Structure and Dynamics of Confined Polymers

NATO Science Series

A Series presenting the results of activities sponsored by the NATO Science Committee. The Series is published by IOS Press and Kluwer Academic Publishers, in conjunction with the NATO Scientific Affairs Division.

A. Life Sciences	IOS Press
B. Physics	Kluwer Academic Publishers
C. Mathematical and Physical Sciences	Kluwer Academic Publishers
D. Behavioural and Social Sciences	Kluwer Academic Publishers
E. Applied Sciences	Kluwer Academic Publishers
F. Computer and Systems Sciences	IOS Press
1. Disarmament Technologies	Kluwer Academic Publishers
2. Environmental Security	Kluwer Academic Publishers
3. High Technology	Kluwer Academic Publishers
4. Science and Technology Policy	IOS Press
5. Computer Networking	IOS Press

NATO-PCO-DATA BASE

The NATO Science Series continues the series of books published formerly in the NATO ASI Series. An electronic index to the NATO ASI Series provides full bibliographical references (with keywords and/or abstracts) to more than 50000 contributions from international scientists published in all sections of the NATO ASI Series.
Access to the NATO-PCO-DATA BASE is possible via CD-ROM "NATO-PCO-DATA BASE" with user-friendly retrieval software in English, French and German (WTV GmbH and DATAWARE Technologies Inc. 1989).

The CD-ROM of the NATO ASI Series can be ordered from: PCO, Overijse, Belgium

Series 3. High Technology – Vol. 87

Structure and Dynamics of Confined Polymers

edited by

John J. Kasianowicz
Biotechnology Division,
National Institute of Standards and Technology,
Gaithersburg, U.S.A.

Miklós S.Z. Kellermayer
Department of Biophysics,
Pécs University Medical School,
Pécs, Hungary

and

David W. Deamer
Biophysics Laboratory,
Department of Chemistry and Biochemistry,
University of California, Santa Cruz, U.S.A.

Springer-Science+Business Media, B.V.

Proceedings of the NATO Advanced Research Workshop on
Biological, Biophysical & Theoretical Aspects of Polymer Structure and Transport
Bikal, Hungary
20–25 June 1999

A C.I.P. Catalogue record for this book is available from the Library of Congress.

ISBN 978-1-4020-0698-2 ISBN 978-94-010-0401-5 (eBook)
DOI 10.1007/978-94-010-0401-5

Printed on acid-free paper

Contents

Preface

Polymers are essential to biology because they can have enough stable degrees of freedom to store the molecular code of heredity and to express the sequences needed to manufacture new molecules. Through these they perform or control virtually every function in life.

Although some biopolymers are created and spend their entire career in the relatively large free space inside cells or organelles, many biopolymers must migrate through a narrow passageway to get to their targeted destination. This suggests the questions: How does confining a polymer affect its behavior and function? What does that tell us about the interactions between the monomers that comprise the polymer and the molecules that confine it? Can we design and build devices that mimic the functions of these nanoscale systems?

The NATO Advanced Research Workshop brought together for four days in Bikal, Hungary over forty experts in experimental and theoretical biophysics, molecular biology, biophysical chemistry, and biochemistry interested in these questions. Their papers collected in this book provide insight on biological processes involving confinement and form a basis for new biotechnological applications using polymers.

In his paper Edmund DiMarzio asks: What is so special about polymers? Why are polymers so prevalent in living things? The chemist says the reason is that a protein made of N amino acids can have any of 20 different kinds at each position along the chain, resulting in 20^N different polymers, and that the complexity of life lies in this variety. This argument is part of the answer, but the chemist is speaking only of the variety contained in a homogeneous, isotropic bag of stuff.

However, polymeric systems can also have many configuration degrees of freedom that undergo phase transitions, and these have profound consequences. There are 5 classes of phase transitions that occur only in polymeric systems. DiMarzio solves the problem of a polymer threading a membrane, shows that it has a phase transition, and uses it to explain why the other 4 classes also have phase transitions. With a suitable change of variables, each phase transition becomes a stable coordinate useful for storing data. A multimeric system has a very large number of these and thus can store huge amounts of data. DiMarzio argues that this provides a basis for biological self-assembly.

The processes of viral infection by phage, DNA transduction in bacteria, RNA translation, protein secretion, and muscle contraction all require biopolymers to migrate through, or function within, pores that are 1 to 10 nm in size. Lucienne Letellier discusses experimental studies on the transport of DNA across membranes by a phage, which tightly confines the molecule of

life in a capsid and delivers it into a target cell through a narrow portal. Sanford Simon, Stephan Nussberger and Walter Neupert, and Kathleen Kinnally extensively review the molecular mechanisms for targeting proteins to specific locations within cells and translocating them across membranes through nanoscale protein pores. The problem's significance is underscored by the fact that each of the $\sim 10^9$ proteins in each cell is replaced on a more or less regular basis. Without an efficient method to transport and target proteins to their proper locations, the cell's hierarchical organization would not exist.

Advances in experimental and theoretical methods have opened new opportunities to understand the physical properties of polymers confined in nanometer length-scale regions. Oleg Krasilnikov shows how the partitioning of linear, nonelectrolyte polymers can be used to deduce the diameter and other structural features of protein ion channels. Sergey Bezrukov and John Kasianowicz demonstrate that this simple method can also reveal information about the interactions between a nanopore and nonelectrolyte polymers that partition into it. Elie Raphaël and his colleagues discuss physical theories on how branched polymers partition into narrow pores. Nanopores might eventually be used to measure the physical properties of these complex polymers.

Bezrukov and Kasianowicz also observed that the mean occupancy time for nonelectrolyte polymers in a nanopore can be much greater than that predicted for a 1-dimensional diffusion process. These studies led to the direct measurement of individual polynucleotides through threading through a single ion channel (Kasianowicz, et. al., David Deamer, et al., Daniel Branton, et al., and Mark Akeson, et al.). Because of the great disparity in pore length scales and polymer persistence lengths, it is interesting to compare the processes of polynucleotide transport in a single nanopore with Björn Akerman's experimental results on the migration of single double-stranded DNA molecules through gels and other microscopic porous media (e.g. track-etched membranes and porous glasses). These molecules can evidently become trapped on features of widely disparate length scales. These features behave like snags and dominate the polymer diffusive motion through gels, whereas the rate of polynucleotide transport through a nanopore might be dominated by the polymer structure.

Murugappan Muthukumar, David Lubensky, and Wokyung Sung, and DiMarzio discuss several different theoretical approaches that describe the transport of polymers through gels and narrow pores. Their theories capture some of the essential features of polymer transport and provide a solid framework that will aid in the design of new experiments with these systems.

Imre Derenyi and Dean Astumian describe analytically the effects of different confinement geometries that create Brownian ratchet potentials. They illustrate models that use the random potentials to separate macromolecules and other models that use them to transport molecules across membranes,

even against a gradient in the chemical potential. Their models agree with experiment in every detail so far.

Many biopolymers, including those in muscle, function in tightly organized domains. Zoya Podlubnaya provides an overview of muscle structure and the mechanisms by which muscle contracts. Miklós Kellermayer shows how single molecule experiments can reveal detailed physical information about structural transitions in muscle proteins. In some cases, the results suggest that the behavior of single molecules accounts in part for some of the bulk tissue's properties. Ultimately, one would like to use single molecule detection methods to probe these polymers in a state of confinement similar to that of their native environment. Zeno Farkas, Derenyi, and Tamas Vicsek explore the dynamics of actin filaments using elegant motility assays.

Alexei Khoklov and his colleagues are using Monte Carlo simulations to show that the properties of AB-copolymer globules depend strongly on whether the primary sequence of the A and B monomers is random, random-block, regular, or designed. A protein-like AB-copolymer is designed such that in the most dense globular conformation, all the hydrophobic B-units are in the core of the globule and the hydrophilic A-units form the envelope of the core. One of their interesting results shows that the A monomers in a protein-like 1-dimensional AB-copolymer are organized into blocks or domains of higher relative concentration with a long-range power-law correlation, which is fractal behavior, the signature of scale invariance.

New approaches are needed to understand the physics of polymers in extreme confinement. Advances here could have a major impact in biology, physics and chemistry and ultimately lead to the development of new methods in biotechnology. Peter Goodwin and colleagues illustrate a method for single molecule nucleic acid analysis by fluorescence flow cytometry. Jingyue Ju discusses the potential use of fluorescence energy transfer reagents for DNA sequencing. Deamer, et al., Branton and Meller, and Kasianowicz, et al. discuss the potential for using single nanopores to rapidly sequence DNA. Kasianowicz, et al. and Akeson et al. demonstrate how polymers and single nanopores might be used to detect and quantitate a wide variety of analytes in solution.

We are extremely grateful to the NATO Science Committee for its generous financial support that made the workshop and this book possible. Also appreciated is the additional financial support provided by Avanti Polar Lipids, the Hungarian Research and Development Committee, Incyte Pharmaceuticals, MATÁV Communications, and the Biotechnology Division at NIST. Finally, we thank the staff at the Puchner Castle for providing a lovely and comfortable meeting venue and Baldwin Robertson for assistance in editing this volume.

Contributing Authors

Björn Åkerman
Department of Physical Chemistry, Chalmers University of Technology, Goteborg, Sweden

Mark A. Akeson
Biophysics Laboratory, Department of Chemistry and Biochemistry, University of California, Santa Cruz, CA 95064

Sergey M. Bezrukov
9/1E122, NICHHD, National Institutes of Health, Bethesda, MD 20892-0924

Daniel Branton
Department of Molecular and Cellular Biology, Harvard University, Cambridge, MA 02138
The Rowland Institute for Science, Cambridge, MA 02142, USA

David W. Deamer
Biophysics Laboratory, Department of Chemistry and Biochemistry, University of California, Santa Cruz, CA 95060

Imre Derényi
Department of Surgery, MC 6035, University of Chicago,
5841 S. Maryland Ave., Chicago, IL 60637
derenyi@rainbow.uchicago.edu

Peter M. Goodwin
M888 Bioscience Division, Los Alamos National Laboratory, Los Alamos, NM 87545
pmg@lanl.gov.

Jingyue Ju
Dept. of Chemical Engineering and the Columbia Genome Center, Columbia University, 1150 St. Nicholas Ave., NY, NY 10032

John J. Kasianowicz
Biotechnology Division, National Institute of Standards and Technology, Gaithersburg, MD 20899-8313
john.kasianowicz@nist.gov

Miklós S.Z. Kellermayer
Department of Biophysics, Pécs University Medical School, Pécs H-7624 HUNGARY

Alexei R. Khokhlov
Physics Department, Moscow State University, 117234 Moscow, Russia

Kathleen W. Kinnally
Division of Basic Sciences, New York University College of Dentistry, 345 East 24th St., New York, NY 10010

O. V. Krasilnikov
Laboratory of Membrane Biophysics, Department of Biophysics and Radiobiology, Federal University of Pernambuco, 50670-901, Recife, PE, Brazil
Laboratory of Molecular Physiology, Institute of Physiology and Biophysics, 700095 Tashkent, Uzbekistan

Lucienne Letellier
Institut de Biochimie et Biophysique Moléculaire et Cellulaire, UMR 8619 CNRS, Université Paris Sud, Bât 430, 91405 Orsay cedex, France.

David K. Lubensky
Department of Physics, Harvard University, Cambridge, MA 02138
lubensky@cmts.harvard.edu

Edmund A. DiMarzio
Department of Chemical Engineering, Bld. 090, University of Maryland, College Park, MD 20742

Murugappan Muthukumar
Dept. of Polymer Science and Engineering, U. Massachusetts at Amherst, Amherst, MA

Stephan Nussberger
Institute of Physiological Chemistry, University of Munich, Goethestraße 33, D-80336 München, Germany

Zoya A. Podlubnaya
Institute of Theoretical and Experimental Biophysics of Russian Academy of Sciences, Pushchino, Moscow Region, 142292, Russia

Elie. Raphaël
Collège de France, Physique de la Matière Condensée, URA 792 du CNRS
11, place Marcelin Berthelot, 75231 Paris cedex 05, France

Sanford M. Simon
Laboratory of Cellular Biophysics, Rockefeller University, 1230 York Ave., Box 304, New York, NY 10021-6399

Wokyung Sung
Department of Physics and Institute of Polymer Research,
Pohang University of Science and Technology, Pohang, 790-784, Korea
sung@galaxy.postech.ac.kr

Tomas Vicsek
Collegium Budapest/Institute for Advanced Studies, Budapest, Szentháromság u. 2, 1114 Hungary

Workshop Participants

Björn Åkerman
Department of Physical Chemistry, Chalmers University of Technology, Goteborg, Sweden

Mark A. Akeson
Biophysics Laboratory, Department of Chemistry and Biochemistry, University of California, Santa Cruz, CA 95064

Gyorgy Bathory
Dept, of Physiology, Semmelweis University of Medicine, H-1088 Budapest, VIII. Puskin u. 9. Budapest 8. P.O.B. 259, H-1044

Tomas Bleha
Polymer Institute, Slovak Academy of Sciences, 84236 Bratislava, Slovakia

Daniel Branton
Department of Molecular and Cellular Biology, Harvard University, Cambridge, MA 02138

David W. Deamer
Biophysics Laboratory, Department of Chemistry and Biochemistry, University of California, Santa Cruz, CA 95060

Imre Derényi
Department of Surgery, MC 6035, University of Chicago, 5841 S. Maryland Ave., Chicago, IL 60637

derenyi@rainbow.uchicago.edu

Peter Galajda
Deptartment of Biophysics, Hungarian Academy of Science, Szeged Biological Center, Szeged, Hungary

Peter M. Goodwin
M888 Bioscience Division, Los Alamos National Laboratory, Los Alamos, NM 87545

Alexander Y. Grosberg
Visiting Scientist, MIT, Dept. of Physics, 13-2009, Cambridge, MA 02139

Parvez Haris
Dept. of Biological Sciences, Dr Montfort University, Hawthorn Building, The Gateway, Leicester, LE1 9BH, United Kingdom

György Hegyi
Eotvos Lorand University, Department of Biochemistry, Budapest, Puskin utca 3, H-1088, Hungary

Jingyue Ju
Dept. of Chemical Engineering and the Columbia Genome Center, Columbia University, 1150 St. Nicholas Ave., NY, NY 10032

John J. Kasianowicz
Biotechnology Division, National Institute of Standards and Technology, Gaithersburg, MD 20899-8313

Miklós S.Z. Kellermayer
Department of Biophysics, P écs University Medical School, P écs H-7624 HUNGARY

Alexei R. Khokhlov
Physics Department, Moscow State University, 117234 Moscow, Russia

Kathleen W. Kinnally
Division of Basic Sciences, New York University College of Dentistry, 345 East 24th St., New York, NY 10010

O. V. Krasilnikov
Laboratory of Membrane Biophysics, Department of Biophysics and Radiobiology, Federal University of Pernambuco, 50670-901, Recife, PE, Brazil; Laboratory of Molecular Physiology, Institute of Physiology and Biophysics, 700095 Tashkent, Uzbekistan

Lucienne Letellier
Institut de Biochimie et Biophysique Moléculaire et Cellulaire, UMR 8619 CNRS, Université Paris Sud, Bât 430, 91405 Orsay cedex, France.

David K. Lubensky
Department of Physics, Harvard University, Cambridge, MA 02138

András Lukács
Dept. Biophysics, Pecs Univ. Med. School, Pécs, Szigeti ut 12. H-7624, Hungary

M. Muthukumar
Dept. of Polymer Science and Engineering, U. Massachusetts at Amherst, Amherst, MA

Stephan Nussberger
Institute of Physiological Chemistry, University of Munich, Goethestraße 33, D-80336 München, Germany

Pal Ormos
Dept. Biophysics, Hungarian Acad. Sci., Szeged Biological Center, Szeged, Hungary, Temporary address: Biophysics Group (P-21), D454, Los Alamos National Laboratory, Los Alamos, NM 87545, USA

V. Adrian Parsegian
NIH, NICHHD, Bethesda, MD 20814

Zoya A. Podlubnaya
Institute of Theoretical and Experimental Biophysics of Russian Academy of Sciences, Pushchino, Moscow Region, 142292, Russia

E. Raphaël
Collège de France, Physique de la Mati ère Condensée, URA 792 du CNRS
11, place Marcelin Berthelot, 75231 Paris cedex 05, France

Sanford M. Simon
Laboratory of Cellular Biophysics, Rockefeller University, 1230 York Ave., Box 304, New York, NY 10021-6399

Béla Somogyi
Dept. Biophysics, Pecs Univ. Med. School, Pécs, Szigeti ut 12. H-7624, Hungary

Wokyung Sung
Department of Physics and Institute of Polymer Research, Pohang University of Science and Technology, Pohang, 790-784, Korea

J.P Tommassen
Dept. Mol. Cell. Biol., University of Utrecht, Padualaan 8, NL-3584 CH Utrecht, The Netherlands

T. Vicsek
Collegium Budapest/Institute for Advanced Studies, Budapest, Szenth áromság u. 2, 1114 Hungary

PROFOUND IMPLICATIONS FOR BIOPHYSICS OF THE POLYMER THREADING A MEMBRANE TRANSITION

Edmund A. DiMarzio
Department of Chemical Engineering, University of Maryland, College Park, MD 20742

Abstract There are 5 phase transitions unique to polymers. They are the:

1) helix to random-coil transition in polypeptides, DNA, and collagen,
2) polymer adsorption transition,
3) collapse transition,
4) equilibrium polymerization transition, and the
5) polymer threading a membrane transition (PTM).

The derivation of the PTM transition contained here allows us to understand why the 5 phase transitions exist. The 5 transitions, plus the 5 phase transitions common to both polymers and non-polymeric material, plus the many couplings of these transitions to each other give in total 1023 a priori possible transitions. Three examples taken from the 45 a priori possible coupled pairs are described in the paper. They are the:

1) polymerization transition coupled to the isotropic to nematic liquid crystal transition,
2) helix to random-coil transition coupled to surface adsorption, and the
3) PTM transition coupled to the helix to random-coil transition.

Three areas of future work are mentioned:

a) study of the equilibrium, kinetic, and pattern formation aspects of the 10 phase transitions and their couplings
b) self-assembly viewed as polymer phase transition phenomena, and
c) a proof that all evolved life-forms must necessarily be polymeric.

Finally two applications of the PTM transition are given: 1) interpretation of viral DNA injection into a cell as a PTM transition, and 2) the "going fishing" model of transport of material across a cell membrane.

Keywords: Self-assembly, biological self-assembly, macromolecular phase transitions, collapse transition, membrane translocation, equilibrium polymerization, helix formation, adsorption of biopolymers.

J.J. Kasianowicz et al. (eds.), Structure and Dynamics of Confined Polymers, 1–21.

1. Introduction

The subject of this NATO workshop is polymer structure and dynamics in confined spaces as they relate to biology. The polymer threading a membrane (PTM) transition involves confined spaces in three separate senses. First, the polymer is restricted to thread the membrane, viewed as a rigid plane partition in which a small hole is made, only at the one place. Second, the monomers on one side of the partition are confined to an infinite half-space so that the number of configurations rather than being z_l which is appropriate to a chain of l_1 segments in free space is instead a smaller number [1,2]. The third space confinement is the self-excluded volume: two monomers cannot occupy the same space simultaneously. If we wished, we could also consider the partition to have a finite thickness and the pore to be a cylinder of a given diameter. However, the simpler model considered here (partition thickness equals zero) is so rich in its consequences that we concentrate on it and leave the problem of a polymer in a cylindrical pore to others.

We will gain insight to the question, so obvious and pervasive that it is often overlooked: what is so special about polymers that they provide the basis of living things? How the various biological polymers, DNA, the several RNA's, the myriad Proteins, and polysaccharides can service life-forms is the subject of modern biology. We will provide an answer in this manuscript to the question of why polymers are so prevalent in living things, going so far as to claim that **all life-forms are necessarily polymeric.**

The chemist says that the reason that polymers are so important to life is that for a protein of degree of polymerization N one can have any of 20 different kinds of amino acids at each position along the chain resulting in 20^N different polymers and that the complexity of life lies in this variety. This argument is part of the answer, but the chemist is speaking of the variety contained in a homogeneous, isotropic bag of stuff. To get the variety of the spatial and temporal structures that one sees in life-forms one has to do some physics. We shall see that what is special about polymers are the 5 classes of phase transitions that occur only in polymers. They are the:

1) polymer threading a membrane transition,
2) helix to random-coil transition,
3) isolated polymer molecule attracted to a surface transition,
4) polymer collapse transition, and the
5) equilibrium polymerization transition.

These 5 transitions, unique only to polymers, along with the 5 other classes of transitions common to all materials (both polymeric and non-polymeric) provide a basis for understanding the self-assembled structures of biology.

In Section 2 we discuss each of the 5 transitions unique to polymers, but with special emphasis on the PTM transition since it gives insight into why

these five transitions exist. We then argue in Section 3 that the transitions individually, and coupled to each other in pairs, triplets, etc. provide the basis for biological self-assembly. Three examples of coupled pairs of transitions are given:

a) polymerization coupled to the isotropic liquid to nematic liquid-crystal transition,
b) helix to random-coil transition coupled to surface adsorption, and
c) PTM transition coupled to the helix to random-coil transition.

The number of a priori possible coupled transitions is shown to be very large. The paradigm of Section 3, to the effect that polymeric phase transitions model biological self-assembly, shows that there is a vast field of unsolved problems awaiting solution. Some of these are discussed in Section 4 titled Future Work. Finally in Section 5 two applications of the PTM transitions to biology are given. They are the transport of viral nuclear material to inside the cell, and the "going fishing" model of membrane translocation.

2. Theory

A unified understanding of the 5 classes of phase transitions unique to polymers is obtained by first deriving the polymer threading a membrane (PTM) transition, which we now do.

2.1 Polymer threading a membrane transition (PTM) [3]

The math needed is of the simplest kind, and all the thermodynamic relations are obtained from $F = -kT\ln(Q)$, where Q is the sum over all states weighted with the Boltzmann exponential $\exp(-E/kT)$.

$$Q = \Sigma \exp(-E_j/kT), \tag{1}$$

$$S = -\partial F/\partial T, \quad P = \partial F/\partial V, \quad \mu_j = \partial F/\partial N_j. \tag{2}$$

Here F is the Helmholtz free energy, S the entropy, and the standard symbols for thermodynamic quantities are used. Now suppose a thin rigid plane partition separates two solutions and suppose that a polymer of l monomers is threaded through a small hole in the partition. The polymer can slide back and forth through the hole so that at any one time l_1 monomers are on side 1 and l_2 monomers are on side 2 ($l_1 + l_2 = l$), but the solutions are not allowed to mix. Then we can write the sum over states Q for the polymer as

$$Q = \Sigma {x_1}^{l_1} {x_2}^{l-l_1}, \quad x_j = z_j \exp(-\varepsilon_j/kT), \tag{3}$$

where z_j is the freedom per monomer in solution j and ε_j is the energy of attraction of the monomer for solution j. This geometric series is easily

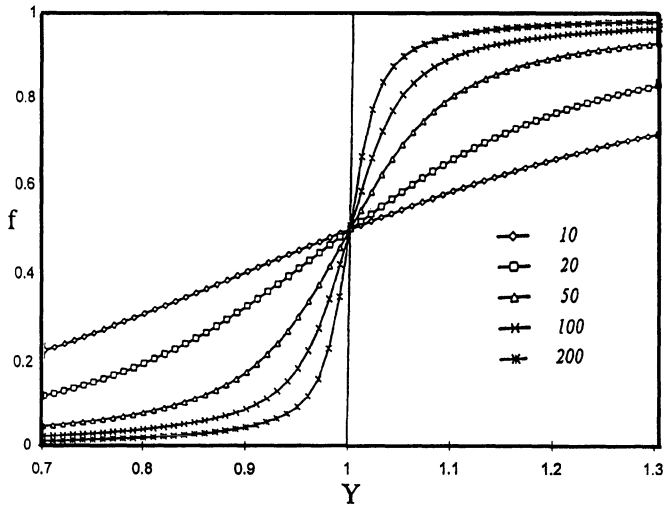

Figure 1. The fraction f of segments residing in region 1 versus the ratio Y of partition functions per monomer, for polymer chains of different length l. A 1st-order transition occurs in the limit of infinite molecular weight.

summed, and we obtain

$$Q = (x_2^{l+1} - x_1^{l+1})/(x_2 - x_1). \tag{4}$$

From this expression all the thermodynamic quantities are easily derived. The number of monomers in region one is

$$< l_1 >= Y/(1-Y) - (l+1)Y^{l+1}/(1-Y^{l+1}). \tag{5}$$

In Figure 1 we plot the fraction f of monomers of type 1 versus $Y = x_1/x_2$ for various values of chain length l. Notice that there is a first-order transition. As $l \to \infty$ there is a discontinuity in f at $Y = 1$.

Now let us compare this result to that of a very similar problem, which however does not display a transition. Consider two containers of monomers of volumes V_1 and V_2 connected by a thin tube of very small volume compared to that of the containers. The energy of a monomer molecule in volume j is given by ε_j. We obtain for the sum over states

$$Q = \Sigma x_1^{l_1} x_2^{l-l_1}/l_1!(l-l_1)!, \qquad x_j = V_j \exp(-\varepsilon_j/kT). \tag{6}$$

The only difference between Equations 6 and 3 are the factorials in the denominator of Equation 6. These factorials arise from the fact that the monomers within each container are indistinguishable from one another. The fraction f

of molecules in region 1 is easily calculated from Equation 6 to be

$$f = V_1 \exp(-\varepsilon_1/kT)/[V_1 \exp(-\varepsilon_1/kT) + V_2 \exp(-\varepsilon_2/kT)]. \quad (7)$$

This equation shows no phase transition. Indeed, we have just solved the problem of a perfect gas partitioned between two containers, and as is known it does not have a phase transition. The important point is that the only difference between the two equations, 3 and 6, is in the factorials in the denominator of Eq. 6. So, the phase transition in the linear polymer occurs because the covalent connectedness of the monomers makes the monomers distinguishable from one another! The indistinguishability of the molecules in the case of gases results in no phase transition. Thus the existence of the transition is intimately related to the Gibbs' paradox [4]. This is a highly significant result because it means that for linear polymers we should expect phase transitions in abundance.

We now wish to examine the other 4 phase transitions that occur in linear polymers. However, before we do this we need to solve the PTM problem more carefully. In Figure 2 we have listed the number of configurations that a polymer of length l_1 sees when it is attached at one end to the plane surface.

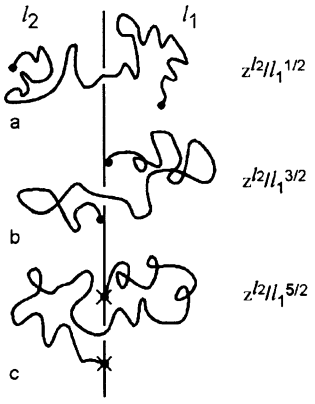

Figure 2. Polymer threading a membrane. A polymer molecule is singly threading through a small hole in an otherwise impermeable partition separating solutions 1 and 2. In 1a the ends are free, in 1b the ends can roam freely on the surface, while in 1c the ends are fixed to the surface. The formulas give the number of configurations of a chain of l_1 monomers attached at one end to the surface and confined in solution 1 as described above. The number of configurations per monomer is z_1, and the attractive energy of the monomer for solution 1 is ε_1. The thermodynamics of this system is easily derived, and a 1st-order transition is obtained (see Figure 3).

The presence of the surface reduces the number of possible configurations in a simple way depending on how the other end is constrained [1,2]. When one end is tied to the surface and the other end is free, the number of configurations is $z^{l_1}/l_1^{1/2}$; if the free end is constrained to roam on the surface then the number of configurations allowed to the chain is reduced to $z^{l_1}/l_1^{3/2}$; finally, with both ends fixed near each other on the surface the number of configurations is reduced even further to $z^{l_1}/l_1^{5/2}$. The sum over states Q is easily evaluated for each of these cases.

$$Q = \Sigma \frac{x_1^{l_1} x_2^{l_2}}{l_1^{\Theta_1} l_2^{\Theta_2}}, \qquad \Theta_1 = \Theta_2 = 1/2, \quad 3/2, \quad 5/2, \tag{8}$$

where $l_1 + l_2 = l$. Figure 3 illustrates the fraction of monomers in side 1 for a molecular weight of 50 for the various Θ. Notice that the larger the Θ the sharper the curve. Therefore the transition is again first-order for each value of Θ.

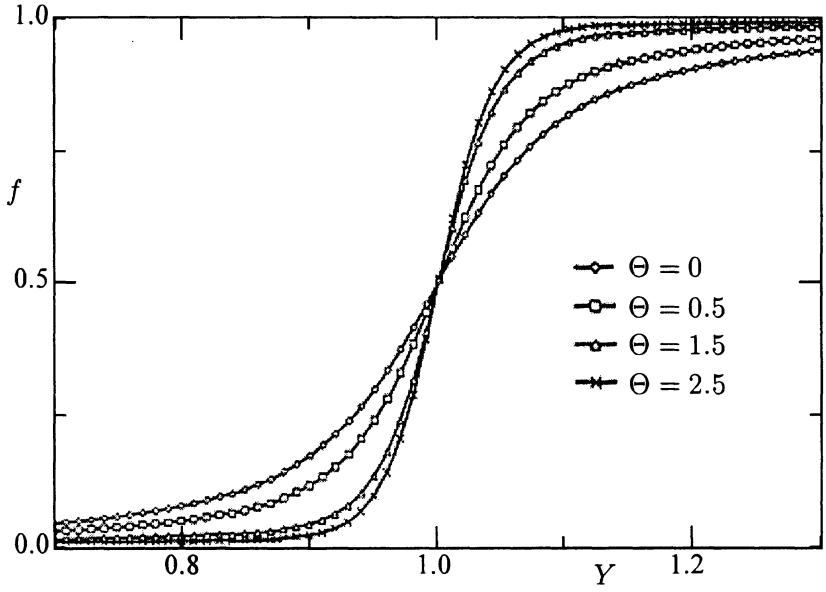

Figure 3. The fraction of segments residing in region 1 versus the ratio Y of partition functions per monomer, for a chain of 50 monomer units suffering various degrees of confinement. The larger the value of $\Theta = \Theta_1 = \Theta_2$ the more the confinement, and the sharper the transition.

The existence of the first-order phase transition is not affected by changes in parameters such as Θ, or by changes in geometry. To high accuracy [5],

the only result of inter-segment excluded volume is to shift the values of Θ and z. Thus even when we include the effects of inter-segment excluded volume as well as segment-surface excluded volume, we have a first-order phase transition. Furthermore geometries other than plane surfaces also result in Equation 8 but with non-integer Θ's. If the allowable volumes were the interiors of cones [6] or wedges [7], and if the polymer were imagined to be threaded at the apex of the cones or wedges, then Equation 8 still holds with the values of Θ_1, Θ_2 appropriate to those geometries [6,7]. Finally, the values of Θ_j need not be equal; the surface of one side can be a plane while the surface on the other side can be a cone.

We now discuss briefly the other four classes of phase transitions.

2.2 The helix to random-coil transition

By considering infinitely long single-, double-, and triple-stranded polymers (Fig. 4), one finds the character of the helix to random coil transition. In a polypeptide, because three hydrogen bonds need to be broken for rotation about a covalent bond to occur, the transition is sharp, but diffuse [8,9]. The matching model for DNA shows a second-order transition in the Ehrenfest sense. Bruno Zimm, who derived the result [10], was initially perplexed because in the series by Landau and Lifshitz a "proof" exists [11] to the effect that a linear system should not show phase transitions. We now know that because it is a linear system it shows a phase transition. Poland and Scheraga showed that what we assume to be the entropy of the individual loops separating the helical strands in partially denatured DNA determines the kind of phase transition observed [12]. Using Az^n/n^C for the number of configurations of a loop of n monomers, they determined that for $C = 0$ there is no transition, for $C = 3/2$ a 2nd-order transition occurs, while for $C > 2$ a 1st-order transition obtains. Since for a single-stranded molecule $C = 0$, polypeptides have no sharp transition. Simple Gaussian statistics show that a loop of n monomers would have $z^n/n^{3/2}$ configurations so that $C = 3/2$, and this results in a 2nd-order transition for the DNA molecule. If C were greater than 2 the transition would be 1st-order. As Applequist showed, the perfect matching model for collagen has a first-order transition [13]. This can be understood by treating the perfect matching model for a k stranded infinitely long molecule. For a k-stranded loop with each strand containing n monomers, the number of configurations is proportional to $z^{kn}/n^{3(k-1)/2}$. To obtain this result write the number of configurations W_3 of a (denatured) k-stranded loop as

$$W_3 = \int [z^n(2\pi nl^2/3)\exp(-3\mathbf{r}^2/2nl^2)]^k d\mathbf{r} \quad \propto \quad z^{kn}/n^{3(k-1)/2}. \qquad (9)$$

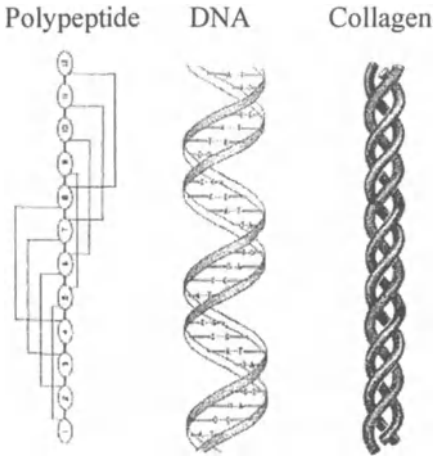

Figure 4. Schematics of the helical portions of a single-stranded polypeptide, double-stranded DNA, and triple-stranded collagen. Rotation about covalent peptide bonds occurs when three consecutive hydrogen bonds are broken. A random coil portion in DNA occurs when the hydrogen bonds between adenine and thymine and/or guanine and cytosine side groups are broken. Also an alternation of helical and random coil portions of collagen occurs when the hydrogen bonds (not shown) between strands of collagen are broken. For the perfect matching model, the transition obtained by changing temperature or chemical potential in collagen is 1st-order, in DNA is 2nd-order, and in polypeptides is diffuse.

The Poland-Scheraga criteria show that for $k \geq 3$ we obtain 1st-order transitions.

2.3 Polymer attached to a surface

An interesting feature of the adsorbed polymer problem in Subsection 2.1 is that it is isomorphic to the DNA problem in the limit of infinite molecular weight [14]. The basic reason for this is that each consists of loops alternating with different segments, which are either trains of the adsorbed polymer or helical regions of the DNA. The trains of adsorbed polymer and the helical regions of DNA each have entropies and energies that are proportional to their lengths. The loops of DNA and the loops of the adsorbed molecule each have $Az^n/n^{3/2}$ configurations (see Section 2.2 and Figure 2.b). So an adsorbed polymer has a 2nd-order transition just as DNA does.

Perhaps the simplest exact treatment of an adsorbed polymer molecule is the original treatment [15]. One imagines a one-dimensional random walk to

begin at the origin and to be confined to the positive x axis by a barrier. This problem is readily solved. The relevant mathematics is contained completely in Chapter 3 of Feller's book on probability theory [16]. The crucial step [17] is the use of the reflection principle which allows us to express the number of configurations in the presence of a barrier in terms of the numbers in the absence of a barrier. Suppose the two ends of a random walk are located at points A and B on the same side of the barrier which is located at the origin. The number of walks from A to B that do not touch or cross the origin is equal to the total number of walks from A to B in the absence of the barrier minus the total number of walks that touch or cross the origin. This latter number is by the reflection principle [16] equal to the number of walks from A' (the reflection of point A through the origin) in the absence of a barrier. Thus the problem of a walk in the presence of a barrier is related to the number of walks in the absence of a barrier. By weighting each time the walk touches the surface with an energy ε, one can easily obtain the partition function for this one dimensional problem and evaluate the thermodynamics [15]. But it is clear that we have also solved the adsorption problem for the body centered cubic lattice as well. The only difference is that in the one-dimensional problem there is one way to step away or to step towards the origin while in the d dimensional bcc lattice there are 2^{d-1} ways to step away or to step towards the surface. Rubin [18], using recurrence relation techniques, has solved the problem of a polymer molecule near a surface for a variety of lattices. In all cases there is a second-order transition. Figure 5 shows the adsorption curves for various lattices. The transition point is given by [18] $\varepsilon/kT = \ln(2/(2-a))$, where ε is the contact energy of a monomer for the surface and $1-a$ is the fraction of steps running parallel to the surface.

Some of the results are not intuitive and quite surprising. This lack of intuition derives from the lack of intuition that most people have for the conclusions of probability theory itself, as Feller nicely explains [16]. This being the case we can expect to be surprised!

If one end is tied to the surface, the other end free, then when there is no monomer surface attraction the normal polymer scientist would expect the number of contacts with the surface to be proportional to the square root of molecular weight. In reality for an infinite chain the expected number of monomer contacts with the surface is only 1 as Figure 6 shows! At the transition temperature the expected number of contacts is indeed proportional to the square root of molecular weight but the fraction of contacts is zero as figure 5 clearly shows; in the adsorption region the expected number of contacts is proportional to molecular weight. Another result [15], not shown here, is that in the adsorption region the monomer density decreases exponentially as we go from the surface and the adsorption profile is independent of molecular weight for modestly large molecular weight, while in the desorption region

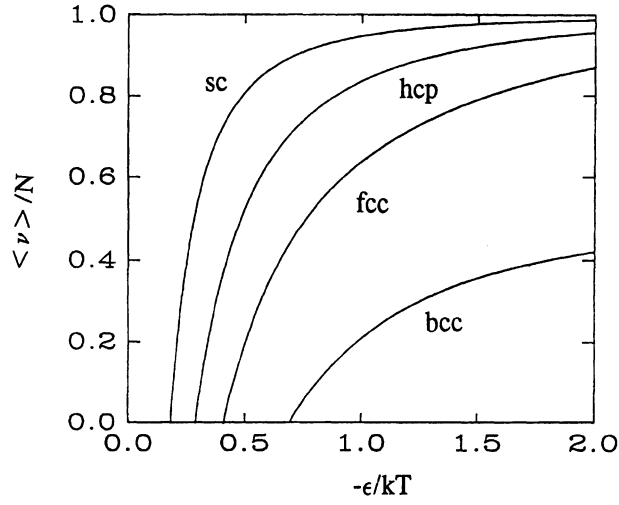

Figure 5. Polymers confined to a lattice and lying on one side of a surface, with one end fixed to the surface, undergo a 2nd-order transition as the strength of the attraction of the monomers for the surface is increased. A monomer has an energy zero unless it is on the surface, in which case the energy is ϵ. The lattice types label the curves. sc = simple cubic; hcp = hexagonal close-packed; fcc = face-centered cubic; bcc = body-centered cubic.

the monomer density increases as we go out from the surface, reaching a maximum at a distance which is equal to the square root of two times the molecular weight. Thus the presence of the surface swells the polymer. The transition point occurs when the density gradient at the surface is zero perpendicular to the surface and is therefore given by the reflecting boundary condition.

L. I. Klushin, A. M. Skvortsov and A. A. Gorbunov have treated the adsorbed polymer exactly in the Gaussian limit including a consideration of the behavior of the polymer under a force applied to one end [19,20]. Significantly, they have shown that Landau theory fails [20]. This is an example of an exact treatment showing that seemingly reasonable assumptions about complex systems are often wrong.

2.4 The collapse transition

Flory [21] was the first to quantify the competition between the attractive interaction among monomers wanting to collapse the polymer onto itself and the entropy of the polymer chain wanting to expand the polymer. His treatment gave the proper (accurate but not exact) 6/5ths law regarding the end-to-end dimension, $\langle R^2 \rangle = An^{1.2}$, in the expanded region but his method did not establish the character or existence of the transition. Perhaps the simplest

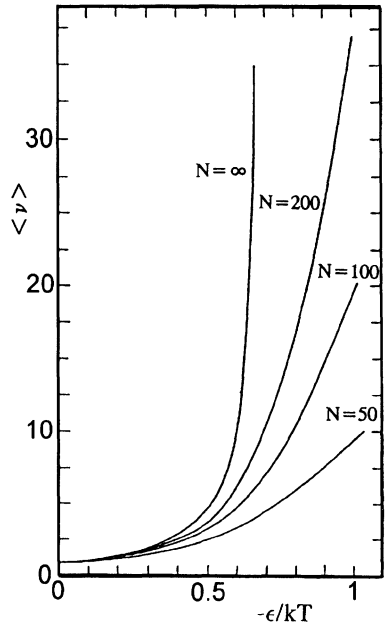

Figure 6. Number of contacts with the surface versus monomer energy of contact with the surface for various molecular weights. Although the fraction of contacts in the desorbed region is zero (for infinite molecular weight) the actual number of contacts is finite as this figure shows. For 1-dimension the number of contacts varies from 1 when the adsorption energy is zero to $(\mathrm{MW})^{1/2}$ when the adsorption energy has the value appropriate to the transition point ($-\varepsilon/kT = \ln 2$, which is the reflection boundary condition).

approach that both displays the transition and retains the flavor of the original Flory ideas is to deal directly with the more fundamental probabilities [22] rather than the thermodynamic properties derived from them as Flory did. We now give an abbreviated version of this approach.

The probability of a polymer chain having an end to end length R is given by the product of three factors

$$W = \left[R^2 \exp(-b^2 R^2)\right] \left[\prod_{j=0}^{n-1} \left(1 - j\frac{l^3}{R^3}\right)\right] \times \left[\exp\left(-n\chi\left(1 - n\frac{l^3}{R^3}\right)\right)\right], \tag{10}$$

where the first factor is the Gaussian distribution function for the end-to-end length, the second factor corrects for excluded volume, and the third factor gives the energy. The notation is standard: $b^2 = 3/2nl^2$, l^3 is the volume of a

bead monomer, n the number of monomer units, and χ is the χ parameter. The first and third factors are clearly correct and do not need discussion although they are approximations that can be improved. To understand the second factor imagine that the polymer is being built up one monomer at a time. The kth monomer can be placed if there is no interference from monomers placed previously on the chain. To evaluate the probability of successful placement of the jth monomer imagine that the previous (j-1) segments are distributed at random in the volume of the sphere. This gives the factor $(1 - jl^3/R^3)$, and the product of these factors constitutes the second factor of equation 10.

From equation 10 we can find the expectation value of R through the relation $\langle R^2 \rangle = \int R^2 W dR / \int W dR$, but this can not be done analytically. Instead we find the value of R which maximizes W by differentiating equation 10 to obtain [22]

$$\begin{aligned} a^5 - a^3 &= -n^{1/2}\left[na^6\left(\ln\left(1 - n^{-1/2}a^{-3}\right) + n^{-1/2}a^{-3}\right) + \chi\right], \quad (11) \\ a &= R/(nl^2)^{1/2}, \end{aligned}$$

which reduces to the Flory result for large R,

$$a^5 - a^3 = n^{1/2}[1/2 - \chi]. \quad (12)$$

Thus, the $R^2 = An^{1.2}$ law is obtained. Additionally, equation 11 can be solved through the transition to obtain the law $R^2 = Bn^{2/3}$ in the collapsed region. This does not mean however that the collapsed phase has unit monomer density; it is in fact less than unity. Figure 7 shows that the transition is 2nd-order. An interesting result occurs when the solvent is polymeric. Then, depending on the relative molecular weights and energetics, the transition can be 1st-order as well as 2nd-order [23]. A recent review of collapse in polymers is [24].

2.5 Equilibrium polymerization transition

This is a classic problem that has been solved in various approximations by Tobolsky and Eisenberg [25] and more recently and more correctly by Wheeler and associates [26]. It seems to be a second-order transition when we allow the molecules to compete with each other for space.

A model for an isolated polymer undergoing equilibrium polymerization, but not in competition with other polymer molecules for space, is as follows. Imagine placing children's blocks one upon another in piles one block wide. The individual blocks represent monomer units and placing them atop another represents polymer chain growth. If the rate of adding to a pile is α and the rate of taking off of the pile is β, then the growth rate G is

$$G = \alpha - \beta \quad (13)$$

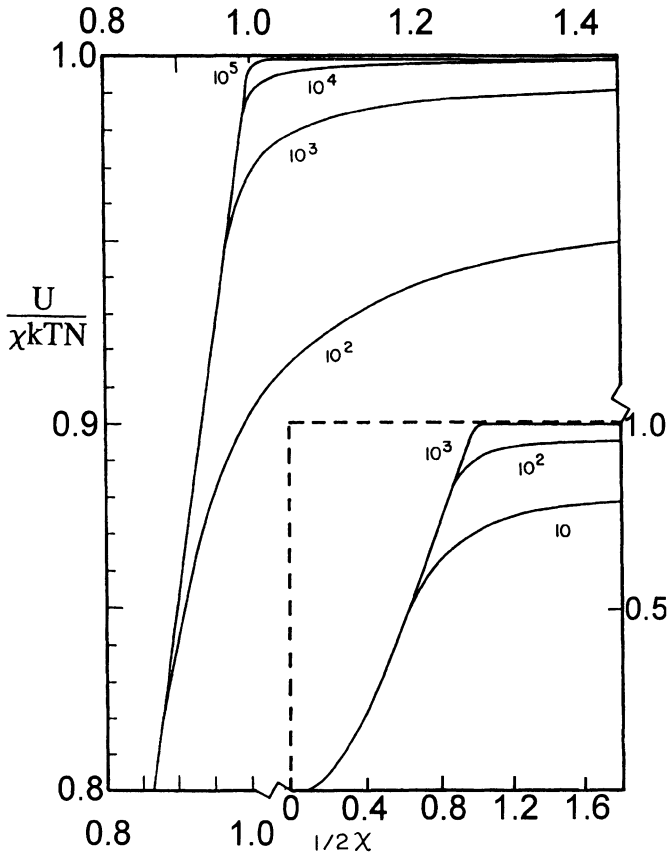

Figure 7. The normalized energy per monomer unit of a collapsing polymer versus normalized temperature for various molecular weights (numbers of monomer units). The transition displayed here is 2nd-order but if the polymer were collapsing in a field of other polymers, rather than in low molecular weight solvent as displayed here, the transition could be 1st-order.

If $\alpha > \beta$ then the pile grows to infinity, while if $\beta > \alpha$ the pile ungrows. From the principle of detailed balance we know that

$$N_\nu \alpha = N_{\nu+1}\beta, \quad or \quad \alpha/\beta = N_{\nu+1}/N_\nu, \tag{14}$$

where N_ν is the number of piles of height ν. But the ratio $N_{\nu+1}/N_\nu$ is known from simple statistical mechanics to be

$$N_{\nu+1}/N_\nu = \exp\left(-(\mu - \varepsilon)/kT\right), \tag{15}$$

where μ is the chemical potential and ε is the energy of attraction of the monomers for each other. From the above equations we see that the ratio α/β goes from being less than 1 to being greater than 1. Thus within an

infinitesimal ΔT the chain goes from being finite in length to being infinite in length. Therefore the chains undergo a first-order phase transition. This result could have also been derived from the grand canonical ensemble.

In summary, we have displayed the 5 classes of phase transitions that occur in linear polymers. They show 1st or 2nd-order transitions in the Ehrenfest sense. The models we have described have been treated exactly; were it not for self-excluded volume these would be exact solutions of real systems; self-excluded volume, however can be treated with good accuracy. In biology the important transition control variables are not usually pressure P or temperature T, but more usually chemical potential μ_j. The force on the end of the polymer chain may also be important in some circumstances.

We reiterate that the reason these transitions occur is because the monomers are distinguishable from one another by virtue of them being connected covalently along the chain. This is a profound result intimately related to the Gibbs' paradox.

3. Coupling of the phase transitions to each other [27]

Phase transitions in polymers

The 10 classes of phase transitions in polymers comprise 5 that occur within an isolated polymer and 5 within collections of polymer molecules.

Phase transitions of an isolated polymer

1) Helix-random coil transition
   a) Single-stranded polypeptides; diffuse order
   b) Double-stranded DNA; 2nd-order
   c) triple-stranded collagen; 1st-order
2) Polymer threading a membrane; 1st order
3) Adsorption onto a surface; 2nd-order
4) Polymerization / 1-d crystallization; 1st-order
5) Collapse transition; 2nd- or 1st-order, depends on solvent

Phase transitions in collections of molecules

6) Liquid-liquid / polymer blends; 1st-order
7) Crystallization; 1st-order: 32 point groups, 230 space groups
8) Liquid Crystals / plastic crystals; 1st-, 2nd-order: nematic, smectic, cholesteric, lyotropic

9) Glass transition / sol-gel transition; 2nd-, 1st-order

10) Block copolymers / membranes / soaps / micelles / vesicles; 1st-, 2nd-order

The first 5 phase transitions are unique to individual polymers, and the second 5 phase transitions are common to both polymers and non-polymeric materials. At first it may seem that we have merely doubled the number of phase transitions allowed to biological polymers. But the number of different classes of phase transition is not just 10. It is actually much greater because of couplings of the phase transitions to each other and because of the manifold ways they can express themselves in space and time.

There are ${}_2C_{10} = 45$ ways that 2 different phase transitions can be selected from the 10. Thus there are 45 classes of pairwise couplings of polymeric phase transitions. Most of them are unexplored. Several that have been investigated are listed below. Additionally, there are ${}_3C_{10} = 120$ triplets of coupled transitions, and so on. Obviously much work is required before polymer phase transitions can be understood in their full generality.

3.1 Polymerization coupled to the isotropic to nematic phase transition

In sickle cell anaemia, a genetic defect causes the hemoglobin molecules which exist within red blood cells at a volume fraction of about 0.4 to aggregate and form long straight hollow microtubules under low oxygen pressure. But these microtubules cannot pack at random when the asymmetry ratio of length to width r reaches a critical value given approximately by the Flory formula [28]

$$rV_{\mathrm{r}} = 8, \tag{16}$$

where V_{r} is the volume fraction of rods. They then form a nematic phase within each red blood cell. This results in a distortion of the red blood cells into their sickle shapes, which in turn impede blood flow within the fine capillaries of the circulatory system. Minton [29] and Herzfeld [30] have discussed this problem at some length.

3.2 Helix-random coil coupled to surface adsorption

Bringing a DNA molecule near a surface couples the two phase transitions, that of a polymer at a surface and that of DNA. Since they both display 2nd-order transitions one expects that the coupled transition becomes 1st-order. Not surprisingly this is indeed the case [2]. More surprisingly, when a single-stranded polypeptide is adsorbed, the cooperativity within the alpha helix is enough to cause the 2nd-order surface adsorption transition to become 1st-order even though the single-stranded transition is only diffuse. See the recent

exact solution of this problem in the Gaussian limit by Carri and Muthukumar [31].

One wonders how this problem relates to that of inducing or impeding enzymatic activity of proteins near surfaces.

3.3 The PTM transition coupled to the helix-random coil transition [27]

This problem can be solved formally by replacing x_1 and x_2 of Eq. A by $q_1(l_1)$ and $q_2(l_2)$, where the q's are the per monomer partition functions for protein or DNA strands in solutions 1 and 2. For large l, the l dependence disappears and for sharp helix-random coil transitions we have the following scheme, where H1 means helix in region 1, $\mathcal{R}_2$ means random coil in region 2 etc. The horizontal arrow means transition (either translocation or helix to random coil) and we are cooling the system. We assume that the helix is always the low temperature phase in both solutions. The case of inverted transitions is easily handled. We obtain

R1→H1; R1→H2:
R2→H2; R2→H1

R1→R2→H1; R1→R2→H2; R1→H1→H2:
R2→R1→H2; R2→R1→H1; R2→H1→H1

R1→R2→H1→H2; R1→R2→H2→H1; R1→H1→R2→H2
R2→R1→H2→H1; R2→R1→H1→H2; R2→H2→R1→H1

The transition behavior is extremely complicated. For example

R1→R2→H1→H2

means that the polypeptide is a random coil in region 1 and on lowering the temperature it translocates to region 2 where it remains a random coil. On further cooling it moves back into region 1 becoming a helix in the process. On cooling further it translocates again to region 2 and remains there as a helix. Of course the usual method of causing a bio-transition is not by changing temperature. It is by means of chemical potential, pH, pK, and ionic strength changes.

Think of the complexity if we couple surface adsorption to PTM to the helix to random coil transitions. Wow!

We now begin to appreciate the complexity of structure embodied in the ten polymer phase transitions and their coupling into pairs, triples etc. Let us

count the number of a priori possible transitions among the 5 isolated polymer transitions There are 5 individual transitions, plus 5x4/2 =10 pairs, plus 5x4x3/2x3=10 triplets, plus 5x4x3x2/2x3x4=5 quadruplets, plus 1 one coupling involving all 5 transitions. This equals 31 total. When it is recognized that the terms listed above are binomial coefficients we see that the answer can be written as $2^5 - 1 = 31$. Similarly, the total number of couplings for the ten phase transitions is $2^{10} - 1 = 1023$. There are 1013 a priori possible couplings plus the 10 individual transitions. Thus discovering the 5 pure polymer transitions did much more than merely double the total number available to a polymer system. Rather the complexity has been increased by a factor of 1023/31=33.

If we count the different kinds of liquid crystals, block copolymers, liquid-liquid phases, etc. then there are many thousands more. It is obvious to this observer that the vast numbers of structures and kinetic pathways implicit in these transitions are responsible for adaptive complexity (evolution) at the molecular level in life-forms.

4. Future work

Although it usually ineffectual to attempt to predict the directions of future work, the paradigm that we have developed to the effect that polymeric phase transitions are central to understanding biological self-assembly allows us to state what work is necessary to implement this paradigm

4.1 The Ten Phase Transitions

We need to study the equilibrium, kinetic and pattern formation aspects of each the ten phase transitions and their manifold couplings into pairs, triplets etc. The present situation is that we have a fair understanding of the equilibrium aspects of the ten isolated transitions but very little work on the various couplings has been attempted. All non-equilibrium aspects of the transitions are poorly understood as are also pattern formation aspects. It is probable that much of our understanding will come from computer modeling. On the other hand, exact treatments whenever found provide benchmarks that are needed to guide our thinking about these most difficult problems. Obviously much future work is needed.

4.2 Biological self-assembly is an orchestration of polymer phase transitions in space and time [27]

To prove this assertion we need to make a catalogue of self-assembling structures and then show to what extent phase transitions are at the heart of the self-assembly process. One way to test for self-assembly is to a) excise

the structure from its biological environment, b) dissolve it in solution, c) reconstitute it, d) reintroduce it into the environment. If it retains its biological function it is a self-assembled entity. Tobacco mosaic virus and some membranes are self-assembled structures in this sense. However, sometimes formation of a self-assembled entity involves the creation of chemical bonds and is not a reversible process. In this case phase transitions are only part of the story. The role of chaperon molecules needs also to be examined. Obviously their role cannot be understood without first understanding the kinetics of the self-assembly process.

A catalog of the diseases of self-assembly might provide insights to their treatment.

An attempt to provide the categories for the classification of the catalog has been made [27]. Much future work is needed.

4.3 All evolved life-forms, no matter where they occur throughout the universe must necessarily be polymeric [27]

Plan for proof: Life requires the most complex of materials to provide the structures and to perform the necessary functions. But the most complex of materials are polymer materials. Therefore life requires polymer materials. It is my belief that the chemical complexity of 20^N different kinds of proteins combined with the physical complexity of many thousands of "orchestrations" of the polymer phase transitions are what makes the evolution of life possible. Presumably, over eons of time, there has been a sampling of various combinations of different polymers and of different orchestrations of polymer phase transitions and viable ones have been found.

A corollary of these ideas is that evolution cannot be understood without first understanding polymeric self-assembly.

5. Two possible applications of the PTM transition [3]

5.1 Behavior of a virus

After the virus compromises the cell wall, the end of the DNA molecule samples the interior of the cell and if it is free-energy favorable it just gets sucked into the cell. The PTM transition shows that this process is 1st-order. Virtually all of the DNA is sucked into the cell. After the DNA makes many copies of itself and the viral proteins, the viruses need to be assembled. The shells first form and then the job of getting the DNA into the virus cores is dealt with. This process usually requires chaperon or helper molecules. It would be interesting to see if there are primitive viruses for which the process

is the reverse of the infection mode. It is implied that such viruses could never infect a dead cell.

5.2 Going fishing

Let region $\mathcal{R}_1$ be the favored region so that most of the polymer resides in $\mathcal{R}_1$, which is outside of the cell. The region $\mathcal{R}_2$ is the inside of the cell. Small molecules (food, medicines, poisons) bind to the molecule effectively changing the values of z_1 and ε_1. With these values of z_1 and ε_1 the inside of the cell $\mathcal{R}_2$ is favored. So the polymer translocates to the interior of the cell $\mathcal{R}_2$. But in $\mathcal{R}_2$ the food or medicine or poison molecules peel off of the polymer and dissolve in the protoplasm. This process can be entropic or energy driven. The polymer, now freed of its hitchhiking molecules translocates to $\mathcal{R}_1$ and begins the process all over again.

Acknowledgments

I am grateful to M. Muthukumar for delivering this talk at the NATO meeting during my indisposition. Sections 2.1 and 5 are more fully developed in [3]. Similarly, sections 3, 3.3, 4.2, 4.3, and 4.3 were described in detail by [27].

References

[1] Di Marzio, E.A. (1967) Some contributions to crystal growth kinetics with applications to ciliation and fractionation in polymers, *J. Chem. Phys.* **47**, 3451-3469.

[2] Di Marzio, E.A. and Bishop, M. (1974) The nature of the helix-random coil transition of biological macromolecules attached to a surface, *Biopolymers* **13**, 234-2348.

[3] Di Marzio, E.A. and Mandell, A. (1997) Phase transition behavior of a linear macromolecule threading a membrane *J. Chem. Phys.* **107**, 5510-5514.

[4] The Gibbs paradox observes that if two particles are distinguishable then an interchange of their positions results in a different state and the sum over states Q must count each state. However if the two particles are indistinguishable then their interchange does not result in a new state and in the sum Q, we count it only once. This can be rationalized as follows. Particles are not points but are extended objects. A field corresponding to n electrons, say, has n intensity concentrations of the field in space and these concentrations can be labeled in n! ways, but there is only one field.

[5] Douglas, J.F., Nemirovsky, A.M. and Freed, K.F. (1986) Polymer polymer and polymer surface excluded volume effects in flexible polymers attached to an interface - comparison of renormalization-group calculations with Monte-Carlo and direct enumeration data, *Macromolecules* **19**, 2041-2054.

[6] Guttman, C.M. Di Marzio, E.A. and Hoffman, J.D. (1980) The polymer in a cone-A model for the surface free energy of a polymer crystal with emergent cilia, *J. Res. NBS* **85**, 273-282.

[7] Lauritzen, J.I. and Di Marzio, E.A. (1978) The configurational statistics of a polymer confined to a wedge of interior angle alpha, *J. Res. NBS* **83**, 381-385.

[8] Gibbs, J.H. and Di Marzio, E.A. (1959) Statistical mechanics of helix-coil transitions in biological macromolecules, *J. Chem. Phys.* **30**, 271-282.

[9] Zimm, B.H. and Bragg, (1959) Theory of the phase transition between helix and random coil in polypeptide chains, *J. Chem. Phys.* **31**, 526-535.

[10] Zimm, B.H. (1960) Theory of "melting" of the helical form in double chains of the DNA type, *J. Chem. Phys.* **33**, 1349-1356.

[11] Landau, L.D. and Lifshitz, E.M. (1958) *Statistical Physics*, Pergamon Press, London, 1958, Section 149.

[12] Poland, D.C. and Scheraga, H.A. (1966) Occurrence of a phase transition in nucleic acid models, *J. Chem. Phys.* **45**, 1464-1469; Poland, D.C. and Scheraga, H.A. (1970) *Theory of the Helix-Coil Transition*, Academic Press, NY.

[13] Applequist, J. (1969) First-order phase transition in multistranded macromolecules, *J. Chem. Phys.* **50**, 609-612.

[14] Hoeve, C.A., Di Marzio, E.A. and Peyser, P. (1965) Adsorption of polymer molecules at low surface coverage *J. Chem. Phys.* **42**, 2558-2563.

[15] Di Marzio, E. A. and McCrackin, F.L. (1965) One-dimensional model of polymer adsorption, *J. Chem. Phys.* **43**, 539-547.

[16] Feller, W. (1948) *An Introduction to Probability Theory and its Applications* 3rd ed., John Wiley and Sons, NY

[17] Di Marzio, E.A. (1965) Proper accounting of a polymer near a surface, *J. Chem. Phys.* **42**, 2101-2106.

[18] Rubin, R.J. (1965) Random-walk model of chain-polymer adsorption at a surface, *J. Chem. Phys.* **43**, 2392-2407; (1969); Comment on conformation of an adsorbed polymer chain II, **51**, 4681.

[19] Skvortsov, A.M., Gorbunov, A.A. and Llushin, L.I. (1994) Adsorption-stretching analogy for a polymer chain on a plane: Symmetry property of the phase diagram, *J. Chem. Phys.* **100**, 2325-2334.

[20] Klushin, L.I., Skvortsov, A.M. and Gorbunov, A.A. (1997) Adsorption of a macromolecule in an external field: An exactly solvable model with biocritical behavior, *Phys. Rev. E* **56**, 1511-1521.

[21] Flory, P.J. (1949) The configuration of real polymer chains, *J. Chem. Phys.* **17**, 303-310.

[22] Di Marzio, E.A. (1984) A simple explanation of the polymer collapse transition, *Macromolecules* **17**, 969-971.

[23] Di Marzio, E.A. and Briber, R. (1995) Collapse of a polymer in a polymeric solvent. *Macromolecules* **28**, 4020-4022.

[24] Grosberg, Yu A. and Kuznetsov, D.V. (1992) Quantitative theory of the globule-to-coil transition, Parts 1-4 *Macromolecules* **25**, 1970-2003.

[25] Tobolski, A.V. and A. Eisenberg, A. (1959) Equilibrium polymerization of epsilon-caprolactam, *J. Am. Chem. Soc.* **81**, 2302-2305; (1960) **82**, 289; (1962) Transition phenomena in equilibrium polymerization, *J. Coll. Sci.* **17**, 49-65.

[26] Wheeler, J.C. Kennedy, S.J. and Pfeuty, P. (1980) Equilibrium polymerization as a critical phenomenon, *Phys. Rev. Lett.* **45**, 1748-1752; Wheeler, J.C. and Pfeuty, P. (1981) The n approaches zero vector model and equilibrium polymerization, *Phys. Rev.* **A24**, 1050-1062.

[27] Di Marzio, E.A. (1999) The ten classes of polymeric phase transitions: Their use as models for self-assembly, *Prog. Polym. Sci.* **24**, 329-377.

[28] Flory, P.J. (1985) in *Recent Advances in Liquid Crystalline Polymers*, ed. Chapoy, L.L. Elsevier Applied Science Publishers, NY, p. 99.

[29] Minton, A.P. (1974) A thermodynamic model for gelation of sickle-cell hemoglobin, *J. Mol. Bio.* **82**, 483; (1975) Thermodynamic analysis of the chemical inhibition of sickle-cell hemoglobin gelation, **95**, 289-307; (1976) Relation between oxygen saturation and aggregation of sickle-cell hemoglobin, **100**, 519-542.

[30] Herzfeld, J. (1996) Entropic driven order in crowded solutions: From liquid crystals to cell biology *Accounts Chem. Res.* **29**, 31-37.

[31] Carri, G.A. and Muthukumar, M. (1999) Coupling between adsorption and the helix-coil transition *Phys. Rev. Lett.* **82**, 5405-5408.

PHAGE DNA TRANSPORT ACROSS MEMBRANES

Lucienne Letellier
Institut de Biochimie et Biophysique Moléculaire et Cellulaire, UMR 8619 CNRS, Université Paris Sud, Bât 430, 91405 Orsay cedex, France.

Abstract Phage nucleic acid transport is atypical among membrane transport and thus poses a fascinating problem: transport is unidirectional, and it concerns a unique molecule the size of which may represent 50 times that of the bacterium. The rate of DNA transport can reach values as high as 3,000 to 4,000 base pairs s^{-1}. This raises many questions which will be addressed in this review. Is there a single mechanism of transport for all types of phage? How does the phage genome overcome the hydrophobic barrier of the host envelope? Is DNA transported as a free molecule or in association with proteins? Is such transport dependent on phage and/or host cell components? What is the driving force for transport? Data will be presented on tailed phage which are the most common type of phage, occurring in over 100 genera of bacteria and for which DNA transport has been the most extensively studied. We will show that it is possible to analyse these mechanisms both in vivo and in vitro by using biochemical as well as biophysical approaches.

Keywords: bacteriophage, cryo-electron microscopy, DNA condensation, DNA delivery, DNA packaging, DNA transport, Escherichia coli, FhuA, liposomes, outer membrane receptors, phage DNA, polyamines, proton electrochemical gradient.

1. Introduction

The transport of nucleic acids across cell membranes is an essential natural process that occurs in all living organisms. In bacteria, nucleic acid transport takes place at the early stages of many processes: conjugation, genetic transformation, T-DNA transfer from bacteria to plant cells, and bacteriophage infection. During the last few years many genes involved in DNA transport have been identified and sequenced, and their gene products have been characterized. These studies have demonstrated striking functional and structural similarities in the processes of conjugation and T-DNA transfer and transformation (reviewed in [1]). In contrast, we still have a poor understanding of phage nucleic-acid transport mechanisms. This is particularly

J.J. Kasianowicz et al. (eds.), Structure and Dynamics of Confined Polymers, 23–36.

surprising having in mind that many concepts, as well as methods of modern genetics have originated from experiments with phage. The question of how a large, hydrophilic, polyanionic molecule crosses membranes had drawn, in the 80's, the attention of some bioenergeticists who thought that Peter Mitchell's chemiosmotic theory [2] would apply to DNA transport and that there would be a "universal" mechanism of DNA transport. The discouraging results obtained (see below) in conjunction with a disinterest of scientific foundations for projects on phage nucleic acid transport took almost all of these scientists away from such studies. The state of the art in phage DNA transport is reflected in the small number of pages (10 of 500) devoted to DNA transport in the 1994 monograph on bacteriophage T4 by Goldberg et al [3].

Phage nucleic-acid transport is atypical membrane transport and thus poses a fascinating problem: transport is unidirectional and concerns a unique molecule the length of which may be 50 times that of the bacterium (50 μm for the double-stranded DNA of T4 phage). The rate of DNA transport, although varying from one phage to another, can reach values as high as 3000 to 4000 base pairs/sec, a value significantly greater than that attained by DNA during conjugation and natural transformation (100 bases/sec). This raises many questions. Knowing that phage genomes display a great diversity ranging from small single-stranded RNA (a few hundred bases) to large double-stranded DNA (170 000 bp) [4], is there a single mechanism of transport for all types of phage? How does the phage genome overcome the hydrophobic barrier of the host envelope? Is DNA transported as a free molecule or in association with proteins? Is the transport dependent on phage and/or host cell components? What is the driving force for transport? Some of these questions have been the subject of recent reviews [3,5–7]. Therefore, they will be only briefly surveyed here. This review will essentially focus on tailed phage, which are by far the most common type of phage, occurring in over 100 genera of bacteria, and for which DNA transport has been the most extensively studied. It is our belief that some of the conclusions on these *in vivo* and *in vitro* DNA transport studies might not be restricted to Escherichia coli phage but may have broader significance. Indeed, Archaea are also the target of phage. Interestingly, some of these phage are of the same head and tail types as T phage and lambdoid phage. This is exemplified in the case of the haloarcheophage ϕH, which resembles E. coli phage P1 in terms of structure and replication of its DNA and lysogeny [8]. These observations strongly suggest that the common ancestor of bacteria and archaebacteria contained viruses. Studies on evolutionary relationships among phage virus might therefore be rich in information [9].

2. Tailed phage DNA: a long, linear and charged polymer confined in a small protein capsid

2.1 Morphology of tailed phage

Tailed phage are formed of an isometric proteinaceous head (capsid), the size of which varies generally between 50 and 100 nm and which contains the viral genome. Almost all tailed phage contain a linear duplex DNA. The capsid is connected to the tail by a complex protein machinery. The tail ends with a tail tip and fibres which ensure the binding of the phage to the host envelope. Tail length varies greatly between phage types and can be up to 200 nm.

2.2 Mechanism of packaging of DNA into phage capsids

Phage T4 has one of the largest genomes (172 kbp). When released in aqueous solution, the DNA has a radius of gyration of about 1000 nm, and a worm-like coil volume of 4×10^9 nm^3. When confined into a 50 nm capsid, the DNA and density occupies a volume of 5×10^5 nm^3 [10]. Packing of the DNA therefore represents an increase of its density by a factor of 10^4, leading to an internal DNA concentration of about 450 mg/ml.

The mechanism of packaging into phage heads during morphogenesis has been the subject of extensive studies, and many models have been proposed (reviewed in [11–14]). Briefly, packaging of the non-condensed DNA takes place into precursor capsids (procapsids). The DNA passes through a portal (connector) protein located at the vertex of the procapsid in a region where the tail will then be connected to the head. Transport of DNA is an ATP-driven process. It is accompanied by important structural changes of the capsid which adopts its final maturated morphology [15]. In the case of phage T3, it was shown that DNA transport proceeds at a rate of 140 bp/sec by the action of terminases and at the expense of 1 ATP hydrolysed per 1.8 bp packaged [16]. Once encapsulated, the DNA is cut by terminases. This cutting is either sequence specific or determined by the mass of the DNA inside the capsid [17]. Morphogenesis of the phage particle ends with attachment of the tail to the head.

The clever combination of appropriate phage mutants, of cryo-electron microscopy techniques, which makes it possible to observe objects in their native state [18], and of image processing has led to two noteworthy studies. Tao et al [19] have presented 3D reconstruction images of the assembly pathway of phage Φ29, a tailed phage infecting Bacillus subtilis. Their study revealed the dynamic process of nucleic acid packaging within the phage capsid and the subsequent genome ejection. Cerritelli et al [20] have visualized the packing of phage T7 DNA (40kbp) into isolated capsids. Their observations are in

agreement with the coaxial spool model proposed by Harrison [21]: the DNA is wrapped axially around the connector core into 6 concentric shells in a quasi-crystalline packing. Based on Cerritelli's data, Odijk [22] has formulated and tested a theory of DNA packing. He concluded that the structure of encapsulated DNA is best explained by balancing electrostatic self-repulsion forces against curvature stress within the DNA spool.

2.3 Putative role of polyamines in DNA condensation

It was originally proposed that polyamines would participate in the neutralization of the viral DNA within the phage capsids. The role of polyamines in DNA condensation, however, is still controversial. Polyamines are found in some phage (T4) and absent in others (T3, T7) [23]. Black [12] concluded that polyamines are peripheral to the energetics of DNA packaging, because E. coli mutants lacking polyamines allow phage formation.

3. Phage DNA transport across the envelope of Gram negative bacteria

3.1 The bacterial envelope: a complex structure

A common feature of almost all bacterial viruses is that only their genome is transferred to the host cytoplasm while the phage capsid and tail remain bound to the cell surface. This situation is very different from that found in most eukaryotic viruses, the envelope of which fused with the host plasma membrane so that the genome is delivered without contacting directly the membrane. In the case of viruses infecting Gram negative bacteria, the naked hydrophilic DNA has to overcome two hydrophobic barriers: the outer and the inner membrane. Furthermore, it has to cross the periplasm, the space separating the two membranes, which contains nucleases and the rigid polymeric sugar structure of the peptidoglycan.

3.2 Phage - host cell envelope recognition and DNA release from the phage capsid

Infection of Gram negative bacteria by tailed phage follows almost the same general scheme: the tail fibers first make contact with the cell surface. This non-specific binding is followed by specific and irreversible binding of one of the proteins located at the tip of the tail to an outer membrane component. Almost all surface components including flagella, pili, capsules, lipopolysaccharides and proteins serve as receptors for phage [24]. Phage binding is followed by release of the DNA from the capsid. For such release to occur, a signal has to be transmitted from the tip of the tail to the head-tail connector, triggering its opening. How this signal is transmitted through

the proteinaceous coat is not understood. Interestingly, for certain phage no component other than the phage and the receptor are required for DNA release. This has allowed analyzing the molecular mechanisms of DNA release in a simplified in-vitro system (see below).

3.3 Crossing the envelope: different phage adopt different strategies

The phage genome begins to be transferred into the host cytoplasm within a few seconds following binding to the receptor. Available evidence indicates that the DNA of phage T4, T5 and T7 crosses the host membranes linearly, nucleotide pair by nucleotide pair, and in a direction opposite to that in which it was packaged. The complexity of phage DNA transport is attested by the fact that none of these phage use similar strategies. This is illustrated in Fig. 1.

Transport of phage T4, 75 and T7 DNA through membranes was followed indirectly by measuring the efflux of host cytoplasmic potassium which takes place concomitantly with DNA transport [7,25,26]. In the case of T4, binding of the phage to the lipopolysaccharide triggers tail contraction; the tip of the internal tube of the tail is then brought close to the cytoplasmic membrane, and the 172 kbp of the DNA cross the membranes in about 30 sec. This

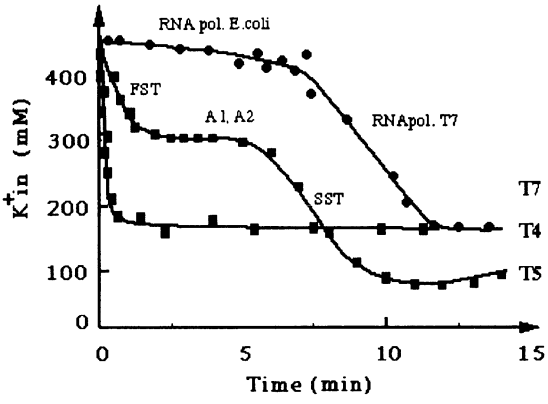

Figure 1. DNA transport strategies of the tailed phage T4, T5 and T7 . Phage DNA transport is followed indirectly by measuring the concomitant efflux of cytoplasmic potassium during DNA transport. Conditions were as described in [26]. E. coli cells(2×10^9 in 3 ml) were incubated at 37°C at physiological pH in a buffer with divalent cations, casamino acids, a carbon source, and 0.5 mM KCl.Phage were added at time = 0 and at a multiplicity of infections of 3 ml. Internal K^+ was determined by measuring the potassium concentration in the external medium with a potassium-valinomycin selective electrode. (RNA pol: RNA polymerase, and FST and SST: First and second step transfer DNA).

represents the highest rate (approximately 4000 bp/sec) observed for DNA transport. From the quantitative analysis of the K^+ efflux induced by phage T4, it was concluded that DNA transport takes place through a voltage-gated channel that opens only above a threshold of membrane potential and remains open only during DNA transport [25].

Phage T7 and T5, in contrast to T4, do not contain a contractile, penetrating tail. Transport of the small phage T7 genome (40 kbp) is slow and takes between 9 and 12 min. DNA transport is coupled first to transcription by the bacterial RNA polymerase and then by the T7 enzyme [27]. DNA transport is associated with an efflux in two steps of K^+ [28]. A feature unique—and mysterious—to phage T5 is that its DNA (121 kbp) is transferred in two steps [29]: 8% of the DNA (First Step Transfer or FST DNA) first enters the cytoplasm. Then, there is a pause of about 4 minutes during which two proteins (A1 and A2) encoded by this fragment are synthesized. The transfer of the remaining DNA (92%) or second step transfer (SST) DNA, takes place only if these proteins have been synthesized. If one prevents synthesis, then the SST DNA still connected to the phage head and attached to the FST fragment, crosses both membranes without being degraded, suggesting that the DNA is protected from periplasmic nucleases during its transport. As shown in Fig. 2, T5-induced K^+ efflux strictly follows the timing of DNA penetration. Just as for T4, the amplitude of the K^+ efflux suggests that it is due to the opening of a channel in the cytoplasmic membrane [26].

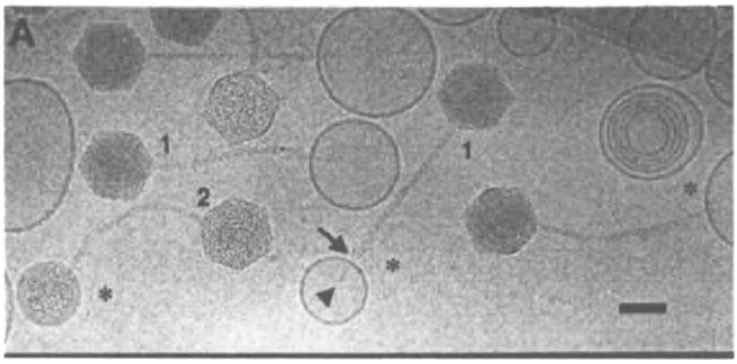

Figure 2. Typical cryo-electron micrographs illustrating the different steps of transfer of phage T5 DNA FhuA-containing liposomes. Liposomes were made from a mixture of phosphatidyl choline/phosphatidic acid (9/1 M/M) as described in [32]. (1) T5 bound to proteoliposomes; phage DNA (electron dense material) is condensed in the capsid. (2) DNA ejection into proteoliposomes; vesicles and capsids contain DNA. (3) empty capsid associated with a DNA-containing proteoliposome. The straight tail fiber formed by pb2 (black arrow) crosses the liposomal membrane. The bar represents 50 nm.

Given the different characteristics of the T4, T5 and T7 K^+ efflux, we postulated that the channels originate from the phage rather than from the host. Fractionation of the envelope of T5-infected E. coli cells suggested that pb2, the protein forming phage T5 straight fiber (Fig 2) would constitute the DNA channel [30]. pb2 (MW = 123 kDa) is an oligomeric polypeptide the length of which (50 nm) would be sufficient to span the entire envelope and gain access to the inner membrane. Except for a short stretch of amphiphilic amino acids, pb2 is essentially hydrophilic. This raises the question as to how it could be inserted into membranes. Interestingly, the region of amphiphilic amino acids shows sequence homologies with fusogenic peptides of eukaryotic envelope viruses [31]. What could be the function of such fusogenic sequences? It is noteworthy that pb2 changes conformation upon binding to FhuA: the pb2 becomes sensitive to proteases, and its morphology is modified [32]. It is tempting to propose that this change in conformation renders the peptide accessible to the host envelope and that it contributes to the fusion of the two membranes. This fusion may have two functions, ensuring the contact between the two membranes and forming the DNA channel, that protect the DNA from periplasmic nucleases.

3.4 Driving force for *in vivo* DNA transport

Many hypotheses of DNA injection into host cells have been formulated since the 1960's (for a review, see [33] and references therein). It was proposed that the translocating apparatus may simply introduce DNA under sufficient pressure to allow spontaneous ejection when packaging has been completed [34]. Gabashvili and Grosberg [33] have analyzed the dynamics of DNA release theoretically: the process they considered is reptation through the phage tail driven by the decrease of condensed DNA free energy.

On the basis of Mitchell's chemiosmotic theory [2], Grinius [35] postulated that the driving force for DNA transport would be the electrochemical gradient of protons $\Delta\mu^{H^+}$ across the cytoplasmic membrane and that the polyanionic DNA molecule would be transported in symport with the protons. This hypothesis was supported by experiments showing that phage T4 DNA transport took place only in energized membranes and above a threshold of membrane potential of -90 mV [36]. However, further experiments suggested that the requirement for a membrane potential was not for transport but rather for opening of the DNA channel [25]. Furthermore, it was shown that both the FST and the SST DNA of phage T5 could cross the cytoplasmic membrane of de-energized cells [37].

Experiments with phage T5 have also proved that the energy for DNA transport cannot be provided only by relief of the capsid internal pressure. Indeed, the capsid and tail of phage T5 can be sheared off the bacterial cell

surface once the FST DNA has been transported into the cytoplasm. Under these conditions the SST DNA (approximately 27 μm in length) floats in the surrounding medium, but is still attached to the FST DNA crossing the envelope. If one provides the energy for the synthesis of the FST-encoded proteins, then the free DNA is transported through the membranes [37].

What then drives the transport of the free DNA molecule? The most reasonable hypothesis is that the DNA crosses the membrane by facilitated diffusion through the pb2 channel, the driving force being its condensation in the cytoplasm by histone-like (A1 and A2) proteins.

4. *In vitro* studies of phage-receptor interactions

4.1 Channeling DNA through a membrane protein?

An interesting feature of T5 is that DNA release from the phage can be triggered in vitro simply by interaction of the virus with its isolated and purified outer membrane receptor, the FhuA protein [38]. DNA release was demonstrated using a fluorescent DNA intercalant YO-PRO-1 [39], the fluorescence of which increased in proportion to the amount of DNA freed from the capsid. Phage bound to FhuA solubilized in detergent ejected virtually all their DNA into the surrounding medium within a few seconds. Interestingly, and in contrast to in vivo DNA transport that occurs in two steps, in vitro DNA release proceeds in one step. Thus, there must be additional host factors that contribute to the unusual transfer of DNA in vivo.

In vitro studies have also highlighted the peculiar properties of the receptor protein. FhuA (MM: 78.9 kDa) belongs to the family of "high-affinity transporters", proteins of the outer membrane of Gram negative bacteria that catalyze the transport of nutrients present at very low concentration in the environment (iron, vitamin B12, etc.) [40,41]. These proteins have long been considered to belong to a class separate from that of porins, the major outer membrane proteins of Gram negative bacteria, which form large water-filled channels allowing the diffusion of hydrophilic solutes up to 800 Da ([42] and references therein). Recently, however, it was shown that high-affinity transporters also carry the function of channel [7,43]. FhuA showed no channel activity when incorporated in a planar lipid bilayer. Yet, binding of phage T5 to FhuA triggered the opening of a large (single channel conductance: 4 nS in 1.5 M KCl) channel in the protein. An estimate of its size from permeability experiments carried out on the closely-related protein, FepA, suggested a diameter of 2 nm [44]. This led us to propose that the FhuA channel might be large enough to permit the passage of the phage DNA. Interestingly, Kasianowicz et al. [45] using an electrophysiological approach, demonstrated that polynucleotides could be transported through the channel-forming toxin α-hemolysin ($>$ 1.6 nm in diameter) incorporated into a lipid bilayer and upon

applying an electric field (see also in this volume the chapters by Kasianowicz, et al., Deamer, et al., and Branton and Meller).

The hypothesis that the channel in FhuA could be large enough for the passage of a DNA molecule was supported by electron crystallography studies of 2-dimensional crystals of the protein. A projection map at 0.8 nm resolution revealed the presence of a low density region approximatively 2 nm in diameter, which may correspond to this channel [48]. However, the determination of the crystal structure at atomic resolution of FhuA [49,50] has highlighted an unexpected feature of the protein, which is also shared by another member of this family, FepA [51]. FhuA consists of a 22-stranded antiparallel β barrel. Within the barrel is a channel, the entrance of which is partially constricted by three surface-located hydrophilic loops, one of them carrying the phage-binding site. The unexpected feature is that the channel is totally obstructed on the opposite side by a domain (a "plug" or "cork") which is structurally distinct from the β barrel. Unplugging of the channel and the disruption of many interactions between the plug, the β barrel and the loops is therefore required for DNA to go through FhuA. It remains an open question whether such a drastic conformational change can take place.

4.2 Delivering a phage genome into liposomes

In an attempt to decipher the mechanisms of DNA transport, we reconstituted FhuA into unilamellar liposomes containing the fluorescent dye YO PRO 1. Binding of T5 resulted in an increase in fluorescence consistent with the transport of part of the DNA into the vesicles [52]. A cryo-electron microscopic study further allowed the visualization of the phage-proteoliposome interactions and to demonstrate unequivocally that the phage genome was delivered into the liposome [32]. Fig 2 shows typical electron micrographs. T5 phage were bound to the proteoliposomes by the tip of their tails. Some of the capsids of phage attached to the proteoliposomes were filled with a dark grey striated material corresponding to DNA. Many were only partially filled with DNA or totally empty as evidenced by their lower electron densities. Phage, with partially or completely empty capsids, were associated with proteoliposomes that contained the same dark grey material as in capsids and which was identified as DNA. pb2, the protein forming the straight tail fibre of the phage was visible inside some vesicles. Notably, the morphology of the liposomes was not disturbed by DNA, although its concentration within the vesicles may have reached values as high as 130 mg/ml.

The mechanism by which DNA is transported into the vesicles is not known. The relief of the capsid internal pressure is probably the major force driving the DNA out of the capsid and allowing it to cross the tail and to emerge from the straight tail fiber. DNA transport, in contrast to DNA pack-

aging into capsids, is clearly not an ATP-driven process since it takes place in the absence of any added energy source. If it is a passive diffusion process, then we expect DNA transport to cease when DNA concentration in the two compartments (capsid and liposome) has reached equilibrium. Alternatively, if polyamines are present in the phage capsid, they might diffuse with the DNA and contribute to its condensation in the liposomes.

We have recently demonstrated that polyamines entrapped in the liposomes can condense phage DNA [53]. FhuA was reconstituted into liposomes containing variable concentrations of spermine. In the presence of 50 mM spermine, typical toroidal structures of DNA wrapped circumferentially were observed inside the liposomes. Their formation depended upon spermine concentration and their sizes varied with the amount of DNA transferred, reaching diameters up to 300 nm. Interestingly, the progressive release of phage DNA in a solution containing the solubilized FhuA receptor and spermine led to the formation of hollow cylinders of DNA which increased in size with the amount of DNA released to reach a diameter of 300 nm and a height of 100 nm.

5. Conclusions

We are far from understanding the mechanism by which a virus genome can be delivered into a bacterial cell. In-vivo studies have been rather poorly informative. Phage genetics has contributed to identifying and characterizing phage receptors, but similar approaches to analyzing DNA transport are lacking because mutations affecting this specific step until now, have not been characterized. On the other hand, in-vitro studies have been particularly stimulating because they allow approaching, at a molecular level, the functioning of receptors as well as the mechanism of DNA transport and condensation. These studies open new perspectives. DNA-containing liposomes might serve as alternative vehicles to transfer foreign genes into eukaryotic cells. Vectorization of foreign DNA is currently achieved by using cationic lipids which form complexes with DNA through charge interactions [54]. The DNA-containing proteoliposomes described here are conceptually very different from the DNA-cationic lipid complexes since the DNA is truly entrapped in the liposomes. Furthermore, since DNA does not interact with the lipids, the lipid composition of the vesicles may be varied to contain different ratios of neutral to charged lipids, glycosylated lipids, or even cholesterol. The reconstitution procedure also allows other proteins and/or other molecules to be co-reconstituted with the phage receptor or entrapped within the liposomes to favor gene delivery or to protect the DNA from degradation. Finally, the origin of the DNA allows its manipulation by means of phage molecular biological strategies.

For those working in the field of polymer and condensed matter physics, the possibility of progressively delivering, base pair after base pair, a large DNA molecule, either in a liposome or in solution will allow approaching the mechanics of toroid formation in a way different from that of the classical studies [10,55,56], where a condensing agent is simply added to a highly-dilute solution of naked DNA.

References

[1] Dubnau, D.(1999), DNA uptake in bacteria. *Ann. Rev. Biochem.* **53**, 217-244.

[2] Mitchell, P. (1968), Chemiosmotic coupling and energy transduction L. Glynn Research, Bodmin and Cornwall (eds).

[3] Goldberg, E., Grinius, L. and Letellier, L. (1994), Recognition, attachment and injection, in The Molecular Biology of Bacteriophage T4, Karam, A. et al. (eds). American Society for Microbiology, Washington DC, pp. 347-357.

[4] Reanney, D., and Ackermann, H.W. (1982), Comparative biology and evolution of bacteriophages, *Adv. Vir. Res.* **27**, 205-280.

[5] Dreisekelman, B. (1994), Translocation of DNA across bacterial membranes, *Microbiol. Rev.* **58**, 293-316.

[6] Palmen, R., Driessen, A.J. and Hellingwerf, K.J. (1994), Bioenergetic aspects of the translocation of macromolecules across bacterial membranes, *Biochem. Biophys. Acta,* **1183**, 417-451.

[7] Letellier, L. and Bonhivers, M. (1996), Intrinsic and extrinsic channels in bacteria in Transport Processes in Eukaryotic and Prokaryotic Organisms, *Handbook of Biological Physics*, **2**, Konings, W., Kaback, H.R. and Lolkema, J.S. (eds.), Elsevier, NY, pp. 615-637.

[8] Zillig, W., Prangishvilli, D., Schleper, C., Elferink M., Holz, I., Albers, S., Janekovic, D. and Götz, D. (1996), Viruses, plasmids and other genetic elements of thermophilic and hyperthermophilic Archae, *FEMS Microbiol. Rev.* **18**, 225-236.

[9] Hendrix, R., Smith, M., Burns, R., Ford, M. and Hatfull, G.(1999), Evolutionary relationships among diverse bacteriophage and prophage: all the world's a phage. *Proc. Natl.Acad.Sci. (USA)* **96**, 2192-2197.

[10] Bloomfield, V. (1996), DNA condensation, *Curr. Opin. Struct. Biol.* **6**, 334-341.

[11] Earnshaw, W. and Casjens, S. (1980), DNA packaging by the double-stranded DNA bacteriophage, *Cell* **21**, 319-331.

[12] Black, L.W. (1989), DNA packaging in ds DNA bacteriophage, *Ann. Rev.Microbiol.* **43**, 267-292.

[13] Black, L.W., Showe, M. and Steven, A. (1994), Morphogenesis of the T4 head in Molecular Biology of Bacteriophage T4; Karam A., et al. (eds). Washington DC; American Society for Microbiology; pp. 218-248.

[14] Hendrix, R. (1998) Bacteriophage DNA packaging, RNA gears in a DNA transport machine, *Cell* **94**, 147-150.

[15] Dube, P., Tavares, P., Lurz, R. and van Heel, M. (1993), Bacteriophage SPP1 portal protein: a DNA pump with 13-fold symmetry, *EMBO J.* **12**, 1303-1309.

[16] Morita, M., Tasaka, M. and Fujisawa, H. (1993), DNA packaging ATPase of bacteriophage T3, *Virology* **193**, 748-752.

[17] Casjens, S., Wyckoff, E., Hayden, M., Sampson, L., Eppler, K., Randall, S., Moreno, E. and Serwer, P. (1992), Bacteriophage p22 portal protein is part of the gauge that regulates packing density of intravirion DNA, *J. Mol. Biol.* **224**, 1055-1074.

[18] Lepault, K., Dubochet, J., Baschong, W. and Kellenberger, W. (1987)¡ Organization of double stranded DNA in bacteriophages: a study by cry-electron microscopy of vitrified samples, *EMBO J.* **6**, 1507-1512.

[19] Tao,Y., Olson, N., Xu, W., Anderson, D., Rossmann, M. and Baker T. (1998), Assembly of a tailed bacterial virus and its genome release studied in three dimensions, *Cell* **95**, 431-437.

[20] Cerritelli, M.E., Cheng, N., Rosenberg, A., McPherson, C., Booy, F. and Steven, A. (1997), Encapsidated conformation of bacteriophage T7 DNA, *Cell*, **91**, 271-280.

[21] Harrison, S. (1983), Packaging of DNA into bacterial heads: a model. *J. Mol. Biol.* **171**, 577-580.

[22] Odijk, T. (1998), Hexagonally packed DNA within bacteriophage T7 stabilized by curvature stress, *Biophys. J.* **75**, 1223-1227.

[23] Cohen S.S. (1998), in *A Guide to the Polyamines*, Oxford Press, pp. 366-395.

[24] Heller, K.J. (1992), Molecular interaction between bacteriophage and the Gram-negative cell envelope. *Arch. Microbiol.* **158**, 235-248.

[25] Boulanger, P. and Letellier, L. (1988), Characterization of ion channels involved in the penetration of phage T4 DNA into E. coli cells, *J.Biol.Chem.* **263**, 9767-9775.

[26] Boulanger, P. and Letellier, L. (1992), Ion channels are likely to be involved in the two steps of phage T5 DNA penetration into E. coli cells, *J. Biol. Chem.* **267**, 3168-3172.

[27] René Garcia, L.R. and Molineux, I. (1996), Transcription-independent DNA translocation of bacteriophage T7DNA into Escherichia coli, *J. Bacteriol.* **178**, 6921-6929.

[28] Bonhivers, M. (1996), Thesis, University of Paris VI, France.

[29] Lanni, Y. (1968), First step transfer DNA of bacteriophage T5, *Bacteriol. Rev.* **32**, 227-242.

[30] Guihard, G., Boulanger, P. and Letellier, L. (1992), Involvement of phage T5 tail proteins and contact sites between the outer and inner membrane of Escherichia coli in phage T5 DNA injection, *J. Biol. Chem.* **267**, 3173-3178.

[31] Boulanger, et al., In preparation.

[32] Lambert, O., Plançon, L., Rigaud, J-L- and Letellier, L. (1998), Protein-mediated DNA transfer into liposomes, *Mol. Microbiol.* **30**: 761-765.

[33] Gabashvili, I. and Grosberg, A. (1992), Dynamics of double-stranded DNA reptation from bacteriophage, *J. Biomol. Struct. and Dynamics* **9**, 911-920.

[34] Rau, D., Lee, B. and Parsegian, V. (1984), Measurement of the repulsive force between polyelectrolyte molecules in ionic solution: hydration forces between parallel double helices, *Proc. Natl. Acad. Sci. (USA)* **81**, 2621-2625.

[35] Grinius, L. (1980), Nucleic acid transport driven by ion gradient across cell membranes, *FEBS Lett.*, **113**, 1-10.

[36] Labedan, B. and Goldberg, E. (1979), Requirement for a membrane potential in injection of phage T4 DNA, *Proc. Natl. Acad. Sci. (USA)* **76**, 4669-4673.

[37] Filali Maltouf, K. and Labedan, B. (1983), Host metabolic energy is not required for injection of bacteriophage T5 DNA, *J. Bacteriol.* **153**, 124-133.

[38] Boulanger, P., le Maire, M., Bonhivers, M., Dubois, S., Desmadril, M. and Letellier, L. (1996), Purification and structural and functional characterization of FhuA, a transporter of the E. coli outer membrane, *Biochemistry* **35**, 14216-14224.

[39] Carlsson, C. Jonsson, M. and Akerman, B. (1995), Double bands in DNA gel electrophoresis caused by bis-intercalating dyes, *Nucleic Acid Res.* **23**, 2413-2420.

[40] Nikaido, H. and Saier, M.H. (1992), Transport proteins in bacteria: common themes in their design, *Science* **258**, 936-942.

[41] Moeck, G.S. and Coulton, J.W. (1998), TonB-dependent iron acquisition: mechanisms of siderophore -mediated active transport, *Mol. Microbiol.* **28**, 675-681.

[42] Schirmer, T., Keller, T.A., Wang, Y.F. and Rosenbusch, J.P. (1995), Structural basis for sugar translocation through maltoporin channels at 3.1 Å resolution. *Science*, **267**, 512-514.

[43] Bonhivers, M., Ghazi, A., Boulanger, P. and Letellier, L. (1996), FhuA, a transporter of the Escherichia coli outer membrane, is converted into a channel upon binding of bacteriophage T5, *EMBO J.* **15**, 1850-1856.

[44] Rutz, J.M., Liu, J., Lyons, J.A., Goranson, J., Armstrong, S.K., McIntosh, M.A., Feix, J.B. and Klebba, P.E. (1992), Formation of a gated channel by a ligand-specific transport protein in the bacterial outer membrane, *Science* **258**, 471-475.

[45] Kasianowicz, J.J., Brandin, E., Branton, D. and Deamer, D.W. (1996), Characterization of individual polynucleotide molecules using a membrane channel, *Proc. Natl. Acad. Sci. (USA)* **93**, 13770-13773.

[46] Akeson , M., Branton, D. Kasianowicz, J.J. Brandin, E. and Deamer, D.W. (1999), Microsecond time-scale discrimination between polycytidylic acid and polyadenylic acid segments within single RNA molecules, *Biophys. J.* **77**, 3227-3233.

[47] Henrickson, S.E, Misakian, M., Robertson, B. and Kasianowicz, J.J. (2000), Asymmetric driven DNA transport in a nanometer-scale pore. *Phys. Rev. Lett.* **85**, 3057-3060.

[48] Lambert, O., Moeck, G., Levy, D., Plan‡on, L., Letellier, L and Rigaud J.-L. (1999), An 8A projected structure of FhuA, a ligand gated channel of the E. coli outer membrane, *J. Structural Biol.*, **126**, 145-155.

[49] Löcher, K., Rees, B., Koebnick, R., Mitschler, A., Moulinier, L., Rosenbusch, J. and Moras, D. (1998), Transmembrane signaling across the ligand-gated FhuA receptor: crystal structures of free and ferrichrome bound states reveal allosteric changes. *Cell* **95**, 771-778.

[50] Ferguson, A., Hofman, E., Coulton, J., Diederichs, K. and Welte, W. (1998), Siderophore-mediated iron transport: crystal structure of FhuA with bound lipopolysaccharide, *Science* **282**, 2215-2220.

[51] Buchanan, S., Smith, B., Venkatramani, L., Xia, D., Esser, L., Palnitkar, M., Chakraborty, R., van der Helm, D. and Deisenhofer, J. (1999), Crystal structure of the outer membrane active transporter FepA from E. coli. *Nat. Struct. Biol.* **6**, 56-63.

[52] Plançon, L., Chami, M. and Letellier, L. (1997), Reconstitution of FhuA, an E. coli outer membrane protein into liposomes. Binding of phage T5 to FhuA triggers the transfer of DNA into the proteoliposomes, *J. Biol. Chem.* **272**, 16868-16872.

[53] Lambert, O., Letellier, L., Gelbart, W. and Rigaud, J.-L. (2000), DNA delivery by phage as a new strategy for encapsulating toroidal condensates of arbitrary size into liposomes. *Proc. Natl. Acad. Sci. (USA)*, in press.

[54] Behr, J.P. (1994), Gene transfer with synthetic cationic amphiphiles; prospects for gene therapy. *Bioconj. Chem.* **5**, 382-389.

[55] Pelta, J., Livolant, F., Sikorav, J.L. (1996a), DNA aggregation induced by polyamines and cobalt-hexamine. *J. Biol. Chem.* **271**, 5656-5662.

[56] Pelta, J., Durand, D., Doucet, J. and Livolant, F. (1996b), DNA mesophases induced by spermidine: Structural properties and biological implications. *Biophys. J.* **71**, 48-63.

TRANSLOCATION OF MACROMOLECULES ACROSS MEMBRANES AND THROUGH AQUEOUS CHANNELS

Translocation across membranes

Sanford M. Simon
Laboratory of Cellular Biophysics, Rockefeller University, 1230 York Ave., Box 304, New York, NY 10021-6399

Abstract Maintaining the permeability barrier of membranes is essential for cell viability. Cells allow the passage of small hydrophilic ions across the membrane by selectively gating transmembrane aqueous pores. Over the past decade an increasing amount of evidence supports a model for which transport of larger molecules such as proteins, DNA and phage also occurs through the selective gating of transmembrane aqueous channels. Studies are presented on the mechanisms by which proteins are translocated across the endoplasmic reticulum and *E. coli* plasma membrane through transmembrane protein-conducting channels. The model of a protein-conducting channel raises a number of challenging questions. First, if proteins are moving across through a transmembrane aqueous channel, then what is moving the protein across the membrane? Second, membrane proteins are synthesized using the same membrane-bound machinery as is used for translocating proteins across the membranes. Thus, how could a transmembrane protein-conducting channel account for the biogenesis of proteins which themselves must eventually end up spanning the bilayer multiple times? The evidence for protein-conducting channels is reviewed, and the mechanism(s) proposed for transport will be evaluated. The experiments also focus on tests for the role of aqueous channels for the biogenesis of membrane proteins.

Keywords: protein translocation, phage export, membrane protein assembly

1. Introduction

Most proteins of the cell are synthesized on ribosomes in the cytosol. However, many proteins whose synthesis is initiated in the cytosol end up in other cellular compartments. This includes the proteins that will be secreted as well as those that become membrane proteins or lumenal components of organelles. These proteins reach their destinations by one of two routes. Some go di-

J.J. Kasianowicz et al. (eds.), Structure and Dynamics of Confined Polymers, 37–66.

rectly from their biosynthetic ribosome to their final destination. In bacterial cells these include all proteins of the plasma membrane or periplasm; in eukaryotic cells, these include proteins destined for the endoplasmic reticulum, mitochondria or chloroplast. In a process called translocation, the proteins are either transported across the membrane or integrated into the membrane. Meanwhile, other proteins reach their destination taking an indirect route. They travel from their biosynthetic ribosome to the endoplasmic reticulum. After translocation, they traverse a series of sorting and vesicular transport steps to their final destination [1].

A great deal is known about how proteins are targeted to an organelle. Targeting requires a signal in the primary amino acid structure of the protein, called a signal sequence, which is necessary and sufficient for targeting. If a protein is synthesized without its signal sequence, it is no longer targeted. If a signal sequence is added, the protein is then able to be targeted to an organelle. Cytosolic factors interact with the signal sequence and facilitate targeting. For the endoplasmic reticulum, the cytosolic factor is the signal recognition particle (SRP) which, upon binding to a newly synthesized signal sequence, also binds to its biosynthetic ribosome [2]. Upon interacting with the ribosome, the SRP slows and sometimes arrests protein synthesis until the SRP-nascent protein-ribosome complex is targeted to the proper organelle and the SRP interacts with its receptor [3], and the entire complex engages the translocation machinery. In a reaction requiring GTP [4, 5], the SRP is displaced from both the signal sequence and the SRP receptor, the ribosome resumes protein synthesis [3], and the nascent protein is translocated across the membrane. Both secretory and membrane proteins share four similar steps: They are made with signal sequences, start their synthesis on ribosomes free in the cytosol, target to the membrane using SRP, and translocate using the same machinery in the membrane of the endoplasmic reticulum.

This chapter will examine the subsequent steps in this process. The first question to be addressed is how secretory proteins cross the membrane. The second is how membrane proteins are integrated into the lipid bilayer with their proper topology.

2. Do proteins cross membranes through the hydrocarbon core of the lipid bilayer, or through transmembrane aqueous channels?

Two different models have been presented to account for the transport of proteins across the membrane of the endoplasmic reticulum.endoplasmic reticulum,membrane In 1975 Gunter Blobel proposed, as part of a refinement of the signal hypothesis [6], that proteins translocate across the membrane through protein-conducting channels [7]. The alternative (and until recently the gen-

erally accepted) hypothesis was that proteins translocate directly through the hydrocarbon core of the lipid bilayer. It was accepted that there would be a large energy barrier for proteins to partition into the lipid bilayer. However, this energy would be regained when the proteins exited the bilayer on the opposite side [8].

Over one hundred years ago Overton had proposed that the rate at which molecules cross membranes was proportional to their partitioning in oil. Based on this, he suggested that the interior of cell membranes was a hydrocarbon phase! Overton realized that many molecules, such as ions, did not adhere to this relation. He further proposed that there were specific transporters in the membrane that facilitated the transport of those molecules that did not readily partition into the lipid.

The sequences which target proteins to membranes usually have a hydrophobic stretch. It was assumed that this hydrophobicity indicated an interaction with the hydrocarbon core of the lipid bilayer. However, most proteins do not readily partition into lipid (and those that do, do not readily leave once they are on the other side). Since proteins of very different physical chemical properties could cross the membrane, Blobel proposed that proteins translocate through an environment shielded from the lipids.

2.1 Electrophysiological analysis of mammalian endoplasmic reticulum

Initially, several options were considered for testing the possibility that proteins translocated through transmembrane aqueous channels. One was to freeze a protein in the process of translocation, and then test whether it is in an aqueous or hydrophobic environment. This experiment could be done using two experimental tricks. First, if the protein was synthesized with an mRNA that ended without a termination codon, when the ribosome reached the end of the mRNA, the nascent polypeptide would remain attached via its final amino acid to the ribosome and the mRNA (the termination codon is normally the physiological signal to terminate protein synthesis and release the ribosome). Second, if the protein synthesis mix contained amino acids that are conjugated to fluorophores, then the amino acid-fluorophore conjugate would be synthesised into the growing nascent protein. The lifetime of many fluorophores is sensitive to their environment. This approach could indicate the environment of the translocation chain.

There were three limitations to this approach. First, when an mRNA is used without a termination codon, some of the nascent polypeptides remain attached to their biosynthetic ribosomes, but many fall off. This produces a mixed population. Thus, the fluorescent signal would come both from those proteins that are still attached to the ribosome (and therefore trapped

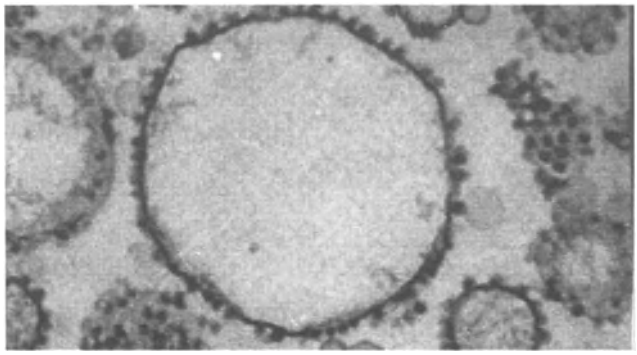

Figure 1. An electron micrograph of a vesicle derived from pancreatic endoplasmic reticulum. The average size of a microsomal vesicle is 200 nm. From [9].

in the process of translocation) and from proteins that have already fallen off the ribosome and therefore are not longer intermediates in translocation. A second problem is that there is no independent method of telling when during synthesis a particular amino acid has left the ribosome and is positioned within the translocon - the machinery in the endoplasmic reticulum that is responsible for translocation. Third, if the fluorophore reports a hydrophilic environment, it does not mean that there is a continuous hydrophilic pathway across the membrane.

The most direct way to test for a continuous hydrophilic pathway across the membrane (also known as a protein-conducting channel) was to test for an aqueous pathway that allowed ionic flow. Thus, the hypothesis that there are protein-conducting channels was initially tested using the same electrophysiological technologies used to test for the presence of ion-conducting channels. It was assumed that a protein-conducting channel should be considerably larger than a conventional ion-conducting channels. Since single ion-conducting channels can be studied on a individual basis (the only true molecular biology) it was reasonable to assume any protein-conducting channels would be similarly detectable. The purest known preparation for membranes that translocate proteins is the rough microsomal preparation of endoplasmic reticulum from the pancreas. The pancreas is a secretory organ and the membranes are coated with ribosomes. The term "rough" microsomes refers to the rough bumps that ribosomes form around the edge of these organelles (see figure 1).

Endoplasmic reticulum vesicles were fused to a planar lipid bilayer separating two aqueous compartments. With each fusion of a vesicle there was an increased permeability of the membrane and the appearance of approximately

5-10 large ion channels [10]. These channels were large based both on their conductance (50-115 pS in 50 mM KCl) and on their permeability to molecules like glutamate. However, the number of large ion channels observed per fused vesicle (5-10) did not correlate with the hundreds of ribosomes that were observed on these vesicles by electron microscopy (see figure 1). Each of these ribosomes was potentially synthesizing and translocating proteins. The discrepancy between the number of channels and the number of bound ribosomes could be explained two ways. Potentially the channels were not involved in the translocation of proteins. Alternatively, when a protein was translocating through the protein-conducting channel the lumen of the channel was occluded to the free flow of ions. This would be in a fashion similar to the block observed in potassium channels when a peptide from the channel enters the pore [11].

To distinguish between these two possibilities, the nascent chains were released from their biosynthetic ribosomes. If the channels were occluded by the translocating chains, release of the nascent chains should unblock the channels. Nascent chains can be released from their biosynthetic ribosomes with the antibiotic puromycin. Puromycin has structural similarity to an amino acid bound to a tRNA. It is recognized by the peptidyl-transferase in the ribosome which adds puromycin to the carboxyl-terminus of the elongating nascent chain. The peptidyl-puromycin then falls off the ribosome [12]. When puromycin is added to ribosomes that are bound to the endoplasmic reticulum and synthesizing nascent secretory proteins, the peptidyl-puromycin, upon release from the ribosome, enters the lumen of the endoplasmic reticulum [13]. This peptidyl-puromycin is then transported through the secretory pathway and, eventually, secreted from the cell. When puromycin is added to ribosomes bound to isolated membranes from the endoplasmic reticulum, the peptidyl-puromycin is released from the ribosomes and enters into the lumen of the endoplasmic reticulum vesicles. In solutions of roughly physiological concentrations of salts (150 mM) , the ribosomes dissociate from the membranes of the endoplasmic reticulum. However, in salt concentrations that are substantially below physiological levels, the ribosome remains associated with the membrane [14].

We wanted to test the effect of releasing the nascent translocating proteins, without affecting the ribosomes. We added puromycin in the presence of 50 mM salt. Puromycin effectively blocks protein synthesis in the range of 0.1-1.0 mM. When we added 100 mM puromycin to the cytoplasmic surface of the endoplasmic reticulum membranes, there was an immediate and substantial increase of the conductance of the membrane (figure 2, top).

A number of tests were done to determine if puromycin was causing a non-specific effect on the permeability of the membrane. First, the same concentration of puromycin was added to a pure lipid bilayer (that is, with-

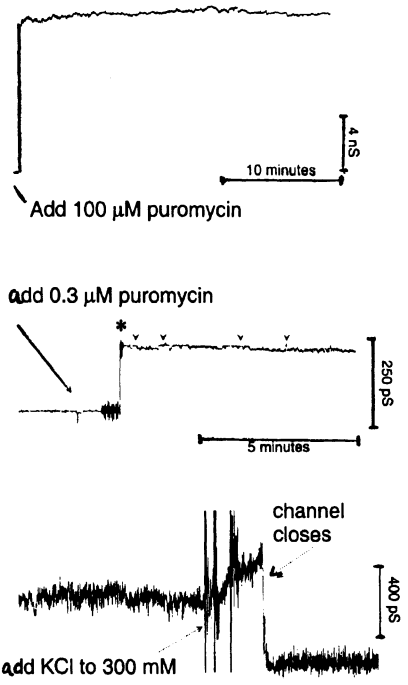

Figure 2. Puromycin reveals the presence of protein-conducting channels in the endoplasmic reticulum. Top. After the endoplasmic reticulum vesicles fused to the bilayer, puromycin was added up to 100 mM resulting in a very large increase of membrane conductance. Middle. In the presence of only 0.3 mM puromycin, discrete channels of 220 pS are observed in 50 mM KCl. Bottom. Upon raising the KCl to concentrations which dissociate the ribosome from the membrane, the channels close. From [15].

out membranes of the endoplasmic reticulum). There was no effect on the conductance of the membrane. Second, endoplasmic reticulum vesicles were fused to a bilayer and 200 mM puromycin was added to the opposite face of the membrane (the equivalent of the lumen of the endoplasmic reticulum) no effect was seen on the conductance of the membrane. However, subsequent addition of puromycin to the cytoplasmic face of the same bilayer elicited a large increase of the conductance [15].

The results were consistent with puromycin releasing the nascent polypeptides from the ribosomes, thereby "unplugging" the putative protein-conducting channels. If this was the case, then by lowering the concentration of puromycin, we should be able to catch the "unplugging" of individual protein-conducting channels. In a subsequent experiment, vesicles of endoplasmic reticulum membranes were fused to a planar bilayer and puromycin was added to only a concentration of 0.3 mM. In the presence of 50 mM KCl, the conduc-

tance was seen to increase in steps of 220 pS (see figure 2, middle). This conductance is considerably larger than observed for most conventional ion channels.

Under these experimental conditions, the ribosome should still be attached to the membrane of the endoplasmic reticulum and the translocon. To test for a role for the ribosome, the concentration of the salt in the bathing medium was raised to physiological levels and above. Raising the salt concentration is known to dissociate the ribosome from the endoplasmic reticulum. As the concentration of salt was raised, the conductance of all ion channels increased (because of the increased number of charge carriers flowing through the channels). However, as the concentration reached the range of 150 to 450 mM, each of the large channels (that were initially 220 pS) closed down (figure 2, bottom). The results indicated that the channels, once unplugged of their translocation nascent polypeptides, remained open as long as the ribosomes were still bound. Only upon dissociation of the ribosomes did the channels close.

The use of puromycin to release the nascent translocating polypeptide and subsequent treatment of raising the salt is not a particularly physiological treatment. However, in the context of protein biosynthesis it made sense for the physiology of the cells that if there were protein-conducting channels, that they would close at the termination of protein synthesis. Otherwise, a large pore would remain between the cytosol and lumen of the endoplasmic reticulum. This would quickly dissipate any gradients of metabolites or ions between these two compartments.

2.2 Electrophysiological analysis of bacterial plasma membrane

The preceding experiments suggested that proteins were translocating across the membrane of the endoplasmic reticulum through protein-conducting channels and that these channels close when a protein completes its translocation across the membrane. This implies that the channels must open at the initiation of translocation across the membrane. The opening could potentially be elicited by the signal sequence, the signal recognition particle, the signal recognition particle receptor, the ribosome, or any combination of these components. Each one of these components was purified and tested. However, testing for the involvement of the ribosome could be problematic. The ribosome is required for synthesis of the nascent chain. In mammalian systems, proteins translocate across the membrane only while still attached to their biosynthetic ribosome. Thus, it would be difficult to resolve between requirements for the ribosome in the biosynthesis of a protein from requirements for the ribosome in translocation. To side-step this problem, we examined

translocation across the inner membrane of Escherichia coli. Translocation across this membrane is very homologous to translocation across mammalian endoplasmic reticulum. When a secretory protein from a mammalian cells is expressed in *E. coli*, the protein's signal sequence is properly recognized, the protein is targeted to the inner plasma membrane, the signal sequence is cleaved at the appropriate spot and the protein is translocated across. Similarly, when a bacterial protein is expressed in a mammalian cell, its signal sequence is properly recognized by the signal recognition particle, the nascent protein is targeted to the endoplasmic reticulum, the signal sequence is cleaved and the protein is translocated across. One of the primary differences is that, in the *E. coli* system, many proteins (as long as they are maintained in an unfolded form) can translocate across the membrane after they have been made. Thus, the role of the ribosome in biosynthesis can be separated from any potential role in translocation.

Plasma membrane vesicles from *E. coli* were fused to a planar lipid bilayer membrane. In general, few ion channels were observed. Upon addition of 200 nM signal peptide, there was a large increase in the membrane conductance (figure 3, top). Because the volume of a single *E. coli* is $\sim 10^{-15}$ l, there are $\sim$ 125 signal peptides per bacterium. When the experiment was repeated at lower concentrations of signal peptide (200 pM, or approximately 1 signal peptide per eight *E. coli*), single discrete channels were observed of 220 pS in 50 mM KCl (figure 3, bottom). These channels were the same size as the channels observed after treatment with puromycin. However, these channels observed in the presence of signal peptide flickered open and shut - that is, they did not remain open. These results are consistent with the signal sequence binding to a site on the translocon, which opens the channel, and then the signal sequence dissociating, resulting in channel closure.

These experiments were repeated in varying salt conditions and membrane potentials to correlate the behavior (conductance, gating, selectively) of the channels observed in the presence of signal peptide with those observed after release of the nascent chain. As was expected, at higher salt concentrations the conductance of the channels increased (this is from increasing the number of charge carriers available to move through the channel). What was not expected was that at increased salt concentrations the channels remained open for a longer period of time. There are two features common to all signal sequences. They have positive charges near their amino terminus and they have a stretch of hydrophobic amino acids. If the stretch of hydrophobic amino acids is important for binding to a site on the translocon then raising the salt should strengthen the interaction. Thus, at higher salt concentrations the signal sequence would be expected to bind to the translocon, thereby opening the channel, but then remaining bound for a longer period of time, resulting in a longer open time for the channel.

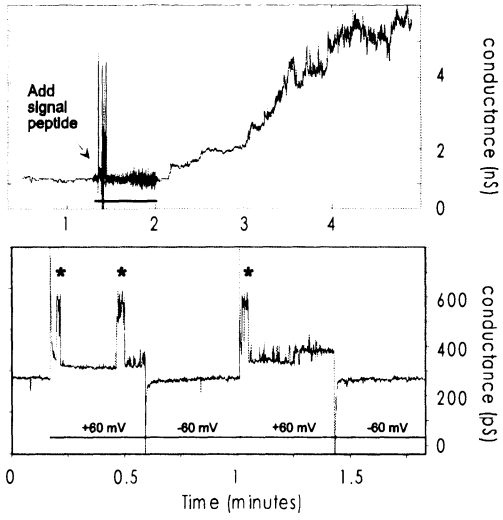

Figure 3. Effect of signal sequences of conductance of the bacterial plasma membrane. Top. Addition of 200 nM signal peptide to the cytoplasmic surface of the bacterial plasma membrane caused a macroscopic increase of membrane conductance. Bottom. Addition of 200 pM signal peptide opened a channel of 200 pS (in 50 mM KCl). From [16].

2.3 Studies of macromolecular transport

The two independent electrophysiological results described above are consistent with the presence of protein-conducting channels for moving proteins across the membrane. There are a number of membranes in the cell that must function as permeability barriers, but must also allow large molecules to selectively cross. We wanted to know if aqueous channels were used more generally as a mechanism for transporting macromolecules and, if so, what is the largest substrate which could cross the membrane through an aqueous channel, while still maintaining the membrane as a permeability barrier.

The model system we examined is the assembly and export of f1 filamentous phage. These exit their *E. coli* host without killing the bacterial cell. Phage are secreted through the outer membrane via a phage-encoded protein, pIV. pIV has sequence homology to proteins in type IV pilus assembly and in transport pathways, including type II and type III secretion systems [17] which mediate the export of folded and assembled oligomeric proteins across the outer membrane of Gram-negative bacteria.

When pIV was purified and reconstituted into planar lipid bilayers, there was initially no indication that it formed channel. One possible interpretation was that pIV did not form an aqueous channel for phage export. Alternatively,

if pIV did form a channel, its opening should be tightly coupled to the export of the filamentous phage. Otherwise, the viability of the *E. coli* would be severely compromised. We reasoned that if we made random mutations in pIV, it should be possible to generate mutations that would still allow phage export, but would result in the channel opening more frequently - at times even uncoupled from the export of phage. Such mutations should be detectable by making the *E. coli* sensitive to environmental stresses such as bile salts, detergents or large hydrophilic antibiotics. We studied one particular mutation (pIVS324G) which was still permissive for phage export. However, this mutation, increased the sensitivity of the *E. coli* to SDS and the hydrophilic antibiotic vancomycin [18]. Both of these assays detect cell death. Thus they may be indicating a channel that may only transiently and infrequently open. However, we were able to demonstrate that the pIVS324G was frequently open because it would allow *E. coli* to live on large maltodextrins (e.g. maltohexose, maltoheptaose) normally unable to permeate through the outer membrane of bacteria [18].

The pIVS324G was then purified and reconstituted into liposomes and fused planar lipid bilayers. Liposomes reconstituted with this protein consistently revealed ion channels of 1.2 nS in 150 mM KCl. While these channels were open at very low voltages, they opened more frequently as the membrane potential was polarized [18]. The channels showed two consistent asymmetries in their behavior. First, they tended to open more often when the voltage on the trans side of the membrane was negative. Second, once a channel was open, it had a greater conductance when the voltage on the trans side was positive.

After we consistently observed channels from the pIVS324G in numerous preparations, we returned to examining the wild-type pIV protein in bilayers. When we increased the membrane polarization, we observed channels opening at $Vm(trans) \sim -120$ mV or $Vm(trans) \sim 180$ mV. These channels had five features in common with the pIVS324G. First, they had the same relative ionic selectivity. Second, they had similar conductance of the open channel. Third, they opened more frequently as the membrane potential was polarized. Fourth, they tended to open more often when the voltage on the trans side of the membrane was negative. Five, once a channel was open, it had a greater conductance when the voltage on the trans side was positive.

The only consistent difference between the pIVwt and pIVS324G was that the mutant protein opened more frequently. This strongly indicated that the channels observed were from the purified pIV rather than a contaminant that co-purified. If the channels were from a contaminant, they should show the same conductance in both preparations. The observation that a point mutation changed a single parameter in the channel behavior - channel gating - strongly implies that the channel is due to pIV. The increased time in the open state

of pIVS324G in planar lipid bilayers was consistent with its effect of making *E. coli* sensitive to vancomycin, or able to grow on large maltodextrins.

Bacteria with type II or III secretion systems include such notorious animal and plant pathogens as Yersinia, Salmonella, Shigella, and Erwinia, all of which express a pIV homologue necessary for secretion or virulence. This is the first direct evidence that pIV and its homologues function as outer membrane channels. Our results demonstrate that opening these channels inappropriately compromises the viability of the host bacteria. This suggests two strategies for fighting these pathogens: drugs that open these channels (thereby compromising the host bacteria) or drugs that lock these channels closed, thereby blocking virulence.

3. What moves proteins across membranes?

If proteins are sitting in an aqueous channel, it begs the question of what is moving the protein across. Many textbooks have presented models which are variations on what I call the "magic fingers" or the "wheels of karma" (see figure 4). These are models which continue to treat proteins as gear boxes with springs rather than polymers made of links of amino acids. The first physical model to try to account for movement proposed that proteins in an aqueous pore were primarily moving by thermal fluctuations. The net direction of movement would be the result of a variety of chemical modifications of the nascent translocating protein. As proteins emerge into the lumen of the endoplasmic reticulum they undergo numerous modifications such as binding to lumenal proteins, forming intra-chain disulfide bonds and modification with a branched chains of sugars (asparagines-linked glycosylation). If, for example, the energetics of the binding of the sugar chains were greater than the energetics of thermal fluctuations, then the nascent protein would be less likely to thermally fluctuate back out into the cytosol. Thus, eventually there would be a net movement into the lumen of the endoplasmic reticulum.

The key issue is whether "eventually" meant that the nascent translocating protein would move into the lumen with a time course fast enough to be of physiological relevance. This was initially tested by modelling the movement of the nascent polypeptide by a series of balls connected with springs. Using either an analytical or numerical simulation, it was found that the nascent chain would move across with a timer course of milliseconds - easily fast enough to account for physiological rates [23].

The first experimental test of the hypothesis came from studies in which the membranes were broken open and depleted of their lumenal contents. Under these conditions, the nascent polypeptides would target to the endoplasmic reticulum, sometimes even have their signal sequences cleaved, but then they

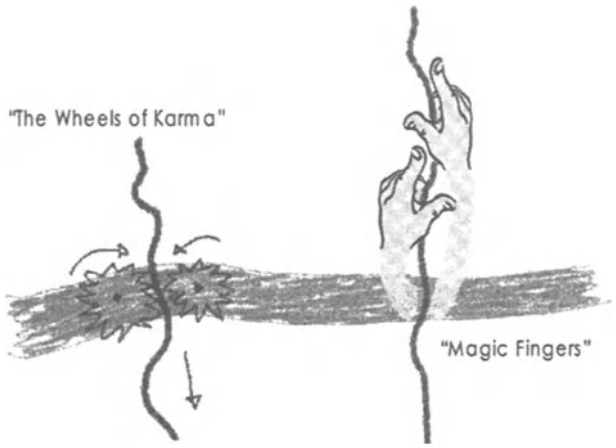

Figure 4. "Tales from the textbooks" Variations on models presented to describe protein translocation.

fell back out. If, on the other hand, the lumenal contents were restored to the vesicle, the directionality of translocation was restored [24].

These results indicated that the directionality of translocation was determined by interactions with components outside the membrane. There are two possible interpretations of these results. On one hand, the lumenal proteins which bind to the nascent chains may be functioning as ratchets. By binding to the nascent chain they block thermal fluctuations of the nascent chains back out of the channel. An alternative model that has been proposed to describe the movement of the nascent translocating chain is that there is an ATP-dependent conformation change that produces a "power-stroke" that pulls the nascent polypeptide across the membrane [25]. There are two independent experimental observations that are cited as consistent for this model. One lumenal component of the endoplasmic reticulum, BiP, was shown to be sufficient to restore the directionality of translocation of pre-pro-alpha factor [26]. BiP is a member of the 70 kD heat-shock protein family of ATPases. Similarly, for the translocation of proteins into mitochondria, a member of the heat-shock protein family of ATPases is required [27,28]. The strongest evidence cited in support of the model comes from the study of a few proteins that are imported into the mitochondria that can, to a limited extent, fold prior to translocating. Since it is generally accepted that a protein must be in a linear "unfolded" conformation to translocate, this implies that the protein must unfold. Calorimetry was used to determine the energy required to completely unfold the protein. The energetics are such that thermal fluc-

tuations are unlikely to ever result in a complete unfolding. Based on this observation it has been argued that a protein could never completely unfold from thermal fluctuations to be able to permeate the protein-conducting channel. However, to initiate translocation, only a fragment of the protein needs to unfold. Once part of the polypeptide is threading across the membrane and bound (ratcheted) inside the organelle, the protein would only need to "unfold" in segments - not all at once. Thus, the amount of energy needed to unfold the entire protein is not relevant. It is already been demonstrated the vast majority of proteins cannot translocate once they have started to fold. The critical question is whether for those rare examples that translocate once they start to fold, what the energetics are to unfold each domain of the protein - not the energetics to unfold the entire molecule.

The notion that BiP in the endoplasmic reticulum is an ATP-dependent motor that pulls the nascent chain across the bilayer is currently the most widely accepted model in the field (other organelles, such as the mitochondria, have their own specific heat-shock type ATPases). However, there are a few problems with this hypothesis. First, BiP is a lumenal protein. It is not clear what BiP could be "pulling" against for moving the nascent chain. Second, BiP only hydrolyzes ATP upon dissociation from the nascent chain. It is not clear how ATP hydrolysis is coupled to mechanical movement. The Brownian ratchet hypothesis requires an energy dependent displacement of the nascent chain to recycle the lumenal proteins to aid in the translocation of subsequence. Finally, it has been recently demonstrated that translocation of a protein can occur if the lumenal contents are replaced with antibodies to the nascent translocating protein [29]. Since antibodies do not undergo an ATP-dependent conformation change, these results indicate that ratcheting of a nascent chain is sufficient for translocation. However, this result only demonstrates that a thermal ratchet is efficient enough to translocate proteins, but not that the lumenal proteins actually function only as ratchets. The result does not rule out the possibility that in situ there are lumenal proteins that facilitate protein translocation through a "power-stroke" – an ATP-dependent conformation change.

There are a number of problems with the experimental tests that have been done so far. Perhaps the primary problem is that all of the studies have been done on proteins that are translocated after they are made - that is, post-translationally. In mammalian systems all known proteins can only cross the endoplasmic reticulum while they are still attached to their biosynthetic ribosome. In yeast, a subset of proteins can go across after they are made - but only if they are maintained in an unfolded state. Experimentally this is done by keeping the protein in 8M urea. However, in the cell it is possible that they translocate across the membrane as they are being synthesized. Similarly, in

mitochondria, many proteins can translocate after they are made if they are maintained in an unfolded, or relatively unfolded state.

Proteins are initially synthesized inside the ribosome by the sequential addition of amino acids at the peptidyl-transferase. The nascent amino acid chain elongates through a narrow tunnel approximately 20 nm long in the large ribosomal subunit [30]. Given the physical constraints of the narrow tunnel in the ribosome, it seems that the nascent polypeptide is maintained in an extended state until it emerges from the ribosome. Thus, the nascent linear polypeptide polymer does not have an opportunity to move in three dimensions until it emerges from the ribosome. Movements of the polypeptide are likely to be strongly influenced by thermal fluctuations. Any thermal fluctuation that allows the nascent chain to move further out of the ribosome, will allow more of the nascent chain to flop and fold in three dimensions. The parts of the protein that have emerged from the ribosome will only very rarely be in a fully extended conformation. Therefore, the nascent chain is unlikely to spontaneously fluctuate back into the pore. The chemical potential gradient that favors the polypeptide moving in three dimensions may be sufficient to account for the nascent chain moving out of the ribosome.

The translocation complex of the endoplasmic reticulum binds to the large ribosomal subunit right at the exit site of the nascent polypeptide [31]. The protein-conducting channel of the endoplasmic reticulum is aligned with the exit site of the 20 nm long tunnel through the large ribosomal subunit. The membrane-bound protein-conducting channel would extend the ribosomal channel by only 4 nm. Thus, when proteins translocate across the membrane as they are being made, the movement of the protein across the membrane may be just an extension of the movement of the protein out of the ribosome. There may be no additional motive force. The various heat-shock protein ATPases may only contribute (either as a ratchet or using a power stroke) for those rare cases of post-translational translocation. Indeed, they may have evolved, and still primarily function as part of an emergency rescue response: In the rare cases where a nascent chain gets stuck while translocating (due to inappropriate folding or ligation to cytosolic factors such as ubiquitin, etc.), the heat-shock proteins bind to and contribute to extracting the translocating chain so that the translocation machinery may be rescued. Thus, they may not contribute to the translocation of most proteins.

For the moment, the mechanism(s) of translocation have not yet been resolved. It remains to be determined if protein movement is solely determined by a ratchet, a power-stroke, or a combination of the two. More careful characterization of each of the models is required to make predictions that can be distinguished experimentally. Part of the limitation is experimental. For example, there is no clean way to measure the speed of polypeptide translocation or the force that would stop it completely.

4. How are membrane proteins targeted to and integrated into the membrane?

Integral membrane proteinsprotein,membrane appear to use the same translocation machinery as secretory proteins. This is based on a number of independent observations. First, secretory proteins and membrane proteins compete with each other for translocation across the endoplasmic reticulum membrane [32]. Second, they both require the signal recognition particle (SRP) for targeting to the endoplasmic reticulum [33]. Indeed, each transmembrane domain of a protein that threads back-and-forth across the bilayer can use SRP to independently target to the endoplasmic reticulum [34]. Third, there are examples in nature that strongly support the hypothesis that a common machinery is used for secretory and membrane proteins. For example, some proteins appear in alternatively spliced forms: one which is secreted and one which has a transmembrane segment at its carboxyl-terminus [35]. Translocation of the amino domains of these proteins occurs before the carboxyl transmembrane segment is synthesized, suggesting that translocation is initiated with a common machinery. Fourth, either translocating secretory or membrane proteins can be cross-linked to a group of proteins that are believed to form the protein-conducting channel (sec61a, sec61b, sec61g) [36,37]. Fifth, mutations in sec61 affect both translocation of secretory proteins and biogenesis of membrane proteins [38]. Finally, reconstitution of the sec61 complex into liposomes is sufficient to either translocate secretory proteins into the lumen of the liposome or integrate nascent membrane proteins with a single transmembrane domain into the lipid bilayer [37,39]. It is not yet known if such a system is sufficient to allow biogenesis of a polytopic membrane protein into a mature functional form.

There is one major difference in the biogenesis of secretory and membrane proteins: the latter do not fully translocate across the membrane. At some point they must stop moving across (perpendicular to the membrane) and partition laterally to integrate their latent transmembrane segments into the hydrocarbon core of the lipid bilayer [15]. Thus, there must be a mechanism by which the translocation machinery "recognizes" a transmembrane segment. Many observations suggest that hydrophobicity alone is not sufficient. First, there are numerous proteins, such as viral fusion proteins, with long hydrophobic stretches that do not embed into the bilayer: They fully translocate across the membrane. The translocation machinery has to ensure that a transmembrane domain is not allowed to fully translocate across and to protect against improperly integrating a wrong domain. Second, when a protein, which is normally integrated in the endoplasmic reticulum membrane is re-targeted (by changing its amino-terminus signal sequence) to the chloroplast, the full protein including its transmembrane domain translocates across

both membranes [40]. When the same protein is targeted to the mitochondria, it crosses the outer membrane and becomes an integral membrane protein of the inner membrane [41]. Thus, there are specific and different signals that are recognized as "stop transfer" signals that allow a domain to move laterally out of the protein-conducting channels and into the hydrocarbon core of the lipid bilayer. This specificity of transmembrane domains for integrating into specific membranes should not perhaps be surprising since: 1) transmembrane segments are signal sequences; 2) signal sequences are specific for translocating certain membranes; 3) when a signal sequence is placed in the interior of a protein it becomes a transmembrane segment [42].

Biogenesis is even further complicated for polytopic membrane proteins - those membrane proteins that cross the bilayer multiple times. These proteins (usually) do not have a cleavable signal sequence at their amino terminus [43]. Instead, the first transmembrane segment functions as the first "signal sequence". Parts of the protein that are on the amino or carboyxl-side of the transmembrane domain are not sufficient to target a reporter protein to the endoplasmic reticulum. However, the transmembrane segment is sufficient to target a reporter protein to the endoplasmic reticulum [34]. Their biogenesis requires at least four discrete steps: 1) targeting to the endoplasmic reticulum membrane; 2) translocating perpendicular to the membrane through protein-conducting channels; 3) folding of the protein; 4) moving the protein parallel to the plane of the membrane out of the protein-conducting channel and integrating into the hydrocarbon core of the lipid bilayer.

It is not known if this is the order in which the steps occur or if the steps are mutually independent. The situation is further complicated by the observation that some transmembrane segments of proteins can embed in the lipid bilayer post-translationally via mechanisms other than via the endoplasmic reticulum-dependent translocation pathway [44, 45].

The rest of this chapter focuses on the biogenesis of polytopic membrane proteins. There are two questions that will be addressed. First, as each latent transmembrane segment is synthesized and emerges from the ribosome, does it sequentially translocate the endoplasmic reticulum to span the bilayer? An alternative hypothesis is that the latent transmembrane segments first accumulate on the cytosolic side as pairs (to form a loop?) or larger aggregates prior to translocating. Second, once a transmembrane segment has translocated into the protein-conducting channels to span the membrane, does it integrate into the bilayer immediately? In an alternative model they would accumulate in the channel until there are pairs of latent transmembrane segments, or larger groups, to integrate into the lipid bilayer.

4.1 Do latent transmembrane segments cross the membrane sequentially, one-at-a-time, as they emerge from the ribosome?

This question was examined by studying the biogenesis of the polytopic membrane protein P-glycoprotein (Pgp). The Pgp was initially identified in tumor cell lines that had been selected for resistance to chemotherapeutics [46–48]. The sequence of Pgp demonstrated homology to a group of membrane-transporters referred to as the ATP-binding cassette proteins. Pgp has both its amino and carboxyl-termini on the cytosolic side of the membrane. Analysis of the sequence together with mapping of glycosylation sites suggested that the protein had six transmembrane domains followed by a large cytoplasmic loop with an ATP-binding site, six additional transmembrane domains and then a final cytoplasmic domain with a second ATP-binding site [49, 50]. This structure is similar to what has been proposed for other members of the ATP-binding cassette family.

4.2 Philosophy of approach: trapping intermediates in translation and translocation.

Biogenesis of membrane proteins is a transient event that involves the synthesis of the nascent protein, its movement across the membrane (translocation), its folding, and its subsequent movement into the lipid bilayer (integration). More than one of these events may occur at the same time. Our experimental strategy has been to catch "snapshots" of a membrane protein (in this case Pgp) in incremental steps of biosynthesis and to analyze how of much of the molecule has bound SRP, targeted to the endoplasmic reticulum, translocated, folded, and integrated into the bilayer. Pgp is trapped at defined points in its synthesis by using mRNA that is truncated within the coding region without a termination codon. When the ribosome reaches the end of the mRNA, protein synthesis terminates with the nascent polypeptide chain attached to a tRNA and hanging onto the ribosome. In the absence of a termination codon, and under carefully controlled conditions, translation is frozen at this step with the nascent Pgp still covalently attached by its carboxyl-termimus amino acid to the tRNA and bound to its biosynthetic ribosome. This traps Pgp as both a true translation and, as shown below, as a true translocation intermediate. This technique requires a method that ensures the maintenance of the bond between the last amino acid and its tRNA. If the tRNA bond is broken, it is no longer an intermediate, but merely a side-reaction. Therefore a major part of the experimental technique is the optimization of translation under conditions that are compatible with maintaining this bond, both during the in vitro reactions and subsequent analysis.

4.2.1 The importance of using true intermediates in protein synthesis and translocation. In all of our work we emphasize the importance of examining Pgp during biogenesis – specifically examining nascent Pgp that is still attached by its carboxyl-terminus amino acid to a tRNA and its biosynthetic ribosome. We believe that examining this kind of Pgp arrested in translation is important for understanding Pgp biogenesis.

The following is one example to support this point (data later in this chapter will provide further support). The first example is from some current work we are doing with opsin. Opsin has been synthesized as a peptide that terminates (with a termination codon) 30 amino acids after the first transmembrane segment. This shortened opsin was properly targeted to the endoplasmic reticulum and integrated into the lipid bilayer. However, its topology was reversed from normal: its amino terminus faced the cytosol. When we synthesized the same peptide but kept it attached to its biosynthetic ribosome, it was targeted to the endoplasmic reticulum and, similarly to native opsin, translocated its amino terminus across the endoplasmic reticulum with 100% efficiency.

4.2.2 Evidence for true translation intermediates. Three criteria are used to test our translations to ensure that the nascent Pgp is a true intermediate in translation. 1) Is the Pgp still attached to its carboxyl-terminus tRNA? If the tRNA is still attached, the nascent peptide will migrate slower on SDS-PAGE as if it is 25 kD heavier. 2) Is the Pgp still bound to the ribosome? This is tested by co-migration with the ribosome in a sucrose gradient. 3) Is the nascent Pgp still at the peptidyl-transferase site in the ribosome? This is tested by adding puromycin which releases nascent Pgp from its tRNA only when the Pgp is still attached to the proper site in the ribosome. When mRNA for Pgp that was truncated after the first transmembrane segment was synthesized, there was a translation product at 10 kD (the expected MW) and 32 kD (figure 5, lane 1). The addition of puromycin at the end of the translation shifts much of the 32 kD translation product to 10 kD. This shows that the band of greater apparent MW was the tRNA bound nascent Pgp. The sensitivity of this band to puromycin shows that it is still bound to the ribosome at the peptidyl-transferase. When these translation reactions are solubilized and separated on a sucrose gradient the nascent polypeptide migrates with the ribosome [51].

4.2.3 Evidence for true translocation intermediates. Two criteria are used to determine whether an intermediate in translation is also an intermediate in translocation. First, do the translation intermediates harvest with the membranes under conditions that discriminate polysomes from membranes? Second, has the translation intermediate been modified by enzymes that are restricted to the lumen of the endoplasmic reticulum such as the oligosaccha-

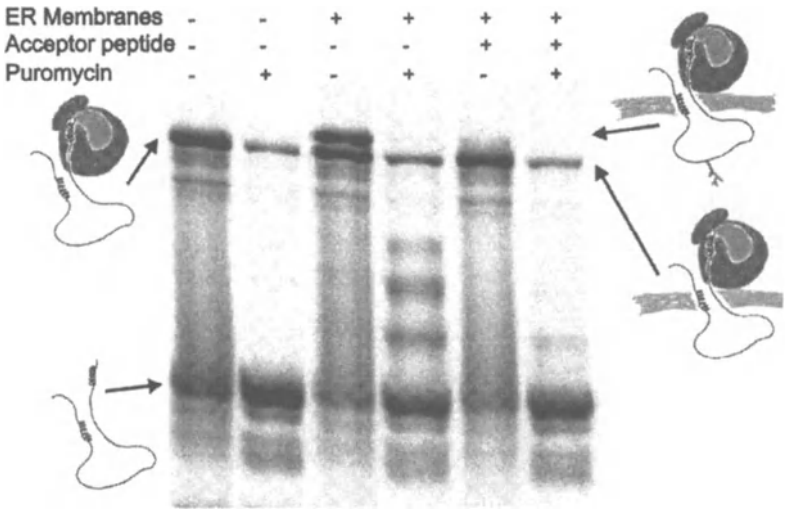

Figure 5. Protein synthesized from mRNA truncated after the 1st transmembrane segment of Pgp is still attached to its tRNA (gray tear drop) and ribosome (dark gray). The tRNA bound-Pgp is a lower moving (higher band) on SDS-PAGE (lane 1). The Pgp is released from its tRNA by puromycin demonstrating that it is still attached to its biosynthetic ribosome (lane 2). This truncated Pgp protein can translocate across the endoplasmic reticulum (as measured by glycosylation, the higher MW band in lane 3). This glycosylated band decreases in the presence of an acceptor peptide (lanes 5, 6) which is a competitive inhibitor of glycosylation. From Borel and Simon [52]. The cartoons adjacent to the gel illustrate the interpretation: The membrane is the horizontal gray line, the tRNA is a gray tear drop, the ribosome is in dark gray and glycosylation on a nascent peptide is illustrated as a branching structure.

ryltransferase which adds sugars onto asparagines? Nascent Pgp that can be shown to be asparagine-linked glycosylated, still bound to its tRNA, migrating with ribosome in sucrose gradients, and can be released from its tRNA with puromycin is judged to be a true intermediate in Pgp biogenesis.

When translation intermediates of Pgp were synthesized in the presence of endoplasmic reticulum one additional protein band was observed that migrated slightly slower than the tRNA-conjugated Pgp (figure 5, lane 3). If this reaction was repeated in the presence of a tripeptide (NYT) that inhibits asparagine linked glycosylation, then this band was not present (lane 5). Thus this slower moving band was the glycosylated Pgp bound to a tRNA. This protein was still bound to its biosynthetic ribosome because it could still be released by puromycin (lanes 4 and 6). Thus, this is a true intermediate in translocation: It has been modified by the oligosaccharyltransferase in the lumen of the endoplasmic reticulum and it is still attached to its biosynthetic ribosome in the cytosol.

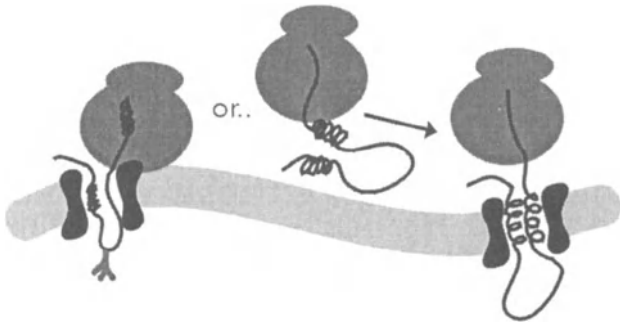

Figure 6. Schematic of experiment to determine if the 1st transmembrane segment of Pgp translocates across the membrane prior to the 2nd transmembrane segment. The mRNA was truncated at a point where the 2nd transmembrane segment is still in the ribosome. Whether the first transmembrane segment had translocated the endoplasmic reticulum was tested by assaying for glycosylation (addition of branched structure, bottom of loop segment).

4.3 When during synthesis does the first transmembrane segment of P-glycoprotein translocate across the endoplasmic reticulum membrane?

We have examined when the first transmembrane segment of Pgp translocates across the membrane [51]. Specifically, we have asked if the first transmembrane domain translocates as soon as it emerges from the ribosome, or if it first accumulates in the cytosol and translocates only after the second transmembrane segment is synthesized. This was tested by synthesizing Pgp from an mRNA truncated in the coding region such that the second transmembrane segment has not yet been synthesized. Then the Pgp was assayed to determine if the first transmembrane segment had translocated across the membrane (see figure 6). To assay translocation, we looked for an asparagine-linked glycosylation of the loop between the first and second transmembrane segments. (This oligosaccharyltransferase glycosylates on Asp/X/Thr-Ser and it is only localized in the lumen of the endoplasmic reticulum – a very reliable assay for translocation).

When the truncated mRNA was translated in the absence of endoplasmic reticulum membranes (Figure 5 lane 1), two bands are seen: A peptide at the expected molecular weight for the shortened protein and a higher molecular weight band which is the nascent peptide bound to its carboxyl-terminus tRNA. When this sample was treated with puromycin (lane 2) the upper band disappeared. This observation confirms that the upper band was the nascent chain bound to its tRNA and that it was still attached to its biosynthetic ribosome adjacent to the peptidyl-transferase (only this enzyme can

add puromycin to release a tRNA bound-nascent peptide). When this same construct was synthesized in the presence of membranes from the endoplasmic reticulum (lane 3), a higher molecular weight band was seen. This is consistent with glycosylation of the loop between the first and second transmembrane segments. This higher molecular weight peptide was not present when the translation mix includes a tripeptide, Asn-Tyr-Thr (a competitive inhibitor of asparagine linked glycosylation, lane 5). This confirms that the loop between the first and second transmembrane segments had translocated across the bilayer. Thus, the first transmembrane segment can span the lipid bilayer prior to emergence of the second transmembrane segment from the ribosome: their translocation is sequential.

4.4 When during the synthesis do the transmembrane segments integrate into the lipid bilayer?

The results of the preceding sections show that the first transmembrane segment of Pgp spans the lipid bilayer before the second transmembrane segment has emerged from the ribosome. However, has this first transmembrane domain integrated into the lipid bilayer or is it still sitting in the aqueous protein-conducting channel of the translocation machinery? Two different assays were used to determine if a transmembrane segment had integrated into the lipid bilayer. First, was the transmembrane segment labeled by hydrophobic probes from within the lipid bilayer? Second, could the latent transmembrane domain be extracted from the membrane without detergents?

4.4.1 Proteins with a single transmembrane segment. The first assay to examine when transmembrane segments integrate into the lipid bilayer used a hydrophobic molecule, (Trifluoromethyl)-3-(m-[I125]iodophenyl) diazirine ([I125]TID) [53] which, upon photoactivation, binds to any amide bond. TID has been used to map conformational changes in the transmembrane domains of the ACh receptor amongst other membrane proteins [54,55].

In preliminary experiments we tested the utility of TID to assay when during biogenesis the transmembrane domains are accessible to the hydrocarbon core of the lipid bilayer [9]. TID labelling of membrane proteins was tested with a protein that has a single transmembrane segment: the vesicular stomatitus virus glycoprotein (VSV Gprotein). Full-length VSV Gprotein is labelled in its transmembrane segment by membrane-embedded TID (Figure 7 middle lane). A construct of the VSV Gprotein which was truncated after its transmembrane segment and synthesized in the presence of rough microsomes could not be labelled by membrane-bound [I125]TID (Figure 7, left lane). A parallel sample of truncated VSV Gprotein was treated with puromycin prior to photoactivation of the [I125]TID. The same truncated construct, released

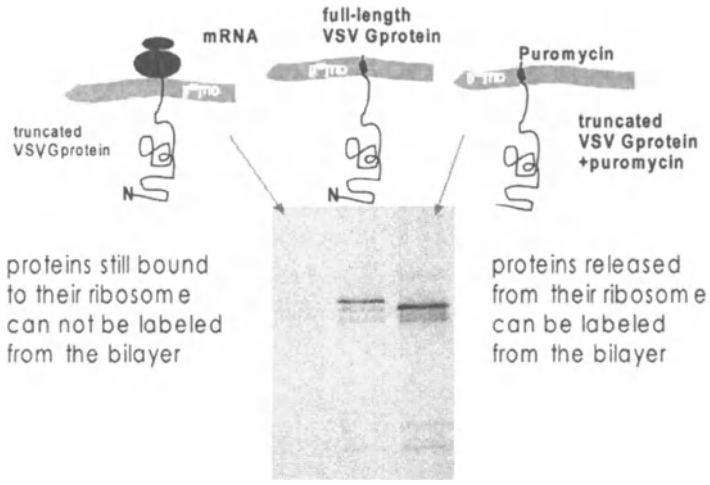

Figure 7. A protein with a single transmembrane segment cannot be labelled from within the lipid bilayer during synthesis. From [9].

from the ribosome so its transmembrane domain could interact with the bilayer, became labelled with [I125]TID (right lane). This indicates that the transmembrane domain in the truncated protein had neither reached nor embedded in the bilayer. The addition of puromycin demonstrated there was enough VSV Gprotein synthesized that, if it were in contact with the lipid domain, it would be labelled with [I125]TID. The puromycin control also indicated that the transmembrane domain could still embed in the bilayer. That is, it was no longer extracted from the membrane with NaOH, urea or Na2CO3 and it could be labelled from within the lipid domain.

This technique requires immunoprecipitation of the protein after photolabeling. Unfortunately, many immunoprecipitation conditions also hydrolyze the tRNA-peptide bond. We are currently working on trying to optimise these conditions for Pgp that will leave the tRNA-peptide bond intact.

4.4.2 When do the transmembrane domains of P-glycoprotein integrate into the lipid bilayer?. If a protein can only be extracted from membranes by solubilization with detergents, the protein is operationally defined as being integrated into the lipid bilayer. Most extractions use base, either hydroxide or carbonate, at pH 11. Unfortunately, base hydrolyzes the bond between the nascent Pgp and its tRNA. Thus, we used urea to test if nascent transmembrane Pgp was integrated into the lipid bilayer. Upon treatment with 4.5 M urea, secretory proteins fractionate away from the membranes and in-

tegral membrane proteins continue to harvest with the membranes (Figure 8, left).

To test whether an arrested truncated Pgp is integrated in the membrane, it is first synthesised in the presence of endoplasmic reticulum vesicles. These vesicles are then harvested. This ensures that we are examining only proteins that have been successfully targeted to the endoplasmic reticulum. The harvested membranes are treated with urea and then the membranes are re-harvested. We measure extraction only for tRNA-conjugated protein.

When such a tRNA-ribosome-bound nascent Pgp was tested with urea, this intermediate in biogenesis was almost (but not totally) extracted from the membrane (Figure 8) [52]. In contrast, upon treating the nascent chain with puromycin to release it from its tRNA, the nascent protein integrated into the lipid bilayer and could no longer be extracted with urea.

Nascent translation-translocation intermediates of Pgp including up to five transmembrane domains were tested [51]. In all cases, the intermediate in biogenesis was predominantly extracted from the membrane and the nascent chain, and upon release from its biosynthetic ribosome, was fully integrated into the lipid bilayer.

There are two observations to note. First, the arrested protein does not fractionate as a membrane protein until it is released from the ribosome. This indicates that the transmembrane segments of translocating polypeptide do not integrate into the lipid bilayer until the nascent chain is released from the ribosome. Second, a translocating membrane protein extracts as neither a secretory protein nor a membrane protein, but as something in between.

Most transmembrane domains have two distinctive characteristics: a stretch of hydrophobic amino acids and charges on either side (see Figure 9). The intermediates in translocation did not fully extract from the membrane. We wondered whether they were being stabilized with the membrane via hydrophobic interactions (with lipids or the transmembrane segments of other proteins) or whether they were being stabilized via electrostatic interactions. These two hypotheses can be distinguished by varying the salt concentration. The previously described extractions were done in physiological salt ($\sim$ 150 mM). If the translocation intermediates were stabilized by electrostatic interactions, they would be de-stabilized at higher salt concentrations (facilitating extraction) and stabilized at lower concentrations (decreasing extraction from the membrane). In contrast, a hydrophobic interaction would be stabilized at higher salt concentrations (decreasing extraction from the membrane) and de-stabilized at lower salt concentrations (favoring extraction) as shown in Figure 9.

The concentration of salt in the urea buffer had no effect on the extraction of control membrane proteins or control secretory proteins [51]. However, raising the salt substantially increased the extraction of the nascent translo-

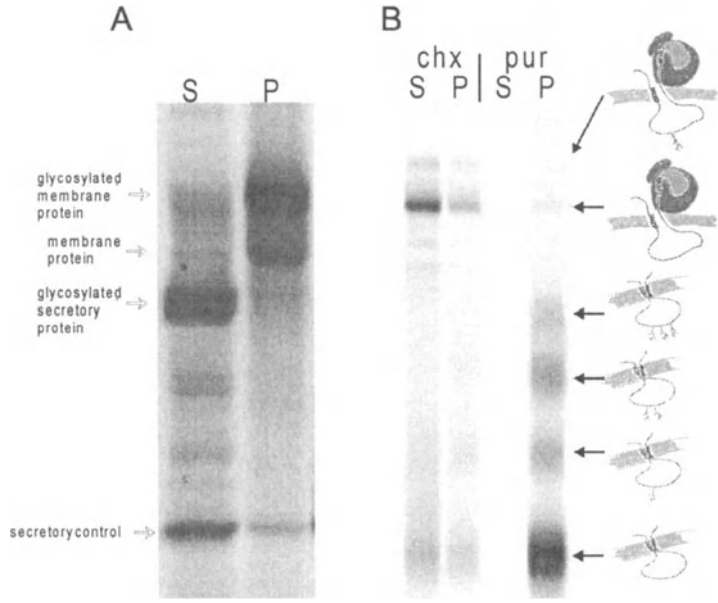

Figure 8. Urea extractions. Left. After treatment with 4.5 M urea, membrane proteins remain with the membranes (M) and secretory proteins are extracted into the cytosol (C). Right. Translocation intermediates that are still associated with their tRNA are extracted from the membrane (C). Nascent peptides that are explicitly released from their ribosomes with puromycin remain with the membranes (M). From Borel and Simon 1996 [51]. The cartoons at the right characterize the results. The nascent Pgp is the black line, the membrane is the horizontal gray line and the tRNA is the gray tear-drop shape. Glycosylation is indicated by a branched structure on the nascent Pgp.

cation intermediates. Lowering the salt decreased the extraction (Figure 10). Similar results have been observed on a large number of different translocation intermediates [51]. These results demonstrate that the nascent translocation intermediates are in a salt accessible, and thus aqueous, compartment. These results are consistent with the photochemical cross-linking that indicates that the nascent intermediates in the biogenesis of membrane proteins are not integrated in the hydrocarbon core of the lipid bilayer. Further, the results indicate that these intermediates in biogenesis are being stabilized via electrostatic interactions, which would leave the transmembrane domains of a protein available to fold amongst themselves.

4.4.3 Summary of integration. These results with the urea extraction and TID labelling have two significant conclusions. First, nascent translocat-

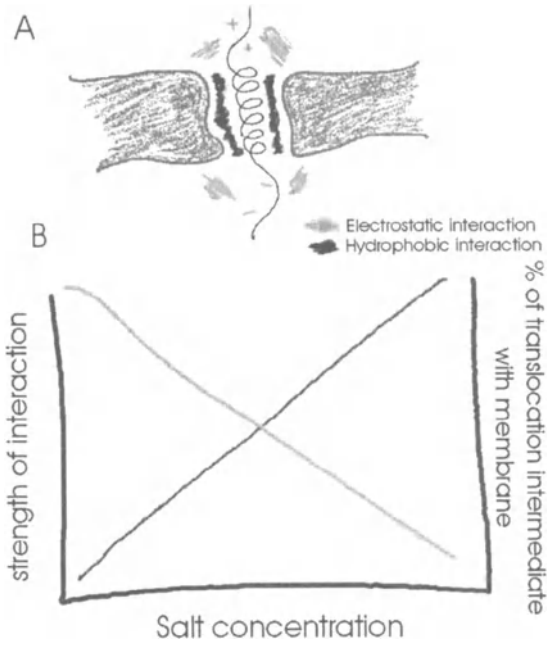

Figure 9. Increasing the salt concentration destabilizes electro-static interactions and strengthens hydrophobic inter-actions. If the translocation intermediates are stabilized with the membrane by electrostatic interactions, then increasing the salt should decrease the number remaining with the membranes. If they are stabilized by hydrophobic interactions, then increasing the salt concentration would increase the tRNA bound intermediates staying with the membrane.

ing chains are not in contact with the hydrocarbon core of the lipid bilayer. This both confirms our electrophysiological recordings, indicating an aqueous protein-conducting channel [15, 16], and enlarges upon them, by demonstrating that the pore is completely insulated from the lipid. Second, we can synthesize a protein such that its transmembrane domain is competent to partition into the bilayer, although it cannot do so until released from the ribosome. The arrested protein fractionates as a transmembrane protein only after it is released from the ribosome. Before the arrested protein is released from the ribosome it is easily extracted from the membrane. This indicates that the transmembrane segments of translocating polypeptides do not integrate into the lipid bilayer until the nascent chain is released from the ribosome.

There are potential reasons for not integrating the protein in the lipid until it is released from the ribosome. There are occasionally charged groups in one transmembrane segment that are salt bridged to charge groups in other transmembrane segments. Each transmembrane segment by itself might not

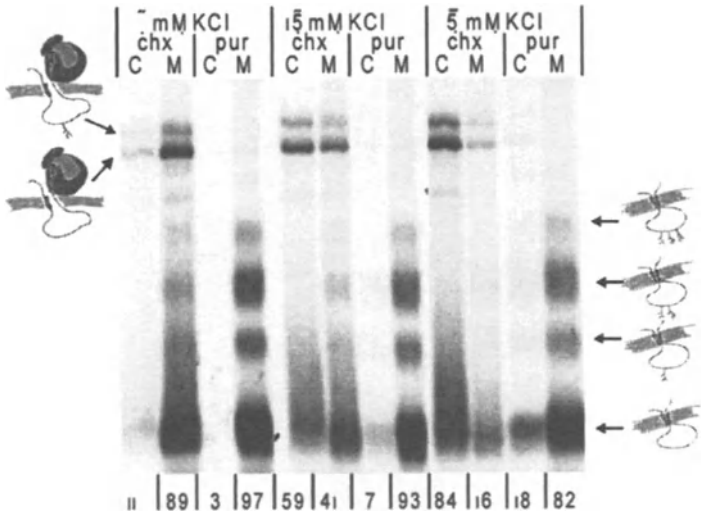

Figure 10. The effect of salt on urea extraction of translocation intermediates of Pgp. In physiological salt 59% of the tRNA bound Pgp is extracted into the cytosol C and away from the Membrane M. Raising the salt extracts 85% of these translocation intermediates and lowering the salt decreases the extraction to 11%. The cartoons illustrate the bands on the gel: the membrane is a horizontal gray line, the ribosome is dark gray, the tRNA is the gray tear-drop shape and glycosylation is indicated by the branched structure.

be particularly stable in the lipid bilayer. It is advantageous to have all of the transmembrane segments folded in their final orientation prior to partitioning into the lipid phase. Indeed, studies of the T-cell receptor have demonstrated that charge substitutions in these domains can lead to endoplasmic reticulum retention and significantly lowered levels of properly inserted membrane proteins [56]. There is no signal that we know of by which the translocation machinery can tell if a particular transmembrane segment is the final transmembrane segment of a protein. However, translation is over once the nascent chain is released from the ribosome. Thus, if the translocation machinery holds nascent chains until the ribosome dissociates from the endoplasmic reticulum membrane, the protein can self-assemble prior to partitioning into the lipid phase. While this explanation is just conjecture at this point, it is consistent with a totally independent electrophysiological experiment. When translocating polypeptides are prematurely released from their ribosomes with puromycin under conditions where the ribosome remains bound to the membrane, the transmembrane protein-conducting channels remain open [15]. Upon dissociation of ribosomes from the membrane, the channels close. This supports an interaction between the ribosome and the opening/closing of the translocating protein-conducting channels.

References

[1] Palade, G.E. (1975) Intracellular aspects of the process of protein secretion. *Science* **189**, 347-358.

[2] Walter, P. and Blobel, G. (1981) Translocation of proteins across the endoplasmic reticulum III. Signal recognition protein (SRP) causes signal sequence-dependent and site-specific arrest of chain elongation that is released by microsomal membranes. *J. Cell Biol.* **91**, 557-561.

[3] Gilmore, R., Walter, P., and Blobel, G. (1982) Protein translocation across the endoplasmic reticulum. II. Isolation and characterization of the signal recognition particle receptor. *J. Cell Biol.* **95**, 470-477.

[4] Connolly, T. and Gilmore, R. (1989) The signal recognition particle receptor mediates the GTP- dependent displacement of SRP from the signal sequence of the nascent polypeptide. *Cell* **57**, 599-610.

[5] Connolly, T., Rapiejko, P.J. and Gilmore, R. (1991) Requirement of GTP hydrolysis for dissociation of the signal recognition particle from its receptor. *Science* **252**, 1171-1173.

[6] Blobel, G. and Sabatini, D.D. (1971) Ribosome-membrane interaction in eukaryotic cells. In *Biomembranes 2*, Manson, L.A. ed. (New York: Plenum), pp. 193-195.

[7] Blobel, G. and Dobberstein, B. (1975) Transfer of proteins across membranes. II. Reconstitution of functional rough microsomes from heterologous components. *J. Cell Biol.* **67**, 852-862.

[8] Engelman, D.M. and Steitz, T.A. (1981) The spontaneous insertion of proteins into and across membranes: the helical hairpin hypothesis. *Cell* **23**, 411-422.

[9] Simon, S.M. (1995) Protein-conducting channels for the translocation of proteins into and across membranes. *Cold Spring Harbor Symposia on Quantitative Biology* **60**, 57-69.

[10] Simon, S.M., Blobel, G. and Zimmerberg, J. (1989) Large aqueous channels in membrane vesicles derived from the rough endoplasmic reticulum of canine pancreas or the plasma membrane of *Escherichia coli*. *Proc. Natl. Acad. Sci. (USA)* **86**, 6176-6180.

[11] Zagotta, W.N., Hoshi, T., and Aldrich, R.W. (1990) Restoration of inactivation in mutants of Shaker potassium channels by a peptide derived from ShB. *Science* **250**, 568-571.

[12] Traut, R.R. and Monro, R.E. (1964) The puromycin reaction and its relation to protein synthesis. *J. Mol. Biol.* **10**, 63-72.

[13] Redman, C.M. and Sabatini, D.D. (1966) Vectorial discharge of peptides released by puromycin from attached ribosomes. *Proc. Natl. Acad. Sci. (USA)* **56**, 608-615.

[14] Adelman, M.R., Sabatini, D.D. and Blobel, G. (1973) Ribosome-membrane interaction. Nondestructive disassembly of rat liver rough microsomes into ribosomal and membranous components. *J. Cell Biol.* **56**, 206-229.

[15] Simon, S.M. and Blobel, G. (1991) A protein-conducting channel in the endoplasmic reticulum. *Cell* **65**, 371-380.

[16] Simon, S.M. and Blobel, G. (1992) Signal peptides open protein-conducting channels in *E. coli*. *Cell* **69**, 677-684.

[17] Russel, M. (1998) Macromolecular assembly and secretion across the bacterial cell envelope: type II protein secretion systems. *J. Mol. Biol.* **279**, 485-499.

[18] Marciano, D., Russel, M., and Simon, S.M. (1999) An aqueous channel for filamentous phage export. *Science* **284**, 1516-1519.

[19] Künkele, K.P., Heins, S., Dembowski, M., Nargang, F.E., Benz, R., Thieffry, M., Walz, J., Lill, R., Nussberger, S. and Neupert, W. (1998) The preprotein translocation channel of the outer membrane of mitochondria. *Cell* **93**, 1009-1019.

[20] Ahting, U., Thun, C., Hegerl, R., Typke, D., Nargang, F.E., Neupert, W. and Nussberger, S. (1999) The TOM core complex: the general protein import pore of the outer membrane of mitochondria. *J. Cell Biol.* **147**, 959-968.

[21] Bulychev, A., Pilon, M., Dassen, H., Van 't Hof, R., Vredenberg, W. and De Kruijff, B. (1994) Precursor-mediated opening of translocation pores in chloroplast envelopes. *FEBS Lett.* **356**, 204-206.

[22] Crowley, K.S., Liao, S., Worrell, V.E., Reinhart, G.D. and Johnson,A.E. (1994) Secretory proteins move through the endoplasmic reticulum membrane via an aqueous, gated pore. *Cell* **78**, 461-471.

[23] Simon, S.M., Peskin, C.S., and Oster, G.F. (1992) What drives the translocation of proteins? *Proc. Natl. Acad. Sci. (USA)* **89**, 3770-3774.

[24] Nicchitta, C.V. and Blobel, G. (1993) Lumenal proteins of the mammalian endoplasmic reticulum are required to complete protein translocation. *Cell* **73**, 989-998.

[25] Glick, B.S. (1995) Can Hsp70 proteins act as force-generating motors? *Cell* **80**, 11-14.

[26] Brodsky, J.L., Hamamoto, S., Feldheim, D. and Schekman, R. (1993) Reconstitution of protein translocation from solubilized yeast membranes reveals topologically distinct roles for BiP and cytosolic Hsc70. *J. Cell Biol.* **120**, 95-102.

[27] Schneider, H.-C., Berthold, J., Bauer, M.F., Dietmeier, K., Guiard, B., Brunner, M. and Neupert, W. (1994) Mitochondrial Hsp70/MIM44 complex facilitates protein import. *Nature (London)* **371**, 768-774.

[28] Ungermann, C., Neupert, W. and Cyr, D.M. (1994) The role of Hsp70 in conferring unidirectionality on protein translocation into mitochondria. *Science* **266**, 1250-1253.

[29] Matlack, K.E., Misselwitz, B., Plath, K. and Rapoport, T.A. (1999) BiP acts as a molecular ratchet during posttranslational transport of prepro-alpha factor across the ER membrane. *Cell* **97**, 553-564.

[30] Bernabeu, C. and Lake, J.A. (1982) Nascent polypeptide chains emerge from the exit domain of the large ribosomal subunit: immune mapping of the nascent chain. *Proc. Natl. Acad. Sci. (USA)* **79**, 3111-3115.

[31] Beckmann, R., Bubeck, D., Grassucci, R., Penczek, P., Verschoor, A., Blobel, G. and Frank, J. (1997) Alignment of conduits for the nascent polypeptide chain in the ribosome-Sec61 complex. *Science* **278**, 2123-2126.

[32] Lingappa, V.R., Katz, F.N., Lodish, H.F. and Blobel, G. (1978) A signal sequence for the insertion of a transmembrane glycoprotein. Similarities to the signals of secretory proteins in primary structure and function. *J. Biol. Chem.* **253**, 8667-8670.

[33] Anderson, D.J., Walter, P. and Blobel, G. (1982) Signal recognition protein is required for the integration of acetylcholine receptor delta subunit, a transmembrane glycoprotein into the endoplasmic reticulum membrane. *J. Cell Biol.* **93**, 501-506.

[34] Friedlander, M. and Blobel, G. (1985) Bovine opsin has more than one signal sequence. *Nature (London)* **318**, 338-343.

[35] McCune, J.M., Lingappa, V.R., Fu, S.M., Blobel, G. and Kunkel, H.G. (1980) Biogenesis of membrane-bound and secreted immunoglobulins. I. Two distinct translation products of human mu-chain, with identical N- termini and different C-termini. *J. Exp. Med.* **152**, 463-468.

[36] High, S., Andersen, S.S.L., Görlich, D., Hartmann, E., Prehn,S., Rapoport,T.A. and Dobberstein, B. (1993) Sec61p is adjacent to nascent type I and type II signal- anchor proteins during their membrane insertion. *J. Cell Biol.* **121**, 743-750.

[37] Oliver, J., Jungnickel, B., Görlich,D., Rapoport,T. and High, S. (1995) The Sec61 complex is essential for the insertion of proteins into the membrane of the endoplasmic reticulum. *FEBS Letters* **362**, 126-130.

[38] Stirling, C.J., Rothblatt, J., Hosobuchi, M., Deshaies,R. and Schekman, R. (1992) Protein translocation mutants defective in the insertion of integral membrane proteins into the endoplasmic reticulum. *Mol. Biol. Cell* **3**, 129-142.

[39] Görlich, D. and Rapoport, T.A. (1993) Protein translocation into proteoliposomes reconstituted from purified components of the endoplasmic reticulum membrane. *Cell* **75**, 615-630.

[40] Lubben, T.H., Bansberg, J. and Keegstra, K. (1987) Stop-transfer regions do not halt translocation of proteins into chloroplasts. *Science* **238**, 1112-1114.

[41] Nguyen, M. and Shore, G.C. (1987) Import of hybrid vesicular stomatitis G protein to the mitochondrial inner membrane. *J. Biol. Chem.* **262**, 3929-3931.

[42] Wessels, H.P. and Spiess, M. (1988) Insertion of a multispanning membrane protein occurs sequentially and requires only one signal sequence. *Cell* **55**, 61-70.

[43] Mostov, K.E., DeFoor, P., Fleischer, S. and Blobel, G. (1981) Co-translational membrane integration of calcium pump protein without signal sequence cleavage. *Nature (London)* **292**, 87-88.

[44] Simon, S.M. (1994) Ion channels: Enter the 'swinging gate'. *Nature (London)* **371**, 103-104.

[45] Slatin, S.L., Qiu, X.Q., Jakes, K.S., and Finkelstein, A. (1994) Identification of a translocated protein segment in a voltage- dependent channel. *Nature (London)* **371**, 158-161.

[46] Biedler, J.L. and Riehm, H. (1970) Cellular resistance to actinomycin D in Chinese hamster cells in vitro: cross-resistance, radioautographic, and cytogenetic studies. *Cancer Res.* **30**, 1174-1184.

[47] Biedler, J.L., Riehm, H., Peterson, R.H. and Spengler, B.A. (1975) Membrane-mediated drug resistance and phenotypic reversion to normal growth behavior of Chinese hamster cells. *J. Natl. Canc. Inst.* **55**, 671-680.

[48] Ling, V. (1975) Drug resistance and membrane alteration in mutants of mammalian cells. *Can. J. Genet. Cytol.* **17**, 503-515.

[49] Chen, C.J., Chin, J.E., Ueda, K., Clark, D.P., Pastan, I., Gottesman, M.M. and Roninson, I.B. (1986) Internal duplication and homology with bacterial transport proteins in the mdr1 (P-glycoprotein) gene from multidrug- resistant human cells. *Cell* **47**, 381-389.

[50] Gerlach, J.H., Endicott, J.A., Juranka, P.F., Henderson, G., Sarangi, F., Deuchars, K.L., and Ling, V. (1986) Homology between P-glycoprotein and a bacterial haemolysin transport protein suggests a model for multidrug resistance. *Nature (London)* **324**, 485-489.

[51] Borel, A.C. and Simon, S.M. (1996) Biogenesis of Polytopic Membrane Proteins: Membrane segments of P-glycoprotein sequentially translocate to span the ER membrane. *Biochemistry* **35**, 10587-10594.

[52] Borel, A.C. and Simon, S.M. (1996) Biogenesis of polytopic membrane proteins: membrane segments assemble within translocation channels prior to membrane integration. *Cell* **85**, 379-389.

[53] Brunner, J. and Semenza, G. (1981) Selective labeling of the hydrophobic core of membranes with 3- (trifluoromethyl)-3-(m-[125I]iodophenyl)diazirine, a carbene- generating reagent. *Biochemistry* **20**, 7174-7182.

[54] White, B.H. and Cohen, J.B. (1988) Photolabeling of membrane-bound Torpedo nicotinic acetylcholine receptor with the hydrophobic probe 3-trifluoromethyl-3-(m-[125I]iodophenyl)diazirine. *Biochemistry* **27**, 8741-8751.

[55] White, B.H. and Cohen, J.B. (1992) Agonist-induced changes in the structure of the acetylcholine receptor M2 regions revealed by photoincorporation of an uncharged nicotinic noncompetitive antagonist. *J. Biol. Chem.* **267**, 15770-15783.

[56] Cosson, P., Lankford, S.P., Bonifacino, J.S. and Klausner, R.D. (1991) Membrane protein association by potential intramembrane charge pairs [see comments]. *Nature (London)* **351**, 414-416.

PROTEIN TRANSLOCATION ACROSS THE OUTER MEMBRANE OF MITOCHONDRIA

Structure and function of the TOM complex of Neurospora crassa

Stephan Nussberger and Walter Neupert
Institute of Physiological Chemistry, University of Munich, Goethestraße 33, D-80336 München, Germany

Abstract Transport of nuclear encoded proteins into mitochondria is mediated by distinct translocation machinery in the outer and inner mitochondrial membranes. At the outer membrane, import is facilitated by a multi-subunit complex called TOM. The role of individual TOM components in recognition and translocation of pre-proteins will be discussed. Specific characteristics of the protein-conducting channel and the three-dimensional structure of the TOM complex isolated from *Neurospora crassa* and determined by electron microscopy are described.

Keywords: electron microscopy, electron tomography, electrophysiology, mitochondrial outer membrane, molecular ratchet, *Neurospora crassa*, protein import, protein translocation, protein-conducting channel, TIM complex, TOM complex

1. Introduction

Transport of a "chain of amino acid beads" across biological membranes plays a central role in a multitude of cellular processes. Prominent examples are the protein secretion pathways of bacteria as well as the movement of proteins across membranes of eukaryotic organelles such as the endoplasmic reticulum, chloroplast and mitochondria. These processes require a series of proteins which (a) recognize the polypeptide to be translocated, (b) keep its conformation in a translocation-competent form and (c) facilitate the actual translocation across the membranes. In recent years, considerable progress was made as numerous components involved in the targeting, insertion and translocation of proteins into mitochondria were identified [1–3]. Genetic and biochemical studies in *Saccharomyces cerevisiae* and *Neurospora crassa* shed light on the molecular properties and cellular roles of these proteins and the mechanism of the transport of preproteins into different mitochondrial subcompartments. Recently, studies on protein translocation into mitochondria

J.J. Kasianowicz et al. (eds.), Structure and Dynamics of Confined Polymers, 67–84.

took another twist when the translocation machinery of the outer membrane of mitochondria (TOM complex) was isolated. The availability of purified TOM complex opened new ways of analyzing the structure and function of this protein-transport system.

The focus of this chapter is on the recent insights into the molecular structure of the TOM complex. We discuss the isolation of the TOM complex from the filamentous fungus *Neurospora crassa* and the specific characteristics of the protein-conducting channel. We address its electrophysiological properties and the structural role of the individual components. We also review recent advances in characterizing the structure of the TOM complex by electron tomography. Negative-staining electron microscopy of isolated TOM complex revealed particles with one, two and three apparent pores of 25 Å. The pore size is similar to the protein-conducting channel of the endoplasmic reticulum [4] indicating that substrate proteins would have to be in an, at least partially, unfolded conformation in order to penetrate the pore. While most preproteins traverse the outer membrane of mitochondria as extended chains, it is intriguing that in bacteria exoproteins engaging the outer membrane export apparatus are fully folded. From a mechanistic perspective, a comparison of the TOM complex with bacterial protein-secretion systems and the protein-conducting channel of the endoplasmic reticulum is quite interesting (see the chapter by Simon, this volume). Recent advances associated with the protein translocation across the mitochondrial inner membrane are beyond the scope of this review and are discussed elsewhere [5]. Certain aspects of the TIM machinery are described in the chapter of K. Kinnally (this volume).

2. Protein import into mitochondria

2.1 The translocation machinery of the outer and inner membranes

The vast majority of mitochondrial proteins are encoded by nuclear genes. They are synthesized as precursors with specific presequences in the cytosol on free ribosomes and imported into mitochondria through distinct proteinaceous channels that are embedded in the mitochondrial membranes (Fig. 1). Cytosolic factors [6,7] maintain the precursors in an import-competent state. The TOM complex mediates the recognition, insertion and translocation of precursor proteins into and across the outer membrane. Binding of unfolded protein segments to specific receptor components and protein domains at the intermembrane space side of the TOM complex appear to provide a pulling force for the initial translocation of the precursors across the mitochondrial outer membrane. Translocation of proteins into the inner membrane or the mitochondrial matrix is mediated by the TIM machineries. At least two import translocases exist which differ in their substrate specificity [2,8–11].

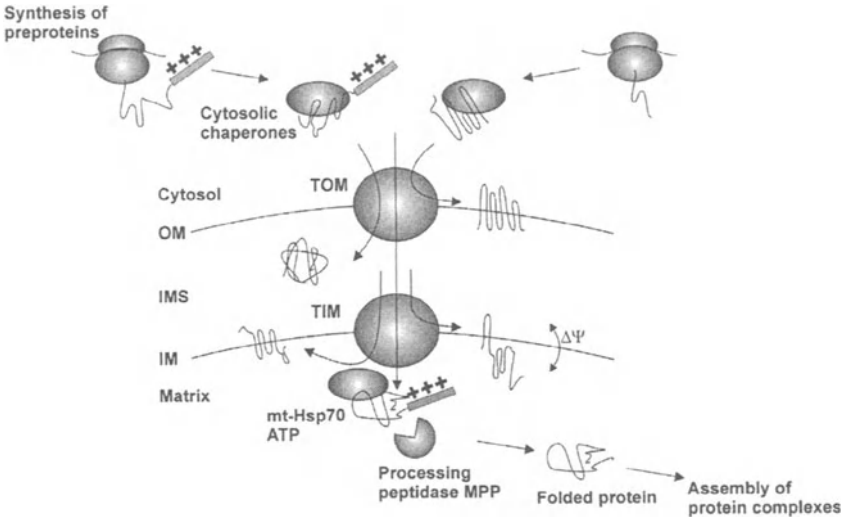

Figure 1. Translocation of nuclear encoded proteins into mitochondria. Preproteins synthesized in the cytosol and destined for translocation into mitochondria are transported across or into the mitochondrial outer (OM) and inner (IM) membranes. Preproteins are targeted to mitochondria via signals which (in most cases) are located at their N-termini or (in fewer cases) within the preprotein. The binding of cytosolic chaperones to preproteins maintains them in an import-competent state. Specific import receptors of the TOM complex bind to the preproteins and pass them on to the general import pore. After translocation across the outer membrane the preproteins bind to components of the TIM machinery located in the inter membrane space (IMS), the innermembrane and the mitochondrial matrix. Upon translocation of the preproteins into the mitochondrial matrix, the signal sequences are proteolytically removed by the matrix-processing peptidase MPP and proteins are folded into their native conformation. Translocation across the inner membrane requires an inner membrane potential ($\Delta\Psi$) and hydrolysis of ATP.

The TIM17-23 complex, together with the chaperone mt-Hsp70, mediates the translocation across the inner membrane into the matrix [12–14]. Upon import into the mitochondrial matrix, proteins are folded with the aid of mitochondrial chaperones [15]. The Tim22-54 complex is involved in the import and membrane insertion of certain inner membrane proteins, such as the ADP/ATP carrier and components of the TIM machinery itself. Import generally requires a membrane potential ($\Delta\Psi$) across the mitochondrial inner membrane.

2.2 The translocation substrates

Proteins destined for import into the mitochondrial matrix are generally synthesized as precursor proteins (or "preproteins") which possess so called matrix targeting sequences (MTS) located at their N-termini. Upon import into the matrix, these signal sequences are cleaved by the matrix processing peptidase MPP [16]. Most MTS have a length of 20 to 60 amino acid residues. They are rich in basic amino acids, generally devoid of negatively charged amino acid side chains, and often have a high content of hydroxylated residues. They are predicted to form positively charged amphiphilic α-helices [17]. Recently, a cleavable MTS was detected at the C-terminus of the precursor of a mitochondrial DNA helicase from yeast [18]. Proteins with N-terminal targeting information traverse both mitochondrial membranes in a linear fashion in a N- to C- terminal direction [19,20]; while C-terminally targeted proteins were shown to move into mitochondria in reverse direction [18].

Proteins which are sorted into the mitochondrial outer membrane, the intermembrane space and many precursor proteins destined to the inner membrane, generally do not carry cleavable targeting signals. They contain internal targeting signals. As an example, a segment of positively charged amino acid residues close to a single transmembrane domain has been shown to function as an internal targeting signal in the inner membrane proteins, Bcs1 and cytochrome c1 [21,22]. The majority of internal targeting signals, however, have not yet been characterized.

3. Molecular characteristics of the TOM complex

3.1 The components of the TOM complex

Genetic and biochemical studies with *Neurospora crassa* and *Saccharomyces cerevisiae* have shown that the TOM complex contains several import receptors. Three receptors (the nomenclature reflects an approximate mass in kDa) Tom20 [23,24], Tom22 [25–28] and Tom70 [29,30] were identified in both *Neurospora crassa* and *Saccharomyces cerevisiae*. Two other components with predicted receptor function, Tom71 [31], a homolog of Tom70, and Tom37 [32], were found only in *Saccharomyces cerevisiae* to date. All these proteins are anchored to the outer membrane by a single transmembrane segment and contain a hydrophilic domain reaching out into the cytosol. In addition, Tom22 has a hydrophilic domain in the intermembrane space. The receptor molecules Tom20 and Tom22 were found to preferentially bind preproteins with N-terminal matrix targeting sequences and proteins destined for insertion into the outer membrane [33,34]. Tom70 binds preproteins with

internal targeting information but in its absence Tom20 can also act as a receptor for this latter class of preproteins [31,34].

Transfer of preproteins across or into the mitochondrial outer membrane is mediated by a specific protein-conducting channel, also defined as general import pore (GIP). Its central component is Tom40 [36–42]. Tom40 is largely membrane-embedded [40,41]. Secondary structure prediction [43] and circular dichroism data [41] of Tom40 suggest an amphipathic β-sheet structure. Tom22 may also constitute an essential part of the GIP because it is highly associated with Tom40. Further components of the GIP include three smaller proteins, Tom7 [44], Tom6 [45–47] and Tom5 [48].

The role of the small Tom proteins is not entirely clear. Tom6 and Tom7 are thought to be important for the stability of the TOM complex by modulating the interaction between the individual Tom components. Tom6 might tighten the interaction of the import receptors with the GIP acting as an assembly factor for Tom22 [45–47]. On the other hand, Tom7 was suggested to destabilize receptor GIP interactions [44]. The Tom5 protein might play a role in the initial insertion of signal sequences into the translocation pore [48]. Tom5 has been detected only in yeast.

Homologs of the *Neurospora* and yeast TOM complex proteins have been identified in organisms including human [49,50], rat [51], *Caenorhabditis elegans* [52], and potato [53,54] indicating that the TOM machinery is conserved in all eukaryotes. Mammalian Tom34 [55,56], a recently described component is peripherally associated with mitochondrial outer membranes with a possible, yet unidentified, function in protein import.

3.1.1 The isolated TOM complex of *Neurospora crassa*. The TOM complex was initially identified through co-immunopreciptation of its components. Due to the lack of isolated purified TOM complex, information about its structure was only recently made available. To prepare the TOM complex we uesd the filamentous fungus *Neurospora crassa* as a source of the proteins. This organism was deemed particularly suitable for the isolation of the TOM complex on a preparative scale because it can easily be cultivated in large quantities and it yields a large amount of mitochondria per unit cell mass. In addition, it allows any TOM component to be genetically modified. We have constructed a *Neurospora* strain in which the gene for Tom22 was deleted and replaced by a version of Tom22 which contained a hexahistidinyl-tag at its C-terminus. From this strain a hetero-oligomeric protein complex containing the Tom components was isolated in the presence of the detergent digitonin and it was termed the TOM holo complex [39,40]. SDS polyacrylamide gel electrophoresis of the TOM complex shows several bands corresponding to the subunits Tom70, Tom40, Tom22, Tom20, Tom7 and Tom6 (Fig. 2). The TOM holo complex has a molecular mass of $\sim$ 450

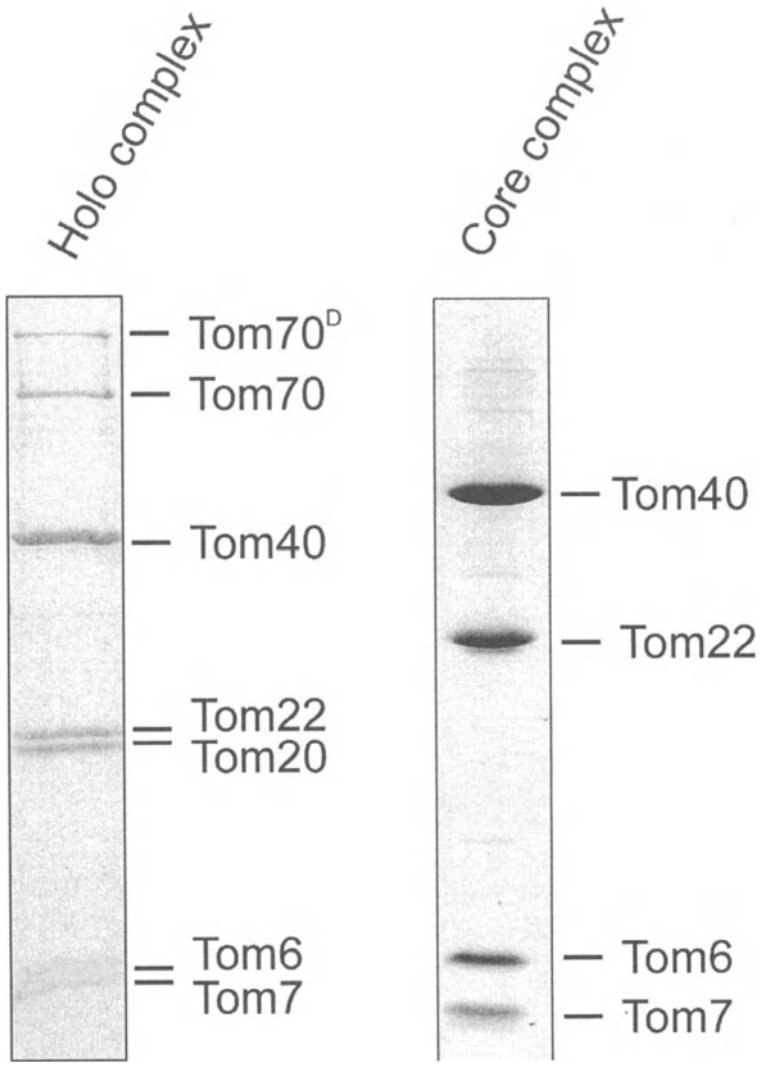

Figure 2. Resolution of TOM holo (left) and TOM core complex (right) from *Neurospora crassa* mitochondria by SDS-PAGE. The TOM holo complex contains the receptors Tom20 and Tom70 (and its dimeric form Tom70D) as well as the constituents of the general insertion pore (GIP) Tom40, Tom22, Tom6 and Tom7. The TOM core complex corresponding to the GIP lacks bands corresponding to the receptors Tom70 and Tom20.

kDa as shown by non-denaturing polyacrylamide gel electrophoresis and size exclusion chromatography [39, 40].

Genetic studies with *Neurospora* and yeast have indicated that Tom40 is the only component of the TOM holo complex which is strictly essential for translocation and cell viability. Disruption of the ISP42 gene in yeast was lethal to the cells [37]. By contrast, mitochondria completely lacking Tom70, Tom22, Tom20 or the small TOM components still facilitate import of preproteins, though at a reduced rate [23,57–60]. Tom22 might be crucial for the structural integrity of the complex [60]. Consistent with this, treatment of isolated TOM holo complex with non-ionic detergents such as n-dodecyl-b,D-maltoside or Triton X-100 specifically releases Tom20 and Tom70 but leaves a remaining "TOM core complex", which is composed of Tom40, Tom22, Tom6 and Tom7, intact (Fig. 2). Tom20 and Tom70 molecules are associated with the core components at the periphery rather than representing integral elements of the core complex. The TOM core complex was also directly isolated from mitochondria after solubilizing it in the presence of the detergent n-dodecyl-b,D-maltoside. Its composition was indistinguishable from that of complex isolated from the TOM holo complex by treatment with the same detergent.

3.1.2 Stoichiometry of the components of the TOM complex. The molar ratios of the individual constituents of the TOM holo and core complexes was determined. *Neurospora* cells growing in the presence of 35S-sulfate homogeneously label cysteine and methionine residues in the TOM proteins. The TOM complexes were isolated and the protein components resolved by SDS-PAGE. Phosphorimaging analysis was then used to determine the molar rations of the TOM proteins and the stoichiometry calculated using the molecular masses of the native complexes [39,40]. The holo complex contains $\sim$ eight Tom40, three to four Tom22, two Tom20, one to two Tom70 and two Tom6 and Tom7 molecules, each. The stoichiometry of the TOM core complex yielded similar molar ratios for Tom40, Tom22, Tom6 and Tom7.

Other groups [38] quantified the amounts of Tom70, Tom40, Tom22 and Tom20 by standardized immunoblotting, comparing signals with mitochondrial extracts and purified recombinant Tom proteins or domains of Tom proteins. Based on these studies, the TOM core complex of *Saccharomyces cerevisiae* was reported to contain about four to six molecules of Tom40 and three to six molecules of Tom22. A likely explanation for these diverging results could be that yeast and *Neurospora* TOM complex exhibit different structural organizations. On the other hand, it is also possible that the differences are due to different estimates of the total molecular mass of the TOM complex which is a prerequisite for the determination of the number of subunits present in the complex.

4. Functional properties of the isolated TOM complex

The protein-conducting channels of the endoplasmic reticulum and bacterial inner membrane open upon interaction with the signal peptide of the translocating preprotein (for review, see [61]). In this way, ion gradients are maintained across the membranes. In the absence of preprotein, these are closed and the membranes sealed. By contrast, there is no need for a sealed outer membrane of mitochondria. Small organic solutes and ions can freely diffuse this membrane, a reaction that is mediated by porin.

The first direct evidence that the TOM complex forms a hydrophilic channel came from electrophysiology measurements. The purified TOM complex forms large ion-conducting channels when integrated into planar lipid bilayers [39]. Under low voltage conditions ($| V | < 60$ mV) the TOM complex exhibited open pores. The average conductance of the TOM complex channel is $\sim$ 2.3 nS in the presence of 1 M KCl. Single channel recordings of the TOM complex shows three conducting states that have been described as closed, half-open and open. These may represent the opening and closing states of two distinct pores in the complex (see below). Conductance measurements in the presence of non-electrolyte polymers (e.g. see the chapter by Krasilnikov, this volume) indicated that the TOM complex allows passage of organic solutes of a molecular mass of up to about 6 kDa [40]. Higher molecular mass polymers of that type did not fit into the TOM protein-conducting channel. Another important characteristic of the TOM complex channel is its small, but nonzero selectivity for cations. The ratio of cation to anion permeability, $\sim$ 3.0 [39], agrees well with the high affinity of TOM complex to positively charged signal sequences.

Earlier reports described a cationic channel in the outer membrane of mammalian and yeast mitochondria, the peptide sensitive channel PSC. The PSC has been reported to be partially blocked by basic peptides, including mitochondrial presequences [62]. Comparison of the electric properties of purified TOM complex and PSC suggested that the two are identical. The isolated TOM complex, as well as the PSC in mitochondrial membranes, binds mitochondrial presequences which partially block the protein-conducting channel [63].

The removal of the solvent-exposed loops or domains of the receptor molecules Tom70, Tom20 and Tom22 by limited proteolysis did not alter the electric properties of the TOM complex channel. The TOM core complex lacking the receptor molecules Tom70 and Tom20 had practically the same electric properties as the holo complex [40]. Apparently, the two receptors are structurally not involved in the pore formation. Also the hydrophilic domains of Tom22 reaching out into the cytosol and the intermembrane space do not play a major role in the formation of the translocation channel. Similar results

were obtained with yeast Tom40 expressed in *E. coli* when integrated into planar lipid bilayers [41]. It is unclear whether single molecules of Tom40, or Tom40 assembled into a multi-subunit structure causes pore formation. Isolation of the yeast TOM complex and analysis after insertion into a lipid bilayer should help to resolve this issue.

Purified TOM holo complex was reconstituted into lipid vesicles and its ability to facilitate translocation and membrane insertion of preproteins was studied. Both reactions were reproduced in this *in-vitro* system [39]. In addition, association of preproteins with the isolated TOM complexes was observed with both the holo and the core complex [64]. Thus, the TOM complex is sufficient for protein translocation.

5. Electron microscopy of isolated TOM complex

5.1 Projection map of the TOM holo complex

The structure of the TOM complex was investigated by electron microscopy [39]. Analysis of negatively-stained TOM holo complex by image processing yielded a projection map of the complex at $(24\ \text{Å})^{-1}$ resolution. The averaged projection images exhibited particles with a diameter of $\sim$ 140 Å. The particles contained one, two and three centers of stain accumulation. This apparent heterogeneity may be caused by the treatment of the complex with a high detergent concentration, relative to that of the protein (the detergent was required for column chromatography). This treatment may have weakened the interaction between the individual protein components and led to a partial breakdown of the three ring structure into two- and single-ring structures. It is conceivable that column chromatography removes small molecules from the complex (e.g. lipids) which may be essential for the stability of the complex. The purified TOM complex may also be unstable under the conditions used during its placement on EM grids and upon negative staining with uranyl acetate.

5.2 3D map of the TOM protein conducting channel

Electron tomography and image analysis of the isolated TOM core complex revealed mainly double-ring structures but a significant fraction of single ring particles was also observed (19%) (Figs. 3 and 4) [40]. Similar structures were observed for the TOM core complex lacking the hydrophilic domains of Tom22 [40]. The 3D reconstruction of the TOM core complex shows several globular elements. Given that the TOM core complex is composed of $\sim$ eight Tom40 molecules these elements could represent dimers of Tom40 [42]. At present the cytosolic and intermembrane space sides of the TOM core complex cannot be distinguished. Probing both surfaces of the molecule

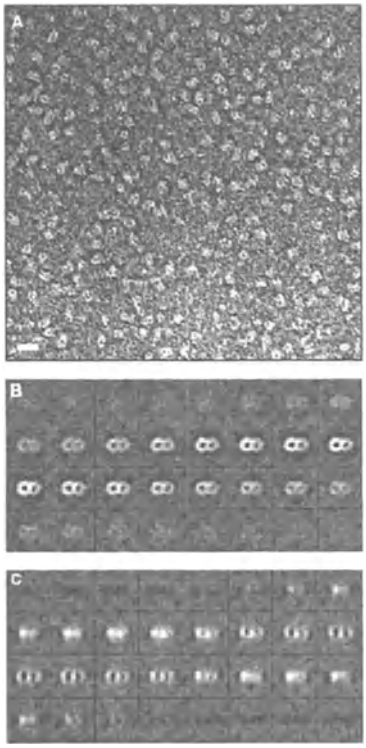

Figure 3. Electron micrograph of purified TOM core complex and three dimensional map of the TOM core complex obtained by electron tomography. (A) TOM core complex was adsorbed to carbon-coated grids and negatively stained with 2% uranylacetate. Bar, 110 Å. (B,C) Electron tomography was carried out using a Philips 200 FEG electron transmission microscope. A total of 321 TOM core complex particles were reconstructed individually from 6741 projections by means of weighted back-projection, before the data set was subjected to three-dimensional alignment, classification and averaging. Grey level representation of (B) horizontal, and (C) vertical slices through the average volume of the most prominent class containing 116 reconstructions at a distance of 3.44 Å. The resolution of the data set was (24 Å)-1 based on the Fourier shell correlation function [65] of two independent averages calculated from images with odd and even numbers. Bar, 70 Å.

with tags or antibodies should help to determine the sideness. The size of the pores of the TOM complex, as derived from single particle analysis, is consistent with that estimated from the conductance measurements.

An interesting question is whether the two ring structure is a dynamic assembly. The structural flexibility of the TOM complex, in terms of alterations of subunit interactions upon binding of preproteins, has indeed been observed [42]. The analysis of translocation intermediates of the ADP/ATP carrier upon transfer across the mitochondrial outer membrane indicated that these

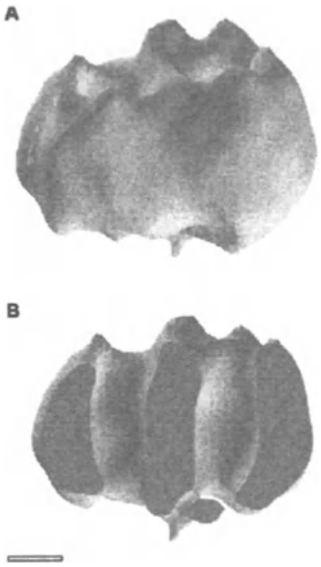

Figure 4. Isosurface representation of the TOM core complex. (A) Side view. (B) Side view of TOM core complex cut along the x,z plane. The threshold of the isosurface representation was set to 64 % of the molecular mass of 410 kDa in order to achieve noise free representation. Bar = 2.8 nm.

intermediates assume a distinct folded state [66]. Therefore, the ADP/ATP carrier upon interacting with the TOM complex may require larger pores than those observed in electrophysiological and electron-microscopy studies. The diameter of the protein-conducting channel of $\sim$ 2.5 nm may be too small to accommodate "hairpin" loops known to form during import of certain types of preproteins. Whether the two rings can undergo a rearrangement to form a structure with a single large pore is presently a matter of speculation [42, 66]. In the case of import of integral proteins of the outer membrane, the rings may open to release the preprotein into the lipid phase. Extensive structure-function studies will be required to solve this question. Furthermore it remains to be determined whether the assembled TOM complex is in equilibrium with its individual subunit constituents e.g. with monomers or dimers of Tom40 [67].

6. Driving force for transport into and across the outer membrane

The forces that drive translocation preproteins into or across the mitochondrial outer membrane are poorly understood. Precursors of endogenous proteins of the outer membrane (e.g. porin or constituents of the TOM complex)

can be inserted via TOM directly into the lipid bilayer. Integration of their hydrophobic, membrane spanning segments may provide sufficient energy to drive this process.

Initial translocation of preproteins bearing matrix targeted signals across the outer membrane does not require hydrolysis of ATP or a membrane potential (the energy required to release the preproteins from cytosolic chaperones is not used for the import reaction). Instead, translocation is thought to be driven by sequential interaction of domains of the TOM complex which bind the precursors with increasing affinity. Movement of presequences from low affinity "cis" sites to high affinity "trans" sites located on the intermembrane side of the TOM complex may also be required for import of preproteins across the outer membrane [68–70]. According to the "acid chain hypothesis" positively charged presequences may move along negatively charged patches of amino acid residues within the TOM machinery [48, 71–73]. To complete translocation across the outer membrane, the incoming polypeptide chain has to associate with other components, in particular the TIM machinery, that provide the driving force for translocation and directionality of movement through the channel. Thus, the TOM complex itself might just provide the pore for polypeptides to cross the outer membrane.

The translocation of polypeptides across the inner membrane requires a membrane potential $\Delta\Psi$ across the inner membrane and ATP [19]. According to the "Brownian ratchet model" or "hand over hand model" the precursor chain diffuses within the pore. The binding of mitochondrial mt-Hsp70 and the TIM component Tim44 to the lumenal portion of the chain would prevent the polypeptide from sliding backwards into the cytosol [74]. Alternatively, it has been suggested that mt-Hsp70 undergoes nucleotide-dependent conformational changes thereby generating a pulling force on incoming preproteins [75, 76]. According to this model the mt-Hsp70 might function as the motor fueled by the hydrolysis of ATP which drives incoming polypeptide chains across the inner membrane.

7. Conclusions and perspectives

The recent progress in the isolation and purification of the TOM holo complex and TOM core complex has advanced our understanding of the characteristics of TOM mediated protein translocation. The purification of the TOM complex in chemical amounts opened the door for studying the mechanism of protein translocation using biophysical tools. Electrophysiology studies may permit the further characterization of the protein-conducting channel. What is the driving force for the protein translocation through the TOM channels? The immobilization of isolated TOM complex on biosensor chips, e.g. plasmon resonance chips, may allow to study the pathway of vectorial movement

of preproteins from binding sites of the TOM complex with low affinity to such with larger affinity in more depth.

The tertiary structure of the TOM complex must be studied at higher resolution. So far, there is no clue as to how the individual components of the TOM complex are assembled in three dimensions. One important question is how many Tom40 molecules form the protein-conducting channel. The structure of TOM/preprotein complexes should be studied by electron tomography. Structural details of the preprotein channel itself are essential for a deeper insight into the translocation process. The conformational dynamics of TOM is another issue of prime importance. The mechanisms of insertion of resident proteins of the outer membrane (e.g. of the TOM complex itself) into the lipid bilayer need to be addressed, including questions such as whether such preproteins can exit the channel in a lateral fashion. An interdisciplinary approach will be required to understand one of the molecular mechanisms for directed movement of polypeptide chains across membranes. The TOM complex might be one paradigm for such an attempt.

Acknowledgments

We would like to thank K.P. Künkele, C. Thun, U. Ahting, U. Staudinger, Drs. F.E. Nargang, R. Hegerl, and D. Typke for their contributions to the progress in the molecular structure of the TOM complex, and Dr. W. Baumeister for his continued support. Financial support from the Deutsche Forschungsgemeinschaft (SFB 184, Teilprojekt B23 to S.N and W.N.) and the Münchener Medizinische Wochenschrift (S.N.) is gratefully acknowledged.

References

[1] Schatz, G. and Dobberstein, B. (1996) Common principles of protein translocation across membranes. *Science* **271**, 1519-1526.

[2] Neupert, W. (1997) Protein import into mitochondria. *Annu Rev Biochem.* **66**, 863-917.

[3] Haucke, V. and Schatz, G. (1997) Import of proteins into mitochondria and chloroplasts. *Trends Cell Biol.* **7**, 103-106.

[4] Hanein, D., Matlack, K.E., Jungnickel, B., Plath, K., Kalies, K.U., Miller, K.R., Rapoport, T.A. and Akey, C.W. (1996) Oligomeric rings of the Sec61p complex induced by ligands required for protein translocation. *Cell* **87**, 721-732.

[5] Bauer, M.F., Hofmann, S., Neupert, W. and Brunner, M. (2000) Protein translocation into mitochondria: the role of TIM complexes. *Trends Cell Biol.* **10**, 25-31.

[6] Komiya, T., Hachiya, N., Sakaguchi, M., Omura, T. and Mihara, K. (1994) Recognition of mitochondria-targeting signals by a cytosolic import stimulation factor, MSF. *J. Biol Chem.* **269**, 30893-30897.

[7] Komiya, T., Sakaguchi, M. and Mihara, K. (1996) Cytoplasmic chaperones determine the targeting pathway of precursor proteins to mitochondria. *EMBO J.* **15**, 399-407.

[8] Köhler, C.M., Jarosch, E., Tokatlidis, K., Schmid, K., Schweyen, R.J. and Schatz, G. (1998) Import of mitochondrial carriers mediated by essential proteins of the intermembrane space. *Science* **279**, 369-373.

[9] Pfanner, N. and M. Meijer. (1997) The Tom and Tim machine. *Curr-Biol.* **7**, R100-103.

[10] Sirrenberg, C., Bauer, M.F., Guiard, B., Neupert, W. and Brunner, M. (1996) Import of carrier proteins into the mitochondrial inner membrane mediated by Tim22. *Nature (London)* **384**, 582-585.

[11] Sirrenberg, C., Endres, M. Folsch, H., Stuart, R.A. Neupert, W. and Brunner, M. (1998) Carrier protein import into mitochondria mediated by the intermembrane proteins Tim10/Mrs11 and Tim12/Mrs5. *Nature (London)* **391**, 912-915.

[12] Schneider, H.C., Berthold, J., Bauer, M.F., Dietmeier, K., Guiard, B., Brunner, M. and Neupert, W. (1994) Mitochondrial Hsp70/MIM44 complex facilitates protein import. *Nature (London* **371**, 768-774.

[13] Kronidou, N.G., Oppliger, W., Bolliger, L., Hannavy, K., Glick, B.S., Schatz, G., and Horst, M.S.O. (1994) Dynamic interaction between Isp45 and mitochondrial hsp70 in the protein import system of the yeast mitochondrial inner membrane. *Proc. Natl. Acad. Sci. (USA)* **91**, 12818-12822.

[14] Rassow, J., Maarse, A.C., Krainer, E. Kubrich, M. Muller, H., Meijer, M., Craig, E.A. and Pfanner, N. (1994) Mitochondrial protein import: biochemical and genetic evidence for interaction of matrix hsp70 and the inner membrane protein MIM44. *J. Cell Biol.* **127**, 1547-1556.

[15] Ostermann, J., Horwich, A.L., Neupert, W. and Hartl, F. U. (1989) Protein folding in mitochondria requires complex formation with hsp60 and ATP hydrolysis. *Nature (London)* **341**, 125-130.

[16] Hawlitschek, G., Schneider, H., Schmidt, B., Tropschug, M., Hartl, F.U. and Neupert, W. (1988) Mitochondrial protein import: identification of processing peptidase and of PEP, a processing enhancing protein. *Cell* **53**, 795-806.

[17] von Heijne, G. (1986) Mitochondrial targeting sequences may form amphiphilic helices. *EMBO J.* **5**, 1335-1342.

[18] Lee, C.M., Sedman, J., Neupert, W. and Stuart, R. A. (1999) The DNA helicase, Hmi1p, is transported into mitochondria by a C-terminal cleavable targeting signal. *J. Biol. Chem.* **274**, 20937-20942.

[19] Schleyer, M. and Neupert, W. (1985) Transport of proteins into mitochondria: translocational intermediates spanning contact sites between outer and inner membranes. *Cell* **43**, 339-350.

[20] Eilers, M., Hwang, S. and Schatz, G. (1988) Unfolding and refolding of a purified precursor protein during import into isolated mitochondria. *EMBO J.* **7**, 1139-1145.

[21] Fölsch, H., Guiard, B., Neupert, W. and Stuart, R. A. (1996) Internal targeting signal of the BCS1 protein: a novel mechanism of import into mitochondria. *EMBO J.* **15**, 479-487.

[22] Arnold, I., Fölsch, H., Neupert, W. and Stuart, R.A. 1998. Two distinct and independent mitochondrial targeting signals function in the sorting of an inner membrane protein, cytochrome c1. *J. Biol. Chem.* **273**, 1469-1476.

[23] Ramage, L., Junne, T., Hahne, K., Lithgow, T. and Schatz, G. (1993) Functional cooperation of mitochondrial protein import receptors in yeast. *EMBO J.* **12**, 4115-4123.

[24] Söllner, T., Griffiths, G., Pfaller, R., Pfanner, N. and Neupert, W. (1989) MOM19, an import receptor for mitochondrial precursor proteins. *Cell* **59**, 1061-1070.

[25] Hönlinger, A., Kübrich, M., Moczko, M., Gärtner, F., Mallet, L., Bussereau, F., Eckerskorn, C., Lottspeich, F., Dietmeier, K., Jacquet, M. and Pfanner, N. (1995) The mitochondrial receptor complex: Mom22 is essential for cell viability and directly interacts with preproteins. *Mol Cell Biol.* **15**, 3382-3389.

[26] Kiebler, M., Keil, P., Schneider, H., van der Klei, I.J., Pfanner, N. and Neupert, W. (1993) The mitochondrial receptor complex: a central role of MOM22 in mediating preprotein transfer from receptors to the general insertion pore. *Cell* **74**, 483-492.

[27] Lithgow, T., Junne, T., Suda, K., Gratzer, S. and Schatz, G. (1994) The mitochondrial outer membrane protein Mas22p is essential for protein import and viability of yeast. *Proc Natl Acad Sci (USA)* **91**, 11973-11937.

[28] Nakai, M. and Endo, T. (1995) Identification of yeast MAS17 encoding the functional counterpart of the mitochondrial receptor complex protein MOM22 of *Neurospora crassa*. *FEBS Lett.* **357**, 202-206.

[29] Hines, V., Brandt, A., Griffiths, G., Horstmann, H., Brutsch, H. and Schatz, G. (1990) Protein import into yeast mitochondria is accelerated by the outer membrane protein MAS70. *EMBO J.* **9**, 3191-3200.

[30] Söllner, T., Pfaller, R., Griffiths, G., Pfanner, N. and Neupert, W. (1990) A mitochondrial import receptor for the ADP/ATP carrier. *Cell* **62**, 107-115.

[31] Schlossmann, J., Dietmeier, K. Pfanner, N. and Neupert. W. (1994) Specific recognition of mitochondrial preproteins by the cytosolic domain of the import receptor MOM72. *J. Biol Chem.* **269**, 11893-11901.

[32] Gratzer, S., Lithgow, T., Bauer, R.E., Lamping, E., Paltauf, F., Kohlwein, S.D., Haucke, V., Junne, T., Schatz, G. and Horst, M. (1995) Mas37p, a novel receptor subunit for protein import into mitochondria. *J Cell Biol.* **129**, 25-34.

[33] Mayer, A., Nargang, F.E., Neupert, W. and Lill, R. (1995). MOM22 is a receptor for mitochondrial targeting sequences and cooperates with MOM19. *EMBO J.* **14**, 4204-4211.

[34] Brix, J., Dietmeier, K. and Pfanner, N. (1997) Differential recognition of preproteins by the purified cytosolic domains of the mitochondrial import receptors Tom20, Tom22, and Tom70. *J Biol Chem.* **272**, 20730-20735.

[35] Schlossmann, J., Lill, R., Neupert, W. and Court, D. A. (1996) Tom71, a novel homologue of the mitochondrial preprotein receptor Tom70. *J Biol Chem.* **271**, 17890-17895.

[36] Kiebler, M., Pfaller, R., Sollner, T., Griffiths, G., Horstmann, H., Pfanner, N. and Neupert, W. (1990) Identification of a mitochondrial receptor complex required for recognition and membrane insertion of precursor proteins. *Nature (London)* **348**, 610-616.

[37] Baker, K.P., Schaniel, A., Vestweber, D. and Schatz, G. (1990) A yeast mitochondrial outer membrane protein essential for protein import and cell viability. *Nature (London)* **348**, 605-609.

[38] Dekker, P.J.T., Ryan, M.T., Brix, J., Müller, H., Hönlinger, A. and Pfanner, N. (1998) Preprotein translocase of the outer mitochondrial membrane: molecular dissection and assembly of the general import pore complex. *Mol Cell Biol.* **18**, 6515-6524.

[39] Künkele, K.P., Heins, S., Dembowski, M., Nargang, F.E., Benz, R., Thieffry, M., Walz, J., Lill, R., Nussberger, S. and Neupert, W. (1998a) The preprotein translocation channel of the outer membrane of mitochondria. *Cell* **93**, 1009-1019.

[40] Ahting, U., Thun, C., Hegerl, R., Typke, D., Nargang, F.E., Neupert, W. and Nussberger, S. (1999) The TOM core complex: The general protein import pore of the outer membrane of mitochondria. *J. Cell Biol.* **147**, 959-968.

[41] Hill, K., Model, K., Ryan, M.T., Dietmeier, K., Martin, F., Wagner, R. and Pfanner, N. (1998) Tom40 forms the hydrophilic channel of the mitochondrial import pore for preproteins. *Nature (London* **395**, 516-521.

[42] Rapaport, D., K. P. Künkele, M. Dembowski, U. Ahting, F. E. Nargang, W. Neupert, and R. Lill. 1998. Dynamics of the TOM Complex of Mitochondria during Binding and Translocation of Preproteins. *Mol Cell Biol.* **18**, 5256-5262.

[43] Court, D.A., Lill, R. and Neupert, W. 1995. The protein import apparatus of the mitochondrial outer membrane. *Can. J. Bot.* **73**, 193-197.

[44] Hönlinger, A., Bömer, U., Alconada, A., Eckerskorn, C., Lottspeich, F., Dietmeier, K. and Pfanner, N. (1996) Tom7 modulates the dynamics of the mitochondrial outer membrane translocase and plays a pathway-related role in protein import. *EMBO J.* **15**, 2125-2137.

[45] Kassenbrock, C.K., Cao, W. and Douglas, M. G. (1993) Genetic and biochemical characterization of ISP6, a small mitochondrial outer membrane protein associated with the protein translocation complex. *EMBO J.* **12**, 3023-3034.

[46] Alconada, A., Kubrich, M., Moczko, M., Honlinger, A. and Pfanner, N. (1995) The mitochondrial receptor complex: the small subunit Mom8b/Isp6 supports association of receptors with the general insertion pore and transfer of preproteins. *Mol Cell Biol.* **15**, 6196-6205.

[47] Cao, W. and Douglas, M.G. (1995) Biogenesis of ISP6, a small carboxyl-terminal anchored protein of the receptor complex of the mitochondrial outer membrane. *J. Biol Chem.* **270**, 5674-5679.

[48] Dietmeier, K., Hönlinger, A., Bömer, U., Dekker, P.J.T., Eckerskorn, C., Lottspeich, F., Kübrich, M. and Pfanner, N. (1997) Tom5 functionally links mitochondrial preprotein receptors to the general import pore. *Nature (London)* **388**, 195-200.

[49] Goping, I.S., Millar, D. G. and Shore, G.C. (1995) Identification of the human mitochondrial protein import receptor, huMas20p. Complementation of delta mas20 in yeast. *FEBS Lett.* **373**, 45-50.

[50] Mori, M. and Terada, K. (1998) Mitochondrial protein import in animals. *Biochim Biophys Acta* **1403**, 12-27.

[51] Iwahashi, J., Yamazaki, S., Komiya, T., Nomura, N., Nishikawa, S., Endo, T. and Mihara, K. (1997) Analysis of the functional domain of the rat liver mitochondrial import receptor Tom20. *J. Biol Chem.* **272**—, 18467-18472.

[52] Voos, W., Martin, H., Krimmer, T. and Pfanner, N. (1999) Mechanisms of protein translocation into mitochondria. *Biochim. Biophys. Acta* **1422**, 235-254.

[53] Jänsch, L., Kruft, V., Schmitz, U.K. and Braun, H.P. (1998) Unique composition of the preprotein translocase of the outer mitochondrial membrane from plants. *J. Biol. Chem.* **273**, 17251-17257.

[54] Glaser, E., Sjoling, S., Tanudji, M. and Whelan, J. (1998) Mitochondrial protein import in plants. Signals, sorting, targeting, processing and regulation. Plant *Mol Biol.* **38**, 311-338.

[55] Nuttall, S.D., Hanson, B. J., Mori, M. and Hoogenraad, N.J. (1997) hTom34: a novel translocase for the import of proteins into human mitochondria. *DNA-Cell-Biol.* **16**, 1067-1074.

[56] Chewawiwat, N., Yano, M., Terada, K., Hoogenraad, N. and Mori, M. (1999) Characterization of the novel mitochondrial protein import component, Tom34, in mammalian cells. J Biochem (Tokyo). 125, 721-727.

[57] Pfaller, R., Pfanner, N. and Neupert, W. (1989) Mitochondrial protein import. Bypass of proteinaceous surface receptors can occur with low specificity and efficiency. *J Biol Chem.* **264**, 34-39.

[58] Söllner, T., Griffiths, G., Pfaller, R., Pfanner, N. and Neupert, W. (1989) MOM19, an import receptor for mitochondrial precursor proteins. *Cell* **59**, 1061-1070.

[59] Harkness, T.A., Nargang, F.E., van der Klei, I., Neupert, W. and Lill, R. (1994) A crucial role of the mitochondrial protein import receptor MOM19 for the biogenesis of mitochondria. *J. Cell Biol.* **124**, 637-648.

[60] van Wilpe, S., Ryan, M.T., Hill, K., Maarse, A.C., Meisinger, C., Brix, J., Dekker, P.J., Moczko, M., Wagner, R., Meijer, M., Guiard, B., Honlinger, A. and Pfanner, N. (1999) Tom22 is a multifunctional organizer of the mitochondrial preprotein translocase. *Nature (London)* **401**, 485-489.

[61] Matlack, K.E.S., Mothes, W. and Rapoport, T A. (1998) Protein translocation: Tunnel vision. *Cell* **92**, 381-390.

[62] Fèvre, F., Henry, J.P. and Thieffry, M. (1994) Reversible and irreversible effects of basic peptides on the mitochondrial cationic channel. *Biophys J.* **66**, 1887-1894.

[63] Künkele, K.P., Juin, P., Pompa, C., Nargang, F. E., Henry, J. P., Neupert, W., Lill, R. and Thieffry, M. (1998b) The isolated complex of the translocase of the outer membrane of mitochondria. Characterization of the cation-selective and voltage-gated preprotein-conducting pore. *J. Biol Chem.* **273**, 31032-31039.

[64] Ahting, U. Unpublished results.

[65] Saxton, W.O. and Baumeister, W. (1982) The correlation averaging of a regularly arranged bacterial cell envelope protein. *J. Microsc.* **127**, 127-138.

[66] Endres, M., Neupert, W. and Brunner, M. (1999) Transport of the ADP/ATP carrier of mitochondria from the TOM complex to the TIM22-54 complex. *EMBO J.* **18**, 3214-3221.

[67] Rapaport, D. and Neupert, W. (1999) Biogenesis of Tom40, core component of the TOM complex of mitochondria. J. Cell Biol. **146**, 321-331.

[68] Mayer, A., Neupert, W., Lill, R. and Matlin, K.S. (1995) Mitochondrial protein import: reversible binding of the presequence at the trans side of the outer membrane drives partial translocation and unfolding. *Cell* **80**, 127-137.

[69] Nargang, F.E., Rapaport, D. Ritzel, R.G., Neupert, W. and Lill, R. (1998) Role of the negative charges in the cytosolic domain of TOM22 in the import of precursor proteins into mitochondria. *Mol. Cell. Biol.* **18**, 3173-3181.

[70] Rapaport, D., Neupert, W. and Lill, R. (1997) Mitochondrial protein import. Tom40 plays a major role in targeting and translocation of preproteins by forming a specific binding site for the presequence. *J Biol Chem.* **272**, 18725-18731.

[71] Schatz, G. (1997) Just follow the acid chain. *Nature* **38,**, 121-122.

[72] Komiya, T., Rospert, S., Koehler, C., Looser, R., Schatz, G. and Mihara, K. (1998) Interaction of mitochondrial targeting signals with acidic receptor domains along the protein import pathway: evidence for the 'acid chain' hypothesis. *EMBO J.* **17**, 3886-3898.

[73] Bolliger, L., Junne, T., Schatz, G. and Lithgow, T. (1995) Acidic receptor domains on both sides of the outer membrane mediate translocation of precursor proteins into yeast mitochondria. *EMBO J.* **14**, 6318-6326.

[74] Ungermann, C., Neupert, W. and Cyr, D.M. (1994) The role of Hsp70 in conferring unidirectionality on protein translocation into mitochondria. *Science* **266**, 1250-1253.

[75] Glick, B.S. (1995) Can Hsp70 proteins act as force-generating motors? *Cell* **80**, 11-14.

[76] Voisine, C., Craig, E.A., Zufall, N., von Ahsen, O., Pfanner, N. and Voos, W. (1999) The protein import motor of mitochondria: Unfolding and trapping of preproteins are distinct and separable functions of matrix Hsp70. *Cell* **97**, 565-574.

PROTEIN TRANSLOCATION CHANNELS IN MITOCHONDRIA

TIM & TOM channels

Kathleen W. Kinnally
Division of Basic Sciences, New York University College of Dentistry, 345 East 24th St., New, NY 10010

Abstract Protein translocation across membranes is a fundamental cellular process that is especially vital for mitochondrial biogenesis. More than 95% of all mitochondrial proteins must be imported from the cytoplasm. The protein-translocating channels of mitochondria have many identical properties including conductance, voltage dependence and regulation by synthetic peptides whose sequences mimic the targeting domains of precursors. Viewing protein translocation across membranes as movement of polymers through confined pathways has provided a novel perspective of channel function. These considerations suggest the observed flickering of the channels in the presence of targeting peptides represents an interaction of the peptides with the channel rather than translocation events.

Keywords: protein import, mitochondria, TIM channel, TOM channel, targeting peptides

1. Introduction

Protein translocation across membrane barriers is important in many cellular functions including signalling, secretion, biogenesis of organelles, compartmentation, and programmed cell death. Since about half of the proteins synthesised in a cell must cross at least one membrane before reaching their final destinations, protein translocation across membranes is a fundamental cellular process [1]. This process is especially vital for mitochondrial biogenesis since $> 95\%$ of all mitochondrial proteins must be imported. Viewing protein translocation across membranes as movement of polymers through confined pathways may provide a different perspective, and, ultimately, a better understanding of the mechanisms underlying this process.

Certain basic principles seem to apply to protein translocation regardless of the membranes being traversed. In 1975, Blobel and Dobberstein proposed that water-filled pores, or channels, play an integral role in the protein

J.J. Kasianowicz et al. (eds.), Structure and Dynamics of Confined Polymers, 85–95.

translocation processes and provide a pathway through which proteins may cross membranes [2]. Evidence supporting this idea was provided by the studies of Simon and Blobel [3, 4] in which electrophysiological techniques were used to identify potential protein-translocating channels in the endoplasmic reticulum and bacterial cell membranes. More recently, the protein translocating channels of the mitochondrial outer and inner membranes were identified [5]. In the general protein translocation scheme, targeting domains on precursors interact with receptors and the translocation channel opens to reveal an aqueous pathway through the hydrophobic interior of the bilayer. Typically, the targeting regions are located at the amino-terminal end of the precursors and are cleaved after translocation. Polypeptides are translocated in an unfolded state, as linear polymers. A molecular motor is thought to "pull" the precursors through the channel and then chaperones catalyse folding of the proteins [1].

2. Protein translocation in mitochondria

Mitochondrial proteins are, for the most part, synthesized in the cytoplasm and carry signal sequences (or presequences) at their amino-termini. The presequences contain the information that targets proteins to mitochondria and they are removed during or after import into the organelles [6, 7]. Presequences typically carry a net positive charge and assume an amphipathic α-helical structure even though there is little or no sequence homology among mitochondrial targeting regions. Synthetic peptides whose sequences mimic these regions are referred to as "targeting peptides" and they competitively inhibit protein import into mitochondria [8, 9]. This inhibition is thought to reflect a competition between mitochondrial precursors and targeting peptides for binding sites on receptors on the outer membrane. More recent studies indicate targeting peptides may also inhibit protein import across the inner membrane by opening a channel that causes the mitochondria to depolarize [10].

The translocation of polypeptides into mitochondria is a multi-step process involving several proteins. These proteins are organised into complexes, called TIM (translocase of the inner membrane) and TOM (translocase of the outer membrane), that catalyse import across the two membranes [11] (Figure 1). Both complexes have receptors necessary for recognition and sorting of precursors as well as a pore for selective translocation across the membranes. The acronyms "TIM" and "TOM" followed by a molecular weight specify components of the translocase complexes. As shown in the model of Figure 1, the MCC (multiple conductance channel) [5] and PSC (peptide sensitive channel) [12, 13] are the import pores of the TIM and TOM complexes, respectively (reviewed in [14]). Hence, MCC and PSC are now referred to as

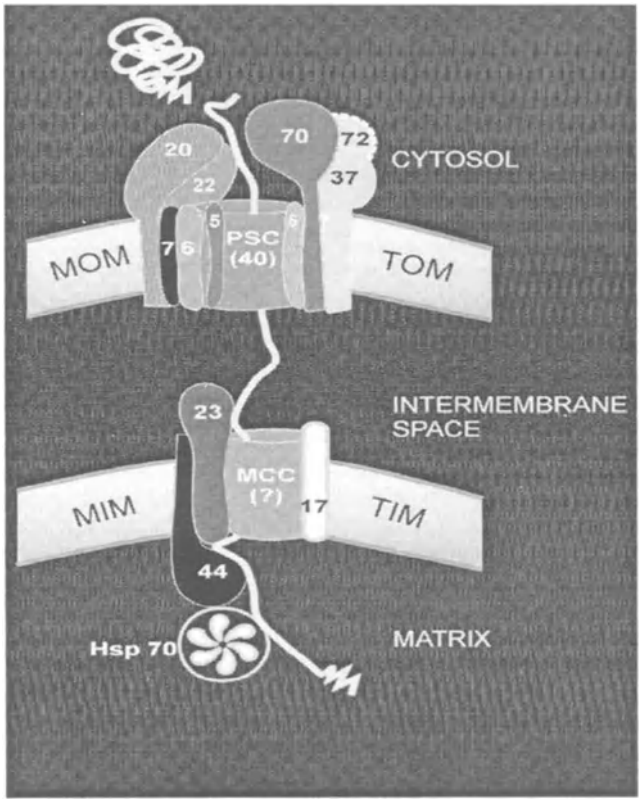

Figure 1. The protein import machinery of mitochondria. Multi-subunit complexes called TIM and TOM are located in the mitochondrial inner (MIM) and outer (MOM) membranes. MCC and PSC form channels in these complexes that allow the passage of precursors from the cytoplasm to the matrix. Model was modified from [14].

the TIM and TOM channels, respectively. A comparison of the single channel behavior of these two activities as well as the effects of targeting peptides follows a short description of the mitochondrial protein import machinery.

2.1 The TOM complex

The outer membrane is a physical barrier representing the first level of selection for precursors synthesised in the cytoplasm, regardless of their final destination within the mitochondrion. The TOM complex is responsible for recognition of the mitochondrial presequences and for translocation of precursors across the outer membrane (Figure 1). Importantly, protein translocation was reconstituted in proteoliposomes containing purified TOM complex in the

elegant studies of Künkele and colleagues [12]. Furthermore, incorporation of the purified TOM complex reconstituted into planar bilayer membranes imparted a channel activity that was modified by targeting peptides. These findings clearly demonstrate the association of a channel activity with a complex capable of translocating proteins across membranes. In addition, single particle electron microscopic image analysis showed the presence of two, and possibly three, apparent pores associated with each purified TOM complex (see the chapter by Nussberger and Neupert, this volume).

While several ancillary proteins (e.g., TOM22p) act as receptors, the essential protein TOM40p was identified as the import pore of the TOM complex. Hill et al. [15] found that bacterially expressed TOM40p imparted channel activity to planar bilayers. Targeting peptides modified the channel activity associated with TOM40p, like that of the TOM complex [12]. Interestingly, none of the TOM proteins have been assigned a "motor" activity for "pulling" the precursor through the pore of the complex.

2.2 The TIM complex

The TIM complex, or translocase of the inner membrane, catalyses the import of proteins across the inner membrane of mitochondria (see Figure 1). While import through the TIM complex can operate independently of the TOM complex, current models favour their transient linkage at contact sites (junctions where the two membranes are closely apposed). In an elegant, electron-microscopic study by Schulke and colleagues [16], the inner and outer membranes were "zippered" together by stalling precursors in the import machinery.

It has been suggested that TIM23p and TIM17p form part of the channel in the inner membrane through which precursors are translocated into the matrix [17]. Both TIM23p and TIM17p are essential proteins with several transmembrane domains that are closely associated in the TIM complex [18]. Both proteins can be chemically cross-linked to a precursor arrested in transit across the inner membrane [19], and depletion of TIM23p from cells results in a defect in protein import [20]. Furthermore, antibodies against TIM23p inhibit import of several mitochondrial proteins across the inner membrane [20]. However, TIM channel activity has the same conductance, ion selectivity, and voltage dependence in the presence and absence of TIM23p. In addition, depletion of TIM23p modifies the targeting peptide sensitivity of the TIM channel (see below). These findings indicate TIM23p is most likely a receptor and is not required for the basic structure of the pore of the TIM complex. Therefore, the molecular identity of the protein(s) forming the polypeptide translocation pathway of the TIM complex has not yet been firmly established.

2.3 Comparison of protein import through the TIM and TOM complexes

A large electrochemical gradient across the inner membrane drives ATP production in mitochondria. The permeability of the inner membrane must remain very low in order to maintain this gradient. Therefore, the TIM channel must be exquisitely regulated or its opening would short-circuit oxidative phosphorylation. As expected, the conductance pathway through the TIM channel is normally closed in mitochondria unless activated, e.g., by calcium or targeting peptides [10]. The TOM channel is not subject to such limitations and could normally remain in an open conductance state.

Other differences in import properties have emerged between the TIM and TOM complexes. Translocation of polypeptides through the TOM complex requires ATP. However, translocation across the inner membrane requires ATP and an electrochemical potential which is normally established by the electron transport chain [21–23]. The membrane potential is thought to play a role in translocation of the presequence across the inner membrane. While none is apparently associated with the TOM complex, the TIM complex has a "motor" to facilitate transport of the precursors through the pore. A member of the hsp70 family (mt-hsp70p) associates with TIM44p to form a subcomplex on the matrix face of the inner membrane [24, 25]. These two proteins form, at least in part, an ATP-driven import motor. The subcomplex binds the precursor and a conformational change in mt-hsp70p (brought on by ATP hydrolysis) generates the torque that "pulls" precursors through the transmembrane pore of the TIM complex [26, 27]. The mt-Hsp70p retained by the precursor after its release from TIM44p prevents the unfolded polypeptide from sliding back through the pore.

2.4 TIM and TOM, two mitochondrial channels

TIM and TOM channel activities, previously referred to as MCC and PSC, respectively, are recorded from mitoplasts and mitochondria using patch-clamp techniques. The electrophysiological characteristics of the TIM and TOM channels are virtually identical. The peak conductances are 1000 pS and predominant sub-conductance levels are 500 pS. These values were used to estimate diameters of 2.7 nm for single pores, and 2 nm for double barrel pores [14]. Single particle analysis indicates the TOM complex has a double barrel pore (see Nussburger and Neupert, this volume and [12]), as expected from the single channel behavior. Importantly, the pores of the TIM and TOM complexes are large enough to accommodate an unfolded polypeptide during translocation. Both channels are slightly cation-selective with permeability ratios for K^+/Cl^- of about 5. After reconstitution into proteoliposomes, the voltage dependencies of the TIM and TOM channels

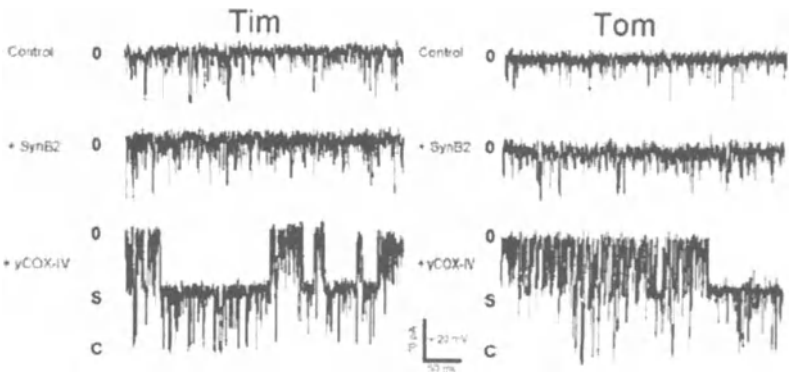

Figure 2. The activities of two mitochondrial channels are regulated by synthetic targeting peptides. Typical current traces of TIM and TOM were recorded at 2 kHz from patches excised from proteoliposomes containing mitochondrial inner and outer membranes, respectively. Traces were obtained in the absence (control) and presence of targeting peptide (yCOX-IV from cytochrome oxidase subunit IV) or control peptide (SynB2) in symmetrical 0.15 M KCl, 5 mM HEPES, pH 7.4, under voltage-clamp conditions at 20 mV. O, S, and C indicate the open, substate and closed current levels.

are asymmetrical around zero mV with closure at voltages larger than +40 or -50 mV. These two channel activities were distinguished by mutations and protease sensitivity as well as the effects of antibodies (reviewed in Kinnally et al., 2000 [14]). TIM and TOM are the protein translocation channels of the inner and outer membranes of mitochondria, respectively. Considering that these two channels have the same function, it is not surprising that their electrophysiological characteristics are identical.

2.4.1 Channel conductances are regulated by targeting peptides. The open probability and mean open time of yeast and mammalian TIM and TOM channels are decreased specifically by synthetic signal peptides whose sequences mimic the targeting regions of mitochondrial precursors, e.g., cytochrome oxidase subunit IV and VI. Two other mitochondrial channel activities, mCS and VDAC, are unperturbed by targeting peptides [28]. Furthermore, TIM and TOM channel activities are not affected by control peptides, e.g. synB2, a cationic alpha-helical peptide whose sequence does not support mitochondrial protein import.

TIM and TOM channel activities respond similarly to the presence of signal peptides. As shown in figure 2, the frequency of closing, visualised as downward inflections in the current traces, dramatically increases upon introduction of the targeting peptides like yCOX-IV, but not control peptides like SynB2. As shown in Table 1, this effect is specific for targeting peptides.

Table 1. Targeting peptides regulate TIM channel activity[a]

Peptide	*Sequence*	*Net Charge*	*Pre-sequence*	*TIM Flicker*
COX-IV$_{1-13}$	^{1}MLSLRQSIRFFKY$_{13}$	+3	+[b]	+
COX-IV$_{1-22}$	^{1}MLSLRQSIRFFKPATRTLCSSR$_{22}$	+5	+[b]	+
COX-VI	^{1}MLSRAIFRNPVINRTLLRAR$_{20}$	+5	+[c]	+
FCOX-IV	^{3}RAPALRRSIATTVVRCNAET$_{22}$	+3	+[c]	+
SynB2	MLSRQQSQRQSRQQSQRQSR	+5	-[d]	-
pAT-III	RNASVLKSSKNAKRYLRCNLKA	+7	-[b]	±[e]
iVDAC	^{109}RGAKFNLHFKQ$_{119}$	+3	-[c]	-
nVDAC	^{1}MAVPAFSDIAKSANDLLNKD$_{20}$	-1	-[c]	-
cVDAC	^{272}THKVGTSFTFES$_{283}$	0	-	-

[a]Modified from [5]. [b]Ref. [8]. [c]Predicted but not determined. [d]Ref. [7]. [e]pAT-III blocked from the bath side but not micropipette side.

The nature of the closures of these two channels is not as yet understood. However, the peptide effect is dose- and voltage-dependent as shown in Figure 3. The frequency of closing increases with dose and the magnitude and polarity of the potential that drives the positively charged peptide across the membrane. The peptides have little effect if the polarity is reversed. Hence, it has been suggested that the closures correspond to the intermittent blockade of the conductance pathway as the peptides are translocated across the membrane. Alternatively, the closures have relatively long durations of microseconds, suggesting the closures represent some interaction of the peptide with the translocation apparatus that results in a de-stabilization of the open state. It is expected that translocation events for polypeptides of this size would be in the 10 nanosecond time domain (personal communication, J.J. Kasianowicz). Perhaps, the fast translocation events are obscured by the long duration blockade associated with peptide interaction with receptors.

Deletion of receptors known to recognize signal sequences of precursors abolishes the peptide sensitivities of the TIM and TOM channels. Depletion of TIM23p by mutation [5] or TOM22p by protease treatment [29] eliminates the rapid flickering induced by signal peptides for TIM and TOM channels, respectively. These findings provide further evidence that the peptide-induced closures do not simply represent translocation events. However, Kasianowicz and colleagues have demonstrated nucleotide translocation across the hemolysin pore when current blockades were examined on a faster time scale [30–32] (see also the chapters by Kasianowicz, et al.; Deamer, et al., Branton and Meller, and Akeson, et al., this volume). Their work has provided the justification to re-examine the receptor-less complexes on the $\sim$ μsecond time

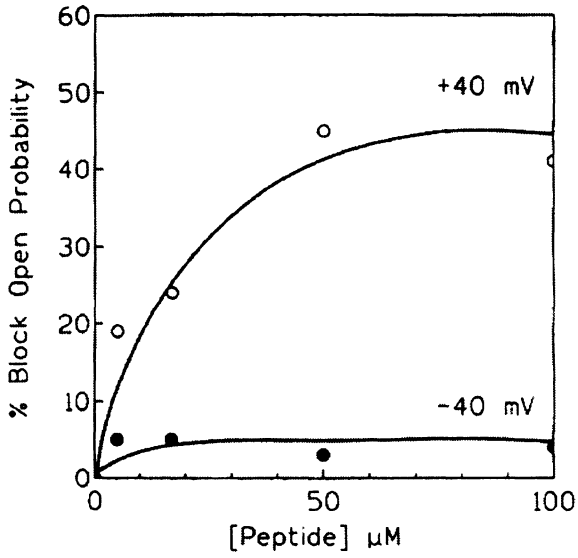

Figure 3. The effect of peptides is dose and voltage dependent. The % block (or % decrease) in open probability of the Tim channel caused by varied levels of the targeting peptide COX-IV peptide is shown at ±40 mV. The open channel probability is calculated from amplitude histograms (bin width of 0.4 pA) as the fraction of total time spent in the fully open state. Activity was recorded from a patch excised from a proteoliposome derived from inner membranes isolated from yeast mitochondria. Modified from [28]. Similar results were observed with the Tom channel.

scale in order to determine if current blockade associated with translocation events can be detected.

3. Conclusions

Our understanding of the mechanisms of protein translocation across membranes has advanced significantly in recent years. Many components of the mitochondrial import machinery have been discovered and their roles in protein transport have been unraveled by genetic and biochemical analysis. Electrophysiology, in particular patch clamping, is now playing a major role in the characterization of the channels of the TIM and TOM complexes. However, several important questions remain unanswered about protein translocation in mitochondria. In particular, what proteins make up the pore of the TIM complex, what forces promote protein translocation through the TOM complex in the apparent absence of a motor, and can polypeptide translocation be detected as current fluctuations through pores?

Acknowledgments

KWK is supported by NSF grants MCB9513439 and MCB-9816950, and NIH grant GM57249. I thank C.A. Mannella for his long-standing intellectual support and J.J. Kasianowicz for his helpful discussions.

References

[1] Schatz, G. and Dobberstein, B. (1996) Common principles of protein translocation across membranes. *Science* **271**, 1519-1526.

[2] Blobel, G. and Dobberstein, B. (1975) Transfer of proteins across membranes. I. Presence of proteolytically processed and unprocessed nascent immunoglobulin light chains on membrane-bound ribosomes of murine myeloma. *J. Cell Biol.* **67**, 835-51.

[3] Simon, S.M. and Blobel, G. (1991) A protein-conducting channel in the endoplasmic reticulum. *Cell* **65**, 371-380.

[4] Simon, S.M. and Blobel, G. (1992) Signal peptides open protein-conducting channels in *E. coli*. *Cell* **69**, 677-684.

[5] Lohret, T.A., Jensen, R. and Kinnally, K.W. 1997. The Tim23 import protein is required for normal activity of a mitochondrial inner membrane channel. *J. Cell Biol.* **137**, 377-386.

[6] Roise, D. and Schatz, G. (1988) Mitochondrial presequences *J. Biol. Chem.* **263**, 4509-4511.

[7] Allison, D.S. and Schatz, G. (1986) Artificial mitochondrial presequences. *Proc. Natl. Acad. Sci. (USA)* **83**, 9011-9015.

[8] Glaser, S.M., and Cumsky, M.G. (1990) Localization of a synthetic presequence that blocks protein import into mitochondria. *J. Biol. Chem.* **265**, 8817-8822.

[9] Hugosson, M., Andreu, D., Boman, H.G. and Glaser, E. (1994) *Eur. J. Biochem.* **223**, 1027-1033.

[10] Kushnareva, Y.E., Campo, M.L., Kinnally, K.W. and Sokolove, P.M. (1999) Effects of signal presequences and non-signal peptides on mitochondrial permeability and membrane conductance. *Arch. Biochem. Biophys.* **366**, 107-115.

[11] Pfanner, N., Douglas, M. G., Endo, T.. Hoogenraad, N. J.. Jensen, R. E., Meijer, M., Neupert, W., Schatz, G., Schmitz, U. K., Shore, G. C. 1996. *Trends in Biochemical Sciences* **21**, 51-52.

[12] Künkele, K.P., Heins, S., Dembowski, M., Nargang, F.E., Benz, R., Thieffry, M., Walz, J., Lill, R., Nussberger, S., and Neupert, W. (1998) The preprotein translocation channel of the outer membrane of mitochondria. *Cell* **93**, 1009-1019.

[13] Juin, P., Pelleschi, M., Sagné, C., Henry, J.-P., Thieffry, M. and Vallette, F.-M. (1995) Involvement of the peptide sensitive channel in the translocation of basic peptides into mitochondria. *Biochim. Biophys. Res. Comm.* **211**, 92-99.

[14] Kinnally, K.W., Muro, C., and Campo, M.L. (2000) MCC and PSC, the putative protein import channels of mitochondria. *J. Bioenerg. Biomemb.* **32**, 47-54.

[15] Hill, K., Model, K., Ryan, M.T., Dietmeier, K., Martin, F., Wagner, R. and Pfanner N. (1998) TOM40 forms the hydrophilic channel of the mitochondrial import pore for preproteins. *Nature (London)* **395**, 516-21.

[16] Schulke, N., Sepuri, N.B.V. and Pain, D. (1997) In vivo zippering of inner and outer mitochondrial membranes by a stable translocation intermediate. *Proc. Natl. Acad. Sci. (USA)* **94**, 7314-7319.

[17] Berthold, J., Bauer, M.F., Schneider, H.-C., Klaus, C., Dietmeir, K., Neupert, W. and Brunner, M. (1995) The MIM complex mediates preprotein translocation across the mitochondrial inner membrane and couples it to the mt-Hsp70/ATP driving system. *Cell* **81**, 1085-1093

[18] Ryan, K.R., Roxanne, S.L. and Jensen, R. (1998) Characterization of the mitochondrial inner membrane translocase complex: the TIM23p hydrophobic domain interacts with Tim17 but not with the other TIM23p molecules. *Molec. and Cell. Biol.* **18**, 178-187.

[19] Ryan, K.R., and Jensen, R.E. (1993) mas6p can be cross-linked to an arrested precursor and interacts with other proteins during mitochondrial protein import. *J. Biol. Chem.* **268**, 23743-23746.

[20] Emtage, J.L.T. and Jensen, R.E. (1993) mas6 encodes an essential inner membrane component of the yeast mitochondrial protein import pathway. *J. Cell Biol.* **122**, 1003-1012.

[21] Gasser, S.M., Daum, G. and Schatz, G. (1982) Import of proteins into mitochondria. Energy-dependent uptake of precursors by isolated mitochondria. *J. Biol. Chem.* **257**, 13034-13041.

[22] Martin, J., Mahlke, K. and Pfanner, N. (1991) Role of an energized inner membrane in mitochondrial protein import. *J. Biol. Chem.* **266**, 18051-18057.

[23] Schleyer, M., Schmidt, B. and Neupert, W. (1982) Requirement of a membrane potential for the posttranslational transfer of proteins into mitochondria. *Eur. J. Biochem.* **125**, 109-116.

[24] Kang, P.-J., Ostermann, J., Shilling, J., Neupert, W., Craig, E.A. and Pfanner, N. (1990) Requirement for hsp70 in the mitochondrial matrix for translocation and folding of precursor proteins. *Nature (London)* **348**, 137-143.

[25] Ungermann, C., Guiard, B., Neupert, W. and Cyr, D.M. (1996) The delta psi- and Hsp70/MIM44-dependent reaction cycle driving the early steps of protein import into mitochondria. *EMBO J.* **15**, 735-744.

[26] Schneider, H.C., Berthold, J., Bauer, M.F., Dietmeier, K., Guiard, B., Brunner, M. and Neupert, W. (1994) Mitochondrial hsp70/MIM44 complex facilitates protein import. *Nature (London)* **371**, 768-774.

[27] Rassow, J., Maarse, A.C., Krainer, E., Kubrich, M., Muller, H., Miejer, M., Craig, E.A. and Pfanner, N. (1994) Mitochondrial protein import: biochemical and genetic evidence for interaction of matrix hsp70 and the inner membrane protein MIM44. *J. Cell Biol.* **127**, 1547-1556.

[28] Lohret, T.A. and Kinnally, K.W. (1995) Targeting peptides transiently block a mitochondrial channel. *J. Biol. Chem.* **270**, 15950-15953.

[29] Muro, C., Campo, M.L., Stanley, S., Schatz, G. and Kinnally, K.W. Structure and function studies define essential components of the TIM and TOM channels of the mitochondrial protein import complexes. *In preparation*.

[30] Kasianowicz, J.J.; Brandin, E.; Branton, D.; Deamer, D.W. (1996) *Proc. Natl. Acad. Sci. (USA)* **93**, 13770-13773.

[31] Akeson, M., Branton, D. Kasianowicz, J.J. Brandin, E. and Deamer, D.W. (1999) Microsecond time-scale discrimination between polycytidylic acid and polyadenylic acid segments within single RNA molecules, *Biophys. J.* **77**, 3227-3233.

[32] Henrickson, S.E, Misakian, M., Robertson, B. and Kasianowicz, J.J.. (2000) Asymmetric driven DNA transport in a nanometer-scale pore. *Phys. Rev. Lett.* **85**, 3057-3060.

SIZING CHANNELS WITH NEUTRAL POLYMERS

O. V. Krasilnikov
Laboratory of Membrane Biophysics, Department of Biophysics and Radiobiology, Federal University of Pernambuco, 50670-901, Recife, PE, Brazil
Laboratory of Molecular Physiology, Institute of Physiology and Biophysics, 700095 Tashkent, Uzbekistan

Abstract We have developed a method for determining the physical dimensions of nanometer scale pores formed by protein ion channels. This was possible because of the availability of a wide range of size-selected nonelectrolyte polymers of poly(ethylene glycol), PEG, and because PEG decreases the bulk conductivity of ionic solutions. The method is simple. PEGs that are sufficiently small enter the channel's pore and decrease the channel's ionic conductance. PEGs that are larger than the pore's diameter rarely partition into the pore and therefore do not decrease the channel conductance. Thus, the dependence of the channel conductance on the PEG molecular weight determines the pore's PEG molecular weight cut-off, and by inference, the pore's radius. We recently extended the technique to determine the shape of a channel's lumen including the sizes of both openings and the size and location of constrictions inside the pore. We discuss here the details of the method, the properties of PEG, and some limitations of using the technique to determine channel size.

Keywords: poly(ethylene glycol), PEG, α-hemolysin, α-toxin, ion channel, protein structure, nonelectrolyte polymer

1. Introduction

There are many techniques for determining protein structure. These include, but are not limited to, spectroscopies (absorbance, fluorescence, circular dichroism, IR, and MALDI-TOF), x-ray scattering, dynamic light scattering, size exclusion chromatography, ultracentrifugation, intrinsic viscosity, electrophoresis, microscopies (electron and AFM), NMR, ESR, EPR and protein sequencing. Some of these techniques can also be used for deducing structural features of transmembrane proteins. Solid-state NMR spectroscopy [1,2] has proved particularly useful for studies of small polypeptides. In some instances, the protein must first be modified with a probe, as is the case with EPR and ESR [3–5], or first extracted from a lipid bilayer using detergents, as is done in x-ray crystallography [6–9].

J.J. Kasianowicz et al. (eds.), Structure and Dynamics of Confined Polymers, 97–115.

A protein ion channel has a unique functional feature, a transmembrane ion-conducting portal, that can be interrogated using electrophysiology (i.e. measuring the channel's conductance). For example, scanning cysteine mutagenesis and subsequent covalent modification were used to identify amino acid residues that line the nicotinic acetylcholine receptor channel's pore [10]. In addition, nonelectrolyte polymers were used to probe the geometric features of unmodified channels. Specifically, they permitted the determination of both the change in a channel's pore volume upon gating [11] and the size of a channel's pore (e.g. it's radius) [12]. We discuss the latter method in this chapter.

2. Probing Ion Channels with Nonelectrolyte Polymers

The method for using nonelectrolyte polymers (herein called polymers) to determine the physical dimensions of protein ion channels is simple. The polymer decreases the bulk conductivity of ionic solutions. Thus, polymers that are sufficiently small to enter the channel's pore will decrease the channel's conductance. Polymers with radii larger than those of the two pore entrances rarely partition into the pore and therefore will not affect the channel conductance. Thus, the dependence of the channel conductance on the polymer molecular mass is used to deduce the pore's radius.

An ideal probe of channel size would be a polymer that is a hard sphere, i.e. one that has a well-defined radius and that binds neither to the pore's wall nor with other substances in solution. The hydrodynamic radius of the smallest member of that homologous polymer class should be smaller than narrowest radius of the channel and the largest one should be larger than the largest pore opening.

We used poly(ethylene glycol), PEG, as a probe for ion channel size because it is commercially available in a wide range of well-defined sizes with a lower hydrodynamic radius limit of $\sim$ 0.4 nm. However, there are some features which could limit the use of PEG, and other nonelectrolyte polymers, in estimating channel size. For example, the polymer might interact with the channel, which would complicate the data analysis. In addition, as mentioned above, the effect of polymer on the channel conductance is the primary measurement in this method of estimating pore size. Unfortunately, the method is empirical and a theory that completely describes the effects of PEG on channels is non-extant (however, see the chapter by Bezrukov and Kasianowicz, this volume).

In this chapter, we discuss the effects of nonelectrolyte polymers on the bulk conductivity, viscosity and ionic activity of aqueous solutions. We also discuss the dependence of polymer size on pH and ionic strength, the conductance of ion channels in the absence and presence of nonelectrolyte polymers, and

how to deduce the radius of the largest pore entrance of the channel. Finally, we mention how polymers can be used to gain insight into the mechanisms of ion transport through ion channels.

3. Results

3.1 Nonelectrolytes in aqueous solutions

Nonelectrolytes decrease the bulk conductivity of aqueous solutions. This effect is virtually independent of the nonelectrolyte polymer type [12–14]. For example, hydroxyl-containing substances (ethylene glycol, glycerol, glucose, and sucrose) decreased the conductivity only slightly less than did PEGs.

According to the Stokes-Einstein law, the diffusion coefficient and mobility of ions, and hence the bulk conductivity of solutions, depend on the viscosity of the medium in which the ion is embedded. The macroscopic viscosity of aqueous solutions increases in the presence of nonelectrolytes, and also depends strongly on the nonelectrolyte's type and molecular mass [15]. Because the dependence of the bulk conductivity and the macroscopic viscosity on molecular mass are different, we conclude that the solution macroscopic viscosity, as altered by nonelectrolyte polymers, does not completely dominate ion diffusion.

The viscosity study permits the estimation of both the equivalent hydrodynamic radii R_h of nonelectrolytes and the value of their molar volume in solution. The former has a nonlinear dependence on the molecular mass M_r of the polymer. The empirical equation can be expressed as:

$$r_h = 0.508 + 0.37 \times 10^{-3} M_r - 0.703 \times 10^{-8} M_r^2 \qquad (1)$$

with an average deviation from the experimental values approximately 0.065 nm. The results in comparison with the nonelectrolyte crystal radius data are shown in Table 1.

The dependence of the volume occupied by a hydrated PEG on polymer molecular mass, estimated using eq. 1, is illustrated in Fig. 1. For solutions containing 10%, 20% and 30% PEG (weight/volume, w/v), the total solution volume occupied by the polymer is reached in the presence of PEG 10000, PEG 4600 and PEG 3500 respectively. These highly concentrated PEG solutions are obviously far from either the dilute or semi-dilute regimes. Because we use an oversimplified expression of the hydrated polymer radius, the solution volume occupied by PEG can exceed 100% in the calculation presented here (Fig. 1).

Table 1. Hydrodynamic and crystallographic radii of selected nonelectrolytes.

Nonelectrolyte	*Hydrodynamic radius, nm*	*Crystal radius, nm*	*Hydrodynamic volume / Crystal volume*
Ethyleneglycol	0.26	0.28	0.93
Glycerol	0.31	0.31	1.00
Glucose	0.37	0.36	1.04
Sucrose	0.47	0.44	1.20
PEG 300	0.60	0.47	2.05
PEG 400	0.70	0.52	2.44
PEG 600	0.78	0.60	2.25
PEG 1000	0.94	0.70	2.37
PEG 1450	1.05	0.80	2.27
PEG 2000	1.22	0.89	2.59
PEG 3000	1.44	1.02	2.84
PEG 3400	1.63	1.06	3.63
PEG 4000	1.92	1.12	5.04
PEG 4600	2.10	1.17	5.73
PEG 6000	2.50	1.28	7.42
PEG 20000	5.10	1.92	18.89

The hydrodynamic radius is obtained using viscometry [12, 13, 15]. The crystal radius is estimated to be $(3M/4\pi\rho N)^{1/3}$, where M is the average molecular mass, ρ is the density ($\sim$ 1.13 for PEG, Merck), and N is Avogadro's number.

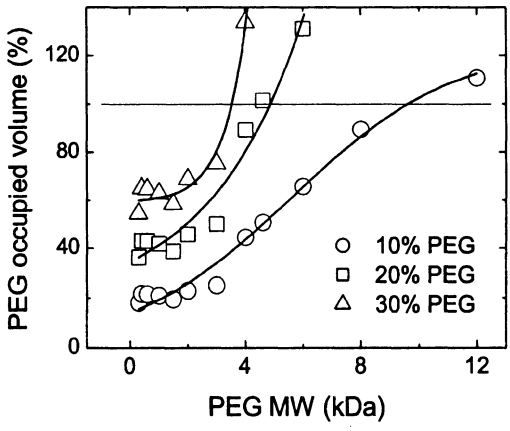

Figure 1. The percentage of solution volume occupied by hydrated PEG in the aqueous phase depends on the PEG molecular weight and the polymer concentration. The values were calculated from the hydrodynamic radii for each of the PEGs (Table 1) using Eq. 1.

3.2 Accessibility of polymer containing solutions to dissolved ions

We now consider the effects of nonelectrolyte polymers on ions in solution. Dissolved electrolytes cannot occupy the volume occupied by the polymer,

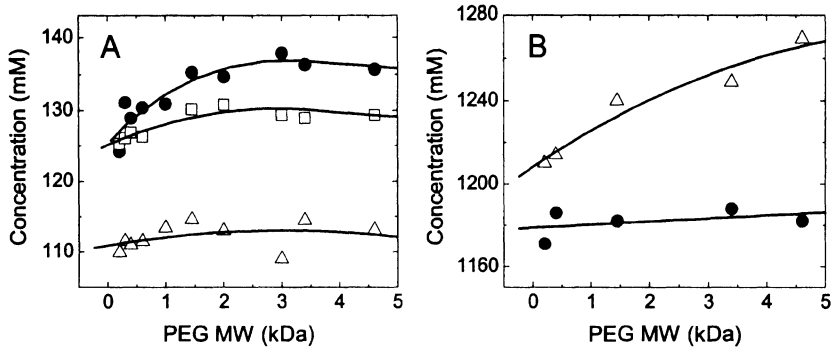

Figure 2. The apparent ion concentrations in 20% (w/v) PEG solutions in either (A) 0.1 M KCl or NaCl or (B) 1 M KCl. The solutions also contained 5 mM Tris-citric acid and were titrated to pH 7.5. The concentrations of K^+(triangles), Na^+ (squares) and Cl^- (circles) were measured with ion-selective electrodes. Data are the mean values of 5 to 7 experiments.

but they have access to water molecules that are free in solution. Using ion-selective electrodes, we compared the effective concentration of ions in solutions that contain polymers of different size (Fig. 2).

At fixed weight percent of PEG (20% w/v), the ion activities depend on the ion type, molecular mass of PEG and the electrolyte concentration. (Figs. 2A and 2B). For the smallest PEG used and in 0.1 M KCl, the activities of Cl^- and Na^+ were $\sim$ 13% greater than that of K^+. The difference in the activities is probably due to the selective binding of ions to PEG. Some of the ion activities increase with increasing PEG molecular mass. The increase in Cl^- activity with PEG molecular mass is consistent with the notion that two or three water molecules are bound per PEG repeat unit [16–19] and the gradual increase in the amount of water bound to PEG for PEG molecular mass greater than $\sim$ 800 to 1000 Da [19]. The smaller increase in K^+ activity (in 0.1 M KCl solution) with the increase in PEG molecular mass suggests that, under these conditions, K^+ binds more strongly to PEG than does Cl^-. It is curious that when the concentration of KCl is increased from 0.1 M to 1 M, increasing the PEG molecular mass has a larger effect on the activity of K^+ compared to that of Cl^- (Fig. 2B). Also note that at lower ionic strength, the PEG apparently binds K^+ more than it does Cl^- (Fig. 2A). However, at higher ionic strength, the opposite is true. It is well known that PEG forms complexes with metal cations [20,21], apparently because PEGs can adopt pseudo-helical conformations with cavities of preferred sizes [21–23]. The results therefore suggest that the structure of PEG changes with ionic strength.

3.3 Influence of pH and KCl concentration on the PEG hydrodynamic radius

We and others have used relatively high concentrations of electrolytes and different pH values when using nonelectrolytes to study the physical properties (e.g. of the "apparent" size) of ion channels [14, 24–29]. In these experiments, it is usually assumed that the hydrodynamic radius of the nonelectrolyte polymers, including PEG, is independent of the electrolyte type and electrolyte concentration. We tested this assumption.

By measuring the viscosity of PEG solutions, we demonstrated that the hydrodynamic radius of PEG is virtually unchanged with increasing pH. For example, the radius of PEG3400 increased only from (1.62 ± 0.15) nm at pH 3 to 1.65 ± 0.16 nm at pH 10. High concentrations of 2:2 electrolytes, like $MgSO_4$, have destabilizing effects on PEG [30]. We therefore wondered what effects relatively high concentrations of 1:1 electrolytes (e.g. KCl and NaCl) used in ion channel studies might have on the hydrodynamic radius of PEGs. We found that increasing the electrolyte concentration only slightly decreases PEG's hydrodynamic radius and that the greater the PEG molecular mass, the greater the influence the KCl concentration has on the R_h. The dependence of R_h on [KCl] (in M) for PEG4000 and PEG1500 can be expressed as R_h4000 = 2.048 - 0.058[KCl] and R_h1500 = 1.164 - 0.019[KCl]. For example, the hydrodynamic radii of PEG4000 and PEG1500 are about 2.5% and 1.5% smaller, respectively, in 1 M KCl than they are in 0.1 M KCl.

4. Effect of Nonelectrolytes on the Ion Current Through Single Channels

4.1 Molecular information deduced using nonelectrolyte polymers

PEG is commercially available in a wide-range of sizes. If the dispersion of the polymer molecular mass of a stated size PEG is minimal, the polymer can be used to estimate the maximum radius of the channel, as was mentioned above. This is possible if we assume the PEG molecules act as hard spheres, not as flexible coils [31] (i.e. they do not interact with the channel's walls; see below, the chapter by Bezrukov and Kasianowicz, and [26]). The polymer can also be used to deduce information about the mechanism of ion transport through the channels (e.g. the relation between the effect of low molecular mass polymers on the ion channel conductance and the bulk conductivity can help elucidate the mechanism of ion transport through the channels).

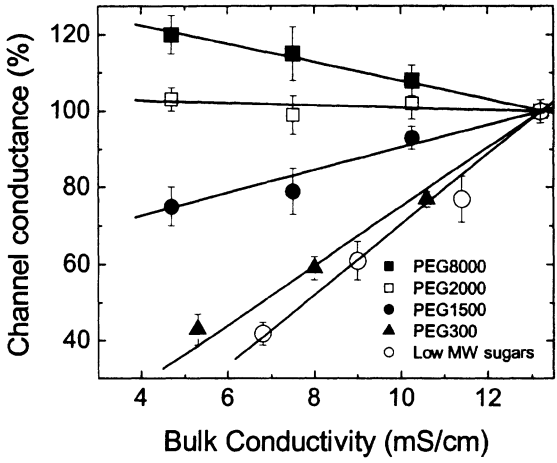

Figure 3. The αHL channel conductance ratio (i.e. 100 times the ratio of the channel conductance in the presence to that in the absence of nonelectrolytes) as a function of the bulk conductivity. The bulk conductivity decreased as the nonelectrolyte concentration was increased. The solutions on both sides of the membrane initially contained 0.1 M KCl. The PEGs or low molecular weight sugars were subsequently added to each side. Data adapted from [41].

4.2 Effect of PEG on *S. aureus* α-hemolysin channel conductance

α-Toxin (also known as α-hemolysin, αHL) is a virulent factor produced by *Staphylococcus aureus* [32]. As a monomer, it contains 293-amino acid residues with a total molecular mass of 33.2 kDa [33]. The monomer is water-soluble, but spontaneously binds to a lipid membranes. Upon binding, it oligomerizes into a water-filled, slightly anion-selective channel [34–39]. The channel is formed from seven identical monomers [39]. It is generally accepted that the transmembrane pore-formation is a major mechanism by which *S. aureus* damages target cells.

We demonstrated that when the concentration of low molecular mass PEGs (e.g. 300 to 600 Da) was increased, both the conductance, g, of the αHL channel and the bulk conductivity, σ, of a KCl solution decreased in a similar manner (Fig. 3) [12, 13, 15]. This suggests the mechanism of ion transport in the channel is similar to that in the bulk. From the PEG partitioning experiments (Fig. 3), the largest radius of the αHL channel is approximately 1.3 nm. In the presence of 0.1 M KCl, this value of the maximum channel radius is independent of pH [12, 24].

By measuring the dependence of both the single channel conductance and the polymer-induced current fluctuations, Bezrukov and Kasianowicz [26, 27]

demonstrated that in 1 M NaCl, the apparent size of the αHL channel is smaller at pH 4.5 than at pH 7.5, even though the channel's conductance, in the absence of PEG, is larger at the lower pH value. Their results suggest that, under these conditions, PEG interacts with the walls of the αHL channel. Specifically, neither a hard-spheres interaction model nor scaling theory adequately describes their PEG partitioning data. They demonstrated that an ad-hoc two parameter model, based on simple physical concepts, was sufficient to describe their results. The authors also concluded that that interaction between PEG and the pore's wall is modulated by a change in the channel induced by a change in pH. Because the properties of PEG are virtually unchanged by changes in the solution pH and ionic strength, their conclusion seems reasonable. However, it is conceivable that ions bound to PEG (Figs. 2A and 2B) might account, in part, for the interaction of PEG with the αHL's titratable side chains in the channel.

Based on the linear relationship between the channel conductance, g, and the solution bulk conductivity, σ, on the PEG concentration, we defined an empirical parameter F, a filling factor to describe the extent to which the pore is filled with polymer [40]:

$$F = \left(\frac{g_o - g_i}{g_o}\right)\left(\frac{\sigma_o}{\sigma_o - \sigma_i}\right) \tag{2}$$

where the subscripts o and i denote the absence and presence of PEG, respectively.

The value of the filling factor is greater if nonelectrolyte polymer partitions into the pore. Figure 4 illustrates the dependence of F on the PEG molecular mass. We assume the value of the hydrodynamic radius at which F starts to increase is the largest radius of the channel.

As was shown for PEG partitioning into the αHL channel [26,27], the dependence of the filling factor F on the PEG hydrodynamic radius of PEG is sharp. Because the filling factor is another representation of the PEG partitioning data, it too cannot be described adequately by scaling theory [31] whether or not the PEG molecules inside the channel are assumed to repel each other (Fig. 5).

At relatively low ionic strength (0.1 M KCl), a hard-sphere model that excludes PEG-PEG repulsive interactions inside the channel does not fit the data well. However, if these interactions are included in the model, the fit is better, but still not acceptable (Fig. 5). Curiously, under certain experimental conditions, even highly flexible PEG molecules (i.e. with a Kuhn length of about several Angstroms) phenomenologically behave as hard spheres that repel each other when confined in a nanometer-scale pore. Neverthless, despite the lack of a complete physical understanding of how PEG interacts with the αHL channel, and how the PEG molecules interact with each other when they

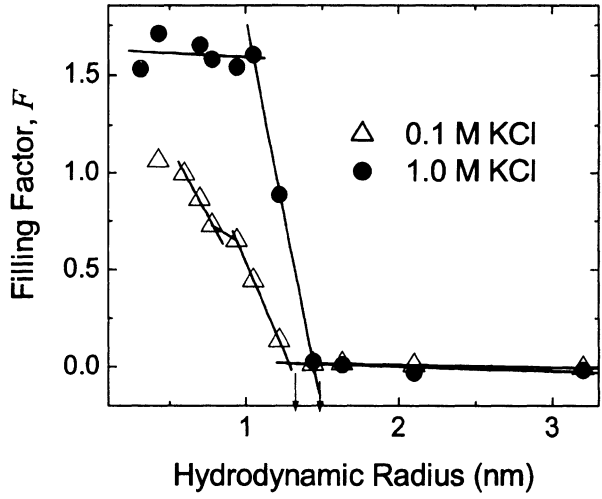

Figure 4. The dependence of the filling factor F on the PEG hydrodynamic radius for the αHL channel. The arrows indicate the value of the maximum radii of the channel in 0.1 M KCl and 1 M KCl, respectively. The membranes were comprised of phosphatidylcholine-cholesterol mixtures (3:1 mass ratio). αHL was added to the *cis*-compartment and the applied potential was - 40 mV (*cis* side negative). The PEG solutions were prepared by mixing 2 g of polymer with 8 ml of either of the buffered electrolyte solution at pH 7.5.

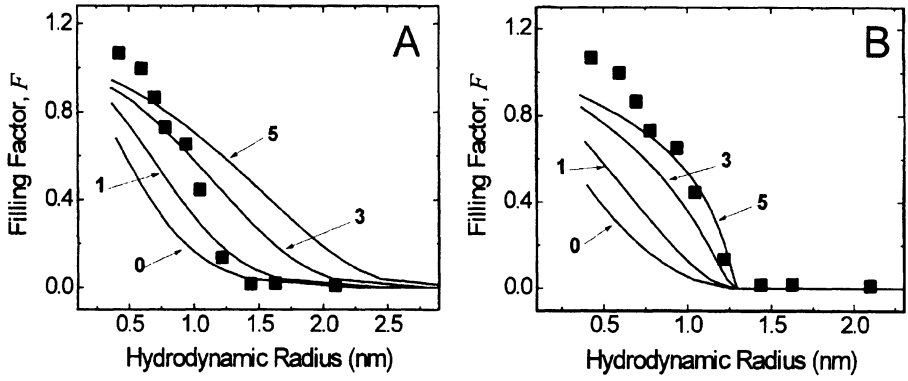

Figure 5. PEG partitioning into the αHL channel as a function of the polymer's hydrodynamic radius. The plot illustrates the experimental results for solutions that contained 0.1 M KCl (squares) and two theoretical predictions (lines) which account for polymer-polymer repulsion: (A) the scaling approach [26, 31]; (B) the hard sphere approach [26, 31]. The numbers inside the plot indicate the excess free energy of polymer-polymer repulsion (in units of kT).

are inside the pore, partitioning experiments still appear useful as probes for this channel's size.

4.3 αHL-channel asymmetry probed using nonelectrolyte partitioning

The partitioning experiments described above were performed in the presence of identical concentrations and sizes of nonelectrolytes in both aqueous phases bathing the αHL channel. To determine the size of each entrance of the αHL channel, and whether the geometry of the channel varies along the pore's axis, we repeated the PEG partitioning experiments with non-electrolyte solution in contact with either the *cis* or *trans* openings, but not both. The approach here is completely empirical. To interpret the experimental results, we will assume, for the sake of simplicity, that polymer partitioning occurs in an "all-or-none" fashion.

The conductance of αHL ion channels in the presence of the polymer in the *cis* or the *trans* sides of the chamber was measured (Table 2). By definition, the protein is added to the *cis* chamber. This table also includes conductance data measured in the presence of PEG on both sides of the channel (g^{both}). Note that the values of g^{cis} are almost always larger than g^{trans} . This is consistent with the known structure of the αHL channel [42]. However, the minimum molecular mass of PEG at which the maximal values g^{cis} and g^{trans} are reached was $\sim$ PEG2000. Thus, the entry of PEG into the αHL channel is limited by both of the narrow pore mouths.

If the αHL pore's geometry is invariant along the pore axis, the dependence of the *cis* and *trans* side filling factors on the PEG hydrodynamic radius should be identical and vary sharply from zero to a maximum value as the polymer radius is decreased. The results in Fig. 6 show that PEG molecules with radii larger than 1.22 nm do not enter the channel from either entrance (i.e. $F \sim 0$) and the maximum values of F observed for either case was 0.6. However, the two filling factors differ in their dependence on PEG size and they both exhibit a second step for PEGs with hydrodynamic radii between $\sim$ 0.5 nm and 1 nm.

These results can be interpreted in a simple manner. When the solution contains PEGs that are too large to partition into a pore entrance, $F = 0$. As the R_h is decreased to a size small enough to enter the pore, F increases. F continues to increase as R_h decreases until the polymers encounter another constriction, smaller than the channel's mouth, further inside the pore. Here, F remains constant with decreasing R_h. Finally, as the polymer hydrodynamic radius is reduced further, the polymer is able to penetrate further into the pore past the second constriction, and further increase the value of F.

Table 2. Conductance of a single αHL channel with PEG at one or both ends.

	χ, mS/cm	R, nm	g^{both}	g^{cis}	g^{trans}
Standard	12.95		107.5±3.1		
Glycerol	7.10	0.308	55.1±6.5	71.6±3.7	72.7±5.6
PEG200	6.15	0.430	49.4±3.6	69.1±5.3	65.0±5.2
PEG300	6.00	0.600	50.0±7.4	75.8±5.5	62.5±5.0
PEG400	5.92	0.700	53.1±5.7	75.1±3.7	68.9±3.9
PEG600	5.95	0.780	57.9±3.5	75.1±5.1	69.0±3.2
PEG1000	5.72	0.940	59.0±5.1	75.9±5.8	73.7±7.4
PEG1450	5.70	1.050	68.7±5.2	81.5±5.1	83.1±4.4
PEG2000	5.71	1.220	91.9±6.0	100.0±4.8	104.2±6.5
PEG3000	5.73	1.440	105.6±3.2		
PEG3400	5.66	1.630	105.3±4.4	105.5±4.2	104.6±7.6
PEG4600	5.65	2.100	106.4±7.3		

χ (mS/cm) is the bulk solution conductivity. R (nm) is the hydrodynamic radius of the non-electrolyte obtained using viscosimetry by [12, 53, 54]. The single channel conductance g(pS) is expressed as mean ± SD. The number of the single channel events counted in the main pool obtained from the computer analysis of the histogram and the number counted in the whole cumulative histogram are all larger than 40. g^{both} is obtained with the same nonelectrolyte on both sides of the bilayer; g^{cis} is measured with a given nonelectrolyte on the cis side and PEG 4600 on the trans side, and g^{trans} is the conductance measured with the given nonelectrolyte on the trans side and PEG 4600 on the cis side. Because there is a transmembrane potential V_{rev} and the system is asymmetric, the conductances g^{cis} and g^{trans} are calculated as follows:

$$g^{\text{cis}} = I_m/(V_m + V_{\text{rev}})$$
$$g^{\text{trans}} = I_m/(V_m - V_{\text{rev}}).$$

V_m is the potential applied across the membrane and Other conditions are described in the Text.

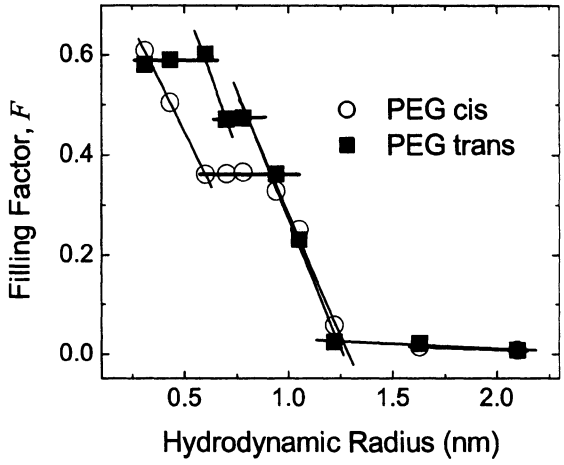

Figure 6. The dependence of the filling factors for the αHL channel (in the presence of PEG in either the *cis* or the *trans* membrane side) on the PEG hydrodynamic radius. The differences in these two results reflect the asymmetry in the channel's structure.

4.4 Summary of Probing the αHL Channel With Non-electrolyte Polymers

From the crystal structure, the αHL channel is 10 nm long and the radii of the *cis* and *trans* openings are both ~ 1.4 nm. There is a large vestibule inside the cap domain that has a maximum radius of 2.3 nm. The narrowest constriction inside the channel has a radius of ~ 0.7 nm and is located at the nexus between the cap and β-barrel stem domains. The radius of the stem segment varies from 0.7 to 1.2 nm depending on the volume of the side chains protruding into the 1.3-nm radius (nominal) of this segment.

The results of the polymer partitioning data (Fig. 6) suggest that the *cis* and *trans* channel entrances of the αHL channel are about the same size (~ 1.25 nm) and that the inner pore geometries for the *cis* and *trans* sides of the channel are different. The larger width of the filling factor plateau for the *cis* polymer addition indicates that the *cis* side of the pore is more steeply conical and than that on the *trans* side. The second constrictions from the *cis* and *trans* pore entrances have radii that range from 0.9 nm to 0.6 nm and 0.8 nm to 0.7 nm, respectively. The results also suggest that minimum radius of the channel is ~ 0.6 to 0.7 nm. These conclusions are in good agreement with the channel's crystal structure [42] (Fig. 7).

5. Limitations with the Method and Possible Future Applications

The simple method described here to determine the size of nanometer-scale pores has several limitations. First, there is no complete physical theory that adequately describes the experimentally determined polymer partitioning results constrictions closer to the bulk solution (e.g. the vestibule in the *cis* side of the αHL channel, Fig. 7) are indeterminate. Third, the interpretation of polymer partitioning experiments may be complicated because PEG interacts with proteins. For example, in high concentrations, it lowers the transition temperature for some proteins [44, 45].

PEG is presumed to bind to hydrophobic sites of proteins, in part, because it has non-polar moieties [46,47] and generally is repelled by fixed charges [30]. If the repulsion is purely electrostatic, then the interaction between PEG and an ion channel due to charged amino acid side chains, will become more attractive. The first evidence for this was provided by Bezrukov and Kasianowicz [26,27] from an analysis of the low-frequency spectral density of αHL channel current noise in the presence of differently sized PEG in 1 M NaCl. In our channel sizing experiments performed in the presence of 0.1 M KCl, we did not observe this effect.

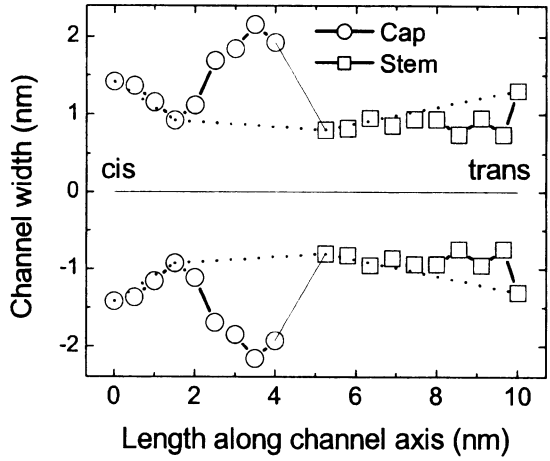

Figure 7. A cross-section of the αHL channel based on the crystallographic data (open circles) [42] and the results of PEG paritioning experiments (dotted line). The structure of the channel in lipid bilayers near the *trans* side entrance ([43]) is identical to that of the crystal structure. The radius of the large vestibule in the *cis* side cannot be ascertained using the polymer partitioning method described here.

Table 3. Transmembrane potential in Cis- and Trans-filling experiments and osmolalities with 0.1 M KCl containing 20% (w/v) PEG.

	V_{rev}	P_{osm}	ΔP_{osm}
Standard		191.8 ±1.0	
Glycerol	-3.50	3046 ±14.5	2372.6
PEG200	-2.60	1905.8±9.3	1231.8
PEG300	-1.85	1512.2±7.9	838.2
PEG400	-1.60	1292.4±2.9	618.4
PEG600	-1.50	1077.6±4.3	403.6
PEG1000	-1.00	918.6±6.0	244.6
PEG1450	-0.50	835.2±1.9	161.2
PEG2000	-0.30	789.3±20.1	115.3
PEG3000	-0.30	734.5±0.7	60.5
PEG3400	0.00	721.4±3.6	47.4
PEG4600	0.00	674.0±5.0	0.0

P_{osm} (mOsm/kg) is the osmolality of a solution prepared by mixing 20 g of the given nonelectrolyte and 80 ml of standard solution (0.1 M KCl, 5 mM Tris-citric acid buffer with pH 7.5. V_{rev} (mV) - is the potential needed on the side with the smaller nonelectrolyte to keep the current through the channel equal to zero. The other compartment always contains PEG4600. The data are mean ± SD for 5-7 experiments. Osmolality of solutions is measured with a Fiske Mark-3 freezing-point osmometer.

There are several other issues that must be considered when using non-electrolyte polymers to size nanometer-scale pores. We address each of these below.

If polymer of one mass is added to the solution on one side of the pore, and that of a different mass is added to the solution on the other side of the pore, a transmembrane potential can develop. Using the αHL channel and high concentrations of PEGs, we found that the value of this potential depended on the difference in the osmolality of both solutions (Table 3). Smaller polymer molecules that correspond to higher osmotic pressure differences [48] increase the magnitude of the potential and the potential was negative on the side that contained the lesser molecular mass PEG.

The observed transmembrane potential should be the sum of a) the streaming potential produced by solution flow through the channel, b) the potential generated by an electrolyte gradient caused by the dilution in an unstirred layer from the side of higher (lower) osmotic pressure due to unidirectional flow of water through the lipid bilayer [49,50], and c) the potential generated by the difference in the KCl activities of the solutions on either side of the membrane. The latter effect is small (Fig.2) and cannot explain the values of the transmembrane potential that we measured (Table 3).

The polymer sizing method requires the single channel conductance be measured to high accuracy. For example, a change of 1% in the mean value

of the single channel conductance leads to a 3% change in the value of the filling factor [40].

In one study, it was shown that a dispersion in polymer molecular mass results in an overestimate in the effective pore radius [51]. Experiments with *Chara coralina* "ghosts" also demonstrated the need to account for the polymer mass dispersion in channel sizing experiments [52]. However, the dispersion of PEG molecular mass (e.g. Merck) show that standard deviation in molecular mass and in hydrodynamic radii of nonelectrolyte, obtained from viscosimetric studies [12,53,54], is usually small (5%).

6. Conclusion

Nonelectrolyte polymers have been used to deduce the size of a wide variety of channels reconstituted into planar bilayer membranes. These channels include the Ca^{2+}-channel induced by neurotoxin from black widow spider venom [55], the Ca^{2+}-channel formed by protein of *Characeae* algae *Nitellopsis* [56], channels formed by *S. aureus* αHL [24,40,57,66], B-subunit of cholera enterotoxin [58,67], *Vibrio cholerae* hemolysin [41,59], *Pasteurella multocida* dermonecrotic toxin [60], colicin Ia [25], mitochondrial porin [28], malaria parasite's nutrient channel [61], Syringomycin E [62], amphotericin B [63], alamethicin [14], chrysospermin [64] and the nonpeptidic fungal toxin [65].

Despite its limitations, the nonelectrolyte polymer partitioning technique is a simple and powerful method to study the geometrical features of relatively large ion channels.

Acknowledgments

I thank Sergey Bezrukov, John Kasianowicz, Stephen Slatin, Roland Benz, Frederich Thinnes, Wamberto Varanda, Steve Aird and Antonio Carvalho for fruitful collaboration and my collaborators Ravshan Sabirov, Vadim Ternovsky, Petr Merzlyak, Javdat Muratkhodjaev, Liliya Yuldasheva, Romildo Nogueira, Jackson da Cruz, Carlos Carneiro and Claudio Rodrigues for their excellent work on which this review is largely based.

References

[1] North C.L., Barranger-Mathys, M. and Cafiso, D. (1995) Membrane orientation of the N-terminal segment of alamethicin determined by solid-State 15N NMR. *Biophys. J.* **69**, 2392-2397.

[2] Opella S.J. (1994). Solid-state NMR structural studies of proteins. *Ann. Rev. Phys. Chem.* **45**, 659-683.

[3] Altenbach, C., Froncisz, W., Hubbell, W. and Hyde, J. (1988) The orientation of membrane-bound, spin-labeled mellitin as determined by electron-paramagnetic resatu-

ration recovery measurements. *Biophys. J.* **53**, A94-A94.

[4] Cafiso, D.S . (1994) Alamethicin - a peptide model for voltage gating and protein membrane interactions. *Ann. Rev. Biophys. Biomol. Struct.* **23**, 141-165.

[5] Barranger-Mathys, M. and Cafiso, D.S. (1996) Membrane Structure of Voltage-Gated Channel Forming Peptides by Site-Directed Spin-Labeling. *Biochemistry* **35**, 498-505.

[6] Tsukihara, T. and Aoyama, H. (2000) Membrane protein assemblies - towards atomic resolution analysis. *Curr. Opin. Struct. Biol.* **10**, 208-212.

[7] Fleming, K.G. (2000) Riding the wave: structural and energetic principles of helical membrane proteins. *Curr. Opin. Biotechnol.* **11**, 67-71.

[8] Sakai, H. and Tsukihara, T. (1998). Structures of membrane proteins determined at atomic resolution. *J Biochem. (Tokyo)* **124**, 1051-1059.

[9] Ostermeier, C. and Michel, H. (1997) Crystallization of membrane proteins. *Curr. Opin. Struct. Biol.* 7, 697-701; Beauchamp, J.C. and Isaacs, N.W. (1999) Methods for X-ray diffraction analysis of macromolecular structures. *Curr. Opin. Chem. Biol.* **3**, 525-529.

[10] Akabas, M.H., Stauffer, D.A., Xu, M. and Karlin, A. (1992) Acetylcholine-receptor channel structure probed in cysteine-substitution mutants *Science* **258**, 307-310.

[11] Zimmerberg, J. and Parsegian, V.A.P. (1986) Polymer inaccessible volume changes during opening and closing of a voltage-dependent ionic channel. *Nature (London)* **323**, 36-39.

[12] Krasilnikov, O.V., Sabirov, R.Z., Ternovsky, V.I., Merzliak, P.G. and Muratkhodjaev, J.N. (1992a) A simple method for the determination of the pore radius of ion channels in planar lipid bilayer membranes. *FEMS Microbiol. Immunol.* **105**, 93-100.

[13] Sabirov, R.Z., Krasilnikov, O.V., Ternovsky, V.I., Merzliak P.G. and Muratkhodjaev, J.N. (1991) Influence of some nonelectrolytes on conductivity of bulk solution and conductance of ion channels. Determination of pore radius from electric measurements. *Biologicheskie Membrany* **8**, 280-291.

[14] Bezrukov, S.M. and Vodyanoy, I. (1993) Probing alamethicin channels with water-soluble polymers. Effect on conductance of channel states. *Biophys. J* **64**, 16-25.

[15] Sabirov R.Z., Krasilnikov O.V., Ternovsky V.I., Merzliak P.G. (1993): Relation between ionic channel conductance and conductivity of media containing different non-electrolytes. A novel method of pore size determination. *Gen. Physiol. Biophys.* **12**, 95-111.

[16] Hager, S.L. and MacRury, T.B. (1980) Investigation of phase-behavior and water binding in poly(alkilene oxide) solutions. *J.Appl. Polym. Sci.* **25**, 1559-1571.

[17] Tilcock, C.P.S. and Fisher D. (1982) The interaction of phospholipid membranes with poly(ethylene glycol). Vesicle aggregation and lipid exchange. *Biochim. Biophys. Acta* **688**, 645-652.

[18] Breen J., Huis D., Bleijser J. and Leyte J.C. (1988) Solvent dynamics in aqueous PEO-salt solutions studied by nuclear magnetic relaxation. *J.Chem.Soc., Faraday Trans.I* **84**, 293-307

[19] Antonsen, K.P., Hoffman A.S. (1992) Water structure of PEG solutions by differential scanning calorimetry measurements. In: *Poly(Ethylene Glycol) Chemistry: Biotechnical and Biomedical Applications*, Edited by Harris, J.M., Plenum Press, New York-London, 15-28.

[20] Bailey F.E. and Koleske, I.V., (1976) *Poly(Ethylene Oxide)*, Academic Press, New York

[21] Bailey F.E. and Koleske I.V. (1991) *Alkylene Oxides and Their Polymers*, Marcel Dekker, New York

[22] Harris J.M. (1992) Introduction to biotechnical and biomedical applications of poly(ethylene glycol). In: *Poly(Ethylene Glycol) Chemistry: Biotechnical and Biomedical Applications*, Edited by Harris, J.M., Plenum Press, New York-London, 1-13.

[23] Harris J.M., Hundley N.H., Shannon, T.G., Struck, E.C. (1982) Poly(ethylene glycols) as soluble, recoverable, phase-transfer catalysts. *J. Org. Chem.* **47**, 4789-4791.

[24] Korchev, Y.E., Bashford, C.L., Alder, C.M., Kasianowicz J.J. and Pasternak C.A. (1995) Low conductance states of a single ion channel are not "closed". *J. Membr. Biol.* **147**, 233-239.

[25] Krasilnikov, O.V., Yuldasheva L.N., Nogueira, R.A. and Rodrigues, C.G. (1995) The diameter of water pores formed by colicin Ia in planar lipid bilayers. *Brazilian J. of Med. and Biol. Res.* **28**, 693-698.

[26] Bezrukov, S.M., Vodyanoy, I., Brutyan, R.A. and Kasianowicz, J.J. (1996) Dynamics and free energy of polymers partitioning into a nanoscale pore. *Macromolecules* **29**, 8517-8522.

[27] Bezrukov, S.M. and Kasianowicz, J.J. (1997) The charge state of an ion channel controls neutral polymer entry into its pore. *Eur. Biophys. J.* **26**, 471-476.

[28] Carneiro, C.M.M., Krasilnikov, O.V., Yuldasheva, L.N., Campos de Carvalho, A.C. and Nogueira R.A. (1997). Is the mammalian porin channel, VDAC, a perfect cylinder in high conductance state? *FEBS Lett.* **416**, 187-189.

[29] Krasilnikov, O.V., Merzlyak, P.G., Yuldasheva, L.N., Azimova, R.K. and Nogueira, R.A. (1997) Pore-forming properties of proteolytically nicked staphylococcal α-toxin. The ion channel in planar lipid bilayer membranes. *Med. Microbiol. and Immunol.* **186**, 53-61.

[30] Lee, J.C. and Lee, L.L. (1981) Preferential solvent interactions between proteins and polyethylene glycols. *J. Biol. Chem.* **256**, 625-631.

[31] Merzlyak, P.G., Yuldasheva, L.N., Rodrigues, C.G., Carneiro, C.M., Krasilnikov O.V. and Bezrukov, S.M. (1999) Polymeric Nonelectrolytes to probe pore geometry: Application to the α-toxin transmembrane channel. *Biophys. J.* **77**, 3023-3033.

[32] Bhakdi, S. and Tranum-Jensen, J. (1991) *S. aureus* α-toxin. *Microbiol. Rev.* **55**, 733-751.

[33] Gray, G.S. and Kehoe, M. (1984) Primary sequence of the α-toxin gene from Staphylococcus aureus Wood 46. *Infect. Immunity* **46**, 615-618.

[34] Valeva, A., Weisser, A., Walker, B., Kehoe, M., Bayley, H., Bhakdi S. and Palmer, M. (1996) Molecular architecture of a toxin pore: a 15-residue sequence lines the transmembrane channel of Staphylococcal alpha-toxin. *EMBO J.* **15**, 1857-1864.

[35] Vecsey-Semjen, B., Lesieur, C., Mollby, R. and vander Goot, F.G. (1997) Conformational changes due to membrane binding and channel formation by staphylococcal alpha-toxin. *J. Biol. Chem.* **272**, 5709-5717.

[36] Tomita, T., Watanabe, M. and Yasuda, T. (1992) Influence of membrane fluidity on assembly of *Staphylococcus aureus* a-toxin, a channel-forming protein, in liposome membrane. *J. Biol. Chem.* **267**, 13391-13397.

[37] Krasilnikov, O.V., Ternovsky, V.I., Musaev, Yu.M. and Tashmukhamedov, B.A. (1980). Influence of staphylotoxin on conductance of bilayer phospholipid membranes. *Doklady AN UzSSR* **N7**, 66-68.

[38] Krasilnikov, O.V., Ternovsky, V.I. and Tashmukhamedov, B.A. (1981). Properties of ion channels induced by alpha-staphylotoxin in bilayer lipid membranes. *Biofisica* **26**, 271-275.

[39] Gouaux, J.E., Braha, O., Hobaugh, M.R., Song, L., Cheley, S., Shustak, C. and Bayley, H. (1994). Subunit stoichiometry of staphylococcal alpha-hemolysin in crystals and on membranes: A heptameric transmembrane pore. *Proc. Natl. Acad. Sci. (USA)* **91**, 12828-12831.

[40] Krasilnikov, O.V., Cruz, J.B.Da., Yuldasheva, L.N. and Nogueira, R.A. (1998) A novel approach to study the geometry of the water lumen ion channel. Colicin Ia channels in lipid bilayers. *J. Membr. Biol.* **161**, 83-92.

[41] Krasilnikov, O.V., Muratkhodjaev, D.N. and Zitzer, A.O. (1992b) The mode of action of V.cholerae cytolysin. The influences of both erythrocytes and planar lipid bilayers. *Biochim. Biophys. Acta* **1111**, 7-16.

[42] Song, L., Hobaugh, M.R., Shustak, C., Cheley S., Bayley, H., and Gouaux, J.E. (1996) Structure of staphylococcal α-hemolysin, a heptameric transmembrane pore. *Science* **274**, 1859-1866.

[43] Kasianowicz, J.J., Burden, D.L., Han, L., Cheley, S. and Bayley H. (1999) Genetically engineered metal ion binding sites on the outside of a channel's transmembrane b-barrel. *Biophys. J.* **76**, 837-845.

[44] Arakawa, T. and Timasheff, S.N. (1985) Mechanism of poly(ethylene glycol) interaction with proteins. *Biochemistry* **24**, 6756-6762.

[45] Lee, L.L. and Lee, J.C. (1987) Thermal stability of proteins in the presence of poly(ethylene glycols). *Biochemistry* **26**, 7813-7819.

[46] Hammes, G.G. and Schimmel, P.R.. (1967) An investigation of water-urea and water-urea-polyethylene glycol interactions. *J. Am. Chem. Soc.* **89**, 442-446.

[47] Ingham, K.C. (1977) Polyethylene glycol in aqueous solution: solvent perturbation and gel filtration studies. *Arch. Biochem. Biophys.* **184**, 59-68.

[48] Parsegian, V.A., Rand, R.P., Fuller, N.L. and Rau, D.C. (1986) Osmotic stress for the direct measurement of intermolecular forces. *Method Enzymol.* **127**, 400-416.

[49] Pohl, P., Saparov, S.M. and Antonenko, Y.N. (1997) The effect of a transmembrane osmotic flux on the ion concentration distribution in the immediate membrane vicinity measured by microelectrodes. *Biophys. J.* **72**, 1711-1718.

[50] Pohl, P., Saparov, S.M. and Antonenko, Y.N. (1998) The size of the unstirred layer as a function of the solute diffusion coefficient. *Biophys. J.* **75**, 1403-1409.

[51] Scherrer, R. and Gerhard, P. (1971) Molecular sieving by the Bacillus megaterium cell wall and protoplast. *J.Bacteriol.* **107**, 718-735.

[52] Berestovsky, G.N., Ternovsky, V.I. and Cataev, A.A. *Private communication.*

[53] Sabirov, R.Z., Krasilnikov, O.V., Ternovsky, V.I., Merzliak, P.G. and Muratkhodjaev, J.N. (1991) Influence of some nonelectrolytes on conductivity of bulk solution and conductance of ion channels. Determination of pore radius from electric measurements. *Biologicheskie Membrany* **8**, 280-291.

[54] Sabirov, R.Z., Krasilnikov, O.V., Ternovsky, V.I. and Merzliak, P.G. (1993) Relation between ionic channel conductance and conductivity of media containing different non-electrolytes. The novel method of pore size determination. *Gen. Physiol. Biophys.* **12**, 95-111.

[55] Krasilnikov, O.V. and Sabirov, R.Z. (1992) Comparative analysis of latrotoxin channels of different conductance in planar lipid bilayers. Evidence for cluster organization. *Biochim. Biophys. Acta* **1112**, 124-128.

[56] Ternovsky, V.I. and Berestovsky, G.N. (1998) Effective diameter and structural organization of reconstituted calcium channels from the Characeae algae Nitellopsis. *Membr. Cell Biol.* **12**, 79-88.

[57] Krasilnikov, O.V., Sabirov, R.Z., Ternovsky, V.I., Merzliak, P.G. and Tashmukhamedov, B.A. (1988) Structure of ion channels induced by a-toxin from *Staphylococcus aureus*. *Gen. Physiol. Biophys.* **7**, 467-473.

[58] Krasilnikov O.V., Muratkhodjaev D.N., Voronov S.E., Ezepchuk Yu.V. (1991) The ionic channels formed by cholera toxin in planar bilayer lipid membranes are entirely attributable to its B-subunit. *Biochim. Biophys. Acta* **1067**, 166-170.

[59] Zitzer, A.O., Nakisbekov, N.O., Li, A.V., Semiotrochev, V.L., Kiseliov, Yu.L., Muratkhodjaev, J.N., Krasilnikov, O.V. and Ezepchuk, Yu.V. (1993) Entero-cytolisin (EC) from Vebrio cholerae non-01 (some properties and pore-forming activity). *Int. J. Med. Microbiol. Virol. Parasitol. Infect. Dis.* **279**, 494-504.

[60] Krasilnikov, O.V., Ternovsky, V.I., Navasardyants, D.G. and Kalmykova, L.I. (1994) The characterization of ion channels formed by Pasteurella multocida dermonecrotic toxin. *Med. Microbiol. and Immunol.* **183**, 229-237.

[61] Desai S.A., Rosenberg R.L, (1997) Pore size of the malaria parasite's nutrient channel. *Proc. Natl. Acad. Sci. (USA)*, **94**, 2045-2049.

[62] Kaulin Y.A., Schagina L.V., Bezrukov S.M., Malev V.V., Feigin A.M., Takemoto J.Y., Teeter J.H.., Brand J.G. (1998) Cluster organization of ion channels formed by the antibiotic Syringomycin E in bilayer lipid membranes. *Biophys. J.* **74**, 2918-2925.

[63] Sabirov R.Z., Tadjibaeva G. Sh., Krasilnikov O.V., El Sufi S.A.F., Tashmukhamedov B.A. (1992) Influence of the hydrophilic nonelectrolytes on the single amphotericin channels. *DAN UzSSR* **N1**, 52-54.

[64] Ternovsky V.I., Grigoriev P.A., Berestovsky G.N., Schlegel R., Dornberger K., Grafe U. (1997) Effective diameters of ion channels formed by homologs of the antibiotic chrysospermin. *Membr. Cell Biol.* **11** 497-505.

[65] Goudet C, Benitah J.P., Milat M.L., Sentenac H., and Thibaud J.B. (1999) Cluster organization and pore structure of ion channels formed by beticolin 3, a nonpeptidic fungal toxin. *Biophys. J.* **77**, 3052-3059.

[66] Coates G.M.P., Bashford C.L., Smart O.S. (1998) Using HOLE to predict the effects of PEG's on the conductance of α-toxin. *Biochem. Soc. Trans.* **26**, S193.

[67] Smart O.S., Breed J., Smitgh G.R. and Samsom M.S.P. (1997). A novel method for structure-based prediction of ion channel conductance properties. *Biophys. J.* **72**, 1109-1126

DYNAMIC PARTITIONING OF NEUTRAL POLYMERS INTO A SINGLE ION CHANNEL

Sergey M. Bezrukov
LPSB, NICHD, National Institutes of Health, Bethesda, MD 20892-0924 and St.Petersburg Nuclear Physics Institute, Gatchina, Russia 188350

John J. Kasianowicz
Biotechnology Division, National Institute of Standards and Technology, Gaithersburg MD 20899-8313

Abstract Polymers partitioning into highly confined spaces can be studied using single nanometer-scale pores formed by protein ion channels. The ionic conductance of a channel depends on the state of occupancy of the pore by polymer and serves as a measure of polymer partitioning. Specifically, the movement of neutral polymer into the pore causes a reduction of the channel's conductance. The mean conductance is used to determine the polymer partition coefficient and the conductance fluctuations report the rates at which polymer exchanges between the bulk and the pore. Three theoretical approaches to describe the steric interaction of polymer and a single pore (hard spheres, random flight model, and scaling theory) fail to describe the partitioning of poly(ethylene glycol) into two structurally and chemically different ion channels (*Staphylococcus aureus* α-hemolysin and alamethicin). In particular, these theories cannot account for the sharp molecular weight dependence of the partition coefficient.

Keywords: polymer confinement, poly(ethylene glycol), PEG, PEO, structure-function

1. Introduction

The physics of polymer transport through porous media with micron-sized apertures is important for the science and technology of separating a wide variety of molecules (see the chapter by Åkerman, this volume). However, most fundamental processes of biology, including molecular interaction and recognition, molecular synthesis, ion transport, and polymer translocation happen at nanoscale dimensions. The latter typically occurs through nanometer-scale pores in the membranes of cells and cellular organelles. It is crucial for many biological functions including protein secretion [1–3] (see also Simon, this volume), bacterial gene transduction, and some mechanisms of viral in-

J.J. Kasianowicz et al. (eds.), Structure and Dynamics of Confined Polymers, 117–130.

fection [4] (see also the chapters by Letellier and Kasianowicz, et al., this volume). To understand the mechanism by which polymers are transported through such small portals, we study how differently-sized molecules of a neutral polymer, poly(ethylene glycol), partition into a nanopore of a protein ion channel. water-soluble polymer have also been used as molecular probes of ion channel functional structure [5–14] (see also Krasilnikov, this volume). Interpretation of results obtained in such studies relies on either complete exclusion or partial partitioning of polymers between the bulk and the channel pore, a process that is governed by complex polymer-pore interactions.

Using the polymer-induced changes in single channel conductance as a measure of pore occupancy by polymers, we deduce polymer partitioning as a function of polymer size for two structurally and chemically different channels, *Staphylococcus aureus* α-hemolysin (αHL) and alamethicin. We compare experimental results with the predictions of three theoretical approaches: hard spheres partitioning (e.g. [15]), random flight model [16], and scaling [17, 18]. We find that for both channels, the experimentally obtained dependence of polymer exclusion (or partitioning) on polymer weight is *sharper* than any of these models of pure steric repulsion describes. We show that several possible complications stemming from a) the deviation of pore shape from that of a regular cylinder, b) the polydispersity of PEG samples, or c) the non-ideality of concentrated polymer solutions do not solve the problem. In fact, each of them predict the opposite effect—the *flattening* of the dependence of partitioning on polymer molecular weight.

2. General principles

2.1 Equilibrium partitioning

We consider here the problem of polymers partitioning into a nanometer-scale pore. In the case of a large pore (i.e. large with respect to the characteristic size of the polymer coil), one would expect a simple equi-partitioning of polymer between the bulk and the pore (Fig. 1, top). It is clear that the action of polymer on the single pore conductance would be identical to that on the bulk conductivity because the average polymer density inside the pore is the same as that in the bulk. Primarily, neutral polymers (e.g. PEG) reduce the bulk conductivity of electrolyte solutions because their addition decreases the ionic concentration and increases the solution microviscosity. Also, if ions bind to the polymer, this will further reduce the bulk conductivity.

In contrast, for a small pore (i.e. small with respect to the characteristic size of the polymer coil), there is a high entropic cost for confining a polymer in the pore because a number of possible polymer configurations are lost (Fig. 1, bottom). As a result, the average occupancy of the pore by polymer is decreased, and the polymer concentration in the pore will be less than

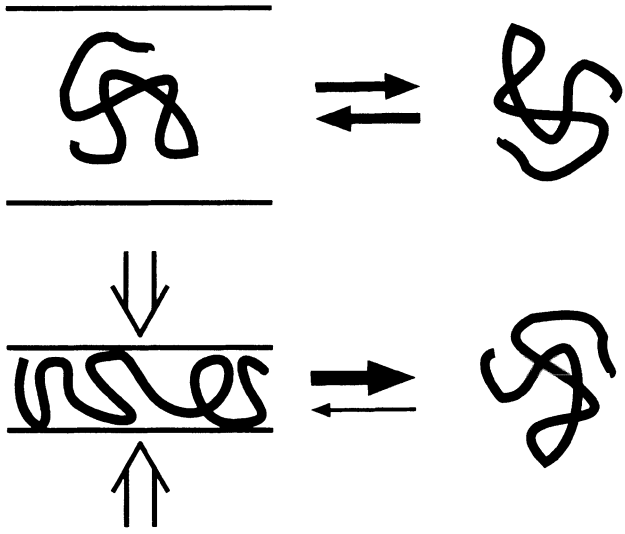

Figure 1. Polymer confinement in two idealized pores. Top: the polymer equilibrates between the bulk and a relatively large pore without being distorted. Bottom: the polymer partitioning into a relatively small pore is reduced by the entropic repulsion between the polymer and the pore.

that in the bulk. Correspondingly, the relative polymer-induced conductance reduction will be less than that for a large channel. In the case of very large, and therefore completely excluded polymers, there is no reduction in the conductance of the channel itself. In all cases, there is a small, and sometimes measurable, influence of polymer on the access resistance of the channel.

There are several approaches to formulating a quantitative description of entropy-driven polymer exclusion. We discuss three of them which provide analytical closed-form solutions: hard spheres partitioning [15], random flight model [16], and scaling [17,18]. In the hard spheres model, we consider the polymer radii r_h to scale as $\sim$ (molecular weight)$^{3/5}$. The corresponding partition coefficient between the bulk and a cylindrical pore of radius R is given by [15]

$$p^{HS} = \begin{cases} (1 - r_h/R)^2 & \text{for } r_h \leq R \\ 0 & \text{for } r_h > R. \end{cases} \quad (1)$$

Note that even in the hard sphere model, the partition coefficient varies smoothly and monotonically with molecular weight and is manifestly zero for particles that are larger than the pore. The random flight model [16] represents a polymer chain as a three dimensional random walk and accounts

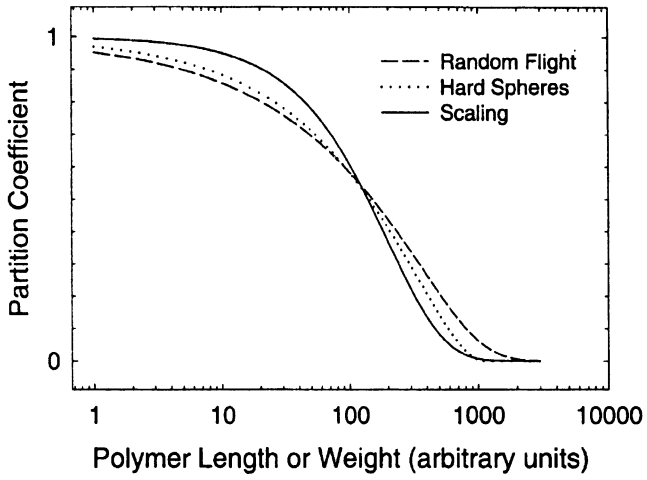

Figure 2. Comparison of three theoretical approaches to describe the steric interaction of polymer and a single pore: hard spheres (dotted line), random flight model (dashed line), and scaling theory (solid line). The polymer molecular weights are normalized to permit the midpoint of the three curves to coincide.

for the walks that are lost as a result of confinement. The partition coefficient is given by

$$p^{RW} = 4 \sum_{m=1}^{\infty} \frac{1}{\beta^2{}_m} \exp\left[-(\beta_m r_i/R)^2\right], \tag{2}$$

where β_m are the roots of a zero order Bessel function of the first kind and r_i is the root-mean-square radius of an ideal chain, $r_i \sim$ (molecular weight)$^{1/2}$. Unlike the hard sphere model, this description predicts a finite value of the partition coefficient for particles that are larger than the pore.

The scaling theory approach considers the entropic cost of confining a large polymer chain in a narrow and long cylinder. Increasing the length of the polymer increases the number of "blobs" trapped in the cylindrical pore and the change in entropy is proportional to the polymer length (or molecular weight) [17,18]. Therefore, because r_h scales as $\sim$ (molecular weight)$^{3/5}$, the partition coefficient is described by

$$p^{SC} = \exp\left[-\theta\,(r_h/R)^{5/3}\right], \tag{3}$$

where the parameter θ is not definable by scaling arguments. All three descriptions give rise to a smooth transition from equi-partitioning to complete exclusion (Fig. 2). Scaling theory gives the sharpest transition between these two regimes.

2.2 Dynamics of partitioning

The previous descriptions do not address the fact that polymer partitioning is a dynamic process. Even at equilibrium, polymer molecules continuously exchange between the pore and the bulk because of Brownian motion. While the average partitioning is characterized by the decrease in the mean pore conductance, the polymer exchange between the bulk and the pore causes fluctuations around the mean conductance value. The characteristic polymer lifetime in the pore is about $L^2/12D$ [19,20], where L is the pore length and D is the polymer diffusion coefficient in the pore. For a 5 nm long pore, and a 1 nm radius polymer in water ($D \sim 3 \times 10^{-6}$ cm^2/s), the lifetime is $\sim$ 10 ns. The temporal resolution of these pore conductance measurements is $\sim$ 10 μs, some three orders of magnitude too slow to resolve such fast events. Nevertheless, one does observe polymer-induced conductance fluctuations by noise spectral analysis. As we show below, in some cases, the fluctuations are so pronounced that they are evident even at low temporal resolution. This occurs because the time scale of polymer partitioning is markedly increased by polymer-pore interactions. Even when polymer exchange between the bulk and the pore is fast, the effective diffusion coefficient of the polymer in the pore can be estimated from the low frequency spectral density of polymer-induced conductance (or current) fluctuations according to [21–23]:

$$D = \Delta g_s \langle \Delta g \rangle L^2 V^2 / 3 S_i(0), \tag{4}$$

where Δg_s is the reduction in pore conductance induced by a single particle (polymer molecule), $\langle \Delta g \rangle$ is the average reduction in pore conductance, V is the transmembrane applied potential, and $S_i(0)$ is the low-frequency power spectral density of particle-induced current fluctuations. The main assumptions implicit here are that the pore is homogeneous and long (i.e. $L \gg R$, where R is pore radius) and particle-particle interactions are negligible.

3. Experiments and their analysis

3.1 Methods

We determined the ability of differently-sized polymers to partition into a pore that spans a lipid bilayer membrane. Specifically, we measured the ionic current that flows through the pore at a constant applied potential in the presence of differently-sized poly(ethylene glycols), PEGs. Single channels were formed by adding either αHL or alamethicin to one side of a planar lipid bilayer membrane which was bathed by symmetric aqueous solutions containing 1 M NaCl, 2.5 mM MES (or HEPES) at pH 7.5 and 15% (w/w) of a given molecular weight PEG added to the salt solution. We used PEGs with molecular weights between 200 and 17000 Da. Solvent-free membranes were formed from diphytanoyl phosphatidylcholine in high purity pentane and

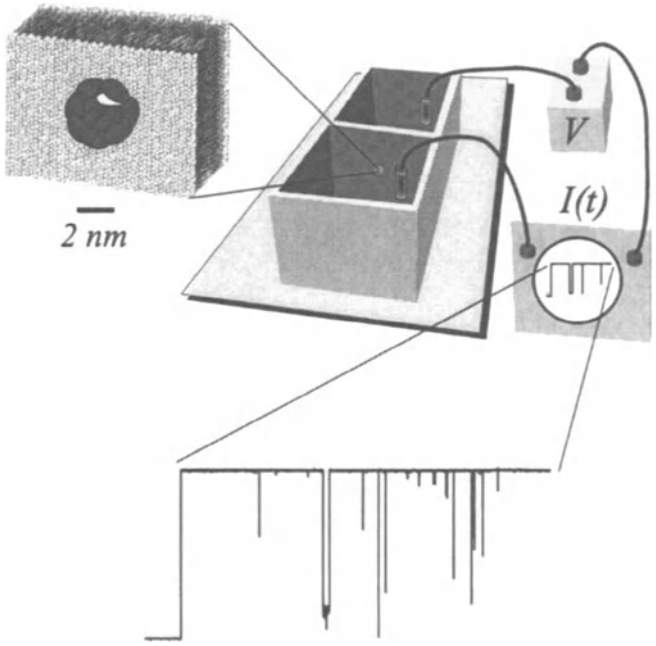

Figure 3. Schematic of single channel recording apparatus. A single channel is formed by adding pore-forming compound to the solution on one side of a 50 μm diameter lipid membrane. The current flowing through the pore is measured using a high impedance, low noise amplifier.

the current was measured and analyzed as described earlier [7, 10, 24]. The temperature was T = (24.0 ± 1.5) °C. An illustration of the apparatus is shown in Fig. 3.

3.2 Experimental results from two chemically and structurally different channels

Figure 4 illustrates the current through a fully open single αHL channel in the absence of polymer and in the presence of differently-sized PEGs [10]. The current varies with PEG molecular weight in two ways. First, the mean current increases with increasing polymer weight. Second, there is a marked difference in the current noise of the pore's open state, depending on the polymer molecular weight. The noise corresponding to the current through the pore in the presence of PEG 2000 is much greater compared to that in the presence of higher and lower molecular weight polymers. Low molecular weight PEGs penetrate the pore and cause a significant decrease in the mean channel conductance. Intermediately-sized polymers cause a smaller

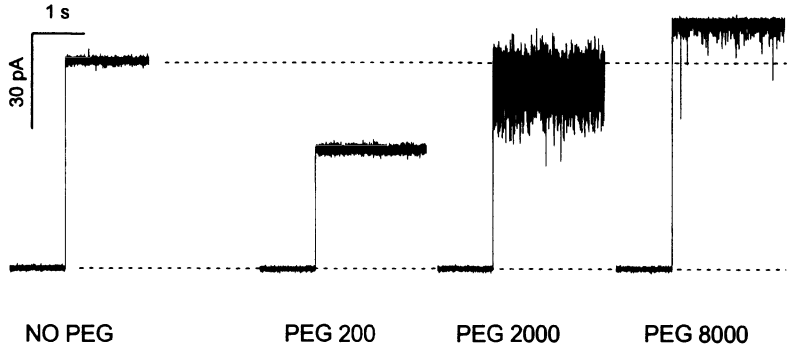

Figure 4. The effect of different molecular weight PEGs on the single αHL channel current. The leftmost trace illustrates the current jump caused by the spontaneous formation of a pore in the absence of polymer. The three recordings on the right show the influence of differently-sized polymers on the open pore current. The current noise varies non-monotonically in polymer molecular weight. The concentration of polymer was 15% for all PEGs and the applied potential was 100 mV. The signal was filtered with a low-pass Bessel filter at 1 kHz.

decrease in the conductance but induce marked fluctuations in the channel current. Large polymers, which are mostly excluded from the pore, increase the mean conductance. Qualitatively similar results were observed with single alamethicin ion channels [7,21]. However, in this case, the low-frequency polymer-induced noise was not as pronounced.

A comparison of the steady-state mean conductance measurements for a single αHL and alamethicin channels in the presence of differently-sized PEG molecules is shown in Fig. 5. Level 1 of the multi-state alamethicin channel is chosen because its conductance, about 0.7 nS in 1M NaCl, in this state is close to that of the fully open αHL channel ($\sim$ 0.9 nS). We first consider the effect of PEG on the αHL channel conductance. Three features are clearly seen. First, PEGs with molecular weights $\leq$ 3400 partition into the pore and decrease the pore's conductance. Second, higher molecular weight PEGs, which apparently do not partition into the pore, increase the conductance. The latter effect is caused by the water binding properties of PEG which increases the electrolyte activity [7]. Third, the lowest molecular weight PEGs (molecular weights $\leq$ 1000) decrease the pore conductance more effectively than they do the bulk solution conductivity (compare the data with the horizontal dotted line). The latter result suggests there is an attractive interaction between the polymer and pore. The mean conductance of a single alamethicin channel also decreases

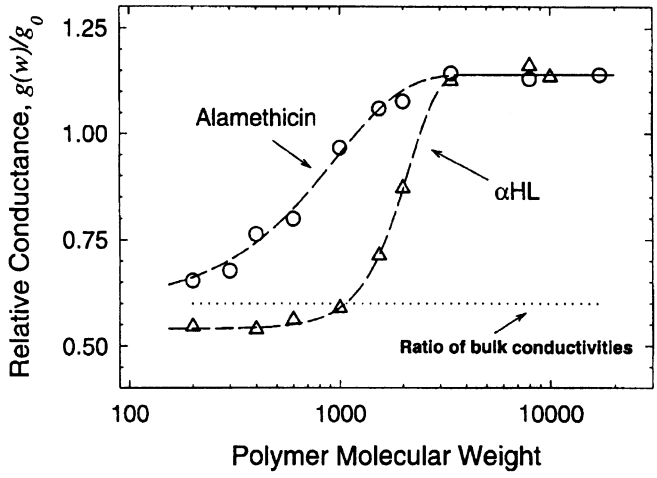

Figure 5. The dependence of single αHL and alamethicin ion channel mean conductances on PEG molecular weight. The conductance values in the presence of PEG, $g(w)$, are normalized to that in the absence of polymer, g_0.

with decreasing PEG molecular weight. However, it does so less sharply. We discuss the significance of this difference below.

The partitioning of polymer into a channel is a dynamic process which causes fluctuations about the mean conductance value (Figs. 4 and 5). To quantify the polymer-induced current noise, we use power spectrum analysis, which facilitates the decomposition of a noise signal from different sources [25, 26]. This statistical method gives the frequency content of the mean square fluctuation. The low-frequency current spectral density for single αHL and alamethicin channels in the presence of PEG is illustrated in Fig. 6. The position of the current noise peak for both channels correlates with the position of the maximum slope in the mean conductance dependence on polymer molecular weight (Fig. 5). However, the peak intensity observed for αHL is more than an order of magnitude greater than that for alamethicin (note the 5-fold difference in scales used for the αHL and alamethicin data and the difference in the applied potentials – see Fig. 6 legend). From equation 4, it follows that the effective diffusion coefficient of the polymer in the αHL channel is dramatically smaller than that in the alamethicin channel. This mobility reduction and the time scale of the polymer-induced current fluctuations for the αHL channel (Fig. 4 and results presented elsewhere [10]) suggest that PEG and the αHL channel interact strongly whereas the interaction between the polymer and the alamethicin channel is not evident.

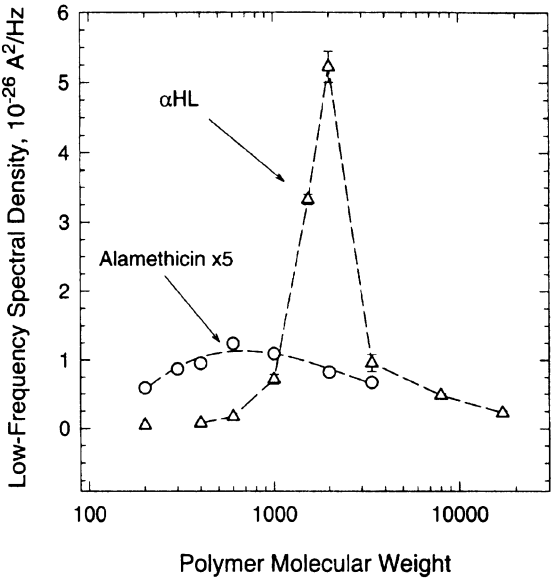

Figure 6. Molecular weight dependence of the low-frequency current spectral density for single αHL (triangles) and alamethicin (circles) channels. The peak in the current noise for αHL is much greater than that for alamethicin's level 1 conductance state and is shifted to higher polymer molecular weight. The applied potential was 100 mV and 150 mV for the experiments with αHL and alamethicin, respectively.

3.3 Comparison of experimental results to available theories

To determine the polymer partitioning into these two channels, we use the mean conductance data in Fig. 5 and assume that the polymer-induced conductance reduction is proportional to the polymer partition coefficient [10]. The results are plotted in Fig. 7. There is a significant difference between the polymer partition coefficients for αHL and alamethicin. First, for αHL, the slope of the partition coefficient dependence on polymer weight is much steeper. Second, for alamethicin, the midpoint of the partition coefficient is shifted towards smaller polymer weights by at least two-fold.

The solid lines are the predictions for the partition coefficient using scaling theory. The fit is not particularly good because it does not adequately describe the steepness of the molecular weight dependence. Although, as is shown in Fig. 2, scaling theory gives the *sharpest* transition between partitioning and exclusion compared to the hard-spheres and random-flight models, it is not sharp enough. The deviation is most pronounced for the αHL channel, but is also clearly seen for the alamethicin channel. We conclude that independent of the size, structural features, and chemical composition of these two pores,

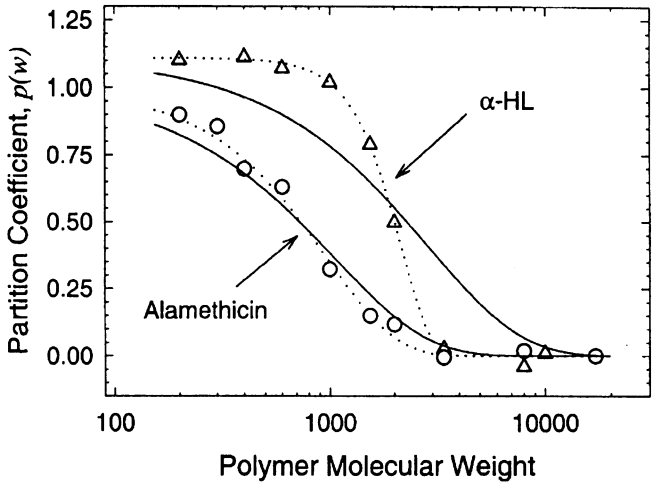

Figure 7. The dependence of polymer partitioning into single αHL (triangles) and alamethicin (circles) ion channels on PEG molecular weight. The solid lines are the least-squares best-fit predictions for the partition coefficient using scaling theory [17,18]. The dashed lines are drawn to guide the eye. For αHL, we used an additional multiplicative factor of 1.1 to account for partitioning exceeding unity for small PEGs.

the three theoretical approaches do not quantitatively describe the empirically obtained polymer partitioning data.

3.4 Possible reasons for the discrepancies between theory and experiment

The polymer partition coefficient is obtained here from conductance data. Implicit is the assumption that the effect of polymer on bulk conductivity and on channel conductance are caused by the same two primary mechanisms – an increase of the solution microviscosity and by dilution. This assumption appears valid because channel pores are large both with respect to the PEG monomer size and the Debye screening length in 1 M electrolytes. Second, for small PEGs that partition easily into the channel, the relative reduction in the pore conductance is close to the relative reduction in bulk solution conductivity (Fig. 5). Thus, there is no compelling reason to expect any pronounced non-linearity between polymer partitioning and channel conductance reduction.

Using the above assumption, we consider three other possible complications that, at first glance, may account for deviations from the "ideal partitioning". They include:

- the pore's shape differs from that of a regular cylinder,

- the PEG samples are poly-disperse mixtures with a number of polymer sizes present,
- the polymer solutions are not ideal at 15% (w/w) concentrations used in partitioning measurements.

However, it is easy to see that each of these complications results in the opposite effect – the *flattening* of the dependence of partitioning on polymer molecular weight. Indeed, deviations in the shape of the pore from a regular cylinder (e.g., to a conical shape) will lead to a wider transition range because the molecular weight cut-off will be converted from one value of polymer size to a spectrum of sizes.

Polymer size polydispersity also widens the transition range. For example, consider a polydisperse PEG sample with a primary size that is excluded from the pore. The low molecular weight components in the PEG sample will still partition into the pore and reduce the pore conductance, which would not occur if the PEG sample was monodisperse. In the other extreme of polymer partitioning (i.e. a low molecular weight PEG sample), high molecular weight components of the sample will be excluded from the pore. Thus, the pore conductance will decrease to a lesser extent compared to monodisperse low molecular weight PEG sample. A recent study addressed this question [27].

The effects of polymer solution non-ideality were discussed previously [14]. It was shown that only the highly artificial hard spheres model gives some sharpening of the transition. However, it is well known that PEG in water forms flexible coils with a Kuhn length of several Ångstroms. Polymer models (e.g. scaling arguments) predict a shift in the partition coefficient curve to higher polymer molecular weights if polymer-polymer repulsion is included. Moreover, if we consider the increase in this repulsion as the polymer molecular weight is increased (solutions of higher weight PEGs are less ideal at the same weight/weight concentration [28]), the polymer solution non-ideality will broaden the transition between partitioning and exclusion. Indeed, larger polymers are driven into the pore with a stronger force of polymer-polymer repulsion.

4. Conclusions

The empirical study of polymer partitioning into nanometer-scale pores reveals a simple qualitative picture. Large polymers are excluded from the pores and thus do not significantly influence the pore conductance whereas small polymers equi-partition into the pore and reduce its conductance to the same degree as they decrease the bulk solution conductivity. The transition between complete exclusion and partitioning reveal the characteristic size of the pore. The larger the pore, the higher the polymer molecular weight at which this transition occurs. However, a rigorous quantitative analysis

of the data clearly shows that three available theoretical models for entropic repulsion fail to describe the sharpness of the transition. Hard spheres, random flight model, and scaling theory predict a smoother dependence of polymer partition coefficient on molecular weight than is observed.

Our analysis suggests that several possible complications caused by either the deviation of the pore shape from a regular cylinder, polydispersity of PEG samples, or non-ideality of concentrated polymer solutions all predict the opposite effect, i.e. a flattening of the dependence of partitioning on polymer molecular weight.

One might ascribe the deviation of the empirical polymer partitioning (Fig. 7) from the theoretical predictions discussed here to complications due to the finite size of the polymer. For example, polymers with small degrees of polymerization, e.g. PEGs with molecular weight less than 1000 Da, undoubtedly do not represent good random coils. The smallest polymers used in our study probably have an appearance more like a curved rod than a coil. Thus, the concepts of statistical polymer physics discussed above should be applied with caution.

However, the results in Fig. 7 demonstrate that the larger pore (αHL) has a steeper dependence of the partition coefficient on polymer molecular weight than does the smaller pore (alamethicin). This shows that the deviation of the data from theoretical predictions is greater for the larger pore and therefore for *larger* polymers. Specifically, for αHL, the transition between partitioning and exclusion occurs over a PEG molecular weight range of 1000 Da and 4000 Da. This observation seems to disagree with the finite size argument discussed above, but does not necessarily exclude this possibility.

We conclude that more theoretical and experimental research is needed to reach a quantitative understanding of the mechanisms controlling flexible polymer partitioning at these biologically important length scales. New models for polymer partitioning must consider interactions between the polymer and the nanometer pore other than the purely entropic repulsion of polymer by an inert geometric constriction.

Acknowledgments

We thank V. Adrian Parsegian, Don Rau, and Victor Bloomfield for fruitful discussions.

References

[1] Simon, S.M., Blobel, G. (1991) A protein-conductive channel in the endoplasmic reticulum. *Cell* **65** 371-380.

[2] Walter, P., Johnson, A.E. (1994) Secretory proteins move through the endoplasmic reticulum via an aqueous, gated pore. em Cell, **78** 461-471.

[3] Bustamante, J.O., Hanover, J.A., Leipins, A. (1995) The ion channel behavior of the nuclear pore complex. *J Membrane Biol.* **146**, 239-252.

[4] Miller, R.V. (1998) Bacteria gene swapping in Nature. (1998) *Scientific American* **278**, 66

[5] Zimmerberg, J., Parsegian, V.A. (1986) Polymer inaccessible volume changes during opening and closing of a voltage-dependent ionic channel. *Nature (London)* **323**, 36-39.

[6] Krasilnikov, O.V., Sabirov, R.Z., Ternovsky, V.I., Merzliak, P.G., Muratkodjaev, J.N. (1992) A simple method for the determination of the pore radius of ion channels in planar lipid bilayer membranes. *FEMS Microbiol. Immun.* **105**, 93-100.

[7] Bezrukov, S.M., Vodyanoy, I. (1993) Probing alamethicin channels with water soluble polymers. *Biophys. J.* **64**, 16-25.

[8] Parsegian V.A., Bezrukov, S.M., Vodyanoy, I. (1995) Watching small molecules move: Interrogating ionic channels using neutral solutes. *Bioscience Repts.* **15**, 503-514.

[9] Korchev, Y.E., Bashford, C.L., Alder, G.M., Kasianowicz, J.J., Pasternak, C.A. (1995) Low conductance states of a single ion channel are not "closed". *J. Membrane Biol.* **147**, 233-239.

[10] Bezrukov, S.M., Vodyanoy, I., Brutyan, R.A., Kasianowicz, J.J. (1996) Dynamics and free energy of polymers partitioning into a nanoscale pore. *Macromolecules*, **29**, 8517-8522.

[11] Desai, S.A., Rosenberg, R.L. (1997) Pore size of the malaria parasite's nutrient channel. *Proc. Natl. Acad. Sci. (USA)* **94**, 2045-2049.

[12] Bezrukov, S.M., Kasianowicz, J.J. (1997) The charge state of an ion channel controls neutral polymer entry into its pore. *Eur. Biophys. J.* **26**, 471-476.

[13] Kaulin, Y.A., Schagina, L.V., Bezrukov, S.M., Malev, V.V., Feigin, A.M., Takemoto, J.Y., Teeter, J.H., Brand, J.G. (1998) Cluster organization of ion channels formed by the antibiotic syringomycin E in bilayer lipid membranes. *Biophys. J.* **74**, 2918-2925.

[14] Merzlyak, P.G., Yuldasheva, L.N., Rodrigues, C.G., Carneiro, C.M.M., Krasilnikov, O.V., Bezrukov, S.M. (1999) Polymeric nonelectrolytes to probe pore geometry: Application to the α-toxin transmembrane channel. *Biophys. J.* **77**, 3023-3033.

[15] Colton, C.K., Satterfield, C.N., Lai, C.-J. (1975) Diffusion and partitioning of macromolecules within finely porous glass. *AIChE J.* **21**, 289-298.

[16] Casassa, E.F. (1967) Equilibrium distribution of flexible polymer chains between a macroscopic solution phase and small voids. *Polymer Lett.* **5**,773-778.

[17] de Gennes, P.-G. (1979) *Scaling Concepts in Polymer Physics*, Cornell University Press, Ithaca, NY.

[18] Grosberg, A.Yu., Khokhlov, A.R. (1994) *Statistical Physics of Macromolecules*, AIP Press, New York, NY.

[19] Feher, G., Weissman, M. (1973) Fluctuation spectroscopy: determination of chemical reaction kinetics from the frequency spectrum of fluctuations. *Proc. Nat. Acad. Sci. (USA)* **70**, 870-875.

[20] Berg, H. (1993) *Random Walks in Biology*, Princeton University Press, Princeton, NJ.

[21] Bezrukov, S.M., Vodyanoy, I., Parsegian, V.A. (1994) Counting polymers moving through a single ion channel. *Nature (London)* **370**, 279-281.

[22] Bezrukov, S.M. (2000) Ion channels as molecular Coulter counters to probe metabolite transport. *J. Membrane Biol.* **174**, 1-13.

[23] Bezrukov, S.M., Berezhkovskii, A.M., Pustovoit, M.A., Szabo, A. (2000) Particle number fluctuations in a membrane channel. *J. Chem. Phys.* **113**, 8206-8211.

[24] Kasianowicz, J.J., Bezrukov S.M. (1995) Protonation dynamics of the alpha-toxin ion channel from spectral analysis of pH-dependent current fluctuations. *Biophys. J.* **69**, 94-105.

[25] Neher, E., Stevens, C.F. (1977) Conductance fluctuations and ionic pores in membranes. *Ann. Rev. Biophys. Bioeng.* **6**, 345-381.

[26] DeFelice, L.J. (1981) *Introduction to Membrane Noise*, Plenum Press, New York, NY.

[27] Berestovskii, G.N., Ternovskii, V.I., Kataev, A.A. (2000) Allowing for polymer polydispersion as a necessary condition for determination of aqueous pore diameters in cells walls and membranes using polymers. *Biofizika* **45**, 69-78.

[28] Parsegian, V.A.; Rand, R.P.; Fuller N.L., Rau, D.C. (1986) Osmotic stress for the direct measurement of intermolecular forces. *Methods Enzymol.* **127**, 400-416.

BRANCHED POLYMERS INSIDE NANOSCALE PORES

C. Gay, P.-G. de Gennes, E. Raphaël
Collège de France, Physique de la Matière Condensée, URA 792 du CNRS
11, place Marcelin Berthelot, 75231 Paris cedex 05, France

and F. Brochard-Wyart
PSI, Institut Curie
11 rue P.M. Curie, 75005 Paris, France

Abstract A non adsorbing, flexible polymer (in dilute solution with a good solvent) enters a pore (of diameter D smaller than its natural size R_F only when it is sucked in by a solvent flux J higher than a threshold value J_c. For linear polymers $J_c \simeq kT/\eta$ (where T is the temperature and η the solvent viscosity). We discuss here the case of statistically branched polymers, with an average number n of monomers between branch points. We find that, depending on the tube diameter, there are two regimes: "weak confinement" and "strong confinement" depending on the tube diameter. By measuring J_c in both regimes, we should determine both the molecular weight of the polymer and the number n of monomers in it.

Keywords: statistically branched polymer, threshold solvent flux, determining molecular weight and number of monomers in a polymer.

1. Introduction

A major breakthrough in polymer production occurred some years ago with the discovery of metallocene catalysts [1]. Thanks to these new catalysts, it is nowadays possible to produce polyolefins with a controlled level of branching and tacticity. The simplest object that one might think of is a statistically branched polymer, with an overall degree of polymerization N, and a number n of monomers between successive branch points. The aim of characterization is to obtain N and n from a minimum number of measurements in dilute solutions. A new method of characterization, based on permeation studies using nanoscale pores, was recently proposed by two of us [2]. In the present paper, we study how this new method of characterization, initially developed

J.J. Kasianowicz et al. (eds.), Structure and Dynamics of Confined Polymers, 131–139.

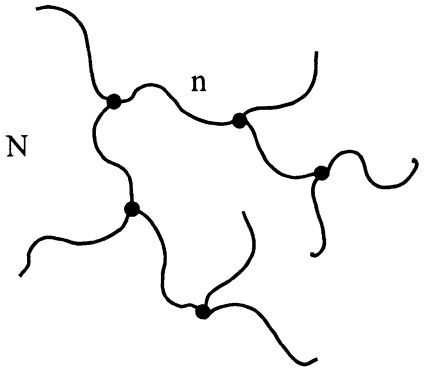

Figure 1. A statistically branched polymer, with a overall degree of polymerization N and a number n of monomers between branch points. The molecule is flexible and tree-like (i.e., it does not contain any closed cycle).

for star polymers, can be extended to statistically branched polymers [3,4]. Througout the paper we assume that the molecule is flexible and tree-like (*i.e.*, it does not contain any closed loop), see Fig.1.

2. Penetration of a linear chain in a nanoscale pore

2.1 Permeation without flow

Let us start from a single linear chain, with degree of polymerization N, dissolved in a good solvent. The coil behaves like a self-avoiding chain with a radius of the Flory form [5]

$$R_F \simeq aN^{3/5}, \tag{1}$$

where a is the monomer size. We now confine the chain into a cylindrical pore of diameter D and assume that the polymer adsorption on the solid wall is negligible. As long as $D \gg R_F$, no change in the behavior of the chain is expected. But if $D < R_F$, the chain is squeezed into the pore and can be pictured as a sequence of blobs of size D, each containing g monomers. At scales smaller than D the chain behaves as an unconstrained chain, and D and g are related by

$$D \simeq ag^{3/5}. \tag{2}$$

The total number of blobs is N/D, and the overall length of the confined chain is $L \simeq (N/g)D \simeq aN(a/D)^{2/3}$. The free energy F required to confine the chain is kT per blob, that is

$$F \simeq kT\frac{L}{D} \simeq kTN\left(\frac{a}{D}\right)^{5/3} \simeq \left(\frac{R_F}{D}\right)^{5/3}. \tag{3}$$

The free energy F can be obtained by measuring the partition coefficient p (*i.e.* the ratio of concentration inside the pore to the concentration outside) for a pore exchanging chains with a bulk solution

$$p \simeq \exp\left(-\frac{F}{kT}\right) \simeq \exp\left[-\left(\frac{R_F}{D}\right)^{5/3}\right]. \tag{4}$$

The partition coefficient becomes rapidly negligible for $D \ll R_F$: chains of size R_F larger than D do not spontaneously penetrate into the pore.

2.2 Forced penetration

We now want to force the chain to enter in the pore. In order to do that, we impose a certain solvent flux J inside the pore. Figure 2 shows a chain that has partially entered into the pore (over a length $l > D$). The free energy of this state can be written

$$E = E_{\text{conf}} + E_{\text{drag}}, \tag{5}$$

where $E_{\text{conf}} \simeq kT(l/D)$ describes the confinement of the l/D blobs. The term E_{drag} represents the effect of viscous forces on the confined blobs and can be evaluated as follows. Each blob is subject to a Stokes force of order ηVD, where η is the solvent viscosity. The flow velocity V is simply related to J and D by $V \simeq J/D^2$. The overall hydrodynamic force is thus $\eta VD(l/D) \simeq \eta Vl$. The work done by this force is $\eta Vl^2/2$; hence $E_{\text{drag}} \simeq -\eta Vl^2/2$. Returning now to the free energy eq. (5), we see that it is maximum for

$$l^* \simeq \frac{kT}{\eta}\frac{D}{J}, \tag{6}$$

corresponding to an energy barrier

$$E^* \simeq \frac{(kT)^2}{\eta J}. \tag{7}$$

Aspiration occurs when $E^* \simeq kT$. This gives a critical current [6]

$$J_c \simeq kT/\eta. \tag{8}$$

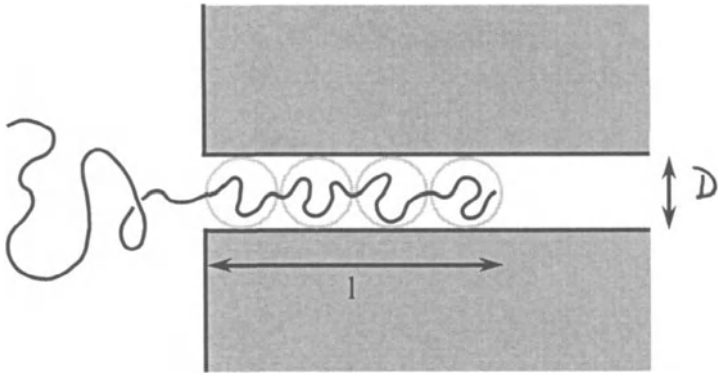

Figure 2. The entry process for a linear polymer: only a certain length, l, has penetrated in the pore.

It is important to note that J_c is independent of the tube diameter D and of the molecular weight N of the polymer. At room temperature, with viscosities comparable to the viscosity of water, $J_c \sim 5 \cdot 10^{-13}\mathrm{cm}^3 \cdot \mathrm{s}^{-1}$. For a pore of diameter $D \sim 5$ nm, the corresponding velocity is $V \simeq J_c/D^2 \sim 20\mathrm{cm} \cdot \mathrm{s}^{-1}$. Experimentally, the crossover from zero permeation to high permeation has been observed by Léger and coworkers for polystyrene in good solvent inside polycarbonate nanotubes [7].

It is also possible to derive the critical current eq. (8) by considering what happens in the entry region outside the pore [8]. There, in a naive picture, we have a convergent flow of velocity $v(r) \simeq J/r^2$, where r is the distance to the pore entry. The velocity gradient is $\dot{\gamma}(r) \simeq J/r^3$. Let $\tilde{r}$ be the distance at which $\dot{\gamma}(\tilde{r}) \simeq 1/\tau$, where $\tau \simeq \eta(R_F)^3/kT$ is the coil relaxation time (Zimm time). We have $\tilde{r} \simeq \left(\frac{\eta J}{kT}\right)^{1/3} R_F$. At a distance $R < \tilde{r}$, the deformation is fast, the chain cannot relax and deforms affinely. The lateral dimension r_f of the distorted coil near the pore entry is of order $r_f \simeq R_F(D/\tilde{r})$. For the chain to penetrate into the pore, R_f has to be smaller than D. This correponds to $J \geq J_c$, where J_c is again given by eq. (8).

3. Statistics of branched polymers

3.1 Overall size in dilute solution

Let us consider the overall size of a statistically branched polymer in dilute solution. An interesting approach based on a Flory type of calculation was

set up by Lubensky and Isaacson [9] and later implemented by Daoud and Joanny [10]. It has been shown long ago by Zimm and Stockmayer [11] that, in the absence of excluded volume interactions, the size of a statistically branched object (containing no loops) was given by $R_0 \simeq aN^{1/4}n^{1/4}$. If we now incorporate excluded volume (with a volume a^3 per monomer), we can write a coil free energy F in terms of the size R as follows:

$$F \simeq kT\left[\frac{R^2}{R_0^2} + \frac{N^2a^3}{R^3}\right]. \tag{9}$$

Here the first term is an elastic energy, and the second term is the effect of intermonomer repulsions (Na^3/R^3 is the internal volume fraction). Optimizing eq. (9) with respect to R, we arrive at [9, 10]:

$$R_F \simeq aN^{1/2}n^{1/10} \tag{10}$$

One can check that for $n = N$, *i.e.* for a linear chain, we recover the standard result $R_F \simeq aN^{3/5}$. Some verifications of eq. (10) have been obtained (on dilute solutions of branched polymers) by M. Adam and coworkers *et al.* [12].

3.2 A statistically branched polymer inside a nanoscale pore

What happens if we now confine our statistically branched object into a cylindrical pore of diameter D ? This problem has been first studied by Vilgis *et al.* some years ago [13]. The main result can been understood in terms of a Flory like free energy

$$\frac{F}{kT} \simeq \frac{L^2}{a^2N^{\frac{1}{2}}n^{\frac{1}{2}}} + \frac{N^2a^3}{LD^2}, \tag{11}$$

where L is the molecule extension along the tube. The first term in eq. (11) is an elastic energy for a molecule of extension L and unperturbed radius $R_0 \simeq aN^{1/4}n^{1/4}$. The second term is the effect of intermonomer repulsions. Optimizing (11) with respect to L, we arrive at

$$L \simeq aN^{5/6}n^{1/6}\left(\frac{a}{D}\right)^{2/3} \simeq D\left(\frac{R}{D}\right)^{5/3}. \tag{12}$$

The internal concentration is

$$\phi \simeq \frac{Na^3}{LD^2} \simeq \left(\frac{D_{min}}{D}\right)^{4/3}, \tag{13}$$

where the minimum diameter

$$D_{min} \simeq aN^{1/8} \tag{14}$$

correspond to maximum squeezing ($\phi = 1$). Of particular importance is the corresponding value of L:

$$L_A \simeq aN^{3/4}n^{1/4} \tag{15}$$

We call L_A the *Ariadne length.* Ariadne helped Theseus through the Minoan labyrinth by giving him a reel of thread, which kept track of his march. L_A represents the length of the shortest path from the starting point to the monster: in our language, the thread distance between two arbitrary points on the cluster. When we squeeze the polymer at its utmost, we arrive at a length L of order L_A.

3.3 The equivalent semi-dilute solution

As usual for semidilute solutions in good solvents, we can think of the squeezed polymer as a compact stacking of blobs, each with a diameter ξ [5].

There are two regimes, depending on the size of the correlation length ξ when compared to the size $\xi_n \simeq an^{3/5}$ of one linear piece of n monomers in good solvent.

1 When the tube diameter D is larger than a certain cross-over value D^*, we have $\xi > \xi_n$. We call this "weak confinement". In this regime, the number g of monomer per blob of size ξ is given by the relation (see eq. (10))

$$\xi \simeq ag^{1/2}n^{1/10}. \tag{16}$$

Writing that $\phi \simeq ga^3/\xi^3$ (compact arrangement) and comparing with eq. (13), we arrive at the correlation length

$$\xi \simeq a\left(\frac{D}{a}\right)^{4/3} N^{-1/6}n^{-1/30}. \tag{17}$$

2 The cross-over occurs when $\xi = \xi_n$. The corresponding tube diameter is given by:

$$D^* \simeq aN^{1/8}n^{19/40}. \tag{18}$$

Note that $D^*/D_{min} \simeq n^{3/5} > 1$.

3 In the interval $D^* > D > D_{min}$, we have a new regime of "strong confinement". There are many blobs between two adjacent branch

points, and the correlation length ξ versus volume fraction ϕ follows the classical law for semidilute solutions of *linear* polymers $\xi \simeq a\phi^{4/3}$. Since $\phi \simeq (D_{min}/D)^{4/3}$ we then arrive at a very simple result:

$$\xi \simeq a(D/D_{min}) \simeq aN^{-1/8}n^{-1/8}. \tag{19}$$

3.4 Critical currents

Knowing the correlation length ξ, we can derive the osmotic pressure Π of the squeezed molecule

$$\Pi \simeq kT/\xi^3. \tag{20}$$

We now consider a branched polymer that has partially entered into the pore over a length l. The corresponding confinement energy is

$$E_c \simeq \Pi D l^2 \simeq kTDl^2/\xi^3. \tag{21}$$

The hydrodynamic force acting on one blob of size ξ is $\eta\xi V$ (Stokes force). The number of blobs is Dl^2/ξ^3. The corresponding energy is thus given by

$$E_h \simeq -\frac{1}{2}\frac{l^2}{\xi^2}\eta J. \tag{22}$$

The total energy $E_c + E_h$ is maximum for

$$l^* \simeq \frac{kT}{\eta J}\frac{D^2}{\xi}, \tag{23}$$

corresponding to an energy barrier

$$E^* \simeq kT\frac{kT}{\eta J}\left(\frac{D^2}{\xi}\right)^4. \tag{24}$$

The critical current J_c corresponds to $E^* \simeq kT$ and is thus given by

$$J_c \simeq \frac{kT}{J}\left(\frac{D^2}{\xi}\right)^4. \tag{25}$$

Inserting eqs. (17) and (19) into (25), we find

$$J_c \simeq \frac{kT}{\eta}(a/D)^{4/3}N^{2/3}n^{2/15}, \qquad D > D^* \tag{26}$$

and

$$J_c \simeq \frac{kT}{\eta} N^{1/2} n^{-1/2}, \qquad D < D^*. \tag{27}$$

Equations (26) and (27) are the central predictions of the model.

4. Concluding remarks

1 According to eqs. (26) and (27), a measurement of the critical current J_c, performed at *two* diameter ($D < D^*$ and $D > D^*$) should allow for the determination of *two* unknowns: the overall number of monomers N and the average distance n between branch points. Thus the permeation may be a rather powerful characterization method. However, our discussion is still rather far from real applications. Several complications can be expected : (a) The largest molecules might clog the pore, (b) The strenght of the pore material should be quite high in order to resist the pressure drop corresponding to the critical current, (c) In some cases, the hydrodynamic forces may be large enough to break the polymer. For a detailed discussion of this last point, see [4] .

2 In order to study the dynamics and free energy of polymers partitioning into a nanoscale pore, Kasianowicz and coworkers [14] have recently performed very interesting experiments where they measure, with high resolution, the ionic conductance of a proteinaceaous channel in the presence of water-soluble polymers. For more details, see Chapter 7 of the present volume.

3 The Ariandne length (15) is related to the so-called *spectral dimension* of a branched polymer. For more details, see [3].

Acknowledgments

We thank S. Havlin, T. Mc Leish, S. Milner and T. Vilgis for helpful discussions.

References

[1] W. Raminsky and M. Arndt (1997), *Adv. Polymer Sci.* **127**, 144.

[2] F. Brochard-Wyart and P.-G. de Gennes (1996), *C. R. Acad Sci. II, Paris* **323**, 473.

[3] C. Gay, P.-G. de Gennes, E. Raphael, and F. Brochard-Wyart (1996), *Macromolecules* **29**, 8379.

[4] P.-G. de Gennes (1999), *Adv. Polymer Sci.* **138**, 92.

[5] P.-G. de Gennes *Scaling Concepts in Polymer Science* (1985), Ithaca, NY: Cornell University Press.

[6] F. Brochard-Wyart and P.-G. de Gennes (1977), *J. Phys. Chem.* **67**, 52.

[7] G. Guillot, L. Léger, and F. Rondelez (1985), *Macromolecules* **18**, 2531.

[8] S. Daoudy and F. Brochard-Wyart (1978), *Macromolecules* **11**, 751.

[9] J. Isaacson and T. C. Lubensky (1980), *J. Physique Lett.* **41**, 469.

[10] M. Daoud and J. F. Joanny (1981), *J. Physique* **42**, 359.

[11] B. Zimm and W. H. Stockmayer (1949), *J. Chem. Phys.* **17**, 1301.

[12] M. Adam, M. Delsanti, J.-P. Munch, D. Duran, M. Daoud, and J. F. Joanny (1987), *J. Physique* **48**, 1809.

[13] T. A. Vilgis, P. Haronska, and M. Benhamou (1994), *J. Phys. II, France*, **4**, 2187.

[14] S. M. Bezrukov, I. Vodyanov, R. A. Brutyan, and J. J. Kasianowicz (1996), *Macromolecules*, **29**, 8517.

PHYSICS OF DNA THREADING THROUGH A NANOMETER PORE AND APPLICATIONS TO SIMULTANEOUS MULTIANALYTE SENSING

John J. Kasianowicz, Sarah E. Henrickson, Martin Misakian, Howard H. Weetall, Baldwin Robertson, and
Biotechnology Division, National Institute of Standards and Technology, Gaithersburg MD 20899-8313

Vincent Stanford
Information Technology Laboratory, National Institute of Standards and Technology, Gaithersburg MD 20899-8113

Abstract Polymer transport is central to many biological processes, including protein translocation, bacterial gene transduction and some modes of viral infection. To better understand the mechanisms of macromolecular transport, we are studying the ability of polymers to partition into and thread through single protein ion channels. It was recently shown in our laboratory that individual molecules of single-stranded DNA and RNA can be detected and characterized as they are driven electrophoretically through a single channel formed by *Staphylococcus aureus* α-hemolysin. We demonstrate that polynucleotides partition more readily into one entrance of this channel than the other and that the rate at which the polymer enters the pore increases exponentially with the magnitude of the applied electrostatic potential. A simple model provides an estimate for both the height of the energy barrier that limits polynucleotide entry into the channel and the number of charges on polyanionic ssDNA that initiate voltage-driven transport through the pore. We show that polynucleotides can be used to probe the geometric properties of an ion channel, and that the interaction between the polynucleotides and a nanopore can be used to estimate the concentration of analytes in solution. A statistical analysis of the current blockades provides information about the structures of both the polymer and the nanopore.

Keywords: alpha-hemolysin, ion channel, DNA, polynucleotide, polymer transport, protein structure, sensor, analyte detection

J.J. Kasianowicz et al. (eds.), Structure and Dynamics of Confined Polymers, 141–163.

1. Introduction

Ion channels are nanometer-scale pores formed from transmembrane proteins. The most well-known channels are the Na^+ and K^+ selective pores which provide the molecular basis of nerve activity [1–4]. More than fifty years of research into the structure and function of ion channels has demonstrated that the same motif, a nanopore, appears in many different roles in cells and organelles including: antibiotic activity [5], the transduction of signals within and between cells [1–4, 6], and the selective transport of ions and macromolecules [1–4, 6–19].

In order to understand the physics of macromolecular transport through biological nanopores including, e.g.

- protein translocation [10–12] (see also the chapters by Simon, Nussburger, and Kinnally, this volume),
- gene transduction between bacteria [4],
- and the transfer of genetic information from some viruses and bacteriophage to host cells (see Letellier, this volume),

we are studying the threading of flexible linear polymers of single stranded RNA and DNA through single channels formed by *Staphylococcus aureus* α-hemolysin (αHL) [20–23]. We describe some of these efforts below.

Experimental methods have only recently permitted the detection of either several polymers [24–28] or single polymers [20–23] in narrow proteinaceous pores. Theoretical analyses of polymer partitioning into simple model geometries are now providing valuable insight into the physics of DNA confinement in structures with biologically relevant length scales [29–34].

Ion channels have recently been considered as a good model system for detecting and quantitating analytes in solution [35–43]. We demonstrate the proof-of-concept that the interaction between polymers and a single nanometer-scale pore provides the physical basis for a new class of sensor that is capable of detecting simultaneously more than one analyte [44].

As is shown elsewhere in this book, nonelectrolyte polymers are good probes for estimating the diameter of protein ion channels (see the chapters by Krasilnikov and by Bezrukov and Kasianowicz; see also [25–28]). As an extension of that work, we show here that polynucleotides can be used as molecular rulers to estimate the length of a channel and the location of constrictions along the pore axis [45].

2. Properties of a model nanopore; the α-hemolysin ion channel

αHL is a protein secreted by the bacteria *Staphylococcus aureus* as a 33.1 kDa monomer [46]. It spontaneously binds cell membranes and self-assembles into a heptameric pore from seven identical subunits [47,48]. The channel has a stem region that spans the membrane [32] and a large head domain that protrudes well beyond one of the membrane-solution interfaces [48] (Fig. 1).

The αHL channel has several properties that make it ideal for studying polymer transport in a nanometer-scale pore. Like many other protein ion channels (e.g. [4,49]), the αHL channel gates (i.e. switches) between different conducting states [26,50,51]. Specifically, the rate at which the αHL channel switches from a fully open state to lesser conducting states increases with the magnitude of the applied potential. Under certain conditions, the αHL channel can remain fully open for tens of minutes [51]. Also, αHL, unlike the Na^+, K^+ and Ca^{2+} selective ion channels, has a relatively large pore diameter that is $\sim$ 1.6 nm at the narrowest constriction [25–28,48] (see also the chapters by Krasilnikov and by Bezrukov and Kasianowicz, this volume). Finally, the crystal structure of the channel has been resolved to 0.19 nm [48] (see Fig. 1)

Figure 1. A model nanopore for DNA transport studies. The α-hemolysin ion channel crystal structure with a single-stranded DNA molecule superposed in the channel. The channel is approximately 10 nm long and 10 nm wide at its widest segment. The narrowest constriction within the pore is about 1.6 nm in diameter and is located approximately halfway down the pore axis. The *cis* and *trans* entrances of the pore are located at the large cap domain (top) and small stem segment (bottom), respectively.

The αHL channel has an additional property that makes it ideal for polymer transport studies. The residence times of some neutral and anionic polymers in its pore are much greater than one would predict using either a one dimensional diffusion equation or any other simple relationship for polymer mobility in the bulk aqueous phase. Because of this, the transit of a single polymer through the pore is easily detected using conventional electrophysiological techniques. For example, random-flight polymers of poly(ethylene glycol), i.e. PEG, that are small enough to partition into the αHL pore should diffuse the length of the channel in about 100 nanoseconds as they apparently do in the alamethicin channel [34]. In contrast, PEGs that enter the αHL channel spend some 100 μs in the pore [29] (see also the chapter by Bezrukov and Kasianowicz). A similar decrease in mobility relative to the mobility in the bulk was observed with single-stranded DNA and RNA transport through this channel [20].

3. Methods

Details of the experimental methods for reconstituting the αHL channel into planar lipid bilayer membranes [35,36] and for detecting polynucleotides threading through it are described elsewhere [20,22,44] (see also Fig. 2, Bezrukov and Kasianowicz). Briefly, a solvent-free diphytanoyl phosphatidylcholine lipid membrane is formed on a 20 μm to 60 μm diameter hole in a 17 μm thick Teflon partition that separates two halves of a Teflon chamber (after [52]). The two compartments contain identical aqueous solutions (e.g. 1 M KCl, 10 mM HEPES, pH 7.5). The αHL protein is added to one compartment. After a single channel forms, excess protein is removed. A transmembrane electric field is applied via two Ag-AgCl, electrodes and the resulting current is converted to voltage (after [53])using a patch clamp amplifier (Axopatch 200B, Axon Instruments). The signal is electronically filtered and digitized by an A/D converter (Axon Instruments Digidata 1200 or 1321, or National Instruments AT-MIO16X A/D board). In our sign convention for the applied potential, a negative voltage drives anions from the *cis* side (i.e. top of the pore, Fig. 1) to the *trans* side (i.e. bottom of the pore). Single-stranded homopolymeric DNA was initially suspended in 10 mM Tris-HCl, 1 mM EDTA, pH 7.5 and added in small aliquots ($<$ 1% of each chamber volume) to either the *cis* or *trans* compartments.

4. Electrically driven transport of single-stranded RNA and DNA in a nanopore

It was shown in our laboratory that a transmembrane electric field can drive single-stranded DNA (ssDNA) through single αHL channels [20]. The

passage of individual polynucleotides through the channel causes transient single channel blockades (Fig. 2).

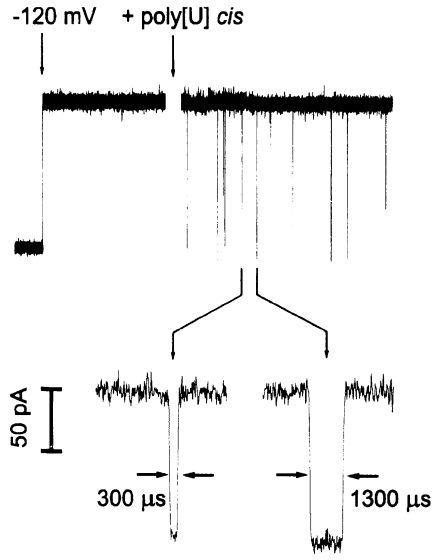

Figure 2. The transport of individual polynucleotides through a single αHL channel causes transient ionic current blockades. (Left) In the absence of ssDNA, the single channel current is stable. (Right) Adding 210-nucleotide long poly[U] caused transient current blockades. The blockades are well defined in amplitude and lifetime. An all-points histogram analysis demonstrated that the distribution of poly[U]-induced current blockade lifetimes were described well by three Gaussians. From [20].

The results of several experiments suggest that ssDNA completely threads through the pore as an extended rod and blocks the current during its transit. First, the mean lifetimes of the blockades induced by poly[U] RNA are proportional to the polymer's contour length (Fig. 3) [20]. Second, the mean lifetimes decrease with an increase in the applied potential [20]. Third, the polymerase chain reaction method confirmed that ssDNA, but not blunt-ended double-stranded DNA, traverses the pore [20]. We discuss below a fourth method that confirms that the polymer threads completely through this channel.

4.1 Voltage-dependent polynucleotide entry into a single nanopore

In general, the current-voltage relationship of the αHL channel is nonlinear and rectifying. Thus, the ability of monovalent cations and anions (e.g. K^+ and Cl^-), to partition into and transport through this channel depends on an asymmetry in the channel's structure.

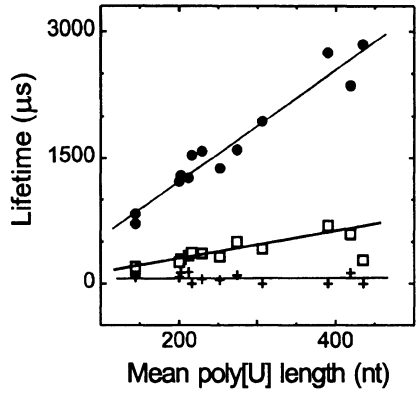

Figure 3. Two of the three most probable lifetimes for poly[U]-induced current blockades were proportional to the mean polymer length (filled circles and open squares). The results suggest that the polynucleotides thread through the αHL channel as linear extended rods. The third class of blockades (+) did not scale with the polymer length and may be caused by brief interludes between the polymer and pore that do not result in polynucleotide transport events. From [20].

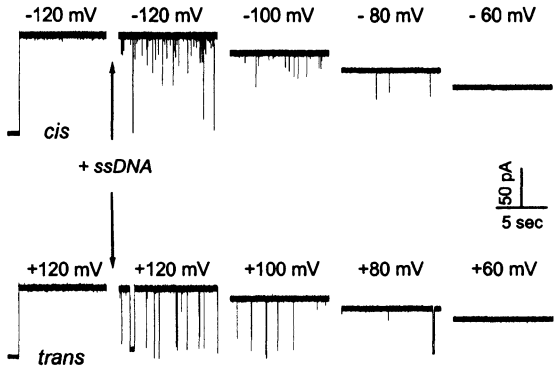

Figure 4. The rate of αHL channel blockade by polynucleotides is voltage dependent. In the absence of ssDNA (leftmost recording), the single channel current is quiescent. Adding 30-nucleotide long 5'biotinylated poly[dC]: bT-poly[dC]$_{30}$) to the *cis* side causes transient single channel current blockades. The number of polymer-induced blockades decreases as the magnitude of the applied voltage decreases (top). Similar results are obtained when ssDNA is added to the *trans* side and applied potential is reversed (bottom). The polynucleotide concentration is 400 nM and 800 nM on the *cis* and *trans* sides, respectively. Qualitatively similar results are observed for a wide variety of DNA and RNA homopolymers. From [22].

In order to understand the mechanism by which individual ssDNA molecules enter a nanometer-scale pore, we studied the concentration, voltage, and sidedness dependence of polynucleotide-induced current blockades of a

single αHL ion channel (Fig. 4). We found that for relatively short polynucleotides, the blockade frequency is proportional to the polymer concentration (Fig. 5, inset) and increases exponentially with the applied potential, and ssDNA enters more readily into the pore from the *cis* side (Fig. 5) [22].

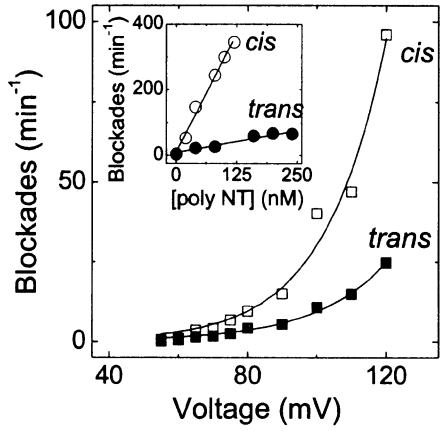

Figure 5. Polymer-induced current blockade rate is dependent on the polynucleotide concentration and the applied potential. For $|V| = 120mV$ and for relatively short polynucleotides, the time-averaged blockade rate increases linearly with the polymer concentration (inset) and exponentially with the magnitude of the applied potential. Similar results are obtained with different DNA and RNA homopolymers. From [22].

To describe theoretically the voltage dependence of the polynucleotide-induced blockade rate R, we used a classical Van't Hoff-Arrhenius rate law or transition state relation

$$R = \kappa\nu \exp[(\Delta U - U^{\ddagger})/kT], \tag{1}$$

where $\kappa \sim 1$ is a probability factor, ν is the frequency factor, $U^{\ddagger}$ is the activation energy (or barrier height) for polymer tranport through the pore [22], ΔU is the energy that drives a polynucleotide into the channel, and kT has its usual meaning. This relation can be derived from a diffusion equation for polymer migration assuming that the barrier for polymer transport is high, such that polymer barrier crossing is a rare event [54].

We assume that the electrostatic energy driving a polymer segment with charge ze into the nanopore by an applied transmembrane potential is $\Delta U = ze|V|$ [4], where e is the fundamental electronic charge. Thus,

$$R = R_0 \exp(ze|V|/kT), \tag{2}$$

where R_0 is independent of V. Fitting equation 2 to the data in Fig. 5 yields $z = 1.9$ and $z = 1.4$ for the entry of polymer into the *cis* and *trans* sides of the channel, respectively.

To obtain a value for the barrier height, we estimate the rate R_0 by using an expression from a simple barrier penetration problem [54]. This rate is assumed to be $\nu = CDA/l$, where C, D, A and l are the polymer concentration, polymer diffusion coefficient, channel cross sectional area and the barrier width. When C = 400 nM (Fig. 4), *cis*), $D = 10^{-7}$ cm^2 s^{-1}, $A = 3\text{x}10^{-14}$ cm^2, and $l = 10^{-6}$ cm (the length of the channel), we have $R_0 \sim 0.04$ min^{-1} and $U^{\ddagger} = 8kT$.

The results in Figs. 4 and 5 demonstrate that polynucleotide entry into the αHL channel is a relatively rare event. An upper bound for polynucleotide flux to the pore is estimated by assuming that the polymers are point particles diffusing to a perfectly adsorbing disk with diameter d using $J = 4CDd$ [55, 56]. If we use the bulk values for C and D, and d = 2 nm [25–28, 48], then $J \sim 3{,}000$ min^{-1} for C = 1,000 nM and $D = 10^{-7}$ cm^2 s^{-1}. The experimental results in Fig. 4 show that for V = -120mV and C = 1,000 nM, $\sim$ 300 blockades min^{-1} occured. Under these experimental conditions, approximately 10% of the *cis*-side ssDNA-pore collisions result in single channel current blockades. This is a suprisingly high rate because the polynucleotides are not point particles and the entropy of the chains reduces the probability that one of the two ends will find the pore entrance.

To explain the voltage dependence of polynucleotide entry into the channel, we assume there is a single barrier for polymer entry and ignore the barriers or wells that are the physical cause of the asymmetric partitioning of polymer into the two entrances (Figs. 4 and 5). The energy required for polymer penetration into the narrow confines of the channel is evidently decreased by an applied electrical potential. Because the electrostatic potential profile along the pore axis is not known, we assume that the applied potential drops linearly across the barrier. The results of fitting the data in Fig. 5 to the above model show that the value of the polymer valence that is driven into the barrier by the applied potential is $z \sim 2$. Because there is at most one charge per nucleotide on the phosphate backbone, on average at least two nucleotides interact with the barrier and initiate polynucleotide translocation.

The inset in Figure 5 shows that at a given polynucleotide concentration the polymer enters the *cis* side more readily than it does the *trans* side. A cartoon cross section of the αHL channel illustrated in Figure 6 suggests two possible factors that could account for the asymmetry. First, the vestibule on the *cis* side is larger than that on the *trans* side. Second, there is a greater density of negatively charged amino acid side chains close to the *trans* entrance that could inhibit polymer entry into the pore. Our preliminary results obtained with genetically engineered versions of the αHL channel suggest that

electrostatic repulsion plays a significant role in excluding polynucleotides from the αHL channel (data not shown).

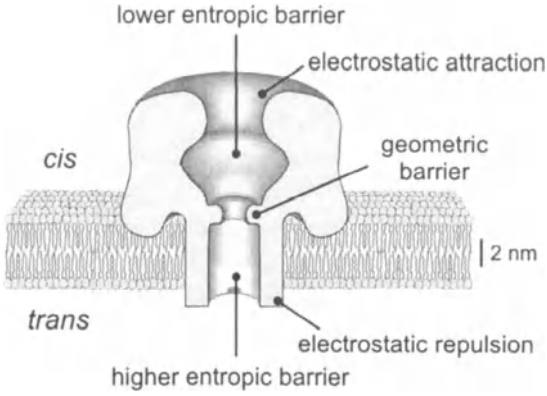

Figure 6. Several hypothetical mechanisms for the asymmetric partitioning of ssDNA into the αHL ion channel. Polymer entry from the *trans* side may be less favorable because of either the negatively charged side-chains at that entrance, the smaller pore diameter on that side, or both. From [22].

5. Sizing a nanopore with polymeric molecular rulers

The previous section demonstrated how threading ssDNA through a narrow pore can be used to characterize some of the physical properties of both the polymer and the pore. However, those experiments do not determine how deep the polymer translocation barrier is located within the pore. We addressed this problem by studying the ability of polymers that were modified with a bulky macromolecule (e.g., a protein or antibody), herein called a cap, to partition into either side of the channel (Fig. 7). The cap prevents the polymer from completely threading through the channel. Different length capped polymers were used as molecular rulers to determine both how far the polymer must thread into the pore before it is committed to completely transport through the channel. We also used polymers that can be capped at both ends to determine the total length of the pore.

Figure 7 illustrates how singly capped ssDNA molecules were used to probe the structure of the αHL channel. In the absence of the cap protein (neutravidin), polynucleotides of different length cause transient blockades in the single channel current. Avidin (i.e., + neutravidin), which binds to the 5'-end of the polynucleotides, causes relatively long polynucleotides (30mers) to occlude the pore from the *cis* side, whereas shorter capped ssDNA (20mers) do not (Fig. 7, current recordings, top). Similar experiments demonstrated

that the critical polynucleotide length to occlude the pore from the *trans* side was between 10 and 20 bases (Fig. 7, current recordings, bottom)).

To determine the length of the pore, we used different length homopolynucleotides with binding sites for ligands on the 5'- and 3'- ends of the polymer. In the absence of ligands, the polynucleotides caused transient single channel blockades. The subsequent addition of one of the ligands on the same side the polymer was added caused the polymer to occlude the pore. Reversing the voltage caused the current to increase to the fully open state because the polymer exited the channel from the same side it entered. After adding the second ligand to the opposite side, reversing the potential could not clear the polymer from the channel if the polymer length was greater than 45 nucleotides (data not shown) [45]. Because the channel length is $\sim$ 10 nm, we conclude that the mean distance between each base inside the pore is $\sim$ 0.22 nm.

The latter result, and the data in Fig. 7 suggest that the segment inside the αHL channel that commits polynucleotides to transport is located quite close to the smallest constriction inside the pore (Fig. 6, geometric barrier). By assuming that Ohm's law is approximately valid inside the pore, we find that the drop in the electrostatic potential is evidently greatest in this segment. Because both ends of a sufficiently long polymer can become bound to ligands on both sides of the channel, these data also confirm that polynucleotides thread completely through the pore ([20]).

6. Novel nanopore-based sensors

During the past decade, it was posited that single ion channels might prove useful as components of sensors for specific analytes (e.g., [35,36,41,42]). The principle of analyte detection and identification is simple. The binding of analyte to a site inside the pore or near the pore mouth causes fluctuations in the single channel current [35,36]. These conductance fluctuations could be caused by changes in the electrostatic potential inside or near the pore, by changes in the conformation of the channel, or by occlusion of the pore. In a different approach, modified gramicidin channels were reconstituted into complex membranes on solid support electrodes [39]. Because the latter system uses a large number of channels, the kinetic information contained in the reactions between an individual molecule and a single channel is lost.

We discuss here another mechanism by which a single nanopore can be used to detect analytes in solution. Specifically, instead of placing the binding site on the nanopore itself, we put it on a polymer. The ability of the polymer to partition into the pore, or transport through it is altered by the presence of analyte [44].

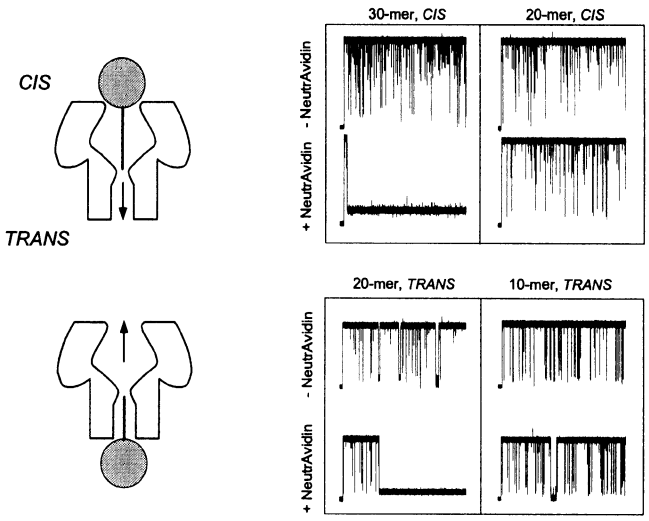

Figure 7. Polynucleotide molecular rulers are used to probe the αHL channel's structure. *Left.* Polynucleotides bound to avidin are driven into the pore from the *cis* and *trans* sides and occlude the pore. *Right.* Cap-free polymers cause transient blockades in single channel current (- neutravidin). The subsequent addition of a avidin as a capping protein (i.e. neutravidin), causes the polymer to occlude the pore if the polymer is longer than a critical length. This length is between 20 to 30 bases and 10 to 20 bases for *cis*- and *trans*-side polymer additions, respectively. The magnitude of the applied potential was 120 mV. From [45].

6.1 Model for nanopore-based sensor

In one realization of a nanopore-based sensor, for low concentrations of relatively short polymers and in the absence of analyte, the mean number of current blockades is proportional to the polymer concentration (as shown Fig. 5, inset; see also Fig. 8, top). Analyte binding to a site on the polymer alters the ability of the polymer to transport through the pore. The polymer would either be rendered pore-impermeant (Fig. 8, middle) or occlude the pore for a time that is commensurate with $1/k_{off}$ (Fig. 8, bottom). In the first case, the analyte concentration is deduced from the decrease in the mean number of blockades per unit time (Fig. 8, middle). For the second detection scheme (Fig. 8, bottom), the analyte concentration is deduced from the mean time that it takes the nanopore to be occluded by the analyte/polymer complex after the electric field is applied [44].

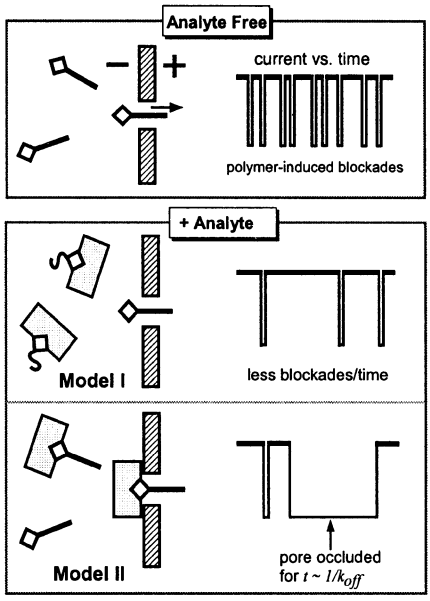

Figure 8. Two models for analyte detection and quantitation using polymers and a single nanopore. In the absence of analyte, polymers with covalently attached ligand binding sites traverse the pore and cause transient current blockades (top). Analyte alters the polymer's ability to transport through the pore: the polymer becomes unable to partition into the pore (Model I) or the complex blocks the pore for a time that is commensurate with the mean lifetime of the complex (i.e. $1/k_{off}$) (Fig. 8, bottom). From [44].

6.2 Analyte alters polymer-induced nanopore current blockades

Proof-of-concept for the sensor scheme in Fig. 8 is shown in Fig. 9. In the absence of polymers, the single channel current is stable (Fig. 9, left). The addition of relatively short 5'-bT-poly[dA]$_{10}$ causes short-lived single channel current blockades (Fig. 9, top middle). The subsequent addition of avidin, in excess of the polymer concentration, essentially eliminated the polymer-induced blockades (Fig. 9, top right). The loss of signal may be caused either by a significant reduction in the residence time of the polymer in the pore as it partitions into and out of the same channel entrance, or by the polymer being rendered pore-impermeant. This result is consistent with the first of the two sensor models shown in Fig. 8 (middle).

In a separate experiment, a relatively long biotinylated polynucleotide, 5'-bT-poly[dA]$_{50}$, also causes short-lived current blockades (Fig. 9, bottom middle). In this case, the subsequent addition of avidin causes the channel to

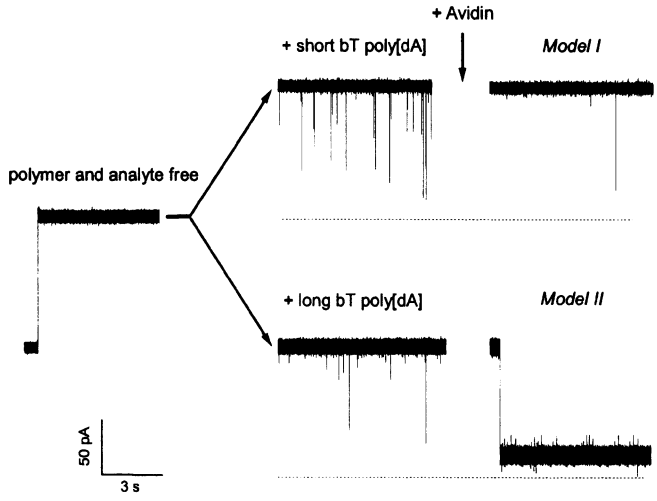

Figure 9. Proof-of-concept for the analyte detection method described in Fig. 8. The leftmost recording shows open channel current in the absence of polymer, with an applied potential of -120 mV. The middle recording shows the effect of adding 250 nM 10-nucleotide bT-poly[dA]$_{10}$ (top) or 30 nM 50-nucleotide bT-poly[dA]$_{50}$ (bottom). Excess neutravidin (2.6 mM to the 10-mer and 670 nM to the 50-mer) bound virtually all of the bT-poly[dA] and caused either a reduction in blockades (10-mer, sensor in Fig. 8, middle) or long-lived occlusions (50-mer, sensor in Fig. 8, bottom). From [44].

become occluded virtually indefinitely (Fig. 9, bottom right). This is expected for a nanopore sensor operating as in Fig. 8 (bottom).

Longer biotinylated polymers (e.g., 5'-bT-poly[dA]$_{50}$) also cause current blockades (Fig. 9, bottom). However, in this case, the subsequent addition of avidin causes the channel to become occluded for times much greater than the mean time for polynucleotide transport through the pore (Fig. 9, bottom right).

For the first model of the nanpore sensor system (Fig. 8, middle), the mean rate of polymer-induced transient current blockades decreases monotonically with increasing analyte concentration. This was verified experimentally by measuring the rate of 5'-bT-poly[dA]$_{10}$ induced blockades as a function of avidin concentration (Fig. 10). By the principle of mass action, for a completely irreversible reaction between analyte and sensing polymer, the blockade rate should decrease linearly with analyte concentration. The results in Fig. 10 are consistent with this prediction over most of the analyte concentration range. It is easy to show theoretically that if the reaction is reversible, as the polymer concentration increases, the polymer-induced blockade rate will decrease nonlinearly to zero.

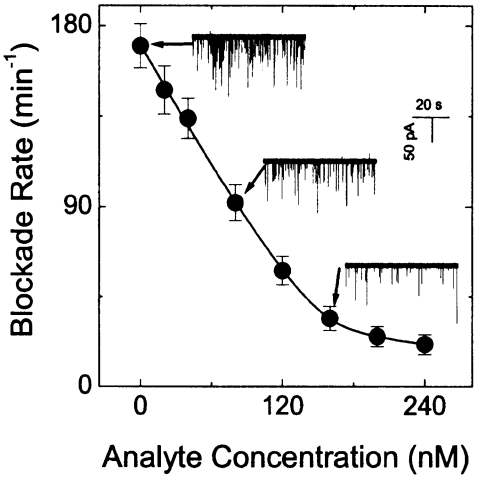

Figure 10. The analyte detection method described in Fig. 8 (middle) is quantitative. The concentration of analyte is estimated from the decrease in the time-averaged polymer-induced single-channel current blockades. Here, adding 40 nM ssDNA (bT-poly[dA] $_{10}$) causes transient current blockades (upper left recording), and increased amounts of avidin decreased the average number of transient blockades per unit time. Arrows indicate representative current recordings at the indicated concentrations. From [44].

6.3 Multi-analyte detection

At relatively low polymer concentration, the αHL channel is almost always polymer free (Fig. 9, top and bottom middle) because the rate of polymer entry is low and the current blockades are relatively short-lived. It follows that the sensor mechanism illustrated in Fig. 8 could be used to detect multiple analytes if different ligand binding sites could be attached to polymers that have unique current blockade signatures. The single channel recordings in Fig. 11 demonstrate that even identical length homopolymers comprised of 100 nucleotide long thymine, adenine, and cytosine can readily be distinguished in both the lifetimes and amplitudes of the current blockade patterns. The marked difference in blockade lifetimes is most likely caused by the different structures the various homopolynucleotides adopt (e.g., [57], see also [23] and the chapter by Akeson, et al.).

The possibility of detecting more than one analyte simultaneously with single nanpore was tested using two different polymers, each with a unique binding site for a specific analyte and each causing a distinctive current blockade pattern. The two polymers, 5'-bT-poly[dC] $_{10}$ and 5'-BRDU-poly[dT] $_{50}$ could bind avidin or the antibody to BRDU (α-BRDU), respectively. In the

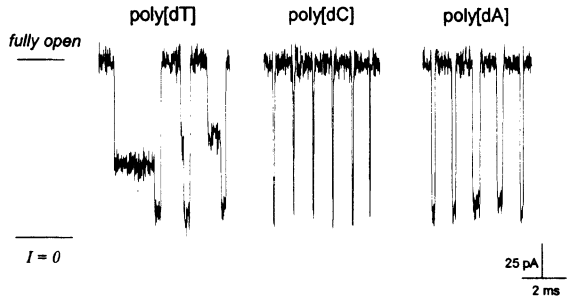

Figure 11. Identical length homopolymers of poly[dT], poly[dC] and poly[dA] cause single channel current blockades that are characteristic of the polynucleotide. Note the distinctive double-step polythymine blockade pattern. Qualitiatively similar results were obtained many times using these three types of homopolynucleotides over a wide range of polymer lengths. From [44].

absence of the two polymer types, the single channel current is stable (Fig. 12, leftmost recording). As expected, adding 400 nM bT-poly[dC] $_{10}$ to the *cis* side causes transient current blockades that are characteristic of poly[dC] (Fig. 12, second recording). The subsequent addition of 400 nM BRDU-poly[dT] $_{50}$ to the same side further increases the mean polymer-induced blockade rate and the additional blockades are characteristic of poly[dT] (Fig. 12, third recording). Avidin markedly reduces the rate of current blockades because the bT-poly[dC]$_{10}$-induced blockades disappeared as expected (e.g. Fig. 8, middle and Fig. 10). The addition of an antibody that is specific to BRDU (α-BRDU, 240 nM) causes the pore to be occluded for relatively long times by the complex of α-BRDU:BRDU-poly[dT]$_{50}$, as expected for a relatively long polymer bound to a large analyte (Fig. 8, bottom). If only relatively short polymers were used in this type of experiment, the system could be used to detect simultaneously many analytes and is limited only by the number of unique current blockade patterns that can be generated by the polymers.

BRDU-poly[dT]$_{50}$ further increases the total number of blockades per unit time and causes the characteristic double-step poly[dT] signature, as seen in the middle expanded view (Fig 12). The addition of 600 nM streptavidin eliminates virtually all the bT-poly[dC] $_{10}$ current blockades, as expected for the sensor shown in Fig. 8 (middle), shown both by the reduction in total events as well as the lack of characteristic poly[dC] events in the data, (right-most expanded curent recording). Finally, the addition of 240 nM α-BRDU polyclonal antibody causes virtually infinite channel current blockades, most remaining until the potential is reversed. This is expected for the sensor shown in Fig. 8 (bottom).

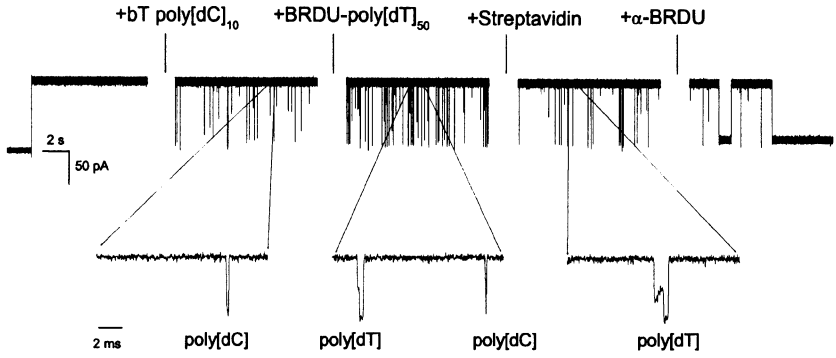

Figure 12. Simultaneous detection of two analytes using a single nanopore and two different polymers. The applied potential is -120 mV. See the text for details. From [44].

6.4 Alternative nanopore detector schemes

The sensor mechanism described here could detect any analyte that alters a polymer's ability to partition into or completely traverse the pore. The first type of sensor illustrated in Fig. 8 (middle) sensor could also work in reverse. For example, if an analyte converts a pore-impermeant polymer into a pore-permeant form, then the number of blockades per unit time will increase with analyte concentration, i.e. opposite to that suggested in Fig. 8, middle and shown in Fig. 10. A similar principle was demonstrated by the cleavage of RNA homopolymers (e.g. poly[U] but not poly[A]) into more numerous and shorter polymers by ribonuclease A [20].

7. Statistical analyses of polynucleotide transport events

The αHL ion channel is used to measure current flow signatures caused by individual molecules as they traverse a single nanopore. The diameter of the smallest constriction in the αHL channel is close to that of ssDNA. Under the experimental conditions reported here, only several hundred ions per μs flow through the pore when it is partially occluded by a polynucleotide. Thus, there will be significant noise caused by random fluctuations in ion concentration within the pore (e.g. Figs. 2 and 10). Statistical techniques are therefore a fundamental tool to estimate the blockade states associated with the molecules as they transit.

The magnitude of the single αHL channel current is asymmetric with respect to the sign of applied potential. We demonstrated above that polynucleotides are more likely to enter one pore entrance than the other (Fig. 5). We show here that the current blockade patterns for polymers threading through the pore in one direction are different from those driven from the other direction. Specifically, using a statistical analysis, we found that the characteris-

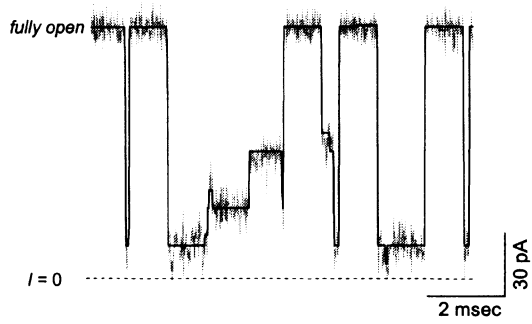

Figure 13. Statistical identification of polynucleotide-induced current blockade states. The single-channel current blockades caused by poly[dT]$_{100}$ (gray) show a rich structure with relatively long-lived substates. Time-coherent segments in the blockades are well described by individual Gaussian components. The solid black lines illustrate the mean current values of the Gaussian components, that are estimated from an all-points histogram of the current (Fig. 14), subject to the constraint imposed by a Hidden Markov state machine which applies a penalty for state transitions (see text). Not all of the states, which seem obvious to the eye, are estimated by the state decoder because of the need to separate closely spaced states whose amplitude distributions overlap but are separate in time. The applied potential was $V = -120mV$) which drives the polymer from the *cis* to the *trans* side of the channel. The actual times between the blockades is random and much longer than is shown.

tics of the current blockades induced by poly[dT] depend on the direction the polynucleotide travels through the pore. We used an Expectation Maximization (EM) technique to fit Gaussian Mixture Models (GMMs) to the channel amplitude distribution [58]. The channel asymmetry was pronounced for the *trans* versus *cis* transit event characteristics including frequency, average amplitude, and event sub-state structure. We employ an ergodic Hidden Markov Model (HMM) to represent the piece-wise stationary sub-state distributions [59,60]. Figure 13 shows an example of the maximum likelihood estimate of the sub-state sequence for a segment of data for poly[dT]$_{100}$ driven into the *cis* pore entrance. The sequence of state mean current values is superimposed on the raw current data. This state sequence is estimated from the transit data using the HMM [61] and a Viterbi decoder [62] with the components of the channel Gaussian mixture as the output distributions of the HMM state transitions.

7.1 Open channel statistics

We computed the amplitude distributions for the *trans* and *cis* open channel conditions using $\sim$ three million time samples. The absolute mean current values were approximately 88 pA and 120 pA, with standard deviations of *sim* 4.9 pA and 4.8 pA, respectively. Under these experimental conditions,

the αHL channel is highly asymmetric in mean open single channel current; the *cis* mean current is thirty-six percent higher than that of the *trans*. The Kolmogorov-Smirnov (K-S) statistic [63] shows small but significant deviations from a Gaussian distribution in both the *trans* and *cis* open channel data, with values of 3.2 and 8.4 respectively. Both support rejecting the hypothesis that the data are Gaussian distributed at better than 0.01 probability level. We found that a two and three component Gaussian mixture was required to fit the *cis* and *trans* open channel data, respectively.

7.2 Transit event statistics

We have adapted signal analysis methods to characterize and decode reproducible sub-states that are evident in polynucleotide-induced single channel current blockades. We show here how this analysis was used to describe a population of ~ 43,000 individual poly[dT] $_{100}$-induced current blockades. Most of the events (~40,000) were caused by polymer driven into the *cis* entrance versus ~ 2,600 *trans*, owing to the lower rate of events per unit time in the *trans* data set. The rate of polymer entry into the *cis* entrance was ~ 16-fold greater than that for *trans* polymer entry. These results are consistent with the asymmetry in bT-poly[dC]$_{30}$) driven into the pore (Fig. 5).

Non time coherent Gaussian mixtures can be fit to the observed amplitude distributions for *trans* and *cis* event sets well enough that the K-S goodness of fit tests provided no basis for rejection at the 0.05 level of confidence. However, we found pronounced differences in the number and location of the mixture components needed to model transit amplitude distributions for the two channel conditions. In order to improve the resolution of closely spaced states we applied a seven point median filter to the transit time series. For this filtered data, a thirty nine component model was required to adequately represent the amplitude distribution for the *cis* events (K-S = 1.32) while a twenty component model was needed for *cis* transit event amplitude distribution (K-S = 1.10). Figure 14 shows the amplitude distributions with the estimated mixture models plotted against the observed distributions for *cis* and *trans* transit event sets.

Generally, we also observed that the current blockades appears to be well characterized by a piece-wise stationary multi-component Gaussian mixture amplitude distribution. We modeled the piecewise stationarity of the states with an HMM which favors self persistent state transitions over transitions to other states. As shown in figure 13, this technique shows promise as a means of measuring sub-states within transit events caused by single molecules. This method may provide another technique to probe the structure of ion channels [64].

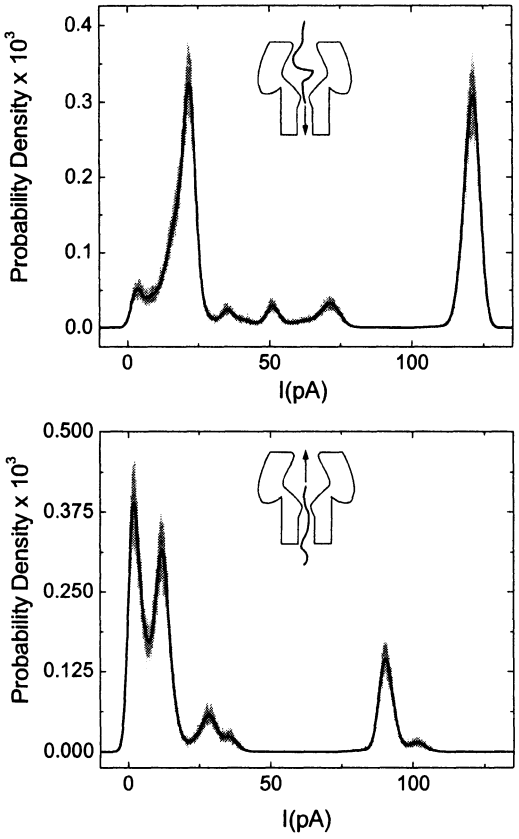

Figure 14. All-points histogram for single αHL channel current in the presence poly[dT]$_{100}$. The current blockade pattern for polymers threading from *cis* to *trans* (top, $V = -120mV$) and vice versa (bottom, $V = +120mV$) are markedly different. The solid black line represents the best-fit nodel of the least number of Gaussian components that adequately represent the amplitude data as measured by the Kolmogorov-Smirnov statistic (see text). This fitting procedure does not consider temporal information in the data (e.g., time-correlations of current values). However, when combined with a Hidden Markov Temporal State Model (HMM) it provides a good description of the segments within polynucleotide-induced current blockade signals (see Fig. 13). The actual fraction of time the channel is occupied by polymer is very small. However, the open channel data shown here excludes most of the time between blockade events. The spectrum of the open channel noise is nearly flat.

Finally, although the signals caused by the polymers in Figs. 4 and 5 are easy to differentiate by eye, a wide variety of statistical measures (e.g. mean, variance, mean lifetime, autocorrelation or spectral analysis [27,28,35,36,65, 66], Hidden Markov Models [61] and Viterbi decoding algorithms [62] should prove useful for decoding the complex structures of polynucleotide-induced

current blockades [64] and for automatically distinguishing current blockades caused by many different types of polymers.

8. Conclusion

We demonstrated how a protein ion channel is a good model system for measuring directly the energetics of polynucleotide transport in a single αhemolysin ion channel. Perhaps these techniques can also be used to study DNA transport in other channels (e.g., [67]). It is our hope that this new technique combined with the sophisticated theoretical approaches being developed to describe and anticipate the physics of this process will provide a better understanding of biological transport processes and spur the development of new technologies for detecting a wide variety of molecules.

Acknowledgments

We thank Mr. Sean Lee and Mr. Jason Rubenstein for writing some of the computer programs used in the data acquisition and analysis. Supported in part by the NIST Advanced Technology Program and the National Academy of Sciences/National Research Council (JJK). Figure 1 was assembled by Sean Connelly, Texas A&M University.

References

[1] Hodgkin, A.L., Huxley, A.F. (1952) Currents carried by sodium and potassium ions through the membrane of the giant axon of *Loligo. J. Physiol.* **116**, 446-472.

[2] Hodgkin, A.L., Huxley, A.F. (1952) The components of membrane conductance in the giant axon of *Loglio. J. Physiol.* **116**, 473-496.

[3] Katz B. (1966) *Nerve, Muscle, and Synapse.* McGraw-Hill, New York, NY.

[4] Hille, B. (1992) Ionic channels of excitable membranes (Sinauer Assoc., Sunderland, MA, ed. 2, 1992).

[5] Leippe, M., Andra, J., Mullereberhard, H.J. (1994) Cytolytic and antibacterial activity of synthetic peptides derived from amoebapore, the pore-forming peptide of entamoebahistolytica. *Proc. Nat'l. Acad. Sci. (USA)* **91**, 2602-2606.

[6] Tsien, R.W., Tsien, R.Y. (1990) Calcium channels, stores and oscillations. *Annu Rev. Cell Biol.* **6**, 716-760.

[7] Columbini M. (1987) Regulation of the mitochondrial outer membrane channel, VDAC. *J. Bioenergetics and Biomembranes* **19**, 309-320.

[8] Andersen, O.S. (1989) Kinetics of ion movement mediated by carriers and channels. *Methods in Enzymology* **171**, 62-112.

[9] Blachly-Dyson, E., Peng, S.Z., Colombini, M., Forte, M. (1990) Selectivity changes in site-directed mutants of the VDAC ion channel-structural implications. *Science* **247**, 1233-1236.

[10] Simon, S.M., Blobel, G. (1991) A protein-conductive channel in the endoplasmic reticulum. *Cell* **65** 371-380.

[11] Crowley, K.S., Liao, S., Worrell, V.E., Reinhart, G.D., Johnson, A.E. (1994) Secretory proteins move through the endoplasmic reticulum via an aqueous, gated pore. *Cell*, **78** 461-471.

[12] Walter, P., Johnson, A.E. (1994). Signal sequence recognition and protein targeting to the endoplasmic reticulum membrane. *Annu. Rev. Cell. Biol.* **10**, 87-119.

[13] Garcia, L.R., Molineux, I.J. (1996) Transcription-independent DNA translocation of bacteriophage T7 DNA into Escherichia coli. *J. Bacteriology* **178**, 6921-6929.

[14] Miller, R.V. (1998) Bacteria gene swapping in Nature. *Scientific American* **278**, 66.

[15] Gene Transfer in the Environment, S. B. Levy and R.V. Miller, eds. (McGraw-Hill, New York, NY, 1989)

[16] Young, R. (1992) Bacteriophoage lysis- mechanism and regulation. *Microbiol. Rev.* **56**, 430-481.

[17] Jakes, K.S., Kienker, P.K., Slatin, S.L., Finkelstein, A. (1998) Translocation of inserted foreign epitopes by a channel-forming protein. *Proc. Natl. Acad. Sci. (USA)* **95**, 4321-4326.

[18] Parsegian, V.A. (1969). Energy of an ion chrossing a low dielectric membrane: solutions to four relevant electrostatic problems. *Nature (London)* **221**, 844-846.

[19] Bustamante, J.O., Hanover, J.A., Leipins, A. (1995) The ion channel behavior of the nuclear pore complex. *J Membrane Biol.* **146**, 239-252.

[20] Kasianowicz, J.J., Brandin, E., Branton, D., Deamer, D.W. (1996) Characterization of individual polynucleotide molecules using a membrane channel. *Proc. Natl. Acad. Sci. (USA)* **93**, 13770-13773.

[21] Akeson, D., Branton, D., Kasianowicz, J.J., Brandin, E., Deamer, D.W. (1999) Microsecond time-scale discrimination between polycytidylic acid and polyadenylic acid segments within single RNA molecules. *Biophys. J.* **77**, 3227-3233.

[22] Henrickson, S.E., Misakian, M., Robertson, B., Kasianowicz, J.J. (2000) Asymmetric driven DNA transport into a nanometer-scale pore. *Phys. Rev. Lett.* **85**, 3057-3060.

[23] Meller, A., Nivon, L., Brandin, E., Golovchenko, J., Branton D. (2000). Rapid nanopore discrimination between single polynucleotide molecules. *Proc. Natl. Acad. Sci. (USA)* **97**, 1079-1084

[24] Bezrukov, S.M., Vodyanoy, I., Parsegian, V.A. (1994) Counting polymers moving through a single ion channel. *Nature (London)* **370**, 279-281.

[25] Krasilnikov, O.V., Sabirov, R.Z., Ternovsky, V.I., Merzliak, P.G., Muratkodjaev, J.N. (1992) A simple method for the determination of the pore radius of ion channels in planar lipid bilayer membranes. *FEMS Microbiol. Immun.* **105**, 93-100.

[26] Korchev, Y.E., Bashford, C.L., Alder, G.M., Kasianowicz, J.J., Pasternak, C.A. (1995) Low conductance states of a single ion channel are not "closed". *J. Membrane Biol.* **147**, 233-239.

[27] Bezrukov, S.M., Vodyanoy, I., Brutyan, R.A., Kasianowicz, J.J. (1996) Dynamics and free energy of polymers partitioning into a nanoscale pore. *Macromolecules* **29**, 8517-8522.

[28] Bezrukov, S.M., Kasianowicz, J.J. (1997) The charge state of an ion channel controls neutral polymer entry into its pore. *Eur. Biophys. J.* **26**, 471-476.

[29] de Gennes, P.-G. (1979) *Scaling Concepts in Polymer Physics*, Cornell University Press, Ithaca, NY.

[30] Grosberg, A.Yu., Khokhlov, A.R. (1994) *Statistical Physics of Macromolecules*, AIP Press, New York, NY.

[31] DiMarzio, E.A., Mandell, A.J. (1997) Phase transition behavior of a linear macromolecule threading a membrane. *J. Chem. Phys.* **107**, 5510-5514.

[32] Lubensky, D.K., Nelson, D.R. (1999) Driven polymer translocation through a narrow pore. *Biophys J.* **77**, 1824-1838.

[33] Muthukumar, M. (1999) Polymer translocation through a hole. *J. Chem. Phys* **111**, 10371-10374.

[34] DeGennes, P. (1999) Passive entry of a DNA molecule into a small pore. *Proc. Natl. Acad. Sci. (USA)* 96, 7262-7264.

[35] Bezrukov, S.M., Kasianowicz, J.J. (1993) Current noise reveals protonation kinetics and number of ionizable sites in an open protein ion channel. *Phys. Rev. Lett.* **70**, 2352-2355.

[36] Kasianowicz, J.J., Bezrukov S.M. (1995) Protonation dynamics of the alpha-toxin ion channel from spectral analysis of pH-dependent current fluctuations. *Biophys. J.* **69**, 94-105.

[37] Kasianowicz, J.J., Walker, B., Krishnasastry, M., Bayley, H. (1994) Genetically engineered pores as metal ion biosensors. *Mat. Res. Soc. Symp. Proc.* **330**, 217-223.

[38] Walker, B., Kasianowicz, J.J., Krishnasastry, M., Bayley, H. (1994) A pore-forming protein with a metal actuated switch. *Protein Engineering* **7**, 655-662.

[39] Cornell B.A., Braach-Maksvytis V.L.B.,King, L.G., Osman, P.D.J., Raguse, B, Wieczorek, L., Pace R.J. (1997) A biosensor that uses ion-channel switches. *Nature (London)* **387**, 580-583.

[40] Van Wie, B.J.; Davis, W.C.; Moffett, D.F.; Koch, A.R.; Silber, M.; Reiken, S.R.; Sutisna, H. 1998, USP 5,736,342.

[41] Kasianowicz J.J., Burden D.L., Han L., Cheley S., Bayley H. (1999) Genetically engineered metal ion binding sites on the outside of a channel's transmembrane beta-barrel. *Biophys. J.* **76**,837.

[42] Braha, O., Walker, B., Cheley, S., Kasianowicz, J.J., Hobaugh, M.R., Song, L., Bayley, H. (1997) Designed protein pores as components for biosensors. *Chemistry & Biology* **4**, 497-505.

[43] Gu, L.Q., Braha, O., Conlan, S., Cheley, S., Bayley, H. (1999) Stochastic sensing of organic analytes by a pore-forming protein containing a molecular adapter. *Nature (London)* **398**, 686-690.

[44] Kasianowicz, J.J., Henrickson, S.E., Weetall, H., Robertson, B. (2001) Simultaneous multianalyte detection with a nanometer-scale pore. *Anal. Chem.* **79**, 2632.

[45] Henrickson, S.E., DiMarzio, E.A., Kasianowicz, J.J. Polymeric molecular rulers for probing the structure of a nanoscale pore. *submitted*

[46] Tobkes, N., Wallace, B., Bayley, H. (1985) Secondary structure and assembly mechanism of an oligomeric channel protein. *Biochemistry* **24**, 1915-1920.

[47] Gouaux J.E., Braha, O., Harbaugh, M., Song, L., Cheley, S., Shustak, C., Bayley, H. (1994) Subunit stoichiometry of staphylococcal alpha-hemolysin in crystals and on membranes: a heptameric transmembrane pore. *Proc. Natl. Acad. Sci. (USA)* **91**, 12828-12831.

[48] Song, L., Hobaugh, M.R., Shustak, C., Cheley, S., Bayley, H., Gouaux, J.E. (1996) Structure of Staphylococcal alpha-hemolysin, a heptameric transmembrane pore. *Science (USA)* **274**, 1859-1866.

[49] Oiki, S., Koeppe, R.E., Andersen, O.S. (1995) Voltage-dependent gating of an asymmetric gramicidin channel. *Proc. Nat'l. Acad. Sci. (USA)* **92**, 2121-2125.

[50] Menestrina, G. (1986) Ionic channels formed by *Staphylococcus aureus* alpha-toxin - voltage-dependent inhibition by divalent and trivalent cations. *J. Membrane Biology* **90**, 177-190.

[51] Kasianowicz, J.J. (1994). Voltage-dependent gating kinetics of an ion channel modulated by ionic strength. *Biophys. J.* **66**, A430. abstract; Lerman, J.C., Li, R., Kasianowicz, J.J. Voltage- and pH-dependent gating kinetics of the α-hemolysin channel altered by changes in electrolyte type and concentration. *Submitted.*

[52] Montal M., Mueller P. (1972) Formation of bimolecular membranes from lipid monolayers and a study of the electrical properties. *Proc. Nat'l. Acad. Sci. (USA)* **69**, 3561-3566.

[53] Sakmann, B. and Neher, E. (1995). Single Channel Recording, 2nd ed. Plenum Press, NY, NY.

[54] Ma, S. (1985) *Statistical Mechanics* World Scientific, Philadelphia, PA.

[55] Berg, H. (1993) *Random Walks in Biology*, Princeton University Press, Princeton, NJ.

[56] Einstein, A. (1956) *Investigations on the Theory of Brownian Movement*, Dover Press, New York, NY.

[57] Saenger, W. *Principles of Nucleic Acid Structure.* Springer Verlag, NY, NY. pp. 301 and 303 and references therein.

[58] Xu,L., Jordan, M. (1996) On convergence properties of the EM algorithm for Gaussian mixtures; *Neural Computation* **8**, 129-151.

[59] Baum, L.E., Petrie, T. (1966) Statistical inference for probabilistic functions of finite state Markov chains. em Annals of Mathematical Statistics **37**, 1559-1563.

[60] Baum, L. (1972) An inequality and associated maximization technique in statistical estimation of probabilistic functions of a Markov process. *Inequalities* **3**, 1-8.

[61] Rabiner, L.R. (1989) A tutorial on hidden Markov models and selected applications in speech recognition. *Proceedings of the IEEE* **37**, 257-286.

[62] Viterbi, A.J. (1967) Error bounds for convolutional codes and an asymmetrically optimum decoding algorithm. em IEEE Transactions on Information Theory **IT-13**, 260-267

[63] Chakravarti, I.M., Laha, R.G., Roy, J. (1967) Handbook of Methods of Applied Statistics Vol. I em John Wiley & Sons Inc., New York, 260-267.

[64] Stanford, V., Wang, Q., Kasianowicz, J.J. *Submitted.*

[65] deFelice, L.J. *Membranes and Current Noise*, Plenum Press, NY, NY.

[66] Stevens, C.F. 1977. Study of membrane permeability changes by fluctuation analysis. *Nature* **270**, 391-396.

[67] Szabo, I., Bathori, G., Tombola, F., Brini, M., Coppola, A., Zoratti, M. (1997) DNA translocation across planar bilayers containing *Bacillus subtilis* ion channels. *J. Biol. Chem.* **272**, 25275-25282.

MECHANISM OF IONIC CURRENT BLOCKADES DURING POLYMER TRANSPORT THROUGH PORES OF NANOMETER DIMENSIONS

David W. Deamer, Hugh Olsen, Mark A. Akeson,
Biophysics Laboratory, Department of Chemistry and Biochemistry, University of California, Santa Cruz, CA 95064

and John J. Kasianowicz
Biotechnology Division, National Institute of Standards and Technology, Gaithersburg, MD 20899-8313

Abstract Linear anionic polymers driven through the α-hemolysin channel produce ionic current blockades. Three parameters of the blockades can be measured, including blockade amplitude, duration and modulations of amplitude within a single event. To test the hypothesis that blockade amplitude is related to the molecular volume of a linear polymer traversing the pore, the effects of four different polymers on the ionic current flowing through single α-hemolysin channels were compared. The amplitude of the blockade is proportional to the fraction of the pore volume occupied by the translocating polymer. We conclude that the primary contribution to the amplitude of a blockade is molecular volume, although other factors may also play minor roles. These results suggest that single nucleotide resolution will require a pore volume near the size of the individual monomers in a polynucleotide ($\sim$ 0.3 nm^3), which will require an improvement of nearly two orders of magnitude over the current limiting volume provided by the α-hemolysin pore ($\sim$ 18 nm^3).

Keywords: α-hemolysin, ion channel, polynucleotide, DNA transport

1. Introduction

As discussed in other chapters of this book, the ability of a nanoscopic pore to detect and characterize single molecules of linear polymers has led to a variety of novel applications. These range from determinations of concentration and polymer length [1], to discriminating between monomer compositions [2, 3], detecting analytes in solution [3], and reading encoded sequences [1], and perhaps even to DNA and RNA sequencing [1] if single nucleotide reso-

J.J. Kasianowicz et al. (eds.), Structure and Dynamics of Confined Polymers, 165–175.

lution can be achieved. In order to use nanopores for such applications, it is important to understand the mechanism by which ionic current blockades are produced when a polymer traverses a pore. Here we will use the α-hemolysin channel as a model, but a similar analysis can be more generally applied to any pore of nanoscopic dimensions.

2. Properties of the α-hemolysin pore

We begin by summarizing the properties of α-hemolysin and the ionic current that is driven through the pore by an electric field. α-hemolysin is a 33 kD protein isolated from *Staphylococcus aureus*, which self-assembles as heptamers in lipid bilayers to form a transmembrane ionic channel. Song et al. determined the structure of the channel to 0.19 nm resolution [4]. Figure 1 illustrates a cross section of the channel with dimensions taken from the X-ray crystallographic coordinates.

The cap domain of the channel has an entry of approximately 2.6 nm diameter that contains a ring of lysine side chains. Other lysines are exposed on the surface of the cap region that, depending on the proximity of nearby negatively charged side chains, may provide a net positive charge that attracts anionic polymers to the neighborhood of the pore [5]. This entry opens into a vestibule with the largest interior dimension $\sim$ 3.6 nm, which then leads into the stem segment and the pore that spans the lipid bilayer. The transmembrane pore segment has an average diameter of 2.1 nm, and the entrance to this section of the channel from the cap region's vestibule has a diameter of 1.5 nm. This limiting aperture is composed of alternating lysine and glutamatic acid side chains. The stem segment of the pore is lined with neutral side chains of glycine, threonine, asparagine and serine, and has two hydrophobic rings of exposed leucine and methionine side chains [4,6]. The opening at the other end of the pore has a 2.2 nm ring of alternating lysine and aspartate residues. At neutral pH ranges and high ionic strength, this channel remains open even at potentials up to 200 mV [7], an essential characteristic for the applications to be described here.

3. Ionic Current Blockades

Typical ionic current blockades caused by individual molecules of single stranded poly(C) as they traverse the α-hemolysin pore are shown in Figure 2. Note that as each RNA molecule enters the pore, a large fraction of the ionic current is blocked for several hundred microseconds. The pore aperture limits the diameter of the linear polymers that produce blockades. For instance, single stranded nucleic acid molecules can enter the pore and produce blockades [1], but blunt-ended duplex DNA with a diameter of 2.6 nm does not thread through the pore [1].

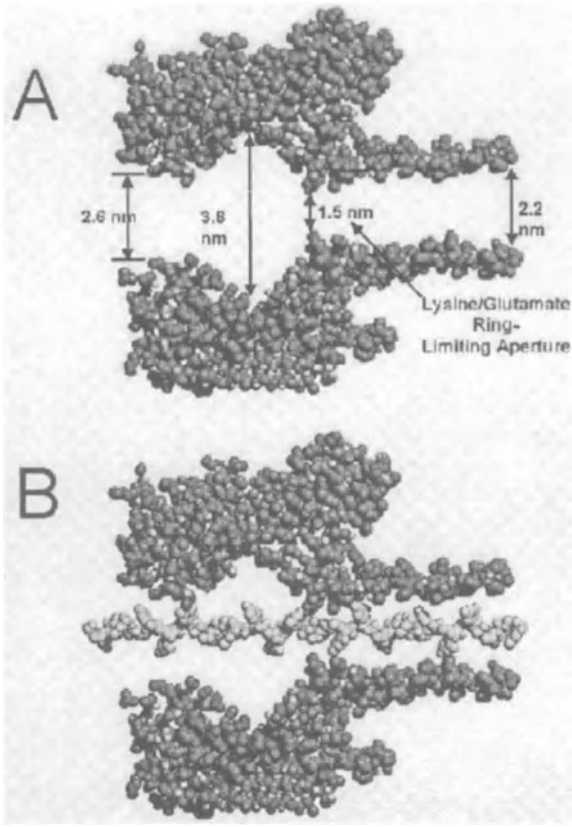

Figure 1. Structure of the α-hemolysin channel. A. Sagittal cross section shows the general configuration of the pore and approximate dimensions. B. Side view of pore with single-stranded oligo(dC) translocating from left to right. Original figure of the channel modified from Song et al. [4]. The channel was not co-crystallized with oligo(dC).

3.1 Capture phase

For applications involving translocation through the α-hemolysin channel, the channel and bilayer are typically bathed by 1 M KCl containing 10 mM pH 7.5 HEPES buffer. When a voltage of 120 mV is imposed on the pore, a 117 pA ionic current, caused by the movement of K^+ and Cl^- ions through the channel, results. If single stranded nucleic acids are present, a given molecule will occasionally diffuse into a small volume near the mouth of the channel and be captured by the field [5]. It is improbable that the entire molecule will be moved by the field. It is more likely that the relatively mobile 3' or 5' ends of the nucleic acid strand will be captured [5]. The voltage-dependent

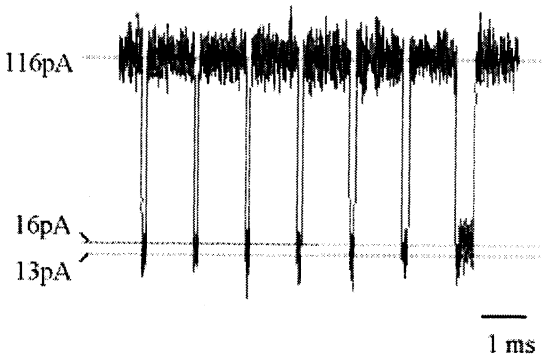

Figure 2. Ionic current blockades produced by deoxycytidylic acid. Data from [2]. The fact that individual single stranded nucleic acid molecules produce detectable current blockades is a surprising result (but see [6] and the chapter by Bezrukov and Kasianowicz, this volume), and it is worth describing the process in sufficient detail so that the blockade mechanisms to be described later can be clearly understood. The production of an ionic current blockade entails three basic processes: capture, entry, and translocation. (See also [1,5,8], and the chapters by Kasianowicz, et al., by Bezrukov and Kasianowicz, by Lubensky, and by Muthukumar).

entry of polynucleotides into the αHL channel is discussed elsewhere ([5], see also the chapter by Kasianowicz, et al.).

3.2 Entry phase

At this point three outcomes are possible. The first is that the diffusing nucleic acid molecule simply collides with the pore's entry. During the collision, the ionic current is interrupted for a few tens of microseconds, but the duration of this transient blockade is independent of chain length [1]. The second possibility is that one end of the molecule partially enters the vestibule and remains indefinitely for periods ranging from tens of microseconds to several milliseconds, after which it either falls out or is drawn completely into the pore (see [5]). While the molecule occupies the vestibule it causes a partial blockade with a characteristic amplitude about half that of the full blockade. The third possibility is that one end of the nucleic acid will be drawn completely through the pore by the applied electrical field, producing a full blockade with a duration that is a function of chain length [1].

3.3 Translocation phase

Translocation occurs as a result of an electrophoretic force acting on the anionic phosphate groups of the chain. The pore is only 10 nm long, but the nucleic acid strands can range from short oligomers to polymers thousands of nucleotides in length. Given the small diameter of the pore, the polynu-

cleotides must move through as extended linear polyanions [1]. We assume that the electric field acts only on some of the oligonucleotide's phosphate groups within the channel, and not on the entire molecule (see [5] and the chapter by Kasianowicz, et al.). The result is a constant force drawing the strand through the pore. Although it may at first seem improbable that a field of 100 mV could exert enough force to overcome diffusion, the field strength across the membrane itself is equivalent to $2x10^5$ volts cm^{-1}. This electrical field is apparently just sufficient to capture polymers, since a field half that strength (50 mV, or 10^5 volts cm-1) does not produce RNA- or DNA-induced current blockades ([5], see also the chapter by Kasianowicz, et al.).

As each polynucleotide molecule traverses the channel, it gives rise to a discrete ionic current blockade. The reason for the blockade is clear from Figures 1B and 1C, which show the pore with a pyrimidine oligonucleotide filling a significant fraction of the volume available. Furthermore, the polyanion will drag along waters of hydration, which will increase the apparent volume of the molecule in the pore and form transient hydrogen bonds with the water of hydration lining the channel's polar interior.

Table 1 summarizes the physical properties of the pore that are relevant to understanding ionic current blockades. Here we will assume that the major component of the blockade occurs when a nucleic acid occupies the 5 nm long pore in the stem of the channel, and neglect contributions by the larger vestibule. The pore volume is $\sim$ 17.9 nm^3. This volume is obtained by adding up the separate volumes of the 17 amino acid rings that compose the pore. Each ring has a diameter varying from 1.4 (the lysine-glutamate ring representing the limiting aperture at the entry of the pore) to 2.6 nm (the 5 glycine rings), equivalent to an average diameter of 2.1 nm.

In 1 M KCl, the pore volume contains $\sim$ 600 water molecules and 11 K^+ and 11 Cl^- ions if the ionic concentration in the pore reflects the bulk phase solution. About 120 pA of current is driven through the pore by a voltage of 120 mV, which is typical for our experimental conditions. This is equivalent to a current of 700 ionic charges per microsecond flowing through the pore, 350 ions each of K+ and Cl-, which have nearly identical transference numbers. However, the ionic current is reduced to approximately a tenth of the open channel current when a polynucleotide occupies the pore, so that the number of ions decreases to 70 ionic charges per microsecond.

Polynucleotides pass through the pore at rates ranging from 1 to 3 ms per nucleotide for DNA - poly(dC) compared to poly(dA) - and from 3 to 20 μs per nucleotide monomer for RNA - polyC compared to polyA. Clearly there is some form of "frictional" interaction between the polynucleotide and the pore that considerably reduces its mobility. The electrical force acting on the polynucleotide works against the frictional drag so that a given strand is translocated through the pore at a more or less constant velocity.

Table 1. Properties of the α-hemolysin ion channel

Pore volume:	$\sim$17.9 nm^3
Water molecules in pore:	597
Ions in pore (1 M KCl):	11 K^+ and 11 Cl^-
Ionic current (120 mV)	120 pA
Ions passing through pore:	$7x10^8$ s^{-1}
Ionic velocity in pore:	200 nm ms^{-1}
Polymer velocity in pore:	0.25 - 1.7 nm ms^{-1}
Transit time range:	1 μs/nt (poly(dC)) - 22 μs/nt (poly(A))

We can also calculate the relative velocities of ions and nucleotide phosphates in the pore. In order to carry 120 pA of ionic current, the K^+ and Cl^- ions must move through the open pore at a velocity of 200 nm ms^{-1}, equivalent to 20 cm s^{-1}, a surprisingly high velocity. The corresponding velocity of nucleotide phosphates moving through the pore ranges from 0.25 to 1.7 nm ms^{-1}, two orders of magnitude slower than the ionic velocity in the open pore. It follows that, even though the polynucleotide responds electrophoretically to the fixed electrical field that drive it through the pore, the anionic phosphate groups do not contribute significantly to the total current.

4. Measurable parameters of ionic current blockades

Three parameters provide information about the nature of the linear polymer passing through a nanopore. The first is blockade amplitude, with units of picoamps, which simply represents the difference between the open channel current and the current during the blockade. This parameter can be normalized as I/I_o where I is the blockade current and I_o is the open channel current. Blockade amplitude has a characteristic value for many homopolymers of RNA and DNA, suggesting that it will be an important feature of analytical applications of nanopore technology.

Blockade duration is the time required for a polymer to pass through the pore. Typical values for different homopolymers range from 1 ms per nucleotide monomer for oligo(dC) to 22 ms per nucleotide monomer for oligoA RNA. Blockade signature is defined as a measurable variation in blockade amplitude during translocation. When all three variables are taken into account, the pattern of blockades is different for virtually every linear polymer we have tested, again suggesting that nanopore analysis of polymers will provide useful information [1,3].

5. What factors could affect blockade amplitude?

There are at least five factors that could contribute to the reduction in ionic current caused by a linear polymer traversing a nanopore. It has been known since the earliest research on particles (such as red cells) passing through 100 mm pores in cell counters that the primary contributing factor to the resulting decrease in conductance (D_g) is the volume of the particle [9]. This relation is described by the equation $D_g = 2\pi r^3\sigma/L^2$, where r is the radius of a spherical particle, L is the length of the pore, and σ is the bulk solution conductivity. Although this equation is not directly applicable to a linear molecule occupying the α-hemolysin pore, we can still ask whether volume is the primary factor. For instance, $\sim$ 20 ions are present in the open pore at any given time, but if a molecule of DNA occupies half of the pore volume, this number would be reduced to 10 ions with a corresponding decrease in the ionic current. It follows that volume of the polymer in the pore is likely to be a major factor.

However, other factors may also contribute to the blockade. For instance, because the velocity of the molecule in the pore is much less that that of the ions carrying the current, ions necessarily must move around the molecule, and the longer path length could also reduce the total ionic current. Another consideration is energy loss to the pore components. The channel's resistance to ionic current may be greater than that of the same volume and geometry of free solution, so that energy available in ionic current is lost as heat. Ions moving through the fully open pore may lose less energy than when a molecule occupies the pore. One of the reasons is that the polyanion has water of hydration, as do the current-carrying ions, and the ionic current does work to make and break hydrogen bonds as they move past the polyanion.

Electrostatic interactions between the linear molecule and the ions carrying current must also be considered. A polyanion in the pore could produce a transient cation selectivity to the pore, so that Cl^- carry less of the total current through the pore. The anionic phosphate groups in the polyanion may also provide ion exchange sites for K^+ ions, slowing their transit rate by the extra time required to bind to and be released from the phosphate. Lastly, there may be unknown effects of the polyanion on the pore's conformation. For instance, the phosphate groups moving past the rings of lysine at the entry and exit of the pore could exert an electrostatic force that would tend to reduce the diameter of these limiting apertures, thereby increasing the pore's resistance to ionic current.

Most of these factors are not yet amenable to experimental tests, but we do have information related to molecular volume. If the volume of the molecule occupying the pore is the primary factor contributing to blockade amplitude, we should be able to measure blockades produced by polyanions having dif-

ferent molecular volumes. If the hypothesis is correct, blockade amplitude should vary as a function of molecular volume relative to pore volume. We will use the molecular volumes and blockade amplitudes of oligo(dC) and oligo(dA). We can compare the nucleic acid molecules to the blockade amplitudes produced by a strand of alternating deoxyribose and phosphate (the abasic backbone of DNA) and a 65mer of polyphosphate. These linear polyanions have markedly different molecular volumes, yet if they are mor or less extended rods, they have approximately the same charge density of phosphate.

As an example, we will first estimate the volume of a poly(dA) molecule in the pore. Assuming an average molecular weight of 300 for dAMP in DNA, and a density of 1.7, a mole of dAMP would have a volume of 1.76×10^{23} nm^3, or 0.29 nm^3 per nucleotide. The conformation of a single strand of DNA in the channel is unknown, but for the purposes of this calculation we can assume 0.34 nm per base, which is the repeat distance of bases in a double helix. About 15 nucleotides would then be in the pore at any instant. The total volume of 15 dAMPs in the pore is then $15 \times 0.29 = 4.35$ nm^3. This is only 27% of the pore volume, but we must also take into account water of hydration bound to the polymer and to the pore surface that is unavailable to conduct ionic current. We will assume that each monomer of the nucleic acid has four waters of hydration (60 total), and that a single layer of water is bound to the interior surface of the pore (320 total). With these assumptions, 70% of the pore volume would be occupied by a single strand of oligo(dA).

Similar calculations were made for oligo(dC), for the abasic strand, and for polyphosphate. Figure 3 (top) shows blockades produced by polyphosphate 65mers, abasic strands of DNA, and oligo(dC), and the graph below plots calculated against experimental results for blockade amphitude related to fractional molecular volume occupied by the polymers in the α-hemolysin pore. The slope of the plotted line is 1.4, because the experimental values are generally somewhat larger than the calculated values. This suggests that the other factors discussed earlier may be contributing to the absolute measured magnitude of a blockade.

We conclude that blockade amplitude is largely a function of the fractional volume occupied by a linear polymer traversing a nanopore. The difference in total volume between purine and pyrimidine deoxyoligonucleotides in the α-hemolysin pore is only 0.3 nm^3, which represents a 6% difference in the volume occupied by the molecules in the pore after correcting for water of hydration. In current nanopore detectors this difference is just barely detectable as an average signal over noise. It follows that an improved pore having a smaller volume than that of the α-hemolysin channel is likely to be required for single nucleotide resolution in nanopore sequencing applications.

Similar calculations were made for oligo(dC), for the abasic strand, and for polyphosphate. Figure 4 shows a comparison of the calculated and ex-

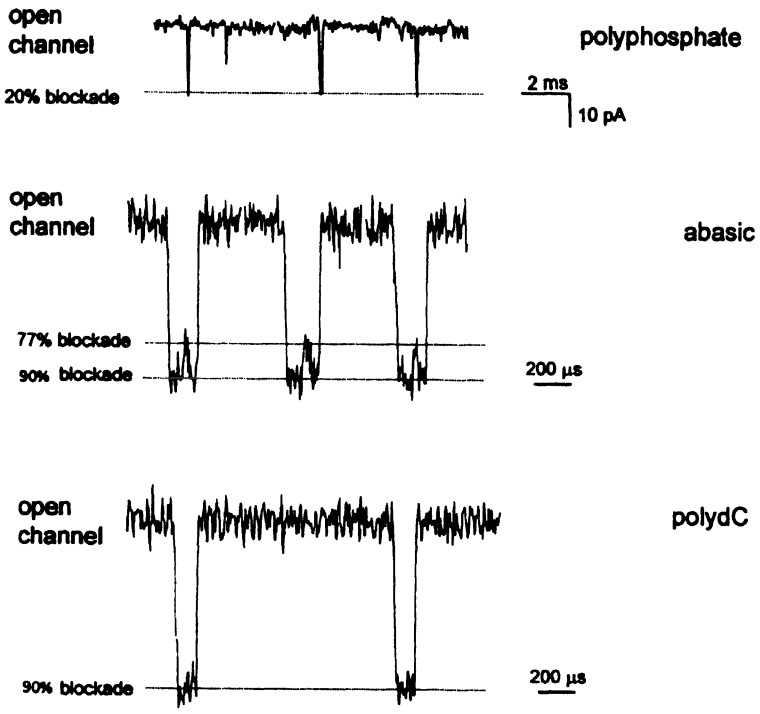

Figure 3. Single channel current recordings illustrating the blockades caused by polyphophosphate, poly(abasic) and poly(dC).

perimental values. The slopes of the two plotted lines are similar, but the experimental values are somewhat larger than the calculated values in all cases, suggesting that one of more of the other factors discussed earlier is contributing to the absolute magnitude of a blockade.

Comparison of calculated and measured current blockades. The upper portion of the figure shows examples of current blockades for polyphosphate 65mers, an abasic strand of DNA, and oligo(dC). (Blockade amplitudes of pure abasic strands have not yet been determined. The value of 77% is taken from an abasic strand that is part of a larger synthetic DNA construct, which produces the upward modulation of the blockade shown in the figure.) The lower portion of the figure shows experimental and calculated blockade amplitudes plotted against the fractional molecular volume occupied by 4 polymers in the pore - polyphosphate, abasic strands, oligo(dC) and oligo(dA).

6. Conclusions

We conclude that blockade amplitude is largely a function of the fractional volume occupied by a linear polymer traversing a nanopore. The difference

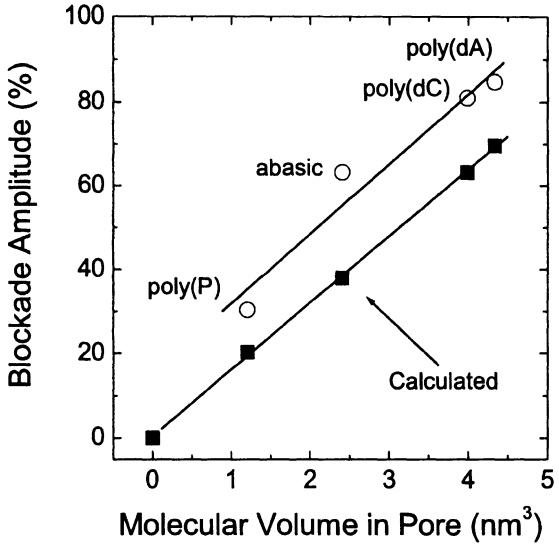

Figure 4. Comparison of calculated and measured current blockades.

in total volume between purine and pyrimidine deoxyoligonucleotides in the α-hemolysin pore is only 0.3 nm^3, which represents about a 6% difference in the volume occupied by the molecules in the pore after correcting for water of hydration. In current nanopore detectors this difference is just barely detectable as an average signal over noise. It follows that single nucleotide resolution required for nucleic acid sequencing will require an improved pore of smaller volume than that of the α-hemolysin channel.

Acknowledgments

Supported in part by NIST NAS/NRC, NIST Advanced Technology Program (JJK) and the NIH (DWD).

References

[1] Kasianowicz, J.J., Brandin, E., Branton, D. and Deamer, D.W. (1996) Characterization of individual polynucleotide molecules using a membrane channel, *Proc. Natl. Acad. Sci. (USA)* **93**, 13770-13773.

[2] Akeson, M., Branton, D., Kasianowicz, J.J., Brandin, E. and Deamer, D.W. (1999) Microsecond time-scale discrimination between polycytidylic acid and polyadenylic acid as homopolymers or as segments within single RNA molecules. *Biophys. J.* **77**, 3227-3233.

[3] Kasianowicz, J.J., Henrickson, S.E., Weetall, H.H. and Robertson, B. (2001) Simultaneous multianalyte detection with a nanopore. *Analytical Chemistry* **73**,2268-2272.

[4] Song, L., Hobaugh, M.R. Shustak, C., Cheley, S., Bayley, H. and Gouaux, J.E. (1996) Structure of staphylococcal α-hemolysin, a heptameric transmembrane pore, *Science* **274**, 1859-1855.

[5] Henrickson, S.E, Misakian, M., Robertson, B. and Kasianowicz, J.J. (2000) Asymmetric driven DNA transport in a nanometer-scale pore *Phys. Rev. Lett.* **85**, 3057-3060.

[6] Bezrukov, S.M., Vodyanoy, I., Brutyan, R.A., Kasianowicz, J.J. (1996) Dynamics and free energy of polymers partitioning into a nanoscale pore. *Macromolecules*, **29**, 8517-8522.

[7] Lerman, J., Li, R., Kasianowicz, J.J. Voltage- and pH-dependent gating kinetics of the α hemolysin ion channel altered by monovalent electrolytes *Submitted.* Kasianowicz, J.J. (1994)Voltage-dependent gating kinetics of an ion channel modulated by ionic strength *Biophys. J.* bf 66, A430.

[8] Lubensky, D.K. and Nelson, D.R. (1999) Driven polymer translocation through a narrow pore. *Biophys. J.* 77, 1824-1838.

[9] DeBlois, R.W. and Bean, C.P. (1970) Counting and sizing of submicron particles by the resistive pulse technique, *Rev. Sci. Instrum.* **41**, 909-916.

USING NANOPORES TO DISCRIMINATE BETWEEN SINGLE MOLECULES OF DNA

Daniel Branton
Department of Molecular and Cellular Biology, Harvard University, Cambridge, MA 02138, USA
The Rowland Institute for Science, Cambridge, MA 02142, USA

Amit Meller
Department of Molecular and Cellular Biology, Harvard University, Cambridge, MA 02138, USA
The Rowland Institute for Science, Cambridge, MA 02142, USA
Center for Advanced Biotechnology, Biomedical Engineering, Boston University, Boston, MA 02215, USA

Abstract Discrimination and characterization of unlabeled, low copy number DNA molecules may become a central requirement for many future biotechnology applications where low cost, high throughput genomic analysis is essential. To date, approaches to such analysis usually require many copies (femto-moles or more) of DNA that are amplified from a specific small region of DNA. In many cases, preparing this DNA is the rate-limiting step that significantly contributes to the overall cost of the analysis. Recently, new tools and techniques that allow detection and manipulation of single DNA molecules have been reported. These tools may eliminate the necessity for DNA amplification. One example consists of sequence-specific DNA detection using molecular beacons which offer a superior signal-to-background efficiency compared with standard DNA probes, and thus are much more suitable for single molecule detection [1]. Single DNA molecules have also been sorted and sized using electric fields [2] or stretched by electrophoretic force in a specially micro-fabricated cell [3].

Keywords: α-hemolysin, DNA sequencing, nanopore

1. Introduction

In this volume, we have been introduced to the energetic barriers and dynamics that may explain aspects of polymer translocation through channels in membranes (see the chapters by Muthukumar, Akerman, Lubensky, and Sung, this volume). Others [4] (see also the chapters by Kasianowicz, Deamer, and

J.J. Kasianowicz et al. (eds.), Structure and Dynamics of Confined Polymers, 177–185.

Akeson) have shown that a biological channel in an insulating membrane separating two ion-containing solutions can in fact be used to detect and characterize single polynucleotide molecules. Meller et al. [5] have taken advantage of these discoveries to show how several different DNA polymers can each be identified by a unique pattern in event diagrams. These diagrams are plots of translocation duration versus blockade current for an ensemble of events. The results are an excellent example of how the coincident recording of several independent parameters can provide a unique fingerprint that distinguishes between DNA molecules which differ from each other only by their sequence [5].

When a polynucleotide molecule is forced to traverse the α-hemolysin channel, it occupies, and thus blocks, much of the otherwise open pore, enabling straightforward detection of the passing molecule [4]. Meller et al. [5] characterized each molecule's passage through the nanopore in an α-hemolysin channel as an event whose duration time, t_D and its averaged normalized blockade current level, I_B, were recorded. Figure 1 displays two typical events labeled by the facing arrow pairs. I_B was calculated by averaging the blockade current during the event and dividing this average by the averaged open pore current. Although the basic apparatus Meller et al. [5] used was similar to the horizontal bilayer apparatus described by Akeson et al. [6], a special heat-conducting design and the use of a thermoelectric device made it possible to maintain the buffer solutions, bilayer, and channel at any fixed temperature between 0°C and 50°C. The effects of temperature on the movement of DNA polymers through a nanopore were found to be stronger than the those expected due to frictional drag alone, and, as we shall see below, have provided several new insights into the translocation process.

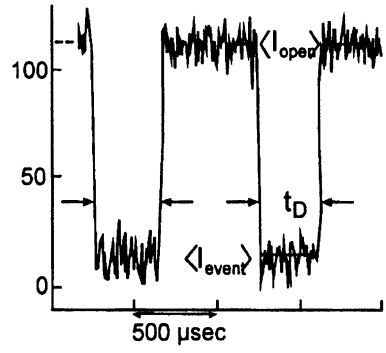

Figure 1. Definition of the translocation duration time ,t_D, and the normalized blockade level,I_B, for two typical events.

At room temperature some polymers, such as poly(dA) and poly(dC), translocate through the α-hemolysin channel at rates that differ from each

other markedly. As a consequence, an event diagram (fig. 2), in which each translocating DNA molecule is characterized by the duration of the blockade it produces, t_D, and the average blockade current, I_B, show that the events corresponding to the two polymers each cluster in well-separated regions. Less than 1% of the poly(dA)$_{100}$ events fall in the poly(dC)$_{100}$ region and vice versa. Thus, discrimination between the two polymer types is readily achieved. Strikingly, the poly(dA)$_{100}$ events separate into two groups, as do also the poly(dC)$_{100}$ events. The two separate groups are evident as two peaks in the current histograms for each polymer type (fig. 2b). The histograms also show that the current peaks are well fitted by the sum of two Gaussian curves whose peak values (I_{P1} and I_{P2}) are among the statistical translocation properties that can be measured for each polymer, e.g. for poly(dA) I_{P1}= 0.115 and I_{P2}= 0.152.

Histograms of the translocation durations for groups 1 and 2 also exhibit clear peak values which are defined as t_{P1} and t_{P2}. For events of short duration (e.g., $t_D < t_{P1}$) the distributions display Gaussian behavior as shown by the fits (solid lines in fig. 2c). But for events of long duration (e.g., $t_D > t_{P1}$), the distribution of t_D values is not Gaussian (fig. 2c) and is most reliably approximated by an exponential with time constant t_τ. As shown in figure 2c, which plots the translocation duration histograms for groups 1, this time constant was found to be much longer for the poly(dA)$_{100}$ events than for the poly(dC)$_{100}$ events. (Likewise, the group 2 values of τ_{T2} were greater for poly(dA) than for poly(dC)). Other polymer types, reported below, as well as many other polymers (unpublished data) exhibit a similar non-Gaussian time distribution of t_D. Because this non-Gaussian time distribution is observed for all the polymers that have been tested, it most likely a reflection of the basic underlying mechanism responsible for polymer translocation rather than of the particular base sequence traversing the nanopore. This non-Gaussian time distribution should be taken into account in future attempts to model polymer translocation through small diameter channels.

Although the separation into 2 groups is not as clear for poly(dC)$_{100}$ as it is for poly(dA)$_{100}$, the tendency of these DNA polymers to fall into two groups begs the obvious question: Why two groups? The same question has been raised with respect to the similar phenomena observed for many RNA polymers [4] (see also the chapter by Kasianowicz), where it was suggested the two groups seen for many polymers could represent translocation of the same structure in either of two orientations (3' to 5' or 5' to 3'). If this were the case, one might expect that all DNA polymers, which contain the same deoxyribophosate backbone would, irrespective of their base composition, give rise to two groups in event plots such as shown in figure 2. In fact, several polymers, such as poly(dCdT)$_{50}$, were found to produce only one group,

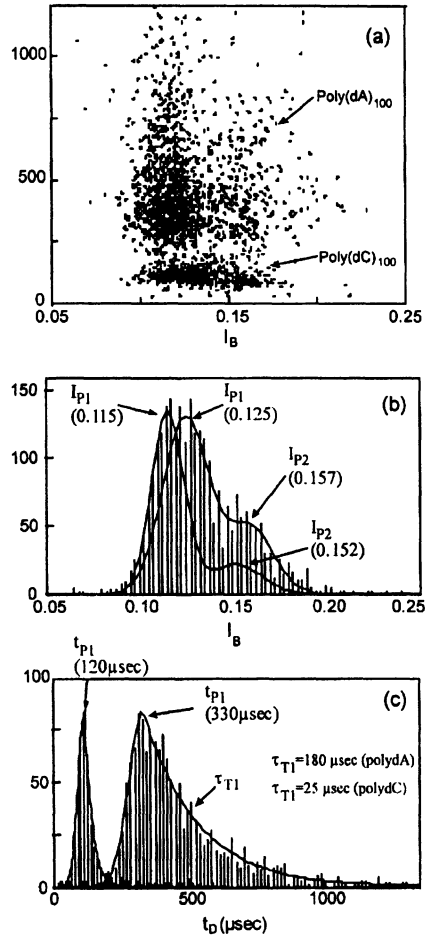

Figure 2. (a) Event diagram showing translocation duration versus blockade level for poly(dA)$_{100}$ (black) and poly(dC)$_{100}$ (gray) at 20°C. Each point on this diagram represent the translocation of a single molecule that was characterized by its translocation duration, t_D, and blockade current, I_B. (b) Current histogram projected from the above event diagram, same color codes. The two peaks corresponding to the two groups of events are denoted by I_{P1} and I_{P2}. The solid lines are fits of the data to a sum of two Gaussians. (c) Duration histogram projected from (a) for the first group of events. The solid lines are fits, see text. From [5].

suggesting that the grouping phenomena may be a function of the particular purines or pyrimidines that are attached to the backbone sugars.

Using the procedure described above for poly(dA) and poly(dC), we measured the translocation properties of six different polymers. By fitting the translocation duration time and blockade current distribution we obtained the characteristic parameters of each of the polymer shown in Table 1. Together,

Table 1.

Polymer	I_{P1}	t_{P1} (μs)	τ_{T1} (μs)	I_{P2}	t_{P2} (μs)	τ_{T2} (μs)
$(dA)_{100}$	0.126±0.012	192±10	55±3	0.178±0.013	291±20	111±7
$(dC)_{100}$	0.134±0.010	76±4	15±1	0.170±0.013	64±4	10±1
$(dA)_{50}(dC)_{50}$	0.128±0.010	136±7	32±2	0.168±0.014	231±16	176±12
(dAdC)50	0.141±0.011	177±9	38±2	0.182±0.011	163±11	41±3
$(dC)_{50}(dT)_{50}$	0.140±0.011	137±7	25±1	No group 2	–	–
$(dCdT)_{50}$	0.144±0.012	82±4	91±5	No group 2	–	–

Summary of the statistical translocation properties of six different polymers characterized at 25.0 deg C. The standard error of the mean is shown for at least 5 groups of measurements of the same polymer. From [5].

these ensemble properties can provide a unique fingerprint that distinguishes between DNA molecules, several of which differ from each other only by their sequence. The I_P, t_P and τ_T values for the group 1 and group 2 events of six different polymers unambiguously characterizes each of the polymer types.

The differences between the translocation behavior of polymers measured at 25°C are accentuated at lower temperature. Using again poly(dA) $_{100}$ and poly(dC) $_{100}$ as an example, examination of representative data at 15.0°C, 25.0°C and 33.0°C (fig 3), make it clear that the two polymers show different trends:

The poly(dA) events remain as two separate groups throughout the entire temperature range, but the poly(dC) events that begin to fall into two groups at 20°C (fig. 2) merge into a single widely dispersed group above 25° (fig. 3b and 3c).

The relative number of events in the two poly(dA) groups varies with temperature. At 15°C, nearly 50% of the total number of events are in the second group while at 40°C this fraction is reduced to only 20-25%. Particularly for poly(dA), the scattered events in group 2 become even more dispersed at low temperatures (fig. 3a).

An extensive series of measurements from 15°C to 40°C with five polymer types showed that for all of the polymers tested, the temperature dependence of t_{P1} is best approximated by $\sim a/T^2 + b$ (figure 4, full lines) where a is a constant that depends on the polymer type, T is the temperature in °C and b is an additive constant. Exponential and T^{-1} temperature dependencies failed to fit this data. The T^{-1} temperature dependence of cannot be accounted for by viscous drag alone since viscosity would be expected to contribute only a factor of T^{-1}. The strong temperature dependence of t_{P1} probably arises from a complex of factors affecting those portions of the polymer that are in the channel and those that are outside of the channel. We thus would expect

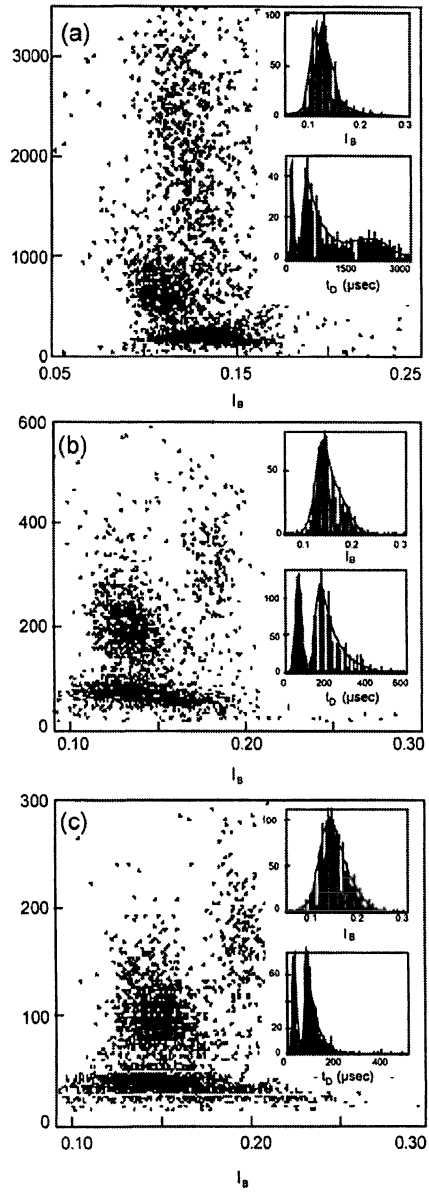

Figure 3. Event diagrams for poly(dA)$_{100}$ (black) and poly(dC)$_{100}$ (gray) at: (a) 15°C, (b) 25°C and (c) 33°C. The insets are the corresponding translocation current (top) and duration time histograms, same color codes. The solid lines are fits similar to those shown in figure 2. From [5].

weaker temperature dependence for shorter polymer, especially those that are

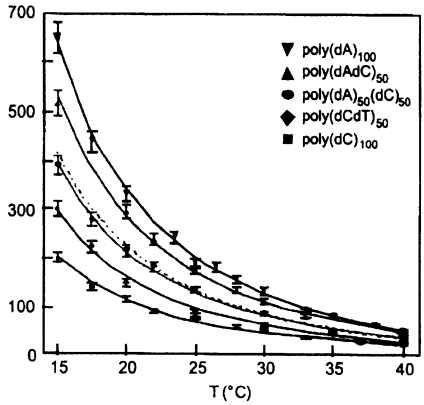

Figure 4. Dependence of t_P for group 1 events for poly(dA)$_{100}$, poly(dC)$_{100}$, poly(dA$_{50}$dC$_{50}$), poly(dAdC)$_{50}$, and poly(dCdT)$_{50}$). The error bars indicate the standard error of the mean of more than 5 groups of measurements. With rising temperature between 15°C and 40°C there is a 12-fold decrease of t_{P1} for the slowest polymer poly(dA), and an 8 fold decrease of t_D for the fastest poly(dC). The dotted black line that matches closely to the poly(dA$_{50}$dC$_{50}$) data is the algebraic average between t_D of poly(dA)$_{100}$ and t_{P1} of poly(dC)$_{100}$. Note that the temperature dependence is not exponential; rather, T^{-2} scaling (solid lines) yielded the best fit to the data. From [5].

short enough to reside entirely within the pore. This is indeed confirmed by a preliminary set of measurements with polymers as short as 10 bases (unpublished).

Inspection of Figure 4 makes it clear that at high temperatures, the differences between polymers are diminished. For example, the ratio of t_{P1} for poly(dA)$_{100}$ to t_{P1} for poly(dC)$_{100}$ (the slowest and fastest polymers in our experiments) decreases with temperature from $\sim$ 3.2 at 15°C to $\sim$ 2.1 at 40°C. Further experiments at higher temperatures will be needed to determine if all polymers approach a common value. If so, translocation through a nanopore could be used as a rapid measure of polymer length regardless of the polynucleotide's composition or sequence.

At low temperatures, the differences between polymers are striking. This implies that experiments at 15°C or lower should optimize the identification of individual polymers in a mixed population. For example, the discrimination between poly(dA)$_{100}$ and poly(dC)$_{100}$ at 20°C shown in figure 2c is enhanced at 15°C where there is less overlap in the distribution of t_D values of the two components. Other experiments with poly(dC)$_{100}$ and poly(dCdT)$_{50}$ show that the t_{P1} values for these polymers differ by 50% (300μs versus 200 μs) at 15°C even though both polymers contain only pyrimidines. Recent experiments at low temperatures demonstrate that as few as 10 substitutions

of thymines spaced evenly throughout a 100 nucleotide poly(dC) polymer are readily detectable (unpublished data).

The effects of temperature on the movement of DNA polymers through a nanopore have begun to provide new insights into the origin of the two event groups observed with many polymers, such as poly(dA)$_{100}$ and poly(dC)$_{100}$ at low temperatures. Originally, the presence of two groups was interpreted as translocation of similarly structured polymers in either of two orientations, 3' to 5' or 5' to 3'. But the measurements of temperature dependent translocation parameter values have now begun to suggest that the presence of two groups may be the result of an equilibrium between polymers that contain stacked structures and polymers that are in an essentially random coil [7–10]. The stacked structure is favored at low temperature, whereas the unstacked random state is favored at high temperature. If, at low temperatures, any existing stacked structure must be broken as the DNA is translocated through the narrow α-hemolysin pore, the added time to disrupt this structure would shift t_P to longer times and broaden the distribution of translocation durations, as measured by τ_T. At the high salt concentrations used for our experiments, the time scales for unstacking the polymer bases are commensurate with the difference between the t_{P1} and t_{P2} values we observed [5].

Meller et al. [5] advanced four observations that implied secondary structure and base stacking could be a major explanation for the existence and the statistical properties of group 2 events: There is a particularly strong temperature dependence of t_{P2} and τ_{T2} in those polymers which contain long poly(dA) sequences. This phenomena is pronounced with poly(dA)$_{100}$, which is known to have a strong tendency for base stacking at low temperatures. In contrast, the translocation duration of poly(dAdC)$_{50}$, which cannot form strong purine-purine base stacking, is approximated by an exponential over the entire temperature range.

If entry into the narrow space of the α-hemolysin requires that DNA base stacking structure be broken, the energy associated with this process should yield events with a greater temporal scattering. Indeed, τ_{T2}, (which provides a direct measure of temporal dispersion in group 2) for poly(dA)$_{100}$ and poly(dA$_{50}$dC$_{50}$) diverges at low temperatures to much larger values compared with τ_{T1} for poly(dA)$_{100}$ and poly(dA$_{50}$dC$_{50}$) whereas the τ_{T2} values for poly(dAdC)$_{100}$, which cannot form strong purine-purine base stacking, did not show such divergence.

If lower temperatures stabilize purine stacking, it is expected that the number of the events associated with structured polymers will grow with decreasing temperature. This is observed. The fraction of the events in group 2 increase from about 20% at 25°C to 45% at 15° for poly(dA)$_{100}$ and poly(dA$_{50}$dC$_{50}$), while remaining nearly constant for poly(dAdC)$_{50}$. For both

poly($dC_{50}dT_{50}$) and poly$(dCdT)_{50}$, in which only weak pyrimidine stacking is possible [11], the pattern of translocation events do not exhibit two groups, even at 15°C.

Thus, the group 2 events may represent the mostly structured (base-stacked) polymers and the group 1 events the more unstructured, randomly conformed polymers. While Meller et al.'s [5] data does not exclude specific polymer-pore interactions that could explain the two groups as two states of the channel, such interactions would not readily explain the strong temperature effects.

References

[1] Bonnet, G., Krichevsky, O., Libchaber, A. (1998). *Proc. Natl. Acad. Sci. (USA)* **95**, 8602-06.

[2] Chou, H., Spence, C., Scherer, A., Quake, S. (1999). *Proc. Natl. Acad. Sci. (USA)* **96**, 11-13.

[3] Bakajin, O.B., Duke, T.A.J., Chou, C.F.S., Austin, R.H., Cox, E.C. (1998). *Phys. Rev. Lett.* **80**, 2737-2740.

[4] Kasianowicz, J.J., Brandin, E., Branton, D., Deamer, D.W. (1996). *Proc. Natl. Acad. Sci. (USA)* **93**, 13770-13773.

[5] Meller, A., Nivon, L., Brandin, E., Golovchenko, J., Branton D. (2000). *Proc. Natl. Acad. Sci. (USA)* **97**, 1079-1084

[6] Akeson, M., Branton, D., Kasianowicz, J. J., Brandin, E., Deamer, D.W. (1999). *Biophys. J.* 77, 3227-3233.

[7] Luzzati, V., Mathis, A., Mason, F., Witz, J. (1964). *J. Mol. Biol.* **10**, 28-41.

[8] van Holde, K.E., Brahms, J., Michelson, A.M. (1965). *J. Mol. Biol.* **12**, 726-739.

[9] Holcomb, D.N., Tinoco, I., Jr. (1965). *Biopolymers* **3**, 121-133.

[10] Dewey, T.G., Turner, D.H. (1979). *Biochemistry* **18**, 5757-5762.

[11] Solie, T.N., Schellman, J.A. (1968). *J. Mol. Biol.* **33**, 61-77.

USE OF A NANOSCALE PORE TO READ SHORT SEGMENTS WITHIN SINGLE POLYNUCLEOTIDE MOLECULES

Mark Akeson, David W. Deamer, Wenonah Vercoutere, Rebecca Braslau, and Hugh Olsen
Biophysics Laboratory, Department of Chemistry and Biochemistry, University of California, Santa Cruz, CA 95064

Abstract Single-stranded polynucleotide molecules impede ionic current when they are driven through a nanoscale pore formed by the α-hemolysin heptameric channel (see J. Kasianowicz, D. Deamer, D. Branton, this volume). The duration and frequency of these blockades correlate with the length and concentration of the polymer examined. This suggests that translocation of RNA and DNA strands through the nanopore might also be used to derive a direct, high-speed read-out of each molecule's linear composition. We have recently shown that this is possible. Homopolymers of polycytidylic acid (poly C), polyadenylic acid (poly A), and polyuridylic acid (poly U) cause blockades of current through the α-hemolysin pore that are distinguishable from one-another based on amplitude and duration. These differences are due to the predominant secondary structure adopted by each homopolymer at room temperature in neutral buffer. We have also demonstrated that the nanopore instrument has sufficient sensitivity and resolution to detect short, discrete blocks within single polynucleotide molecules during translocation. For example, within an individual RNA strand, the transition from a 30-nucleotide poly A segment to a 70-nucleotide poly C segment can be read as an abrupt, 10 pA current change. A larger current change can also be observed at the transition between nucleotides and an abasic deoxyribose-phosphate segment inserted into a synthetic DNA strand. These polymers may be used to encode targeting molecules such as antibodies, gene specific oligonucleotides, and peptide agonists.

Keywords: α-hemolysin, nanopore, polycytidylic acid, polyadenylic acid, polyuridylic acid, sequencing DNA

1. Introduction

We and our colleagues (Deamer et al., Branton et al., Kasianowicz et al., this volume) are developing nanopore instruments designed to read the linear composition of individual encoded polymers including RNA and DNA.

J.J. Kasianowicz et al. (eds.), Structure and Dynamics of Confined Polymers, 187–200.

David Deamer and Daniel Branton first proposed that this technology might one-day achieve single nucleotide resolution, thus permitting sequencing at rates approaching 1000 nucleotides per pore per second [1]. This will require a detector associated with the nanopore that can resolve modest structural differences between two pyrimidines (T and C in DNA) or between two purines (G and A in DNA), at 7 angstrom spatial resolution in 1 to 10 milliseconds per nucleotide. As a preliminary step toward this end, we have used the α-hemolysin prototype nanopore to establish current blockade patterns caused by linear block copoylmers (Deamer et al., this volume, Fig. 1). The blocks in these copolymers are composed of identical repeated monomers in series (20mers or greater) including RNA nucleotides, DNA nucleotides, and synthetic monomers linked by phosphodiester bonds. In this chapter, we describe the signatures of these block copolymers as they traverse the α-hemolysin under an applied voltage. We also describe a new application of the encoded molecules that we refer to as targeted molecular bar codes.

2. Discrimination between RNA homopolymers based on blockade amplitude and duration.

One of our first aims was to determine if the prototype nanopore instrument could distinguish between homopolymers of any of the five common nucleotides (G, A, C, T or U). Based upon differences in molar volume (Deamer et al., this volume) we reasoned that comparisons between a purine polyribonucleotide and a pyrimidine polyribonucleotide would be most likely to result in measurable current differences. Our experimental set-up has been described previously [1,2]. Briefly, single α-hemolysin channels were introduced into high-resistance lipid bilayers formed across a horizontal, conical aperture on a Teflon patch tip separating two baths containing 1M KCl at pH 7.5 to 8.0 (HEPES/KOH). Ribonucleic acid homopolymers (poly A or poly C of about 150 nt in length) were added to the cis bath and ionic current blockades were measured at 120 mV applied potential. Poly A homopolymers caused three classes of blockades [2] (See Fig. 1, dashed arrows). Among these, the larger amplitude blockades reduced the channel current by about 107 pA to 19 pA of residual current (85 % blockades) with durations in the range of 1.5 to 2.5 ms. These blockades were strand-length dependent, a characteristic that correlates with vectorial translocation through the nanopore [1].

The pattern of blockades caused by poly C was easily distinguished from the pattern caused by poly A (Figure 1, solid arrows). Most notably, of the blockades whose duration was strand-length dependent, two distinguishing characteristics emerged: i) poly C RNA reduced the channel current significantly more than did poly A RNA (95 % blockades vs 85 % blockades,

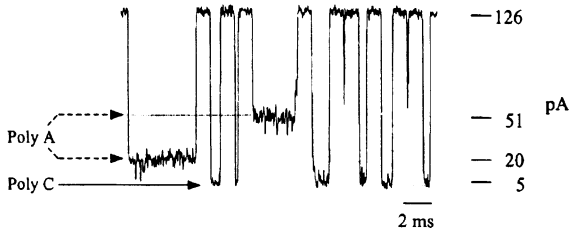

Figure 1. Blockades of the α-hemolysin nanopore caused by poly A or poly C homopolymers. The RNA strands ($\sim 200\mu g/ml$) were captured and driven through a single α-hemolysin pore by a 120 mV applied potential at room temperature. The buffer was 1M KCl at pH 7.5 (HEPES/KOH). From [2].

respectively); and ii) the 95 % blockades caused by poly C were shorter in duration (ca. $3\mu s$ per nucleotide) than were the 85 % blockades caused by poly A (ca. $20\mu s$ per nucleotide). Using these two parameters alone, it was possible to identify each individual blockade in a population of several thousand as due to poly C translocation or due to poly A translocation. This result set the stage for construction of RNA block copolymers that could be read directly by the α-hemolysin nanopore (see below), but it was also opposite of what we expected: the adenylic acid monomer in poly A has a larger molar volume than does the cytidylic acid monomer in poly C, and yet the poly A blockade amplitude was less than the poly C blockade amplitude. Furthermore, on average, poly C RNA translocated across the pore more rapidly than did poly A RNA of similar length despite greater resistance to poly C translocation implied by the larger blockade amplitude. This unexpected result is most likely explained by the predominant secondary structure adopted by each RNA homopolymer in neutral solution at room temperature. X-ray diffraction analysis of poly C fibers (See Fig. 2a, left) [3]
reveals a right-handed helix with six nucleotides per turn and a 1.34 nm diameter which is sufficiently narrow to fit into the α-hemolysin pore without unstacking. In other words, poly C could translocate across the α-hemolysin pore as a narrow single-stranded helix rather than as an extended, random coil (Figure 2b, left). By comparison, X-ray diffraction analysis of poly A RNA [6] (See Fig. 2a right) suggests a right-handed helix with nine nucleotides per turn and a 2.2 nm diameter. This structure is sufficiently narrow to fit into the vestibule of the α-hemolysin pore (see the chapters by Kasianowicz, et al. and by Deamer et al.), accounting for the numerous, long-lived partial blockades associated with this polymer (Fig. 1). However, at 2.2 nm diameter the poly A helix is too large to fit through the 1.5 nm limiting aperture of the α-hemolysin pore. Thus poly A RNA would typically be captured as a helix, but translocated as an extended strand as it is slowly unstacked by the electric field across the nanopore (Figure 2b, right).

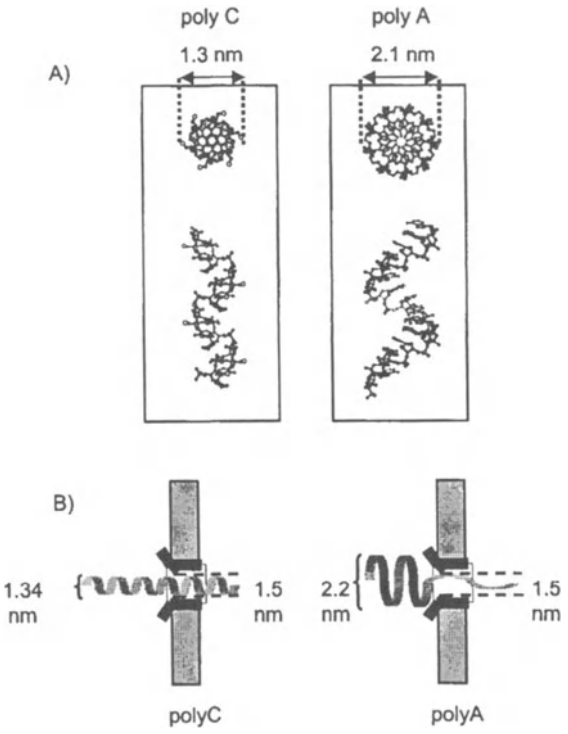

Figure 2. Structure of poly C and poly A RNA homopolymers based on X-ray diffraction analysis. The structure at left is from [3]. The structure at right is from [4]. Dimensions of the α-hemolysin pore are from [5].

Two additional experimental results support this model. First, Adler et al. [7] used circular dichroism to show that poly dC is relatively unstructured compared to poly C at room temperature in neutral buffer. Therefore, if the model in Figure 2b is correct, current blockades caused by poly dC should be faster and of lesser amplitude on average than are blockades caused by equal length poly C. This is in fact the case (Figure 3).

Second, if poly A penetrates the limiting aperture of the α-hemolysin pore as an extended strand formed when a helix unstacks (Figure 2b), then current blockades caused by poly A should be similar in amplitude to those caused by an extended random RNA coil such as poly U [6,8,9] but significantly longer in duration. This is supported by experiment as well: current blockades during poly A translocation cannot be distinguished from poly U translocations based on amplitude, but they can be distinguished from poly U based on average blockade duration [2].

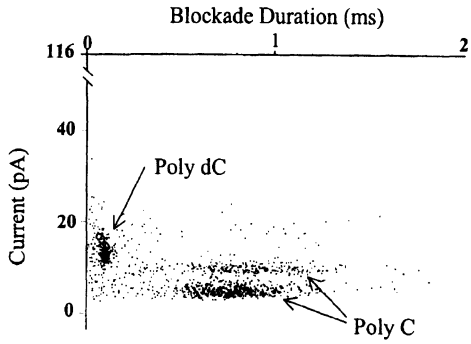

Figure 3. Comparison of the ionic current blockades caused by poly C RNA and by poly dC DNA homopolymers. The polymers (~ 100 nucleotides long) were captured and driven through a single α-hemolysin pore by a 120 mV applied potential at room temperature. The buffer was 1M KCl at pH 8.0 (HEPES/KOH). From [2]. Reading of a poly A/poly C RNA block copolymer using ionic current through the α-hemolysin pore.

The homopolymer data (preceding section) lead us to believe that a transition from poly A to poly C segments within an individual RNA molecule should be detectable by the α-hemolysin pore. We therefore examined blockades caused by an RNA strand composed of covalently linked poly A and poly C blocks (Fig. 4a).

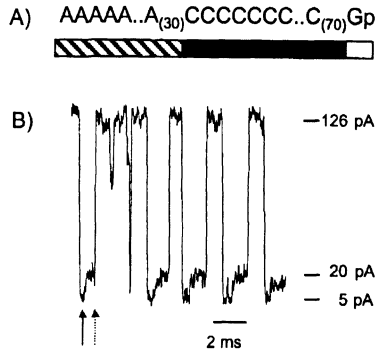

Figure 4. Ionic current blockades caused by a poly A(30)poly C(70) RNA block copolymer. The RNA strands (50 μg/ml) were captured and driven through a single α-hemolysin pore by a 120 mV applied potential at room temperature in 1M KCl.

As predicted by the homopolymer data, translocation of this RNA block copolymer resulted in blockades with two components (Figure 4b), one of which reduced the channel current by ~ 95 % (consistent with poly C), and the other of which reduced the current by ~ 85 % (consistent with poly A). To establish that the two part blockade signature was due to the poly C-to-poly

A transition in A(30)C(70)Gp, we repeated the experiment with the addition of ribonuclease A. Ribonuclease A cuts 3' of pyrimidine nucleotides in RNA, but it does not cut at purine residues. When added to an A(30)C(70)Gp preparation, this would result in a rapid decrease in intact block copolymers, and ultimately result in a mixture of intact poly A 30mers and cytidylic acid monomers (Fig. 5a).

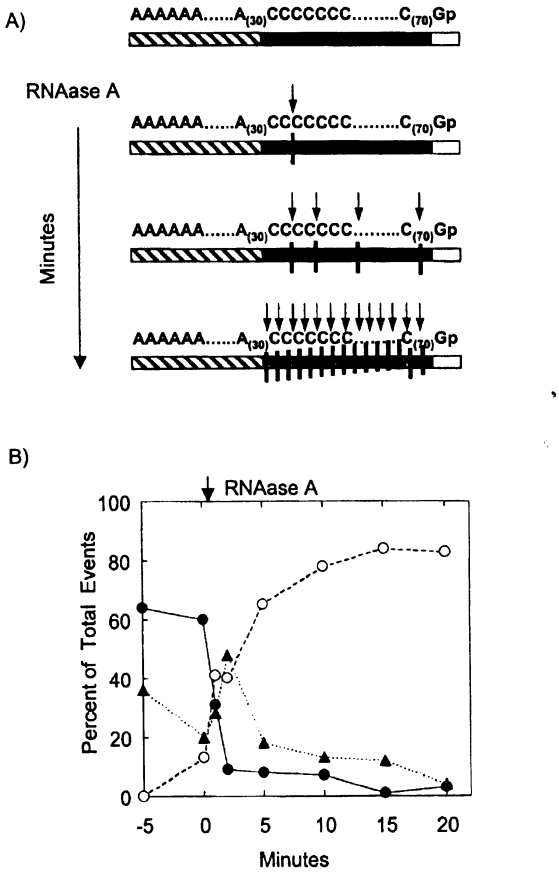

Figure 5. Effect of RNAse A digestion on the proportion of two level vs single level blockade signatures in a solution containing poly A(30)poly C(70) at time zero. The filled circles represent C-to-A bilevel blockades, the open circles represent poly A blockades, and the triangles represent poly C blockades. Experimental conditions described in Fig. 4.

Figure 5b shows that current blockade patterns read by the nanopore instrument follow this pattern. This confirms that current blockades in the α-hemolysin pore accurately report the transition from a poly C helix to a poly A extended strand during translocation of individual RNA molecules.

3. Design and testing of a synthetic DNA strand containing an abasic segment.

The A(30)C(70)Gp data were evidence that an individual encoded linear polymer could be read by a nanopore instrument. However, our ability to read the poly C-to-poly A transition relied upon differences in secondary structure between the two segments. Ultimately, our ability to read polynucleotide sequences (Deamer et al., Branton et al., this volume), or to read the sequence of targeted molecular bar codes (see below), will be optimized if we can detect the primary structure of linear polymers. The synthetic strand depicted in Figure 6 was designed to maximize our ability to read primary structure within a synthetic DNA strand.

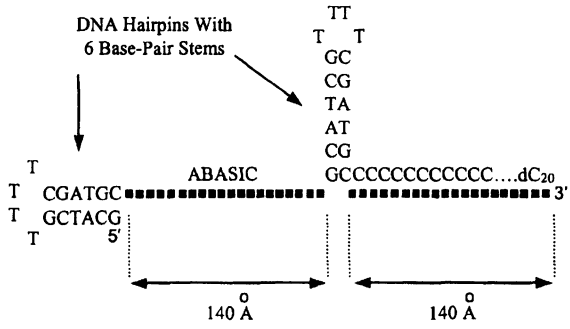

Figure 6. A synthetic DNA strand containing hairpins and an abasic polydeoxyribose-phosphate insert.

This molecule was constructed with three key features: i) a block of twenty dC nucleotides at the 3' end of the molecule to facilitate efficient capture and to provide a well characterized blockade amplitude at the start of translocation. ii) A block composed of twenty 'abasic' monomers in which the base normally found at C1 of the deoxyribose sugar in DNA is replaced by a hydrogen atom (Figure 7).

The molar volume of the abasic monomer is significantly less than that of DNA nucleotides (Deamer et al., this volume) and would therefore be likely to cause a measureably different blockade amplitude than does poly dC. In addition, twenty abasic monomers strung end-to-end would be about 140 angstroms, which is sufficient to span the α-hemolysin pore. iii) DNA hairpins were inserted at the 5' end of each homopolymer segment. These hairpins were inserted because random coils of polynucleotide traverse the α-hemolysin nanopore at 1-3 nucleotide per μs, and it is likely that the abasic segment would traverse the pore much more rapidly than this. Gueron and Leroy [10] have shown that H-bonded base pairs in duplex DNA (such as hairpin stems) have finite lifetimes ranging from 10 ms for G-C pairs internal to a duplex, to

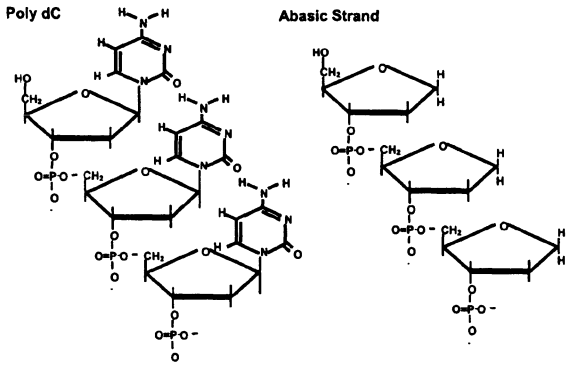

Figure 7. Structure of an abasic deoxyribose-phosphate backbone compared to polydeoxycytidylic acid (poly dC).

substantially less than 1 ms per base pair at the end of a duplex, as would be encountered by a polymerase at a replication fork in DNA, or by a nanopore translocating DNA up to an internal hairpin. Thus, on a molecular scale, transport of DNA in an electric field across a nanopore would be expected to pause at each base-pair in a hairpin stem and only proceed when each of the base-pairs sequentially dissociates. This model is supported by the results in Figure 8, which show that a 10 base-pair hairpin stem inserted into a poly dC synthetic strand slows translocation by about 10 μs per base pair relative to a randomized control [11].

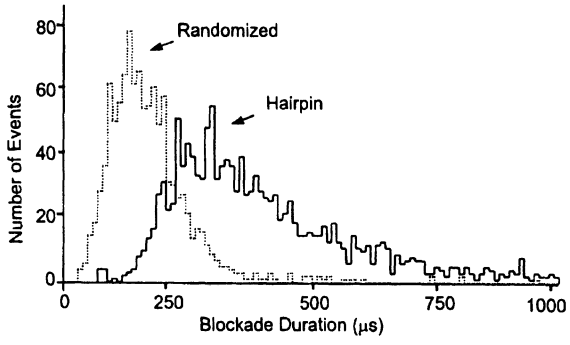

Figure 8. Comparison between blockade durations caused by an oligomer with a 10 bp hairpin insert between two poly dC 20mer overhangs, and a randomized control. Conditions for the experiment are described in the legend to Figure 3.

When the polymer in Figure 6 was examined by the nanopore, a distinct, reproducible three-part blockade signature was observed in 40% of measured events (Figure 9). The first and third components of these events were characterized by 86% current reductions relative to the open channel, consistent

with blockades caused by DNA random coils. The intermediate segment (Figure 9 arrows) was characterized by a 71% current reduction relative to the open channel. This intermediate segment was absent in a control polymer in which the abasic segment was replaced by a poly dC 20mer, therefore the 71% blockade amplitude correlates with translocation of the abasic segment. This constitutes evidence that a nanopore can be used to read the primary structure of a linear polymer.

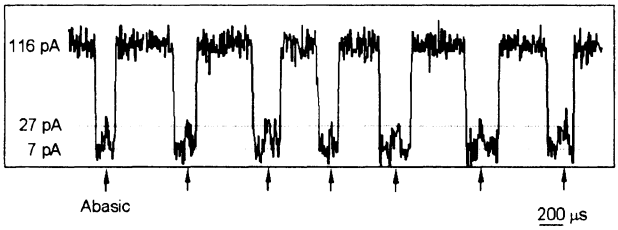

Figure 9. Characteristic blockades caused by the synthetic strand in Figure 6. Conditions for the experiment are described in the legend to Figure 3. The spike in the middle of each event (arrows) was absent in a control where the abasic insert (Figure 6) was replaced by poly dC.

4. Use of synthetic encoded polymers as 'molecular bar codes' targeted to cell surface antigens

We are using synthetic polymers similar to the one described in Figure 6 to examine details of DNA translocation that will be important in development of a sequencing nanopore. These encoded polymers could also be used to tag antibodies, agonists, gene specific sequence and other molecules specifically targeted to biologically important macromolecules. In principle, this technology would permit simultaneous quantification of several thousand polynucleotides or proteins expressed in a human tissue sample at rates approaching ten thousand molecules per second. This speed would require only a small array of nanopores and femtomole amounts of encoded polymers. Our approach can be summarized as follows. Each 'targeted molecular bar code' is a macromolecule comprised of a unique readable segment (a synthetic encoded polymer as in Figure 6) attached through a cleaveable linker to a second segment that specifically targets a macromolecule. Figure 10 illustrates one hypothetical example in which the encoded polymers are attached to antibodies or agonists directed against cell surface proteins. An array of several thousand unique molecular bar codes can be designed using an 'alphabet' composed of interchangeable blocks at each position in series along a linear polymer. For example, an alphabet of four in a series of five blocks can give $4^5 \sim 1000$ unique codes each of which could be attached to a unique agonist

or antibody. The signature used to identify each segment of the alphabet may include: i) average current through or across the nanopore during occupancy of the pore by that segment; ii) duration of pore occupancy by the segment; iii) segment-specific current noise; and iv) catalytic or fluorescent moieties associated with the segment that are detected upon translocation through the pore. In a typical assay, a mixture of targeted molecular bar codes would be added to a population of cells (for example a blood sample or a tissue biopsy) and allowed to bind (Figure 10). Unbound targeted molecular bar codes are washed from the surface, then the bound molecular bar codes are cleaved from the surface at the linker. The recovered molecular bar codes are subsequently read and quantified using a nanoscale pore, thus reporting the amount of each targeted cell surface protein (see also Kasianowicz, et al.).

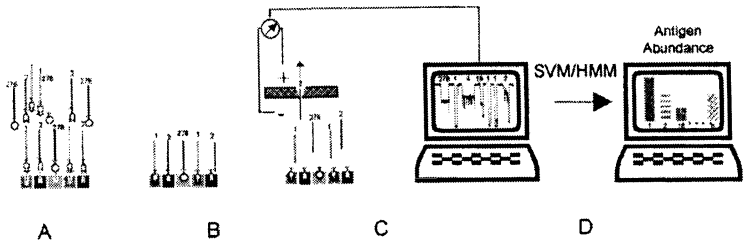

Figure 10. Targeted molecular bar code strategy. Each targeted molecular bar code is a macromolecule comprised of a unique encoded polymer attached through a cleaveable linker to a second segment that specifically binds to a target macromolecule such as a cell surface protein. In the example shown, a mixture of antigen-specific molecular bar codes is added to a population of cells (for example a blood sample or a suspected pathogen) and allowed to bind (A). Unbound molecular bar codes are washed from the surface (B), after which the bound molecular bar codes are cleaved from the surface at the linker and translocated through the nanopore under an applied field (C). Each current signature reported by the nanopore (D) is identified by computational methods (e.g. Hidden Markov Models (HMM) and Support Vector Machine (SVM)), thus quantifying the targeted antigens (E). Using an alphabet of four discernible, interchangeable segments linked in a five-segment-long series would allow construction of $4^5 \sim 1{,}000$) unique codes.

We designed a simple experiment to demonstrate that a single-polymer bar code could be specifically targeted to a macromolecule (Figure 11a). In brief, DNA oligonucleotides corresponding to 50 base segments of human p53 and N-ras open reading frames were synthesized on polystyrene beads. These sequences served as targets. We then synthesized a targeted single-polymer bar code comprised of a poly dT 18mer that served as the code, coupled through a disulfide linkage to an antisense complement to the N-ras target. This N-ras targeted bar code was hybridized to the N-ras and p53 polystyrene beads using standard conditions. The beads were then rinsed twice in 0.2X SSC, followed by 0.1 M DTT for 30 minutes at 37 degrees

C to cleave the disulfide linkage between the targeting strand and the dT 18mer bar code. The product of each reaction was then added separately to the nanopore. The results are shown in Figure 11b. There was more than a fifty-fold excess of the characteristic dT 18mer signature in the N-ras sample compared to the non-specific p53 sample. This demonstrates that an encoded polymer can be targeted to a macromolecule and used to specifically detect that macromolecule.

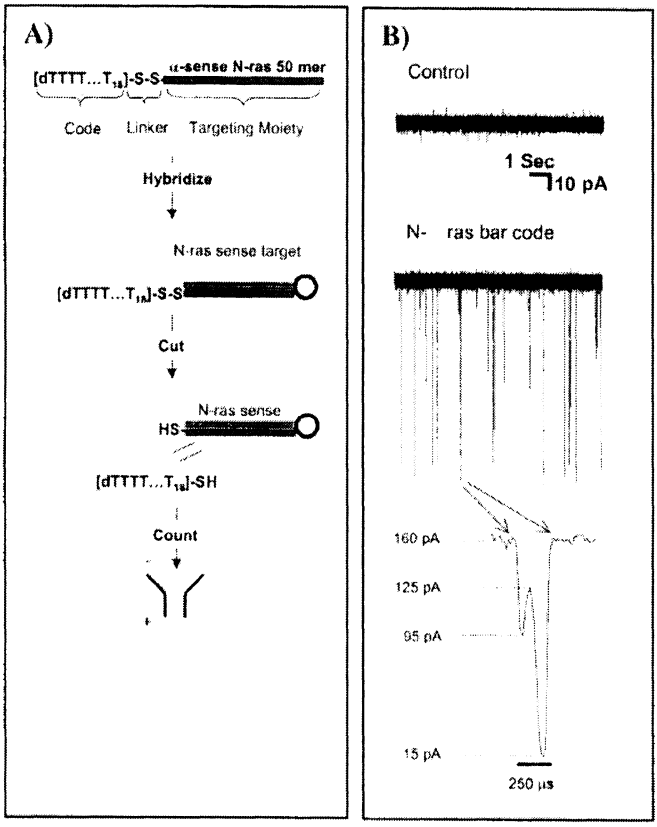

Figure 11. Nanopore detection of a molecular bar code directed against N-ras.

5. Future directions: synthesis of encoded polymers using nitroxide-mediated free-radical polymerization

The phosphodiester-based encoded polymers we have used to date will substantially increase our knowledge of the nanopore detector. One-hundred of such phosphodiester-based bar codes should be easily designed and synthesized providing a foundation for the molecular bar code library. However,

two possible drawbacks are that the phosphodiester bonds may be cut by a variety of enzymes in biological solutions, and the selection of phosphoramidite monomers we can use in our syntheses is limited. For these reasons, we are also now using nitroxide-mediated free radical polymerization to prepare synthetic polymers. A variation on conventional strategies using the 'Braslau/Vladimir Initiator' (Figure 12) effects living polymerization with extremely low polydispersities and controlled molecular weights for a number of monomer families, including styrenes, acrylates, acrylic acids, acrylamides and acrylonitriles [12].

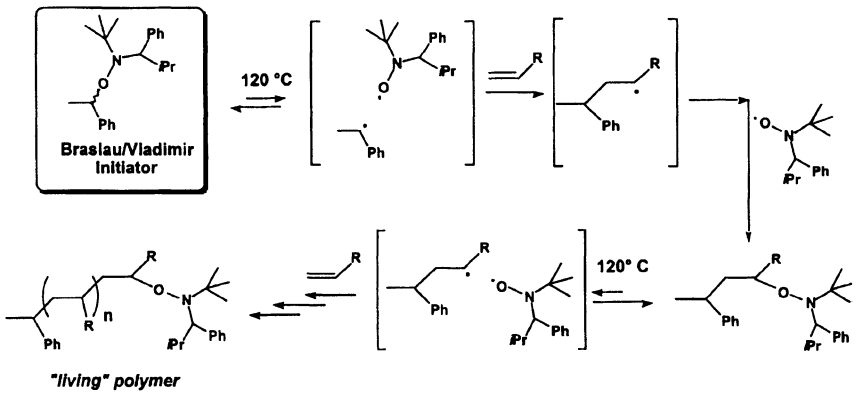

Figure 12. Mechanism of nitroxide-mediated living polymerization using the Braslau/Vladimir Initiator.

The previous "TEMPO" nitroxide based initiator was effective only with styrene monomers. The excellent performance of the Braslau/Vladimir initiator allows preparation of controlled polymers (including block copolymers) bearing a variety of functionalities, including carboxylic acids, epoxides, amines, perfluoroalkyl groups, ethers, esters, amides, nitriles and substituted aromatic groups. A few examples of each monomer class are shown here, all of which are commercially available (Figure 13 top, middle). Derivatizable monomers (Figure 13, bottom) may also be introduced into the polymer bar codes. These can be protected forms of ionizable species. For example, t-butyl acrylate can be used as a protected form of acrylic acid, which upon treatment with TFA should liberate the carboxylic acid. Alternatively, these derivatizable monomers can be used as handles for the introduction of additional charged or fluorescent moieties that can be added once the polymerization has been effected. In addition, the use of monomers with reactive functionality offers the opportunity to introduce graphed arms onto the polymer chain. This can be used to manipulate the effective diameter of the polymer chain, or to design more complex structures such as branched or comb polymers.

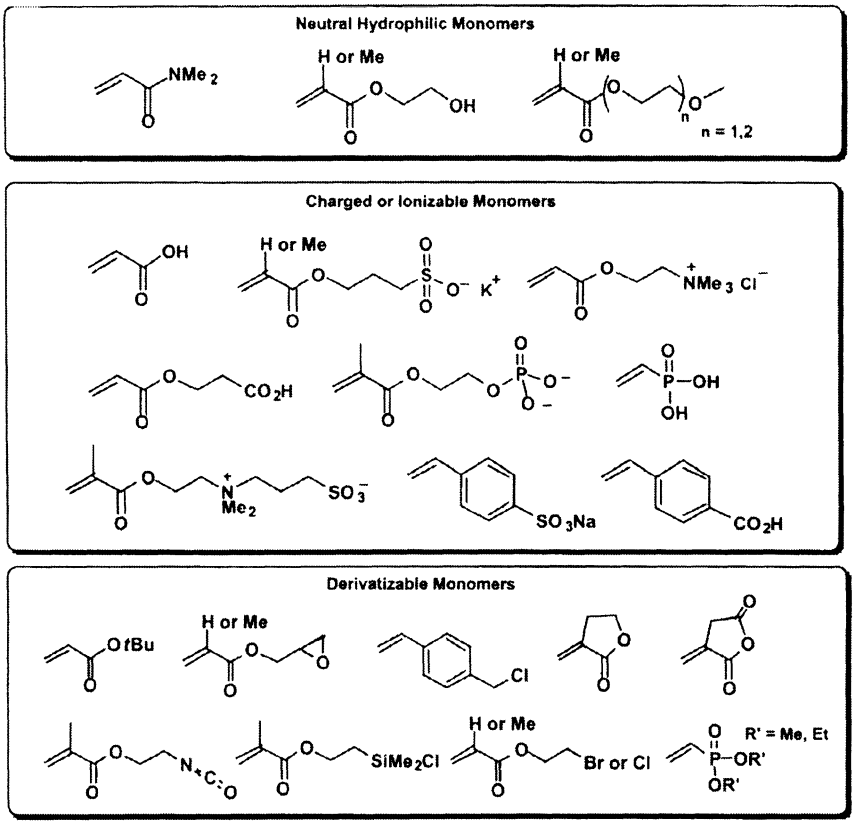

Figure 13. Classes of monomers that may be incorporated into polymers using the Braslau/Vladimir Initiator.

6. Conclusions

We have demonstrated that segments of linear polymers can be read as they are driven through the pore formed by α-hemolysin. To date the encoded polymers we have used were primarily RNA and DNA, but recently we have prepared synthetic polymers using an innovative nitroxide-mediated free radical polymerization strategy. These encoded polymers may be used to tag molecules such as antibodies, peptide agonists and gene specific oligonucleotides in complex mixtures.

References

[1] Kasianowicz, J.J., E. Brandin, D. Branton, and D.W. Deamer. (1996). Characterization of individual polynucleotide molecules using a membrane channel. *Proc. Natl. Acad. Sci. (USA)* **93**,13770-13773.

[2] Akeson, M., D. Branton, J.J. Kasianowicz, E. Brandin, and D.W. Deamer. (1999). Microsecond time-scale discrimination among polycytidylic acid, polyadenylic acid, and polyuridylic acid as homopolymers or as segments within single RNA molecules. *Biophys. J.* **77**, 3227-3233.

[3] Arnott, S., R. Chandrasekaran, and A.G.W. Leslie. (1976). Structure of the single-stranded polyribonucleotide polycytidylic acid. *J. Mol. Biol.* **106**, 735-748.

[4] Saenger, W., J. Riecke, and D. Suck. (1975). A structural model for the polyadenylic acid single helix. *J. Mol. Biol.* **93**, 529-534.

[5] Song, L., M.R. Hobaugh, C. Shustak, S. Cheley, H. Bayley, and J.E. Gouaux. (1996). Structure of staphylococcal α-hemolysin, a heptameric transmembrane pore. *Science (USA)* **274**, 1859-1865.

[6] Cantor, C.R., and P.R. Schimmel. (1980). Biophysical Chemistry, Part I: The Conformation of Biological Macromolecules. W.H. Freeman, San Francisco. 341 pp.

[7] Adler, A., L. Grossman, and G.D. Fasman. 1967. Single-stranded oligomers and polymers of cytidylic and 2'-deoxycytidylic acids: Comparative optical rotatory studies. *Proc. Natl. Acad. Sci. (USA)* **57**, 423-430.

[8] Evans, F.E., and R.H. Sarma. (1976). Nucleotide rigidity. *Nature (London)* **263**, 567-572.

[9] Inners, L.D., and G. Felsenfeld. (1970). Conformation of polyribouridylic acid in solution. *J. Mol. Biol.* **50**, 373-389.

[10] Gueron, M., and J.-L. Leroy. (1995). Studies of base-pair kinetics by NMR measurement of proton exchange. *Methods in Enzymology* **261**, 383-413.

[11] Vercoutere, W.A., M. Akeson, H. Olsen, and D.W. Deamer. 2000. Analysis of hairpin structures within single DNA molecules using a nanopore detector. *Biophys. J.* **78**, 402a (abstract).

[12] Benoit, D., V. Chaplinksi, R. Braslau, and C.J. Hawker. (1999). Development of a universal alkoxyamine for 'living' free radical polymerizations. *J. Am. Chem. Soc.* **121**, 3904-3920.

POLYMER DYNAMICS IN MICROPOROUS MEDIA

Björn Åkerman
Department of Physical Chemistry, Chalmers University of Technology, Goteborg, Sweden

Abstract The transport and conformational dynamics of polymers confined in porous media is reviewed, with emphasis on DNA in gels and polystyrene in track-etched membranes and porous glasses. These systems are used to illustrate the reptation concept, diffusive and electrophoretic transport under different degrees of confinement, and the effect of polymer topology and polymer-pore affinity on such processes.

Keywords: polymer confinement, DNA, polystyrene, gels, porous glass, track-etched membranes, reptation, diffusion, electrophoresis, threading, affinity, electrosmosis

1. Introduction

The motion of polymers in porous systems such as gels have important biotechnical applications in separation science as exemplified by size-exclusion chromatography and gel electrophoresis of biopolymers. Gel systems have a long tradition because they are easy to use for analytical and preparative purposes since they have good resolution and capacity. From the point of view of mechanisms for polymer transport these systems are relatively complicated however, because they are heterogeneous structures usually with a wide pore-size distribution. More recently polymer transport in more well-defined pores such as channels through lipid or inorganic membranes has become an important field of research. These systems usually offer well-defined pore geometry (radius and length), and sometimes even the crystallographic structure is known. The practical use of such channels for instance in analytical applications still remains to be demonstrated, but it is clear they form very interesting systems for mechanistic studies and in addition often have important but poorly understood biological functions of polymer transport.

One aim of this review is to demonstrate that polymer motion in membrane-spanning channels on one hand and in gels (and in porous glasses which have similar characteristics) on the other often is similar in nature. For instance, a polymer which is long compared to the membrane is threaded through a

J.J. Kasianowicz et al. (eds.), Structure and Dynamics of Confined Polymers, 201–225.

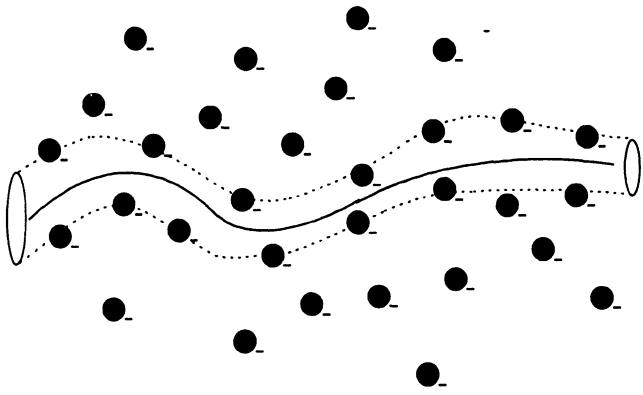

Figure 1. Polymer (solid) reptating in a gel with reptation tube (dotted) connecting the confining gel fibers (circles).

narrow channel end-on. Similarly, the motion of a polymer in a gel is often well-described by reptation, the snake-like end-on motion originally proposed by deGennes [1]. The nearest gel fibers have a confining effect which restrains the lateral motion of the polymer, and the motion is essentially along an imaginary tube (Figure 1) which is channel-like in nature.

Studies in the two types of system therefore can complement each other, and the second aim is to illustrate this. Membrane-based channels are often superior for realising the well-defined geometries commonly used in theoretical work. On the other hand, the range of available experimental techniques is much wider in the gels and glasses. In particular, spectroscopic techniques such as light scattering, fluorescence recovery after photobleaching (FRAP), linear dichroism spectroscopy and dielectric relaxation have been used in gels and porous glasses to establish important concepts such as polymer reptation. A spectroscopic approach is considerably more difficult in membrane-based systems, which in effect are two-dimensional and therefore offer very short optical paths. The combination of spectroscopy with single-molecule observation of the polymer by optical microscopy has proven especially powerful [2, 3]. Microscopy gives mechanistic insight but at the price of a limited spatial resolution, whereas spectroscopy provides high-resolution data at the expense of lost information due to ensemble averaging. The question of spatial and temporal resolution is an important one because usually the pore size is on a length-scale that is below the resolution of the microscope and be-

cause important polymer processes on this length-scale occur in a time range of milliseconds not accessible to video-microscopy.

The present review compares the dynamics of polymers in porous membranes and porous gels/glasses and includes conformational dynamics as well as diffusive and electrophoretic transport. The equally important question of partitioning, the equilibrium distribution of polymer between the pores and the outside bulk-solution, was recently reviewed extensively by Teraoka [4].

2. Principles of Confinement

2.1 Interactions in confining pores

All applications of polymer transport in pores rely on interactions with the matrix. Most basic is the steric type of interaction, which leads to reptation and which underlies the separation according to molecular size obtained by size-exclusion in gel filtration and by sieving in gel electrophoresis [5]. Steric interactions are often also responsible for the difference in behaviour between polymers of the same molecular weight but different shape, such as circular polymers. A gate formed by two gel-obstacles will generally slow down or even stop a circular molecule more than the corresponding linear form because the circle has to bend to pass between the obstacles whereas the linear counterpart can reptate through the narrow passage (Fig. 2a).

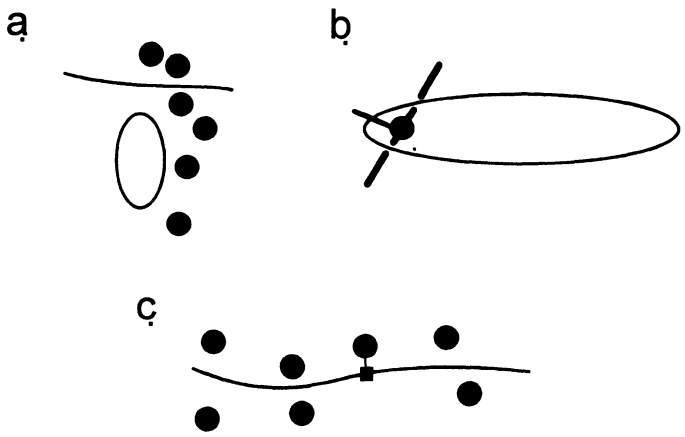

Figure 2. Type of interactions for polymer confined in a gel. a) Steric exclusion of a circular polymer. b) Impalement of circle on dangling gel fibre. c) Affinity between polymer and gel-attached probe.

In addition a circular topology allows for qualitatively new types of polymer-matrix interactions, such as impalement (Fig. 2b). Finally there is the possibility of designing attractive or repulsive interactions between polymer and the pore-wall, as exemplified by a gel modified with a DNA-binding probe used in affinity electrophoresis as is illustrated in Fig. 2c [6].

2.2 Modes of confinement

Because of the omnipresent steric interactions the motion of a polymer in a porous matrix or any other confining geometry will be perturbed compared to the behaviour in free solution. Generally speaking a polymer can be considered to be confined if at least one dimension of the space available to it has an extension which is comparable to or smaller than the radius of gyration R_g of the polymer in the absence of any confinement. The degree of perturbation will depend on the type and degree of confinement. The confinement can be one-dimensional (slit), two-dimensional (pore) or three-dimensional (box or cavity) (Fig. 3a-c). We will also include the situation of a point-like confinement, a slip-ring, through which the polymer is threaded (Fig. 3d).

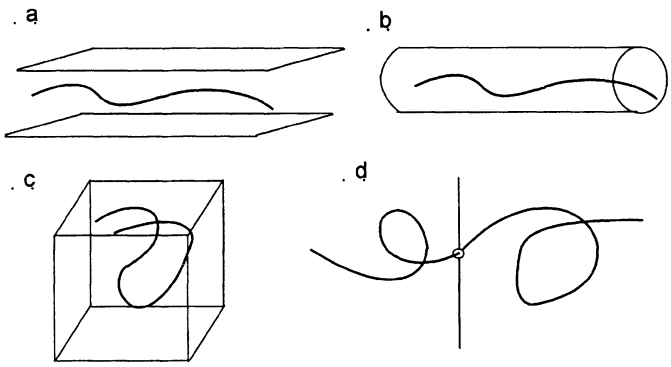

Figure 3. Modes of confinement. a) slit. b) pore. c) cavity. d) slip-link.

In the latter case the confinement is limited to a short piece of the chain (in the ideal slip-link case it is of negligible extension), but it still has interesting and sometimes strong effects on the conformation and dynamics of the rest of the polymer. The slip-link model is often used as a limiting model for the threading of a polymer through a porous membrane. A real membrane L_m will have a finite thickness L_m, but when the polymer contour length L_c is long compared to L_m, the fraction of polymer segments which are actually in

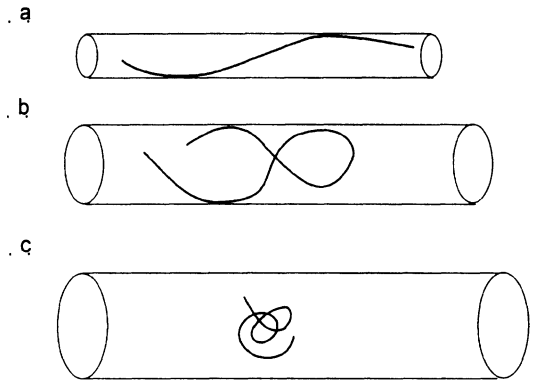

Figure 4. Degrees of confinement in a cylindrical pore

the membrane at any given time is so small that the slip-link model can be considered a good approximation.

For cases where the finite membrane thickness is relevant, such as the opposite limiting case that $L_c << L_m$ (when the pore can be considered to be infinitely long), one can discern several regimes corresponding to different degrees of confinement (Fig. 4).

We will call the confinement intermediate if the pore radius R_p is in the range $P < R_p < R_g$, where P is the persistence length of the chain (Fig. 4b). In this regime the polymer coil will generally be deformed in shape, but the chain is still able to fold inside the channel. The chain is considered to be strongly confined if $R_p < P$, a situation where the polymer stiffness prevents it from doubling over inside the pore (Fig. 4a). This criterion is independent of the polymer length L_c, and the additional relation between P and L_c define different types of strongly confined polymers. The case $L_c << P$ corresponds to a strongly confined rigid rod. However, more relevant to the present discussion is the case $L_c > P$. In this case the polymer is flexible (i.e. has internal degrees of freedom) but the strong confinement means that the pore severely limits its conformational space (Fig. 4a).

When R_p is larger than but comparable to R_g (Fig. 4c), there is still an effect on the motion of the polymer compared to the free solution because the whole pore cross-section is not equally accessible—even if the coil fits inside the pore. In this regime of weak (non-deformed) confinement the polymer can often be modelled as an equivalent sphere.

For a given polymer the mean-square radius of gyration according to the worm-like model can be calculated from P and L_c as [7]

$$\langle R_g^2 \rangle = 2PL_c \left[\frac{1}{6} - \frac{P}{2L_c} + \frac{P^2}{L_c^2} - \frac{P^3}{L_c^3} \left(1 - e^{-L_c/P} \right) \right]. \quad (1)$$

The use of the root-mean-square radius of gyration R_g as the effective polymer size is not undisputed. It is often replaced by the hydrodynamic radius R_h defined as the radius of the rigid sphere that has the same translational diffusion coefficient D as measured for the polymer in free solution [8],

$$R_h = \frac{kT}{6\pi\eta D}, \quad (2)$$

where k is the Boltzmann constant, T the absolute temperature, and η the sample viscosity. We will be using the convenient dimensionless size ratios $\lambda \equiv R_g/R_p$ and $\lambda_h \equiv R_h/R_p$.

3. Experimental systems

3.1 The polymer

Confined polymers have been studied in a wide range of experimental systems. A commonly used synthetic polymer is polystyrene, which has a persistence length of $P = 0.9$ nm in the melt [9] or 1.7 nm in terahydrofuran [10]. The contour length is given by $L_c = 0.0243M$, where M is the molecular weight [10], so typical contour lengths are below 5000 nm [8], corresponding to R_g-values (in THF) up to about 50 nm and R_h values up to 40 nm.

The biopolymer DNA is another very useful model polymer for several reasons. The electrostatic, hydrodynamic and polymer statistical (flexibility) properties of DNA have been characterized in great detail. For double-helical DNA the persistence length varies between 100 and 50 nm for ionic strengths between 1 and 1000 mM [11]. For single-stranded DNA it is sequence-dependent, but when averaged over mixed sequences P is in the range of 3 to 5 nm at 100 mM ionic strength (and 8 M urea) [12]. The polymer is available as truly monodisperse samples in essentially any size-range, from oligonucleotides to chromosomal DNA containing millions of basepairs. The contour length is $L_c = 340$ nm per thousand base pairs (kbp). Commonly used are phage DNA because each phage particle contains exactly one DNA molecule of well-defined size and sequence. Interesting contour lengths are provided by the T7 (39 kbp; $L_c = 13.3$ μm), λ (48 kbp; $L_c = 16.3$ μm) and T2/T4 (166 kbp; $L_c = 56.4$ μm) phages, where the latter has R_g as high as 1 μm. Plasmids are smaller and typically contain 3 - 11 kbp. Also the chemical properties are well established since for any sequenced DNA the

atomic structure is known. DNA can bind ligands such as small ions, dyes, drugs and proteins through groove-binding and/or intercalation between the base pairs [13]. This wide array of reversible interactions can be used to design interactions with the channel walls.

Finally DNA can be long enough so that the global shape of individual molecules can be imaged by fluorescence microscopy, if the DNA is stained with a fluorescent dye. With the usually employed dyes such as the cyanine dye YOYO, the contour length is approximately 50% longer than for native DNA due to the helix-extension by intercalation [14], the charge density (which is very high for DNA anyway) is lower by 15% because the dyes are cationic [15] whereas the persistence length seems to be only little affected [16].

3.2 The channel

3.2.1 Inorganic porous membranes. Track-etched membranes [17] are formed by bombarding polycarbonate membranes with ionic particles such as Kr^{25+} which creates very small holes of a density which depends on the irradiation time. In the next step the holes are etched to cylindrical pores of suitable radius determined by the etching time. The result is a membrane with well-defined thickness (typically 10 μm), porosity (4 to 20%) and of very narrow distribution of pore-sizes. Typical (average) pore radii are in the range 10 nm up to micrometers, and are readily measured by electron microscopy or atomic force microscopy [18, 19]. Mica can be used instead of polycarbonate, but then the holes are rhomboidal in shape [10]. In membrane-based channels the confinement is pore-like (Fig. 3b) or like a slip-link (Fig. 3d) depending on the contour length of the polymer compared to the thickness L_m of the membrane. In a typical track-etched membrane (L_m = 10 μm) confinement of most synthetic polymers such as polystyrene would be pore-like ($L_c < L_m$), whereas the typical phage DNAs (L_c = 15 μm to 60 μm) would be an interesting intermediate case.

3.2.2 Gels. Gels exhibit much stronger heterogeneity than porous membranes do. Agarose [5] is a polysaccharide that forms hydrogen-bonded fibrous gels, which are thermo-reversible. The pore size distribution of agarose gels as determined by atomic force microscopy is wide, but exhibits a well-defined single maximum [20]. The average pore radius is approximately given by

$$R_p = 250\text{nm} \cdot C^{-0.6}, \tag{3}$$

where C is the percentage of the gel.

Polyacrylamide forms by free radical polymerization. Pore sizes as small as a few nm are found in the denser parts of the gel, which form around the nucleation points. However, due to monomer depletion these kernels are surrounded by larger cavities which may approach μm in size [21]. The pore-size distribution is thus bimodal in nature, and it is therefore difficult to ascertain the degree of confinement of a given polymer in a polyacrylamide gel.

The random nature of native gels can be important. The size-separation by sieving of biomolecules during electrophoretic migration in gels relies on there being a distribution of pore sizes. Gel heterogeneity also has other fundamental implications (see review [22]). For example, it can cause a confined polymer to adopt a more compact size. This does not occur in a regular gel [23].

3.2.3 Porous glasses. The channels of controlled porous glasses form a maze which in electron micrographs resembles a porous gel [8]. The pore-size distribution is again wide, and the average pore radii ranges from as small as 7 nm to several hundreds of nm [24]. The pore cross section is irregular in shape, and the pores are neither straight nor much longer than their radii, so in terms of polymer confinement, porous glasses and gels can be considered to be rather similar.

4. Concepts

4.1 The nature of confinement in gels - reptation

The membrane-based channels are easy to identify with the ideal cases outlined in Figures 3 and 4 because the pores in these experimental systems have a well-defined geometry in terms of length and direction. The porous gels and glasses differ from porous membranes in that they have pores in all directions. In these three-dimensional structures one can imagine two types of confinement situations for a polymer, and so one should take into account that there is a distribution of pore-sizes in these systems. For entropic reasons the polymer will seek out larger than average cavities because in those the conformational freedom of the chain is larger. If the radius of gyration is comparable to the (average) pore size the polymer will move between such cavities in the matrix, sometimes passing through restrictions that requires some coil-deformation. This situation corresponds to a three-dimensional confinement in cavities (Fig. 4c) linked by channels. On the other hand, if the radius of gyration is much larger than the average pore size the polymer will split between many cavities, which together with the linking restrictions form a channel in which the polymer is confined in essentially a one-dimensional fashion. This resembles a pore-like confinement (Fig. 4b), but the channel

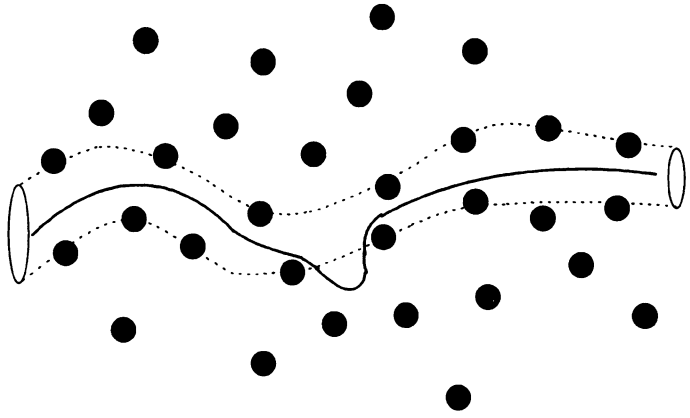

Figure 5. Reptation-tube leakage by loop formation.

is neither straight nor of constant geometry. The shape is in fact defined by the (instantaneous) path of the polymer itself through the three dimensional network. However, if the polymer moves by end-on motion there is little conceptual difference compared to a polymer in a straight channel. In both cases the motion is in effect one-dimensional in the sense that if the polymer slides like an inextensible rope only one co-ordinate is required to describe its motion in both cases, albeit a curvilinear one in the gel case.

A more important difference is that in the gel-case the channel-geometry is not constant, the diameter varies along the channel depending on whether the corresponding part of the polymer is in a cavity or in a restriction. Interestingly, with DNA as the polymer, fluorescence microscopy can be used to visualise both the channels and the polymer path. If the polymer is pulled tight (by say an electric field) the chain will trace the path between the confining gel-fibers thus visualizing the channel topology. If the DNA is allowed to relax locally (by removing the extending force) the chain will fill the channel almost like a liquid, and cavities can be seen as bright spots along the channel [16,25]. The reptation tube can thus be viewed as a confining cylinder of varying radius, or alternatively as a set of larger cavities connected by tighter passages acting essentially as slip-links, the so called lakes-and-straits model [26].

Generally polymers in gels do not move exclusively by reptation. Depending on the height of the confining energy barrier ("the thickness of the tube wall") the polymer can leak out of the tube by forming a loop between gel-fibers (Fig. 5) and thus violate the reptation concept. Both theory [27] and experiments [16] support that the confining energy barrier is determined

by the ratio between the persistence length of the polymer and the interfiber distance (pore size). If the interfiber distance is small compared to P the entropic and/or enthalpic cost for forming a loop is too high, and the polymer has to move end-on. In a gel the effective channel diameter $2R_p$ is equal to the interfiber distance. Since this is also the distance that when compared to P determines the confining barrier, a polymer can in principle be reptating only if it also fulfils the criterion for strong confinement, $R_p < P$. The typical average pore radii of 40 nm to 400 nm in agarose gels are larger than the persistence length of double-stranded DNA. However, reptation has still been unequivocally demonstrated [28], and agarose gels are therefore useful model systems for studying the motion of intermediately confined DNA. The polymer can shrivel up inside the reptation tube but is still confined to a predominantly end-on type of motion.

4.2 Diffusive transport in the weakly confined regime

4.2.1 Theory. In the weakly confined regime the polymer traverses the pore essentially as a spherical coil, and an often used model is that developed by Renkin [29] for a rigid object translocating a cylindrical tube. The ratio of diffusion coefficients in the pore D_p and the bulk D_b is given by

$$\frac{D_p}{D_b} = \phi\frac{f_b}{f_p} = (1-\lambda)^2\left(1 - 2.1\lambda + 22.1\lambda^3 - 0.95\lambda^5\right), \qquad (4)$$

which takes into account: (1) that the solute concentration is lower in the pore than the bulk through the partitioning coefficient ϕ; and (2) the additional drag caused by the viscous interaction with the cylinder walls giving rise to a higher friction coefficient in the pore f_p than in the bulk f_b. Both ϕ and the ratio f_b/f_p depend on the confinement parameter λ, as shown for a spherical particle by the last part of eq (4). This model has been confirmed for rigid solutes such as proteins and latex spheres [30]. It is often used for polymers as well, but then the exact meaning of the "particle" size is not settled. Simulations suggest that R_g is a better descriptor than R_h [31].

A model specifically designed for polymers is the scaling theory of Daoud and deGennes, which again by combining partitioning [32] and enhanced drag [33] effects results in [29]

$$\frac{D_p}{D_b} = \alpha(k\lambda)^{-2/3}e^{-(k\lambda)^{5/3}}, \qquad (5)$$

where α and k are proportionality constants which are not quantified by the scaling theory. Harding and Doi [34] have confirmed the scaling-law predictions in a full hydrodynamic treatment and also calculate the prefactors under certain conditions. The scaling model is derived under the condition

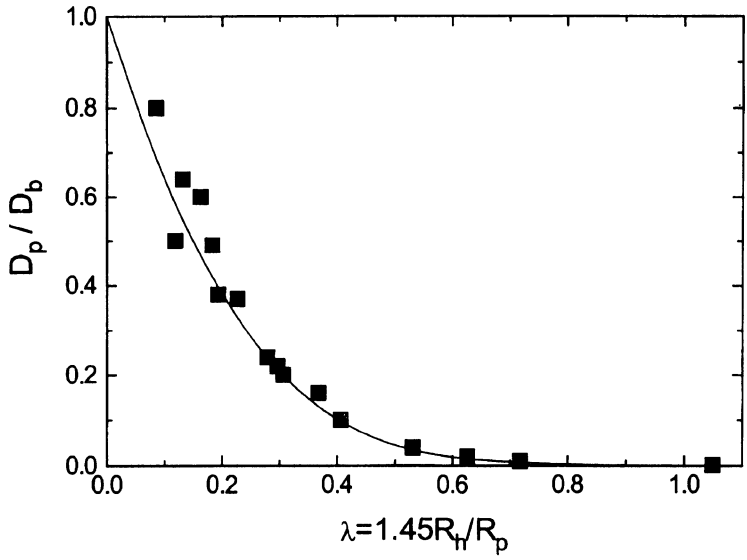

Figure 6. Retardation of weakly confined polystyrene in track-etched polycarbonate membrane. Data from [29]. Curve is calculated from eq. 4.

that the chain has to elongate as it enters the pore. Therefore it applies strictly only for the case of intermediate confinement, but sometimes applies also in the weakly confined case.

4.2.2 Track-etched membranes. Early studies in track-etched membranes [29] showed that in the weakly confined regime ($\lambda_h < 1$) the rate of diffusive transport of polystyrene through the pores decreases in good agreement with the Renkin equation (4) as the polymer size R_h approaches the pore radius ($\lambda_h \rightarrow 1$). Their results show that the behaviour of different polymer and membrane pairs can be described by a universal curve (Fig. 6) if plotted using the dimensionless λ_h parameter, but in their case only by defining $\lambda_h = 1.45R_h/R_p$, i.e. the effective polymer size is taken to be kR_h, where k is in effect used as a fitting parameter.

The value of k being larger than 1 suggests that a polymer diffuses more slowly than a rigid sphere of the same hydrodynamic radius. This interpretation seems to be supported by a study [10], which directly compares a rigid and a flexible solute and their permeation through the same porous mica membranes (again in the weakly confined range $\lambda_h < 1$). The results show that a rigid porphyrine molecule obeys the equation for a rigid sphere whereas polystyrene is more strongly retarded for the same λ-value in the range 0-0.5. However, when polymers of different degrees of flexibility are compared in

the same porous membrane, another picture emerges. Bohrer and colleagues [35] find good agreement with eq. (4) (with $k = 1$) for a cross-linked polymer ficoll, which can be expected to act as a comparatively rigid object, whereas the highly flexible dextran diffuses more rapidly through the membrane for a given ratio of polymer-to-pore size ratio. The authors conclude that the possibility of the polymer to change its configuration is an important factor for rapid pore-translocation. Canell and Rondelez [29] also compared with the theory of Daoud-deGennes and found that eq. (5) describes their data well, but it should be remembered that in this case there is an additional fitting parameter α. Guillot [36] demonstrated that the limiting factor in the accuracy of measuring the diffusion rate in the membrane pores is the boundary layer of gradients in solute concentration outside the pore entrance. This effect can be avoided by direct measurements of polymer motion in-situ in the pores by dynamic light scattering. This approach is difficult in the porous membranes because of their own turbidity and short optical paths but have been successfully applied in porous glasses.

4.2.3 Porous glasses. Porous glasses offer an interesting system where light scattering can be performed if the solvent is indexed-matched to the glass-material [37], and this experimental technique has recently been reviewed [4]. Dynamic light scattering is particularly suitable for studying polymer diffusion in porous media because by changing the wavelength and/or scattering angle (q-vector) it is possible to probe polymer motion on different length scales. In their first application of dynamic light scattering Karasz and co-workers studied polystyrene diffusion in porous glasses [8] and demonstrated the existence of two diffusion regimes for weakly confined chains ($\lambda < 0.5$). One was considerably slower than in bulk and ascribed to diffusion over distances large compared to the pore size. This component exhibits the same decreasing dependence on an increase of λ (still below 1) as has been measured by macroscopic approaches (Fig. 6). This shows that the two techniques monitor the same process, and that the (long-range) diffusion of weakly confined chains in porous glasses is well described by modelling them as equivalent spheres with a radius close to R_{h}. A second faster diffusion mode most likely corresponds to short-range motion within one pore since the transition between the two modes occurs for a q-value (probing distance) corresponding to the pore radius R_{p}. As expected the corresponding effective diffusion coefficient increases as the q-vector value increases. The polymer (segmental) diffusion is faster the shorter the probed distance is since confinement plays less and less role then. This second effective diffusion coefficient always remains lower than the bulk-value (measured with the same q-value). The glass thus slows down diffusion at all the probed length-scales, which typically can be as small as about $R_{\mathrm{p}}/6$. As an example, under conditions ($\lambda = 0.25$)

where the macroscopic diffusion is retarded by 40%, the diffusion coefficient at this shortest length scale is about 90% of that of a free polymer measured at the same q-value.

In an extended study of the macroscopic polymer diffusion process, λ-values between 0 and 1.4 were covered [38]. Three regimes were identified based on the dependence of the macroscopic diffusion coefficient on molecular weight. For $\lambda < 0.3$ the equivalent-sphere model (eq. 4) was appropriate, while for $0.2 < \lambda < 0.5$ the polymer behaves as a Rouse chain. This free-draining behavior is ascribed to screening of hydrodynamic interactions between chain segments by the pore-walls. As λ approaches and exceeds 1 the macroscopic diffusion coefficient exhibits a stronger molecular weight dependence than the $1/L_c$ expected for a Rouse-chain [33] in an infinitely long pore. The third regime is consistent with entropic-trapping predictions, but reptation was also proposed as a possibility. Both explanations seem possible in view of the fact that SEM pictures show that the pores are not much longer than their width, i.e. that the matrix is highly connected. A long enough polymer can form a randomly-oriented three-dimensional path through the matrix and thus exhibit the stronger L_c^{-2} dependence that follows from reptation [1]. Alternatively the connection-points between the pores provide cavities connected by more restricted passages (the pores), an environment heterogeneous enough to be potentially capable of entropic trapping [23].

Stapf and Kimmich [39] used NMR-spectroscopy to investigate the possibility of polymer reptation in porous glass by exploiting one of the original predictions of the reptation theory [40], namely for the spin-lattice relaxation time T_1 of a confined polymer. For a $L_c = 450$ nm long poly(dimethylsiloxane) the predicted $T_1 \sim \nu^{0.75}$ scaling with the NMR-frequency ν was observed in 2 nm porous glass ($\lambda = 3.0$). In agreement with this interpretation the scaling was considerably weaker (0.25 to 0.5 instead of 0.75) for shorter polymers or in wider pores, and in non-crosslinked polymer solutions where the chain undergoes Rouse dynamics. The evaluation requires non-trivial corrections for adsorption-effects, however, so the support for reptation must be considered indirect.

Only quite recently has *static* light scattering been performed in order to measure the structure of a confined polymer chain. Scattering for small q-values show that the radius-of-gyration of polystyrene of a given polymer molecular weight is smaller in the glass than in the bulk [41].

4.2.4 Gels. In gels, weakly confined polymers correspond to what is called the Ogston regime [5]. This is an important case from an application point of view because DNA and proteins in this regime can be separated by electrophoretic filtration (sieving).

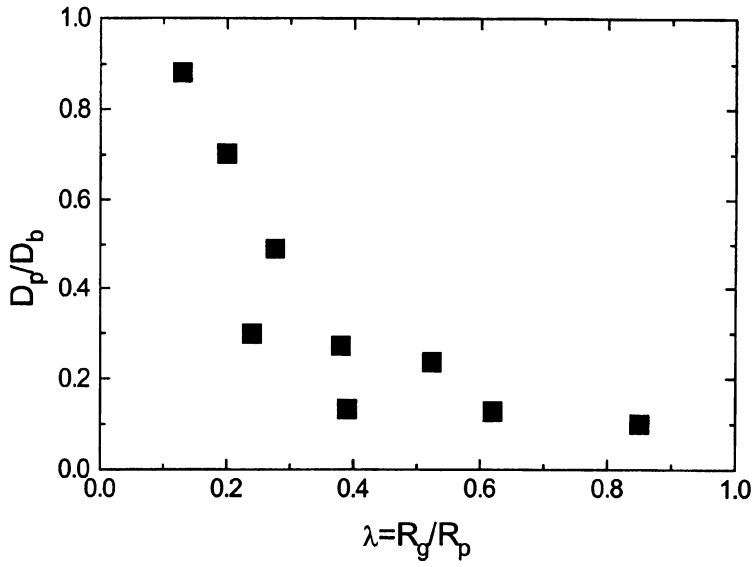

Figure 7. Retardation of rotational diffusion of weakly confined double-stranded DNA in agarose gels. Data from [43].

Gosnell and Zimm [42] measured the translational diffusion coefficient D of weakly confined DNA in 0.5% agarose gels for which $R_p = 380$ nm according to eq. (3). The reduction in diffusion rate compared to free solution agrees with eq. (4), and the L_c^1 scaling of D deviates significantly from the reptation prediction [1] L_c^{-2} as expected since the chains are only weakly confined. Only three DNA sizes were studied however, so the number of polymer/pore-size combinations is too limited to confirm universal behavior in terms of the confinment parameter λ, as in Fig. 6.

A larger set of experimental conditions were studied by Stellwagen [43] who in an instructive demonstration used an electric field to monitor Brownian *rotational* motion of weakly confined DNA in agarose gels. An electric field is used to align monodisperse samples of DNA, and the field-free relaxation back to an isotropic state of the DNA is then monitored by measuring the linear dichroism (or rather birefringence) decay after the field is removed. The relaxation is considerably slower than for the same DNA outside the gel, suggesting a strong confining effect on DNA motion. She studied DNA of sizes 622 to 2936 base pairs in 0.5% to 1.5% agarose gels, a range which corresponds to the $\lambda = R_g/R_p$ range 0.13 to 0.85, where R_p is based on the pore sizes measured with AFM by Tinland and coworkers [20]. The decay is mono-exponential, and Figure 7 shows the ratio of the relaxation rates in gel and in free solution vs λ for the DNA-gel combinations investigated.

The data points fall essentially on a common curve which approaches 0 as λ approaches 1. This shows that the hindering of the rotational motion is very similar to that of the translational diffusion of weakly confined polymers in track-etched membranes and porous glasses (Fig. 6).

Together the two studies show that DNA molecules, which according to the R_g-criterion are weakly confined in agarose, behave as expected when compared to other polymer/matrix combinations.

4.3 Diffusive motion of intermediately and strongly confined polymers

Almost all studies in porous glass have been on weakly confined chains. This is probably because the longer chains that are required to reach the intermediately confined regime usually enter to such low a degree that measurements become difficult. In addition the penetration time can be as long as months [41] for polymers with $\lambda \geq 1$. Secondly the typical pore-size of a few nanometers in porous glasses is not narrow enough to strongly confine the synthetic polymer polystyrene ($P = 0.9$ nm) typically used in these systems. Double-stranded DNA ($P = 50$ nm) would indeed be strongly confined in this system, but to our knowledge no such studies exist.

In contrast, gels have been used extensively to study intermediately and strongly confined polymers, especially DNA. The difference in focus compared to porous glasses perhaps stems from the strong tradition of using electric fields in electrophoretic applications of gels. In confinement studies electric fields drive the polymer into the gel under conditions where diffusive entering would be very slow and only to a low degree. In diffusive motion studies, electric fields perturb the polymer from equilibrium, and then the Brownian motion is monitored during the field-free relaxation back to equilibrium as described for weakly confined DNA above.

4.3.1 Intermediate confinement. The Brownian motion of intermediately confined double-stranded DNA was studied in agarose gels using phage DNA, such as T4, which has R_g about 1000 nm at 50 mM ionic strength compared to an average pore radius of 250 nm in a 1% gel, i.e. $\lambda = 4$. As measured by FRAP in 0.7 and 2% agarose gels, translational motion of 6 different intermediately confined DNA (10 kbp - 164 kbp) is 7 to 500 times slower compared to that in free solution [42]. The observed effect of DNA size is in agreement with the L_c^{-2}-prediction of reptation [1], except for the longest DNA in the denser gel (2%), suggesting that entropic-trapping effects may become important in this case.

The relaxation by Brownian motion of such long DNA chains after field-perturbation is complex. Even a field as low as a few V/cm strongly perturbs

the coil from its equilibrium shape, and forces the molecules to adapt to the gel by converting into extended and field-aligned conformations. As the field is turned off the molecule returns to the equilibrium isotropic coil by two processes (see review [3]). Most rapid is a relaxation of the stretching by a translational retraction of the extended chain along its path in the gel, like a rubber band snapping back inside a tube. This is what happens during the fast step. Then, by a much slower process, the chain reptates out of the original field-aligned tube and adopts an isotropic coil-conformation. The latter process is monoexponential in nature and exhibits a field-independent relaxation time constant which scales [28,42] as L_c^3 as expected for reptation. The faster de-stretching process exhibits a much more complicated multi-exponential time-dependence which is still not fully understood, but most likely involves transfer of DNA segments from smaller to larger cavities along the path of the chain. Taken together the two processes well illustrate the state of DNA-confinement in agarose. The intermediate degree of confinement means the pore-size is big enough compared to the DNA stiffness to allow the chain to relax locally by shrivelling up inside the pores. Still the gel fibers are close enough to prevent the chain from randomizing its conformation by loop-formation between gel fibers [16], and it instead has to rely on an end-on type of diffusive motion to return to the equilibrium coil.

4.3.2 Strong confinement. There are only a few studies of the dynamics of strongly confined chains ($P > R_p$). Polyacrylamide gels contain regions where pore sizes are smaller than the persistence length of double-stranded DNA. Wijmenga and Maxwell [44] have used the electric-field perturbation method to study rotational diffusion of monodisperse DNA in size range of 55 to 256 basepairs (L_c = 19 nm to 87 nm) in 4 and 10% polyacrylamide gels with estimated pore radii R_p of 1.5 and 3.2 nm respectively. The field-free relaxation was considerably slower than for the same DNA outside the gel, suggesting a strong confining effect on DNA motion. The measured effect of DNA size on the relaxation time constant was in good agreement with the L_c^2-scaling predicted by Odijk in a theory for a long ($L > P$) wormlike chain which is strongly confined ($P > R_p$) in a cylinder of radius R_p [45]. There was a clear deviation from the reptation prediction (L_c^3 scaling) and from a Doi-Edwards theory for rigid-rod relaxation which predicts a L_c^5 dependence in the relaxation time constant, as expected if the inferred strong confinement is correct. By contrast, Pajevic and coworkers [46] have used light scattering to show that poly(styrene-sulphonate) most likely reptates in a 11% polyacrylamide gel, because the diffusion coefficient scales as L_c^2 in agreement with the reptation prediction (they did not measure the alignment relaxation time-constant). This observation is consistent with the fact that poly(styrenesulphonate) has a persistence length of P = 4.8 nm at the used

ionic strength of 0.1 M [47]. This is much closer to the pore size (4.1 nm) than is the case for DNA which has P =50 nm, and polystyrene is thus close to be only intermediately confined. Double-stranded DNA cannot be studied in a strongly confined state in normal agarose gels because pore sizes below the typical persistence length of 50 nm are difficult to achieve without having such high gel concentrations that the turbidity tends to preclude spectroscopic studies. The lack of strong confinement is also supported by the fast segmental motion of significant amplitude that occurs both in the millisecond [48] and in the micosecond [49] time ranges. In 2% hydroxyethylated agarose the average pore size is about $R_{\mathrm{p}} = 38$ nm [50], as evaluated through application of the Ogston model, and this would indicate a case on the border between intermediate and strong confinement. Field-free de-stretching of T2-DNA ($L_{\mathrm{c}} = 56$mm) is indeed somewhat slower than in 1% gel ($R_{\mathrm{p}} = 90$nm by the same method), but there is no qualitative difference in the behaviour in the two gels. In fact the reptation time constants were indistinguishable, and the lack of distinguishing relaxation behaviour may be due to that the Ogston model seems to underestimate the average pore size. The more direct (model-independent) AFM measurements [20] indicate about 4 times larger pore sizes in native agarose gels than those derived by the Ogston method. If this is true also for hydroxyethylated gels double-stranded DNA is only intermediately or weakly confined in this gel too, as is the case in non-modified agarose.

4.4 Electrophoretic transport in gels, membranes and porous glasses

Electrophoretic transport of DNA in agarose gels (Fig. 8) clearly reflects the transition from weakly to intermediately confined polymers.

The velocity of a weakly confined chain ($R_{\mathrm{g}} < R_{\mathrm{p}}$ and $L_{\mathrm{c}} < 20$ kbp) depends on molecular weight due to a sieving effect of the gel, often referred to as Ogston migration. The smaller the DNA coil the easier to find a connected path of cavities that are big enough to allow its passage. Intermediately confined DNA ($R_{\mathrm{g}} < R_{\mathrm{p}}$ and $L_{\mathrm{c}} > 50$ kbp), on the other hand, migrates with a velocity that is independent of size because it moves essentially end-on. In simple terms, an extended reptating chain (as opposed to a coiled chain) has a friction coefficient that is proportional to L_{c}. Since this is also true for the total charge Q, the steady state velocity $v = Q/f$ will be independent of L_{c}. A more detailed picture of the different regimes is given by analysis of the field-induced deformation of the DNA coils during migration, as monitored by linear dichroism or birefrigence [28, 42, 52]. The coils of weakly confined DNA are essentially unperturbed. The intermediately confined chains are strongly perturbed and exhibit a characteristic cyclic migration between extended conformations when the coil is hooked around a gel fibre. They

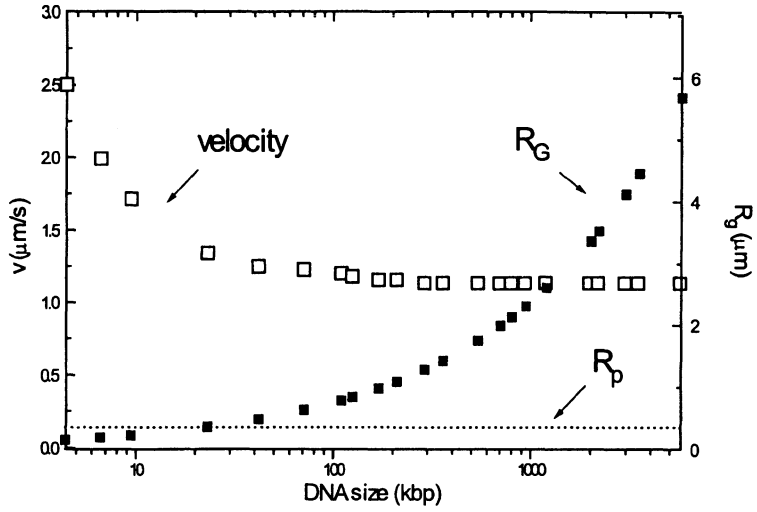

Figure 8. Electrophoretic velocity (v) of double-stranded DNA in 0.8% agarose gel. Radius-of-gyration calculated by eq. 1 using P=50 nm. DNA size is given in kilo base pairs. Data from [51] and B. Akerman (unpublished results).

exhibit compact states that result as the chain slides off the hooking point and contracts due to entropic tension in the chain [53]. The transition between the two regimes occurs around $R_g = R_p$ and is characterised by the coils being deformed without exhibiting cyclic migration [52]. The coils are large enough to be occasionally squeezed through narrow passages between cavities, but not large enough to have to split between several cavities, which is the requirement for hooking.

Intermediately confined DNA in agarose has also been used to mimic the initial phases of the threading of a polymer through several pores in a membrane [54]. The DNA is arranged in a extended but locally relaxed state and then a field is applied perpendicular to the direction of extension. Initially many loops form through different parallel pores, but soon the loops start to compete and finally the chain is threaded in a sliding fashion through one of the pores. A theory by Long and Viovy [27] explains the loop-formation and competition well, and the experimental gel-system was used to demonstrate that the principles of a threading-based separation scheme proposed by the same authors [55] could be realised in agarose. A real device could perhaps be based on gel-filled nylon membranes [56].

To our knowledge no experiment has been performed on the interesting possibility of electrophoretic translocation of a polymer through a track-etched membrane. O'Connor and colleagues [57] have shown that the electrophoretic mass-flux of proteins through a track-etched membrane is the same as the

flux in the absence of a membrane because the enhanced field strength in the pores compensates for the reduced area available for transport through the membrane. The effect of an enhanced field in the pores becomes particularly significant in the case of a single pore, where the whole voltage drop between the electrodes in the two bulk solutions occurs essentially solely over the membrane. Electro-osmosis is often significant in track-etched membranes, because the pore walls are charged. This has been elegantly exploited for analysing rigid particles by electrophoretic transport through membranes with a single pore [58] but so far it has not been applied to polymers. The possibility of imaging and measuring the electro-osmotic flow out of a single membrane pore with a scanning electrochemical microscope [59] may prove valuable for a better understanding of this phenomenon.

4.5 Polymer topology and channel affinity

The effect of circular topology on the behaviour of confined polymers has been investigated by using plasmid DNA in polyacrylamide and agarose gels [60,61]. In agarose both the linear and circular form of the 11 kbp plasmid are only weakly confined, but still their behaviour is quite different. Circular DNA is impaled on protruding gel-fibers (Fig. 2b), a form of interaction which is not available to the linear form. During electrophoresis in strong fields ($>$ 15 V/cm) impaling is detected as a full arrest of the circles and as a strong field alignment because the electric force pulls on the anchored circles. By contrast the linear form migrates essentially nondeformed because it is only weakly confined, as discussed in connection with Figure 8. Also in polyacrylamide gels there is circle-specific impaling and aligning at high fields of a occurs. Figure 9 compares the kinetics of electrophoretic alignment (measured by linear dichroism) of a 5.4 kbp plasmid DNA ($L_c = 1800$ nm and $R_g = 120$ nm) in circular and linear form in a 5% gel, by presenting the degree of orientation S, where $S = 1$ corresponds to perfect field-alignment and $S = 0$ to an isotropic coil. Again the circles are more strongly aligned because of anchoring but orient slowly (minutes) because they have to find gelfibers to impale. The linear form becomes field-aligned much faster (about 30 ms) by cyclic reptation, as reflected by a weak oscillation in S in the early stage of the process shown in the right hand part of Figure 9. The circles also become field-aligned ($S > 0$) by migration on this fast timescale, but to a small degree ($S = 0.008$) compared to the final alignment ($S = 0.031$), which results from anchoring by impalement. The lack of oscillation suggests the circle only becomes compressed without cyclic migration.

At low fields, however, the circles align preferentially perpendicular to the field whereas the linear form is still field-aligned [61]. This surprising effect has been ascribed to flattening of the circles against down-field bottoms of

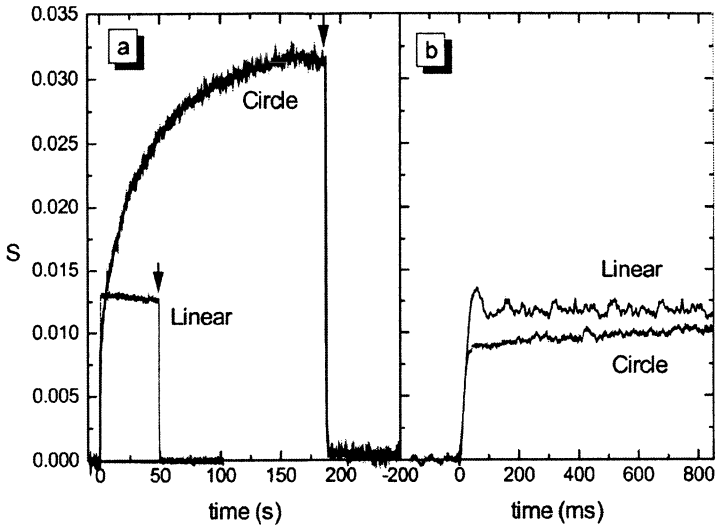

Figure 9. (a) Electrophoretic alignment response S(t) of circular and linear DNA in polyacrylamide gel to a constant field (22.5 V/cm) applied at t = 0 and turned off at the time denoted by the arrow. S = +1 corresponds to perfect parallel alignment, and non-oriented DNA has S = 0. (b) Expansion of initial phase. Data from [60].

"lobster-trap" types of restrictions in the denser parts of the gel, where the average pore size is much smaller the persistence length of the DNA. The circles cannot penetrate such constrictions (c.f. Fig. 2a) because they have to double over, whereas the linear counterpart can reptate between gel-fibers since the pore size is larger than the helix diameter (2 nm).

Bohrer and coworkers [62] compared the diffusion of starshaped and linear poly(isopropene) of various molecular weights in track-etched membranes. When the linear and the 8, 12 or 18 arm stars are all in the weakly confined regime ($\lambda_h < 1$), the branched polymers have very similar diffusivities, but they all diffuse considerably slower than the linear form with the same R_h. The linear polymer satisfies the Renkin equation as was the case for linear polystyrene, but the authors could not determine if the deviating behaviour for the stars stemmed from the partition- or friction-part of eq (4). Direct light-scattering measurements of the diffusion coefficient of weakly confined linear and star-shaped poly(isopropene) in porous glass [63] showed a similar lower diffusivity of the star-shaped forms, indicating that the slower star diffusion is related to the friction factor. Importantly, since the chemistry of the chain is independent of its topology it seems unlikely the difference is related to differences in the interaction with the pore walls.

The importance of designed interaction between the pore wall and the confined polymer has been studied only in a few cases. In an interesting study

Kluijtmans and coworkers [64] used FRAP to study the diffusion of charged silica spheres in (negatively charged) porous glass. Several observations regarding the effect of the repulsive interaction on the motion of this rigid solute are likely to be general enough to apply also to polymers. The ratio of diffusion coefficients in the glass and the bulk fulfils a Renkin-type of behavior (eq. 4, Fig. 7.) if in the size-parameter λ the effective particle-radius is taken to be the sum of the geometric radius and the Debye screening length, i.e. the repulsive interaction can be modeled as an increase in particle size equal to the double-layer thickness. Secondly, at high salt the particles diffuse faster than neutral particles, probably because the repulsive interactions tend to push the particles towards the centre of the pore where the added drag from the wall is minimal.

Attractive polymer-pore interactions have been studied for intermediately confined DNA in agarose gels covalently modified with the DNA-binding intercalator-dye ethidium bromide [6]. The dye is capable of binding to DNA also after immobilisation to the gel, as suggested by a decrease in electrophoretic mobility (compared to the unmodified gel) as the density of attached affinity-label is increased (Fig. 10, left). In a control experiment the same type of gel was covalently modified with fluorescein to a similar extent (Fig. 10, right). In this case the DNA was not retarded, as expected since fluorescein is negatively charged and will repel DNA electrostatically.

Again, several observations [6], made using linear dichroism spectroscopy, are likely to be generally valid for polymers confined in attracting channels. The retarding effect of the affinity on the migration of T4 DNA can be decreased by increasing the field strength, to the extent that the behaviour is essentially indistinguishable from that in the unmodified control gel at 30 V/cm. The simplest explanation is that the strong force field overcomes the affinity forces, in qualitative agreement with simulations of polymer reptation in affinity-gels [65]. Second, the affinity points act as reversible anchors against which the polymer is extended by the field considerably more than in the control gel. The effect resembles the enhanced field alignment observed for permanently anchored DNA [66], with the important difference that with the reversible ethidium-affinity the enhancment effect again disappears at high fields because the anchoring yields. Finally, fast changes in the polymer conformation, such as field-free destretching, which occur on time scales comparable to the dissociation time for the affinity label are strongly retarded. On the contrary, processes which are much slower, such as reptation, are not affected because the anchoring points are released many times on the time scale of polymer motion. Similar retardation of fast polymer motions by adsorption effects has been observed by dielectric relaxation spectroscopy on poly(propylene glycol) in porous glass [67].

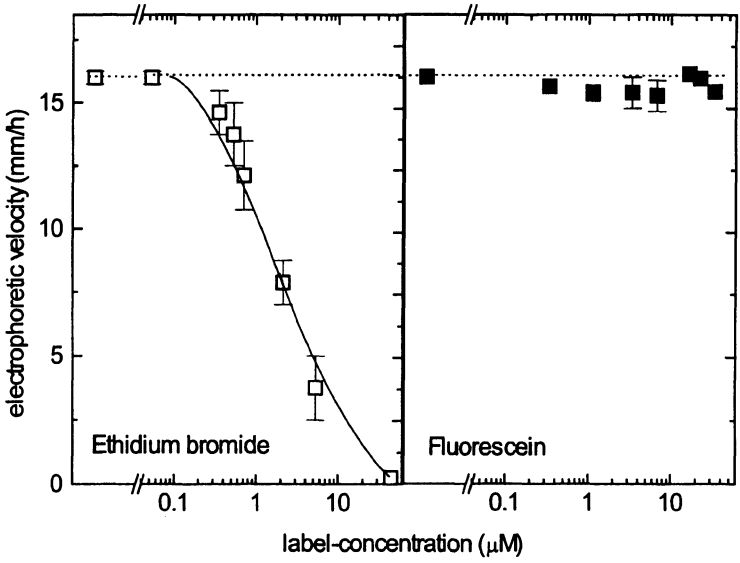

Figure 10. Electrophoretic mobility of DNA in affinity-modified 1% agarose gel. Ethidium bromide is cationic and binds to DNA by intercalating between the basepairs. Fluorescein is anionic and is electrostatically repelled from DNA. In both cases the leftmost point corresponds to unmodified gel. Data from [9] and B. Akerman (unpublished).

References

[1] deGennes, P.G. (1979) *Scaling Concepts in Polymer Physics*, Cornell University Press.

[2] Howard, T.D. and Holzwarth, G. (1992) Fluctuations in the Velocity of Individual DNA Molecules during Agarose Gel Electrophoresis. *Biophys. J.* **63**, 1487-1492.

[3] Akerman, B. (1996) Cyclic Migration of DNA in Gels: DNA Stretching and Electrophoretic Mobility. *Electrophoresis* **17**, 1027-1036.

[4] Teraoka, I. (1994) Polymer Solutions in Confining Geometries. *Prog. Polym. Sci.* **2**, 89-149.

[5] Viovy, J.L. and Lesec, J. (1994) Separation of Macromolecules in Gels: Permeation Chromatography and Electrophoresis. *Adv. Polymer. Sci.* **114**, 2-41.

[6] Akerman, B. (1999) Affinity Gel Electrophoresis of DNA. *J. Am. Chem. Soc.* **121**, 7292-7301.

[7] Bloomfield, V.A., Crothers, D.M. and Tinoco, I. (1974) *The Physical Chemistry of Nucleic Acids*, Harper and Row, p.161.

[8] Bishop, M.T., Langley, K.H. and Karasz, F.E. (1989) Dynamic Light-Scattering Studies of Polymer Diffusion in Porous Materials: Linear Polystyrene in Porous Glass. *Macromolecules* **22**, 1220-1231.

[9] Brulet, A., Boue, F. and Cotton, J.P. (1996) About the Experimental Determination of the Persistence Length of Wormlike Chains of Polystyrene. *J. Phys. II France* **6**, 885-891.

[10] Kathawalla, I.A., Anderson, J.L. and Lindsey, J.S. (1989) Hindered Diffusion of Porphyrins and Short-chain Polystyrene in Small Pores. *Macromolecules* **22**, 1215-1219.

[11] Baumann, C.G., Smith, S.B., Bloomfield, V.A. and Bustamante, C. (1997) Ionic effects on the Elasticity of Single DNA Molecules. *Proc. Natl. Acad. Sci. (USA)* **94**, 6185-6190.

[12] Tinland, B., Pluen, A., Sturm, J. and Weill, G. (1997) Persistence Length of Single-stranded DNA. *Macromolecules* **30**, 5763-5765.

[13] Blackburn, G.M. and Gait, M.J. (Eds). (1990) *Nucleic Acids in Chemistry and Biology*, IRL Press.

[14] Butour, J.L., Delain, E., Coulaud, D., LePecq, J.B., Barbet, J. and Roques, B.P. (1978) Electron Microscopy Studies of the Extension of the DNA Helix by Intercalating Dyes. *Biopolymers* **17**, 873-886.

[15] Carlsson, C., Larsson, A. and Jonsson, M. (1996) Influence of Optical Probing with YOYO on the Electrophoretic Behaviour of the DNA Molecule. *Electrophoresis* **17**, 642-651.

[16] Akerman, B. (1996b) Barriers Against DNA-loop Formation in a Porous Matrix. *Phys. Rev. E.* **54**, 6685-6696.

[17] Guillot, G., Leger, L. and Rondelez, F. (1985) Diffusion of Large Flexible Polymer Chains through Model Porous Membranes. *Macromolecules* **18**, 2531-2537.

[18] Iwata, H., Hirata, I. and Ikada, Y. (1997) Atomic Force Microscopic Images of Solvated Polymer Brushes. *Langmuir* **13**, 3063-3066.

[19] Hernandez, A., Calvo, J.I., Pradanos, P. and Tejerina, F. (1998) Pore Size Distributions of Track-etched Membranes. *Colloids and Surfaces A* **138**, 391-401.

[20] Maaloum, M., Pernodet, N. and Tinland, B. (1998) Agarose Gel Structure Using Atomic Force Microscopy: Gel Concentration and Ionic Strength Effects. *Electrophoresis* **19**, 1606-1610.

[21] Hsu, T.P. and Cohen, C. (1984) Observations on the Structure of a Polyacrylamide Gel from Electron Microscopy. *Polymer* **25**, 1419-1423.

[22] Baumg?rtner, A. and Muthukumar, M. (1996) Polymers in Disordered Media. *Adv. Chem. Phys.* **96**, 625-708.

[23] Briber, R.M., Liu, X.L. and Bauer, B.J. (1995) The Collapse of Free Polymer Chains in a Network. *Science* **268**, 395.

[24] Guo, Y., Langley, K.H. and Karasz, F.E. (1990) Hindered Diffusion of Polystyrene in Controlled Pore Glasses. *Macromolecules* **23**, 2022-2027.

[25] Kantor, R.M., Xuo, X.H., Huff, E.J. and Schwartz, D.C. (1999) Dynamics of DNA Molecules in Gel Studied by Fluorescence Microscopy. *Biophys. Biochem. Res. Commun.* **258**, 102-108.

[26] Zimm, B. (1991) Lakes-straits Model of Field-inversion Gel Electrophoresis of DNA. *J. Chem. Phys.* **94**, 2187-2206; *J. Chem. Phys.* **95**, 3026.

[27] Long, D. and Viovy, J.L. (1996) Theory of Gel Electrophoresis in High Fields: Transient regimes at the field onset. *Phys Rev. E* **53**, 803-811.

[28] Mayer, P., Sturm, J., and Weill, G. (1993) Stretching and Overstretching of DNA in Pulsed Field Gel Electrophoresis. *Biopolymers* **33**, 1347-1357; Pernodet, N., Tinland, B., Sturm, J. and Weill, G. (1999) Brownian Diffusion and Electrophoretic Transport of Double-stranded DNA in Agarose Gels. *Biopolymers* **50**, 45-59.

[29] Cannell, D.S. and Rondelez, F (1980) Diffusion of Polystyrenes through Microporous Membranes. *Macromolecules* **13**, 1599-1602.

[30] Deen. W.H. (1987) Hindered Transport of Large Molecules in Liquid-filled Pores. *AIChE J.* **33**, 1409-1425.

[31] Boyd, R.H., Chance, R.R. and Verstrate, G. (1996) Effective Dimensions of Oligomers in Size Exclusion Chromatography. A Molecular Dynamics Simulation Study. *Macromolecules* **29**, 1182-1190.

[32] Daoud, M. and deGennes, P.G. (1977) Dynamics of Confined Polymer Chains. *J. Phys. (Paris)* **38**, 85.

[33] Brochard, F. and deGennes, P.G. (1977) Dynamics of Confined Polymer Chains. *J. Chem. Phys.* **67**, 52.

[34] Harden, J.L. and Doi, M. (1992) Diffusion of Macromolecules in Narrow Capillaries. *J. Phys. Chem.* **96**, 4046-4052.

[35] Bohrer, M.P., Patterson, G.D. and Carroll, P.J. (1984) Hindered Diffusion of Dextran anf Ficoll in Microporous Membranes. *Macromolecules* **17**, 1170-1173.

[36] Guillot, G. (1987) Diffusion of Polystyrene Solutions through Model Membranes. Diffusion Kinetics of Monodisperse Solutions. *Macromolecules* **20**, 2600-2606.

[37] Bishop, M.T., Langley, K.H. and Karasz, F.E. (1986) Dynamic Light Scattering-studies of Polymer Diffusion in Porous Materials. *Phys. Rev. Lett.* **57**, 1741.

[38] Guo, Y.G., Langley, K.H. and Karasz, F.E. (1990) Hindered Diffusion of Polystryrene in Controlled Pore Glasses. *Macromolecules* **23**, 2022-2027.

[39] Stapf, S. and Kimmich, R. (1996) Field-cycling NMR Relaxometry and Field-Gradient NMR Diffusometry of Polymers Confined in Porous Glasses. *Macromolecules* **29**, 1638-1641.

[40] deGennes, P.G. (1971) Reptation of a Polymer Chain in the Presence of Fixed Obstacles. *J. Chem. Phys.* **55**, 572-579.

[41] Lal, J., Sinha, S.K. and Auvray, L. (1997) Structure of Polymer Chains Confined in Vycor. *J. Phys II France* 7, 1597-1615.

[42] Gosnell, D.L. and Zimm, B.H. (1993) Measurements of Diffusion Coefficients of DNA in Agarose Gels. *Macromolecules* **26**, 1304-1308.

[43] Stellwagen, N. (1985) Orientation of DNA Molecules in Agarose Gels by Pulsed Electric Fields. *J. Biomol. Struct. Dyn.* **3**, 299-314.

[44] Wijmenga, S. and Maxwell, A. (1986) Rotational Diffusion of Short DNA Fragments in Polyacrylamide Gels: An Electric Birefringence Study. *Biopolym.* **25**, 2173-2186.

[45] Odijk, T. (1983) On the Statistics and Dynamics of Confined or Entangled Stiff Polymers. Macromolecules 16, 1340-1344; (1984) Similarity Applied to the Statistics of Confined Stiff Polymers. *Macromolecules* **17**, 502-503.

[46] Pajevic, S., Bansil, R. and Konak, C. (1995) Dynamic Light Scattering Study of Linear Polyelectrolyte Diffusion in Gels. *Macromolecules* **28**, 7536-7542.

[47] Spiteri, M.N., Boue, F., Lapp, A. and Cotton, J.P. (1996) Persistence Length for a PSSNa Polyion in Semidilute Solution as a Function of the Ionic Strength. *Phys. Rev. Lett.* **77**, 5218-5220.

[48] Akerman, B. and Jonsson, M. (1990) Reorientational Dynamics and Mobility of DNA during Pulsed-Field Agarose Gel Electrophoresis. *J. Phys. Chem.* **94**, 3828-3838.

[49] Scalettar, B.A., Selvin, P.R., Axelrod, D., Klein, M.P. and Hearst, J.E. (1990) A Polarized Photobleaching Study of DNA Reorientation in Agarose Gels. *Biochem.* **29**, 4790-4798.

[50] Akerman, B. (1996) Tube Leakage During Electrophoresis Retards Reptating DNA in Unmodified and Hydroxyethylated Agarose Gels. *Phys. Rev. E.* **54**, 6697-6707.

[51] Noolandi, J. and Turmel, C. (1992) Separation of Large DNA Molecules by One-dimensional Pulsed Field Gel Electrophoresis. *Meth. Mol. Biol.* **12**, 73-104. Burmeister, M. and Ulanovsky, L. (Eds.), Humana Press, New Jersey.

[52] Magnusdottir, S., Akerman, B. and Jonsson, M. (1994) DNA Electrophoresis in Agarose Gels: Three Regimes of DNA Migration Identified and Characterized by the Electrophoretic Orientational Behaviour of the DNA. *J. Phys. Chem.* **98**, 2624-2633.

[53] Larsson, A. and Akerman, B. (1995) Period Times and Helix Alignment During the Cyclic Migration of DNA in Electrophoresis Gels Studied with Fluorescence Microscopy. *Macromolecules* **28**, 4441-4454.

[54] Akerman, B. (1997) Threading Dynamics of a Polymer Through Parallel Pores: Potential Applications to DNA Size Separation. *J. Chem. Phys.* **106**, 6152-6159.

[55] Long, D., Harden, J.L. and Viovy, J. L. (1995) Separation de Polyelectrolytes par Permeation de Membranes Poreuses. *C.R. Acad. Sc. Paris* **321**, 239-246.

[56] Ackers, G.K. and Steere, R.L. (1962) Restricted Diffusion of Macromolecules through Agar-gel Membranes. *Biochim. Biophys. Acta* **59**, 137-149.

[57] O'Connor, A.J., Pratt, H.R.C. and Stevens, G.W. (1996) Electrophoretic Mobilities of Proteins and Protein Mixtures in Porous Membranes. *Chem. Engin. Sci.* **51**, 3459-3477.

[58] deBlois, R.W., Bean, C.P. and Wesley, R.K.A. (1977) Electrokinetic Measurements with Submicron Particles and Pores by the Resistive Pulse Technique. *J. Colloid Interface Sci.* **61**, 323-335.

[59] Bath, B.D., Lee, R.D. and White, H.S. (1998) Imaging Molecular Transport in Porous Membranes. *Anal. Chem.* **70**, 1047-1058.

[60] Akerman, B. (1998) Effects of Supercoiling in Electrophoretic Trapping of Circular DNA in Polyacrylamide Gels. *Biophys. J.* **74**, 3140-3151.

[61] Akerman, B. (1998) Ring-Polymer Dynamics in Gels: Supercoiled and Relaxed Circular DNA in Polyacrylamide. *J. Phys. Chem.* **102**, 8909-8922.

[62] Bohrer, M.P., Fetters, L.J., Grizzuti, N., Pearson, D.S. and Tirrell, M.V. (1987) Restricted Diffusion of Linear and Star-Branched Polyisoprenes in Porous Membranes. *Macromolecules* **20**, 1827-1833.

[63] Easwar, N., Langley, K. and Karasz, F.E. (1990) Diffusion of Weakly Confined Star and Linear Polymers and Strongly Confined Linear Polymers in a Porous Material. *Macromolecules* **23**, 738-745.

[64] Kluijtmans, S.G.J.M., de Hoog, E.H.A., Philipse, A.P. (1998) Self-diffusion of Charged Colloidal Tracer Spheres in Transparent Porous Glass Media. *J. Chem. Phys.* **108**, 7469

[65] Hubert, S.J., Krzywinski, M., L'Heureux, I. and Slater, G.W. (1998) Reptation Dynamics with Random Local Interactions. *Macromolecules* **31**, 181-192.

[66] Akerman, B. (1996) Tethering of Double-stranded DNA to Agarose Gels for Studies of Conformation Dynamics During Electrophoresis. *Chem. Comm.* **5**, 661-662.

[67] Schönhals, A. and Stauga, R. (1998) Broadband Dielectric Study of Anomalous Diffusion in a Poly(propyleneglycol) Melt Confined to Nanopores. *J. Chem. Phys.* **108**

ENTROPIC BARRIER THEORY OF POLYMER TRANSLOCATION

Murugappan Muthukumar
Dept. of Polymer Science and Engineering, U. Massachusetts at Amherst, Amherst, MA

1. Introduction

One of the inherent properties of an isolated flexible polymer chain in solutions is its ability to assume very large number of configurations $\mathcal{N}$. Consequently the chain entropy S ($k_B \ln \mathcal{N}$, k_B being the Boltzmann constant) can be very high and its free energy F is given by

$$F = E - TS = E - k_B T \ln \mathcal{N} \tag{1}$$

where E is the energy of interaction among monomers and the surrounding solvent molecules and T is the absolute temperature. When such a chain is exposed to a restricted environment such as a pore or a channel, the number of configurations that can be assumed by the chain is reduced and consequently the chain entropy decreases and chain free energy increases. This effect is depicted in Fig. 1,

F_1, F_2, and F_3 are the free energies of the chain in regions I, II, and III, respectively. Due to the reduction in number of configurations in region III, F_3 is higher than F_1 and F_2. We call $F_3 - F_1$ the entropic barrier for the passage of the chain out of region I. Although this barrier is termed entropic barrier [1–3], it is indeed a free energy barrier, because there can be additional enthalpic contributions to F_3 arising from the interactions of monomers with the pore. In general, the environment of chain in region II can be different from that in region I (due to different electrochemical potentials in these regions) so that F_2 is not necessarily equal to F_1. The net driving potential for polymer transport from I to II is $(F_1 - F_2)$. The polymer chain must negotiate the entropic barrier in order for it to successfully arrive at the opposite side of the pore.

Entropic barriers play a crucial role in dictating polymer transport in media of heterogenous length scales, such as controlled pore glasses and swollen gels in the context of size exclusion chromatography and gel electrophore-

J.J. Kasianowicz et al. (eds.), Structure and Dynamics of Confined Polymers, 227–239.

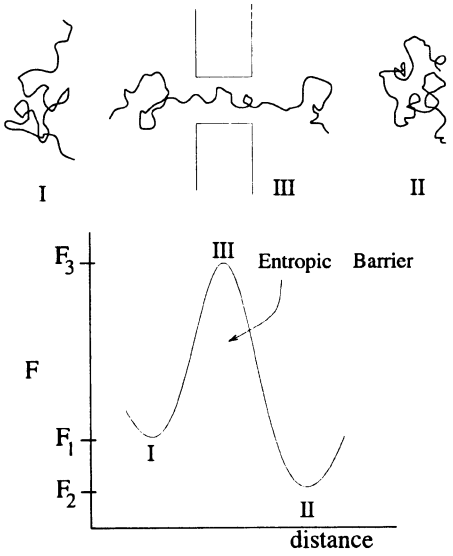

Figure 1. Genesis of entropic barrier due to reduction in number of configurations of the chain by a pore.

sis. These systems consist of cavities with a broad size distribution and large cavities act as entropic traps while narrow passages set up entropic barriers. The calculation of the entropic barrier $(F_3 - F_1)$ and the driving potential $(F_1 - F_2)$ for the above mentioned situations has enabled us to understand the main features of experimental results on polymer diffusion in random media, gel electrophoresis, and polymer threading through protein ion channels. The essential results of the entropic barrier theory and their experimental correspondence are briefly summarized in the following sections.

Since we are interested in large length scale behaviour of the polymer, we have employed polymer physics concepts [4–6] in calculating F_1, F_2, and F_3 by surrogating monomeric chemical details into parameters such as effective segment length l. As an example a homopolymer chain of N_0 monomers with bond length a is considered to be a Kuhn model chain with N segments and segment-to-segment length being l. N is proportional to the molecular weight of the polymer. The chemical details of monomers appear through l. There are three essential polymer concepts required to compute the free energy landscape associated with polymer translocation through narrow constrictions. These are briefly reviewed here for the convenience of the reader.

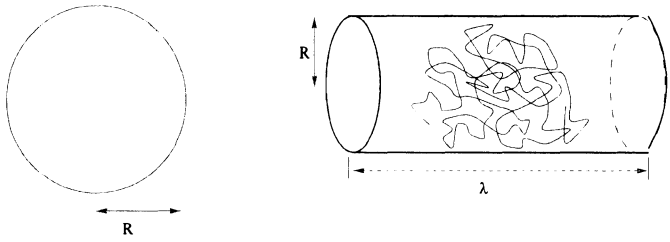

Figure 2. Polymer confinement inside a pore. The length of the cylinder λ is long enough to fully confine the polymer.

(i) When an isolated polymer chain is in a dilute solution, its average radius of gyration R_g is given by

$$R_g \sim N^{\nu} \tag{2}$$

where the effective size exponent ν and the numerical prefactor (not shown in the equation) depend on the nature of the solution. For example,

$$\nu = \begin{cases} \frac{1}{2}, & \text{ideal } \theta \text{ solution} \\ \simeq \frac{3}{5}, & \text{good solutions (high salt)} \\ \simeq 1, & \text{low salt.} \end{cases} \tag{3}$$

As the salt concentration of a dilute solution containing uniformly charged flexible polyelectrolytes is reduced, the polymer chain expands due to electrostatic repulsion between monomers and consequently the effective exponent increases from $3/5$ towards 1.

(ii) When a polymer chain with N segments is confined (Fig. 2) to a restricted space such as a spherical cavity or a cylindrical pore of radius R, the free energy of confinement F_c is

$$\frac{F_c}{k_B T} \sim \frac{N}{R^{1/\nu}} \tag{4}$$

where ν is the value appropriate to the quality of the solution inside the pore.

(iii) The free energy $F_>$ of a polymer chain of N segments in a semi-infinite space with a hard impenetrable surface at the origin and one end of the polymer permanently anchored at the center of the wall (Fig. 3) is given by

$$\frac{F_>}{k_B T} = (1 - \gamma') \ln N + N\mu \tag{5}$$

Figure 3. Polymer tail in semi-infinite space with one end attached permanently to an impenetrable surface.

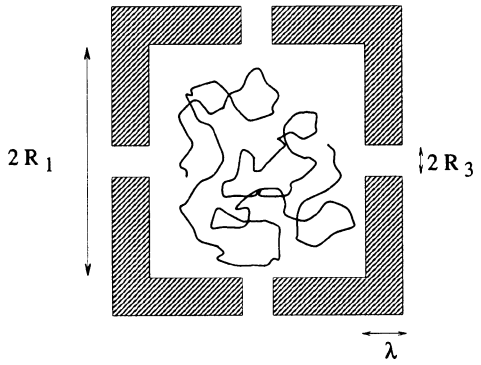

Figure 4. Two-dimensional projection of a cubic cavity.

where μ is the chemical potential of the polymer per segment in the semi-infinite space containing the polymer. γ' is a critical exponent and its effective value is

$$\gamma' = \begin{cases} \frac{1}{2}, & \text{ideal } \theta \text{ solution} \\ \simeq 0.69, & \text{good solution (high salt)} \\ 1, & \text{low salt.} \end{cases} \tag{6}$$

We now proceed to employ these concepts [4–6] in the calculation of entropic barriers and then apply the results to understand polymer transport in random media, gel electrophoresis, and DNA translocation through protein channels.

2. Polymer escape from a cavity in random media

Consider the escape [1–3] of a self avoiding chain ($\nu \simeq \frac{3}{5}$) of N segments from a cubic cavity of inner side $2R_1$ through the gates at the centers of the walls of the cavity as shown in Fig. 4.

Each of the six gates is taken to be a cylindrical pore of radius R_3 and length λ. The system under consideration is a periodic three-dimentional array of this cavity as sketched in Fig. 5.

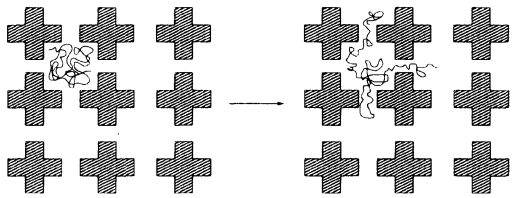

Figure 5. Polymer escape from entropic traps through gates.

Under these conditions, the diffusion coefficient D of the polymer is given by [7, 8]

$$D = D_0 exp\left(-\frac{\Delta F}{k_B T}\right) \tag{7}$$

where D_0 is the diffusion coefficient ($D_0 \sim N^{-1}$, if hydrodynamics is screened) without any geometrical constraints and ΔF is the change in confinement free energy arising from the entropic barrier. If f is the fraction of segments in one of the pores and z is the average number of cavities that contain $(1-f)N$ segments per pore,

$$\Delta F = f F_{c3} + \left(\frac{1-f}{z} - 1\right) F_{c1} \tag{8}$$

where F_{c1} and F_{c3} are the confinement free energies for fully containing the chain in the cavity and the gate, respectively. The above result is only an average result. The precise value of the prefactor in the second term should account for the simultaneous residence of the chain in several cavities and gates. Furthermore, sizes of cavities and gates are broadly distributed in realistic disordered media. Although prefactors will be altered by such distributions, the essential physics will remain unaltered.

For the "toy" addressed in Fig. 4, substitution of Eq.(4) into Eq.(8) gives

$$\frac{D}{D_0} = exp\left\{-N\left[f R_3^{-1/\nu} + \left(\frac{1-f}{z} - 1\right) R_1^{-1/\nu}\right]\right\} \tag{9}$$

To verify the concept of entropic barriers and the validity of Eq.(9), Monte Carlo simulations [1–3] were carried out and the agreement with the predictions of Eq.(9) was excellent. When the pores are not long enough, f is a function of N^{-1}, and consequently D/D_0 is not a simple exponential decrease with N. It can be shown [1–3] that, if the volume of the cylindrical

pore is much smaller than the volume of the polymer then $f \sim \frac{\lambda}{N} R_3^{\frac{1}{\nu}-1}$, so that

$$\frac{D}{D_0} = exp\,[-(BN + s)] \tag{10}$$

where s is proportional to $\lambda R_3^{-1}[1 - z^{-1}(R_3/R_1)^{1/\nu}]$ and B is positive and proportional to $R_1^{-1/\nu}$. Thus λ and R_3 play significant roles in polymer transport. The Monte Carlo data are in agreement with these scaling predictions, and the reader is referred to Refs. [1,2].

If the typical sizes of the cavity and pore are comparable to the segmental length l, then the entropic trap is eliminated and the dominant chain dynamics is via chain ends. Under such extreme conditions, reptation dynamics [4,5], where $D \sim N^{-2}$, is expected to be valid. On the other hand, if there are no pores in the system $(R_1 \to \infty), D = D_0 \sim N^{-1}$. This is the Rouse dynamics [5], where hydrodynamic interactions are ignored (if hydrodynamic interactions are included, $D_0 \sim N^{-\nu}$, called the Zimm dynamics.). For a given random medium, Rouse regime, entropic barrier regime, and the reptation regime can be realized as the molecular weight of the trapped polymer is increased progressively.

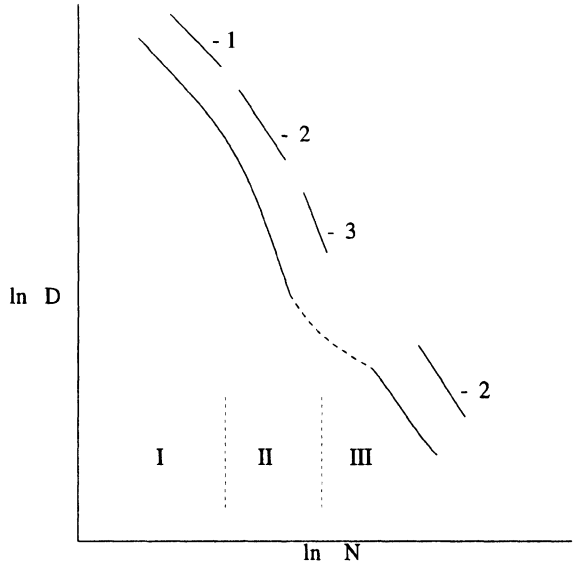

Figure 6. Entropic barrier regime intervenes the Rouse/Zimm and reptation regimes.

This behavior is illustrated in Fig. 6. In Regime I, Rouse's law $D \sim N^{-1}$ is observed. Regime II corresponds to the situation where the chain dynamics is dominated by entropic barriers. In this regime, D has an apparent power

law $N^{-\alpha}$ with α around 3. Instead of such an apparent power law, an exponential law $D \sim exp(-N)$ can also be approximately fitted to simulation and experimental data. For infinitely long chains, the reptation regime III is expected. The conclusion that there is a pronounced intermediate regime due to entropic barriers, between the Rouse and reptation regimes is consistent with all known experimental data [9–17] on D for polymer diffusion in swollen gels and controlled pore glasses.

3. Gel electrophoresis

Gel electrophoresis consists of a sample of electrically charged polymers with different molecular weights being introduced into a gel with an external electric field accross the gel. The seperation of different polymers is achieved due to the differing rates with which charged polymers of diffrent molecular weights migrate through the gel. The gel (e.g., agarose gel) is highly heterogeneous in space and consequently polymer mobility is expected to be dominated by entropic barriers. According to mean field theories [18–21] of electrophoretic mobility μ_e (originally from Hückel),

$$\mu_e \sim QD \tag{11}$$

where the charge Q of the polymer is proportional to N. (Significant deviations [22, 23] from this formula occur in capillary electrophoresis.)

Therefore, by substituting the result of Fig.6 for D in Eq.(11), we can identify three regimes for the molecular weight dependence of the electrophoretic mobility in gel electrophoresis (Fig.7).

We take $\mu_e \sim N^{1-\alpha}$, where α is the effective exponent discussed in the preceding section. Then the N dependence of μ_e in the intermediate regime dominated by entropic barriers is expected [24] to be steeper than the Rouse or reptation regime results. Calladine and coworkers [25] found that $\mu_e \sim N^{-2}$ for DNA in various gels, and Arvanitidou and Hoagland [26] found that $\mu_e \sim N^{-1.4}$ for poly(styrene sulfonate) in polyacrylamide gels, in conformity with the entropic barrier model of gel electrophoresis. These experimental observations are in disagreement with the earlier theoretical prediction, $\mu_e \sim N^{-1}$, based on the reptation model. Furthermore, if the entropic barriers dominate the polymer dynamics, we expect the topology (such as branching) of the polymer to play an insignificant role in the molecular weight dependence of μ_e in agreement with experimental observations [27, 28].

The elegant work of Zimm and coworkers [29] on 'lake and straits' is based on the same theme of dominance of entropic barriers described above.

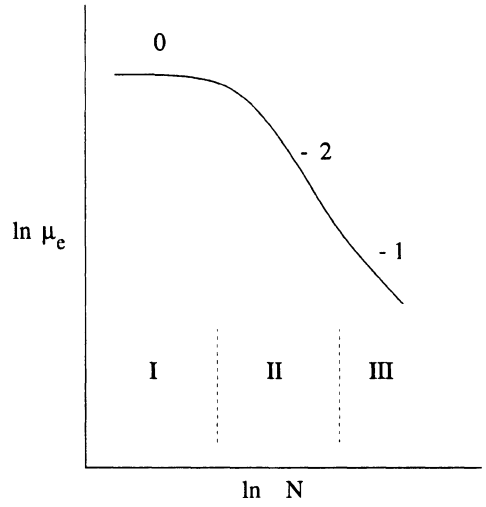

Figure 7. In the intermediate entropic barrier regime, $\mu_e \sim N^{-(\alpha-1)}$, where $(\alpha - 1)$ is greater than 1.

4. Polymer translocation through a hole

Threading a polymer through narrow ion channels and pores under external fields [30–37] involves the transport of the polymer across an entropic barrier as described in section 1. In this section we [37] calculate the entropic barrier and the associated dynamics of a polymer of N segments transporting through a narrow pore (Fig.8)

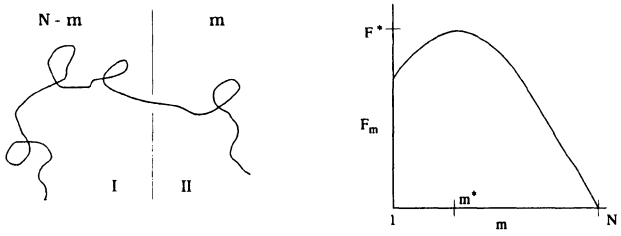

Figure 8. Polymer escape in transition and associated free energy barrier.

from region I to region II under an electrochemical potential gradient $\Delta\mu$. Let these regions be devided by a partition which is taken to be an infinite two-dimentional sheet with a hole in the middle to allow the passage of the chain. As suggested by experimental systems, the hole size is such that hairpins are not allowed. Let m segments be present in region II and $N - m$ segments be in region I. The free energy of this polymer configuration (a tail of m segments in II and a tail of $N - m$ segments in I) follows from Eq.(5) as

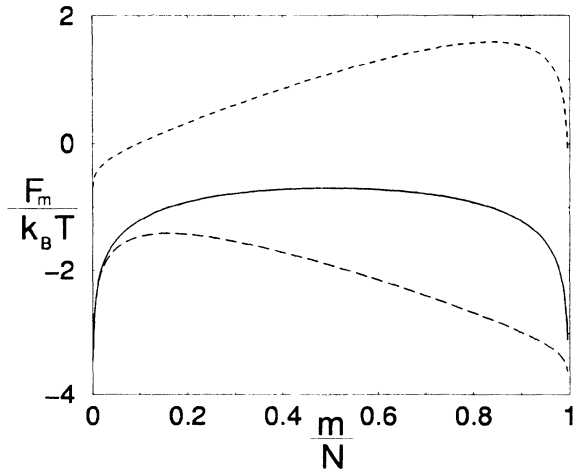

Figure 9. Plot of F_m/k_BT against m/N. Curves represent: solid line, $N\Delta\mu/k_BT = 0$, $\gamma_1' = 0.5 = \gamma_2'$; long-dashed line, $N\Delta\mu/k_BT = 3$, $\gamma_1' = 0.9$, $\gamma_2' = 0.5$; dashed-line,$N\Delta\mu/k_BT = 3$, $\gamma_1' = 0.5$, $\gamma_2' = 0.9$.

$$\frac{F_m}{k_BT} = (1-\gamma_2')\ln m + (1-\gamma_1')\ln(N-m) - m\frac{\Delta\mu}{k_BT} \qquad (12)$$

where the unnecessary constant terms are ignored and $\Delta\mu = \mu_1 - \mu_2.\gamma_1'$ and γ_2' are the values of γ' in regions I and II, respectively. Similarly μ_1 and μ_2 are the chemical potentials of the polymer per segment in regions I and II, respectively. F_m given by Eq.(12) exhibits a free energy barrier as a function of m.

The nature of the free energy barrier depends on (i) conformational statistics on both regions, and (ii) degree of chemical potential mismatch $\Delta\mu$ relative to the entropic part (first two terms on the right hand side of Eq(12)). The barrier is illustrated in Fig. 9 where F_m/k_BT is plotted against m/N for $\gamma_1' = 0.69 = \gamma_2'$. The presence of a free energy barrier implies that a critical number of monomers m^* must be nucleated for the successful polymer translocation to occur. The rate of nucleation of a chain portion larger than m^* in region II is dictated by the free energy F^* at the barrier height. The critical number m^* and the free energy F^* are sensitive functions of $N\Delta\mu/k_BT$ as shown in Figs. 10 and 11.

Thus a very small change in the electrochemical potential gradient can change F^* by an order of magnitude of k_BT. Similar sensitivity of F^* can also be realized by changing the solution conditions in regions I and II. As an example, Fig. 11 gives the dependence of m^* and F^* on γ_1' while γ_2' is kept at 0.69 and $N\Delta\mu = 2k_BT$.

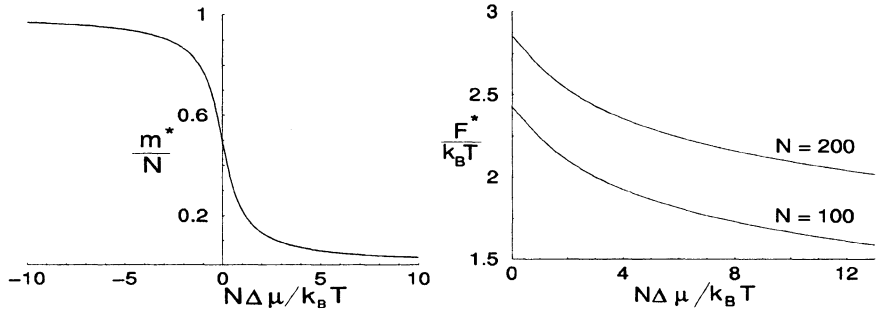

Figure 10. Dependence of critical number m^* of nucleated monomers and free energy F^* at the barrier height on $N\Delta\mu/k_BT$ for $\gamma_1' = 0.69 = \gamma_2'$.

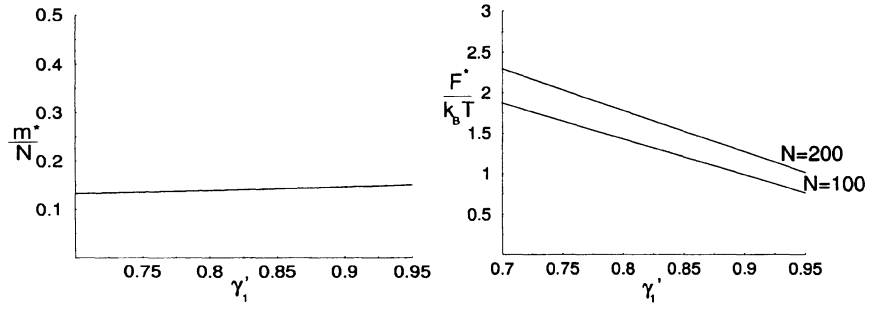

Figure 11. Dependence of m^* and F^* on γ_1' for $\gamma_2' = 0.69$ and $N\Delta\mu/k_BT = 2$.

Following the standard arguments of the theory of nucleation and growth, the transport of the chain through the barrier can be described by (for details, see [37]).

$$\frac{\partial}{\partial t}W_m(t) = \frac{\partial}{\partial m}\left[\frac{k_0}{k_BT}\frac{\partial F_m}{\partial m}W_m(t) + k_0\frac{\partial}{\partial m}W_m(t)\right] \tag{13}$$

where W_m is the probability of finding m segments in region II at time t and k_0 is the rate constant for pushing one segment into region II. k_0 is a nonuniversal parameter and is dictated by the chemical interactions between the segment and the pore. The distribution function W_m and its moments can be calculated from Eq.(13). In particular, the mean first passage time τ (i.e, the average time required by the polymer, having already placed at least one segment in region II, to go from region I to region II) is shown in Fig. 12. τk_0 is plotted against N for different values of $\frac{\Delta\mu}{k_BT}$. While for symmetric barriers ($\Delta\mu = 0$), $\tau k_0 \sim N^2$,

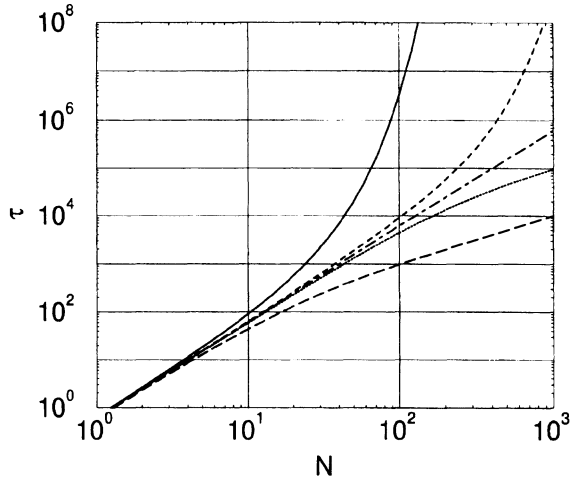

Figure 12. Dependence of τ in units of $1/k_0$ on N for different values of $\Delta\mu/k_BT = 0.1$, long-dashed line; 0.01, dotted-line; 0, dotted-dashed line; -0.01, dashed-line; and -0.1, solid line.

$$k_0\tau \sim \begin{cases} \frac{k_BT}{\Delta\mu}N, & \Delta\mu >> 0. \\ \left(\frac{k_BT}{\Delta\mu}\right)^2 exp\left(\frac{-N\Delta\mu}{k_BT}\right), & \Delta\mu << 0. \end{cases} \tag{14}$$

If the entropic terms in Eq.(12) are weak compared to the third term on the right hand side, τ for translocation along the favorable chemical potential gradient ($\Delta\mu > 0$) is given by

$$\tau = \frac{N}{k_0}\frac{k_BT}{\Delta\mu}\left\{1 - \frac{k_BT}{N\Delta\mu}\left[1 - exp\left(-\frac{N\Delta\mu}{k_BT}\right)\right]\right\} \tag{15}$$

with the limits

$$\tau \sim \begin{cases} \frac{k_BT}{k_0\Delta\mu}N, & N\Delta\mu > 1 \\ \frac{N^2}{2k_0}, & N\Delta\mu < 1 \end{cases} \tag{16}$$

Therefore, for sufficiently large values of N such that $N\Delta\mu > 1, \tau$ is proportional to N and inversely proportional to $\Delta\mu/T$, in agreement with experimental results of Kasianowicz et al. [30] on the blockade of α- hemolysin channel by single stranded DNA and RNA. Furthermore, the above theory predicts that $\tau \sim N^2$, for shorter polymers provided $N\Delta\mu < 1$, even if $\Delta\mu \neq 0$. This prediction has also been seen in recent experiments [34].

5. Conclusions

The entropic barrier model described above explains the major scaling features of polymer dynamics in heterogenous media and polymer translocation through narrow channels. The local details, such as the nature of interaction between monomers and pores, are taken only as phenomenological parameters. One approach in the future is to actually compute these details of chemistry to obtain a firm relationship between the parameters of the entropic barrier theory and their origin. Another approach is to measure these parameters (e.g, the rate constant k_0 to push a monomer through the channel) by fitting the experimental data with formulas derived above and then use the theory to predict behaviours at large length scales. It is hoped that progress will be made on both fronts in the future.

Acknowledgments

I am grateful to John J. Kasianowicz for stimulating discussions on translocation of DNA through pores. Acknowledgement is made to the NSF for Grant No. DMR 9970718 and the Materials Research Science and Engineering Center at the University of Massachusetts.

References

[1] M. Muthukumar and A. Baumgärtner (1989), *Macromolecules* **22**, 1937, 1941.

[2] M. Muthukumar (1991), *J. Non-Cryst. Solids* **131-133**, 654.

[3] A. Baumgärtner M. Muthukumar (1996), *Adv. Chem. Phys.* **XCIV**, 625.

[4] P.-G. de Gennes (1979), *Scaling concepts in Polymer Physics*, Ithaca, NY: Cornell University Press.

[5] M. Doi and S. F. Edwards (1986), *The Theory of Polymer Dynamics*, New York: Oxford Science Publications.

[6] E. Eisenriegler (1993), *Polymers Near Surfaces*, Singapore: World Scientific.

[7] M. Daoud and P.-G. de Gennes (1977), *J. Phys.* **38**, 85.

[8] F. Brochard and E. Raphael (1990), *Macromolcules* **23**, 2276.

[9] H. Kim, T. Chang, J. M. Yohanan, L. Wang, and H. Yu (1986), *Macromolecules* **19**, 2737.

[10] H. Watanabe and T. Kotaka (1987), *Macromolecules* **20**, 530.

[11] N. Nemoto, T. Kojima, T. Inove, M. Kishine, T. Kirayama, and M. Kurata (1989), *Macromolecules* **22**, 3793.

[12] L. M. Wheeler and T. P. Lodge (1989), *Macromolecules* **22**, 3399.

[13] N. Nemoto, M. Kishine, T. Inove and K. Osaki (1990), *Macromolcules* **23**, 659 (1990).

[14] Lodge, T.P. and Rostein, N.A. (1991), *J. Non-Cryst.Solids* **131-133**, 671.

[15] G. D. J. Phillies and P. Paczak (1988), *Macromolecules* **21**, 214.

[16] N. Easwar (1989), *Macromolecules* **22**, 3492.

[17] Y. Guo, K. H. Langley, and F. E. Karasz (1990), *Macromolecules* **23**, 2022.

[18] W. B. Russel, D. A. Saville, and W. R. Schowalter (1989), *Colloidal Dispersions*, Cambridge: Cambridge University Press.

[19] L. S. Lerman and H. L. Frisch (1982), *Biopolymers* **21**, 995.

[20] O. J. Lumpkin and B. H. Zimm (1982), *Biopolymers* **21**, 2315.

[21] G. W. Slater, J. Rousseau, and J. Noolandi (1987), *Biopolymers* **26**, 863.

[22] M. Muthukumar (1996), *Electrophoresis* **17**, 1167.

[23] M. Muthukumar (1997), *J.Chem.Phys.* **107**, 2619.

[24] J. Melenkevitz and M. Muthukumar (1990), *Chemtracts* **1**, 171.

[25] C. R. Calladine, C. M. Collins, H. R. Drew, and M. R. Mott (1991), *J.Mol. Biol.* **221**, 981.

[26] E. Arvanitadou and D. Hoagland (1991), *Phys.Rev.Lett.* **67**, 1464.

[27] D. L. Smisek and D. Hoagland (1990), *Science* **248**, 1221.

[28] D. Hoagland and M. Muthukumar (1992), *Macromolecules* **25**, 6696.

[29] B. H. Zimm and S. D. Levene (1992), *Quart.Rev.Biophys.* **25**, 171.

[30] J. J. Kasianowicz, E. Brandin, D. Branton, and D. W. Deamer (1996), *Proc. Natl.Acad. Sci. USA* **93**, 13770.

[31] S. M. Bezrukov, I. Vodyanoy, R. A. Brutyan, and J. J. Kasianowicz (1996), *Macromolecules* **29**, 8517.

[32] I. Szabo, G. Bathori, F. Tombola, M. Brini, A. Coppola, and M. Zoratti (1997), *J.Biol.Chem.* **272**, 25275.

[33] M. Akeson, D. Branton, J. J. Kasianowicz, E. Brandin, and D. W. Deamer (1999), *Biophys. J.* **77**, 3227.

[34] A. Meller, L. Nivon, E. Brandin, J. Golovchenko, and D. Branton (2000), *Proc. Natl. Acad. Sci. USA* **97**, 1079.

[35] W. Sung and P. J. Park (1998), *Phys.Rev.Lett.* **77**, 783; *J.Chem.Phys.* **108**, 3013.

[36] E. A. DiMarzio and A. J. Mandell (1997), *J.Chem.Phys.* **107**, 5510.

[37] M. Muthukumar (1999), *J.Chem.Phys.* **111**, 10371.

POLYMER TRANSLOCATION THROUGH A "COMPLICATED" PORE

David K. Lubensky *
Department of Physics, Harvard University, Cambridge, MA 02138

Abstract Motivated by experiments in which a polynucleotide is driven through a proteinaceous pore by an electric field, we study the diffusive motion of a polymer threaded through a narrow channel with which it may have strong interactions. We show that there is a range of polymer lengths in which the system is approximately translationally invariant, and we develop a coarse-grained description of this regime. In contrast to previous models, this description holds even when some pore degrees of freedom do not remain equilibrated. General features of the distribution of times for the polymer to pass through the pore are then deduced. Finally, we consider more microscopic models and argue that the available data suggests a translocation mechanism involving coupling between the polymer backbone and other slow degrees of freedom.

1. Introduction

Modern polymer physics has achieved great success with models in which the polymer is regarded as a flexible, uniform "string" whose conformational entropy dominates the system's behavior [1, 2]. Although this is usually an excellent description, in some situations other interactions can become important. One example is the insertion of a polymer into a pore of diameter comparable to the size of the chemical repeat units that make up the polymer. Although perhaps unusual with synthetic polymers, such a situation can easily occur in biological systems. For example, Kasianowicz, Brandin, Branton, and Deamer have detected single strands of RNA passing through a 1.5 nm pore formed by the membrane-bound protein *Staphylococcus aureus* α-hemolysin [3]. Further experiments have generated a wealth of data on this polynucleotide in α-hemolysin (herein PAHL) system [4–8]. Szabo and coworkers [9–11] and Hanss and coworkers [12] have studied similar systems. In addition to their intrinsic interest, these experiments may even-

*Much of this contribution represents work done in collaboration with David Nelson and has been reported previously in [43]. Sections 5 and 6 are new work.

J.J. Kasianowicz et al. (eds.), Structure and Dynamics of Confined Polymers, 241–259.

tually lead to a single-molecule DNA sequencing technique. More generally, most cells must transport macromolecules across membranes in order to function; in a number of cases, relatively "thick" molecules are believed to pass through nanometer-scale channels [12–16]. Several such biological systems are examined elsewhere in this volume [17–21].

There exists a considerable theoretical literature on the confinement of polymers in inert channels that interact with the polymer only through hard-wall potentials [22–36]. Many of the standard techniques of polymer theory then apply. Inspired largely by the experiments on PAHL, in this paper we consider a different scenario: We study the motion of a homopolymer threaded through a narrow pore with which it has strong interactions. The pore is taken to be sufficiently small that no more than one polymer diameter can fit in it at a given time; in particular, hairpin bends are not allowed to pass through the channel. We also put aside the question of how the polymer first enters the hole, focusing instead on the dynamics once one end has been inserted. We then argue that, in the presence of a force driving the polymer through the pore, there should be a regime in which the polymeric degrees of freedom outside of the pore can be neglected, and the system is effectively one-dimensional and translationally invariant. In this limiting case, very general arguments allow us to propose a coarse-grained description of the chain dynamics. Our approach follows several authors [27–31] in viewing the translocation process as essentially diffusion in one dimension; we differ, however, in emphasizing the role that the protein pore itself plays in this diffusion process. The importance of polymer-pore interactions has previously been emphasized by Bezrukov, Kasianowicz, and coworkers [5, 37–39].

Since our analysis relies heavily on the results of PAHL, the next section sketches some salient features of the experiments. We then introduce a long length scale "hydrodynamic" description of one-dimensional diffusion and use it to calculate the distribution of passage times for a polymer being driven through a pore. A more microscopic model and its predictions for the transport coefficients appearing in the coarse-grained description are then analyzed; we find that the available data are not well-described by a picture in which the polymer backbone position is the only degree of freedom. We conclude by looking at what happens outside of the quasi-one-dimensional regime and by giving a more detailed comparison of our theory to other available models.

2. Experimental background

The experiments of interest to us have been amply discussed elsewhere [3–8]. Briefly, the α-hemolysin channel is inserted into a lipid membrane; Kasianowicz and Bezrukov have demonstrated that in concentrated salt solutions it can remain open for periods on the order of tens of seconds [40, 41].

While passing through the pore under the influence of an electric field across the membrane (120mV), single-stranded DNA or RNA partially block the narrow (1.5–2 nm diameter [42]) transmembrane channel, resulting in a detectable decrease in the current flowing through the pore. One can thus obtain a histogram of the times required for individual polynucleotides to traverse the membrane. Since the size of the channel at its smallest constriction is barely larger than the diameter of a single-stranded polynucleotide, one might expect that the physics in the vicinity of the pore would play an important role in determining how the polymer translocates. Indeed, the observed translocation speeds are far slower than predicted by simple hydrodynamic estimates [43], supporting the idea that one must take polymer-pore interactions into account when modeling the PAHL system.

A quantity of considerable interest in what follows will be the mean force F driving the polymer through the pore.[1] Clearly F is primarily the result of the electric field acting on the polymer. Any voltage V applied to the system should fall almost entirely across the narrow α-hemolysin pore. The charge on each nucleotide is just the electron charge e, so the electrostatic energy gained by moving one nucleotide completely through the pore is eV. This suggests that F is roughly

$$F \approx \frac{eV}{a} \approx 5\frac{k_{\mathrm{B}}T}{a}\,, \tag{1}$$

where $a \approx 0.6$ nm is the length of a nucleotide, and the second equality holds for $V \approx 125\mathrm{mV}$. This figure of course is a crude estimate and is almost certainly larger than the true force. Nonetheless, mounting indirect evidence supports the idea that F is of the order of a few $k_{\mathrm{B}}T/a$, and thus is quite large when expressed in appropriate units. For example, Kasianowicz and coworkers [44] and Branton and coworkers have observed current blockades in the PAHL system suggestive of the pulling apart of paired polynucleotide strands; this would require that Fa be larger than the free energy cost of opening a base pair. Similarly, the very fact that the polymers insert into the pore means that they must gain enough electrostatic energy to overcome the entropic cost of confinement [33]. Thus, for most of the rest of the paper, we will assume that $F \approx 5k_{\mathrm{B}}T/a$ and explore the consequences of this hypothesis.

[1] One can define F more precisely as the mean force required to immobilize a given monomer in the pore, where the average is taken over time and over all of the monomers in a given polymer. Thus F does not include hydrodynamic drag forces, nor forces that vanish when averaged over all the monomers.

3. Coarse-grained description

This section and the next are concerned with predicting distributions of translocation times of the sort measured in the PAHL system. To do this, we rely on the fact that if the translocation is sufficiently slow and the polymer is being driven sufficiently strongly, the system is approximately invariant under a discrete set of translations—that is, it is essentially unchanged if the polymer moves an integer number of nucleotides forwards or backwards through the pore. We first establish this symmetry, then use it to derive an effective diffusion equation from which the desired distribution may be calculated.

3.1 Regime of validity of translational symmetry

Begin by dividing the polymer into three parts: the roughly ten nucleotide long piece that is actually *inside* the channel, and the two "ends", comprising the majority of the nucleotides, *outside* the channel. The pore always contains the same number of bases, so, for homopolymers, this part of the polymer always satisfies the requirement of translational symmetry. The length of each end "dangling" outside the pore, in contrast, changes with the x of the polymer's backbone that has passed through the pore, destroying translational invariance (The variable x is defined so that if the polymer backbone has length L, $x = 0$ when the polymer has just started in the pore and $x = L$ when it has reached the other side). In what follows, we shall argue that under certain conditions this variation may be neglected. Our arguments assume that the parts of the polynucleotide outside the pore may be described by the theories usually applied to long, flexible polymers [1,2]; we thus ignore, for example, base-stacking and other specific interactions [45]. We also assume that the ion channel is sufficiently long and narrow that any voltage drop falls entirely across the channel.

There are two criteria for ignoring the ends of the polymer outside of the pore. They should have a characteristic relaxation time that is much faster than the characteristic time for the motion of a monomer through the channel, and the derivative of their free energy with respect to x should be much less than the driving force F. In the absence of interactions between the polymer and the pore, one would expect diffusion on the scale of a few monomers to be much faster than the relaxation of a long polymer coil, and the first inequality could never be satisfied. However, since the nucleotides in the pore can be expected to interact strongly with the confining protein, the requirement is not implausible. The longest time scale of an isolated polymer in a good solvent is the Zimm time $t_{\mathrm{Z}} \approx 0.4\eta R_G^3/(k_{\mathrm{B}}T) \approx 0.4\eta N^{3\nu} b^3/(k_{\mathrm{B}}T)$, where

ν is the Flory exponent,[2] b is the Kuhn segment length (equal to twice the persistence length), η is the solvent viscosity, and $N = L/b$.[3] If we imagine that the polymer moves a monomer through the channel by hopping over an energetic barrier (an idea to be considered in more detail when we introduce our microscopic model), then in the limit of strong driving, the translocation speed is simply $v = a/t_{\rm pore}$, where $t_{\rm pore}$ is the longest relaxation time of the part of the polymer in the pore. Substituting numerical values for poly[U], we see that $t_{\rm Z}$ and $t_{\rm pore}$ become of the same order when N is of order 150, corresponding to a length of polymer of roughly 300 nucleotides protruding from each side of the pore. Of course, for polymers that traverse the membrane more slowly, as is the case for poly[dA], the value of N below which $t_{\rm Z} \lesssim t_{\rm pore}$ can be significantly larger.

As long as the dynamics of the polymer outside of the pore are fast compared to the dynamics in the pore, one need not treat the external degrees of freedom explicitly. Instead, they affect the motion of the polymer only through a contribution $\mathcal{F}(x)$ to its free energy and through the increased drag they contribute. Here, we assume that v is sufficiently small that the parts of the polymer outside the pore are essentially in equilibrium. On purely dimensional grounds, this must be true when $t_{\rm Z} \ll N^y(b/v)$ for some non-negative exponent y, a requirement that is clearly met whenever $t_{\rm Z} \ll a/v$. (Arguments based on the breakdown of the strong pulling limit of section 5 suggest that $y = 1$.) Lee and Obukhov's scaling argument [26] implies that their effect on the drag is independent of the length of polymer on a given side of the membrane. On the other hand, in order for us to be able to neglect $\mathcal{F}$, $d\mathcal{F}/dx$ must be small compared to the force F driving translocation. Denote the free energy of the coil on the *cis* side of the membrane by $\mathcal{F}_{\rm C}(x)$ and that of the coil on the *trans* side by $\mathcal{F}_{\rm T}(x)$; their sum is $\mathcal{F}(x)$. Sung and Park pointed out that $\mathcal{F}_{\rm C}$ and $\mathcal{F}_{\rm T}$ are simply the free energies of a polymer grafted by one end to a planar surface [31]. For a polymer of length x, this entropic free energy is known to be proportional to $k_{\rm B}T\ln(x/b)$, with a coefficient of order unity that depends on whether excluded volume effects are important [46]. Ignoring the few monomers actually in the channel, we have

$$\mathcal{F}(x) \propto k_{\rm B}T\left[\ln\left(\frac{x}{b}\right) + \ln\left(\frac{L-x}{b}\right)\right]. \qquad (2)$$

For a chain that is a fixed fraction of the way through the hole (i.e. for fixed x/L), $d\mathcal{F}/dx$ vanishes like $1/L$. Further, it makes little sense to consider

[2] In principle, $\nu \approx 0.6$ for a long polymer in a good solvent. However, even with the longest available chains, ν is never observed in dynamics experiments to be larger than 0.55 [2], so we use this value for specific numerical calculations.

[3] If base-stacking or similar effects are important, the appropriate relaxation time should be substituted for the Zimm time.

$x < a$, where a is the length of a single monomer, so we must always have $d\mathcal{F}/dx \lesssim k_{\rm B}T/a$. Typical values will be much smaller than this bound. The driving force $F \approx 5k_{\rm B}T/a$ thus greatly exceeds $d\mathcal{F}/dx$. In sum, we have shown that in the window of polymer lengths

$$\frac{k_{\rm B}T}{Fa} \ll N \ll \left(\frac{k_{\rm B}Ta}{\eta b^3 v}\right)^{1/3\nu} \tag{3}$$

the polymer is short enough to relax quickly, but long enough that the entropic barrier to crossing the membrane is not too steep. For lengths between these bounds, the ends of the chain hanging outside of the pore can be neglected compared to the monomers inside the pore. Typical PAHL systems fall within this regime, and thus possess an approximate translational symmetry.

3.2 Governing equation

It is now well-established in condensed matter physics that the form of the slow, long length-scale dynamics of a system is often determined by the system's symmetries and conservation laws. All microscopic details are subsumed in phenomenological coupling constants and transport coefficients. In this spirit, we would like to obtain a coarse-grained equation for the probability $P(x,t)$ that a contour length x of the polymer's backbone has passed through the pore at time t. Such a description should be valid as long as the polymer length L is much larger than the size a of a nucleotide. After averaging over variations on the scale of a single nucleotide, the discrete translational invariance discussed in the last section will give rise to a translationally invariant coarse-grained equation. The (probability) density $P(x,t)$ is the only conserved variable, so it is relatively straight-forward to write down the coarse-grained hydrodynamic equation. Because there is only a single polymer (or, equivalently, a "gas" of non-interacting polymers going through the same hole), the probability current $j(x,t)$ must be linear in P. The lowest order allowed terms in j are then proportional to P and to $\partial P/\partial x$, and the conservation of probability is expressed as the familiar equation for diffusion with drift.

$$\frac{\partial P}{\partial t} = -\frac{\partial j}{\partial x} = D\frac{\partial^2 P}{\partial x^2} - v\frac{\partial P}{\partial x}\,. \tag{4}$$

We emphasize that, beyond those implicit in the requirements for ignoring the polymer outside the pore, the arguments leading to Eq. 4 make no assumptions about how the pore and the polymer interact. The price paid for this generality is that the average drift velocity v and effective diffusion coefficient D are not known. *a priori*. Their values are determined by more microscopic physics depending on the specific properties of the pore and the particular polymer used; in particular, they may depend nonlinearly on the applied electric field

and need not be related by an Einstein relation. Usually, polymer translocation events in the PAHL system fall into two distinct groups, distinguished by different translocation times or blockade currents [3,4,6]. These two groups may in general be characterized by different values of v and D.

On the macroscopic level of Eq. 4, all information on the competition between driving and diffusive spreading is encoded in a parameter that we call the diffusive length $l_d \equiv D/v$. Roughly speaking, on length scales less than l_d, the polymer's motion is little affected by the presence of the bias from the electric field, while on scales larger than l_d, the driving dominates. We will often assume that the length L of the polymer is larger than l_d, a condition satisfied by the data on PAHL.

3.3 Distribution of passage times

We now propose to calculate a distribution $\psi(t)$ of passage times of the sort measured by experiments on PAHL. One can easily estimate the first few cumulants of this distribution. If a polymer of length L moves with average velocity v, the mean time to pass through the channel should be $\langle t \rangle \approx L/v$. Likewise, the variance in the distance traveled in a time $\langle t \rangle$ is $(\Delta x)^2 = 2D\langle t \rangle$, leading to the estimate $\Delta t^2 \equiv \langle (t - \langle t \rangle)^2 \rangle \approx (\Delta x)^2/v^2 \approx 2DL/v^3$ for the variance in arrival times. These conclusions are correct for a sufficiently long polymer. One might expect corrections, however, because some fraction of the polymers that enter the pore will leave again from the same side instead of passing all the way through. On average, these will be the "slower" molecules: Those that spend a significant time with only the tip of the polymer inserted in the channel are far more likely to fall back out than are those that are quickly driven through the hole. Thus, only "faster" chains tend to enter into the calculation of the mean transit time, decreasing $\langle t \rangle$. This effect is most pronounced for small L/l_d, because only molecules within l_d of the *cis* side have an appreciable chance of "backing out" instead of exiting on the *trans* side. Indeed, when $L \ll l_d$, the driving should be negligible, and we expect $\langle t \rangle$ to approach its $v = 0$ value $L^2/6D$. To determine the precise form of this crossover, we must turn to a more detailed calculation.

This calculation can be formulated as one of a well-studied class of problems known as first-passage problems [47,48].[4] For arbitrary L/l_d, one obtains an exact expression for $\psi(t)$ as an infinite series. If terms that become exponentially small as $L^2/(vtl_d) \to \infty$ are neglected, a comparatively

[4] Details of the calculation may be found in [43].

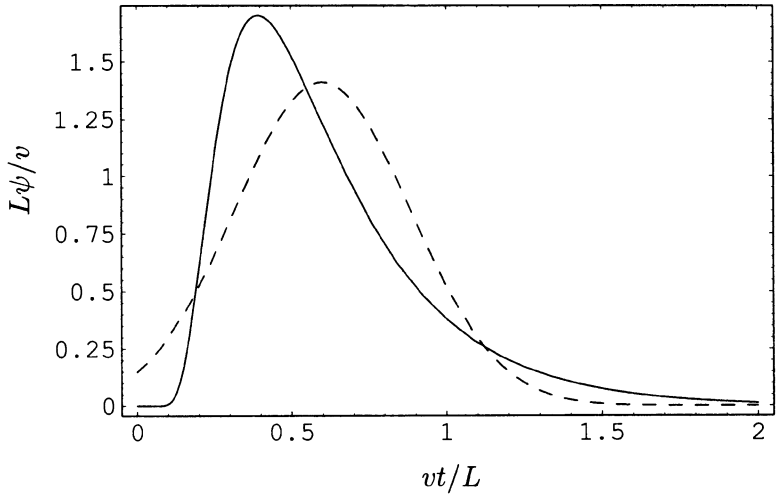

Figure 1. The distribution ψ of passage times plotted versus t for $L/l_d = 5$. Both quantities are appropriately non-dimensionalized, t as vt/L and ψ as $L\psi/v$. The dashed curve is a Gaussian with the same mean and variance as $\psi(vt/L)$.

simple analytic expression results:

$$\psi(t) \simeq \frac{v}{2}\sqrt{\frac{l_d}{\pi}}\left(\frac{L^2}{l_d(vt)^{5/2}} - \frac{2}{(vt)^{3/2}}\right) e^{-(vt-L)^2/(4vtl_d)} \qquad \left(\frac{L^2}{vtl_d} \gg 1\right) . \tag{5}$$

Note that this expression is not valid for sufficiently large t, and in particular not for t so large that it predicts that $\psi(t)$ becomes negative. Nonetheless, for reasonable parameter values it is quite accurate as long as $vt/L \sim \mathcal{O}(1)$. Figure 1 plots $\psi(t)$ for $L/l_d = 5$; a Gaussian with the same mean and variance is included for comparison. Evidently, $\psi(t)$ is quite skewed, and its mean and maximum are correspondingly well-separated. Thus, $\langle t \rangle$ and Δt are not the best parameters for describing experimental data. Indeed, both cumulants are sensitive to how $\psi(t)$ decays for large t, making them very hard to extract accurately from realistic data sets. A more useful choice of parameters to characterize $\psi(t)$ are the position $t_{\max}$ of its maximum (which satisfies $d\psi/dt|_{t_{\max}} = 0$) and the width δt of the peak. The latter is defined as $\delta t \equiv (t_R - t_L)/2$, where t_R and t_L satisfy $\psi(t_R, t_L) = e^{-1/2}\psi(t_{\max})$; we have chosen a factor of $e^{-1/2}$ instead of the more conventional $1/2$ to facilitate comparison with fits of data to a Gaussian. One expects that as $L/l_d \to \infty$, $t_{\max}$ and δt should approach $\langle t \rangle$ and Δt, respectively. For example, for large

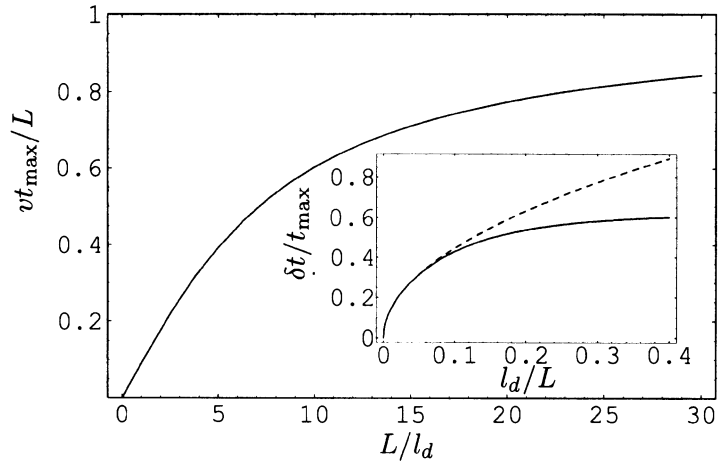

Figure 2. $vt_{\max}/L$ plotted versus L/l_d. Note that $vt_{\max}/L$ varies significantly over the range of L/l_d relevant to the experiments on PAHL, and in particular that it does not reach its asymptotic value of unity until well outside the range of this plot. (*Inset*) Plot of the relative width $\delta t/t_{\max}$ of the peak in the distribution of passage times, versus l_d/L. This curve may be used to obtain the quick estimate $l_d \approx \mathcal{O}(10)$ nucleotides for the PAHL system. The dashed curve gives the $L \to \infty$ asymptotic behavior, $\delta t/t_{\max} \sim \sqrt{2l_d/L}$. We have chosen to put l_d/L instead of L/l_d along the ordinate to allow smooth contact with this large L behavior.

L/l_d we have,

$$t_{\max} = \frac{L}{v}\left(1 - 5\frac{l_d}{L} + \frac{17}{2}\frac{l_d^2}{L^2} + 32\frac{l_d^3}{L^3} + \cdots\right) . \tag{6}$$

The rapidly growing coefficients indicate that although $t_{\max}$ approaches L/v as L approaches infinity, it falls away from its asymptotic form quite rapidly for finite L.

More generally, one can easily find $t_{\max}$ and δt by numerically solving the equations that define them. The inset of figure 2 plots $\delta t/t_{\max}$ versus the polymer length L. This ratio is especially interesting because it depends only on L/l_d, and not on v and D separately; one can thus use it quickly to estimate L/l_d. One finds that l_d is on the order of tens of nucleotides for a typical PAHL experiment. As figure 2 indicates, in this range $t_{\max}$ already deviates significantly from the naive guess $t_{\max} \approx L/v$. In particular, $t_{\max}/L$ varies by a factor of 2 as L/l_d increases from 5 to 25. With sufficiently good data, this deviation from a strict proportionality to L might well be observable, providing strong confirmation of our translationally invariant, quasi one-dimensional picture.

4. Microscopic models of the pore

Until now, we have avoided specifying the physics of the interactions within the pore. The parameters v and D have thus been left completely undetermined. In this section, show how they may be determined from a more microscopic model. We begin by studying a "straw man" model that will turn out not to reproduce the observed values of l_d; we will then speculate on what changes might be necessary to obtain results more in line with experiment.

4.1 One degree of freedom

Start by focusing on the polymer backbone, whose coordinate x tells us what length of the chain has translocated. If we simply assume that the motion of the backbone is slow compared to all the other degrees of freedom in the pore, then we can take x to be the only dynamical variable in the problem. The remaining degrees of freedom are then described by a free energy $\Phi(x)$ that depends on the polymer translocation parameter x. We split Φ into a mean slope F determined by the applied voltage drop and a part $U(x)$ that captures the details of the polymer's interactions with the pore: $\Phi(x) = U(x) - Fx$.[5] For homopolymers (provided we continue to neglect the degrees of freedom outside the pore, as described in section 3.1), $U(x)$ is periodic, with period $a = 1$ nucleotide. F is precisely the mean force introduced in Eq. 1. Our problem is now formally no different from that of a point particle diffusing in a periodic potential U and driven by a constant force F. The probability $P(x)$ of finding such a particle at a point x is governed by a Smoluchowski equation,

$$\frac{\partial P}{\partial t} = D_0 \frac{\partial}{\partial x}\left[\frac{\partial P}{\partial x} + \frac{U'(x) - F}{k_B T} P\right] . \tag{7}$$

The "bare" diffusion constant D_0 is related through an Einstein relation to some suitable hydrodynamic drag force on the polymer in the channel. It is not to be confused with the "effective" diffusion constant D that includes the effects of U and describes the polymer's motion on length scales much larger than a. As is common in theories of electrophoresis, we assume that D_0 is unaffected by the counterion flow.

The parameters v and D that describe the behavior of the PAHL system on long length scales can be calculated from Eq. 7. An approach that relies heavily on ideas of Risken [47] has been described in previous work [43], where mathematical details may be found. In the most general case, v and D have fairly complicated forms, but relatively simple limiting cases capture most of the relevant behavior. Three cases are particularly of interest: large

[5] In principle, U could depend on the applied voltage (and hence on F). We ignore this effect; many of our conclusions will in any case turn out to be insensitive to it.

and small driving force F, and large potential barriers U_0, where U_0 is defined as the difference between the minimum and maximum values of $U(x)$ in a period. For small F, v and D must satisfy an Einstein relation. Indeed, in this limit one finds,

$$v = K\frac{D_0 F}{k_B T}\left[1 + \mathcal{O}(\frac{Fa}{k_B T})\right] \quad \text{and} \quad D = KD_0\left[1 + \mathcal{O}(\frac{Fa}{k_B T})\right] , \qquad (8)$$

where K is a constant defined in terms of integrals of the exponential of $U(x)$. Thus, $v/D = F/k_B T$, as the fluctuation-dissipation theorem requires, but the effective diffusion coefficient D is in general reduced from its bare value D_0. Perhaps more surprising is the fact that a linear-response-like regime is also reached for sufficiently large F. As $F \to \infty$,

$$v = D_0 F\left[1 + \mathcal{O}(\frac{U_0}{Fa})^2\right] \quad \text{and} \quad D = D_0\left[1 + \mathcal{O}(\frac{U_0}{Fa})^2\right] . \qquad (9)$$

The physical content of this result is that when F is much larger than a typical force derived from $U(x)$, $\Phi'(x) \approx -F$, and contributions from U may be neglected entirely. In the opposite limit of large U_0, one might expect that the diffusion process can essentially be described as hopping from one potential minimum to the next. Approximate formulas based on the Kramers escape rate [48] should then apply. In fact, for large U_0 one finds

$$v \simeq K\frac{D_0}{a}\left[e^{\alpha Fa/k_B T} - e^{-(1-\alpha)Fa/k_B T}\right] \qquad (10)$$

and

$$D \simeq K\frac{D_0}{2}\left[e^{\alpha Fa/k_B T} + e^{-(1-\alpha)Fa/k_B T}\right] , \qquad (11)$$

where K is the same constant as in Eq. 8, and α is a parameter varying between 0 and 1 that describes the degree of asymmetry of $U(x)$.

We have already estimated that $l_d \equiv D/v \sim \mathcal{O}(10a)$ from data on previous PAHL experiments. A striking feature of the asymptotic forms Eq. 8 through Eq. 11 just obtained is that all three imply a much smaller value. The linear response results both yield $l_d = k_B T/F$; given our naive estimate $Fa/k_B T \approx 5$, we find $l_d \approx a/5$. For U_0 large enough that the "hopping" approximation of Eq. 11 applies, this order of magnitude is little changed even as $F \to \infty$. Indeed, in this limit Eq. 11 gives $l_d = a/2$. It is of course possible that some particular form of $U(x)$ with finite U_0 and F might lead to a value of l_d larger than $10a$. It seems more likely, however, that l_d interpolates reasonably smoothly among its various limiting values. Although v and D each separately can depend strongly on the shape of $U(x)$, their ratio is thus far less sensitive. This is essentially a consequence of dimensional analysis: The two length scales available in the problem are a and $k_B T/F$, which are

both of order a for the values of F that prevail in experiments on PAHL. We are thus led to an important conclusion: While many aspects of the experimental data agree qualitatively with a model of diffusion in a one-dimensional periodic potential, the observed widths of the translocation time distributions are inconsistent with this model if one takes $Fa \approx 5k_{\mathrm{B}}T$.

4.2 Several degrees of freedom

It is not difficult to suggest reasons for this discrepancy between the observed and the predicted values of l_d. Many, such as the possibility that $Fa/k_{\mathrm{B}}T$ might differ significantly from 5, deserve further investigation. Here, however, we would like to focus on one that seems especially interesting. Our assumption that the motion of the polymer backbone is much slower than the relaxation of every other degree of freedom in the pore was essentially unjustified. In fact, several reasonable scenarios for the microscopic dynamics of translocation violate this assumption. For example, the neutral polymer polyethylene glycol has been shown to specifically bind to certain amino acid residues in the α-hemolysin barrel [5], and something similar could certainly occur with polynucleotides. Or, a polynucleotide with significant base stacking might have to undergo a local unstacking in order to pass through the channel's 1. nm constriction [4]. It is instructive to consider a naive extension of our one-dimensional model meant crudely to describe such situations. Suppose that the pore + polymer system can be in one of two states, state 1, in which the polymer backbone can diffuse freely, and state 2, in which the backbone is trapped and cannot move. Let there be a transition rate (per time) ω_{ij} from state i to state j. This situation bears some similarities to popular models of motor proteins [49], but with the important difference that the ratio ω_{12}/ω_{21} need not violate detailed balance; a similar description has also recently been proposed for the one-dimensional motion of RNA polymerase along a polynucleotide [50]. If $P_i(x)$ is the probability that the system is in state i and that a length x of polymer has passed through the pore, the long time diffusion of the system is governed by equations of the form

$$\frac{\partial P_1}{\partial t} = D_1 \frac{\partial^2 P_1}{\partial x^2} - v_1 \frac{\partial P_1}{\partial x} - \omega_{12} P_1 + \omega_{21} P_2 \tag{12}$$

$$\frac{\partial P_2}{\partial t} = \omega_{12} P_1 - \omega_{21} P_2 \,. \tag{13}$$

In state 2, the motion is arrested, so both the velocity and the diffusion coefficient vanish. Just as in the one-dimensional, periodic case [43], this model leads to a spreading Gaussian wave packet, with velocity and diffusion coefficient determined by the behavior of the eigenvalues near zero. One finds

a velocity

$$v = \frac{v_1}{2}\left(1 + \frac{\Delta\omega}{\omega}\right) , \tag{14}$$

and a diffusion coefficient

$$D = \frac{D_1}{2}\left(1 + \frac{\Delta\omega}{\omega}\right) + \frac{v_1^2}{2\omega}\left(1 - \frac{(\Delta\omega)^2}{\omega^2}\right) , \tag{15}$$

where $\Delta\omega = \omega_{21} - \omega_{12}$ and $\omega = \omega_{12} + \omega_{21}$. Thus, if $v_1 \neq 0$ and ω and $\Delta\omega$ are chosen properly, $l_d = D/v$ can be made arbitrarily large. This is true even if D_1/v_1 remains of order a. Even in this simple example, broad peaks are possible as soon as one relaxes the constraint that the model only contain one degree of freedom. That the experimentally observed peaks are in fact broad is thus an intriguing hint as to the microscopic mechanism of translocation.

5. The strong pulling limit

So far we have always assumed, in accordance with section 3.1, that the parts of the polymer outside the pore relax faster than the degrees of freedom inside the pore. While experiments on relatively short (hundreds of nucleotide) polynucleotides probably fall within this limit, it is interesting to consider what happens when the polymer becomes as slow as the pore. One expects at least two additional regimes: one in which the polymer is still close to equilibrium, but is slower than the pore ($a/v \ll t_Z \ll Nb/v$), and one in which the polymer is far from equilibrium ($t_Z \gg Nb/v$). This section presents preliminary results on the latter case, in the limit in which the polymer is pulled through the pore so fast that it is essentially unable to respond. This is analogous to some situations encountered in gel electrophoresis in high fields, allowing us to adapt theoretical techniques developed to study electrophoresis [51,52] to our problem.

Begin by considering a polymer that has just inserted into the pore. Once the first monomer feels the electric field across the membrane, it exerts a very large tension on the next monomer, which in turn exerts a tension on the third monomer, and so on. The effects of the strong pulling at the pore thus propagate like a front into the quiescent polymer. As sketched in figure 3, behind the front, at distances less than R from the pore, the polymer segments are almost fully aligned by the pulling force, while ahead of the front they retain their unstressed configuration. The radial speed v_f of the front can be related to the speed at which the polymer is pulled through the pore by mass conservation. In a time dt, the number of aligned monomers (including those in the pore) changes by $(v + v_f)dt/b$, and the number of unstressed monomers changes by $(dN/dR)v_f dt$, where $N(R) = (R/b)^{1/\nu}$ is the number

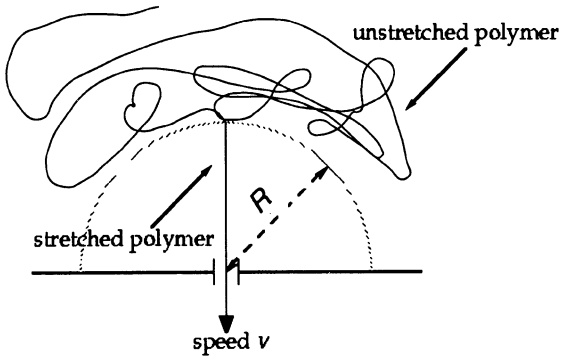

Figure 3. Schematic of polymer translocation in the strong pulling limit. A front, represented by a dotted line, has propagated a distance R into the unstretched, quiescent polymer. Behind the front, the polymer is almost fully stretched by a force that pulls it with a speed v.

of monomers within a distance R of the pore in an equilibrated polymer, and ν is the Flory exponent. Equating these fluxes, we find

$$v = v_f \left[1 + \left(\frac{R}{b}\right)^{1/\nu - 1}\right] \simeq v_f \left(\frac{R}{b}\right)^{1/\nu - 1} , \tag{16}$$

where we are mostly interested in the limit $R \gg b$. The force balance on the aligned section of the polymer then determines the velocities v and v_f. The aligned polymer, of length R, between the front and the pore contributes a hydrodynamic drag $\sim \eta R$, where η is the solvent viscosity.[6] For simplicity, we lump all of the effects of the pore into an additional drag coefficient ζ. This is expected to be correct in the limit in which an extremely strong force is applied to the polymer; at any rate, it should give at least qualitatively reasonable results. These two drag forces must equal the applied force F, whence

$$v = \frac{F}{\zeta + \eta R} . \tag{17}$$

Using Eqs. 16 and 17 to express v_f in terms of R, we can then solve the differential equation $dR/dt = v_f$ to find R, and thus the translocation parameter $x/b \sim (R/b)^{1/\nu} - R/b$, as a function of time. We find the two regimes

$$\begin{aligned} x &\sim t^{1/(2\nu+1)} \qquad (\eta R \gg \zeta) \\ x &\sim t^{1/(\nu+1)} \qquad (\eta R \ll \zeta) . \end{aligned} \tag{18}$$

[6]One can estimate that the rate of dissipation associated with accelerating the equilibrated polymer to a speed v scales like $\eta R v^2$, so we need not account for this effect separately.

Of course, these arguments have left out a number of effects. Most notably, we have not taken account of the fact that monomers will "pile up" on the *trans* side of the pore as they translocate. This is a much more difficult problem to understand than the "pulling out" from the *cis* side, but likely leads to significant additional slowing of the translocation. Even without this effect, however, the non-trivial exponents appearing in Eq. 18 make the important qualitative point that the experimentally observed scaling $x \sim t$ need not occur when the dynamics is not dominated by the pore.

6. Discussion and comparison with other approaches

As a quick perusal of this volume reveals, a number of theories have been proposed to model the behavior of polymers in pores. Despite often treating situations that differ in important particulars, many arrive at results that are at least superficially similar. For example, several authors use one-dimensional Fokker-Planck equations or find that, in the presence of a bias, the polymer's translocation time should be proportional to its length. The reader might easily wonder how (or whether) these theories differ. This section tries to address such questions. In particular we will attempt to clarify how the theory just presented relates to various other approaches in the literature.

Many of the theoretical treatments of polymers in pores are concerned with different questions from those addressed here. For example, di Marzio and Mandell [25, 36] are interested in the *equilibrium* properties of a polymer that is constrained always to remain threaded through a membrane. While their results guarantee that, if there is any electro-chemical potential difference across the membrane, the polymer will eventually translocate, they give very little information about how long this translocation will take. Lee and Obukhov [26] and Yoon and Deutsch [32] consider polymers that are threaded multiple times through a membrane with a very large number of pores. We do not believe that the reptation-inspired arguments used in this case are appropriate when there is only a single pore. A number of authors have studied when the initial insertion of a polymer in a pore is dynamically allowed. In contrast, we ignore this issue and assume that the insertion has already taken place; this assumption should be valid when the applied voltage is sufficiently large. Most of the work on insertion is limited to comparatively large pores with only hard wall interactions with the polymer [22,33]; Sebastian's study of the dynamics after insertion [53] effectively assumes the same situation by taking the polymer chain to be described by the Rouse model, even within the pore. De Gennes, however, has recently treated both the insertion and the translocation stages for the more biologically relevant situation of a narrow pore that can exert a drag force on the polymer [54]. He argues that, at least when the pore is a transient hole in a bare membrane (produced, for exam-

ple, by electroporation), the dominant source of dissipation is the parts of the polymer outside of the membrane, rather than membrane-pore interactions. We believe the opposite to be true for polynucleotides in α-hemolysin.

In addition to de Gennes, two other groups have considered polymers threaded through single, narrow pores. Both ultimately arrived at descriptions in terms of one-dimensional Fokker-Planck equations. Like us, Muthukumar [35] assumes that the translocation dynamics are dominated by the vicinity of the pore, in effect working in our pore-dominated regime. Quantities like drag coefficients are then independent of polymer length. Sung and Park [27,28,31,34], on the other hand, postulate that the standard Rouse or Zimm expressions for polymer mobilities apply to translocation. Despite considerable mathematical and physical similarities, both of these theories differ from ours in important respects. One obvious difference is that, whereas Sung and Park and Muthukumar present results for arbitrary chemical potential difference across the membrane, we have chosen to focus on the limit of strong driving ($Fa/k_{\mathrm{B}}T \gg 1/N$) appropriate to experiments in which polynucleotides are subjected to a 100 mV potential drop. In so doing, we sacrifice generality[7], but gain the ability to make detailed analytic predictions about the shape of the first passage time distribution as well as its moments. More fundamentally, both Sung and Park and Muthukumar implicitly assume that the translocation parameter x (equal to the length of polymer backbone that has passed through the pore) is the only slow degree of freedom, even within the pore. As a result, diffusion coefficients and velocities in their models cannot vary independently, but are related by an Einstein relation or by detailed balance. In contrast, we have taken the point of view that biological pores are complex and incompletely-understood systems; it may not be reasonable to assume that all of their and the polymer's internal degrees of freedom are close to equilibrium during translocation. Although we have argued that a Fokker-Planck-like description still holds without this assumption—at least in the regime where there is an (approximate) translational symmetry—the coefficients D and v are then related in a simple way only in the limit of a very small applied voltage. An Einstein relation is in many ways a very natural assumption, and it is probably valid for many systems. We firmly believe, however, that its predictions are inconsistent with the available data on polynucleotides in the α-hemolysin pore: As discussed in section 4.2, the peaks in the observed distributions of passage times are far broader than the Einstein relation predicts.

[7] Indeed, once gradients of the polymer free energy $\mathcal{F}$ are reintroduced, breaking translational invariance, it is not trivial to come up with a kinetic equation that is always valid, even when there are arbitrary slow degrees of freedom in the pore.

7. Conclusion

The central idea of this paper was first presented in the introduction: In the experiments on PAHL, and likely in other examples of the translocation of biopolymers, the channel through which the polymer passes cannot be taken to be simply a set of hard, homogeneous walls. Rather, any theory that hopes for quantitative accuracy must take into account the fact that the protein pore can both interact with the polymer and have its own dynamics. Indeed, we have argued that there is a regime in which polymer-pore interactions dominate, allowing a quasi-one-dimensional, translationally invariant description of the translocation process. One immediate consequence of this observation is that on long enough length scales, the transport of the polymer through the pore is governed by a simple phenomenological equation. Starting from this equation, we have derived several predictions about the polymer's distribution of passage times. For example, we have shown that deviations from a linear dependence of the polymer's mean translocation time on its length should be observable even for fairly long polymers. It is perhaps worth reemphasizing that these results require neither that the system be near equilibrium nor that any particular microscopic model of the pore be valid. In contrast, to predict the values of the transport coefficients v and D, one must have a more detailed understanding of what goes on within the channel. An analysis of some simple microscopic models hinted that this understanding might eventually involve several slow degrees of freedom in the pore.

Our conclusions suggest several experimental avenues that might be explored in the PAHL system. Perhaps most obvious would be to try to elucidate how translocation occurs on a more microscopic level. For example, site-directed mutagenesis might reveal that the polynucleotides have a tendency to bind to certain amino acid residues. Other experiments of interest could test the existence of a quasi-one-dimensional, translationally invariant regime. With enough data on the length dependence of $t_{\max}$, it should be possible to observe the predicted deviation from the simple guess $t_{\max} \propto L$. Further, if this data could be extended to sufficiently long polymers, deviations from the curve of figure 2 would provide information on the crossover to a regime in which the dynamics of the polymer outside the pore are slower than those inside the pore. Once experimental data of this sort becomes available, a number of new and exciting theoretical problems will doubtless become apparent.

Acknowledgments

It is a pleasure to thank Dan Branton and Jene Golovchenko for introducing us to this problem, and the organizers of this conference for the chance to participate in a stimulating and truly interdisciplinary forum. This work was

supported in part by the Harvard Materials Research Science and Engineering Laboratory through Grant No. DMR94–00396 and by the National Science Foundation through Grant No. DMR97–14725 and through a Graduate Research Fellowship.

References

[1] P.-G. de Gennes (1979) *Scaling Concepts in Polymer Physics*. Ithaca, NY: Cornell University Press.

[2] M. Doi and S. F. Edwards (1986), *The Theory of Polymer Dynamics*. Oxford, Clarendon Press.

[3] J.J. Kasianowicz, E. Brandin, D. Branton, and D.W. Deamer (1996) *Proc. Natl. Acad. Sci. (USA)* **93**, 13770–13773.

[4] M. Akeson, D. Branton, J. J. Kasianowicz, E. Brandin, and D. W. Deamer (1999) *Biophys. J.* 77, 3227-3233.

[5] J.J Kasianowicz, et al., in this volume.

[6] D. Branton and A. Meller, in this volume.

[7] D.W. Deamer, et al., in this volume.

[8] M. Akeson, et al., in this volume.

[9] I. Szabò, G. Bàthori, F. Tombola, M. Brini, A. Coppola, and M. Zoratti. (1997) *J. Biol. Chem.* **272**, 25275–25282.

[10] I. Szabò, G. Bàthori, F. Tombola, A. Coppola, I. Schmehl, M. Brini, A. Ghazi, V. De Pinto, and M. Zoratti (1998) *FASEB J.* **12**, 495-502.

[11] G. Bathori at this meeting.

[12] B. Hanss, E. Leal-Pinto, L.A. Bruggeman, T. D. Copeland, and P. E. Klotman (1998) *Proc. Natl. Acad. Sci. USA* **95**, 1921–1926.

[13] B. Dreiseikelmann (1994) *Microbiol. Rev.* **58**, 293–316.

[14] V. Citovsky and P. Zambryski (1993) *Annu. Rev. Microbiol.* **47**, 167–197.

[15] G. Schatz and B. Dobberstein (1996) *Science* **271**, 1519–1526.

[16] S.M. Simon and G. Blobel (1991) *Cell* **69**, 677–684.

[17] L. Letellier, in this volume.

[18] J.P. Tommassen, at this meeting.

[19] S. Nussberger, in this volume.

[20] S.M. Simon, in this volume.

[21] K. Kinnally, in this volume.

[22] P.-G. de Gennes (1999) *Adv. Poly. Sci.* **138**, 91–105.

[23] W. Carl (1998) *J. Chem. Phys.* **108**, 7921–7922.

[24] J. M. Deutsch and H. Yoon (1997) *J. Chem. Phys.* **106**, 9376–9381.

[25] E. A. DiMarzio and A. J. Mandell (1997) *J. Chem. Phys.* **107**, 5510–5514.

[26] N. Lee and S. Obukhov (1996) *J. Phys II France* **6**, 195–204.

[27] P.J. Park and W. Sung (1998) *Phys. Rev. E* **57**, 730–734.

[28] P.J. Park and W. Sung (1998) *J. Chem. Phys.* **108**, 3013–3018.

[29] C. S. Peskin, G. M. Odell, and G. F. Oster (1993) *Biophys. J.* **65**, 316–324.

[30] S. M. Simon, C. S. Peskin, and G. F. Oster (1992) *Proc. Natl. Acad. Sci. (USA)* **89**, 3770–3775.

[31] W. Sung and P.J. Park (1996) *Phys. Rev. Lett.* **77**, 783–786.

[32] H. Yoon and J. M. Deutsch (1995) *J. Chem. Phys.* **102** 9090–9095.

[33] E. Raphael, in this volume.

[34] W. Sung, in this volume.

[35] M. Muthukumar, in this volume.

[36] E.A. DiMarzio, in this volume.

[37] S.M. Bezrukov and J.J. Kasianowicz (1997) *Eur. Biophys J. Biophys. Lett.* **26**, 471–476.

[38] S.M. Bezrukov, I. Vodyanoy, R.A. Brutyan, and J.J. Kasianowicz (1996) *Macromolecules* **29**, 8517–8522.

[39] Y.E. Korchev, C.L. Bashford, G.M. Alder, J.J. Kasianowicz, and C. A. Pasternak (1995) *J. Membr. Biol.* **147**, 233–239.

[40] J.J. Kasianowicz and S.M. Bezrukov (1995) *Biophys. J.* **69**, 94–105.

[41] S.M. Bezrukov and J.J. Kasianowicz (1993) *Phys. Rev. Lett.* **70**, 2352–2355.

[42] L. Song, M.R. Hobaugh, C. Shustak, S. Cheley, H. Bayley, and J.E. Gouaux (1996) *Science* **274**, 1859–1866.

[43] D.K. Lubensky, and D.R. Nelson (1999) *Biophys J.* **77**, 1824–1838.

[44] J.J. Kasianowicz, S.E. Henrickson, M. Misakian, and B. Robertson (2000), *Phys. Rev. Lett.* **85**.

[45] C.R. Cantor and P R. Schimmel (1980) *Biophysical Chemistry*. Freeman: San Francisco.

[46] K. Binder (1983) in C. Domb and J.L. Lebowitz eds., *Phase Transitions and Critical Phenomena*, vol 8. Academic: London.

[47] H. Risken (1984) *The Fokker-Planck Equation*. Springer-Verlag, Berlin.

[48] N.G. van Kampen (1992), *Stochastic Processes in Physics and Chemistry* (2nd ed.). North-Holland, Amsterdam.

[49] F.Jülicher, A. Ajdari, and J. Prost (1997) *Rev. Mod. Phys.* **69**, 1269–1281.

[50] F. Jülicher and R. Bruinsma (1998) *Biophys. J.* **74**, 1169–1185.

[51] D. Long, and J.L. Viovy (1996), *Phys. Rev. E* **53**, 803–811.

[52] J.M. Deutsch (1987), *Phys. Rev. Lett.* **59**, 1255–1258.

[53] K. L. Sebastian (1999), preprint.

[54] P.-G. deGennes (1999), Proc. Natl. Acad. Sci. USA **96**, 7262–7264.

THE POLYMER BARRIER CROSSING PROBLEM

Wokyung Sung
Department of Physics and Institute of Polymer Research,
Pohang University of Science and Technology, Pohang, 790-784, Korea

Pyeong Jun Park
Biomaterials Research Center,
Korea Institute of Science and Technology, Seoul, 130-650, Korea

Keywords: Barrier crossing rate and time, Brownian ratchet, coil-to-stretch transition, free energy of translocation, Kramers problem for polymers, membrane-curvature effects, nonequilibrium fluctuations, overdamped Langevin equation, polymer adsorption effects, polymer connectivity, polymer flexibility, resonant activation, spring-bead model, Rouse modes, transmembrane chemical-potential differences.

1. Introduction

Dynamics of polymers crossing barriers is not only a basic problem in soft matter physics but also important in biological situations and applications such as polymer transport across membranes, DNA gel electrophoresis etc. While the theories of polymer dynamics in bulk situations have been successful [1], recent developments paid increasing attention to the biologically relevant situations involving polymer interactions with environments as well as the geometric confinements [2]. In this paper we review our theoretical investigations on (1) polymer translocation through a narrow pore in a membrane [3–7] and (2) dynamics of a polymer surmounting a potential barrier [8].

An important characteristic in the biopolymer translocation is the sequential transport of individual nucleic acids or amino acids through a narrow channel in a biomembrane. Once a front segment (N-terminal) passed through the channel, subsequent segments follow until the whole chain is transported completely [9]. To get an insight and relevant informations on this phenomena, simple theoretical models have been suggested and special situations have been explored experimentally. Simon, Peskin, and Oster introduced a naive picture of protein translocation, focusing on the longitudinal diffusion of a

J.J. Kasianowicz et al. (eds.), Structure and Dynamics of Confined Polymers, 261–280.

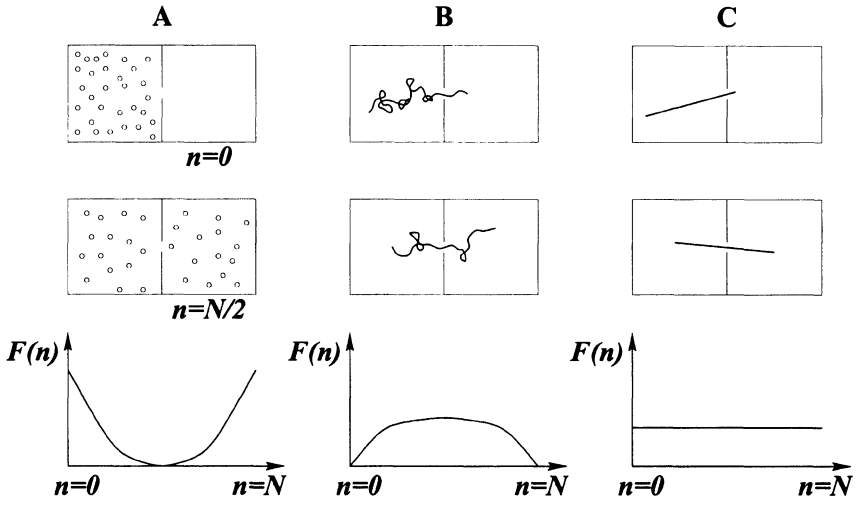

Figure 1. Translocation of (A) small molecules, (B) a flexible polymer, and (C) a rigid rod. n is the number of translocated particles and $F(n)$ is the free energy of translocation.

rigid rod in one-dimension [10]. Although their investigation is successful in demonstrating some important features relevant to the protein translocation, more realistic elements are worth to be considered. To this end, we introduced a model of polymer translocation which can readily be extended to examine much of the relevant driving mechanisms in reality as well as the chain flexibility effects. Experimentally, threading a polymer through a narrow pore under external driving force was investigated in some situations by [11] and in other reports in this book.

Polymers have unique features manifested in crossing barriers, namely, the connectivity, flexibility, and sensitivity to external bias. In contrast to the gas of particles, the linear connectivity of polymers makes the cooperative translocation possible. Consider a textbook example that N gas particles are confined initially in a compartment with a small pore connected to another compartment as shown in Fig. 1 A. Then the molecules spontaneously redistribute to maximize the total entropy of the system, resulting in the equally distributed state in the two compartments. However, a polymer, a linear array of N interconnected particles, threading a pore exhibits completely different behavior. When half of the segments are located in each compartment, the conformational free energy of the polymer has a maximum value. Therefore, the threading polymer will spontaneously be released to either side of the two compartments with equal probability. The polymer translocation from one compartment to the other is essentially a process crossing over an entropic

barrier shown in Fig. 1 B (calculated in Eq. 11), arising from the chain connectivity and also from its flexibility. If, on the other hand, the polymer loses its flexibility and looks like a rigid rod as depicted in Fig. 1 C, the translocation does not accompany any change in its conformational entropy since it has only the translational and rotational degrees of freedom of the whole rod.

Similar effects also manifest in the potential barrier crossing of polymers. In contrast to the gas of N independent particles, or the opposite limit, a rigid globule composed of N beads, a polymer has internal collective degrees of freedom arising from the flexibility and connectivity. These features cause a conformational transition at the barrier peak, depending upon the chain length and the curvature of the potential barrier. Beyond threshold values of the chain length or the potential parameters, for instance, the polymer at the barrier peak assumes a stretched conformation to lower the activation free energy associated with the barrier crossing. This eventually gives rise to a crossing rate of polymers significantly enhanced over those of the two limiting situations. Moreover, the crossing rate may have a resonance behavior as either the chain length or the potential parameters change, which has a potential applicability to the macromolecular separation in practice.

Another related feature to emphasize is the sensitivity of the long chain to an external bias, which is originated from the chain connectivity. In the presence of an external driving, the chain segments respond all hand in hand rather than as individuals. Therefore, a minute strength of external fields may result in a dramatic effect on the dynamics of the whole chain. This cooperativity of chains is the manifestation of the first order phase transition [12] in the chain partitioning behavior between the two compartments, as elsewhere discussed by Di Marzio in this book.

The external biases or the external fields can be time-dependent and fluctuating in general. Recently the noise-assisted phenomena, such as the stochastic resonance or coherence to time-dependent fields and the stochastic ratchet driving the rectified motion [13], have been active research areas. How can these novel stochastic phenomena manifest in polymers? As is well-known, the polymer conformation is a stochastic process in imaginary time and its interplay with the real time stochastic process of barrier crossing is expected to result in many interesting features as will be discussed in this paper.

We are interested in the mean time τ or the rate $\mathcal{R}$ of thermally activated barrier crossing of the whole chain from one side of a membrane or free energy curve to the other side. In dealing with dynamics of complex systems in that level, we must project the description (coarse grain) in terms of a few relevant variables. Assuming that the translocation is the only slow process described by a variable q, we model the process in terms of the overdamped

Langevin equation

$$\Gamma(q)\dot{q} = -\frac{\partial F(q)}{\partial q} + \xi(t), \tag{1}$$

where $\Gamma(q)$ and $F(q)$ are the damping coefficient and the free energy associated with (change of) q. The $\xi(t)$ is the (equilibrium) thermal noise that underlies q, i.e., the white and Gaussian noise that satisfies the fluctuation-dissipation theorem,

$$\langle \xi(t)\xi(0) \rangle = 2\Gamma(q)T\delta(t), \tag{2}$$

where $\langle \cdots \rangle$ is the thermal average and T is the noise strength or the thermal energy ($T \equiv \beta^{-1}$).

A description equivalent to the above Langevin equation is given by the Fokker-Planck equation

$$\frac{\partial}{\partial t} P(q,t) = \mathcal{L}_{FP} P(q,t) \tag{3}$$

where $P(q,t)$ is the time-dependent probability density of the variable q, and $\mathcal{L}_{FP}$ is given by

$$\mathcal{L}_{FP}(q) = \frac{\partial}{\partial q} D(q) e^{-\beta F(q)} \frac{\partial}{\partial q} e^{\beta F(q)} \tag{4}$$

with $D(q) = T/\Gamma(q)$. The average time to cross the free energy barrier from the initial state q_0 to the final state q is the mean first passage time, $\tau(q_0, q)$, satisfying the equation [14]

$$\mathcal{L}^{\dagger}_{FP}(q_0)\tau(q_0, q) = -1, \tag{5}$$

where $\mathcal{L}^{\dagger}_{FP}$ is the adjoint Fokker-Planck operator

$$\mathcal{L}^{\dagger}_{FP}(q) = e^{\beta F(q)} \frac{\partial}{\partial q} e^{-\beta F(q)} D(q) \frac{\partial}{\partial q}. \tag{6}$$

In finding the τ for a variety of situations as next, it remains essential to determine q and to model the $F(q)$ and the $\Gamma(q)$.

2. Translocation through a narrow pore

2.1 Free energy of polymer translocation

Let us assume that the translocation pore is (fixed to be) small enough to allow only a single segment passage and the membrane has a negligible thickness. We choose the q, the relevant coordinate of polymer translocation,

to be n, the number of segments translocated into the *trans* side. Then the threading chain consisting of N segments can be considered as two independent chains of n and $N-n$ segments in *trans* and *cis* sides with one end anchored on the membrane surface, respectively. We calculate the associated free energy, $F(n)$, using polymer partition function Z, which is obtained by the Green's functions $G_n(\mathbf{r}, \mathbf{r}_0)$ and $G_{N-n}(\mathbf{r}, \mathbf{r}_0)$, the probability densities of finding the free ends at $\mathbf{r}$ given the anchors at $\mathbf{r}_0$ on the surface with n and $N-n$ segments respectively [3]:

$$Z = \int d\mathbf{r} G_{N-n}(\mathbf{r}, \mathbf{r}_0) \int d\mathbf{r}' G_n(\mathbf{r}', \mathbf{r}_0) \tag{7}$$

$$F(n) = -T \ln Z \tag{8}$$

$$= \frac{1}{2} T \ln [n(N-n)] + \text{const.} \tag{9}$$

In the above the Green's function is given by

$$G_n(\mathbf{r}, \mathbf{r}_0) = \left[\frac{2\pi n b^2}{3}\right]^{-3/2} \left[e^{-\frac{3(\mathbf{r}-\mathbf{r}_0)^2}{2nb^2}} - e^{-\frac{3(\mathbf{r}+\mathbf{r}_0)^2}{2nb^2}}\right] \tag{10}$$

with b defined as the Kuhn segmental length. We assumed the Gaussian chain statistics and included the steric interaction between the chain and the membrane by imposing the absorbing boundary condition on the membrane surface in calculating the Green's function. Consideration of self-avoiding chain can be easily implemented (M. Muthukumar in this book) but does not incur significant changes in the translocation behavior. With the chemical potential difference $\Delta\mu \equiv \mu_i - \mu_o$ per segment between inside and outside of a cell, the free energy function associated to the polymer translocation is obtained as

$$F(n) = \frac{1}{2} T \ln [n(N-n)] + n\Delta\mu. \tag{11}$$

The shape of the free energy, with $\Delta\mu = 0$, is symmetric as shown in Fig. 1 B, but, remarkably, a minute chemical potential difference per segment can easily break the symmetry for a very long chain, because the first term in Eq. 11 arising from the chain entropy is dominated by the second. For the case of a rigid rod, the entropic term in Eq. 11 is simply vanishing and the free energy is linear in n.

2.2 Analysis of translocation time: the effect of chemical potential bias

The translocation of the whole chain from *cis* to *trans* side can be regarded as a stochastic process $n(t)$ crossing over the free energy barrier given by Eq.

11. Then the translocation time, τ, defined as the mean first passage time from $n = 0$ (reflecting boundary) to $n = N$ (absorbing boundary) can be obtained from the solution of Eq. 5 as follows

$$\tau \equiv \frac{b^2}{D} \int_0^N dn e^{\beta F(n)} \int_0^n dn' e^{-\beta F(n')}. \tag{12}$$

Here D is the constant diffusion coefficient of the whole chain given as $D = T/\Gamma$.

For $\Delta\mu = 0$, τ is integrated to be

$$\tau = \frac{\pi^2}{8} \frac{L^2}{2D}, \tag{13}$$

which can be compared to the translocation time of a rigid rod given by

$$\tau_0 = \frac{L^2}{2D}. \tag{14}$$

Here $L = Nb$ is the chain contour length. Comparing Eq. 13 and Eq. 14, one can see that the chain flexibility retards the translocation by the factor of $\pi^2/8 \approx 1.23$. Now let us focus upon the D, or Γ, the total friction of translocating chain, which should be a sum of contributions from the solvent, Γ_S, and from the pore, Γ_P. In the regime where $\Gamma_S \gg \Gamma_P$, we have $D = T/\Gamma_S$, and then by assuming the Rouse model, $\Gamma_S = N\gamma$ (γ: segmental friction),

$$\tau \sim N^3. \tag{15}$$

In the opposite regime where $\Gamma_S \ll \Gamma_P$,

$$\tau \sim N^2 \tag{16}$$

since the Γ_P should be independent of N. Depending upon how the friction is modeled, therefore, the scaling behavior of τ appears different. Unless specified, we will consider the case of solvent-dominated friction.

For $\Delta\mu \neq 0$,

$$\tau/\tau_0 = Q(\mu^*) = \begin{cases} \frac{2}{|\mu^*|} & (\mu^* \ll -1) \\ \frac{1}{\mu^*} \exp \mu^* & (\mu^* \gg 1) \end{cases} \tag{17}$$

where $\mu^* \equiv N\Delta\mu/T$. As $Q(\mu^*)$ is a function of the scaling variable μ^*, rather than $\Delta\mu$, it is found that a minute chemical potential asymmetry with $|\Delta\mu| \geq T/N$ can make a dramatic change in τ. Regardless of chain flexibility, this extreme sensitivity, already implied in $F(n)$, is a cooperative phenomenon arising from chain connectivity; the segments respond all hand

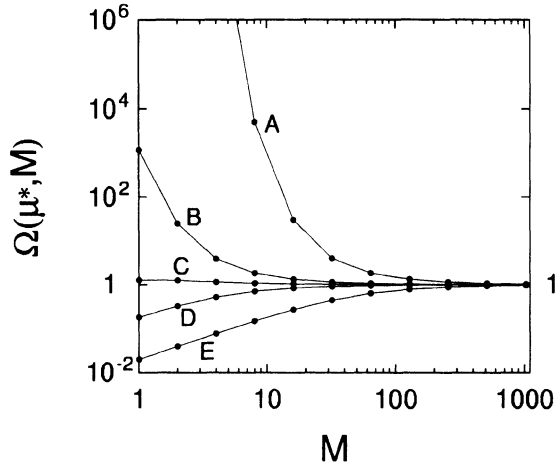

Figure 2. $\Omega(\mu^*, M)$ as a function of M for different values of μ^* ($N = 1026$, and $\mu^* = 100.$(A), 10.74(B), 0.(C), -10.74(D), $-100.$(E)). Note that $\Omega(\mu^*, M)$ goes to 1, when M is sufficiently large ($M \geq |\mu^*|$).

in hand rather than as an individual to an external bias. Depending upon Γ the scaling behavior for a negative chemical potential difference with magnitudes $|\Delta\mu| \geq T/N$ also changes; in the regime of $\Gamma_S \gg \Gamma_P$,

$$\tau \sim N^2/|\Delta\mu|. \tag{18}$$

In the pore friction dominated regime $\Gamma_S \ll \Gamma_P$,

$$\tau \sim N/|\Delta\mu|, \tag{19}$$

in agreements with the experiment of Kasianowicz *et al.* for single-stranded DNA or RNA translocating through an α-hemolysin channel [11].

2.3 Many ratchet effect

The Brownian ratchet (BR) originally suggested by Simon *et al.* [10] as a nonspecific driving mechanism assumes fast binding of chaperone molecules on the chain. We assume here that the chaperones, which is present only in the *trans* side, bind instantaneously and irreversibly on M discrete binding sites distributed uniformly over the contour of the translocating polymer. With this simplified view, the translocation dynamics is reduced to a consecutive unidirectional diffusion within the interval between neighboring binding sites with the boundary conditions that are reflecting and absorbing at left and right edges of each interval. The translocation time can then be written as [3]

$$\tau/\tau_0 = \frac{1}{M}\Omega(\mu^*, M), \tag{20}$$

which shows that the BR enhances the translocation efficiently by the factor of M. In addition, the BR affects the efficiency via the factor $\Omega(\mu^*, M)$ which includes the effects of chemical potential difference as well as chain flexibility (Fig. 2). If there are small number of binding sites such that $M \leq |\mu^*|$, the $\Omega(\mu^*, M)$ behaves in accordance with the sign of $\Delta\mu$; With the reverse bias ($\Delta\mu > 0$), the ratchets accelerate the translocation more effectively while the forward bias ($\Delta\mu < 0$) does not affect the translocation significantly as discussed before. On the other hand, for large enough values of M ($\geq |\mu^*|$), the result, $\Omega(\mu^*, M) \simeq 1$, implies that the BR suppresses the effect of $\Delta\mu$, irrespective of its sign, and the entropic barrier arising from the chain flexibility.

2.4 Polymer adsorption effect

One important factor in the polymer translocation is the polymer interaction with the membrane surface apart from the interaction with the pore. In addition to the steric repulsion, which is the origin of the entropic barrier discussed earlier, membranes can have attractive interaction with the polymer. If a polymer, as the result, can be adsorbed on membrane in the *trans* side but not in the *cis* side, it would be driven to the *trans* side to minimize the total free energy. To quantitatively examine this adsorption effect, we consider a well-known theory of polymer adsorption in terms of the boundary condition:

$$\left[\frac{\partial}{\partial z} \ln G_n(\mathbf{r}, \mathbf{r}')\right]_{membrane\ surface} = c. \tag{21}$$

Here c is the interaction parameter in a function of temperature as well as attraction strength and range, which can be determined using a microscopic description of polymer adsorption on a short-range attractive surface. By integrating the Green's function of the polymer, the free energy as a function of the translocation coordinate n can be obtained as [5]

$$F(n) = \frac{1}{2}T \ln(N-n) - T\left[\frac{nb^2c^2}{6} + \ln \mathrm{erfc}(\sqrt{\frac{n}{6}}bc)\right] \tag{22}$$

where $\mathrm{erfc}(x)$ is the complementary error function. For $T \gg T_c$, with T_c defined as the adsorption-desorption temperature, $c \to \infty$ and the transmembrane polymer does not feel attractive interaction, yielding the free energy and the resulting translocation time given by Eqs. 9 and 13, respectively.

As the temperature is lowered, the attractive interaction drives the polymer to the *trans* side. At $T = T_c$, $c = 0$ and Eq. 22 is reduced to

$$F(n) = \frac{1}{2}T \ln(N-n) \tag{23}$$

yielding a downhill to the *trans* side in the free energy landscape. Then the translocation time for the solvent dominated friction ($\Gamma_S \gg \Gamma_P$) becomes

$$\tau = \frac{2}{3}\left(\frac{L^2}{2D}\right) \sim N^3, \tag{24}$$

with the prefactor reduced from $\pi^2/8$ to $2/3$ compared to the high temperature limit. In this case, the steric interaction in the *trans* side is canceled off by the attractive interaction, but τ still remains proportional to N^3.

For $T \ll T_c$, c behaves as $c \sim -(u_0/T)^{1/2}/b$, with u_0 the attraction potential strength per segment [5], and the free energy becomes

$$F(n) \simeq \frac{1}{2}T\ln(N-n) - T\left[\frac{nb^2c^2}{6}\right]. \tag{25}$$

Then the translocation time is obtained as

$$\tau = \left(\frac{L^2}{2D}\right)\frac{2}{Nb^2c^2/6} = \left(\frac{L^2}{2D}\right)\frac{2}{N\beta u_0}. \sim N^2, \tag{26}$$

In this low temperature regime, the free energy of transmembrane polymer is dominated by the attraction energy which is linearly proportional to n, where the prefactor of n, the u_0, can be interpreted as the energy per segment in *trans* side, or transmembrane segmental energy bias that features as "chemical potential difference" between the two sides of the membrane, as studied in the earlier section.

2.5 Membrane-curvature effect

Suppose that a polymer of N segments is translocating out of a spherical vesicle of radius R through a pore. When n segments are in the outside and $N-n$ segments inside, the polymer free energy is given by [6]

$$\begin{aligned} F(n) &= F^{out}(n;R) + F^{in}(N-n;R) \\ &= -T\ln\left[1+\sqrt{\frac{6R^2}{\pi nb^2}}\right] - T\ln\sum_{k=1}^{\infty} e^{-\frac{\pi^2b^2(N-n)}{6R^2}k^2}. \end{aligned} \tag{27}$$

For $R \gg N^{1/2}b$, $F(n)$ exhibits nearly symmetric barrier as in the case of planar membrane, i.e. $F(n)$ becomes identical to Eq. 9 in the limit $R \to \infty$. However, for R approximately smaller than the radius of gyration $R_G \sim N^{1/2}b$, $F(n)$ becomes a decreasing function of n

$$F(n) \simeq -T\ln\left[1+\sqrt{\frac{6R^2}{\pi nb^2}}\right] + T\frac{\pi^2b^2(N-n)}{6R^2}, \tag{28}$$

thereby the polymer release is favorable due to the polymer confinement entropy. Neglecting the pore friction, the translocation time again exhibits a crossover from $\tau \sim N^3$ to $\tau \sim N^2$ when R_G exceeds R.

For a chain going into the sphere, the uphill of the free energy due to the confinement entropy gives the translocation time as $\tau \sim \exp(N)$. However, the process of polymer capture into a small bud can be achieved easily when a minute chemical potential bias is applied. The critical strength is given by $\Delta\mu_c \sim (b/R)^2 T$, beyond which the capture time goes algebraically as $\tau \sim N^3$ or $\tau \sim N^2$. The excluded volume effect should be important for $R \leq R_G$, but the scaling behavior discussed remains unaltered as argued in [6].

2.6 Effects of nonequilibrium fluctuations

Since the membrane is subject to ceaseless fluctuations due to molecules of the embedding solvent as well as the membrane, the chemical potential of each segment can change in a random fashion. We model the fluctuating chemical potential difference as

$$\Delta\mu(t) = \Delta\mu + \alpha(t), \tag{29}$$

where $\alpha(t) = \pm\alpha$ is a bistable random process with flipping rate ν. It has been extensively studied how the fluctuations in force or potential influence the diffusive process of a Brownian particle [15]. An important finding is the phenomena of resonant activation, that is, minimal τ or maximal flux of particle occurs when the flipping rate becomes comparable to the inverse of the intrinsic characteristic time scale.

Confining ourselves to the translocation of a rigid chain, we introduce a joint probability density $P_\pm(n,t)$ to find $n(t) = n$ and $\alpha(t) = \pm\alpha$ simultaneously [7]. Then the Fokker-Planck equation for $P_\pm(n,t)$ is given by

$$\frac{d}{dt}\begin{bmatrix} P_+(n,t) \\ P_-(n,t) \end{bmatrix} = \begin{bmatrix} -\nu + \mathcal{L}_+ & \nu \\ \nu & -\nu + \mathcal{L}_- \end{bmatrix}\begin{bmatrix} P_+(n,t) \\ P_-(n,t) \end{bmatrix} \tag{30}$$

where $\mathcal{L}_\pm$ is the Fokker-Planck operators for $n(t)$ when $\alpha(t) = \pm\alpha$,

$$\mathcal{L}_\pm = \frac{D}{b^2}\frac{\partial}{\partial n}\left[\frac{\partial}{\partial n} + \beta\left(\Delta\mu \pm \alpha\right)\right]. \tag{31}$$

By solving the Eq. 5, the translocation time τ is found to exhibit a local minimum at some flipping rate, e.g. $\nu \simeq (L^2/2D)^{-1}$, as mentioned above. The resonant (minimum) translocation time as a function of the scaled fluctuation amplitude $q^* = N\alpha/T$ in chemical potential difference is shown in Fig. 3. It can be seen that the translocation tends to be more rapid as the fluctuation amplitude q^* increases. For the reverse chemical potential bias of

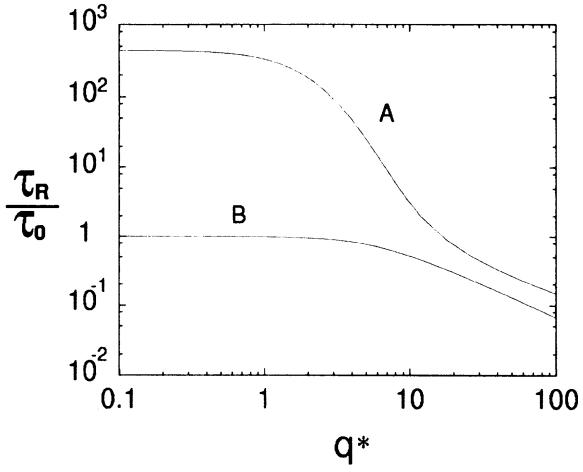

Figure 3. Resonant (minimal) translocation time τ_R in units of $\tau_0 \equiv L^2/(2D)$ versus chemical potential fluctuation amplitude $q^* = N\alpha/T$ (A: $N\Delta\mu/T = 10$, B: $N\Delta\mu/T = 0$). For large fluctuation amplitude, τ_R is determined mainly by q^*.

the magnitude, e.g. $\Delta\mu = 10T/N$ as shown in Fig. 3 A, the speed-up due to the fluctuation is dramatic. Compared with single particle transport, the resonant value of the translocation time becomes much more sensitive to the nonequilibrium fluctuations of chemical potential difference, as much as it does to the constant chemical potential bias, which is another aspect of the cooperativity due to chain connectivity.

3. Crossing a potential barrier

3.1 Generalization of the Kramers problem to polymers

In order to study the effects of the pore on the translocating chain beyond the simple geometrical constraint considered in the last section, we identify the problem as an activated crossing over a potential barrier. A broad class of polymer dynamics in nonhomogeneous media or under external fields fall into this category. As a prototype example, we consider that each monomer is subject to a Kramers metastable potential $U(x)$ (Fig. 4)

$$U(x) = \begin{cases} \frac{1}{2}\omega_0^2 x^2 & \text{near } x = 0, \\ \Delta U - \frac{1}{2}\omega_B^2 (x - x_B)^2 & \text{near } x = x_B, \end{cases} \tag{32}$$

Solving Eq. 5 for the potential with the barrier height ΔU much larger than T, the barrier crossing rate of a Brownian particle (Fig. 4 (a)) initially located in the well is given by the well-known Kramers formula [16, 17]

$$\mathcal{R}_K = \frac{\omega_0 \omega_B}{2\pi\gamma} e^{-\beta\Delta U}. \tag{33}$$

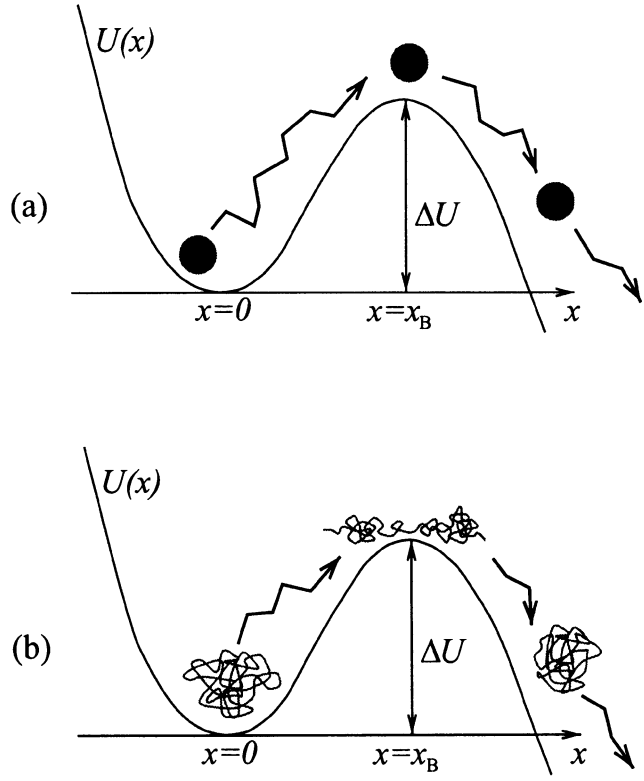

Figure 4. Schematic view of a particle and a polymer escaping from the Kramers metastable potential.

The generalization of this formula to the case of a flexible polymer is in progress. For the potential varying smoothly over the polymer length ($x_B \geq L$), it has been already worked out within the multi-dimensional barrier crossing theory [8]. Since the involved formalism is rather complicated, we give here a more straightforward consideration in the context of the theoretical methodology given in the Introduction. It is important to identify q as the center of mass of the polymer and to consider the polymer free energy with a given value of q, which will be discussed in a later section.

Consider a rigid, collapsed, globule composed of N beads (monomers). Rescaling the parameters, $U(x) \to NU(x)$, $\gamma \to N\gamma$, $\omega_0 \to N^{1/2}\omega_0$, $\omega_B \to N^{1/2}\omega_B$, in Eq. 33, the crossing rate of the globule is given by

$$\mathcal{R}_0 = \left[\frac{\omega_0 \omega_B}{2\pi\gamma}\right] e^{-\beta N \Delta U}. \tag{34}$$

Now suppose that the globule is fully unfolded into a flexible chain. We then expect the rate to be modified to

$$\mathcal{R} = \left[\frac{\omega_0\omega_B}{2\pi\gamma}\right] e^{-\beta\Delta F} \tag{35}$$

$$= \left[\frac{\omega_0\omega_B}{2\pi\gamma}\right] e^{-\beta[N\Delta U+\Delta F']}. \tag{36}$$

Here $\Delta F = F_B - F_0$ is the free energy barrier for a polymer to cross, which is much different from $N\Delta U$, due to polymer fluctuation. Equation 36 can also be derived on the basis of the multi-dimensional barrier crossing theory [8, 18]. Therefore, within the formula (Eq. 36), it remains to determine F_B and F_0, the polymer free energies with the center of mass fixed at the well bottom, $x = 0$, and at the barrier top, $x = x_B$.

3.2 The bead-spring polymer under the Kramers potential

In order to calculate the polymer free energies, we first invoke the Rouse model, where the beads (x_n, $n = 1, 2, \cdots, N$) are harmonically coupled in the nearest neighbors:

$$\gamma\frac{dx_n}{dt} = -\frac{\partial U(x_n)}{\partial x_n} - K(2x_n - x_{n-1} - x_{n+1}) + \xi_n(t). \tag{37}$$

Here $K = 3T/b^2$ is the entropic spring constant, and $\xi_n(t)$ is the thermal Gaussian noise on the n-th segment, characterized by $\langle\xi_n(t)\rangle = 0$ and $\langle\xi_n(t)\xi_m(0)\rangle = 2\gamma T\delta_{nm}\delta(t)$. In terms of the N Rouse modes,

$$x_k = \frac{1}{N}\sum_{n=1}^{N} x_n\cos(kn), \qquad k = \pi j/N \quad (j = 0, 1, 2, \cdots, N-1), \tag{38}$$

the effective Hamiltonian that generate the motion can be written as

$$\mathcal{H} = \frac{1}{2}\sum_{k=0}^{N-1}[\Omega_0(k)]^2 x_k^2 \quad (\text{near } x = 0) \tag{39}$$

and

$$\mathcal{H} = N\Delta U - \frac{1}{2}\sum_{k=0}^{N-1}[\Omega_B(k)]^2(x_k - x_B\delta_{k,0})^2 \quad (\text{near } x = x_B). \tag{40}$$

Here, the modes $\Omega_0(k)$ and $\Omega_B(k)$ are:

$$[\Omega_0(k)]^2 = \begin{cases} N\omega_0^2 & \text{for } k = 0, \\ K_k + 2N\omega_0^2 & \text{for } k \neq 0, \end{cases} \tag{41}$$

and

$$[\Omega_B(k)]^2 = \begin{cases} N\omega_B^2 & \text{for } k = 0, \\ -(K_k - 2N\omega_B^2) & \text{for } k \neq 0, \end{cases} \tag{42}$$

with

$$K_k = 8NK\sin^2(k/2). \tag{43}$$

In terms of x_k, Eq. 37 can be rewritten as

$$\Gamma_k \frac{dx_k}{dt} = -[\Omega_0(k)]^2 x_k + \xi_k(t) \quad (\text{near } x = 0) \tag{44}$$

and

$$\Gamma_k \frac{dx_k}{dt} = [\Omega_B(k)]^2 (x_k - x_B\delta_{k,0}) + \xi_k(t) \quad (\text{near } x = x_B) \tag{45}$$

where $\Gamma_{k=0} = N\gamma$ and $\Gamma_{k\neq 0} = 2N\gamma$ and $\xi_k(t)$ is the Gaussian random force which satisfies $\langle \xi_k(t) \rangle = 0$ and $\langle \xi_k(t)\xi_{k'}(0) \rangle = 2\gamma_k T\delta_{k,k'}\delta(t)$.

The Rouse mode $x_{k=0}$ is the center of mass coordinate and $x_{k\neq 0}$ are the collective conformational coordinate of the chain. The polymer free energy with the center of mass fixed at $x_{k=0} = q$ is given by

$$F(q) = -T \ln \left[\int \prod_{k\neq 0} dx_k \exp(-\beta \mathcal{H}) \right]_{x_{k=0}=q} \tag{46}$$

where we exclude $k = 0$ mode from the variables to integrate. The equation of motion for the polymer center of mass can be explicitly written as

$$(N\gamma)\frac{dq}{dt} = -\frac{\partial F(q)}{\partial q} + \xi_{k=0}(t) \tag{47}$$

$$= \begin{cases} -N\omega_0^2 q + \xi_{k=0}(t) & (\text{near } q = 0) \\ N\omega_B^2(q - x_B) + \xi_{k=0}(t) & (\text{near } q = x_B) \end{cases} \tag{48}$$

which clearly shows that the center of mass mode is stable near $x = 0$ and unstable near $x = x_B$. In view of Eq. 48, the dynamics of the center of mass mode alone yields the escape rate given in Eq. 34. To get the correct rate $\mathcal{R}$, however, we must know ΔF which can be modified by collective Rouse modes x_k other than $x_{k=0}$.

When the center of mass is within the well, the free energy with its free space value taken out is

$$F_0' = -\frac{T}{2} \sum_{k\neq 0} \ln \left[\frac{K_k}{K_k + 2N\omega_0^2} \right] \tag{49}$$

$$\simeq \frac{1}{2}T\ln\left[\frac{\sinh(N\omega_0/\sqrt{K})}{N\omega_0/\sqrt{K}}\right] \tag{50}$$

$$\simeq \begin{cases} N^2\omega_0^2 T/12K = N^2\omega_0^2 b^2/36 & \text{for } s_0 \ll 1, \\ TN\omega_0/2\sqrt{K} = N\omega_0 bT^{1/2}/2\sqrt{3} & \text{for } s_0 \gg 1. \end{cases} \tag{51}$$

Here, $s_0 \equiv N^2\omega_0^2/\pi^2 K = N^2 b^2\omega_0^2/3\pi^2 T$, roughly the ratio of the polymer potential energy in the well to "kinetic energy," is a measure of crossover in the length scaling behavior. The Eq. 49 is in complete agreements with our numerical result of lattice statistics using transfer matrix method [8]. It is noteworthy that the free energy when $s_0 \gg 1$ is the free energy of confinement in the well as confirmed in a scaling theory [8], which is an outcome of polymer flexibility in response to the potential.

The free energy with the center fixed at the barrier top is written

$$F_B = N\Delta U + F_B', \tag{52}$$

$$F_B' = \frac{T}{2}\sum_{k\neq 0}\ln\left[\frac{K_k - 2N\omega_B^2}{K_k}\right]. \tag{53}$$

One remarkable feature to note is that in order to attain the conformational stability of the polymer at the barrier top one must assure $(K_k - 2N\omega_B^2)$ to be positive for $k \neq 0$. If $2N\omega_B^2$ can be large enough to be equal to K_k, say, $K_{k=\pi/N}$ corresponding to the lowest Rouse mode, that is,

$$s_B = \frac{N^2\omega_B^2}{\pi^2 K} = 1, \tag{54}$$

the instability sets in, leading to coil-stretch transition. The transition within the Rouse model results in infinitely negative free energy due to infinite extensibility, yielding the infinite rate! This can be regarded as as a novel resonance phenomena that a soft matter like ideally flexible polymer can reveal in response to external fields. For real polymers of finite extensibility, however, such a singular behavior would not happen, but the coil-stretch transition nevertheless sets in due to the flexible degrees of freedom yet responsive to external fields.

3.3 The polymer free energy and the barrier crossing rate

In order to avoid the infinite extensibility and rate in describing the stretching behavior of polymers, we employ scaling arguments and numerical calculations using the lattice statistics. The free energy F_B' is approximately given

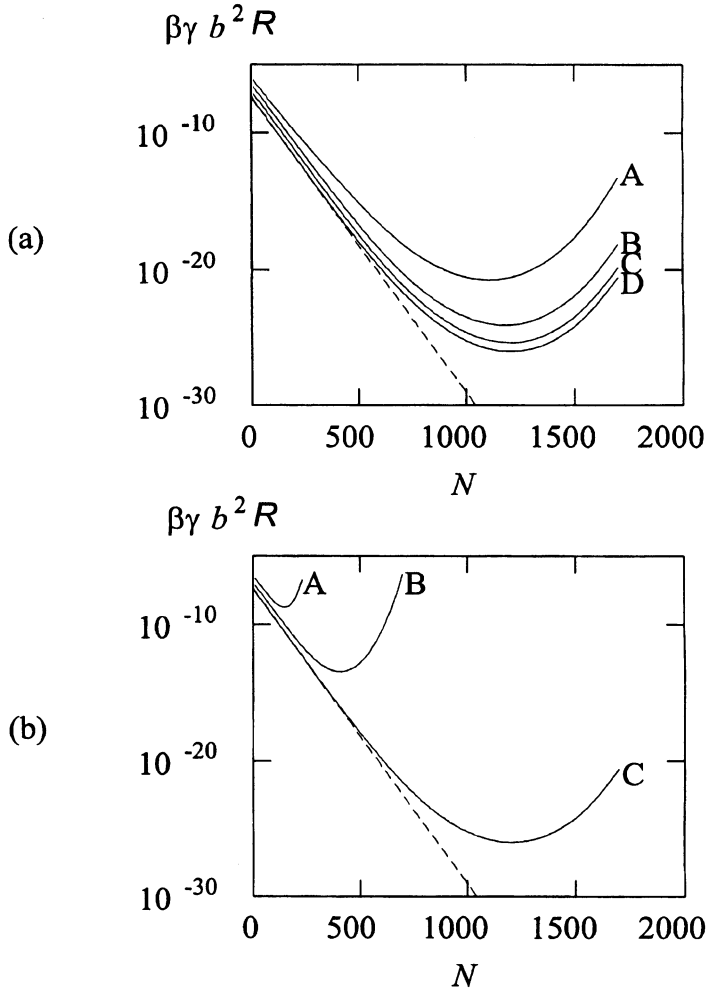

Figure 5. Barrier crossing rate $\mathcal{R}$ (in units of $T/\gamma b^2$) vs. N with $\beta\Delta U = 0.05$. (a) $\beta\omega_B^2 b^2 = 10^{-7}$ (A: $\beta\omega_0^2 b^2 = 10^{-3}$, B: $\beta\omega_0^2 b^2 = 10^{-4}$, C: $\beta\omega_0^2 b^2 = 10^{-5}$, D: $\beta\omega_0^2 b^2 = 10^{-6}$). The dotted line represents $\mathcal{R}_0$, the rate in the globular limit, with the same $\beta\omega_0^2 b^2$ as in D. (b) $\beta\omega_0^2 b^2 = 10^{-6}$ (A: $\beta\omega_B^2 b^2 = 10^{-5}$, B: $\beta\omega_B^2 b^2 = 10^{-6}$, C: $\beta\omega_B^2 b^2 = 10^{-7}$). The dotted line represents $\mathcal{R}_0$ with the same $\beta\omega_B^2 b^2$ as in C.

as

$$F_B' \simeq -\frac{1}{2}\omega_B^2 \left\langle \sum_{n=1}^{N} (x_n - x_B)^2 \right\rangle \tag{55}$$

$$\simeq \begin{cases} -N\omega_B^2 R_G^2/2 \sim -s_B T & \text{for } s_B \ll 1 \text{ (coiled state)}, \\ -N\omega_B^2 \xi^2/2 \sim -N^3 & \text{for } s_B \gg 1 \text{ (stretched state)}, \end{cases} \tag{56}$$

where we have used that the average chain length along the x-axis

$$\left[N^{-1}\sum_{n=1}^{N} x_n^2\right]^{1/2}$$

assumes the free radius of gyration $R_G \sim N^{1/2}b$ in the coiled state and the extended length $\xi \sim Nb$ in the stretched state, respectively [19]. The length scaling behavior is indeed in agreement with the numerical result [8], which we will use below.

In terms of the free energies F_0' and F_B', the rate can be written as

$$\mathcal{R} = \mathcal{R}_0 \exp\left[-\beta(F_B' - F_0')\right]. \tag{57}$$

The free energy difference $\Delta F' = (F_B' - F_0')$, which vanishes in the $N = 1$ limit and in the globule limit, represents the interplay of the conformational degrees of freedom in response to external fields, which is the Kramers potential here. Figure 5 depicts the rate for various values of the potential curvatures as a function of N, as given by the numerical results of the free energies. In any case the rate enhancement due to the fluctuation, $\mathcal{R}/\mathcal{R}_0$, is larger than unity, and increases as the chain length gets larger. Figure 5 (a) shows that as ω_0 increases the rate is more enhanced due to the increased free energy of chain confinement at the well. Similar trends obtains for the increases of ω_B due to decreases of stretch free energy to $-N^3$ scaling behavior along with turnover with a minimum around $s_B \simeq 1$, i.e. coil-stretch transition point as shown in Fig. 5 (b). The details are given below.

For the case of short chains or small curvatures, such that $s_0 \ll 1$ and $s_B \ll 1$, the polymer will behave as a Brownian particle (globule) of size $R_G \sim N^{1/2}b$ during the whole process of barrier crossing. Because $F_0' \simeq F_B' \simeq 0$ in this regime, the activation free energy is simply given by $N\Delta U$ and the crossing rate reads

$$\mathcal{R} = \frac{\omega_0\omega_B}{2\pi\gamma}\exp(-\beta N\Delta U). \tag{58}$$

In B, C and D of Fig. 5 (a) and in A, B, C of Fig. 5 (b), Arrhenius behavior, i.e. $\mathcal{R} \sim \exp(-\beta N\Delta U)$, can be seen in small N regimes for all potential parameters.

For chain lengths and curvatures such that $s_0 \gg 1$ and $s_B \ll 1$, $F_0' \gg T$ and $F_B' \simeq 0$, yielding an activation free energy

$$\Delta F \simeq N\Delta U - F_0' \tag{59}$$

$$\simeq N\left[\Delta U - \omega_0 b T^{1/2}/2\sqrt{3}\right]. \tag{60}$$

The confinement of the polymer in the metastable well reduces ΔF and, as a result, enhances the crossing rate

$$\mathcal{R} = \frac{\omega_0 \omega_B}{2\pi\gamma} \exp\left[-N\left(\beta\Delta U - \beta^{1/2}\omega_0 b/2\sqrt{3}\right)\right]. \tag{61}$$

This is shown most markedly in A of Fig. 5 (a) for small N. The polymer is confined along the x-axis in the metastable well, while it restores the isotropic Gaussian form at the barrier top.

For $s_0 \ll 1$ and $s_B \gg 1$, the internal degrees of freedom of the polymer little affect F_0', while F_B' becomes large and negative, yielding the activation free energy

$$\Delta F \simeq N\Delta U + F_B' \tag{62}$$

$$\simeq N\Delta U - gN^3\omega_B^2 b^2 \tag{63}$$

where g is a constant of the order unity. It is remarkable that F_B' can change much faster than $N\Delta U$ as N varies, giving rise to a local minimum of the escape rate at an intermediate value of N as shown in C and D of Fig. 5 (a), as well as in A, B, C of Fig. 5 (b). The polymer conformation near $x \simeq 0$ is isotropic Gaussian, while it is stretched along the x-direction near $x \simeq x_B$.

Finally, for $s_0 \gg 1$ and $s_B \gg 1$, both the effects of confinement by the well and stretching by the barrier become important in determining the activation free energy, yielding

$$\Delta F \simeq N\Delta U + F_B' - F_0' \tag{64}$$

$$\simeq N\left[\Delta U - \omega_0 b T^{1/2}/2\sqrt{3}\right] - gN^3\omega_B^2 b^2. \tag{65}$$

The resulting escape rate in this case can be significantly enhanced compared with the one given by the bare Arrhenius factor $\exp(-\beta N\Delta U)$, since $F_0' \gg T$ and $|F_B'| \gg T$. Due to the competition between surmounting the potential barrier and stretching the polymer at the barrier top, it also exhibits a minimum at a critical N, N_c, determined by the crossover condition $s_B \simeq 1$, as shown in A and B of Fig. 5 (a). The effects of self-avoidance can be assessed using scaling arguments and is found to be minor for all parameter values.

4. Summary and conclusion

We have reviewed our theoretical investigations on the polymer translocation across a membrane and more general potential barriers. Various relevant effects have been discussed and quantitatively analyzed within our simplified models. The most important lesson from these studies is that the linear connectivity and the conformational flexibility are the characteristics unique to the polymer that are revealed in the barrier crossing under realistic situations.

Due to these characteristics, the polymer behaves in a different way compared with small molecules as well as with a rigid macromolecule. Consequently the novel features involved are conformational adjustments and resonance behavior of polymers in response to the external bias or the environments. Also, it is found genuine crossover behaviors in length scaling of translocation time arise due to the cooperativity, which may have a significance in many practical applications as well as in the natural processes in a living cell.

Possible future issues include the influences from the pore, which has its own complicated structures and dynamics coupled to translocating chain. The theoretical paradigms may have to be changed in incorporating its specific interaction with the inhomogeneous sequence of the biopolymers. Also, more realistic polymer models are worth to be considered to examine the chain semiflexibility as well as the intrachain interactions of various origin. The nonMarkovian and nonequilibrium fluctuation dynamics of the environments requires a special attention. As the living system inherently possesses these characteristics, the dynamics of biopolymers utilizes or fights against them by consuming thermodynamic energy sources in a form of ATP, for instance. Our studies reviewed in this paper may be a starting point to explore this challenging direction.

Acknowledgments

We acknowledge the support from the Korea Research Foundation (1997, 1998, 1999) and the POSTECH special program. W. S. would like to acknowledge financial support of the Forschungszentrum Jülich, Germany, where this article was written.

References

[1] M. Doi and S. F. Edwards (1986), *The Theory of Polymer Dynamics*, Oxford: The Clarendon Press.

[2] A. Baumgärtner and J. Skolnick (1995), *Phys. Rev. Lett.* **74**, 2142.

[3] W. Sung and P. J. Park (1996), *Phys. Rev. Lett.* **77**, 783.

[4] W. Sung and P. J. Park (1998), *Physica A* **254**, 62.

[5] P. J. Park and W. Sung (1998), *J. Chem. Phys.* **108**, 3013.

[6] P. J. Park and W. Sung (1998), *Phys. Rev. E* **57**, 730.

[7] P. J. Park and W. Sung (1998), *Int. J. Bifurcation and Chaos* **8**, 927.

[8] P. J. Park and W. Sung (1999), *J. Chem. Phys.* **111**, 5259.

[9] B. Alberts, D. Bray, J. Lewis, M. Raff, K. Roberts, and J. D. Watson (1994), *Molecular Biology of The Cell*, 3rd ed., New York: Garland Publishing, Inc.

[10] S. M. Simon, C. S. Peskin, and G. F. Oster (1992), *Proc. Natl. Acad. Sci. USA* **89**, 3770.

[11] J. J. Kasianowicz, E. Brandin, D. Branton, and D. W. Deamer (1996), *Proc. Natl. Acad. Sci. USA* **93**, 13770.

[12] E. A. Di Marzio and A. J. Mandell (1997), *J. Chem. Phys.* **107**, 5510.

[13] L. Schimansky-Geier and T. Pöschel (eds.) (1997), *Stochastic Dynamics*, Springer-Verlag.

[14] H. Risken (1984), *The Fokker-Planck Equation*, Springer-Verlag.

[15] L. Gammaitoni, P. Hänggi, P. Jung, and F. Marchesoni (1998), *Rev. Mod. Phys.* **70**, 223.

[16] H. A. Kramers (1940), *Physica (Utrecht)* **7**, 284.

[17] P. Hänggi, P. Talkner, and M. Borkovec (1990), *Rev. Mod. Phys.* **62**, 251.

[18] J. Langer (1969), *Ann. Phys.* **54**, 258.

[19] D. M. Kroll and G. Gompper (1995), *J. Chem. Phys.* **102**, 9109.

BROWNIAN RATCHETS AND THEIR APPLICATION TO BIOLOGICAL TRANSPORT PROCESSES AND MACROMOLECULAR SEPARATION

Imre Derényi and R. Dean Astumian
Department of Surgery, MC 6035, University of Chicago, 5841 S. Maryland Ave., Chicago, IL 60637

Abstract Non-equilibrium fluctuations, whether generated externally or by a chemical reaction far-from-equilibrium, can drive directed motion along an anisotropic structure without thermal gradients or net macroscopic forces, simply by biasing Brownian motion. Systems operating on this principle are often referred to as "Brownian ratchets", and the transport in such systems is called "fluctuation driven transport". Brownian ratchets have been invoked as a possible explanation of the operation of molecular motors and pumps, but may also find application in other fields, such as particle separation or the design of nanoscale motors. Here we present a specific ratchet model for the operation of two microtubule based molecular motors, kinesin and ncd. This model can reproduce all the available mechanical data on the motion of these motors and, in addition, accounts for their directionality. We will also summarize some of the recently proposed macromolecular separation techniques based on geometrical ratchets. The main advantages of these new techniques are that the geometry of the devices can be chosen at will, the devices can be reused, molecules can be sorted continuously, and the separation can be easily automated.

Keywords: Brownian motion, Brownian ratchets, chemical kinetics, fluctuation driven transport, geometrical ratchets, kinesin, membrane transporters, microtubule, molecular motors, ncd, separation, transport processes.

1. Introduction

1.1 Molecular motors

The tiny machines in a living cell that are responsible for transport processes other than pure diffusion are motors—molecular motors. Some well known examples are kinesins that walk along microtubules carrying organelles, and myosins that move along actin filaments inducing muscle contraction. But molecular motors are also responsible for the transcription of the genetic code,

J.J. Kasianowicz et al. (eds.), Structure and Dynamics of Confined Polymers, 281–294.

the synthesis of ATP, and many transport processes across membranes. In general molecular motors use far-from-equilibrium chemical processes (such as ATP hydrolysis, or proton flow through a membrane) to drive a number of processes.

1.2 Physics of microscopic objects

The physics of a microscopic motor is fundamentally different from the physics of its macroscopic counterpart, and requires a completely different description. First, at molecular length and velocity scales, the Reynolds number is small, the motion is overdamped, and inertia plays no role: the velocity and not the acceleration of the objects is proportional to the force acting on it [1]. Second, there is Brownian motion: microscopic objects are randomly kicked around by molecules of the surrounding medium, and any deterministic motion is on top of thermal noise.

The time scale of a motor is determined by that of the velocity and acceleration as well as the electromagnetic properties of its moving parts. For a macroscopic motor the parts and coils are all large so the time constants are long and the thermal fluctuations are usually negligible. These motors suppress stochasticity by design. On the other hand, for a microscopic motor every degree of freedom has inevitably a significant thermal energy $\frac{1}{2}k_{\mathrm{B}}T$ on average (T denotes here the absolute temperature and k_{B} is the Boltzmann coefficient), and the timing of the process is set by thermally assisted events (such as diffusion or activated transitions over energy barriers). Microscopic motors are designed to operate in a stochastic, overdamped environment and harvest rather than suppress thermal fluctuations.

1.3 Brownian ratchets

For the description of molecular motors a new statistical physical principle, the so called "fluctuation driven transport" has been developed [2–4]. To understand this principle, let us imagine a periodic but spatially asymmetric potential, as illustrated by the sawtooth potential in Fig. 1a, and an overdamped Brownian particle moving in it. Such systems are often referred to as "Brownian ratchets". If a Brownian ratchet is in thermal equilibrium, the second law of thermodynamics states that no net motion of the particle can occur, i.e., the average displacement of the particle must be zero. This was illustrated in the famous lectures of Feynman [5]. To generate net motion non-equilibrium fluctuations must be applied. For molecular motors these non-equilibrium fluctuations are supplied by far-from-equilibrium chemical processes, and the interaction between the motor and its track plays the role of the periodic and asymmetric ratchet potential.

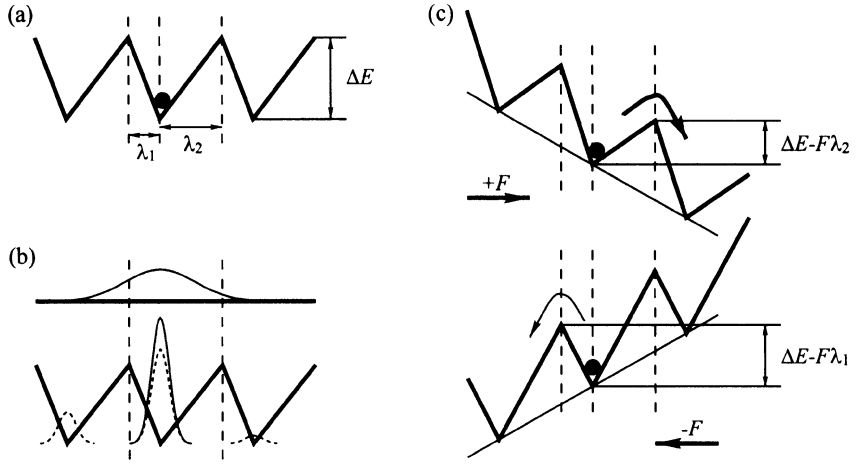

Figure 1. The motion of a Brownian particle (a) in a sawtooth shaped potential due to the effect of (b) a fluctuating potential (flashing ratchet), and (c) a fluctuating external force (rocking ratchet).

One example for Brownian ratchets is the "flashing ratchet", where the ratchet potential fluctuates between two states. In Fig. 1b one of the two states has a sawtooth shape and the other one is flat. Let us now follow the time evolution of the probability density of the particle, illustrated by the Gaussian curves. If the temperature is small enough and the potential is in the sawtooth shaped state, the particle stays near the bottom of a well (solid line). When the potential changes to the flat state, the particle starts to diffuse. After some time, changing back to the sawtooth shaped state, the particle will be captured by the neighboring well on the left with larger probability than on the right (dashed lines). This leads to a net motion to the left. Not surprisingly, when this system is in thermal equilibrium, i.e. when the transition rates between the two states obey detailed balance, the net motion is zero. The non-equilibrium transition rates, required for net motion, can be imposed either externally or by far-from-equilibrium chemical processes.

Another basic example is the "rocking ratchet", where the ratchet potential is tilted to the right and left alternately by an external force with zero time average. When a force F in Fig. 1c points to the right, the energy barrier for jumping to the right becomes shorter by F times the longer distance λ_2. When the same force points to the left, the energy barrier for jumping to the left becomes also shorter but only by F times the shorter distance λ_1. Thus, a net motion to the right is expected. When the fluctuating force is an equilibrium white noise, the net motion is zero. This type of non-equilibrium

fluctuating force is hard to generate by chemical reactions, however, it can be easily realized in man-made devices, such as in particle separators.

2. Kinesin and ncd

Kinesin, a motor protein that moves along microtubules, was discovered in the mid-1980's [6]. Further studies have led to the identification of a large number of proteins that are related in structure to kinesin and constitute the kinesin superfamily of motor proteins. Native kinesin is a dimeric molecule with a tail and two globular head domains (Fig. 2a). The heads are highly conserved, and each contains an ATP and a tubulin binding site. The more or less extended tail interacts with the cargo.

2.1 Experimental results

Recent experimental studies [7–13] have revealed that kinesin moves unidirectionally parallel to the microtubule protofilaments towards the "+" end of the microtubule with discrete steps hydrolyzing one ATP during each step. The step size ($\sim$ 8 nm) is identical to the periodicity of the protofilaments, and

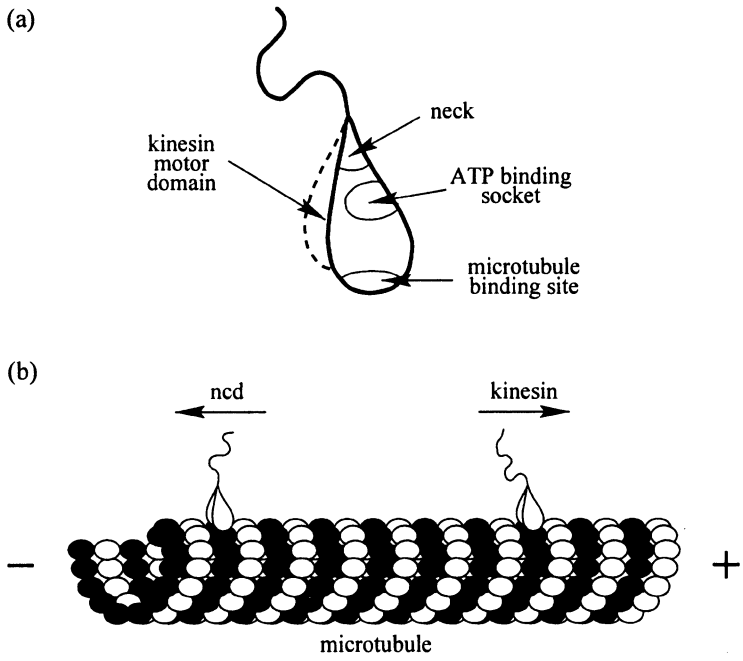

Figure 2. (a) Schematic drawing of the two-headed kinesin molecule. (b) Kinesin and ncd are structurally very similar proteins and bind on the microtubule with similar orientations, yet, they move in opposite directions.

the kinesin heads can bind only to the β-tubulins (black circles in Fig. 2b). Under an increasing load the speed of the kinesin decreases almost linearly and comes to a halt at the stall force ($\sim$ 5 pN).

Most of the models based on Brownian ratchets [14–17] are able to reproduce the experimentally measured mechanical data. These models assume that the asymmetry of the interaction potential between the kinesin head and the microtubule determines the direction of motion.

However, several members of the kinesin superfamily, such as ncd (non-claret disjunctional protein) move in the opposite direction, towards the "–" end of the microtubule (Fig. 2b). This raises a big question: What is the origin of the opposite directionality? The motor domains of kinesin and ncd are structurally very similar and bind on the microtubule with similar orientations [18–20]. So it is hard to imagine that the interaction potential between the motor domain and the microtubule is significantly different for these two motors. The mystery was deepened by a recent elegant experiment [21], in which a chimera was formed by attaching the motor domain of ncd to the neck region of kinesin. Surprisingly, the resulting motor catalyzed "+" end directed motion characteristic of kinesin, from which the neck (and not the motor) region was taken. Attaching the motor domain of kinesin to the neck region of ncd [22] led to similar results: the directionality of the chimera was determined by the neck region. Moreover, changing just a few amino acids in the neck can reverse the directionality of the motor [22,23]. Structural studies also show that it is the neck region, where kinesin and ncd differ the most [23].

For the explanation of the directionality we propose a ratchet model, based on the flashing ratchets, where the direction of motion is controlled by subtle differences in the chemical mechanism of ATP hydrolysis, rather than by differences in the interaction with the microtubule [24,25].

2.2 Chemically reversible model

To understand the model, let us first consider the enzymatic cycle shown in Fig. 3. The enzyme (E) binds a substrate (S), converts it to product (P), then releases it. Assuming that this reaction is far from equilibrium, the reverse processes can be neglected. The interaction between the enzyme and the polymeric filament, along which the enzyme moves, is described by two ratchet potentials. Each period of the ratchet potentials has two energy minima. One of them has a relatively low energy (denoted by L) and the other one has a relatively high energy (denoted by H).

In this system, if substrate binding is slow and the product release is fast, the enzyme moves one period to the right for every cycle. This can be seen easily by following the solid arrows in Fig. 3. Because substrate binding

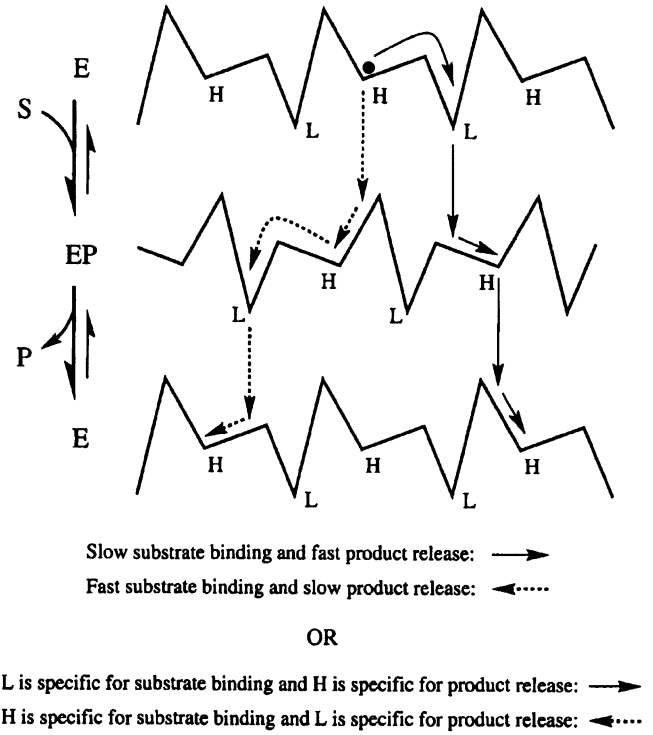

Figure 3. Brownian ratchet description of a chemically reversible motor. The direction can be controlled either by the relative rates of substrate binding and product release, or by the specificity of the H and L states.

is slow, the enzyme in state E has enough time to relax to the position L. Upon binding the substrate the enzyme gets into the position H of state EP. But because the release of the product is fast, the enzyme in state EP cannot spend enough time to relax to position L. Thus, upon releasing the product the enzyme gets into the position H of state E, which is exactly one period to right from the initial position.

On the other hand, if substrate binding is fast and the release of the product is slow, the enzyme moves one period to the left for every cycle (as illustrated by the dotted arrows in Fig. 3): Because substrate binding is fast, the enzyme in state E does not have enough time to relax to position L. Thus, upon binding the substrate the enzyme gets into the position H of state EP. But because now the release of the product is slow, the enzyme in state EP has enough time to relax to the position L. Upon releasing the product the enzyme gets into the position H of state E, which is now exactly one period to left from the initial position.

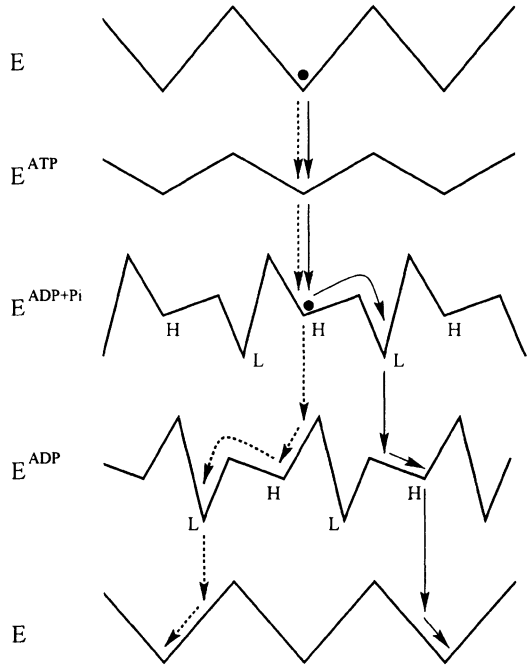

Figure 4. The chemically reversible ratchet model of Fig. 3 incorporated into the ATP hydrolysis cycle of kinesin (or ncd).

Thus, by simply changing the chemical transition rates relative to the mechanical transition rates, one can reverse the direction of the motion. Basically, we have two different asymmetric potentials, and the direction of the enzyme's motion is determined by the amount of time the enzyme spends on these potentials.

But there is a second, even simpler way of reversing the directionality, by changing the chemical specificity of the enzyme in the H and L positions. It is easy to see that if the position L of state E is specific for binding the substrate and the position H of state EP is specific for the release of the product, the motor moves to the right. Or, if the position H of state E is specific for binding the substrate and the position L of state EP is specific for the release of the product, the motor moves to the left.

This simple enzymatic cycle can be easily incorporated into the complicated chemical cycle of kinesin and ncd, as illustrated in Fig. 4. Here a slight change in the release rates of the inorganic phosphate P_i and the ADP molecules can reverse the direction of motion. This is consistent with experimental results: Since the neck region of kinesin is very close to the ATP binding socket, the neck has the potential to modify the chemistry of the ATP hydrolysis

cycle, but has no chance to significantly modify the interaction between the microtubule and kinesin.

Introducing some cooperativity between the two heads of kinesin [25], all the measured mechanical data can be reproduced. For instance, in one possible cooperative two-headed model ATP hydrolysis at the active site of one head cooperatively induces binding of ATP to the other but ATP hydrolysis at this second head cannot proceed until ADP dissociates on the first head. This ensures alternating site kinetics for the ATP hydrolysis which is well established experimentally [26], and also explains how kinesin can advance 8 nm for the hydrolysis of each ATP: Let us imagine that one of the two heads at random binds ATP. Hydrolysis of this ATP induces binding of ATP to the other head, reducing the activation barrier (see E^{ATP} state in Fig. 4) for transition to a neighboring binding site. As the first head continues through its catalytic cycle, moving a period to the right, the second head is more or less "dragged" along for the ride. Then the heads change their role and the cycle starts again.

One prediction of this model, in contrast to previous models, is that a single headed kinesin or ncd should display processivity. This prediction proved to be true in a recent experiment [27] that revealed the average speed of a single headed kinesin is similar to that of a dimer, but the motion is much more erratic. In our model this erratic motion is the consequence of the low barriers in the E^{ATP} state.

3. Membrane transporters

Although Brownian ratchets and the fluctuation driven transport have been introduced to explain the operation of molecular motors, they are also very efficient in describing molecular pumps. Let us just take a look at Fig. 5. Here also a substrate-product reaction powers the fluctuation of a transporter enzyme between two states, E and EP. In most cases this far-from-equilibrium substrate-product reaction is the ATP hydrolysis. The transported particle sees two different potentials in the two states of the transporter. When the transporter is in state E a particle can easily jump from the left side of the membrane to the potential well. A jump from the right is impeded by a high energy barrier. After transition from state E to state EP, the particle will most likely leave the transporter to the right. Thus, if the chemical and mechanical transition rates are in harmony, with this mechanism a far-from-equilibrium chemical reaction can drive the transport of molecules even against an electrochemical gradient $\Delta\mu$.

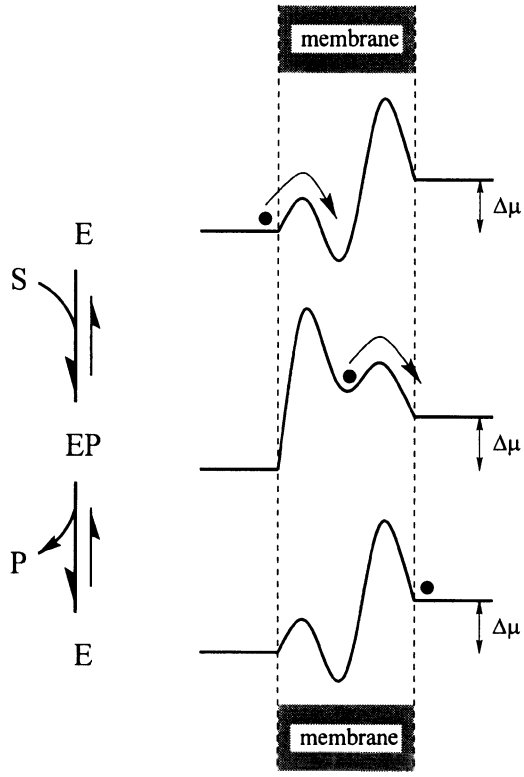

Figure 5. Illustration of a membrane transporter enzyme with two conformational states – one with a high affinity and easy access from the left, and one with low affinity and easy access from the right. Switching between the two conformations is driven by a far-from-equilibrium substrate-product reaction and leads to pumping from left to right.

4. Macromolecular separation

The concept of fluctuation driven transport has inspired researchers to find technological applications of this principle. The applications are particularly promising in particle separation [28–34]. In this section we will present some of the recently proposed macromolecular separation techniques based on geometrical ratchets.

4.1 Separation with microfabricated sieves

A recently introduced microlithographic technique [35] makes it possible to use Brownian ratchets for the separation of macromolecules with quasi-two-dimensional sieves [30–32]. The idea is to etch a two-dimensional array of micron sized obstacles on a silicon chip, which is then sealed and filled up with a medium containing the macromolecules. Fig. 6 depicts two examples

for such arrays. The molecules in these systems can move only in the space between the obstacles. If we apply a constant electrophoretic force in the y direction downwards, the molecules will migrate down. But in the course of their migration they are sometimes able to diffuse freely in the x (lateral) direction, other times they feel the asymmetric geometric constraints imposed by the obstacles. This is analogous to the flashing ratchets.

Let us follow the trajectory of a molecule with a large diffusion coefficient in Fig. 6a. After going through a hole between two obstacles, its probability density starts to spread out, as illustrated with the wider Gaussian curve. So when the molecule reaches the next row of obstacles it gets captured either by the funnel below its starting position or by the next funnel on the right. Thus, on average the molecule will drift to the right. Now let us follow the trajectory of a molecule with a smaller diffusion coefficient. Because its probability density spreads out more slowly, as illustrated with the narrower Gaussian, it will most likely be captured by the funnel below. Thus, the lateral drift of the molecule depends on its diffusion coefficient. Molecules with larger diffusion coefficients have larger lateral drift velocity, providing the basis for separation.

An important feature of this system is that it has a mirror symmetry in the y direction. This means that the lateral drift velocity of the molecules (in the x direction) is independent of the sign of the electrophoretic force (in the y direction), and hence, an alternating force in the y direction has the same

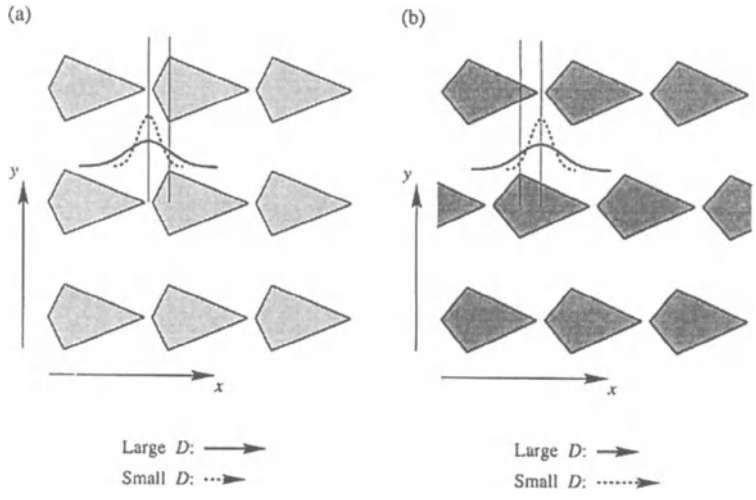

Figure 6. Schematic illustrations of the basic principle of separation with microfabricated sieves. Particles are driven downwards by an external force and drift to the right with different velocities depending on their diffusion coefficient (D).

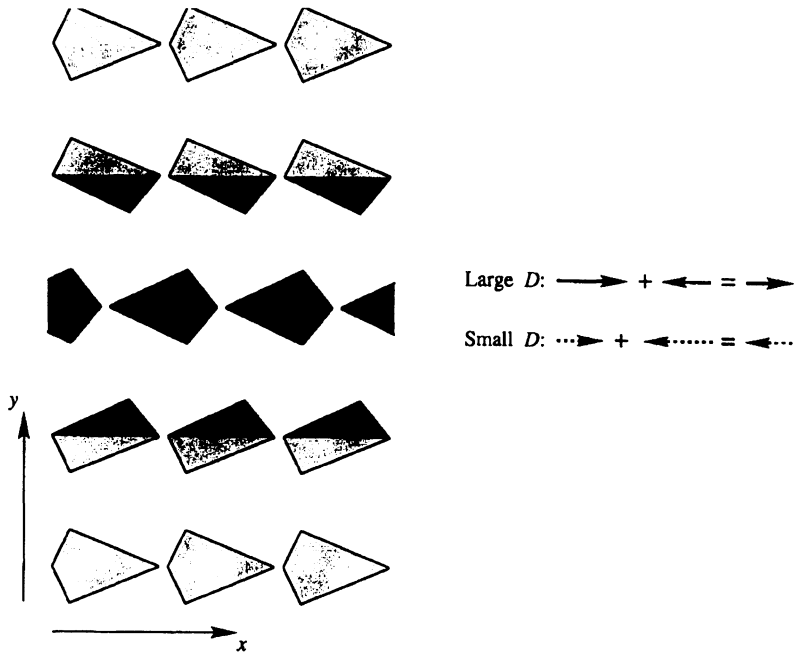

Figure 7. Illustration of how the combination of the sieves in Fig. 6 (a) and (b) can lead to a system in which particles below and above a threshold diffusion coefficient drift in opposite directions.

effect as a constant force. To achieve good lateral segregation it is enough to pull the molecules back and forth across a few rows. This allows to use systems with a very small size in the y direction.

Looking at the system in Fig. 6b one can conclude, that molecules with small diffusion coefficient have large lateral drift velocities, because they basically follow a deterministic trajectory, but molecules with larger diffusion coefficient have a chance to diffuse to the neighboring funnel on the left, reducing the lateral drift velocity. Thus, as opposed to the previous system, here the molecules with larger diffusion coefficients have smaller lateral drift velocity.

This difference between the two systems can be exploited by mixing them with opposite directionality, as indicated in Fig. 7 A remarkable feature of this combined system is, that applying an alternating field in the y direction, molecules with large diffusion coefficient drift to the left, while molecules with small diffusion coefficient drift to the right. The threshold diffusion coefficient, above which molecules drift to the left and below which molecules drift to the right can be controlled by the size and shape of the obstacles, by the ratio of the two different kinds of rows, or by the amplitude of the alternating

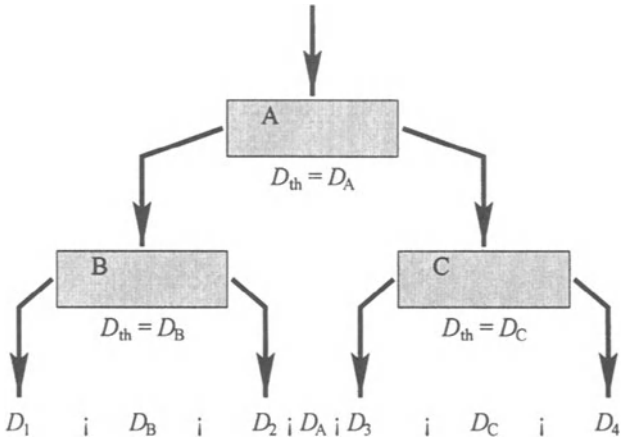

Figure 8. Devices (A, B, and C) from Fig. 7 with different thresholds ($D_B < D_A < D_C$) arranged in a tree topology can be used to sort large amounts of different particles continuously.

field. Such systems can be very useful in the separation of two different kinds of macromolecules. One just has to feed the system continuously in the middle with the solution of the two molecules, and extract the two purified solutions on the left and right sides of the chip.

For the separation of more than two kinds of molecules several chips with different thresholds can be used simultaneously, arranged, e.g., in a tree topology as shown in Fig. 8. The first chip (A) would separate one half of the particles from the other half, then the next two chips (B and C) would continue the separation on these two outputs, and so on.

The resolution or sensitivity of the separation with such microfabricated sieves competes with the resolution of standard gel electrophoresis. The main advantages of this new method of electrophoretic separation are that the shape of the obstacles can be chosen at will, the chips can be reused, the molecules can be sorted continuously, and the separation can be easily automated.

The first experimental realization of a microfabricated sieve was reported recently [33].

4.2 Separation with entropic ratchet

Another separation technique based on geometric ratchets uses the rocking ratchet principle [29]. Here the idea is to manufacture narrow tubes, the width of which is modulated periodically but asymmetrically as illustrated in Fig. 9. If the radius of gyration of a macromolecule is larger than the width of the narrow region, the molecule does not like to be there, because

its internal entropy is smaller due to the geometric confinement. Thus the entropic forces try to push the molecule out of the narrow regions. But because the modulation of the width of the tube is asymmetric, the molecule feels an asymmetric potential. Now, applying an alternating electrophoretic force parallel to the tube, the molecule gets a net velocity, just as we expect from a rocking ratchet. And because molecules with different radii of gyration experience different ratchet potentials, they will drift with different velocities, leading to separation.

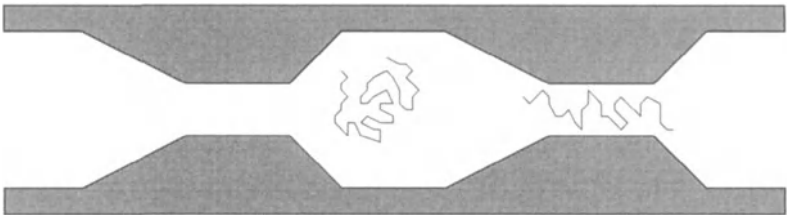

Figure 9. Cartoon of an entropic ratchet. Application of an alternating horizontal force on the macromolecules results in a net velocity, which depends on molecules' radius of gyration.

References

[1] E. M. Purcell, Am. J. Phys. **45**, 3 (1977).

[2] P. Hänggi and R. Bartussek, in *Nonlinear Physics of Complex Systems, Lecture Notes in Physics*, edited by J. Parisi, S. C. Müller, and W. Zimmermann (Springer, Berlin, 1996), vol. 467, pp. 294–308.

[3] R. D. Astumian, Science **276**, 917 (1997).

[4] F. Jülicher, A. Ajdari, and J. Prost, Rev. Mod. Phys. **69**, 1269 (1997).

[5] R. P. Feynman, R. B. Leighton, and M. Sands, *The Feynman Lectures on Physics* (Addison-Wesley, Reading, MA, 1966).

[6] R. D. Vale, T. S. Reese, and M. P. Sheetz, Cell **42**, 39 (1985).

[7] Y.-H. Song and E. Mandelkow, Proc. Natl. Acad. Sci. USA **90**, 1671 (1993).

[8] S. Ray, E. Meyhöfer, R. A. Milligan, and J. Howard, J. Cell. Biol. **121**, 1083 (1993).

[9] K. Svoboda, C. F. Schmidt, B. J. Schnapp, and S. M. Block, Nature **365**, 721 (1993).

[10] K. Svoboda and S. M. Block, Cell **77**, 773 (1994).

[11] M. J. Schnitzer and S. M. Block, Nature **388**, 386 (1997).

[12] C. M. Coppin, D. W. Pierce, L. Hsu, and R. D. Vale, Proc. Natl. Acad. Sci. USA **94**, 8529 (1997).

[13] K. Visscher, M. J. Schnitzer, and S. M. Block, Nature **400**, 184 (1999).

[14] C. S. Peskin and G. Oster, Biophys. J. **68**, 202s (1995).

[15] I. Derényi and T. Vicsek, Proc. Natl. Acad. Sci. USA **93**, 6775 (1996).

[16] T. Duke and S. Leibler, Biophys. J. **71**, 1235 (1996).

[17] I. Derényi and T. Vicsek, Physica A **249**, 397 (1998).

[18] A. Hoenger, E. P. Sablin, R. D. Vale, R. J. Fletterick, and R. A. Milligan, Nature **376**, 271 (1995).

[19] M. Kikkawa, T. Ishikawa, T. Wakabayashi, and N. Hirokawa, Nature **376**, 274 (1995).

[20] E. P. Sablin, F. J. Kull, R. Cooke, R. D. Vale, and R. J. Fletterick, Nature **380**, 555 (1996).

[21] U. Henningsen and M. Schliwa, Nature **389**, 93 (1997).

[22] S. A. Endow and K. W. Waligora, Science **281**, 1200 (1998).

[23] E. P. Sablin, R. B. Case, S. C. Dai, C. L. Hart, A. Ruby, R. D. Vale, and R. J. Fletterick, Nature **395**, 813 (1998).

[24] R. D. Astumian and I. Derényi, Eur. Biophys. J. **27**, 474 (1998).

[25] R. D. Astumian and I. Derényi, Biophys. J. **77**, 993 (1999).

[26] S. P. Gilbert, M. L. Moyer, and K. A. Johnson, Biochemistry **37**, 792 (1998).

[27] Y. Okada and N. Hirokawa, Science **283**, 1152 (1999).

[28] J. Rousselet, L. Salome, A. Ajdari, and J. Prost, Nature **370**, 446 (1994).

[29] G. W. Slater, H. L. Guo, and G. I. Nixon, Phys. Rev. Lett. **78**, 1170 (1997).

[30] T. A. J. Duke and R. H. Austin, Phys. Rev. Lett. **80**, 1552 (1998).

[31] D. Ertas, Phys. Rev. Lett. **80**, 1548 (1998).

[32] I. Derényi and R. D. Astumian, Phys. Rev. E **58**, 7781 (1998).

[33] A. van Oudenaarden and S. G. Boxer, Science **285**, 1046 (1999).

[34] J. S. Bader, R. W. Hammond, S. A. Henck, M. W. Deem, G. A. McDermott, J. M. Bustillo, J. W. Simpson, G. T. Mulhern, and J. M. Rothberg, Proc. Natl. Acad. Sci. USA **96**, 13165 (1999).

[35] W. D. Volkmuth and R. H. Austin, Nature **358**, 600 (1992).

COMPOSITION AND STRUCTURAL DYNAMICS OF VERTEBRATE STRIATED MUSCLE THICK FILAMENTS

Role of myosin-associated proteins

Zoya A. Podlubnaya
Institute of Theoretical and Experimental Biophysics of Russian Academy of Sciences, Pushchino, Moscow Region, 142292, Russia

Abstract We discuss recent data on integral and dynamic (muscle state-dependent) protein components of vertebrate striated muscles thick filaments. Their contribution to the structural dynamics of the filaments and in particular, to Ca^{2+}-dependent reversible structural transitions involving the domains of myosin molecules arranged on the filament surface, is analyzed. The functional importance of these transitions is considered in the context of the mechanisms regulating the contractile process and its coupling with energy metabolism.

Keywords: Skeletal and cardiac muscle, force generation, regulation, structural transitions, myosin filaments, enzymes of energy metabolism, titin and titin-like proteins

1. Introduction

1.1 Structure of vertebrate striated muscle thick filaments

Muscle contraction is usually considered in terms of the "sliding filament model" [1]. According to this model, two systems of contractile filaments (thick, myosin-containing and thin, actin-containing) actively slide past each other, producing the shortening of sarcomeres and thereby of the whole muscle. The interaction of thick and thin filaments, coupled with ATP hydrolysis by the myosin ATPase and regulated by Ca^{2+}, is the central event of this process.

Thick filaments of vertebrate striated muscle consist of bipolar arrays of myosin molecules [2]. The tails of the molecules form the backbone of the filament while the heads (subfragments-1, S1) and the adjacent part of the tail of each myosin molecule (subfragment-2, S2) are located on the filament surface. Bipolar (in the center of the filament) and polar (in each half of the

J.J. Kasianowicz et al. (eds.), Structure and Dynamics of Confined Polymers, 295–309.

Figure 1. Schematic representation of the myosin molecule. The molecule is a hexamer, containing two heavy chains folded together in coiled-coil tail at the C-terminus and separately in two globular heads at the N-terminus, and four light chains. Each head is composed of the heavy chain and an essential (ELC) and a regulatory (RLC) light chain. There are two hinges in the molecule, one is between LMM and S2, and one between S1 and S2. These allow the head and S2 to change orientation (modified from [3])

filament) packing of myosin molecules creates an assembly that has several zones (see below) with different binding properties for adsorption of different non-myosin proteins.

In accordance with the three-dimensional structure of S1 determined at the atomic level [4] each myosin head consists of the motor domain (N-terminus of heavy chain), containing the actin-binding site and active site, and a regulatory domain composed of a long α-helix of the heavy chain and of two light chains (one regulatory light chain, RLC; and one essential light chain, ELC). The ELC is located close to the motor domain (Fig. 1) while the RLC is arranged near the myosin head-S2 junction. Both ELC and RLC are clamped sequentially around an 8.5 nm stretch of α-helical heavy chain, providing the communication between the motor domain of the head and the tail of myosin molecule in the backbone.

In relaxed muscle, the heads are arranged close to the filament backbone, interacting with each other and with the backbone and forming a three-stranded helix with an axial period of 43 nm and a subunit period of 14.5 nm [5–7]. All levels of structural organization of the thick filament assemblies are subordinated to their physiological functions.

1.2 Structural dynamics of the surface domains of the thick filaments

Upon activation of muscle, the myosin heads move away from the backbone and bind to actin, thereby forming cross-bridges that are required to produce force and the relative sliding of the filaments [8]. Recent data on the crystal structure of the myosin head and actin, and the image reconstruc-

tion of actomyosin complex [4, 9–11], clarified the structural basis of myosin functioning as a molecular motor.

It is noteworthy that the above localization of the light chains (LCs) between the motor domain and the S2 "neck" region of myosin allows them to confer stiffness and stability of the α-helix, which is necessary to transmit internal movement of S1 to the backbone of the thick filaments and to amplify this movement in accordance with a revised "tilting crossbridge model" [9,10,12]. In this model, small structural changes which occur in the motor domain of the myosin head upon ATP hydrolysis are magnified by the pivoting of the myosin light-chain domain, which acts as a lever arm. The main structural event accompanying the force generation is not the change in the angle at which the whole head binds to actin filament, as was initially assumed in the "tilting cross-bridge" model [1, 13], instead it is the change in the orientation of the light-chain region of the head.

2. Regulation of contraction of vertebrate striated muscles: enzymatic and structural events

2.1 Types of regulation

It is well known that an increase in the intracellular concentration of Ca^{2+} triggers the contraction of all muscle types. Myofibrillar components responsible for Ca^{2+}-binding are located on the thin or thick filaments or both, depending on the muscle type and species [14]. For instance, contraction of molluscan striated muscle is regulated via direct binding of Ca^{2+} to the binding site in the myosin regulatory domain (myosin-linked regulation) [15]. In vertebrate smooth muscle, at least two regulatory mechanisms operate. The primary one is myosin-linked, in which interaction of Ca^{2+} with myosin light chain kinase results in activation of the latter and in myosin RLC phosphorylation which triggers the cycling of myosin crossbridges and the generation of force. The complementary actin-linked mechanism of regulation in these muscle is also proposed (see references within [16]). An unanswered question is whether a direct binding of Ca^{2+} to RLC may contribute to this process in vertebrate smooth muscle. The contraction of vertebrate striated muscles is believed to be regulated by the binding of Ca^{2+} to troponin C, the Ca^{2+} binding subunits of troponin, which together with tropomyosin forms regulatory system of contractile apparatus (actin-linked regulation). However, some data suggest that the regulation process in these muscles is more complicated, and may involve modification of the myosin by RLC-phosphorylation [17] and direct Ca^{2+} binding to RLC [18, 19].

Numerous biochemical, physiological, structural and *in vitro* motility studies have provided evidence that myosin light chains in the regulatory domain and their interactions with the motor domain appear to be critical not only

for energy transduction but for regulation of myosin enzymatic properties [20–25]. Some authors even assume that S1 is a sufficient structure to move actin filaments and to generate force [26,27]. However the rate of movement induced by S1 appeared to be less than that induced by heavy meromyosin (HMM) or myosin in which the S2 region is present [23,24,26,28].

In Huxley's model [1], the heads and S2 move away from the filament backbone during contraction and that the hinge regions between S1 and S2 as well as between S2 and light meromyosin (LMM) in myosin molecules (Figs. 1 and 2) can maintain the correct orientation of the head binding to actin for force generation. The possible contribution of S2 to force production and regulation is supported by data from various indirect methods [24,28–33]. Moreover, recent papers have reinforced the need for head-head interactions in the processes of force production and regulation, and for S2 being the common element of both heads [24,33,34]. For instance, it has been shown that not only the "neck" region of the myosin molecule, where LCs are located, but also portions of S2 not less than 20 nm long are necessary for normal regulatory ability of myosin. New models of the regulation of vertebrate striated muscles involving the participation of myosin have been suggested [35,36], but the role of the S2 region is still not considered.

2.2 Electron microscopic approaches for studying the structural behavior of the myosin heads on the surface of the thick filaments

Despite the great progress in determining the structure of S1 and actin filaments at atomic resolution, the nature of structural changes in myosin and actin underlying force generation and regulation remains the principal aim of work in the field. Electron microscopy (EM), with its numerous approaches including various cryo procedures, is a promising method for obtaining direct evidence of changes in the structure and disposition of the myosin heads and S2 regions on the surface of myosin filaments under physiological conditions. For example, physiological effectors (e.g. Ca^{2+}) and phosphorylation of the RLC were found to govern the position of the heads, inducing their movement away from the backbone of isolated native or reconstituted myosin filaments of invertebrate muscles ("order - disorder" transitions) [37–39]. Similar phosphorylation-induced "activation" of the structure has been also revealed in isolated skeletal muscle thick filaments [17,40] which correlates with the increased tension developed by the muscle fibre. It follows that phosphorylation of myosin RLC modulates control of contraction of these muscles. Attempts to investigage similar transitions induced by Ca^{2+} in the thick filaments from skeletal and cardiac muscles were unsuccessful so far [17].

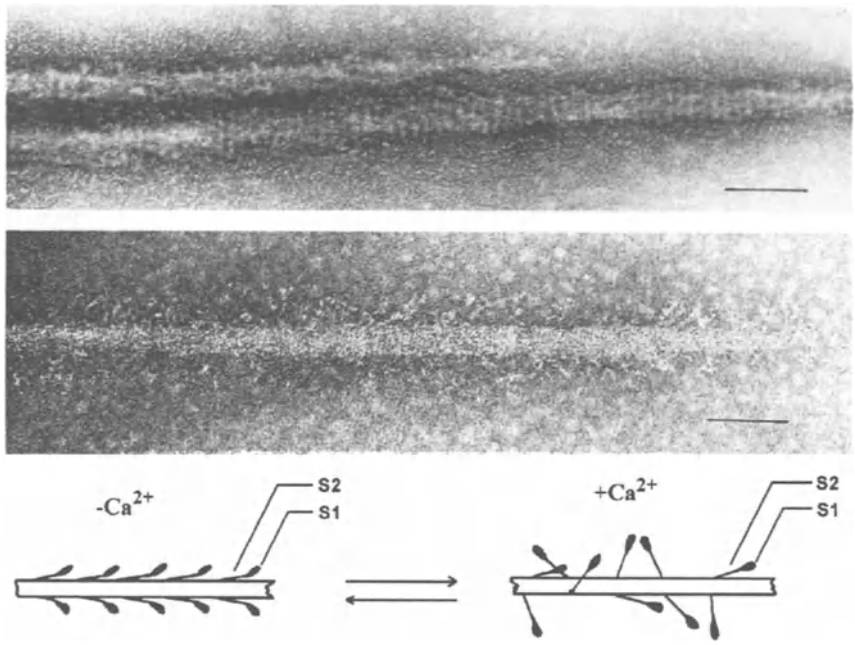

Figure 2. Electron micrographs of synthetic myosin filaments with compact ordered structure in the absence of Ca^{2+} (top) and with spread disordered structure in the presence of Ca^{2+}(middle). The images of the filaments are typical for vertebrate skeletal, cardiac and smooth muscle myosin filaments. Bar, 100 nm. (bottom) - Schematic representation of structural behavior of myosin S2s with the heads in the absence and in the presence of Ca^{2+}. Synthetic myosin filaments for EM examination were prepared from column-purified unphosphorylated myosins (0.2 mg/ml in 0.5 M KCl) by overnight dialysis against the solutions containing: 120 mM KCl, 1 mM $MgCl^{2+}$, 10 mM imidazole-HCl (pH 7.0) and either 0.1-0.01 mM $CaCl^{2+}$, or 1 mM EGTA at 4°C. The suspension of the filaments was placed on collodion or formvar and carbon-coated grids and negatively stained with 1% aqueous uranyl acetate. The same results were obtained with relaxing and activating solutions used by Frado and Craig [39] for demonstration of Ca^{2+}-induced structural transitions in the filaments of "regulated" myosin from molluscan striated muscle.

2.3 Ca^{2+}-induced reversible structural transitions in synthetic myosin filaments

In contrast to previous reports, by the use of negative staining and freeze-drying techniques in EM, we observed that synthetic filaments formed by skeletal, cardiac and smooth muscle myosins with unphosphorylated RLC exhibit Ca^{2+}-induced reversible movement of both the heads and S2s from the backbone of the filaments at neutral pH and physiological ionic strength [16,41]. In the absence of Ca^{2+}(pCa 7-8) the filaments of the above myosins

display prominent rows (crowns) of the heads arranged with an interval of $\sim$ 14.5 nm along the filament (image characteristic for thick filaments in relaxed muscle). Their compact, ordered structure is likely formed by myosin heads and S2s disposed close to the filaments surface due to the interaction of S2s with the backbone and of the heads with each other and with backbone (Figs. 2a, 2c). On the contrary, in the presence of Ca^{2+}(pCa 4.5-5) disordered filaments are usually observed (Figs. 2b, 2c). The myosin heads and S2 subfragments are scattered around the filament, perhaps, due to the weak binding to, and detachment from, the backbone ("activated state" of the filament). This is evidenced by the absence of 14.5 nm axial periodicity in the filaments and by the long distance of heads (up to 50 nm) from the backbone, suggesting that both the heads and S2s move away from the backbone. These transitions are not simply the result of myosin filaments formation during dialysis. They are easily reversible and are due to the effect of Ca^{2+}. Rinsing the filaments with ordered or disordered structure with Ca^{2+}-containing or Ca^{2+}-depleted solutions on EM-grids transforms them tp the "disordered" or "ordered" state, respectively. Because this system, unlike the suspension of isolated native thick filaments usually used for such investigations, did not contain actin and myosin-associated proteins (see below), one can conclude that the Ca^{2+}-dependent S2 release is an intrinsic property of the myosin and is the result of direct Ca^{2+}-binding to its RLC. Perhaps, this is a common property of vertebrate skeletal, cardiac and smooth muscle myosins independently of the regulation type supposed for these muscles (actin-linked regulation in vertebrate striated muscles, or myosin-linked regulation through RLC-phosphorylation in vertebrate smooth muscles).

The reversibility of the Ca^{2+}-induced transitions supports similar effects occuring *in vivo* and the possible contribution of Ca^{2+} sensitivity of myosin of vertebrate striated and smooth muscles to regulation or modulation of the contractile process. *In vivo* the Ca^{2+}-induced S2 release from the backbone of thick filaments could lead to facilitating the interaction of the heads with actin due to the increase in the freedom of their movement and accessibility to thin filaments. Thus, Ca^{2+}-induced structural transitions could regulate the function of the myosin motor due to the communication between the head domains and tails of myosin molecules in thick filaments. Ca^{2+}-induced S2 release itself may result from such a communication route and other EM observations support this assumption. Synthetic filaments formed by skeletal and cardiac myosins with RLC or ELC, in which small peptides at the N-terminus were removed by limited proteolysis, did not display the Ca^{2+}-induced movement of S2: both in the absence and in the presence of Ca^{2+} the filaments retained ordered structure [42]. Unlike RLC, ELC does not bind Ca^{2+} and its truncation does not influence the Ca^{2+} sensitivity of myosin. However if we take into consideration the interaction between LCs sequentially arranged in

the regulatory domain [15], the removal of even small N-terminal fragments in ELC can lead to the loss of functional communication specific to native myosin molecule.

Thus, EM studies reveal the Ca^{2+}-induced movement of functionally important domains of myosin molecules in the highly confined space between the contractile filaments required for their interaction with each other, hydrolysis of ATP, generation of force and shortening of muscle. It should be noted that the above Ca^{2+}-dependent transitions have been revealed in systems containing purified myosins, in the absence of myosin-associated proteins. It is possible that the proteins bound to the myosin filaments in muscle could change their enzymatic and/or structural Ca^{2+} sensitivity.

3. Non-myosin proteins in the thick filament: Structural dynamics and coupling between the contractile (energy-consuming) and energy-supplying systems

3.1 Titin and titin-like proteins

Thick filaments of vertebrate striated muscle contain a number of proteins, usually referred to as minor proteins because of their relatively low concentration, are listed in Table 1. These include enzymes of energy metabolism such as creatine kinase (CK), phosphofructokinase (PFK) and AMP-deaminase (DA) (see review [43]). Other proteins are components of the sarcomeric cytoskeleton and, like the giant elastic protein titin, belong to a family of proteins composed of repeating domains resembling the type III fibronectin and C-2 immunoglobulins (for a detailed discussion of Titin's properties, see Kellermeyer, et al., this volume). Titin is the third most abundant protein in sarcomeres ($\sim$ 10%) after myosin ($\sim$ 44%) and actin ($\sim$ 22%). The titin molecule (MW $\sim$ 3000 kDa, length $\sim$ 1 μm) is arranged along each half of the sarcomere from the M-line to the Z-line (Fig. 3). Titin filaments (longitudinal elastic structural elements of the sarcomere) bind to the thick filaments in the region of the A-disk and are free in the I-line. They overlap with titin filaments of neighboring sarcomeres in the Z-lines. Other proteins, such as M-protein, myomesin and skelemin are located in the region of the M-line with an interval of $\sim$ 43 nm. These can be regarded as transverse elastic structural elements of sarcomeric cytoskeleton.

Titin is believed to play an important role as a template in myofibrillar assembly and in thick filament formation, as well as in maintaining the structural integrity of the sarcomere. It plays a fundamental role in the generation of passive tension of muscle because of its elastic properties (see reviews [44–46] (see also Kellermeyer et al., this volume). The possibility remains that titin (and perhaps the titin-like proteins) bound to thick filaments can contribute to regulatory process affecting the Ca^{2+}sensitivity of actomyosin ATPase and

Table 1. Non-myosin proteins in vertebrate striated muscle thick filament

Enzymes	Titin-like proteins
Myosin ATPase	Titin (connectin)
Creatine kinase	C-protein
Phosphofructokinase	X-protein
AMP-deaminase	H-protein
Adenylate kinase?	Myomesin
	M-protein
	Skelemin

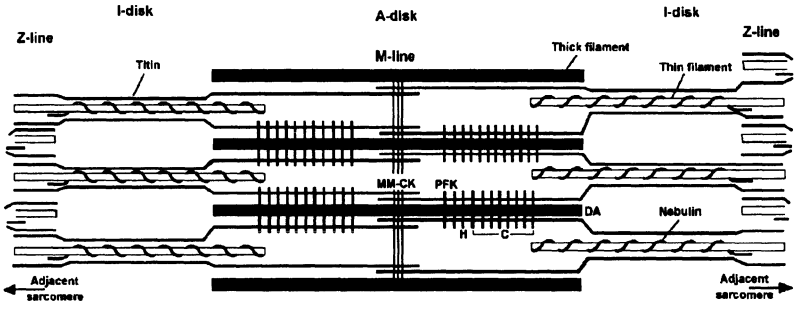

Figure 3. Schematic representation of a sarcomere, the repeating unit of the contractile apparatus of vertebrate striated muscle, showing the location of titin and other proteins bound to the thick filaments. H - H-protein; C - C-protein; MM-CK - M-line-bound creatine kinase; DA - AMP deaminase; PFK - phosphofructokinase (modified from [44].

the structural dynamics of myosin filaments [22,47]. Titin was shown to bind not only to myosin, but also to other components of the thick filaments, such as C-protein, M-protein, myomesin, and AMP-deaminase (DA). Studies of other enzymes of the thick filaments are in progress. It is possible that titin provides a scaffold for enzymes of energy metabolism coupled functionally with myosin ATPase, and thereby supports the concerted and function of the contractile and energy systems of muscle.

3.2 Enzymes of energy metabolism

Functional coupling of myosin ATPase and MM-CK (muscle isoenzyme of CK), AK (adenylate kinase, or myokinase), DA and PFK (a key enzyme of glycolysis) is well established. Later it was demonstrated that they are either integral or dynamic components of the thick filaments. MM-CK is an integral component of thick filaments [48] and is located in the M-line as primary m-crossbridges that connect the thick filaments. Like myosin, MM-CK serves

several functions. Its structural role consists in creating and maintaining a high spatial order of thick filaments that is necessary for rapid contraction. Its enzymatic function is to provide rapid and efficient resynthesis of ATP from ADP and creatine phosphate (CrP) for contracting muscle (reaction 1). However, CK is also bound to thick filaments in the polar halves of the A-disk, where it is a dynamic component of the filaments and the amount of bound CK depends on the functional state of muscle cell [49].

MM-CK localization in M-line has obvious advantages. The enzyme does not interfere with cyclic work of the crossbridges and its presence in the center of the A-disk enables its fast response to the changes in the ADP and H^+ concentration that occur as thin filaments slide toward the center of sarcomere during contraction. Experimental data confirm the functional importance of MM-CK compartmentalization, showing that the amount of M-line-bound MM-CK is sufficient to maintain normal muscle contraction [48]. These data also suggest that in vertebrate striated muscles, especially in fast striated muscles where the CK system is well-developed, the initial phase of contraction is performed at the expense of a reserve of CrP (reaction 1). Upon activation of muscle by Ca^{2+} the myosin ATPase begins to work, leading to the local accumulation of ADP and H^+, the substrates of the reaction catalyzed by MM-CK. These stimulate the reaction 1 in the direction of ATP-regeneration. With depletion of CrP, other systems of synthesis and resynthesis of ATP are activated, whose functional contribution depends on the type of energy metabolism of muscle: AK (reaction 2), glycolysis, and oxidative phosphorylation.

$$ADP + CrP + H^+ \overset{MM-CK}{\rightleftharpoons} ATP + Cr \qquad (1)$$

$$2ADP \overset{AK}{\rightleftharpoons} AMP + ATP \qquad (2)$$

$$AMP + H_2O \overset{DA}{\longrightarrow} IMP + NH_3 \qquad (3)$$

ATP regeneration by MM-CK for muscle contraction is usually regarded in terms of a creatine phosphate shuttle between ATP-consuming, contractile system and ATP-regenerating systems. According to this hypothesis, ADP produced by myofibrillar ATPase does not diffuse into mitochondria, but creatine does. Cr is phosphorylated in mitochondria, and creatine phosphate (CrP) diffuses to myofibrils, where MM-CK catalyzes the reaction (1).

M-line-bound CK is not only a potent intramyofibrillar ATP regenerating enzyme enzyme, but a regulator energy metabolism in muscle [43]. As seen from the above reactions, in the coupled enzyme system "ATPase myosin - MM-CK" as well as in the coupled enzyme system "ATPase myosin - AK

- DA" the product of a previous reaction is the substrate for next reaction. The enzymes in these systems regulate each other. Furthermore, the myosin filament can be also an effective allosteric regulator of activity of the enzymes bound to it (see below).

According to the modern notion, DA and PFK are "ambiquitous" enzymes (terminology of [50]), i.e. they can present in the muscle cell not only in the sarcoplasm, but are bound to strategically important structural elements as well, in particular to the thick filaments. The equilibrium between free and bound forms of enzyme depends on metabolic status of the cell. They can be regarded as dynamic components of the thick filaments. In skeletal muscle DA is located on the ends of the myosin filaments [51,52] or on titin filaments [53]. There are data of *in vitro* experiments on DA binding to titin [54]. If even in some muscles DA is located on titin filaments at the ends of the thick filaments (A-disk), it still appears in the same compartment with myosin ATPase. Our experiments with polyclonal antibodies revealed PFK near the M-line, i.e. near MM-CK in skeletal muscles (Fig. 3) [55]. PFK binding sites on myosin molecule are located in S2. It is worth noting that binding sites for other enzymes have been revealed also in S2 and/or LMM regions of myosin molecules, but not in the head [43]. It should be emphasized that the binding of the enzyme modifies their properties, as a rule, increasing their activity, lowering their sensitivity to inhibitors and thereby intensifying the processes catalyzed by them.

Thus, CK, DA and PFK in muscle can be associated with the thick filaments. The possibility remains that myokinase is also immobilized within myofibrils, since like PFK, it is a permanent impurity of myosin preparations. The stimulation of muscle or the increase of Ca^{2+} concentration in in vitro experiments results in the increase of the amount of the enzymes bound to myosin filaments [43]. Because these enzymes do not bind Ca^{2+}, one can suppose that the Ca^{2+} effects observed are determined by the above Ca^{2+} sensitivity of myosin itself. Because the equilibrium between free and bound forms of the enzymes depends on functional state of muscle, and the binding changes their enzymatic properties, such an "ambiquitous" nature of the enzymes, can be of physiological importance [50]. The existence of easily reversible transitions between soluble and bound states of the enzymes can be regarded as a regulatory mechanism, causing the alterations in their total activity to satisfy changing metabolic demands.

The importance of binding MM-CK, DA, PFK and, possibly, other enzymes, participating in energy metabolism, to the thick filaments first at all consists in their maximal approaching to the places of ATP-consumption, i.e. to myosin heads, which reduces the delivery time of ATP to contractile structures. It is no surprise that the enzymes such as MM-CK, DA, AK and PFK, functionally coupled to each other and to myosin ATPase are gathered and or-

derly distributed for realizing their mutual regulation within one compartment. This order is guaranteed by the thick filament structure. The thick filaments being composite filaments of myosin and titin [56] have bipolar structure and consequently several zones: M-line, P (proximal)-, C- and D (distal)-zones. They are distinct in their binding properties that creates conditions favorable for accommodation of various enzyme systems in the appropriate zones [43,51].

The role of Ca^{2+} in regulating the activities of the enzymes considered here is unknown: their direct activation by Ca^{2+} has not been revealed. However, the processes catalyzed by these enzymes were shown to be activated immediately after stimulation of the muscle. Localization of enzymes on thick filaments near the sites of ADP-production of myosin can provide the possibility of their activation coupled with muscle contraction, i.e. the possibility of synchronous startup of contractile and energy-supplying systems and of their concerted and effective functioning with myosin ATPase. Such a possibility was considered with respect to thin filaments and glycolytic enzymes [57]. This hypothetical mechanism of coupling the executive and glycolytic systems, was based on structural changes in actin filaments depending on Ca^{2+} and an external load. The possibility remains that a similar mechanism can operate in the thick filaments. Because binding sites for the above enzymes are located on S2 and/or on LMM, the enzymes adsorbed on the thick filament should be sensitive to structural changes occurring in these regions of myosin molecules. Undoubtedly, that these suppositions need an experimental confirmation. Testing the influence of the enzymes on Ca^{2+}-dependent structural behavior of S2 is one of important tasks of further investigations. These experiments must include also testing the influence of titin and titin-like proteins, associated with the thick filaments (Table 1). Our preliminary experiments showed that C-protein, whose binding sites are arranged on S2 and LMM of myosin molecule, inhibited Ca^{2+}-dependent mobility of S2. [47].

4. Summary and conclusions

At present the different types of spatial compartmentation of metabolic processes in muscle cell are well known. Along the type of metabolism organization using membranes, the effective compartmentation can be achieved within a single membrane-enclosed confined space by the binding of individual soluble enzymes and their complexes to the filamentous matrical structures (matrical compartmentation, terminology of [58]). This type of compartmentation can provide an additional and sometimes an unique potential for the regulation of cellular processes, for a more rapid and flexible response to the localized dynamic energy needs of the cell in diverse cellular situations. So called "thick filament" of vertebrate striated muscle is an example of such

a compartmentation. It can be regarded as a highly organized multi-enzyme complex, arranged on filamentous titin. The composition of this complex may change with the functional status of the muscle cell. Such a composite filament fulfills several functions: participates in the forming and maintaining of the highly ordered structure of sarcomere, generating of force, regulating of muscle contraction and coordinating of some processes of energy supply for muscle contraction. Thus, this unique compartment creates the possibility for concerted, efficient and economical functioning of contractile and energy-supplying systems of the muscle.

Acknowledgments

This work is supported by the RFBR grant 97-04-48346.

References

[1] Huxley, H.E. (1969) The mechanism of muscular contraction. *Science* **164**, 1356-1366.

[2] Huxley, H.E. (1963) Electron microscope studies on the structure of natural and synthetic protein filaments from striated muscle. *J. Mol. Biol.* **7**, 281-308.

[3] Rayment, I., and Holden, H.M. (1994) The three-dimensional structure of a molecular motor. *Trends Biochem. Sci.* **19**, 129-134.

[4] Rayment, I., Rypniewski, W.R., Schmidt-Bäse, K., Smith, R., Tomchick, D.R., Benning, M.M., Winkelmann, D.A., Wesenberg, G., and Holden, H.M. (1993b) Three-dimensional structure of myosin subfragment-1: a molecular motor. *Science* **261**, 50-58.

[5] Kensler, R.W., and Stewart, M. (1989) An ultrastructural study of crossbridge arrangement in the fish skeletal muscle thick filament. *J. Cell Sci.* **94**, 391-401.

[6] Kensler, R.W., and Stewart, M. (1993) The relaxed crossbridge pattern in isolated rabbit psoas muscle thick filament. *J. Cell Sci.* **105**, 841-848.

[7] Kensler. R.W., and Woodhead, J.L. (1995) The chicken muscle thick filament: temperature and the relaxed cross-bridge arrangement. *J. Muscle. Res. Cell Motil.* **16**, 79-90.

[8] Huxley, H.E., and Brown, W. (1967) The low angle X-ray diagram of vertebrate striated muscle and its behavior during contraction and rigor. *J. Mol. Biol.* **30**, 383-434.

[9] Rayment, I., Holden, H.M., Whittaker, M., Yohn, C.B., Lorenz, M., Holmes, K.C., and Milligan R.A. (1993) Structure of the actin-myosin complex and its implications for muscle contraction. *Science* **261**, 58-65.

[10] Fisher, A.J., Smith, C.A., Thoden, J., Smith, R., Sutoh, K., Holden, H.M., and Rayment, I. (1995) Structural studies of myosin: nucleotide complexes: a revised model for the molecular bases of muscle contraction. *Biophys. J.* **68**, 19s-28s.

[11] Holmes, K.C., Popp, D., Gebhard, W., and Kabsch, W. (1990) Atomic model of the actin filament. *Nature* **347**, 44-49.

[12] Uyeda, T.Q.P., Abramson, P.D., and Spudich J.A. (1996) The neck region of the myosin motor domain acts as a lever arm to generate movement. *Proc. Natl. Acad. Sci. (USA)* **93**, 4459-4464.

[13] Huxley, A.F., Simmons, R.M. (1971) Proposed mechanism of force generation in striated muscle. *Nature* **233**, 533.

[14] Lehman, W., and Szent-Györgyi, A.G. (1975) Regulation of muscular contraction. Distribution of actin control and myosin control in the animal kingdom. *J. Gen. Physiol.* **66**, 1-30.

[15] Xie, X., Harrison, D.H., Schlichting, I., Sweet, R.M., Kalabokis, V.N., Szent-Györgyi, A.G., and Cohen, C. (1994) Structure of the regulatory domain of scallop myosin at 2.8 Å resolution. *Nature* **368**, 306-312.

[16] Podlubnaya, Z., Kulikova, N., and Dabrowska, R. (1999) Effect of Ca^{2+} on the structure of synthetic filaments of smooth muscle myosin. J. Muscle. Res. Cell Motil. (in press).

[17] Levine, R.J.C., Kensler, R.W., Yang, Z., Stull, J.T., and Sweeney, H.L. (1996) Myosin light chain phosphorylation affects the structure of rabbit skeletal muscle thick filaments, *Biophys. J.* **71**, 898-907.

[18] Moss, R.L. (1992) Ca^{2+} regulation of mechanical properties of striated muscle. *Circ. Res.* **70**, 865-884.

[19] Swartz, D.R., Moss, R.L., and Greaser, M.L. (1996) Calcium alone does not fully activate the thin filament for S1 binding to rigor myofibrils. *Biophys. J.* **71**, 1891-1904.

[20] Pulliam, D.L., Sawyna, V., and Levine R.J.C. (1983) Calcium sensitivity of vertebrate skeletal muscle myosin. *Biochemistry* **22**, 2324-2331.

[21] Margossian, S.S., Bhan, A.K., and Slayter, H.S. (1983) Role of the regulatory light chains in skeletal muscle actomyosin ATPase and in minifilament formation. *J. Biol. Chem.* **258**, 13359-13369.

[22] Freydina, N.A., Vishnevskaya, Z.I., Udaltsov, S.N., and Podlubnaya, Z.A. (1986b) Effect of C-protein and DTNB-light chains on actomyosin ATPase activity at various ionic strengths and Ca^{2+}-level. *Acta Biophys. Biochim. Hung.* **21**, 247-256.

[23] Lowey, S., Waller, G.S., and Trybus, K.M. (1993) Skeletal muscle myosin light chains are essential for physiological speeds of shortening. *Nature* **365**, 454-456.

[24] Lowey, S., and Trybus, K.M. (1995) Role of skeletal and smooth muscle myosin light chains. *Biophys. J.* **68**, 120s-127s.

[25] Diffee, G.M., Patel, J.R., Reinach, F.C., Greaser, M.L., and Moss, R.L. (1996) Altered kinetics of contraction in skeletal muscle fibers containing a mutant myosin regulatory light chain with reduced divalent cation binding. *Biophys. J.* **71**, 341-350.

[26] Toyoshima, Y.Y., Kron, S.J., McNally, E.M., Niebling, K.R., Toyoshima, C., and Spudich, J.A. (1987) Myosin subfragment-1 is sufficient to move actin filaments in vitro. *Nature* **328**, 536-539.

[27] Kishino, A., and Yanagida, T. (1988) Force measurements by micromanipulation of a single actin filament by glass needles. *Nature* **334**, 74-76.

[28] Margossian, S.S., Krueger J.W., Sellers, J.R., Cuda, G. Caufield, J.B., Norton, P., and Slayter, H.S. (1991) Influence of the cardiac myosin hinge region on contractile activity. *Proc. Natl Acad. Sci. (USA)* **88**, 4941-4945.

[29] Harrington, W.F., Rodgers, M.E., and Davis, J.S. (1990) Functional aspects of the myosin rod in contraction. In: Squire, J.M. (ed.), Molecular mechanism in muscular contraction. MacMillan, New York, pp. 241-263.

[30] Roulet, A., Burgat, J.M., and Cardinaud, R. (1993) The proteolytic susceptibility of specific sites in myosin light chains is modulated by the filament conformation. *Eur. J. Biochem.* **216**, 89-101.

[31] Kobayashi, T., Kosuge, S., Karr, T., and Sugi, H. (1998) Evidence for bidirectional functional communication between myosin subfragment 1 and 2 in skeletal muscle fibres. *Biochem. Biophys. Res. Commun.* **246**, 539-542.

[32] Tsuchiya, T., Tanaka, H., Shirakawa, I., Karr, T., and Sugi, H. (1998) Evidence for the essential role of myosin subfragment-2 in the ATP-dependent actin-myosin sliding in muscle contraction. Jap. *J. Physiol.* **48**, 383-387.

[33] Trybus, K.M., Freyzon, Y., Faust, L.Z., and Sweeney, H.L. (1997) Spare the rod, spoil the regulation: Necessity for a myosin rod. *Proc. Natl. Acad. Sci. (USA)* **94**, 48-52.

[34] Knight, P.J. (1996) Dynamic behavior of the head-tail junction of myosin. *J. Mol. Biol.* **255**, 269-274.

[35] Lehrer, S.S. (1994) The regulatory switch of the muscle thin filament: Ca^{2+} or myosin heads? *J. Muscle Res. Cell. Motil.* **15**, 232-236.

[36] Head, J.G., Ritchie, M.D., and Geeves, M.A. (1995) Characterization of the equilibrium between blocked and closed states of muscle thin filaments. *Eur. J. Biochem.* **227**, 94-699.

[37] Vibert, P., and Craig, R. (1985) Structural changes that occur in scallop myosin filaments upon activation. *J. Cell. Biol.* **101**, 830-837.

[38] Craig, R., Padron, R., and Kendrick-Jones, J. (1987) Structural changes accompanying phosphorylation of tarantula muscle myosin filaments. *J. Cell Biol.* **105**, 1319-1327.

[39] Frado, L.L.Y., and Craig, R. (1989) Structural changes induced in Ca^{2+} regulated myosin filaments by Ca^{2+} and ATP. *J. Cell Biol.* **109**, 529-538.

[40] Levine, R.J.C., Yang, Z., Stull, J.T., and Sweeney, H.L. (1998) Structural and functional responces of mammalian thick filaments to alterations in myosin regulatory light chains. *J. Struct. Biol.* **122**, 149-161.

[41] Podlubnaya, Z.A., Kakol, I., Moczarska, A., Stepkowski, D., and Udaltsov, S. (1999) Calcium-induced structural changes in synthetic myosin filaments of vertebrate striated muscles. *J. Struct. Biol.*.

[42] Podlubnaya, Z., Stepkowski, D., Udaltsov, S.N., Kakol, I., and Moczarska, A. (1996) Influence of limited cleavage of myosin light chains on cross-bridge mobility in reconstituted filaments of skeletal and cardiac muscle myosins. *J. Muscle Res. & Cell Motil.* **17**, 118.

[43] Podlubnaya, Z.A. (1992) Enzymes in thick filaments of vertebrate striated muscles. *Biochemistry-Moscow* **57**, 1785-1813.

[44] Gregorio, C.C., Granzier, H., Sorimachi, H., Labeit, S. (1999) Muscle assembly: a titanic achievement? *Curr. Opin. Cell Biol.* **11**, 18-25.

[45] Trinick, J. (1994) Titin and nebulin: protein rulers in muscle. *Trends Biochem. Sci.* **19**, 405-409.

[46] Labeit, S., Kolmerer, B., and Linke W.A. (1997) The giant protein titin. Emerging roles in physiology and pathology. *Circ. Res.* **80**, 290-294.

[47] Podlubnaya, Z.A., Udaltsov, S.N., Kakol, I., and Stepkowski, D. (1995) Effect of C-protein on the structural behavior of myosin crossbridges. *J. Muscle Res. Cell Motil.* **16**, 155.

[48] Wallimann, T., and Eppenberger, H.M. (1985) Localization and function of M-line-bound creatine kinase. M-band model and creatine phosphate shuttle. In: Shay, J.W. (ed.), Cell Muscle Motility. Plenum Publish. Corp., New York - London, 6, pp. 239-285.

[49] Ohtsu, N., Hirata, M., Tuboe, S., and Miyatawa, K. (1989) Immunocytochemical localization of creatine kinase M in canine myocardial cells: most creatine kinase M is distributed in the A-band. *J. Histochem. Cytochem.* **37**, 1465-1470.

[50] Wilson, J.E. (1978) Ambiquitous enzymes: variation in intracellular distribution as a regulatory mechanism. *Trends Biochem. Sci.* **3**, 124-125.

[51] Podlubnaya, Z.A., Latsabidze, I.L., and Lednev, V.V. (1989) Structure of thick filaments on longitudinal sections of rabbit psoas muscle. *Biofizika* **34**, 91-96.

[52] Podlubnaya, Z.A., Shpagina, M.D., Lednev, V.V. (1989) Manifestation of the stripes of minor proteins location in A-bands of rabbit cardiac myofibrils. *J. Mol. Biol.* **210**, 655-658.

[53] Cooper, J., and Trinick, J. (1984) Binding and location of AMP deaminase in rabbit psoas muscle myofibrils. *J. Mol. Biol.* **177**, 137-152.

[54] Koretz, J.F., Irving, T.C., and Wang, K. (1993) Filamentous aggregates of native titin and binding of C-protein and AMP-deaminase. *Arch. Biochem. Biophys.* **304**, 305-309.

[55] Freydina, N.A., Shpagina, M.D., Podlubnaya, Z.A. (1986a) Localization of binding sites of F-protein (phosphofructokinase) on myosin molecule. *J. Muscle Res. Cell Motil.* **7**, 481-490.

[56] Kruger, M., Wright, J., and Wang, K. (1991) Nebulin as a length regulator of thin filaments of vertebrate skeletal muscles: correlation of thin filament length, nebulin size and epitope profile. *J. Cell Biol.* **115**, 97-107.

[57] Lednev V.V. (1980) Some aspects of regulation of muscle contraction. In: Ivanitsky, G.R. (ed.), Structural bases and regulation of biological motility. Science, Moscow, pp. 221-270.

[58] Masters, C.J., Reid, S., and Don, M. (1987) Glycolysis - new concepts in an old pathway, *Mol. Cell. Biochem.* **76**, 3-14.

FORCE-DRIVEN FOLDING AND UNFOLDING TRANSITIONS IN SINGLE TITIN MOLECULES

Single polymer strand manipulation

Miklós S.Z. Kellermayer
Department of Biophysics, P'ecs University Medical School, P'ecs H-7624 HUNGARY

Steven Smith, Carlos Bustamante
Dept. of Physics, University of California, Berkeley, CA 94720

Henk L. Granzier
Dept. VCAPP, Washington State University, Pullman, WA 99164-6520

Abstract A polymer strand can be influenced by an array of mechanical effects as it translates through a space with dimensions similar to its own. We summarize our experiments in which the mechanical behavior of single-molecules of the giant protein titin was characterized. Titin is a filamentous polypeptide embedded in the lattice space of the vertebrate muscle sarcomere. A single titin molecule stretches from the Z- to the M-line of the sarcomere, thereby spanning a distance of approximately 1 μm which is huge on the molecular scale. Physiologically, titin is important in generating passive muscle force and in maintaining the structural integrity of the sarcomere through its elastic properties. We analyzed the elastic properties of titin by stretching single molecules with laser tweezers. The force-response of the titin molecule revealed an entropic polymer whose behaviour can be well fitted with the wormlike chain model. Unfolding occurs in titin upon reaching high forces during stretch, and refolding takes place at low forces during the relaxation of the molecule. The force hysteresis implies folding non-equilibrium due to the slow unfolding and refolding rates relative to the stretch and release rates, respectively. Folding non-equilibrium as the source of force hysteresis can be demonstrated by the disappearance of hysteresis upon the addition of chemical denaturant. Repeated stretch and release cycles lead to the mechanical wear-out or fatigue of titin, which may have far-reaching implications for its physiological function.

Keywords: muscle, passive force, entropic chain, globular domains, folding/unfolding, laser tweezer

J.J. Kasianowicz et al. (eds.), Structure and Dynamics of Confined Polymers, 311–326.

Figure 1. Schematic representation of the structure of the vertebrate muscle half sarcomere. Titin extends form the Z- to the M-line. The globular domains of titin are indicated as simple folds. The PEVK segment is thought to be a highly flexible part of titin, indicated by the spring-like representation. Although titin is shown here as if it runs inside the thick filament, the exact arrangement is not precisely known.

1. Introduction

1.1 Structure and function of titin

Titinis a $\sim$ 3.5-MDa filamentous protein that constitutes about 10% of the total mass of vertebrate muscle [1–5]. This giant molecule spans the half sarcomere, from the Z-line to the M-line (Figure 1). Titin is anchored to the Z-line and to the myosin-containing thick filaments of the A-band via its strong myosin-binding property. The I-band segment of the molecule consists of serially-linked tandem immunoglobulin (Ig) domains interrupted with a proline (P)-, glutamate (E)-, valine (V)- and lysine (K)-rich segment (hence named PEVK segment) and other unique sequences [1]. Upon sacomere stretch, passive force is generated by the extension of the I-band segment of titin [6–8]. The A-band segment of titin on the other hand is composed of super-repeats of Ig and fibronectin (FN) domains [1]. Titin's A-band segment does not participate in the generation of passive force under normal, physiological conditions, but remains attached to the stiff thick filaments. This portion of the molecule is thought to provide a structural scaffold for the thick filament [9, 10].

1.2 Previously hypothesized extensibility mechanisms in titin

Not long after its discovery, titin has been hypothesized and shown to be extensible. In indirect experiments on muscle cells the elastic properties of titin have been demonstrated by immunoelectron microscopic [11,14] and mechanical experiments [6,8]. The molecular mechanisms behind titin's elastic behavior, however, have for long been elusive. Early theoretical works hypothesized that titin's elasticity might be attributed to the reversible unfolding and refolding of its globular domains [15]. The discovery of titin's PEVK segment with prospective random coil properties indicated that a highly com-

pliant spring might be present in the molecule, allowing extension even without domain unfolding [1]. To sort out possible mechanisms one would ideally take a single titin molecule, hold it by the ends and stretch it while measuring the extension and the force generated. Through such single-molecule mechanical experiments published recently [16–21], we begin to understand the determinants of titin's elastic behavior.

2. Single-polypeptide manipulation

2.1 The laser tweezer

For stretching single molecules of titin and measuring force we used laser tweezers. In the laser tweezer (or optical trap), radiation pressure is utilized for exerting mechanical forces [22]. According to deBroglie's relation, electromagnetic radiation carries momentum, $P = h/\lambda$, where h is Planck's constant and λ is the wavelength of the radiation. A photon flux interacting with an object will, therefore, impose mechanical force, albeit miniscule, on that object. The interaction between photons and the object may take several forms, including reflection, refraction, diffraction and absorption. In the laser tweezer, reflection and refraction are the most important. As a light beam interacts with an object, say a refractive microscopic bead (Figure 2.a), its direction, hence momentum changes. By the law of conservation of momentum, the momentum of the bead, too, changes equally but in opposite direction. According to the Second Law of Newton, the rate of momentum change produces mechanical force; therefore, the bead will be mobilized in the direction of its momentum change (Figure 2.a).

In the laser tweezer the bead interacts not with a hypothetical, infinitely narrow light beam as in Figure 2.a, but experiences the counteracting op-

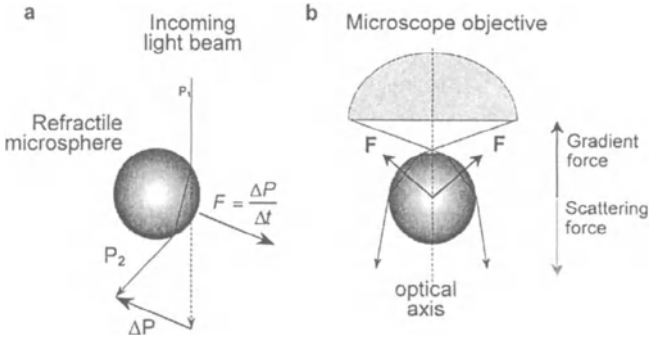

Figure 2. Principles of the laser tweezer. (a) Interaction between a light beam and a refractile microsphere, indicating the change in the momentum of both. (b) Microsphere captured in the laser trap, showing the equilibrium of the gradient and scattering optical forces.

tical forces that arise in a gradient electromagnetic field (Figure 2.b). In equilibrium, the counteracting optical forces, most notably the gradient and scattering forces, acting on the bead are equal and therefore cancel out. For a given optical power the scattering force, which acts in the direction of beam propagation, is proportional to the illuminated area of bead surface, while the gradient force, which acts in the direction of the light intensity change, is proportional to the field gradient. Large field gradients, which correspond to the change in spatial light intensity distribution, typically appear when an intense light beam, for example, a laser beam, is brought to a diffraction-limited focus by an optical lens such as the microscope objective. To displace a bead from its equilibrium position in the center of the optical trap, external mechanical force is required. Conversely, the displacement of the bead from the trap center reflects the effect of external force, whose magnitude, within limits, is linearly proportional to the magnitude of bead displacement. Thus, the laser tweezer can be utilized as a force transducer (in the piconewton range).

2.2 Attachment of titin to beads

Biomolecules are insufficiently refractile to be directly manipulated with laser tweezers. Therefore, we attached levers in the form of microscopic beads to the ends of titin. Titin was prepared from various muscles (rabbit longissimus dorsi, rabbit heart, rabbit soleus, rat heart) by steps described in our earlier works [23,24]. The Z-line end of titin was bound to a latex bead coated with T12 anti-titin antibody. The M-line end of the molecule was attached to a silica bead coated with photo-reactive cross-linkers. The 3.18 μm carboxylated latex beads(SpheroTech) were coated with protein-A, then with T12 [16]. The antibody was then covalently cross-linked to protein-A with DMP (Dimethylpimelimidate-HCl, Pierce). Following blocking of the non-specific binding sites on the beads with 1% BSA and 0.2% Tween-20 in assay buffer (25 mM imidazole-HCl, 25 mM KCl, 4 mM $MgCl_2$, 1 mM EGTA, 1 mM DTT, pH 7.4), the beads were mixed and incubated with titin. The M-line-end bead was prepared by coating 2-µm amino-propyl silica beads (Bangs Laboratories) with the photoreactive cross-linker sulfo-SANPAH (Pierce). For attaching the M-line-end bead to titin, the two different beads were pushed and rubbed against each other in the laser tweezer setup.

2.3 Force and length measurements

We used either a dual-beam, coaxial, counter-propagating laser tweezer system [25] or a single-beam optical trap [19]. In the dual-beam system two 200-mW diode lasers (830 nm, SDL) were used, giving a total optical power of $\sim$ 100 mW at the specimen plane. Force in this system was obtained by directly measuring the change in the light momentum as the beam left the

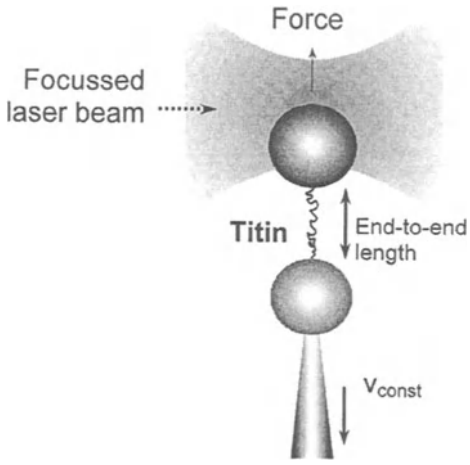

Figure 3. Schematics of the titin stretching experiment.

trap [25]. Using the dual-beam system allowed us to stretch titin with high forces (up to $\sim$ 160 pN) with relatively low optical power. In the single-beam system a high-power laser beam (Nd:YAG, 1046 nm, 4W, Lee Laser) was directed in the sample chamber, where the final optical power was $\sim$ 1.5 W. With the high optical power we were able to stretch titin with forces up to 400 pN. Force in the single-beam system was measured by following the bead displacement from its equilibrium position in the trap center [19]. For force calibration we imposed viscous drag forces on the trapped bead calculated by using Stoke's equation [19,22]. For holding the microscopic bead attached at the other end of titin we used a glass micropipette (outer diameter $\sim$ 40 μm, tip diameter $\sim$ 1 μm mounted in the flow chamber [25]. The micropipette position was adjusted along the XYZ axes by moving the entire flow chamber with a piezoelectric stage (Thorlabs). With the M-line-end bead held by the moveable micropipette and the Z-line specific bead trapped in the force-measuring laser tweezers, titin was stretched by moving the pipette away from the trap (Figure 3). The titin tether was stretched at a constant rate to a maximum predetermined force, while continuously monitoring the force generated in the molecule. When the maximum force was reached, the process was reversed to obtain the release half-cycle. The length of the tethered molecule was calculated by measuring the distance between the centroids of the beads.

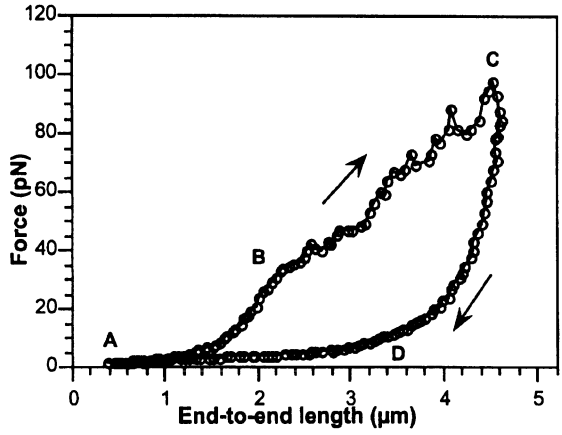

Figure 4. Raw force vs. extension curve obtained for a titin tether. Stretch-release rate, 50 nm/s. Arrows indicate direction of data acquisition (stretch or release). Letters indicate the onset of significant events in the stretch-release cycle (see text).

3. Force versus extension relation of the Titin molecule

3.1 Titin as entropic spring

In the raw force vs. extension curve of titin (Figure 4), force during stretch initially rises nonlinearly (between points A and B). Then titin departs from the initial non-linear elastic behavior, and a force transition begins. This stretch transition (see below) takes place until the maximum experimental force is reached in point C. Upon release, the force drops rapidly, and we initially observe a characteristic non-linear force response. Subsequently, a force transition (release transition, see below) begins at point D. Titin can be extended to lengths exceeding the $\sim 1\mu$m length of the native, folded (but straightened) titin molecule, indicating that part of the extension most likely occurs at the expense of unfolding in the molecule.

The non-linear force response can be explained with the entropic polymer nature of titin. An entropic polymer shortens because of thermally driven bending movements that increase the chain's conformational entropy. To reduce entropy, the chain must be stretched with external force. We find that titin's non-linear elastic behavior can be well described with the wormlike chain (WLC) model [16, 26, 27] that treats the polymer as a bendable or deformable rod of a given persistence length, a measure of the polymer's bending rigidity. The longer the persistence length, the greater the bending

rigidity and the smaller the force required to stretch the chain out. Theoretical WLC force-extension curves were generated using the equation

$$\frac{fA}{k_BT} = \frac{z}{L} + \frac{1}{4\left(1-\frac{z}{L}\right)^2} - \frac{1}{4}, \tag{1}$$

where f is force, A is the polymer's persistence length, z is its end-to-end length, L is the polymer's contour length, k_B is Boltzmann's constant, and T is absolute temperature [26, 27]. The theoretical WLC curves fit the non-linear portions of the data well both during stretch (Figure 5, top) and during release (Figure 5, bottom).

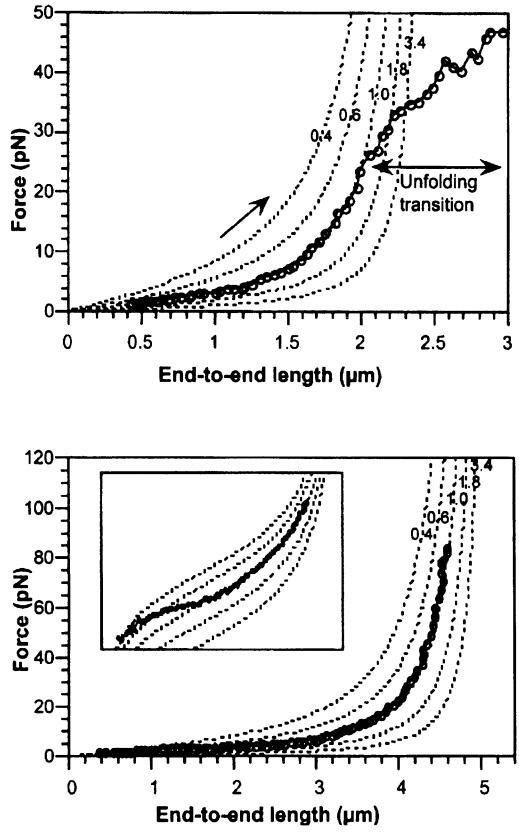

Figure 5. Comparison of the stretch data (top) and the release data (bottom) with theoretical wormlike chain (WLC) curves. The dotted lines are WLC curves for chains of different bending rigidities, with their persistence lengths indicated in nanometers. (bottom, inset) Release data shown on logarithmic force scale. Stretch (unfolding) and release (refolding) force transitions, where the data deviate from WLC behavior, are indicated with arrows.

3.2 Unfolding and refolding transitions in titin

At high forces during stretch the force curve deviates from the predictions of the WLC model (Figure 5, top) because the force drops below the theoretical values. The phenomenon can be reconciled with an overstretch of the polymer which results in the increase of its effective contour length. The process is driven by the unfolding of globular domains in titin.

Hence, we call the stretch transition the unfolding transition. Domain unfolding continues to occur until the maximum experimental force is reached, or as long as folded domains remain in the chain. During release another transition occurs, at low forces (Figure 5, bottom). Here the experimental force increases above the theoretical values, caused by shortening of the effective contour length of the chain, driven by domain refolding. This refolding transition can be particularly well seen when the force is displayed on logarithmic scale (Figure 5, bottom inset).

3.3 Bending rigidity of unfolded titin

The WLC equation allows us to determine the contour and persistence lengths of the titin tether [16,26,27]. At high fractional extension (z/L), as z approaches L, force is dominated by the inverse square term of equation (1) as

$$\frac{fA}{k_BT} = \frac{1}{4\left(1-\frac{z}{L}\right)^2}. \tag{2}$$

Accordingly, at high extensions, $f^{-1/2}$ varies linearly with end-to-end length as

$$f^{-1/2} = 2\left(\frac{A}{k_BT}\right)^{1/2}\left(1-\frac{z}{L}\right). \tag{3}$$

Extrapolation of this linear function to the x- (end-to-end length)-axis, where $f^{-1/2} = 0$, provides the contour length, because $z = L$. The $y - f^{-1/2}$-axis intercept $[2\left(\frac{A}{k_BT}\right)^{1/2}]$, on the other hand, allows to calculate the apparent persistence length of the titin tether as

$$A = \frac{k_BT}{4f}. \tag{4}$$

Figure 6 shows the $f^{-1/2}$ vs. z plot for a stretch and release cycle of a titin tether, with the intercepts highlighted for the extrapolated release curve. The stretch (unfolding) and release (refolding) transitions can also be particularly well observed as these transitions shift the molecule between two states characterized by different contour lengths. Typically, the contour and persistence lengths were more reliably and reproducibly obtained for the release WLC

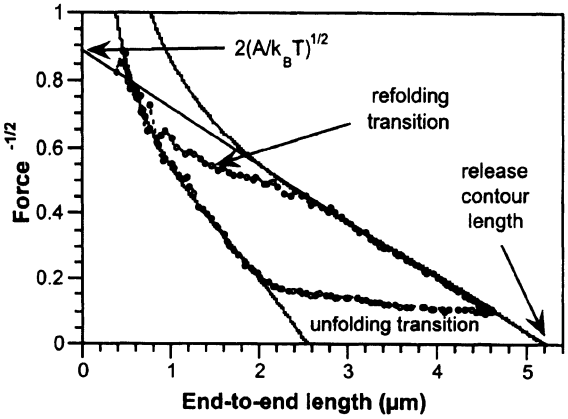

Figure 6. $Force^{-1/2}$ vs. end-to-end length curve obtained in one stretch-release cycle of titin. Both the stretch and release WLC curves were fitted with theoretical WLC curves. For the stretch WLC curve contour and persistence lengths are 2.55 μm and 1 nm, respectively. For the release WLC curve the contour and persistence lengths are 5.2 μm and 1 nm, respectively. Although the apparent persistence lengths are similar here for the stretch and release WLC behavior of titin, more often we find that they are different from each other. The linear extrapolation of the WLC curve at high extensions is also shown, together with the intercepts.

curve, that is, for the unfolded polypeptide. The stretch WLC curve was often distorted by the presence of less characteristic and variable transitions. The persistence length of the single titin molecule A_0 was obtained from the statistical distribution of the apparent persistence length A_{app} derived from many experiments. A_0 was identified as the length corresponding to the peak at the longest A_{app}. Considering that for multi-molecular tethers force at a given fractional extension is the integer multiple of the single-molecule force, using A_0 the number of molecules in any titin tether can be calculated from A_{app} derived from the experimental force-extension curve as

$$n = \frac{A_0}{A_{app}}. \tag{5}$$

Based on 517 stretch-release experiments the persistence length of the single, partially unfolded titin molecule A_0, is 1.69 $\pm$ 0.01 (SD). In addition, the application of the WLC model allowed us to normalize the data to the single molecule. Accordingly, at the employed 50-100 nm/s stretch rate, the onset of the unfolding transition typically occurs between 20 and 30 pN, and refolding during release takes place between 2-3 pN.

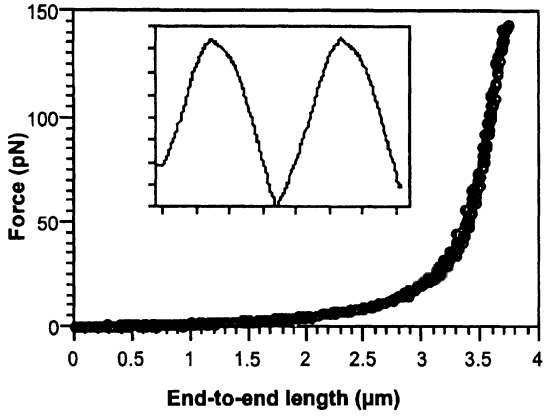

Figure 7. Force vs. extension curve of titin in the presence of 4.5 M of the chemical denaturant guanidine-HCl. Inset shows the stretch-release protocol as the change in titin's end-to-end length as a function of time. Note that the data were obtained in two consecutive stretch-release cycles. Force hysteresis is completely absent.

3.4 Folding non-equilibrium in titin during mechanical manipulation

Hysteresis, characteristic of non-equilibrium processes, was typical for the force-response of titin. Hysteresis appears because the rate at which we stretch or release titin exceeds the rate of unfolding and refolding at equilibrium at the given extension. Thus, application of the external force displaces the domain folding/unfolding reaction from the state of equilibrium. If the stretch and release protocols were carried out at considerably slower (infinitely slow) rates, then the stretch and release curves would merge into a single, equilibrium unfolding/refolding force curve. Alternatively, if titin was kept in the unfolded state, hysteresis should disappear, and we should observe an equilibrium force curve. Indeed, the addition of 4 M guanidine-HCl, a chemical denaturant, abolished hysteresis (Figure 7). Since the release force curve retraces the stretch curve, the molecule is in a state of conformation equilibrium. Thus, the hysteresis in our experiments was indeed related to the kinetics of domain unfolding and refolding.

3.5 Complete mechanical unfolding of titin

Complete domain unfolding in titin can be achieved not only chemically, but also mechanically provided that the forces are sufficiently high or act for a sufficiently long time. To denature the entire ensemble of domains present in the molecule, we stretched titin with high forces (Figure 8) [19]. At forces above $\sim$ 100 pN the unfolding transition stops (point C), because there are

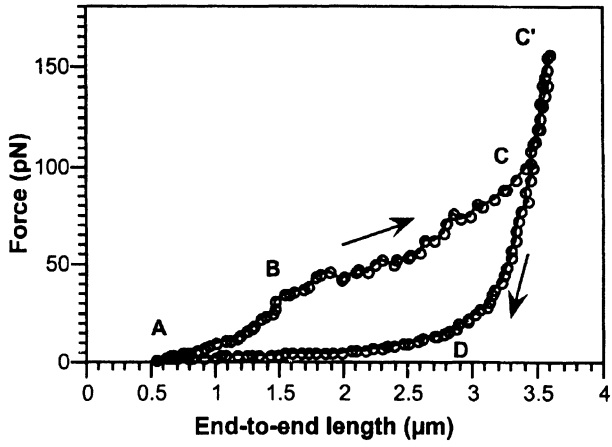

Figure 8. Force vs. extension curve of a titin in which complete, mechanically driven unfolding occurred. Note the congruence of the stretch and release curves at high forces between points C and C'.

no more native domains available to unfold. At this point force begins to rise sharply and follows a WLC curve. Upon release (between points C' and C), force drops rapidly, initially coinciding with the stretch curve. Between points C and C' the stretch and release curves are indistinguishable from each other, indicating that the conformational states of titin are in equilibrium throughout this region of the force vs. extension curve.

4. Mechanical fatigue in repetititively stretched Titin

If a titin molecule is extended in repetitive stretch and release cycles, the stretch force curve progressively approaches the release curve, suggesting that the molecule becomes mechanicaly "worn out" (Figure 9). The process may rightly be called "molecular fatigue". One possible explanation for the appearance of molecular fatigue is that after each stretch/release cycle an increasing fraction of the unfolded titin fails to refold. A slow refolding of titin may be caused by the randomization of proline isomer forms in the Ig and FN domains. Another possibility is that intramolecular structural transitions different from unfolding transition take place in titin during stretch. Such a transition could be the breakage of a pair of intradomain hydrogen bonds [21]. Alternatively, titin's mechanical fatigue may derive from the kinetics of force-driven rupture and formation of non-specific electrostatic bonds that cross-link various sites along a pre-unfolded titin segment [28].

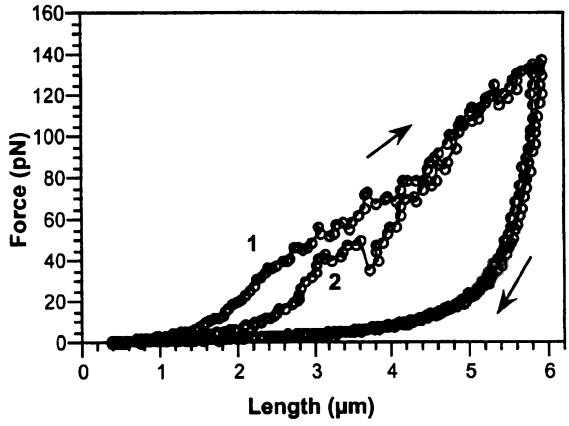

Figure 9. Mechanical fatigue in titin. Force vs. extension curves of a titin tether obtained in two immediately consecutive stretch-release cycles (indicated by the numbers). Note that the strech force curve is shifted toward the release curve in the second cycle. The phenomenon is particularly evident at low forces.

5. Relevance of Titin elasticity to biology

5.1 Comparison of the mechanical behavior of titin and relaxed muscle

It has previously been hypothesized that titin is the major, if not the sole determinant of passive force generation in striated muscle [8,29]. By extrapolating the force measured for the single titin molecule to sarcomeric dimensions (i.e., by scaling the titin force with the number of titin molecules per muscle cross-sectional area), the validity of this hypothesis can be directly tested. We obtained the extrapolated passive muscle force vs. sarcomere length by assuming six titins/thick filament/half sarcomere [8]. Figure 10 shows that the calculated curve is remarkably similar in shape and magnitude to that obtained experimentally for a single skeletal muscle fiber [30]. Thus, titin is indeed the main determinant of the passive force response of muscle [30].

5.2 Mechanical fatigue in muscle

Mechanical fatigue has been observed not only in isolated titin molecules, but also in relaxed muscle [31]. However, the exact mechanisms behind and significance of mechanical fatigue in relaxed muscle have been a puzzle. The observation of fatigue in single titin molecules, and the fact that fatigue occurs in the physiologically relevant force range, may provide a clue to the mechanisms and physiological significance of the phenomenon. Mechanical fatigue

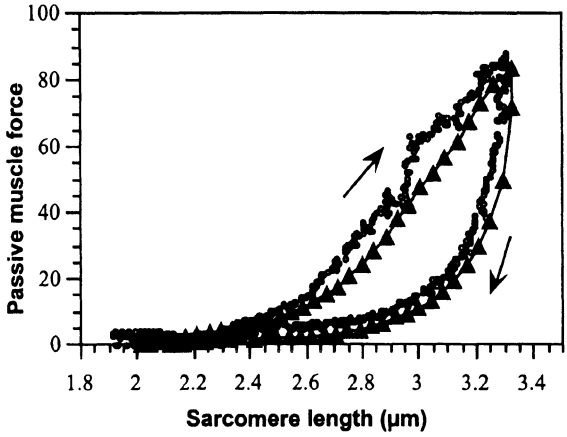

Figure 10. Comparison of the force vs. extension curves obtained for titin and for vertebrate muscle fiber (m. psoas). Open circles, titin force, solid triangles, m. psoas force. The force data of titin were extrapolated with the number of titins per muscle cross-sectional area. Passive force is expressed in kN/m2 tension units.

basically provides contour-length gain to titin and thereby to the passive sarcomere. By varying the effective contour length, a readjustment takes place in the length range across which passive force is generated. That is, following a gain in contour length, the same passive force is reached only upon stretching the muscle to greater lengths. Rate-dependent, repetitive stretch and release experiments indicate that both the contour-length gain and the recovery from it involve kinetic processes. These processes may include unfolding and refolding within different parts of the titin molecule, or the rupture and formation of cross-links along its length. Readjustments in contour length seem to be particularly important in cardiac muscle, as this muscle type operates near the contour length of titin's elastic segment [31].

5.3 Mechanical response of single chromosomes

Although the titin gene is present in the genome of every vertebrate cell, non-muscle titins or titin-like proteins have been scarcely found [32,33]. The recent description of a titin-like protein in Drosophila mitotic chromosomes spurred exciting ideas according to which titin might provide a molecular basis for chromosome structure and elasticity [34]. In fact, the elastic properties of mitotic chromosomes have recently been shown to be quite similar to those of titin, suggesting that there might be a thin, rigid core with titin-like properties within the chromosome [35]. Furthermore, during repetitive cycles of stretch-release, chromosomes, too, displayed mechanical fatigue. Thus, while the exact nature of the chromosome core must be established, it

seems that titin's mechanical behavior (i.e., rate-limited structural transitions superimposed on entropic elasticity) could be considered as a general feature of complex biopolymer systems.

Acknowledgments

This work was supported by grants from the National Institute of Health National Heart, Lung, and Blood Institute (HL61497 and HL62881) to H.L.G., by grants from the National Institutes of Health GM-32543 and the National Science Foundation MBC 9118482 to C.B., and by grants from the Hungarian Science Foundation (OTKA F025353) and the Hungarian Ministry of Health (ETT T-06-021/97) to M.S.Z.K. H.L.G. is an Established Investigator of the American Heart Association.

References

[1] Labeit, S. and Kolmerer, B. (1995) Titins: giant proteins in charge of muscle ultrastructure and elasticity. *Science* **270**, 293-296.

[2] Trinick, J. (1996) Cytoskeleton: Titin as a scaffold and spring. *Current Biology* **6**, 258-260.

[3] Wang, K. Titin/connectin and nebulin: giant protein rulers of muscle structure and function. *Adv. Biophys.* **33**, 123-134.

[4] Maruyama, K. (1997) Connectin/titin, giant elastic protein of muscle. *FASEB J.* **11**, 341-345.

[5] Gregorio, C.C., Granzier, H., Sorimachi, H. and Labeit, S. (1999) Muscle assembly: a titanic achievement? *Curr. Opin. Cell Biol.* **11**, 18-25.

[6] Horowits, R., Kempner, E.S., Bisher, M.E. and Podolsky, R.J. (1986) A physiological role for titin and nebulin in skeletal muscle. *Nature (London)* **323**, 160-164.

[7] Higuchi, H., Suzuki, T., Kimura, S., Yoshioka, T., Maruyama, K. and Umazume, Y. (1992) Localization and elasticity of connectin (titin) filaments in skinned frog muscle fibres subjected to partial depolymerization of thick filaments. *J. Muscle Res. Cell. Motil.* **13**, 285-294.

[8] Granzier, H.L.M. and Irving, T. (1995) Passive tension in cardiac muscle: the contribution of collagen, titin, microtubules and intermediate filaments. *Biophys. J.* **68**, 1027-1044.

[9] Whiting, A., Wardale, J. and Trinick, J. (1989) Does titin regulate the length of muscle thick filaments? *J. Mol. Biol.* **205**, 263-268.

[10] Trinick, J. (1991) Elastic filaments and giant proteins in muscle. *Curr. Opinion Cell. Biol.* **3**, 112-118.

[11] Fürst, D.O., Osborn, M., Nave, R. and Weber, K. (1988) The organization of titin filaments in the half-sarcomere revealed by monoclonal antibodies in immunoelectron microscopy: a map of ten nonrepetitive epitopes starting at the Z line extends close to the M line. *J. Cell Biol.* **106**, 1563-1572.

[12] Itoh, Y., Suzuki, T., Kimura, S., Ohashi, K., Higuchi, H., Sawada, H., Shimizu, T., Shibata, M. and Maruyama, K. (1988) Extensible and less-extensible domains of connectin

filaments in stretched vertebrate skeletal muscle sarcomeres as detected by immunofluorescence and immunoelectron microscopy using monoclonal antibodies. *J. Biochem.* **104**, 504-508.

[13] Trombitás, K. and Pollack, G.H. (1993) Elastic properties of the titin filament in the Z-line region of vertebrate striated muscle. *J. Muscle Res. Cell Motil.* **14**, 416-422.

[14] Trombitás, K., Jin, J.-P. and Granzier, H.L. (1995) The mechanically active domain of titin in cardiac muscle. *Circ. Res.* **77**, 856-861.

[15] Erickson, H.P. (1994) Reversible unfolding of fibronectin type III and immunoglobulin domains provides the structural basis for stretch and elasticity of titin and fibronectin. *Proc. Natl. Acad. Sci. (USA)* **91**, 10114-10118.

[16] Kellermayer, M.S.Z., Smith, S. B., Granzier, H.L. and Bustamante, C. (1997) Folding-unfolding transitions in single titin molecules characterized with laser tweezers. *Science* **276**, 1112-1116.

[17] Rief, M., Gautel, M., Oesterhelt, F., Fernandez, J.M. and Gaub, H.E. (1997) Reversible unfolding of individual titin immunoglobulin domains by AFM. *Science* **276**, 1109-1112.

[18] Tskhovrebova, L., Trinick, J., Sleep, J.A. and Simmons, R.M. (1997) Elasticity and unfolding of single molecules of the giant muscle protein titin. *Nature (London)* **387**, 308-312.

[19] Kellermayer, M.S., Smith, S.B., Bustamante, C. and Granzier, H.L. (1998) Complete unfolding of the titin molecule under external force. *J. Struct. Biol.* **122**, 197-205.

[20] Rief, M., Gautel, M., Schemmel, A. and Gaub, H. (1998) The mechanical stability of immunoglobulin and fibronectin III domains in the muscle protein titin measured by atomic force microscopy. *Biophys. J.* **75**, 3008-3014.

[21] Marszalek, P.E., Lu, H., Carrion-Vazquez, M., Oberhauser, A.F., Schulten, K. and Fernandez, J.M. Mechanical unfolding intermediates in titin modules. *Nature (London)* **402**, 100-103 (1999).

[22] Svoboda, K. and Block, S. Biological applications of optical forces. *Annu. Rev. Biophys. Biomol. Struct.* **23**, 247-285 (1994).

[23] Kellermayer, M.S.Z. and Granzier, H.L.M. Calcium dependent inhibition of in vitro thin-filament motility by native titin. *FEBS Lett* **380**, 281-286 (1996).

[24] Kellermayer, M.S.Z. and Granzier, H.L.M. Elastic properties of single titin molecules made visible through fluorescent F-actin binding. *Biochem. Biophys. Res. Commun.* **221**, 491-497 (1996).

[25] Smith, S.B., Cui, Y. and Bustamante, C. Overstretching B-DNA: The elastic response of individual double-stranded and single-stranded DNA molecules. *Science* **271**, 795-799 (1996).

[26] Marko, J.F. and Siggia, E.D. Stretching DNA. *Macromolecules* **28**, 8759-8770 (1995).

[27] Bustamante, C.J., Marko, J.F., Siggia, E.D. and Smith, S.B. Entropic elasticity of l-phage DNA. *Science* **265**, 1599-1600 (1994).

[28] Kellermayer, M.S.Z., Smith, S., Bustamante, C. and Granzier, H.L. Mechanical fatigue in repetitively stretched single molecules of titin. *In preparation.*

[29] Horowits, R. The physiological role of titin in striated muscle. *Rev. Physiol. Biochem. Pharmacol.* **138**, 57-96 (1999).

[30] Granzier, H. L. M. and Wang, K. Passive tension and stiffness of vertebrate skeletal and insect flight muscles: the contribution of weak cross-bridges and elastic filaments. *Biophys. J.* **65**, 2141-2159 (1993).

[31] Helmes, M., Trombitás, K., Centner, T., Kellermayer, M. S. Z., Labeit, S., Linke, W. A. and Granzier, H. Mechanically driven contour-length adjustment in rat cardiac titin's unique N2B sequence: titin is an adjustable spring. *Circ. Res.* **84**, 1339-1352 (1999).

[32] Eilertsen, K.J. and Keller III, T.C.S. Identification and characterization of two huge proteins of the brush border cytoskeleton: evidence for a cellular isoform of titin. *J. Cell Biol.* **119**, 549-557 (1992).

[33] Eilertsen, K.J., Kazmierski, S.T. and Keller III, T.C.S. Cellular titin localization in stress fibers and interaction with myosin II filaments in vitro. *J. Cell Biol.* **126**, 1201-1210 (1994).

[34] Machado, C. Sunkel C.E. and Andrew D.J. (1998) Human autoantibodies reveal titin as a chromosomal protein. *J. Cell Biol.* **141**, 321-333.

[35] Houchmandzadeh, B. and Dimitrov, S. (1999) Elasticity measurements show the existence of thin rigid cores inside mitotic chromosomes. *J. Cell Biol.* **145**, 215-223.

DYNAMICS OF ACTIN FILAMENTS IN MOTILITY ASSAYS

A microscopic model and its numerical simulation

Zeno Farkas
Dept. of Biological Physics, Eötvös University Budapest, P. Box 32, 1518 Hungary. Collegium Budapest / Institute for Advanced Studies, Budapest, Szentháromság u. 2, 1114 Hungary

Imre Derényi
Dept. of Surgery, MC 6035, University of Chicago, Chicago, IL 60637

Tomas Vicsek
Collegium Budapest/Institute for Advanced Studies, Budapest, Szentháromság u. 2, 1114 Hungary

Abstract We investigate a microscopic model of *in-vitro* motility assays in which actin filaments slide over a layer of myosin heads attached to a glass plate. The resulting set of Langevin equations is solved, and the numerical results are compared to those observed in the related experiments. The agreement is very good, suggesting that our model can predict the behavior under modified conditions or determine some of the parameters that cannot be measured directly, by finding the best fit to the experimentally observed quantities.

Keywords: Actin filament, computer simulation, Langevin equation, microscopic model, motility assays, myosin.

1. Introduction

Motor proteins like myosin or kinesin play an essential role in the motion of living organisms. Much effort has been made to understand how they function. An important experimental tool is the *in-vitro* motility assay [1,2], in which the filaments are placed on a surface coated with motor proteins (see Fig. 1). The filaments may produce various kinds of movements, e.g., they may slide on the surface, rotate around a fixed point, or make a flapping motion [3,4]. In these experiments individual filaments can be analyzed, therefore, valuable

J.J. Kasianowicz et al. (eds.), Structure and Dynamics of Confined Polymers, 327–332.

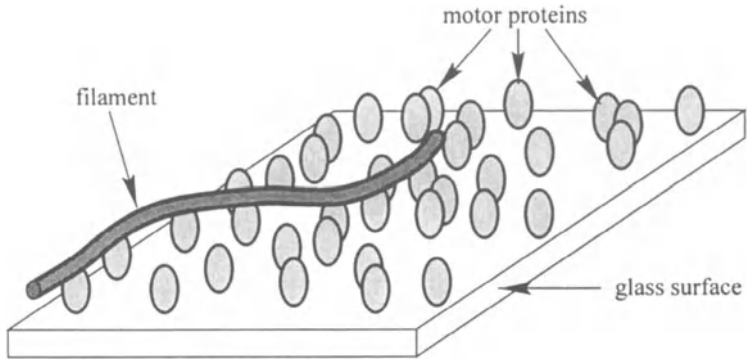

Figure 1. An example of an *in-vitro* motility assay, where a lawn of immobilized motor proteins moves an associated filament.

information can be obtained regarding their elastic properties or the nature of the actin-myosin interaction.

The motion of motor protein filaments has also been the subject of theoretical studies [5, 6]. We have developed a model for the motility assay, and the results of the numerical simulation of the model are presented here.

2. The model

The subject of our investigation is the following motility assay: an actin filament moving over a lawn of randomly distributed myosin heads attached to a horizontal glass plate. The actin filament is modeled by a series of mass points. The neighboring mass points are connected to each other by weightless stiff rods with constant length of a. The model filament is elastic in the transverse direction with *persistence length* L_p (see Fig. 2).

We assume that the myosin molecules can be attached to the actin filament only at certain places called *binding sites.* These binding sites are practically the mass points, although this is not necessary. Since the actin filaments in the experiments move in a liquid, viscous friction forces with viscosity coefficient Γ act on the mass points. The system is in a thermal bath at temperature T, and therefore there also is a random force η_i that satisfies the fluctuation-dissipation relation $\langle \eta_i(t)\eta_j(t')\rangle = 2kT\Gamma\delta_{ij}\delta(t-t')$. Due to high viscosity, the motion of the ith mass point is described by the Langevin equation

$$\Gamma\frac{d\mathbf{r}_i}{dt} = \mathbf{F}_i^{el} + \mathbf{F}_i^{m} + \eta_i, \tag{1}$$

where $\mathbf{F}_i^{el}$ is the elastic force (due to the transversal elasticity), $\mathbf{F}_i^{m}$ is the force exerted by an attached myosin molecule (0 if no myosin is attached), and η_i is the force due to the thermal fluctuations. Our model is microscopic

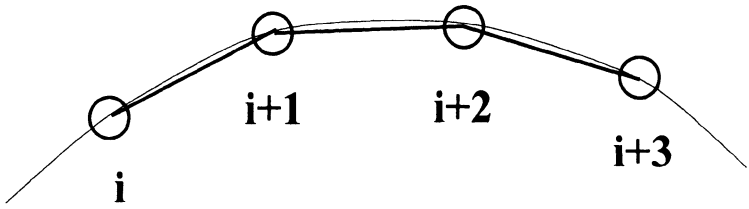

Figure 2. The actin filament is modeled by mass points, which are connected to each other by weightless rods and threaded onto a flexible string.

in the sense that the action of individual myosin heads is taken into account in addition to the microscopic perturbations caused by thermal fluctuations.

To solve the equations of motion with the constraint that the distance between two neighboring points is constant, there are two methods. One method commonly used introduces Lagrange multipliers for the constraints and requires solving a set of nonlinear equations iteratively [7]. The other method transforms coordinates from Euclidian space to a space of angles, taking the constraints into account in a natural way, and requires solving only a set of linear equations [8]. The second method is better, and so we use it. As a consequence, the motion equations for the mass points are transformed into equations for the angles, which will be published separately [9]. These differential equations were solved using the fifth-order Runge-Kutta algorithm with adaptive step size [10].

The combination of the most effective available algorithms allows us to carry out simulations on a time scale compatible with the experimental observation times in spite of the microscopic nature of the model. A more simplistic approach (direct integration of the equations of motion for the mass points) resulted in an algorithm which was 10^3 to 10^4 times *slower*.

The myosin molecules are randomly distributed over the simulation area with surface density σ. In the model, a myosin molecule consists of a rigid head connected to a stretchable string with length l_h and l_s, respectively. One end of the string (the one not connected to the head) is attached to the base. Myosin can freely pivot around this point, and no constraint is imposed on the angle of the head-string connection.

A myosin can attach to a binding site if the point of attachment to the base is within a ring of outer radius l_s and width Δ, and has a center that is l_h from the binding site in a direction that is perpendicular to the actin filament (see Fig. 3). Once a myosin head is attached to an actin unit, it leans backward in a way that the point where the head and the string join each other is moved by a distance of l_{pull} parallel to the actin filament (i.e., the length of the head increases), therefore in most cases the string stretches, and a pulling force is exerted on the actin unit. The absolute value of this force is $D_m(l-l_s)$, where

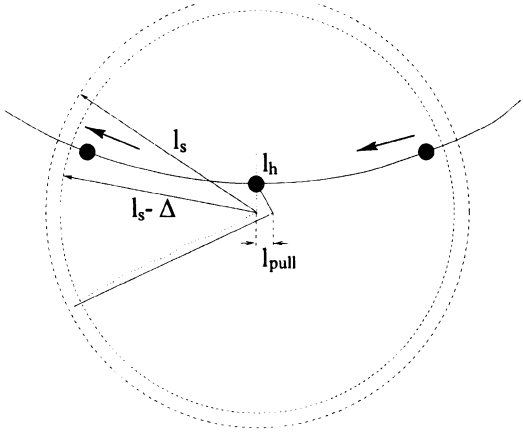

Figure 3. A myosin head can bind to an actin unit if it is located in a proper ring (see text). Once bound, its head changes its configuration by bending backwards a distance l_{pull} in a way that the point where the head and the string joins each other moves parallel to the actin filament. If the sting stretches, a pulling force is exerted to the actin by the myosin string.

l is the length of the stretched string, and its direction is the same as that of the string. It is possible (geometrically) that the string becomes loose and, therefore, no force is exerted. The myosin heads can attach to and detach from the binding sites obeying the following rules:

(i) no more than one myosin head can bind to the same site at any time;

(ii) in case myosin is located in the proper ring, its head can attach to the binding site with "attachment" time constant τ_a (throughout this paper the probabilities are characterized by time constants: the probability of an event with time constant τ to occur during a dt step is dt/τ);

(iii) the myosin head detaches from the binding site with time constant τ_d when it is not stretched too much;

(iv) the myosin head detaches with time constant $\tau_d^{stretch}$ if the string (of length l) is stretched too much, i.e., when $l > l^{max}$.

3. Numerical simulation

The following values were used in the simulations: $\Gamma = 6 \times 10^{-10}$ kg/s, $L_p = 16$ μm, $a = 50$ nm, $D_m = 3 \times 10^{-4}$ kg/s^2, $l_h = 15$ nm, $l_s = 60$ nm, $l_{pull} = 11$ nm, $\Delta = 5$ nm, $\tau_a = 10 \times 10^{-3}$ s, $\tau_d = 4 \times 10^{-3}$ s, $\tau_d^{stretch} = 10^{-6}$ s.

The numerical algorithm has an adaptive step size; it varies between 10^{-5} and 10^{-8} seconds. Except for $\tau_d^{stretch}$, all time constants are greater than 10^{-5}

seconds, therefore it is correct to use the value of dt/τ to give probability in a time step. The simulation program was written in C programming language, and it ran on personal computers with Linux operating system.

4. Results

First we discuss the qualitative results. In the simulation, the motion of the actin filaments is similar to that observed experimentally: (i) if a filament is free to move, it follows a winding path; (ii) if its leading end point gets stuck, the filament starts to rotate around that point and takes on a whirling spiral shape; and (iii) when the filament is attached to the base at two points, it executes an undulating motion. Furthermore, in our simulation we observe occasional reversals of the direction of rotation in case (ii). This was also observed in the experiments, but cannot be described by continuum approximations [4].

As far as the quantitative results are concerned, first we present the velocity dependence on the myosin density of the sliding actin filaments (Fig. 4). It can be seen that the velocity saturates to a value about $5\mu m/s$ near myosin density $400\mu m^{-2}$. This curve is in excellent agreement with the experiments [2].

Another result presented here is the radius of the rotating filament as a function of the myosin density (Fig. 5). The values of the radii are again in very good agreement with experimental results, and fall onto a line when

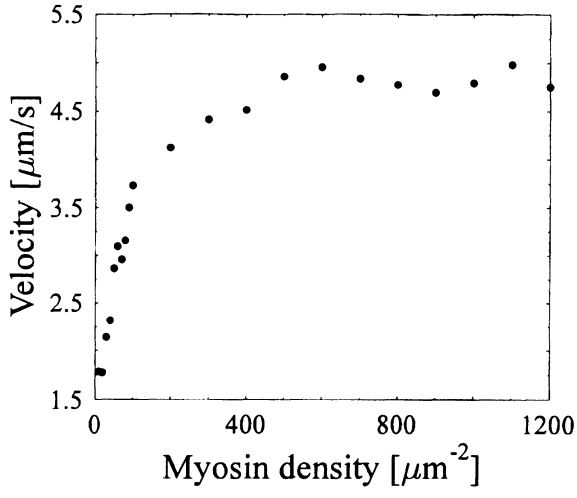

Figure 4. The velocity of sliding actin filaments rapidly saturates to about $5\mu m/s$ as the myosin density is increased past 400 μm^{-2}

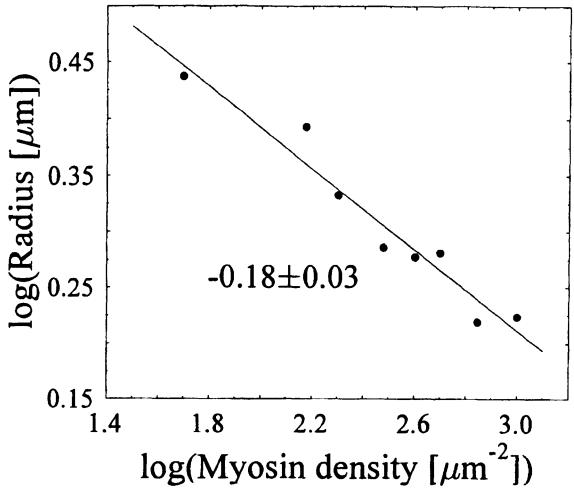

Figure 5. The radius of a rotating filament decreases linearly with the myosin density on log-log scale. This is in agreement with the experimental results; however, the slope is different.

plotted on log-log scale. The slope is -0.18 ± 0.03, which is, however, different from that of the experimental data: -0.36 ± 0.05 [4].

References

[1] K. Sekimoto and K. Tawada (1995), *Phys. Rev. Lett.* **75**, 180–183.

[2] L. Bourdieu, M. O. Magnasco, D. A. Winkelmann, and A. Libchaber (1995), *Phys. Rev. E* **52**, 6573–6579.

[3] K. Sekimoto, N. Mori, K. Tawada, and Y. Y. Toyoshima (1995), *Phys. Rev. Lett.* **75**, 172–175.

[4] L. Bourdieu et al. (1995), *Phys. Rev. Lett.* **75**, 176–179.

[5] T. Duke, T. E. Holy, and S. Leibler (1995), *Phys. Rev. Lett.* **74**, 330–333.

[6] S. Camalet, F. Jülicher, and J. Prost (1999), *Phys. Rev. Lett.* **82**, 1590–1593.

[7] J. M. Deutsch (1988), *Science* **240**, 922-924.

[8] S. He and H. A. Scheraga (1998), *J. Chem. Phys.* **108**, (1), 271–286.

[9] Z. Farkas, I. Derényi, and T. Vicsek. to be published.

[10] W. H. Press, S. A. Teukolsky, W. T. Vetterling, and B. P. Flannery (1992), *Numerical Recepies in C*, Cambridge, England: Cambridge University Press. 2nd ed., Sec. 16.2.

CONFORMATION-DEPENDENT SEQUENCE DESIGN OF COPOLYMERS

Example of bio-evolution mimetics approach

Alexei R. Khokhlov, Victor A. Ivanov, Alexander V. Chertovich, Alexei A. Lazutin
Physics Department, Moscow State University, 117234 Moscow, Russia

and Pavel G. Khalatur
Department of Physical Chemistry, Tver State University, 170002 Tver, Russia

Abstract We present recent data from our Monte Carlo computer simulation study of the properties of AB-copolymer globules that depend strongly on the primary sequence of the A and B monomers. Several primary sequences were studied: random, random-block, regular, and designed sequences. By using the spatial conformation of the homopolymer chain we compared three models: protein-like copolymers, AB-copolymers modeling membrane proteins, and ABC-copolymers modeling proteins with an active enzymatic center. We found evidence that an AB-copolymer chain with a primary sequence prepared on the basis of a particular conformation of a homopolymer chain by a coloring procedure preserves memory about its parent spatial conformation. By analyzing the power spectra of AB-sequences, we find long-range power-law correlations for the copolymers with the designed primary sequences.

Keywords: biomimetics, copolymers, primary sequences with long-range correlations

1. Introduction

For a long time, the chemical industry has been interested in polymers mainly from the viewpoint of obtaining unique construction materials (plastics, rubbers, fibers etc.). Starting from about 1980, the main focus of interest shifted to functional polymers (superabsorbents, membranes, adhesives etc.). In the 1990s, the scientific and industrial polymer community started to discuss smart polymer systems (e.g. soft manipulators, polymer systems for controlled drug release, field-responsive polymers etc.); the meaning behind this term is simply that the functions performed by polymers became more sophis-

J.J. Kasianowicz et al. (eds.), Structure and Dynamics of Confined Polymers, 333–350.

ticated and diverse. This line of research, concentrating on polymer systems with more and more complex functions, will certainly be in the mainstream of polymer science in the 21st century.

In this context, we ask which polymers known at the present time are capable of performing the most sophisticated and diverse functions? The answer is clear. They are biopolymers (e.g. DNA, proteins, RNA etc.), which are responsible for the immensely complicated functions inherent to all living systems. To increase the sophistication of ordinary synthetic polymers, we would need to seek more sophisticated functions. Thus, it is natural to study the functions exhibited by biopolymers *in-vivo* and try to implement similar ideas for synthetic polymer systems. This is the so-called biomimetics approach, which is widely discussed in the recent scientific literature.

Here we propose to address biomimetics from a slightly different viewpoint. The unique features of biopolymers have emerged as a result of long biological evolution. We discuss here globular proteins. The primary sequences of the monomers in globular proteins—the sequences that encode the protein's unique native structure and biological activity—were formed in the process of evolution. This means that the sequences were not always the same: at the early stages of biological evolution they were much less sophisticated, and this resulted in the less sophisticated functions of the early predecessors of today's biopolymers. Returning to biomimetics, we might find it a good idea not to try to mimic biopolymers at the present stage of biological evolution (for synthetic polymer systems this is definitely too complicated and ambitious a task), but rather to try to understand the principles of the biological evolution of sequences at the early stages of evolution and to implement these principles for synthetic copolymers in order to obtain polymer systems with special sophisticated functions. This approach can be called bio-evolution mimetics. Of course, the degree of complexity of functions that we may hope to achieve in this way would be much less than for today's biopolymers. Nevertheless, the behavior of copolymers with designed sequences will exhibit many useful features distinguishing them from scratch (random) sequences.

The studies described here correspond to this approach. The functions of all globular proteins depend on two main factors: (i) the proteins are globular; and (ii) they are soluble in aqueous media. The combination of these two factors is non-trivial; e.g., for homopolymers the transition to the globular conformation is usually accompanied by the precipitation of globules from the solution [1,2]. Protein globules are soluble in water because of the special primary sequence: in the native conformation most of the hydrophobic monomers are in the core of the globule, and the hydrophilic and charged monomer units form the envelope of this core (Fig. 1). Of course, the sorting of the 20 types of monomers available in globular proteins into only two

classes (hydrophobic and hydrophilic) is rather rough. Nevertheless, Fig.1 provides a generalized picture of a protein's structure.

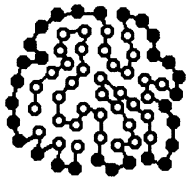

Figure 1. Schematic representation of globular proteins. Hydrophobic units are shown by open circles, while hydrophilic units are represented as filled circles.

Now, having in mind the bio-evolution mimetics approach described above, we can formulate the following problem: is it possible to design a sequence of synthetic AB-copolymers (copolymers that consist of two types of monomers: A-mers and B-mers) such that in the most dense globular conformation, all the hydrophobic B-units are in the core of the globule and the hydrophilic A-units form the envelope of the core? This question was first addressed in [3] (see also [4–6]), and the polymers were called protein-like AB-copolymers.

It is worthwhile here to make two remarks:

(i) Only a very small fraction of all possible AB-sequences are protein-like. Arbitrary AB sequences normally do not provide the perfect fitting of core and envelope shown in Fig.1. Thus, protein-like sequences are already significantly designed in comparison with scratch sequences. None of the copolymers that are normally discussed in the synthetic polymer literature (block copolymers, random copolymers, and copolymers with short-range correlations along the chain) are protein-like. The protein-like sequences may represent the first step of biological evolution selection. In order to perform complicated functions globules should be at least water-soluble. Therefore, studies of AB-copolymers with such sequences may be the simplest exercise for the bio-evolution mimetics approach.

(ii) The protein-like sequences should exhibit long-range correlations along the chain as is clear from Fig. 1. The type of monomer (A or B) depends on the conformation of the globule as a whole, not on the properties of some small part of the chain. We will show below that it is indeed the case and that it determines the long-range correlations quantitatively.

2. Protein-like AB-copolymers: generation and properties of the coil-globule transition

Although it is in principle possible to synthesize protein-like copolymers in the chemical laboratory and find analytical methods for their theoretical description, we discuss here only computer simulation experiments. The pro-

cedure for computer generation of protein-like AB-sequences first proposed in [3] can be described as follows.

We start with an arbitrary homopolymer globule conformation formed by a strong attraction between the monomers (Fig. 2a) and perform a coloring procedure on it (Fig. 2b): monomers in the center of the globule are called B-type (hydrophobic), and monomers belonging to the globular surface are assigned to be A-type (hydrophilic) units. Then the primary structure is fixed, the attraction between monomers is removed, and the protein-like copolymer is ready for further investigation (Fig. 2c). In [3–6] we studied the coil-globule

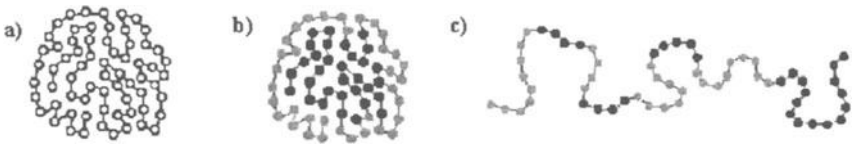

Figure 2. Main steps of the sequence design scheme for protein-like copolymers: (a) homopolymer globule; (b) the same globule after coloring; (c) protein-like copolymers in the coil state.

transition induced in AB-copolymers by the attraction between B-mers (the interactions A-A and A-B were chosen to be repulsive). We compared the properties of this transition with those for random AB-copolymers of the same AB composition and with those for random-block AB-copolymers of the same composition and blockiness. The calculations were performed by the Monte-Carlo method using the bond fluctuation model.

We showed [3–6] that the coil-globule transition in protein-like copolymers occurs at higher temperatures, is more abrupt, leads to the formation of denser globules, and has faster kinetics than for the random and random-block counterparts. The reason for this is illustrated in Fig. 3, where typical snapshots

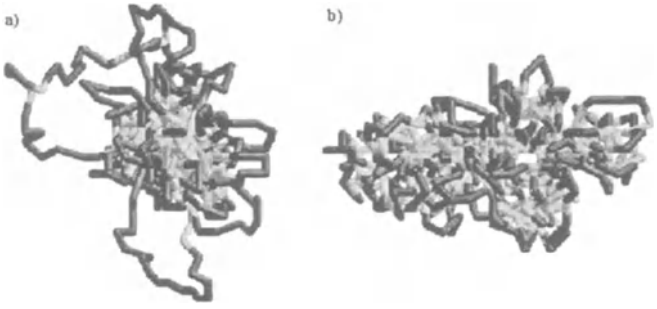

Figure 3. Typical snapshots of globular conformation for (a) protein-like and (b) random copolymers

of globules formed by protein-like and random AB-copolymers with the same AB composition are shown. The core of the protein-like globule (Fig 3a) is much more compact and better formed and is surrounded by hydrophilic loops that stabilize it. Apparently this is due to some memory effect: the core that existed in the parent conformation is simply reproduced upon refolding caused by the attraction of B units. The term "parent" conformation was introduced in [3] to describe the conformation on which the coloring (Fig. 2b) is performed. The features of the parent conformation are inherited by the protein-like copolymer. Looking at the conformations of Fig. 3, it is natural to argue that a protein-like copolymer globule should be soluble in water and thus open to further modification in the course of biological evolution, while random copolymer globules will most probably precipitate and thus drop out of evolution.

3. Long-range correlations in protein-like AB-copolymers

Recently, the existence, origin, and nature of the long-range correlations (i.e., power-law scaling behavior) in DNA sequences has been discussed [8–25]. The presence of such correlations in biopolymers is an indication of the fractal geometry of nature [2, 26–35]. The possible relevance of scale invariance and fractal concepts to the functional features and the structural complexity of biomacromolecules is the subject of considerable interest.

The study of copolymers with specially designed primary sequences (as described above) shows that their behavior is essentially different from that of the random copolymers with the same A/B composition, and from that of random-block copolymers with the same composition and blockiness [3–6]. We concluded that the reason for this is that protein-like copolymers inherit (or memorize) some of the same properties of the parent structures (in particular, the well-formed single B-core coupled with stabilizing A-envelope), which are then manifested in other conditions. An important question is whether the memory effects are manifested in long-range power-law correlations in primary sequences of protein-like copolymers.

The mathematical techniques used for statistical analysis of DNA sequences include autocorrelation analysis and power spectra [36–39], mutual information functions [40], the DNA walk representation and detrended fluctuation analysis [8, 22, 23, 25], ZIPf analysis [41], wavelet-based multifractional formalism [24], etc. To answer the question posed above, we apply two scaling methods to study the primary sequences in protein-like copolymers. The first

method is a standard power spectrum analysis (PSA) [36–39], but with power spectrum estimation using the maximum entropy (all poles) procedure [42]. The second method is the detrended fluctuation analysis (DFA) inxxdetrended,fluctuation,analysis, e.g., [8,22,23,25], which was designed to treat statistically heterogenous DNA sequences.

It is well-known that if a sequence has scale-invariant long-range correlations, then the power spectrum $S(f)$ behaves as $S(f) \sim f^{-\beta}$, and the corresponding log-log plot of $S(f)$ versus f is a straight line with slope $-b$. Here $f = 1/L$, with $L \leq N = N_A + N_B$, where N_A and N_B are the total numbers of A- and B- mers in the sequence) [22,23]. For subsequences of length L with power-law long-range correlations, the detrended fluctuation, $F_D(L)$, can be approximated by the power law $F_D(L) \sim L^{\alpha}$ [36–39]. For ideal power-law correlations, the two scaling exponents α and β are related by $\alpha = (1+\beta)/2 =$ constant [22,23]. Thus, we consider a copolymer A/B sequence to be long-ranged if there are fluctuations in the local A-mer and B-mer densities that significantly depart from Gaussian statistics, i.e., if the fluctuations grow faster than $L^{1/2}$ for a subsequence of a given size L. In contrast, a random infinite sequence is a sequence in which the fluctuations stay within the limits predicted by Gaussian statistics. In this case, the correlations decay exponentially, and we have $\beta = 0$ and $\alpha = 1/2$. Note that many processes, phenomena, and systems are characterized by such behavior. There is, however, a major exception: for a system near the critical point, the exponential decay turns into a power-law decay.

Following the procedure described in [3–6], we prepared the primary sequences of protein-like copolymers for chains of $N \leq 1024$ units using the Monte Carlo (MC) method and the lattice-bond-fluctuation model [43]. For a homopolymer globule in parent conditions (at a temperature slightly below the coil-globule transition), we calculated the distance from the monomer to the center of mass. Half of the monomers were identified as hydrophobic (B-type) and the other half as hydrophilic (A-type) with all hydrophobic monomers closer to the center of mass than any hydrophilic monomer. The results of this sequence design scheme were averaged over 10^3 independent runs with $\simeq 10^6$ MC steps in each run (for details, see [3–6]).

To determine whether the statistical features of the protein-like copolymers are due to the sequence design procedure used here or just due to the different blockiness, we also studied random-block primary sequences. The random-block AB-copolymers have the same composition and the same average length $\langle L \rangle$ of uninterrupted A or B sequences as the protein-like copolymers, but in other respects the AB-sequence is random. The distribution of the values of L was taken in the Poisson form: $\omega(L) = \exp(-\lambda)\lambda^L/L!$, where $\lambda = \langle L \rangle$

and $L = 0, 1, ...\lambda$. Also, we considered random two-letter copolymer as well as regular diblock copolymers with a fixed block length L.

For the power spectrum analysis, we use the MC ensemble of $s = 1000$ independently generated configurations (sequences) of size $N = N_A + N_B \leq 1024$ starting from the beginning and s sequences starting from the end of the sequence. For each sequence, we compute the Fourier transform

$$q_f = \sum_{k=0}^{N-1} u_k \exp(i2\pi kf/N)$$

and the power spectrum

$$S(f) = |q_f|^2 + |q_{N-f}|^2,$$

where $u_k = 1$ for A-mers and $u_k = -1$ for B-mers and where $f = 1/L$ denotes the frequency. Then we average $S(f)$ over the $2s$ sequences

$$S(f) = \frac{1}{2s} \sum_{i=1}^{2s} S_i(f).$$

As mentioned above, if a sequence has long-range power-law correlations, then $S(f) \sim f^{-\beta}$, and consequently a log-log plot of $S(f)$ versus f is a straight line with slope $-b$. Since we dealt with relatively short sequences ($N \leq 210$), the function $S(f)$, obtained via the usual fast Fourier transform (FFT), is very noisy. Therefore, to obtain reasonable power spectrum estimation, we use the so-called maximum entropy (all poles) procedure [42]. In this case, one has

$$S(f) = \frac{a_0}{\left|1 + \sum_{k=1}^{N} a_k z^k\right|^2}, \tag{1}$$

where $z = \exp(i2\pi f/N)$. The a_k are coefficients that satisfy

$$\begin{bmatrix} \phi_0 & \phi_1 & \cdots & \phi_N \\ \phi_1 & \phi_0 & \cdots & \phi_{N-1} \\ \cdots & \cdots & \cdots & \cdots \\ \phi_N & \phi_{N-1} & \cdots & \phi_0 \end{bmatrix} \begin{bmatrix} 1 \\ a_1 \\ \cdots \\ a_N \end{bmatrix} = \begin{bmatrix} a_0 \\ 0 \\ \cdots \\ 0 \end{bmatrix} \tag{2}$$

with $\phi_j = < u_i u_{i+j} >$ for $j = ... - 2, -1, 0, 1, 2, ...$ We have [41]

$$\phi_j = \phi_{-j} = \frac{1}{N+1-j} \sum_{i=0}^{N-j} u_i u_{i+j}, \qquad j = 0, 1, 2, ...N. \tag{3}$$

The basic idea of the DFA technique is to find the dependence of the standard error of a linear interpolation of a statistical sequence on the length L of the

interpolation segment. The original DFA method comprises the following steps [22,23]. First, for each numerical sequence $\{u_i\}$, a running sum

$$\gamma(n) = \begin{cases} \sum_{k=1}^{n} u_k, & n > 0 \\ 0, & n = 0 \end{cases}$$

is computed. Note that this new sequence can be presented graphically as a one-dimensional fractal landscape or topological random walk. The entire sequence $\{\gamma_n\}$ of length N is divided into N/L subsequences (boxes), each of which contains L units and is shifted with respect to the previous box by 1 unit. For each box, linear regression is used to find an interpolated detrended random walk $\gamma_L(n) = a + b(n - n_0)$, where a and b are coefficients of the linear regression. Then we calculate the variances

$$\left\langle [\gamma(n) - \gamma_L(n)]^2 \right\rangle$$

about the local trend for each box and average them over all the boxes of a given size L. To obtain better statistics, we use a moving window. Specifically, we define a sliding observation box of size L that starts at unit i and ends at unit $i + L$. As a result, the $F_D(L)$ function is defined as [22,23]

$$F_D(L) = \frac{1}{(N - L + 1)(L - 1)} \sum_{i=0}^{N-L} \sum_{n=i}^{i+L} [\gamma(n) - \gamma_{i,L}(n)]^2 . \qquad (4)$$

As noted above, for sequences with power-law long-range correlations the detrended fluctuation can be well approximated by a power law $F_D(L) \sim L^{\alpha}$, where, for an ideal (infinite) sequence, the scaling DFA exponent α is related to the spectral correlation exponent β through $\alpha = (\beta + 1)/2$.

We concentrate our study on the statistical analysis of sequences with the requirement that their overall length N is > 512 units, so that the range of scales available to fractal scaling is large enough to make the analysis meaningful with respect to finite size effects. In Fig. 4, we show a log-log plot of the power spectrum $S(f)$ for a protein-like copolymer with $N = 1024$ and average block length $\langle L \rangle = 4.2$. We note in this figure the presence of three spectral regions: low-frequency, mid-frequency, and high-frequency. For the mid-frequency region from a linear regression fit over a reasonable range of scale (more than a decade), one gets $\beta = 0.73 \pm 0.01$. In contrast, random AB-sequences with $\langle L \rangle = 2$ have no correlations [$S(f) \approx 2$ for any f], i.e., the spectral exponent β is equal to zero. The same value of β is obtained for protein-like copolymers in the low-frequency region. In the case of a Poisson random-block copolymer with $\langle L \rangle = 4.2$, the slope found after averaging over 1000 independent realizations undergoes a crossover from zero

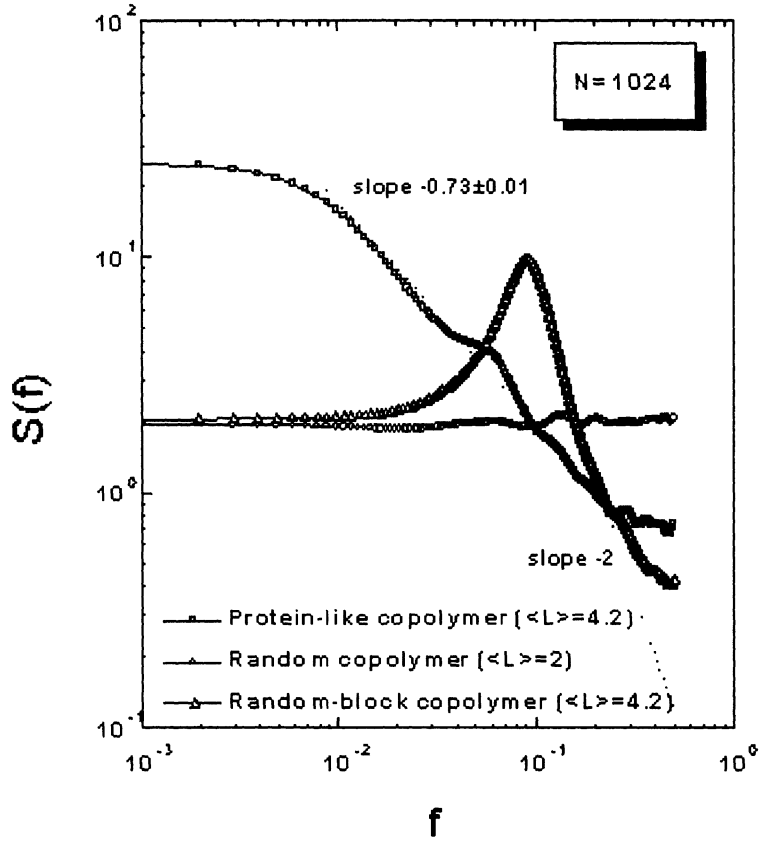

Figure 4. The averaged power spectrum for AB-sequences of 1024-unit protein-like copolymer chains (with $\langle L \rangle = 4.2$), random ($\langle L \rangle = 2$) and random-block ($\langle L \rangle = 4.2$) copolymers.

for small f (corresponding to large L) to 2 for large f, which corresponds to the values of $L < \langle L \rangle$. At $f \approx 1/\langle L \rangle$, the $S(f)$ function has a sharp peak. Note that for protein-like copolymers there is a shoulder in the region $f \approx 1/\langle L \rangle$.

In Fig. 5, we present the DFA results for protein-like, random-block, and regular block copolymers. Only plots obtained for $N = 1024$ are shown in this figure since they are quite representative of the typical features of the data for different values of N. In the case of random copolymers, the DFA method predicts a linear dependence of the $F_D(L)$ function with the exponent $\alpha = 1/2$ at any L. The same exponent is observed for random-block copolymers in the region of sufficiently large L. For regular block copolymers, there is a crossover from $\alpha = 1$ to $\alpha = 0$; this crossover takes place at the value of L corresponding to the block length (=4). On the

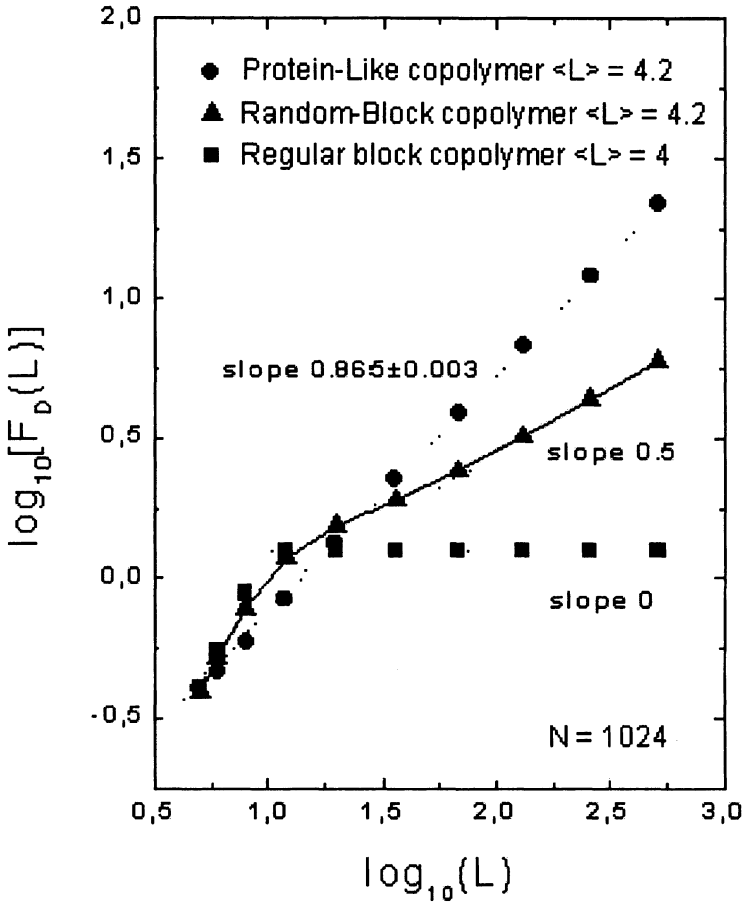

Figure 5. The detrended fluctuation functions for AB-sequences of 1024-unit protein-like copolymer chains (with $\langle L \rangle = 4.2$), random-block copolymer ($\langle L \rangle = 4.2$), and regular block copolymer ($L = 4$).

other hand, we observe distinct long-range power-law correlations which are presented in protein-like AB-copolymers; for the chains with $N = 1024$ we find $\alpha = 0.865 \pm 0.003$. Using the spectral exponent $\beta = 0.73$ found for the same protein-like copolymer, one can obtain $\alpha = (\beta + 1)/2 = 0.87 \pm 0.01$, i.e., a value that within experimental uncertainty is quite consistent with the value a = 0.865 presented above.

Thus, our data show that the monomers in protein-like copolymers are not uniformly distributed throughout the sequence, but rather are organized into blocks or domains of significantly higher relative concentrations. Such a

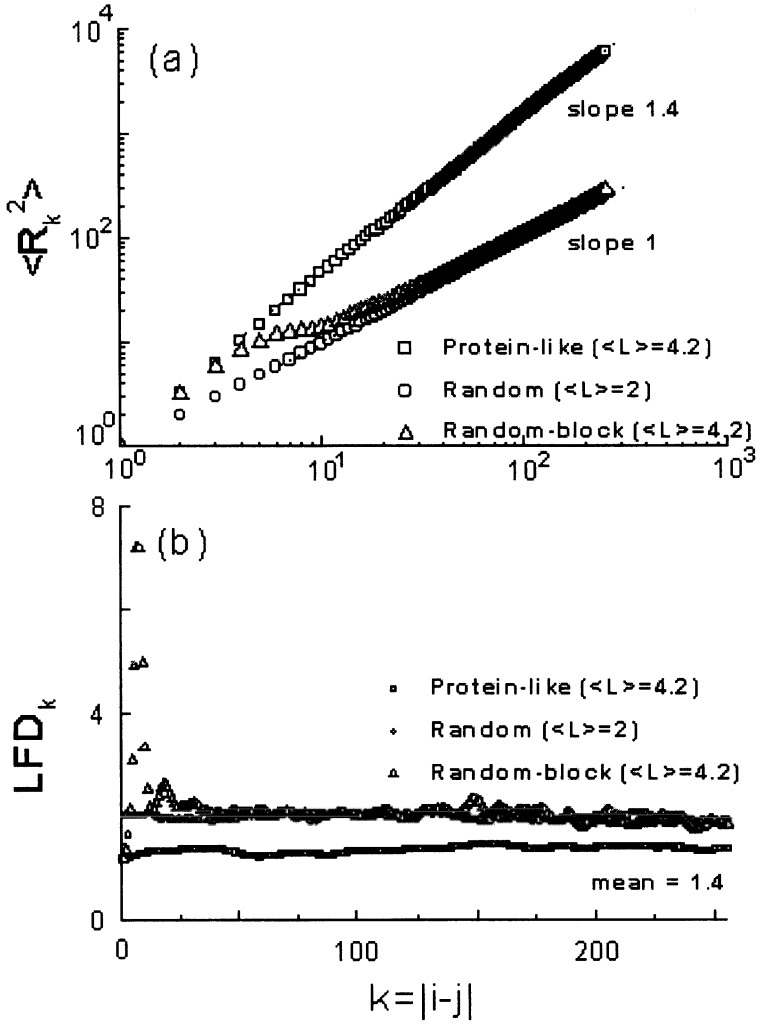

Figure 6. The value of $\langle R_k^2 \rangle$ (a) and the local fractal dimensionality (b) for topological walks corresponding to AB-sequences of N = 1024-unit protein-like copolymer (with $\langle L \rangle = 4.2$), random copolymer ($\langle L \rangle = 2$), and random-block copolymer ($\langle L \rangle = 4.2$).

behavior mirrors fractal properties of this one-dimensional two-letter sequence and is the signature of scale invariance.

In addition to calculating the power spectrum and doing the detrended fluctuation analysis, we have performed a statistical analysis of the internal chain conformation of a topological random walk $\{\gamma_n\}$. To this end, we use the so-called local fractal dimensionality (LFD) [31,44]

$$\mathrm{LFD}_k = \frac{\ln[k/(k-1)]}{\ln\left(\langle R_k^2\rangle/\langle R_{k-1}^2\rangle\right)^{1/2}}, \tag{5}$$

where

$$\langle R_k^2\rangle = \frac{1}{N-k}\sum_{n=1}^{N-k}\langle \gamma_{n,n+k}^2\rangle$$

is the mean-square topological distance between the end points of a chain segment consisting of $k = |i-j|$ units γ_k along the chain. The LFD represents the extent to which the chain is winding. If the chain is a straight line, then $\mathrm{LFD}_k = 1$ and $\langle R_k^2\rangle \sim k^2$, whereas for a freely jointed (Gaussian) chain without the internal correlations, $\mathrm{LFD}_k = 2$ and $\langle R_k^2\rangle \sim k$ for all k. Note that for a real polymer chain, where the chain with excluded-volume interactions behaves as a 3d self-avoiding walk, $\mathrm{LFD}_k = \nu^{-1}(\approx 5/3)$. For the compact polymer globule, $\mathrm{LFD}_k = 3$ and $\langle R_k^2\rangle \sim k^{2/3}$.

In Fig.6(a) the calculated log-log plot of $\langle R_k^2\rangle$ versus k for a protein-like copolymer of length $N = 1024$ is more or less linear with slope ≈ 1.4 for sufficiently large k. In Fig. 6(b), the LFD function is $\mathrm{LDF}_k \approx 1.4$. In contrast, the topological walks of random and random-block copolymers behave like typical Gaussian trajectories with $\langle R_k^2\rangle \sim k$ and $\mathrm{LFD}_k \approx 2$. The results for protein-like copolymers are clearly different from the others. Furthermore, for protein-like copolymers we find that the dependence of $\langle R_k^2\rangle$ appears to be a universal function of the scaling argument $kN^{-1.4}$ for any large $N \geq 256$. This suggests that the topological trajectories can be viewed as fractals and that the topological walk corresponding to a protein-like copolymer exhibits some long-range correlation—specifically a topological excluded-volume effect similar to the usual excluded-volume effect of a real polymer chain in a good solvent.

To conclude this section we emphasize once more that we used power spectrum analysis—specifically the detrended fluctuation method–to explore the distribution of monomeric units in two-letter protein-like copolymer chains obtained via a special sequence design scheme. Power-law long-range correlations are clearly identified and shown to be related to the conformation-dependent sequence design scheme. Our data show that the monomers in the protein-like copolymers are not uniformly distributed throughout the sequence, but rather are organized into blocks or domains of significantly higher relative concentrations. Their behavior reflects fractal properties of these one-dimensional two-letter sequences and is the signature of scale invariance.

Figure 7. Original coloring of a membrane-protein-like globule (on the left), and the final coloring after expansion and subsequent contraction (on the right).

Also, we have found that the topological random walk corresponding to the protein-like copolymers exhibits long-range correlation–specifically a topological excluded-volume effect similar to the usual excluded-volume effect of real polymer chains in a good solvent.

4. AB-Copolymers that mimic membrane proteins

Another way of coloring the monomers inside the dense homopolymer globule mimics some properties of membrane proteins. These proteins are well known to have about 30% of their amino-acid side chains immersed in the lipid membrane, mainly the uncharged and nonpolar side chains, which are hydrophobic. The other 70 % of their side chains are immersed in the aqueous solutions inside and outside the cell and are mainly hydrophilic. In our rough model we took the B-type to be the hydrophobic 30 % in the original globule and the A-type to be the other 70 %. The B-mers are initially inside a cross-section of the parent globule, so the B-part of the parent conformation has the form of a thin disk. We colored the upper and lower hemispheres of A-mers with different colors (black and grey, respectively) to see whether the segregation of the parent is reestablished after equilibration. A snapshot of the original conformation of the AB-copolymer globule is on the left in Fig. 7, and the final conformation is on the right..

We studied the conformations of the AB-copolymer chain with the interaction energies $(\varepsilon_{AA}, \varepsilon_{AB}, \varepsilon_{BB}) = (-1, -1, -2)$, i.e. with a mutual attraction between all monomers, but with the attraction between B-mers twice as strong as the others. We performed the above-described procedure on chains of $N = 256$ units simulated using the Monte CarloMonte Carlo method (MC) method and the bond fluctuation model [43] and averaged the results of this sequence design scheme over $\sim 10^6$ MC steps and over different initial configurations.

We found indeed that the chain has the same structure as the parent, i.e., the segregation structure of the chain is stable. A typical conformation obtained after the expansion and the following contraction of the chain is shown on the right of Fig. 7. Because the interaction is isotropic, the original disk of B-mers, which are colored white in Fig. 7, becomes a sphere of white

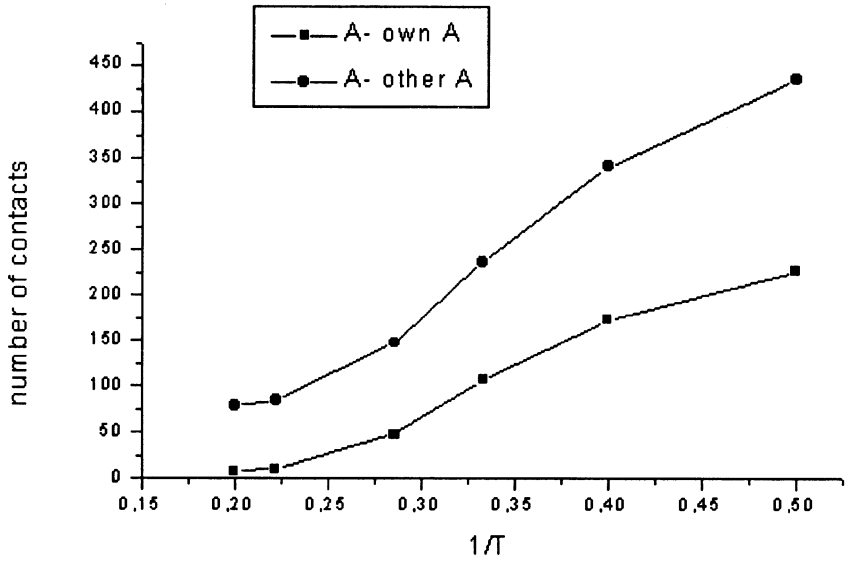

Figure 8. Temperature dependence of the number of contacts between A monomers that belong to different (circles) and the same (squares) hemispheres.

monomers. The grey and black A-mers are still segregated from each other. Thus the grey A-mers have many more contacts with each other than with the black A-mers and vice versa. Figure 8 shows that the number of contacts between all monomers increases with reciprocal temperature because of the transition into the globular state, but the number of contacts between A-mers both in the same hemisphere increases faster than that between A-mers from different hemispheres. In other words, the protein-like copolymer retained some structural features of the parent globule which were then reproduced under the other conditions.

5. ABC-Copolymers that mimic proteins with an enzymic center

The triple coloring of a homopolymer globule is another way of preparing the primary structure of a copolymer chain, the ABC-copolymer. We assigned type A to the surface monomers, type B to the inner monomers (as was done previously for the protein-like copolymers), and type C to the monomers inside a small sphere that is not concentric with the center of mass of the parent homopolymer globule (see Fig. 9).

Our idea was to see whether such a parent conformation can be recombined in the course of equilibration for a different set of interaction parameters including restoring the originally given distance between the centers of the B-

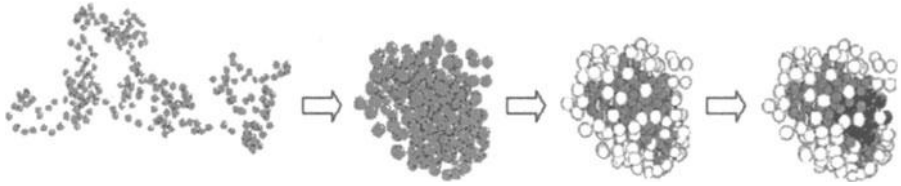

Figure 9. Coloring procedure for ABC-copolymer with active C-center.

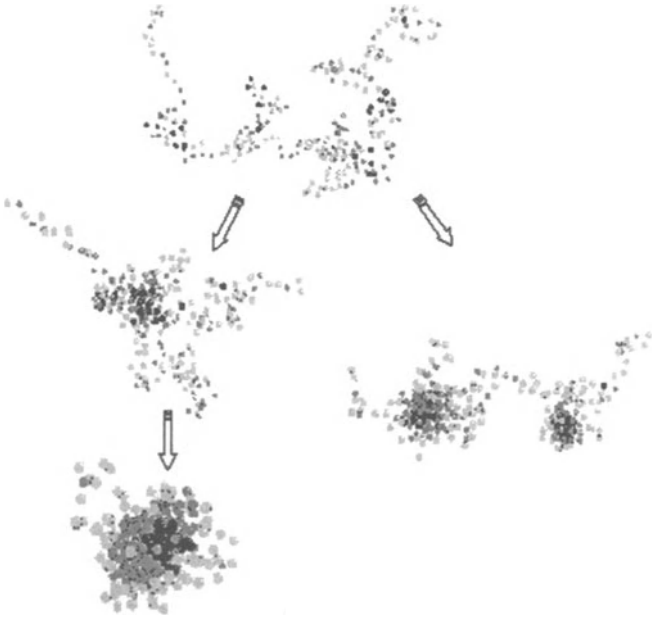

Figure 10. Dependence of the final conformation on the equilibration method.

core and the C-core. We wanted to see whether the position of C-links inside the primary sequence together with a specially chosen interaction potential can lead to stable reconstruction of the spatial conformation of the whole chain.

However, there is a strong dependence on the way we perform the equilibration (see Fig. 10). In that figure the right branch represents the rapid decrease of the temperature during the coil-globule transition, and the left branch represents the slow annealing procedure (smooth decrease of temperature). Decreasing the temperature rapidly brings us to the frozen non-equilibrium conformation. However, we see that using an annealing procedure we are able to achieve a real globule conformation (the global minimum of energy, not just a local minimum).

We performed computer simulations for the chain of N = 256 monomers using attractive interaction potentials for B- and C-links (the attraction for C-link was taken stronger than that for B-links). We found in our computer experiment that such ABC-copolymers normally restore their original structure with B- and C-cores although we have not yet succeeded in determining an interaction potential that would make the center of C-core the same distance from the center of B-core as in the original conformation.

Nevertheless, we definitely found the effect of restoring the active center with the procedure: we switch off the attraction between C-links and let them dissolve inside the dense B-core; and after the switching of attraction between C-links we observe the restoration of C-core again.

6. Conclusions

The approach presented above can be generalized still in another way. To design sequences with special properties it is not necessary to color a dense globule. In fact, any special macromolecular conformation can play the role of a parent one. For example, we considered the conformation of a polymer chain adsorbed on a plane surface [7]. We assigned the A-units to be the monomers closer to the surface at some instant than the other monomers, the B-units and called the AB-chain an adsorption-tuned copolymer. We showed that this copolymer adsorbs onto another plane surface (to which only A-units are attracted) more efficiently than random and random-block copolymers with the same AB-composition and the same degree of blockiness.

In this example, as well as in the other examples in this paper, we have the effect of memorizing some features of the parent conformation in the primary structure (AB-sequence). These features are then manifested when the designed AB-copolymer functions under some other conditions. We think that this might be one of the mechanisms of molecular evolution of biopolymers at the initial stage of evolution.

Acknowledgments

We acknowledge financial support from NATO (grant PST/CLG 974956), INTAS (grant 97-0678), and from the Russian Foundation for Basic Research (grant 98-03-33337a).

References

[1] Lifshitz, I.M., Grosberg, A.Yu. and Khokhlov, A.R. (1978) *Rev. Mod. Phys.* **50**, 683.

[2] Grosberg, A.Yu. and Khokhlov, A.R. (1994) *Statistical Physics of Macromolecules*, American Institute of Physics, NY

[3] Khokhlov, A.R. and Khalatur, P.G. (1998) *Physica A* **249**, 253.

[4] Khalatur, P.G., Ivanov, V.I., Shusharina, N.P. and Khokhlov, A.R. (1998) *Russ. Chem. Bull.* **47**, 855.

[5] Khokhlov, A.R., Ivanov, V.A., Shusharina, N.P. and Khalatur, P.G. (1998) Engineering of synthetic copolymers: Protein-like copolymers. In: *The Physics of Complex Liquids*. Yonezawa, F., Tsuji, K., Kaij, K., Doi, M. and Fujiwara, T. (Eds.). Singapore: World Scientific, p. 155.

[6] Khokhlov, A.R. and Khalatur, P.G. (1999)*Phys. Rev. Lett.* **8**, 3456.

[7] Zheligovskaya, E.A., Khalatur, P.G. and Khokhlov, A.R. *Phys.Rev.E* **59**, 3071.

[8] Peng, C.-K. Buldyrev, S.V., Goldberger, A.L., Havlin, S., Sciortino, F., Simons, M. and Stanley, H.E. (1992) *Nature (London)* **356**, 168.

[9] Nee, S. (1992) *Nature (London)* **357**, 450.

[10] Maddox, J. (1992) *Nature (London* **358**, 103.

[11] Munson, P.J., Taylor, R.C. and Michaels, G.S. (1992) *Nature (London)* **360**, 636.

[12] Amato, I. (1992) *Science* **257**, 747.

[13] Li, W. and Kaneko, K. (1992) *Europhys. Lett.* **17**, 655.

[14] Peng, C.-K., Buldyrev, S.V., Goldberger, A.L., Havlin, S., Sciortino, F., Simons, M. and Stanley, H.E. (1992) *Physica A* **191**, 25.

[15] Stanley, H.E., Buldyrev, S.V., Goldberger, A.L., Hausdorff, J.M., Havlin, S., Mietus, J., Peng, C.-K., Sciortino, F. and Simons, M. (1992) *Physica A* **191**, 1.

[16] Prabbu, V.V. and Claverie, J.-M. (1992) *Nature (London)* **357**, 782.

[17] Yam, P. (1992) *Sci. Amer.* **267**, 23.

[18] Chatzidimitriou-Dreismann, C.A. and Larhammar, D. (1993) *Nature (London)* **361**, 212.

[19] Chatzidimitriou-Dreismann, C.A., Streffer, R.M.F. and Larhammar, D. (1994) *Eur. J. Biochem.* **224**, 365.

[20] Stanley, H.E., Buldyrev, S.V., Goldberger, A.L., Havlin, S., Mantegna, R.N., Ossadnik, S.M., Peng, C.-K., Sciortino, F. and Simons, M. (1994) Fractals in biology and medicine, in: *Diffusion Processes: Experiment, Theory, Simulations*, Pekalski, A. (Ed.), Proc. 5th M. Born Symp., Springer, Berlin, pp. 147-178.

[21] Stanley, H.E., Buldyrev, S.V., Goldberger, A.L., Goldberger, Z.D., Havlin, S., Mantegna, R.N., Ossadnik, S.M., Peng, C.-K. and Simons, M. (1994) *Physica A* **205**, 214.

[22] Buldyrev, S.V., Goldberger, A.L., Havlin, S., Mantegna, R.N., Matsa, M.E., Peng, C.-K., Simons, M. and Stanley, H.E. (1995) *Phys. Rev. E* **51**, 5084.

[23] Viswanathan, G.M., Buldyrev, S.V., Havlin, S. and Stanley, H.E. (1997) *Biophys. J.* **72**, 866.

[24] Arneodo, A., D'Aubenton-Carafa, Y., Audit, B., Bacry, E., Muzy, J.F. and Thermes, C. (1998) *Physica A* **249**, 439.

[25] Buldyrev, S.V., Dokholyan, N.V., Goldberger, A.L., Havlin, S., Peng, C.-K., Stanley, H.E. and Viswanathan, G.M. (1998) *Physica A* **249**, 430.

[26] Mandelbrot, B.B. (1982) *The Fractal Geometry of Nature*, Freeman, San Francisco.

[27] Stanley, H.E. and Ostrowsky, N. (Eds.) (1988) *Random Fluctuations and Pattern Growth: Experiments and Models*, Proc. Cargese NATO ASI, Kluwer Academic Publishers, Dordrecht.

[28] West, B.J. (1990) *Fractal Physiology and Chaos in Medicine*, World Scientific, Singapore.

[29] West, B.J. and Shlesinger, M.F. (1990) *Amer. Sci.* **78**, 40.

[30] Bunde, A. and Havlin, S. (Eds.) (1991) Fractals and Disordered Systems, Springer, Berlin, 1991.

[31] Bunde, A. and Havlin, S. (Eds.), (1994) *Fractals in Science*, Springer, Berlin. 1994.

[32] T. Vicsek. M. Shlesinger, M. Matsushita (Eds.), *Fractals in Natural Sciences*, World Scientific, Singapore, 1994.

[33] West, B.J. and Deering, W. (1994)*Phys. Rep.* **246**, 1.

[34] Buldyrev, S.V., Goldberger, A.L., Havlin, S., Peng, C.-K. and Stanley, H.E. (1994) In: *Fractals in Science*, Bunde, A. and Havlin, S. (Eds.), Springer, Berlin, pp. 49-83.

[35] Bassingthwaighte, J.B., Liebovitch, L.S. and West, B.J. (1994) *Fractal Physiology*, Oxford University Press, New York.

[36] Azbel, M.Ya. (1995) *Phys. Rev. Lett.* **75**, 168.

[37] Herzel, H. and Grosse, I. (1995) *Physica A* **216**, 518.

[38] Voss, R.F. (1992) *Phys. Rev. Lett.* **68**, 3805.

[39] Voss, R.F. (1994) *Fractals* **2**, 1.

[40] Li, W. (1992) *Int. J. Bif. Chaos* **2**, 137.

[41] Mantegna, R.N., Buldyrev, S.V., Goldberger, A.L., Havlin, S., Peng, C.-K., Simons, M. and Stanley, H.E. (1995) *Phys. Rev. E* **52**, 2939.

[42] Press, W.H., Flannery, B.P., Teukolsky, S.A. and Vetterling, W.T. (1986) *Numerical Recipes. The Art of Scientific Computing*, Cambridge University Press, Cambridge, UK, p. 430.

[43] Carmesin, I. and Kremer, K. (1988) *Macromolecules* **21**, 2819; Deutsch, H.P. and Binder, K. (1991) *J. Chem. Phys.* **94**, 2294.

[44] Havlin, S., Ben-Abraham, D. (1982) *Phys. Rev. A* **26**, 1728.

SINGLE MOLECULE NUCLEIC ACID ANALYSIS BY FLUORESCENCE FLOW CYTOMETRY

Peter M. Goodwin, W. Patrick Ambrose, Hong Cai, W. Kevin Grace, Erica J. Larson, Babetta L. Marrone, James H. Jett, James H. Werner, and Richard A. Keller
M888 Bioscience Division, Los Alamos National Laboratory, Los Alamos, NM 87545

1. Introduction

During the past decade the sensitivity and selectivity of laser-induced fluorescence detection methods in liquids have been refined to the point where a molecule labeled with a *single* fluorophore dissolved in solution can be detected and identified as it flows through a focused excitation laser beam. Progress in this field is reviewed in a number of recent papers. [1–5]

Single molecule spectroscopy (SMS), the detection and measurement of properties of individual fluorescent molecules, allows assays to be done that would be difficult or impossible with bulk measurement methods. A useful result of SMS is the measurement of property distribution functions of single fluorescent molecules. Property distribution functions are accessible with SMS since the fluorescence properties of single molecules are measured individually. This information is often inaccessible to bulk measurements due to ensemble averaging. Photophysical properties that have been used for identification of fluorophores at the single molecule level include: gross differences in excitation and emission spectra [6], fluorescence emission lifetime [7–10], fluorescence emission intensity [9], and fluorescence emission polarization anisotropy [11]. Two SMS assays under development in our laboratory, rapid sizing of single DNA fragments and the possibility of single molecule DNA sequencing, are discussed in sections 3 and 4 of this chapter.

2. Single molecule spectroscopy

Figure 1 shows a simplified, schematic representation of single molecule detection (SMD) via laser-induced fluorescence. A solvated, fluorescent molecule crossing a focused excitation laser beam tuned to the transition frequency

J.J. Kasianowicz et al. (eds.), Structure and Dynamics of Confined Polymers, 351–370.

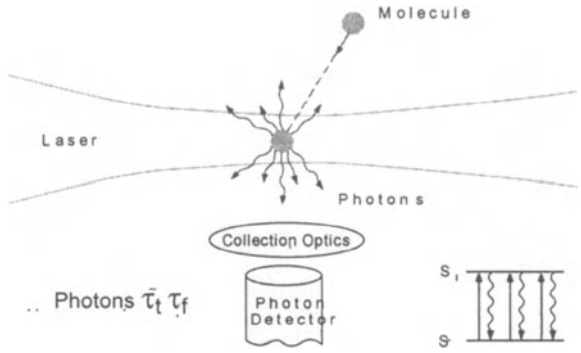

Figure 1. Photon burst detection of single molecules. Reprinted with permission from Davis, et al. (1991). *Genetic Anal.* **8**, 1-7. ©1991 Elsevier Science B.V.

between its ground (S_0) and first excited (S_1) electronic states is rapidly cycled between these two electronic states by the absorption of excitation photons and the emission of fluorescence photons. The optically saturated cycle rate is limited by the fluorescence lifetime, τ_f, of S_1. For highly fluorescent molecules of interest for this work, τ_f is in the range of $1 - 5$ ns. A large fraction of cycles result in the emission of fluorescence photons. This fraction, the fluorescence quantum yield (Φ_f), is typically in the range of $0.2 - 0.9$ in SMS studies. The signature of a single fluorescent molecule crossing the excitation laser is a burst of fluorescence photons. Under the proper conditions this photon burst can be easily detected above the background. The maximum number of photons emitted per molecule, assuming every cycle emits a fluorescence photon, is the molecular transit time across the laser beam, τ_t, divided by the fluorescence lifetime, τ_f. For $\tau_f \sim 1$ ns and a millisecond transit time this number is $\sim 10^6$. In practice, a lower photon yield is realized due to other photophysical characteristics of the fluorophore including its photo-stability, excited triplet state yield, and excited triplet state lifetime. Typically, the most important photophysical characteristic is the photostability or photo-destruction quantum yield, Φ_d, the probability per excitation that the molecule will undergo irreversible photochemical decomposition to a non-fluorescent product. For fluorophores commonly used for SMS, Φ_d is in the range of $10^{-7} - 10^{-5}$ depending on the fluorophore and and solvent combination considered. Most fluorophores useful for SMS have Φ_d in the range of $\sim 10^{-5}$ when dissolved in water. Under extreme excitation conditions where almost all the of molecules photobleach before crossing the excitation laser the average number of fluorescence photons emitted by a molecule is Φ_f/Φ_d. Typical fluorophores used for SMS emit $\sim 10^5$ fluorescence photons under such conditions.

As shown schematically in Fig. 1, high numerical aperture imaging optics are used to efficiently collect emission from the excitation volume and transmit it through an appropriate spectral bandpass filter (not shown in figure) to the photocathode of a sensitive, photon-counting detector. Sensitive optical systems used in our single-molecule studies have overall fluorescence photon collection efficiencies of $\sim 10\%$ resulting in overall fluorescence detection efficiencies of $\sim 1\%$. Under excitation conditions, where most of the molecules do not photobleach, the signature of a single fluorophore crossing the excitation laser beam, on a millisecond time-scale, is a burst of ~ 100 detected photons (photoelectrons, PE). This burst is easily detectable when appropriate steps are taken to reduce the luminescence background. The major source of background is Raman and Rayleigh scattering of the excitation laser by the solvent. This background is most easily reduced by limiting the volume of the laser excited solvent in the field of view of the detector, referred to here as the detection volume. A spatial filter located in the image plane of the collection optics (not shown in the figure) limits the length of the excitation volume in the field of view of the detector. The size of the detection volume is determined by the diameter of the focused laser beam, the magnification of the collection optics, and the size of the spatial filter. For a fixed excitation intensity, the solvent scattering intensity scales linearly with the detection volume, while the fluorescence intensity of a single molecule is essentially independent of the detection volume. We use detection volumes that are as small as practical for our applications. Most of these applications require volumes with linear dimensions larger than the diameter of the analyte sample stream to ensure uniform excitation of the analyte. Hydrodynamic focusing is used produce small analyte sample streams at the center of a flow cell. [12] Typically, samples are introduced into a flowing sheath stream using a small inner diameter ($1-20\ \mu\mathrm{m}$) capillary inserted into the flow cell upstream of the detection volume. Under the flow conditions typically used for SMD ($\sim 1\ \mathrm{cm/s}$ flow velocity), lateral diffusion of low molecular weight ($< 1000\ \mathrm{amu}$) analyte, between the point of introduction and the point of interrogation $\sim 50\ \mu\mathrm{m}$ downstream, results in sample stream diameters of $\sim 10\ \mu\mathrm{m}$ in the detection volume.

Excitation of the entire cross section of the analyte stream is required for efficient SMD and quantitative analysis of single molecule fluorescence burst intensities. [3] We use detection volumes in the range of 1 to 50 picoliters depending on the requirements of the application. Small volumes are used to reduce solvent scattering and fluorescence impurity background for the detection and identification of molecules containing a single fluorophore. Larger volumes are used for DNA fragment sizing where high resolution fluorescence burst intensity measurements are required.

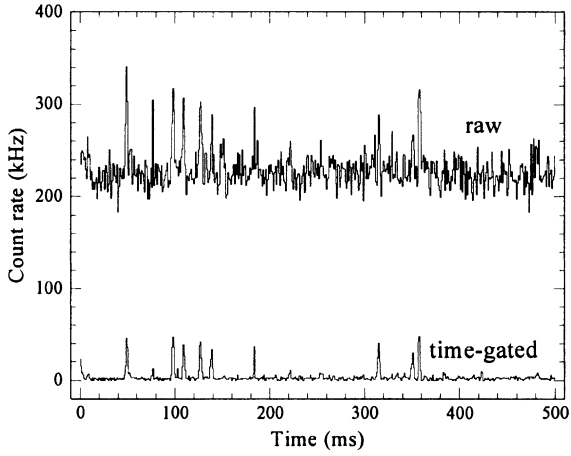

Figure 2. Detection of single Rhodamine 6G (R6G) molecules in a $\sim 3\,\mathrm{pL}$ volume using pulsed excitation and TCSPC to discriminate against water Raman and Rayleigh scattering background. R6G molecules dissolved in water were flowed one-at-a-time through a $16\,\mu\mathrm{m}$ e^{-2} diameter 514.5 nm mode-locked Ar^+ excitation laser beam ($\sim 200\,\mathrm{ps}$ pulse width, 82 MHz pulse repetition frequency, 30 mW average power). Fluorescence emission was detected through a $550 \pm 30\,\mathrm{nm}$ band-pass filter using a single-photon counting avalanche photodiode. Top trace is raw TCSPC data binned into 1 ms intervals. Bottom trace (time-gated) is the same data processed to exclude photons detected within $\sim 1\,\mathrm{ns}$ of the excitation laser pulse. Fluorescence photon bursts from single R6G molecules ($\sim 40\,\mathrm{kHz}$ peaks) are clearly evident in the time-gated TCSPC data. Reprinted with permission from Ambrose et al. (1999). *Chem. Rev.* **99**, 2929-2956. ©1999 American Chemical Society. [5]

For single fluorophore detection and identification, we use pulsed excitation and time-correlated single-photon counting (TCSPC) to further discriminate against solvent Raman and Rayleigh scattering. [13, 14] Briefly, a mode-locked, picosecond laser pulse train is used to excite the sample. TCSPC is used to measure the arrival time of each detected photon with respect to the excitation laser pulse. Prompt photons detected within $\sim 1\,\mathrm{ns}$ of the laser pulse are primarily due to solvent Raman and Rayleigh scattering, instantaneous processes occurring only during the laser pulse, and are not processed. For analytes with fluorescence lifetimes $> 2\,\mathrm{ns}$ most of the fluorescence photons arrive at times $> 1\,\mathrm{ns}$ after the laser pulse and are processed. Figure 2 demonstrates the background reduction afforded by pulsed excitation and TCSPC.

Pulsed excitation and TCSPC also enables the measurement of single molecule fluorescence lifetimes. Since the arrival time with respect to the excitation pulse is measured for each detected photon comprising a fluorescence burst, these arrival times can be used to estimate the fluorescence lifetime of the molecule that caused the burst. Fluorescence photon burst lifetime

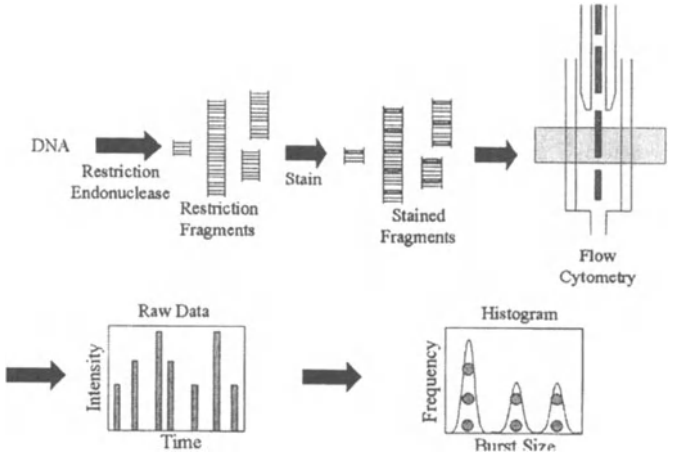

Figure 3. Schematic outline of DNA fragment sizing by flow cytometry. Often the DNA to be analyzed is first digested with a restriction endonuclease to produce a set of restriction fragments. The DNA fragments are then stained with a fluorescent, intercalating dye such as TOTO-1. A dilute solution of these fragments is passed through an ultrasensitive flow cytometer. Fluorescence photon bursts from individual fragments are recorded and a burst size histogram is compiled from the data. Since the fluorescence burst size is proportional to the fragment length, the burst size histogram is a measure of the distribution of DNA fragment lengths in the sample.

measurements have been used by a number of different groups to identify different fluorescent species at the single molecule level. [7–10] In contrast to spectral identification methods that require at least two fluorescence detection channels an possibly multiple excitation wavelengths [6], single molecule identification by fluorescence lifetime and/or fluorescence emission intensity can be accomplished with a single detection channel and a single excitation wavelength.

3. Single molecule DNA fragment sizing

We [15–22], and others [23–27], have developed a method to measure the length of double-stranded DNA fragments based the measurement of fluorescence intensities of individual, dye-intercalated DNA fragments. A simple schematic outlining this approach to DNA fragment sizing is shown in Fig. 3. A sample of DNA fragments to be analyzed is first stained with a fluorescent intercalating dye such as thiazole orange homodimer (TOTO-1). The dye binds stoichiometrically to the DNA such that the amount of dye intercalated in a fragment is proportional to the length of that fragment (base pairs). An additional property of these intercalating dyes is a large increase ($\sim 1000\times$) in the fluorescence quantum yield of the dye upon intercalation into

the DNA. [28] This enhancement eliminates the need to separate unbound dye from stained DNA fragments prior to analyzing the sample. Stained DNA fragments are diluted to a concentration of $\sim 10^{-14}$ M and introduced into an ultrasensitive fluorescence flow cytometer developed in our laboratory. Fragments pass individually through the ~ 50 pL, laser-illuminated detection volume and each fragment produces a burst of fluorescence photons that is detected and recorded. The data set is searched for fluorescence bursts and the number of photoelectrons comprising each burst (burst size) is tabulated. Since the fluorescence burst size is proportional to the fragment size, a histogram of the burst sizes is a measure of the distribution of fragment sizes in the sample.

Compared to conventional gel electrophoresis methods, our technique is extremely sensitive and fast. We typically analyze less than a picogram of DNA in less than 10 minutes. Conventional gel electrophoresis requires hundreds of nanograms of DNA and analysis times ranging from hours to tens of hours. Flow cytometric DNA fragment sizing has a number of other advantages over gel electrophoresis. It is quantitative, individual DNA fragments are counted, and the fluorescence signal is linear with fragment size. In contrast, the migration distance in gel electrophoresis is inversely logarithmic with fragment size, and relative fragment populations must be estimated from band intensities. Finally, in contrast to gel electrophoresis, the resolution of flow cytometric DNA sizing improves with increasing fragment size. More complicated, pulsed-field gel electrophoresis (PFGE) techniques used to separate DNA fragments larger than ~ 50 kb in length typically measure fragment sizes with an uncertainty of $\sim 10\%$. Fragments ranging in size from 0.4 kb [20] to 425 kb [22] have been sized by flow cytometry with measurement uncertainties typically in the range of 2-5%. Currently, flow cytometric DNA fragment sizing is limited to fragments < 500 kb in length because of DNA fragment shearing during handling and analysis.

3.1 Applications

In this section we describe the application of flow cytometry to DNA fragment sizing to characterize P1 artificial chromosomes (PACs) or bacteria artificial chromosomes (BACs), and to discriminate between bacterial species.

3.1.1 Evaluation of PAC and BAC libraries. Since artificial chromosomes and restriction fragments from bacterial genomes digested with rare-cutting endonucleases are typically tens to hundreds of kilobasepairs in length, PFGE is required to characterize these DNA samples. Unfortunately, fragment size analysis with PFGE is relatively slow (~ 20 hours) and requires hundreds of nanograms of DNA. [18,22] Flow cytometry provides a faster and more sensitive method for sizing these large DNA fragments.

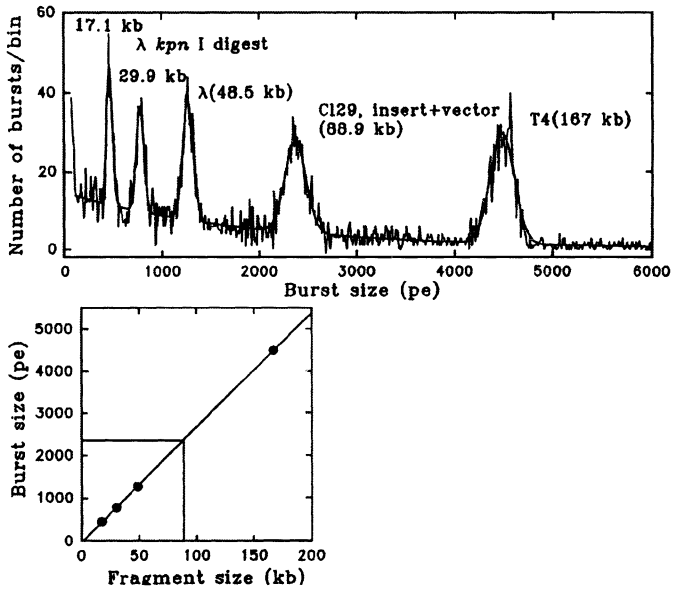

Figure 4. Fluorescence flow cytometry sizing of a PAC clone. The top panel shows a histogram of fluorescence burst sizes obtained from an intact PAC clone. λ Kpn I digest, λ DNA, and T4 DNA were used as size standards. The smooth, solid line is a fit of the histogram to a sum of five Gaussians plus an exponentially decaying background. Experimental conditions: 30 mW continuous wave excitation at 514.5 nm; excitation laser beam e^{-2} diameter, 46 μm; DNA staining dye, TOTO-1; DNA fragment transit time, 1.6 ms; amount of DNA analyzed, < 1 pg; analysis time, 134 s. The bottom panel shows a plot of burst size means, obtained from the centroids of the Gaussian fits, versus the fragment sizes of the standards. The means of the DNA standard peaks were fit by linear regression. The size of the intact PAC clone determined from the calibration line and its mean burst size is 88.9 ± 0.8 kb. Reprinted with permission from Huang et al. (1996). *Nucleic Acids Res.* **24**, 4202-4209. ©1996 Oxford University Press. [18]

BACs and PACs are plasmids that can accept a DNA fragment as large as 300 kb from another organism. [29,30] Typically, the DNA fragment of interest is inserted into a PAC or BAC, and the plasmid is then transferred into a host cell (normally a bacterium), where it is propagated. Sizing of these PAC and BAC clones is important for characterizing the insert. A library consists of a set of PAC or BAC clones that contain DNA inserts of the organism under study. The availability of libraries is very important in the construction of physical maps and is the starting point for sequencing an organism's genomic DNA.

The use of fluorescence flow cytometry to size PAC clones is demonstrated in Fig. 4. PAC clones were prepared by a protocol described in detail elsewhere. [18] The PAC clones were stained with TOTO-1. The top panel shows a burst size histogram obtained from a mixture containing an intact

PAC clone and several size standards. The histogram was fit to a sum of five Gaussians plus an exponentially decaying background. The bottom panel shows a plot of the burst sizes, obtained from the centroids of the Gaussian fits, versus the fragment sizes of the standards. The regression line was used to calculate the size of the PAC clone. The size of the insert was obtained by subtracting the known size of the PAC plasmid from the size of the intact PAC clone determined by flow cytometry. Insert sizes of several PAC clones determined by fluorescence flow cytometry agreed with results obtained with PFGE within the uncertainties of the measurements ($\sim 10\%$ for PFGE). [18]

3.1.2 Bacteria species identification by flow cytometry. Rapid identification of bacteria species and strains is critical in many areas including public health, biological weapons defense, and epidemiology. [31–34] In the case of a food poisoning outbreak or a suspected biological attack, rapid identification of the bacterial species and strain involved is crucial for effective treatment. In a biological attack, symptoms may not appear until it is too late to treat the infection. It is important to determine what pathogen was released in order to begin treatment immediately since pathogenic strains may be resistant to specific antibiotics [35]. Rapid identification methods also allow public health officials to track the course of an outbreak or to determine whether a common food or water source is responsible for multiple outbreaks. Discrimination is achieved by digesting the genomic DNA of the bacterium with a rare-cutting restriction enzyme and determining the sizes of the fragments that result. The set of fragments that is obtained (the fingerprint) depends on the DNA sequence, and is therefore characteristic of a particular species or strain of bacteria. [31] Again, because PFGE is used to size these fragments, hundreds of nanograms of bacterial DNA and ~ 20 hours are required to obtain the fingerprint.

Our flow cytometric DNA fragment sizing technique has been used for this analysis. Genomic DNA from bacterial cells was extracted and digested with a rare-cutting restriction enzyme to produce a set of different sized fragments. These bacterial DNA fragments were stained with TOTO-1 and analyzed in our ultrasensitive flow cytometer. [22] The sizes of the fluorescence bursts obtained from the individual fragments were histogramed to obtain the bacteria fingerprint. Figure 5 shows an example of the use of fluorescence flow cytometry to discriminate among different bacterial species. [22] The three histograms shown were obtained by digesting genomic DNA from three different species of bacteria with the Not I restriction endonuclease. Each species of bacteria can easily be distinguished from the others by its fingerprint pattern. The histograms were fit to a sum of Gaussians with an exponentially decaying background. The insets show a plot of the centroid positions of the

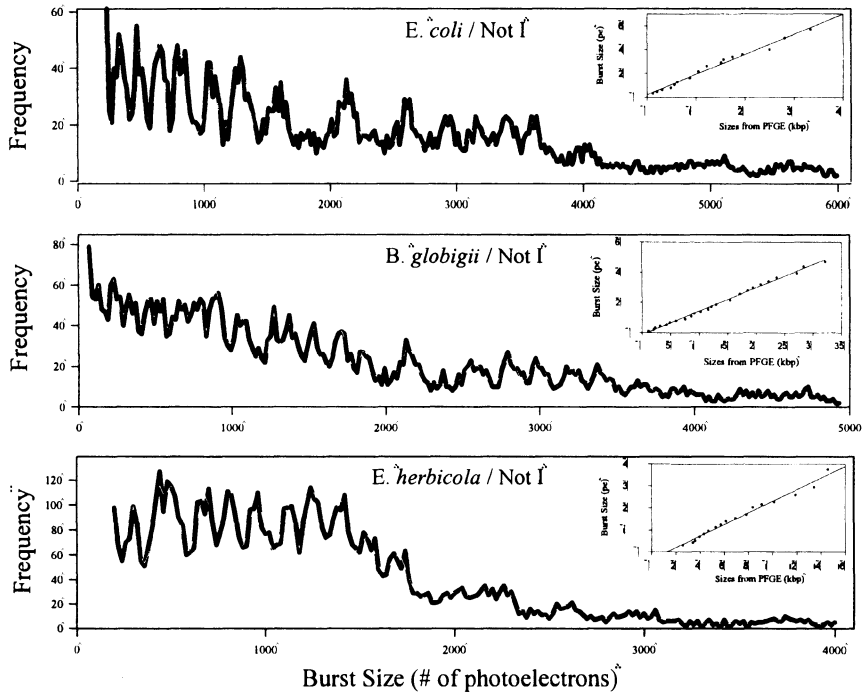

Figure 5. Histograms for the Not I digestion of *Escherichia coli*, *Bacillus globigii*, and *Erwinia herbicola* genomes. The solid line represents the histogram, and the white line represents a fit consisting of a sum of Gaussians with an exponentially decaying background. Experimental conditions: 25 mW continuous wave excitation at 514.5 nm; excitation laser beam e^{-2} diameter, $\sim 50\,\mu$m; staining dye, TOTO-1; transit time, 2.1 ms; DNA analyzed, < 1 pg. The insets are plots of the extracted centroids versus the fragment sizes obtained from pulsed-field gel electrophoresis. Reprinted with permission from Kim et al. (1999). *Cytometry* **36**, 324-332. ©1999 Wiley-Liss, Inc. [22]

peaks versus the fragment sizes obtained from PFGE. As can be seen, burst sizes are linear with fragment sizes. Because we have previously demonstrated that the technique can size fragments ranging from 0.4-425 kb with 2-5% uncertainty, we attribute most of the deviation from linearity to the 10% uncertainty inherent in PFGE. [17,20,21] The relationship between burst size and fragment size can be determined independently of the PFGE measurement by the addition of internal standards. [22]

Fragment analysis times were < 10 minutes and < 1 pg of DNA was analyzed. These results demonstrate a $\sim 100\times$ reduction in sample analysis time and a $\sim 200,000\times$ increase in sensitivity over standard PFGE fragment analysis. However, when the time for sample preparation is included, the total times (several days) required for analysis of a sample by flow cytometry or by PFGE are about the same. Work is underway in our laboratory to reduce

sample preparation times to less than one day to take advantage of the speed of DNA sizing by flow cytometry.

We are presently investigating the applicability of our fluorescence flow cytometric technique to discriminate among bacterial strains. Preliminary results are encouraging. Histograms from a variety of bacteria will be incorporated into a library to form the basis for the rapid identification of bacterial species and strains. Because species or strains that are closely related might have very similar histograms when digested with one particular restriction endonuclease, fingerprint patterns obtained for each bacterium with several different restriction endonucleases will be included in the library. The Centers for Disease Control and Prevention already uses this type of approach for fingerprints obtained by PFGE. Fingerprints of bacterial strains responsible for food-borne illnesses are reported and recorded electronically on the PulseNet web site: http://www.cdc.gov/ncidod/dbmd/pulsenet/pulsenet.htm.

3.2 High throughput DNA fragment sizing

In this section we describe a method for increasing the throughput of DNA fragment-size measurements. There are numerous applications that will benefit from higher measurement rates, including fingerprint analysis of environmental samples and size characterization of plasmids in clone libraries. In particular, higher volume flow rates are needed for dilute, un-amplified samples or when a large number of samples must be analyzed.

The sample measurement rate in a single probe volume is limited to about 100 fragments per second. This limit arises primarily from fluorescence signal saturation and fragment coincidences within the probe volume. The fluorescence signal from an intercalating dye such as TOTO-1 saturates at about 1 detected photon per intercalated dye molecule per millisecond. For a mean burst size of N_s detected (signal) photons, the relative uncertainty from shot noise is $1/\sqrt{N_s}$ in the absence of background. Typically more than 1000 signal photons are required to limit the uncertainty in the measurement to less than a few percent. At an optimal dye staining level, for TOTO-1, of 1 dye homodimer to every 5 base pairs, a 5 kb fragment must be observed for approximately one millisecond. To reduce the fraction of fragment overlaps within the probe volume to less than a few percent, the concentration must be adjusted so that only about 100 fragments per second flow through the probe volume.

A solution to the problem of increasing the throughput is to observe many probe volumes in parallel. Figure 6 shows a method for detecting fluorescence from many DNA fragments in parallel. [36] Instead of using hydrodynamic focusing to produce a narrow sample stream, the sample was flowed within the full width of a square-bore channel with dimensions of $250 \times 250\,\mu\text{m}^2$.

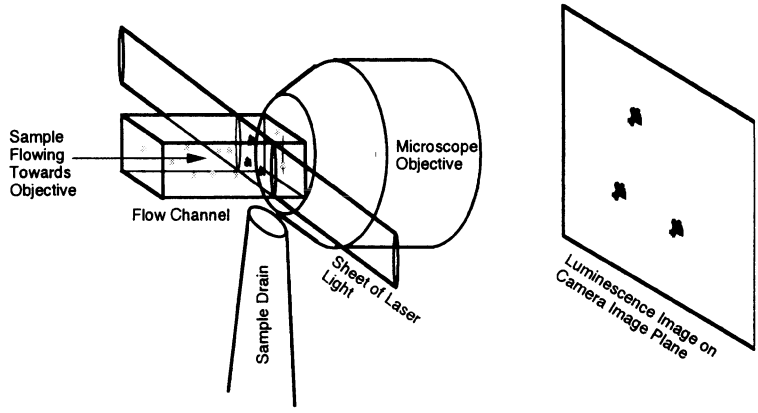

Figure 6. A schematic diagram of the instrument used for parallel fluorescence imaging of fluorescently labeled DNA. The fluorescence photons from many individual, stained-DNA fragments were recorded concurrently by a charge coupled device camera. Reprinted with permission from Van Orden et al. (2000). *Anal. Chem.*, 72(1):37-41. ©2000 American Chemical Society. [36]

The cross section of the flow channel was illuminated with a thin ribbon of laser light; 20 mW from a continuous wave Ar^+ laser operated at 514.5 nm was shaped with cylindrical lenses into a sheet with dimensions of $10 \times 200\ \mu m^2$. The sheet of light intersected the flow stream near the open end of the flow channel. DNA fragments crossed the laser beam at random positions within the cross-section of the flow channel. A water immersion objective with a numerical aperture of 1.0 was used to collect luminescence from the illuminated cross section. Additional lenses and filters (not shown) were used to image fluorescence from each DNA-dye complex onto a cooled, slow-scan, charge coupled device camera (CCD). Each fluorescent spot occupied 9 pixels within an image area of 335×289 pixels, corresponding to the illuminated area of $\sim 200 \times 250\ \mu m^2$. The camera was operated with an image acquisition time of 150 ms and a readout dead time of 280 ms. The transit time across the focused laser beam at the center of the flow channel was adjusted to be 4 ms, much less than the 150 ms integration time, so that truncation effects at the edges of the integration period were reduced. The concentration was adjusted so that an average of 865 fragments were observed in each image.

Figure 7 shows a histogram the fluorescence intensities from a mixture of fragments obtained in 8.6 seconds (20 images, 17,300 fragments) at a rate of ~ 2000 fragments per second. The sample consisted of DNA fragments with lengths of 7.2, 48.5, and 154 kb stained with TOTO-1. [36] Since the flow rate, laser intensity and fluorescence collection efficiency depend on position, the burst sizes also depend on the position within the flow channel. For

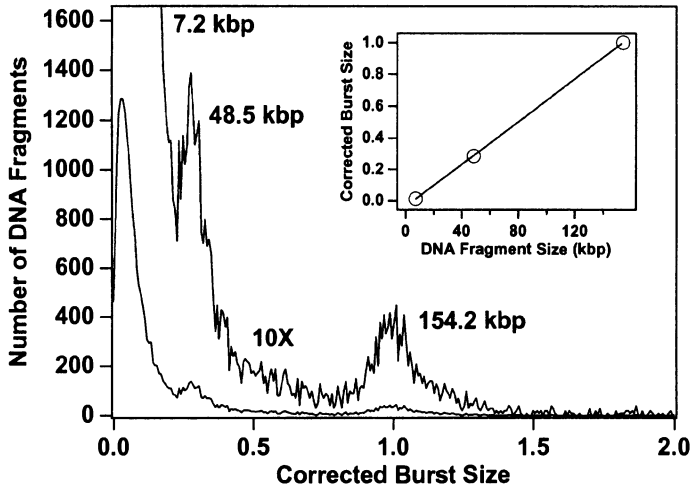

Figure 7. Corrected fluorescence burst size distribution of a mixture of fluorescently labeled DNA fragments obtained with parallel, high-throughput detection. The total data acquisition time was 8.6 s, 17,300 fragments were analyzed. The inset shows the peak positions of the bursts versus the DNA fragment size. Reprinted with permission from Van Orden et al. (2000). *Anal. Chem.*, 72(1):37-41. ©2000 American Chemical Society. [36]

example, bursts from 154 kb fragments produced between 20,000 to 60,000 photoelectrons for fragments in different positions in the flow channel. A calibration surface was obtained to narrow the peak distribution for the 154 kb fragment, and was divided into all the bursts. The abscissa in Fig. 7 is the corrected burst size. Clearly, parallelism improved the speed of measurement. The numerical analysis time averaged to about 1 minute per image. With a frame transfer CCD camera and parallel computing hardware, it is estimated that this technique could approach a measurement and analysis rate of 100,000 fragments per second with a sensitivity sufficient to detect fragments as small as 2 kb in length. [36]

4. Single molecule DNA sequencing

4.0.1 Approach. Several groups are exploring the use of single molecule detection to sequence DNA. [3, 10, 37–43] As diagramed in Fig. 8, our approach consists of: A) replicating a strand of DNA using fluorescently labeled nucleotides, B) anchoring this fluorescently labeled strand in a flow stream, C) adding an exonuclease to the flow stream to sequentially cleave nucleotides from the end of the DNA strand. The cleaved, labeled nucleotides are entrained in the flow and are detected and identified downstream via laser-induced fluorescence.

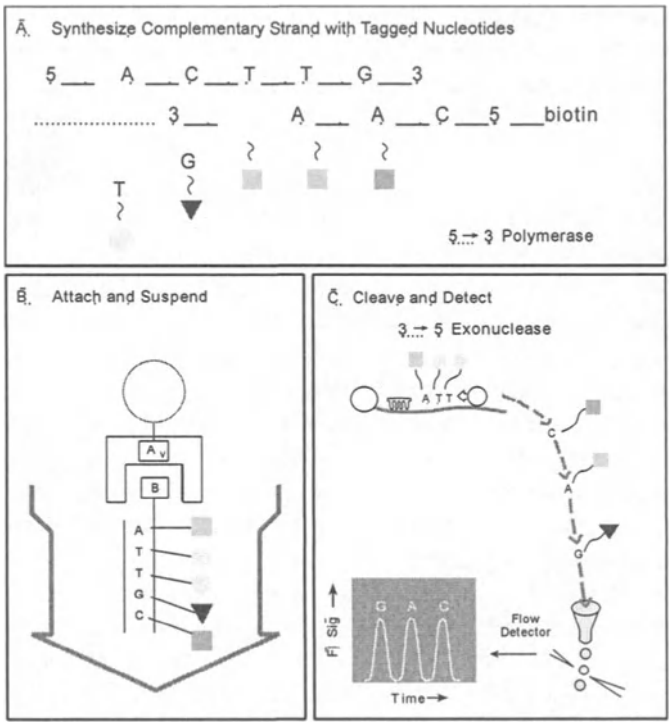

Figure 8. Schematic diagram depicting the steps necessary to sequence DNA by single molecule detection (see text). Reprinted with permission from Davis et al. (1991). *Genetic Anal.* **8**, 1-7. ©1991 Elsevier Science B.V.

DNA sequencing by single molecule detection has the potential to sequence DNA at a rate of hundreds of bases per second. Even more important than the projected sequencing rate is the projected ability to sequence long fragments. Read lengths of tens of kilobases are anticipated, thereby reducing greatly the need of sequencing overlapping regions characteristic of the conventional sequencing process. In contrast to gel electrophoresis, this approach is not limited to read lengths of < 1000 bases or by cloning bottlenecks.

The proposed method of sequencing requires that a *single* fragment of DNA be anchored in the flow stream. If multiple fragments were digested to increase the fluorescence signal, the distribution of enzymatic cleavage rates on the different DNA fragments would cause the released nucleotides to rapidly dephase. Hence, to extract sequence information, one must detect and identify individual fluorescently labeled nucleotides cleaved from a single DNA fragment.

4.0.2 Current status. As a step towards detecting individual fluorescently labeled bases cleaved from a single DNA fragment, we [38] and others [42] have reported the efficient detection and identification of distinct, individual labeled nucleotides enzymatically cleaved from multiple DNA fragments.

In our work [38], three sets of labeled DNA oligimers (each 45 base pairs) were replicated to contain either a single tetramethyl rhodamine-dUMP, a single R6G-dCMP, or one of each labeled base. Approximately 5,000 DNA oligimers were attached to 3 μm diameter microspheres. For each of the three DNA samples, individual DNA laden microspheres were optically trapped [44] in the center of a flow stream that contained *Escherichia coli* Exonuclease III (Exo III). Enzymatically cleaved nucleotides were entrained in the flow and carried downstream through an excitation laser beam. Although many strands of DNA were being simultaneously digested, the turnover rate of Exo III (1 nucleotide/sec/strand at room temperature) was sufficiently low to ensure that, on average, less than one cleaved, fluorescent nucleotide was present in our laser probe volume at any given time.

For every detected single molecule transit, the fluorescence lifetime and burst size were measured. [9] Scatter plots of the burst size versus the fluorescence lifetime are shown in Fig. 9 for cleavage experiments from each DNA sample. It is evident that R6G-dCMP bursts and TMR-dUMP bursts occupy different regions of this two-dimensional space. Based on the correlated measurement of burst size and fluorescence lifetime, a single fluorescent molecule may be identified as either R6G-dCMP or TMR-dUMP with $\sim$87% accuracy. Use of both the burst size and lifetime for base identification is expected to reduce the error rate in consensus DNA sequencing compared to consensus error rates obtained using either the burst size or fluorescence lifetime alone. [38]

The low turnover rate of Exo III on fluorescently labeled DNA compared to the background fluorescence burst rate constrains us to examine the digestion of a large number of DNA fragments ($\sim$100). The Exo III digestion of a single labeled fragment of DNA fully replicated with fluorescent nucleotides will, on average, yield a transit of a single fluorescent base per second. It would be difficult to discern these cleavage events on top of our current background burst detection rate of a few per second [38]. Thus, in order to detect the cleavage from a single DNA fragment, our background burst detection rate must be lowered by approximately an order of magnitude or the exonuclease turnover rate must be increased by a commensurate amount.

We are now using a faster exonuclease that will make the digestion of fewer DNA fragments more discernible. *Escherichia coli* Exonuclease I (Exo I) is known to be fast (275 nucleotides/sec/strand at 37 °C) and highly processive on native, single-stranded DNA. [45] Cleavage experiments performed

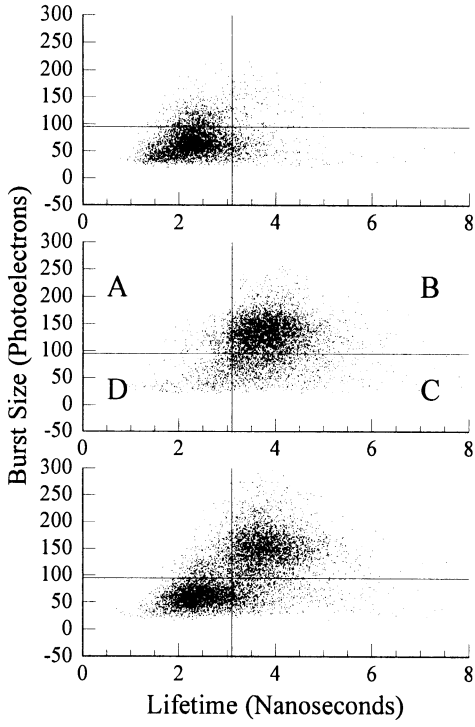

Figure 9. Scatter plots of burst size versus lifetime for three cleavage experiments. The top panel shows ~ 4000 bursts detected during the cleavage of DNA labeled with TMR-dUMP. The middle panel depicts ~5000 bursts detected during the cleavage of DNA labeled with R6G-dCMP. The bottom panel shows ~ 8000 bursts detected during the cleavage of DNA labeled with one TMR-dUMP and one R6G-dCMP. The burst size-lifetime space was divided into four quadrants, A, B, C, and D. See [9, 38] for further discussion. Reprinted with permission from Werner et al. (1999). *Proc. SPIE-Int. Opt. Soc. Eng.* **3602**, 355-366. ©1999 SPIE-The International Society for Optical Engineering. [38]

in our apparatus indicate that Exo I is also fast and processive on fluorescently labeled, single-stranded DNA. Figure 10 shows the fluorescence signal detected during cleavage experiments using two different exonucleases (Exo III and Exo I). The DNA used in these experiments was 5'-biotinylated 40-mers with the last 22 bases (from the 3' terminus) labeled at each of seven U positions with R6G-dUMPs. For the Exo III digestion experiments, double-stranded 40-mers were used. Single-stranded 40-mers were used for the Exo I digestion experiments. Similar numbers (~ 1000) of double-stranded or single-stranded 40-mers were attached to 3 μm diameter, streptavidin coated microspheres. For the Exo I experiment, the DNA-laden microspheres were pre-incubated with Exo I in a buffer that allowed the exonuclease to bind to the 3' terminus, but lacked the magnesium cofactor necessary to induce

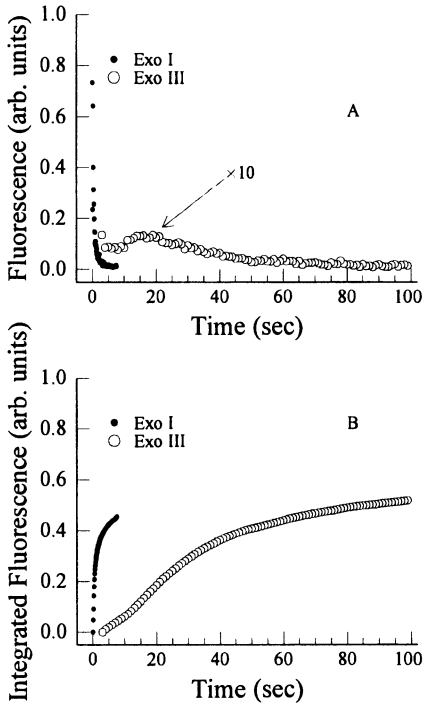

Figure 10. Cleavage experiments with Exo I and Exo III. The disappearance of the fluorescence signal indicates that the labeled DNA is completely digested. From the top panel (A) it is evident that Exo I digests the labeled DNA much more rapidly than Exo III. For ease of comparison, the fluorescence signal from the Exo III digestion experiment (open circles) shown in (A) has been multiplied by a factor of 10. From the integrated fluorescence intensity (B), it is evident that Exo I is processively digesting the labeled DNA (see text).

cleavage; the sheath stream buffer contained magnesium but no exonuclease. For the Exo III cleavage experiment, the DNA-laden microspheres were preincubated with Exo III and Exo III was also added, in addition to magnesium, to the sheath stream buffer. Individual DNA-laden microspheres were optically trapped in the sheath buffer $\sim 50\ \mu$m upstream of the detection volume and the time history of fluorescent nucleotide release measured. Under these experimental conditions, we attribute the disappearance of a measurable fluorescence signal to the complete digestion of the fluorescently labeled DNA on the microsphere.

The fast decay in the Exo I digestion experiment (filled circles) demonstrates clearly that the DNA is being cleaved much more rapidly than it is with Exo III digestion (open circles). From the fluorescence intensity decay rate it is estimated that Exo I is cutting fluorescently labeled DNA at a rate

of ~50 nucleotides per second. For ease of comparison, the Exo III trace in Fig. 10A has been multiplied by a factor of 10.

The integrated fluorescence intensity, which is a measure of the total number of released fluorescent bases, is shown in Fig. 10B to be similar for the two experiments. Both cleavage experiments yielded roughly the same number of cleaved nucleotides per microsphere (integrated fluorescence signal). With Exo I, 6840 ± 320 released R6G-dUMP's were detected downstream of the microsphere; 6500 ± 2200 R6G-dUMP's were detected with Exo III. Smaller (1430 ± 200 R6G-dUMP's) integrated transients (data not shown) were obtained when DNA-laden microspheres pre-incubated with Exo III were trapped in a sheath stream buffer containing only magnesium. We attribute the smaller transients to the dissociation of Exo III, a non-processive exonuclease, from the DNA fragments after cleavage of the first R6G-dUMP at the 3' terminus. In contrast, the results obtained with Exo I are consistent with this exonuclease processively digesting the entire fluorescently labeled DNA fragment.

4.0.3 Future prospects. We have made significant progress towards a demonstration of DNA sequencing via single molecule detection. Two distinguishable, fluorescently labeled nucleotides types enzymatically cleaved from DNA fragments anchored in flow have been detected with high efficiency and identified with high accuracy at the single molecule level. Only two distinguishable, fluorescent labels are required for single molecule DNA sequencing if the necessary combinations of pairs of nucleotide types are labeled and sequenced. [46] Furthermore, a fast exonuclease (Exo I) has been shown to rapidly and processively cleave fluorescently labeled DNA. It is anticipated that in the near future our group and others pursuing similar approaches will be able to discern fluorescence bursts yielded from a single labeled strand of DNA undergoing exonuclease digestion.

Acknowledgments

This research was supported by the Los Alamos Center for Human Genome Studies under United States Department of Energy Contract W-7405-ENG-36, by the Department of Energy (NN20), by the National Institutes of Health funded National Flow Cytometry Resource (RR-01315), and by internal funding from Los Alamos National Laboratory.

References

[1] Barnes, M. D., Whitten, W. B., and Ramsey, J. M. (1995). Detecting single molecules in liquids. *Anal. Chem.* **67**, A418-A423.

[2] Keller, R. A., Ambrose, W. P., Goodwin, P. M., Jett, J. H., Martin, J. C., and Wu, M. (1996). Single-molecule fluorescence analysis in solution. *Appl. Spectrosc.* **50**, A12-A32.

[3] Goodwin, P. M., Ambrose, W. P., and Keller, R. A. (1996). Single-molecule detection in liquids by laser-induced fluorescence. *Accounts Chem. Res.* **29**, 607-613.

[4] Nie, S. and Zare, R. N. (1997). Optical detection of single molecules. In Stroud, R. M., editor, *Annual Review of Biophysics and Biomolecular Structure*, volume 26, pages 567-596. Annual Reviews, Inc., Palo Alto, CA.

[5] Ambrose, W. P., Goodwin, P. M., Jett, J. H., Van Orden, A., Werner, J. H., and Keller, R. A. (1999). Single molecule fluorescence spectroscopy at ambient temperature. *Chem. Rev.* **99**, 2929-2956.

[6] Soper, S. A., Davis, L. M., and Shera, E. B. (1992). Detection and identification of single molecules in solution. *J. Opt. Soc. Am. B* **9**, 1761-1769.

[7] Zander, C., Sauer, M., Drexhage, K. H., Ko, D. S., Schulz, A., Wolfrum, J., Brand, L., Eggeling, C., and Seidel, C. A. M. (1996). Detection and characterization of single molecules in aqueous solution. *Appl. Phys. B* **63**, 517-523.

[8] Enderlein, J., Goodwin, P. M., Van Orden, A., Ambrose, W. P., Erdmann, R., and Keller, R. A. (1997). A maximum-likelihood estimator to distinguish single molecules by their fluorescence decays. *Chem. Phys. Lett.* **270**, 464-470.

[9] Van Orden, A., Machara, N. P., Goodwin, P. M., and Keller, R. A. (1998). Single-molecule identification in flowing sample streams by fluorescence burst size and intra-burst fluorescence decay rate. *Anal. Chem.* **70**, 1444-1451.

[10] Sauer, M., Arden-Jacob, J., Drexhage, K. H., Göbel, F., Lieberwirth, U., Mülegger, K., Müller, R., Wolfrum, J., and Zander, C. (1998). Time-resolved identification of individual mononucleotide molecules in aqueous-solution with pulsed semiconductor-lasers. *Bioimaging*, **6**, 14-24.

[11] Schaffer, J., Wolkmer, A., Eggeling, C., Subramaniam, V., Striker, G., and Seidel, C.A.M. (1999). Identification of single molecules in aqueous solution by time-resolved fluorescence anisotropy. *J. Phys. Chem. A* **103**, 331-336.

[12] Kachel, V., Fellner-Feldegg, H., and Menke, E. (1990). Hydrodynamic properties of flow cytometry instruments. In Melamed, M. R., Lindmo, T., and Mendelsohn, M. L., editors, *Flow Cytometry and Sorting*, pages 27-44, New York, NY. J. Wiley & Sons, Inc.

[13] Harris, T. D. and Lytle, F.E. (1983). Analytical applications of laser absorption and emission spectroscopy. In Kliger, D. S., editor, *Ultrasensitive Laser Spectroscopy*, chapter 7, pages 369-433. Academic Press, New York.

[14] Goodwin, P. M., Wilkerson, Jr., C. W., Ambrose, W. P., and Keller, R.A. (1993b). Ultrasensitive detection of single molecules in flowing sample streams by laser-induced fluorescence. *Proc. SPIE-Int. Soc. Opt. Eng.* **1895**, 79-89.

[15] Goodwin, P. M., Johnson, M. E., Martin, J. C., Ambrose, W. P., Marrone, B. L., Jett, J. H., and Keller, R. A. (1993a). Rapid sizing of individual fluorescently stained DNA fragments by flow cytometry. *Nucleic Acids Res.* **21**, 803-806.

[16] Johnson, M. E., Goodwin, P. M., Ambrose, W. P., Martin, J. C., Marrone, B. L., Jett, J. H., and Keller, R. A. (1994). Sizing of DNA fragments by flow cytometry. *Proc. SPIE-Int. Soc. Opt. Eng.* **1895**, 69-78.

[17] Petty, J. T., Johnson, M. E., Goodwin, P. M., Martin, J. C., Jett, J. H., and Keller, R. A. (1995). Characterization of DNA size determination of small fragments by flow cytometry. *Anal. Chem.* **67**, 1755-1761.

[18] Huang, Z., Petty, J. T., O'Quinn, B., Longmire, J. L., Brown, N. C., Jett, J. H., and Keller, R. A. (1996). Large DNA fragment sizing by flow cytometry: Application to the characterization of P1 artificial chromosome (PAC) clones. *Nucleic Acids Res.* **24**, 4202-4209.

[19] Van Orden, A., Cai, H., Goodwin, P. M., and Keller, R. A. (1999). Efficient detection of single DNA fragments in flowing sample streams by two photon fluorescence excitation. *Anal. Chem.* **71**, 2108-2116.

[20] Ambrose, W. P., Cai, H., Goodwin, P. M., Jett, J. H., Habbersett, R. C., Larson, E. J., Grace, W. K., Werner, J. H., and Keller, R. A. (2000). Flow cytometric sizing of DNA fragments. In Lakowicz, J. R., editor, *Topics in Fluorescence Spectroscopy Volume 7: DNA Technoloy*. Kluwer Academic/Plenum Publishers, Dordrecht, the Netherlands. In press.

[21] Huang, Z., Jett, J. H., and Keller, R. A. (1999). Bacteria genome fingerprinting by flow cytometry. *Cytometry* **35**, 169-175.

[22] Kim, Y., Jett, J. H., Larson, E. J., Penttila, J. R., Marrone, B. L., and Keller, R. A. (1999). Bacterial fingerprinting by flow cytometry: Bacterial species discrimination. *Cytometry* **36**, 324-332.

[23] Castro, A., Fairfield, F. R., and Shera, E. B. (1993). Fluorescence detection and size measurement of single DNA-molecules. *Anal. Chem.* **65**, 849-852.

[24] Schins, J. M., Agronskaya, A., de Grooth, B. G., and Greve, J. (1998). New technique for high-resolution DNA sizing in epi-illumination. *Cytometry* **32**, 132-136.

[25] Agronskaia, A., Schins, J. M., de Grooth, B. G., and Greve, J. (1999a). Polarization effects in flow cytometric DNA sizing. *Appl. Opt.* **38**, 714-719.

[26] Chou, H. P., Spence, C., Scherer, A., and Quake, S. (1999). A microfabricated device for sizing and sorting DNA molecules. *Proc. Natl. Acad. Sci. USA* **96**, 11-13.

[27] Agronskaia, A., Schins, J. M., de Grooth, B. G., and Greve, J. (1999b). Two-color fluorescence in flow cytometry DNA sizing: Identification of single molecule fluorescent probes. *Anal. Chem.*, **71**, 4684-4689.

[28] Glazer, A. N. and Rye, H. S. (1992). Stable dye-DNA intercalation complexes as reagents for high-sensitivity fluorescence detection. *Nature*, **359**, 859-861.

[29] Ioannou, P. A., Amemiya, C. T., Garnes, J., Kroisel, P. M., Shizuya, H., Chen, C., Batzer, M. A., and Delong, P. J. (1994). A new bacteriophage P1-derived vector for the propagation of large human DNA fragments. *Nat. Genet.* **6**, 84-89.

[30] Shizuya, H., Birren, B., Kim, U. J., Mancino, V., Slepak, T., Tachiiri, Y., and Simon, M. (1992). Cloning and stable maintenance of 300-kilobase-pair fragments of human DNA in *Escherichia-coli* using an F-factor-based vector. *Proc. Natl. Acad. Sci. USA* **89**, 8794-8797.

[31] Busch, U. and Nitschko, H. (1999). Methods for the differentiation of microorganisms. *J. Chromatogr. B* **722**, 263-278.

[32] Vos, P., Hogers, R., Bleeker, M., Reijans, M., van de Lee, T., Hornes, M., Frijters, A., Pot, J., Peleman, J., Kuiper, M., and Zabeau, M. (1995). AFLP: A new technique for DNA fingerprinting. *Nucleac Acids Res.* **23**, 407-4414.

[33] Keim, P., Kalif, A., Schupp, J., Hill, K., Travis, S. E., Richmond, K., Adair, D. M., Hugh-Jones, M., Kuske, C. R., and Jackson, P. (1997). Molecular evolution and diversity in *Bacillus anthracis* as detected by amplified fragment length polymorphism markers. *J. Bacteriol.* **179**, 818-824.

[34] Tenover, F. C., Arbeit, R. D., Goering, R. V., Mickelsen, P. A., Murray, B. E., Persing, D. H., and Swaminathan, B. (1995). Interpreting chromosomal DNA restriction patterns produced by pulsed-field gel-electrophoresis: Criteria for bacterial strain typing. *J. Clin. Microbiol.* **33**, 2233-2239.

[35] Smith, T. L., Pearson, M. L., Wilcox, K. R., Cruz, C., Lancaster, M. V., Robinson-Dunn, B., Tenover, F. C., Zervos, M. J., Band, J. D., White, E., and Jarvis, W. R. (1999). Emergence of vancomycin resistance in *Staphylococcus aureus*. *New Engl. J. Med.* **340**, 493-501.

[36] Van Orden, A., Ambrose, W. P., and Keller, R. A. (2000). High throughput DNA fragment length analysis. *Anal. Chem.* **72**, 37-41.

[37] Goodwin, P. M., Cai, H., Jett, J. H., Ishuag-Riley, S. L., Machara, N. P., Semin, D. J., Van Orden, A., and Keller, R. A. (1997). Application of single molecule detection to DNA sequencing. *Nucleos. Nucleot.* **16**, 543-550.

[38] Werner, J. H., Cai, H., Goodwin, P. M., and Keller, R. A. (1999). Current status of DNA sequencing by single molecule detection. *Proc. SPIE-Int. Soc. Opt. Eng.* **3602**, 355-366.

[39] Eigen, M. and Rigler, R. (1994). Sorting single molecules: Application to diagnostics and evolutionary biotechnology. *Proc. Natl. Acad. Sci. (USA)* **91**, 5740-5747.

[40] Dörre, K., Brakmann, S., Brinkmeier, M., Han, K., Riebeseel, K., Schwille, P., Stephan, J., Wetzel, T., Lapczyna, M., Stuke, M., Bader, R., Hinz, M., Seliger, H., Holm, J., Eigen, M., and Rigler, R. (1997). Techniques for single molecule sequencing. *Bioimaging* **5**, 139-152.

[41] Dapprich, J. (1999). Single-molecule DNA digestion by λ-exonuclease. *Cytometry* **36**, 163-168.

[42] Sauer, M., Angerer, B., Han, K. T., and Zander, C. (1999). Detection and identification of single dye labeled mononucleotide molecules released from an optical fiber in a microcapillary: First steps towards a new single molecule DNA sequencing technique. *Phys. Chem. Chem. Phys.* **1**, 2471-2477.

[43] Jett, J. H., Keller, R. A., Martin, J. C., Marrone, B. L., Moyzis, R. K., Ratliff, R. L., Seitzinger, N. K., Shera, E. B., and Stewart, C. C. (1989). High speed DNA sequencing: An approach based upon fluorescence detection of single molecules. *J. Biomol. Struct. Dynam.* 7, 301-309.

[44] Machara, N. P., Goodwin, P. M., Enderlein, J., Semin, D. J., and Keller, R. A. (1998). Efficient detection of single molecules eluting off an optically trapped microsphere. *Bioimaging* **6**, 33-42.

[45] Brody, R. S., Doherty, K. G., and Zimmerman, P. D. (1986). Processivity and kinetics of the reaction of Exonuclease I from *Escherichia coli* with polydeoxyribonucleotides. *J. Bio. Chem.*, 261(16):7136-7143.

[46] Jett, J. H., Keller, R. A., Martin, J. C., Posner, R. G., Marrone, B. L., Hammond, M. L., and Simpson, D. J. (1995). Method for rapid base sequencing in DNA and RNA with two base labeling. US Patent # 5,405,747.

FLUORESCENCE ENERGY TRANSFER REAGENTS FOR DNA SEQUENCING AND ANALYSIS

High-throughput fluorescent DNA sequencing

Jingyue Ju
Dept. of Chemical Engineering and the Columbia Genome Center, Columbia University, NY, NY 10032

Abstract A novel set of fluorescent reagents for DNA sequencing and analyses was developed using a fluorescence energy transfer principle with synthetic chemistry. These reagents are markedly superior when compared to single dye-labeled primers and dideoxynucleotides in DNA sequencing and in PCR-fragment analysis. Examples of construction, characterization, and application of these fluorescent reagents are described.

Keywords: Fluorescence energy transfer, DNA sequencing, oligodeoxynucleotide, ET primer, dideoxynucleotide, fluorophore, donor, acceptor, absorption, emission, electrophoresis.

1. Introduction

The ability to sequence DNA accurately and rapidly is revolutionizing biology and medicine. The confluence of the massive Human Genome Project, the sequencing of other bacterial and eukaryotic genomes, and the explosive growth of DNA sequence-based diagnostics, is driving an exponential growth in the need for high throughput sequencing. The Saenger dideoxy chain-termination method [1] is now accepted as the technique of choice for all large scale sequencing projects. Widely used automated versions of this method employ either four differently end-labeled fluorescent primers or terminators to generate all the possible fragments of the DNA template to be analyzed, where the fragments terminating with the four different bases (A, C, G, T) are separated at single-base pair resolution on a sequencing gel and then identified by the four distinct emissions [2, 3]. In the past fifteen years, significant progress has been made in refining the sequencing instruments and in increasing the throughput of the electrophoretic separation [4, 5]. Im-

J.J. Kasianowicz et al. (eds.), Structure and Dynamics of Confined Polymers, 371–383.

provements in the polymerase led to uniform termination efficiency [6] and the introduction of thermostable polymerases [7] have also significantly improved the quality of sequencing data. Application of laser-induced fluorescence for four-color DNA sequencing is a major advancement for the automated DNA sequencing technology that makes large-scale genome sequencing initiative possible. An "ideal" set of fluorophores for four-color DNA sequencing must consist of four different fluorophores. These dyes should have a similar high molar absorbance at a common excitation wavelength as well as high fluorescence-quantum yields, exhibit strong and well-separated fluorescence emissions, and introduce the same relative mobility shift of the DNA sequencing fragments. These criteria cannot be met optimally by the spectroscopic properties of single fluorescent dye molecules, and indeed are poorly satisfied by the sets of fluorescent tags initially used. By exploiting resonance fluorescence energy transfer (ET), we can overcome the constraints imposed by the use of single dyes. The fluorescent tags for DNA sequencing that meet the performance criteria listed above were developed [8, 9]. The energy transfer dye labeled primers and terminators can be efficiently excited at a common wavelength and exhibit strong and distinct fluorescent emissions [10, 11]. They are markedly superior to single dye-labeled primers and terminators in DNA sequencing and in PCR fragment analysis. The higher sensitivity offered by these new sets of fluorescent dyes also allows the direct sequencing of large-template DNA ($30kb$, such as BAC clones), significantly advanced the large scale sequencing and mapping projects [12, 13]. The incremental improvement of four-color DNA sequencing technology has made a deep impact on the genome sequencing. A new paradigm of revolutionary technology in DNA sequencing is still required for genomics research, as explored by colleagues in this series (single molecule detection and nanopore approach for DNA sequencing: Kasianowicz, et al., Deamer, et al., Branton and Meller).

2. Fluorescence energy transfer

Optical interactions persist between two chromophores even when they are far apart (8 nm). The chromophore with high energy absorption is defined as a donor, and the chromophore with lower energy absorption is defined as an acceptor. Fluorescence energy transfer is mediated by a dipole-dipole coupling between the chromophores that results in resonance transfer of excitation energy from an excited donor molecule to an acceptor [14]. Förster established that the energy transfer efficiency is proportional to the inverse sixth power of the distance between the two chromophores. Thus, fluorescence resonance energy transfer has been used extensively as a spectroscopic ruler for biological structures [15], and energy transfer-coupled tandem phy-

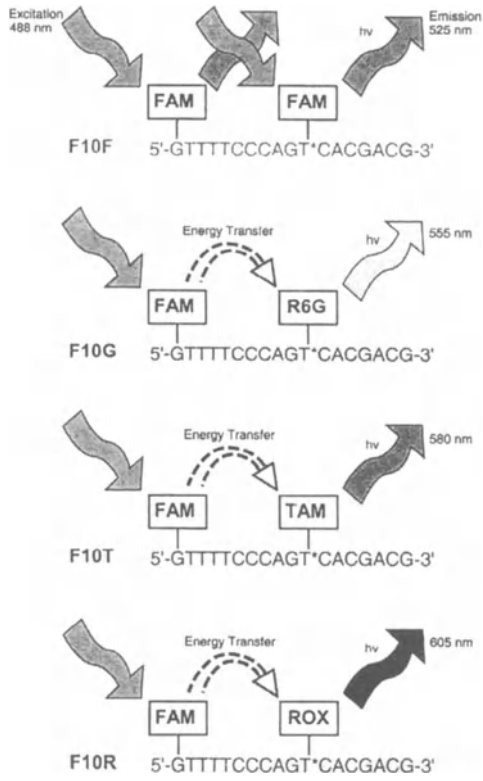

Figure 1. Structures of the four ET primers (F10F, F10G, F10T and F10R)

cobiliprotein conjugates have found wide applications as unique fluorescent labels [16]. A set of polycationic heterodimeric fluorophores that exploit energy transfer and that have high affinities for double-stranded DNA were also developed, offering advantages over monomeric fluorophores in multiplex fluorescence labeling applications [17–19]. By exploiting fluorescence energy transfer, using a common donor and four different acceptors, fluorescent genetic analysis reagents, we constructed ET primers and dideoxynucleotides that are markedly superior to single dye labels in DNA sequencing, and in multiplex PCR-based mapping and sizing protocols.

3. Design and synthesis of energy transfer dye-labeled oligonucleotide primers and dideoxynucleotides

The synthetic reactions to construct four representative ET primers and the structures of these molecules are presented in Figure 1 and 2.

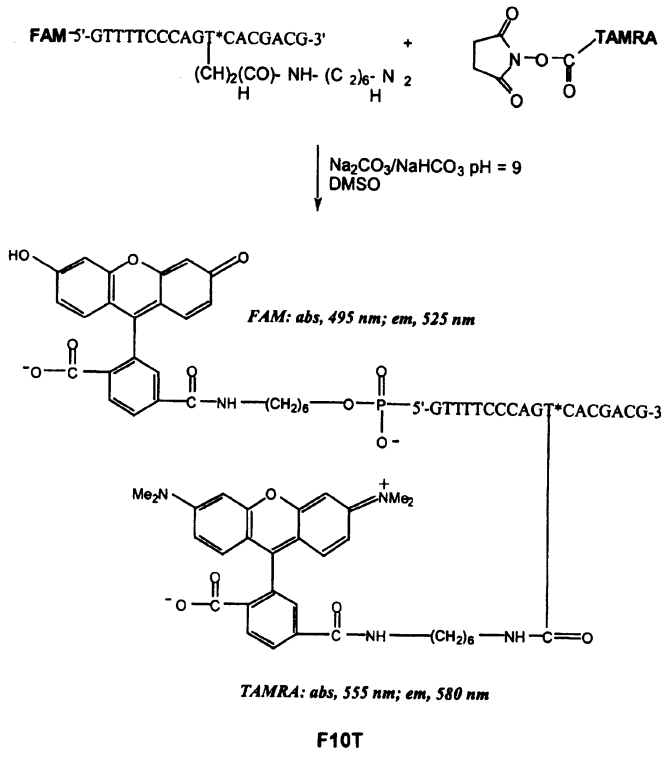

Figure 2. Representative synthetic scheme for the preparation of F10T.

Oligodeoxynucleotides (18-bases long) with the sequence 5'-GTTTTCCCAGTCACGACG-3'(the M13 D 40 universal primer) were synthesized with donor-acceptor fluorophore pairs separated by different distances. The 18-mer contains a modified base (T*) introduced by the use of 5'-dimethoxytrityl-5-[N-(trifluoroacetylaminohexyl)-3-acrylimido] -2'-deoxyuridine,3'-[(2-cyanoethyl)-(N,N-diisopropyl)]-phosphoramidite (Amino-Modifier C6 dT, Glen Research, Sterling, VA), which has a protected primary amine linker arm. The donor dye was attached to the 5' end of the oligomer, and the acceptor dye was attached to the primary amine group on the modified base (T*). The ET primers are named using the abbreviation D-N-A, where D is the donor, A is the acceptor, and N is the number of bases between D and A. In all the primers presented here, 5-carboxyfluorescein (FAM, F) is selected as a common donor, 6-carboxyrhodamine-6G (R6G,G) or 2',7'-dimethoxy-4',5'-dichloro-6-carboxyfluorescein (JOE, J), N,N,N',N'-tetramethyl-6-carboxyrhodamine (TAMRA, T) and 6-carboxy-X-rhodamine (ROX, R) are selected respectively as acceptors. A large library of ET primers can be constructed with the same donor at 5' end and different acceptors at

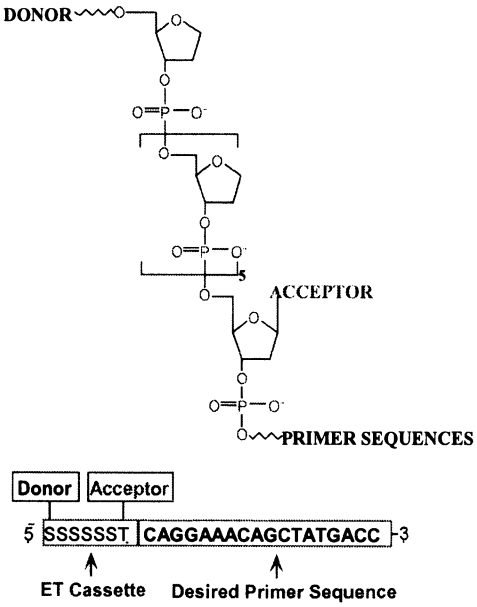

Figure 3. Primers of any sequence can be tagged with energy transfer-coupled dye cassettes devoid of DNA sequence complementarity. The S6 polymer linker is assembled using dSpacer CE Phosphoramidite (Glen Research, Sterling, VA) on a DNA synthesizer and T* introduced as described in the text.

different positions on the primer sequence. The spacing between the two chromophores is altered by varying the position of T* in the synthesis of each primer. It is found that the electrophoretic mobility of the ET primers and the extension DNA fragments depends on the spacing between the donor and acceptor. Within a range of distances determined by the number of intervening bases that allow good energy transfer, it is possible to adjust the electrophoretic mobility of the primers. Application of this principle leads to the selection of four ET primers (F10F, F10G, F10T and F10R) with optimum fluorescence properties and similar electrophoretic mobilities for four-color DNA sequencing. The ET-coupled dye labeling approach can also be used to label primers of any sequence by using an ET cassette.

As shown in Figure 3, a polymer linker SSSSSST* (S6T*) formed by six 1',2'-dideoxyribose phosphates (S) plus a modified thymidine (T*) at the 5' end of the desired primer sequence forms a universal spacer for attaching the ET coupled fluorophores, thereby producing an ET cassette [10,20]. With FAM as a common donor and FAM, JOE, TAMRA, and ROX as acceptors, a set of ET cassette labeled primers (FS6F, FS6J, FS6T and FS6R) were synthesized. This primer set exhibits improvements in fluorescence intensity similar to those presented above. The use of such a universal spacer is

advantageous in several respects: (i) the spacer will not hybridize to any sequences within the DNA template and therefore false priming is avoided; (ii) the spacer linkage maintains the natural nucleic acid phosphate functionality, which avoids possible anomalies in electrophoretic mobility; and (iii) the elimination of the aromatic bases on the deoxyribose rings in the spacer may reduce the likelihood of fluorescence quenching. Using the concept of labeling with an ET cassette, the energy transfer coupled dyes have been recently linked to the four dideoxynucleotides (ddA, ddC, ddT and ddG) to form fluorescent energy transfer terminators [21] (Figure 4). The use of ET terminators allows DNA sequencing reaction to be performed in a single tube, quadrupling the throughput.

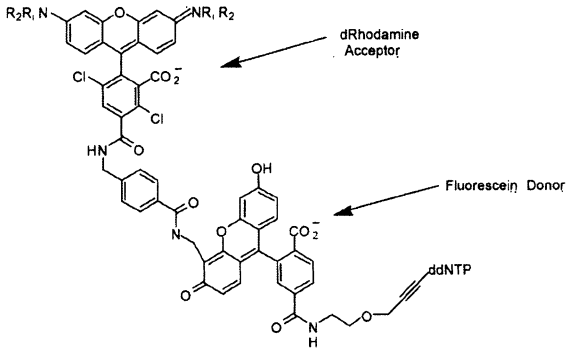

Figure 4. Structure of energy transfer dye-labeled terminators.

4. Spectroscopic properties of energy transfer dye-labeled reagents

As a representative example, the absorption and emission spectra of 4 ET primers are presented in Figure 5. The ratio of the 260 nm to the 496 nm absorbance of F10F is 1.3, while this ratio for the single FAM-labeled 18-mer is 2.2. This is consistent with the incorporation of two FAM molecules in F10F. Each ET primer exhibits the characteristic absorption of FAM at 496 nm as well as strong absorption at 525 nm due to JOE in F10J, at 555 nm due to TAMRA in F3T and at 585 nm due to ROX in F3R. The fluorescence spectra of the ET primers are dominated by the acceptor emissions. While the emission maximum of F10F is at 525 nm, the emission of F10J with 488-nm excitation is Stokes-shifted to 555 nm, that of F3T is shifted to 580 nm, and that of F3R is shifted to 605 nm. In the case of F3R, the Stokes-shift is over 100 nm. Figure 4 also presents emission spectra of the single dye-labeled primers measured at the same molar concentration as that of the corresponding ET primers. Substantial enhancement of the ET primer emission intensity is

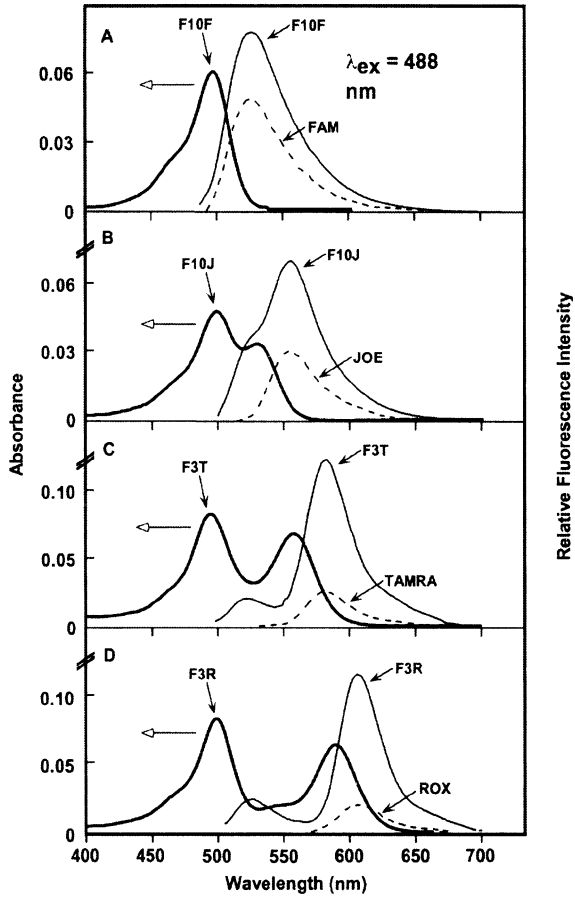

Figure 5. Comparison of the fluorescence emission intensity of the four ET primers with the corresponding single dye-labeled primers with 488 nm excitation (1xTBE, 7 M urea). The thick lines indicate the absorption spectra of the ET primers. (A) F10F vs. FAM, (B) F10J vs. JOE, (C) F3T vs. TAMRA and (D) F3R vs. ROX. The emission spectra for each primer pair were determined using solutions at the same molar concentration.

observed compared to the corresponding single dye-labeled primers, indicating that efficient energy transfer is occurring. Based on a comparison of the residual FAM emission in the ET primers with that of a FAM-labeled primer with same sequence and length, the energy transfer efficiency was calculated to be 65% for F10J, 96% for F3R and 97% for F3T. The fluorescence quantum yields based on the integrated emission from both donor and acceptor for the four primers relative to fluorescein were 0.82 for F10F, 0.63 for F10J, 0.15 for F3T, and 0.13 for F3R. Figures 6A and 6B presents the fluorescence intensity comparison (A) of a library of 20 ET primers (B) with the separation distance

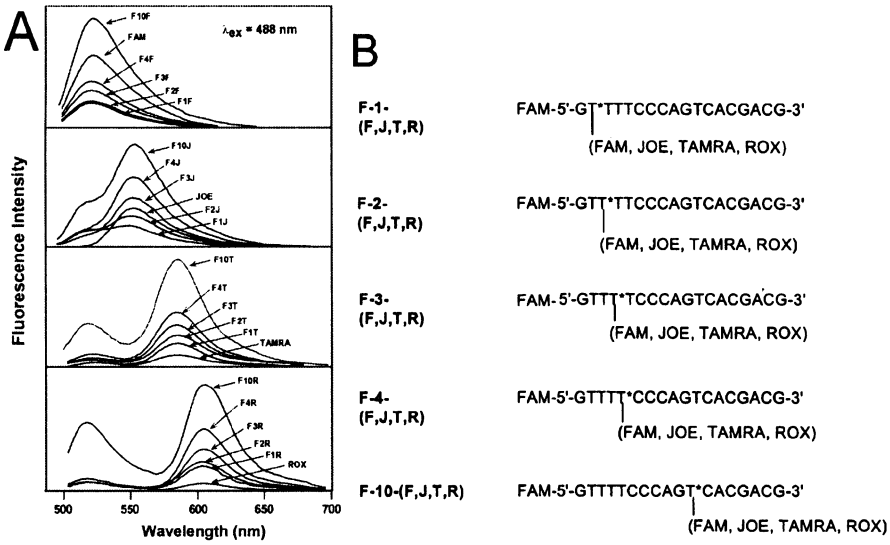

Figure 6. Fluorescence emission spectra (A) of 20 ET primers (B) and the corresponding single dye-labeled primers. The spectra for each primer series were determined at the same molar concentration in 1xTBE buffer with 488-nm excitation.

between the donor and acceptor systematically increased from one to ten nucleotides, as well as the corresponding single dye-labeled primers measured at the same molar concentration. The fluorescence intensity increases with the separation distances between the donor and acceptor. Within the range of separation distance studied in each primer series, the largest fluorescence intensities were obtained when the spacing is ten nucleotides. For example, the fluorescence intensity of F10T and F10R measured in the acceptor emission region is 10 and 14 times that of the corresponding TAMRA and ROX primers, respectively as shown in Figure 7. These results clearly indicate that as the spacing between the donor and the acceptor fluorophores is increased, the fluorescence quenching decreases significantly. The energy transfer efficiency of the ET primers, as expected, decreases as the spacing increases. Thus, the emission spectra of primers F10J, F10T and F10R have higher FAM emission compared to the other ET primers. However, the reduced quenching observed for the larger spacing more than compensates for this loss of ET efficiency. More recently developed ET primers with a cyanine donor fluorophore and employing rhodamine-110 in place of the FAM acceptor exhibit from 1.6- to 24-fold enhanced emission signal and virtually no differential mobility shift [22,23]. In summary, in ET primers and terminators, a common donor with a high absorbance at the excitation wavelength harvests energy and transmits

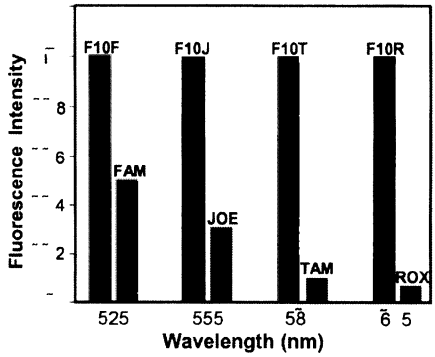

Figure 7. The fluorescence intensity of ET primers is strikingly enhanced over that of conventional single dye-labeled primers. The fluorescence intensities were determined in a fluorimeter with 488 nm excitation on equimolar solutions in DNA sequencing buffer. The fluorescence intensity of each ET primer was normalized to one.

it efficiently to different acceptor fluorophores that emit in strong and distinct wavelength regions.

5. DNA sequencing using energy transfer dye-labeled primers and terminators

Four-color dideoxy DNA sequencing using DyePrimer or DyeTerminator allows highly automation of the sequencing process. The sequencing reagents are commercially available from several sources. The improvements on the DNA polymerase (Thermo Sequenase and Amplitaq FS) [7] as well as the fluorescent tag optimization using energy transfer principle markedly improved the sequencing data quality and the read length. The DyePrimer sequencing requires 4 reactions, each for a particular dideoxynucleotide, generating data with uniform peaks. This procedure sometimes generates false stops because all the DNA fragments extended from the primer carry a fluorescent tag. The DyeTerminator procedure uses one tube reaction and false stops are generally eliminated since only the correctly terminated DNA fragments carry a fluorescent tag. The sequencing peaks, however, are less uniform compared to DyePrimer data. The use of energy transfer fluorescent reagents facilitates the development of capillary array DNA sequencer (Megabace 1000 and ABI 3700), that allows automated loading of 96 samples simultaneously as well as automated sample tracking and analysis. The separation matrix linear polyacrylamide (LPA) for capillary electrophoresis has been shown to be capable of generating up to 1000 bp in an hour [24]. This new generation of automated DNA sequencer coupled with the ET reagents and the separation matrix development is substantially increasing the throughput, the speed and the overall process of larger sequencing projects. Shown in Figure 8 is a

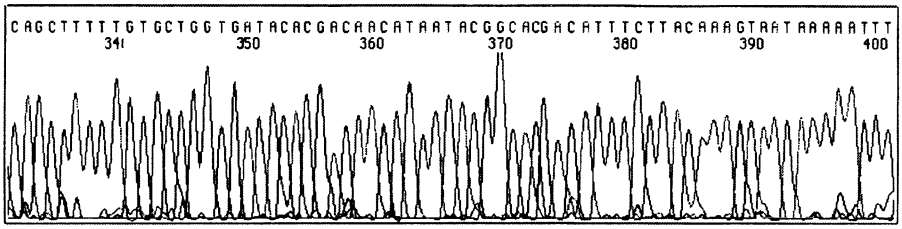

Figure 8. The enhanced emission intensity and decreased spectral overlap afforded by energy transfer terminators significantly improve the quality of DNA sequencing. This figure presents a portion of a electropherogram generated with Thermo Sequenase on a 96 capillary DNA sequencer Megabace 1000 (Amersham Pharmacia Biotech, Inc.).

portion of a four-color electropherogram obtained with ET terminators and a 96-capillary array DNA sequencer Megabace 1000.

However, both of the dye primer and dye terminator methods still have disadvantages, causing either false termination (DyePrimer) or background noise due to the unincorporated dye-labeled terminators (DyeTerminator). A solid phase sequencing chemistry was developed producing much cleaner sequencing data on both slab gel and capillary array sequencers, eliminating the disadvantages of current dye primer and dye terminator chemistries [25]. As shown in Figure 9, the procedure involves coupling fluorescent energy transfer (ET) primers that produce high fluorescent signals and solid phase capturable terminators such as biotinylated dideoxynucleotides. After the sequencing reaction, the extension DNA fragments are captured with magnetic beads coated with streptavidin, while the other components in the sequencing reaction are washed away. Only the pure dideoxynucleotide terminated

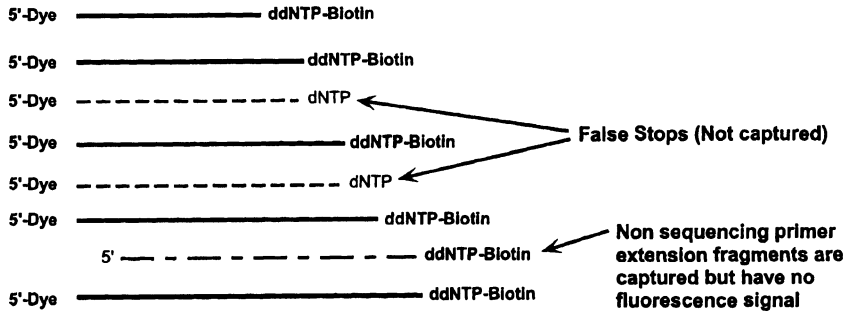

Figure 9. A schematic shows that by purifying the sequencing fragments generated with dye labeled primers and biotin-terminators with streptavidin coated magnetic beads, only true sequencing fragments are loaded and detected in the fluorescence DNA sequencer. False stopped fragments are not captured and non sequencing primer extension fragments resulting from RNA and nicked DNA fragments are not detected.

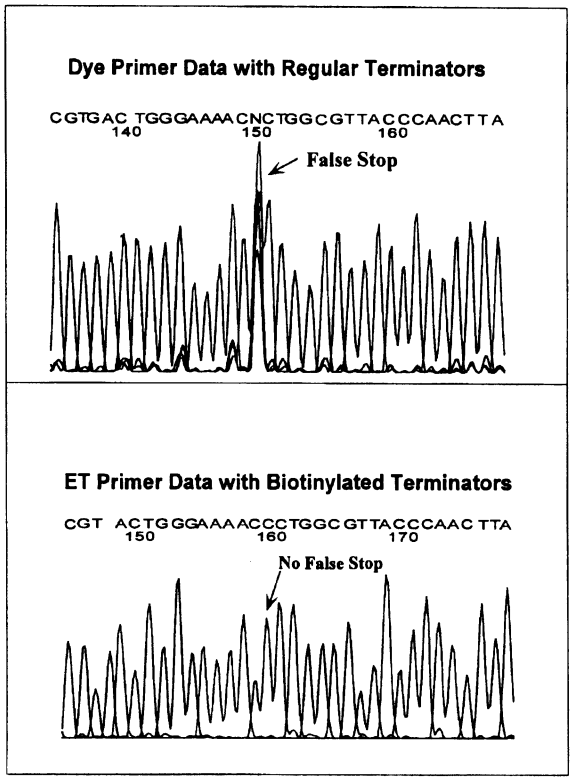

Figure 10. The four color sequencing data generated with biotin-terminators and energy transfer (ET) primers after purification with streptavidin coated magnetic beads (A) are much cleaner than the sequencing data generated with dye primer and regular ddNTPs (B). A false stop peak in B resulted in a sequence error. In the same sequence region no false peak was seen in A.

extension products are released from the magnetic beads and are loaded on the sequencing gel. This sequencing procedure provides an ideal platform for mutation detection as shown in Figure 10. The four-color DNA sequencing data generated with biotin-terminators and energy transfer (ET) primers after purification with streptavidin coated magnetic beads (A) are much cleaner than the sequencing data generated with dye primer and regular ddNTPs (B). A false stop peak in B results in a sequence error. In the same sequence region no false peak is seen in A.

6. Summary and conclusion

The improvement of the spectroscopic properties of fluorescent tags provided by energy transfer dye-labeled primers and terminators has led to a

quantum advance in the detection capabilities in DNA sequencing and in PCR fragment detection. These energy transfer fluorescent reagents are generally applicable to all analyses that employ fluorescent primers/terminators and should increase the sensitivity and throughput in all instances. For example, short tandem repeat (STR) analysis and sizing plays a vital role in diagnostics and in forensic identification [26]. ET primers have been used to analyze STRs using a two-color labeling format and capillary array electrophoresis [27]. Such a technology platform was also used for developing high-throughput methods for the diagnosis of bladder cancer [28]. In addition to DNA sequencing and STR typing, applications to DNA fragment sizing, DNA sequencing by hybridization and fluorescence in situ hybridization are but a few examples of the obvious future applications of energy transfer fluorescent reagents.

References

[1] Saenger, F., Nicklen, S. and Coulson, A.R. (1977). DNA sequencing with chain-terminating inhibitors. *Proc. Natl. Acad. Sci. (USA)* **74**, 5463-5467.

[2] Smith, L.M., Sanders, J.Z., Kaiser, R.J., Hughes, P., Dodd, C., Connell, C.R., Heiner, C., Kent, S.B.H., Hood, L.E. (1986) Fluorescence detection in automated DNA sequencing analysis. *Nature (London)* **321**, 674-679.

[3] Prober, J.M., Trainor, G.L., Dam, R.J., Hobbs, F.W., Robertson, C.W., Zagursky, R.J., Cocuzza, A.J., Jensen, M.A. and Baumeister, K. (1987) A system for rapid DNA sequencing with fluorescent chain-terminating dideoxynucleotides. *Science* **238**, 336-341.

[4] Connell, C. R., Fung, S., Heiner, C., Bridgham, J., Chakerian, V., Heron, E., Jones, B., Menchen, S., Mordan, W., Raff, M., Recknor, M., Smith, L., Springer, J., Woo, S. and Hunkapiller, M. (1987). Automated DNA sequence analysis. *BioTechniques* **5**, 342-348.

[5] Mathies, R.A., Huang, X.C. (1992). Capillary array electrophoresis: an approach to high-speed, high-throughput DNA sequencing. *Nature (London)* **359**, 167-169.

[6] Tabor, S., Richardson, C.C. (1987). DNA sequence analysis with a modified bacteriophage T7 DNA polymerase, *Proc. Natl. Acad. Sci. (USA)* **84**, 4767-4771.

[7] Tabor, S., Richardson, C.C. (1995). A single residue in DNA polymerases of the Escherichia coli DNA polymerase I family is critical for distinguishing between deoxy- and dideoxyribonucleotides. *Proc. Natl. Acad. Sci. (USA)* **92**, 6339-6343.

[8] Ju, J., Ruan, C., Fuller, C.W., Glazer, A.N. and Mathies, R.A. (1995). Energy transfer fluorescent dye-labeled primers for DNA sequencing and analysis. *Proc. Natl. Acad. Sci. (USA)* **92**, 4347-4351.

[9] Ju, J., Kheterpal, I., Scherer, J., Ruan, C., Fuller, C.W., Glazer, A.N., Mathies, R.A. (1995). Design and synthesis of fluorescence energy transfer dye-labeled primers and their application for DNA sequencing and analysis. *Anal. Biochem.* **231**, 231-240.

[10] Ju, J., Glazer, A.N. and Mathies, R.A. (1996) Energy transfer primers: a new fluorescence labeling paradigm for DNA sequencing and analysis, *Nature Medicine* **2**, 246-249.

[11] Lee, L.G., Spurgeon, S.L., Heiner, C.R., Benson, S.C., Rosenblum, B.B., Menchen, S.M., Graham, R.J., Constantinescu, A., Upadhya, K.G., Cassel, J.M. (1997). New energy transfer dyes for DNA sequencing. *Nucleic Acids Res.* **25**, 2816-2822.

[12] Marra, M., Weinstock , L.A. and Mardis, E.R. 1996. End sequence determination from large insert clones using energy transfer fluorescent primers. *Genome Res.* **6**, 1118-1122.

[13] Heiner, C.R., Hunkapiller, K.L., Chen, S.M., Glass, J.I., Chen, E.Y. (1998). Sequencing multimegabase-template DNA with BigDye terminator chemistry. *Genome Res.* **8**, 557-561.

[14] Forster, T. (1965) in Modern Quantum Chemistry, Istanbul Lectures, Part III, eds. Sinanoglu, O., Academic Press, New York and London, pp. 93-137.

[15] Stryer, L. (1978). Fluorescence energy transfer as a spectroscopic ruler. *Ann. Rev. Biochem.* **47**, 819-846.

[16] Glazer, A.N., Stryer, L. (1983). Fluorescent tandem phycobiliprotein conjugates. Emission wavelength shifting by energy transfer. *Biophys. J.* **43**, 383-386.

[17] Benson, S.C., Singh, P., Glazer, A.N. (1993). Heterodimeric DNA-binding dyes designed for energy transfer: synthesis and spectroscopic properties. *Nucleic Acids Res.* **21**, 5727-5735.

[18] Benson, S.C., Mathies, R.A., Glazer, A.N. (1993). Heterodimeric DNA-binding dyes designed for energy transfer: stability and applications of the DNA complexes. *Nucleic Acids Res.* **21**, 5720-5726.

[19] Rye, H.S., Drees, B.L., Nelson, H.C.M. and Glazer, A.N. (1993) Stable fluorescent dye-DNA complexes in high sensitivity detection of protein-DNA interactions. Application to heat shock transcription factor, *J. Biol. Chem.* **268**, 25229-25238.

[20] Ju, J., Glazer, A.N.and Mathies, R.A. (1996) Cassette labeling for facile construction of energy transfer fluorescent primers, *Nucleic Acids Res.* **24**, 1144-1148.

[21] Rosenblum, B.B., Lee, L.G., Spurgeon, S.L., Khan, S.H., Menchen, S.M., Heiner, C.R., Chen, S.M. (1997). New dye-labeled terminators for improved DNA sequencing patterns. *Nucleic Acids Res.* **25**, 4500-4504.

[22] Hung, S-C., Ju, J., Glazer, A.N., Mathies, R.A. (1996). Cyanine dyes with high absorption cross section as donor chromophores in energy Transfer Primers. *Anal. Biochem.* **243**, 15-27.

[23] Hung, S-C., Ju, J., Glazer, A.N. and Mathies, R.A. (1996). Energy transfer primers with 5- or 6-carboxyrhodamine-6G as acceptor chromophores. *Anal. Biochem.* **238**, 165-170.

[24] Salas-Solano, O., Carrilho, E., Kotler, L., Miller, A.W., Goetzinger, W., Sosic, Z. Karger, B.L. (1998). Routine DNA sequencing of 1000 bases in less than one hour by capillary electrophoresis with replaceable linear polyacrylamide solutions. *Anal. Chem.* **70**, 3996-4003.

[25] Ju, J. (1999). United States Patent 5,876,936, Nucleic Acid Sequencing with Solid Phase Capturable Terminators.

[26] Hammond, H.A., Jin, L., Zhong, Y., Caskey, C.T., and Chakraborty, R. (1994) Evaluation of 13 short tandem repeat loci for use in personal identification applications. *Am. J. Hum. Genet.* **55**, 175-189.

[27] Wang, Y., Ju, J., Carpenter, B.A., Atherton, J.M., Sensabaugh, G.F., Mathies, R.A. (1995). Rapid sizing of short tandem repeat alleles using capillary array electrophoresis and energy-transfer fluorescent primers. *Anal. Chem.* **67**, 1197-1203.

[28] Wang Y, Hung S-C, Linn, J. F., Steiner, G., Glazer, A. N., Sidransky, D., Mathies, R.A. (1997). Microsatellite-based cancer detection using capillary array electrophoresis and energy-transfer fluorescent primers. *Electrophoresis* **18**, 1742-1749.

Index